A PERSPECTIVE ON THE STATUS OF COAL RESEARCH FROM SHIPMENTS OF SAMPLES

Karl S. Vorres*, Carl W. Kruse**, Koen A. Nater***, David C. Glick**** and Alan Davis****

*CHM/211, Argonne National Laboratory, Argonne, IL 60439
**Illinois State Geological Survey, 615 E. Peabody Dr., Champaign, IL 61820
***deGrote Vos, Zeeweg 37, 1753 BB St. Martenzee, Netherlands
**** Coal and Organic Petrology Laboratories, 105 Academic Projects Bldg., Pennsylvania State University, University Park, PA 16802

INTRODUCTION

Research on all aspects of coal research, at least for more small scale work, involves the use of samples at the beginning of experimental work. Most research workers for smaller scale work do not collect their own coal samples, but rather order them from a group of sample suppliers. The number of suppliers meeting the major needs in the US, as well as for the world, is not very large. An examination of the shipments of samples from each of these suppliers will give an interesting insight into the general trends in volume of work in the field.

The suppliers involved in this study include the Argonne Premium Coal Sample Program, the Illinois Basin Coal Sample Program, the SBN and the several groups of samples from the Pennsylvania State University Coal Sample Bank. Each of these supplies a different number of samples in varying quantities. The quantities and variety of samples is important to the individual worker in selecting a supplier. The type of work to be done frequently affects the quantities and choice of sample, which in turn affects the choice of supplier. Some suppliers tend to ship samples to smaller scale users who tend to do more fundamental work, while other suppliers tend to ship to larger scale users who tend to do both fundamental and the beginnings of applied work. The number of samples shipped from each supplier over a period of years would indicate something of the relative amounts of work done over that period. This paper provides some insight into this measure of work. Individually the trends would speak only for the experience of one sample supplier. If all suppliers have similar experience, then sample shipments may be a useful measure of coal research in the areas that they serve.

The Argonne Premium Coal Sample Program (APCSP).

This program (1) provides samples of 8 coals from the US in two sample container sizes. Either 5 grams of -100 mesh or 10 grams of -20 mesh are available in individual borosilicate glass ampules. Orders may request as many of the ampules as needed for a research program. There is currently a charge of $1.60 per gram of sample regardless of the sample amount. This program began in late 1982. Samples are processed in a large nitrogen-filled glove box in one ton lots. The samples have been sent to about 350 users in most of the major nations in which coal research is done. Records are kept of the individual shipments, and have been tabulated in terms of the total shipments of ampules on a monthly basis since shipments began. A plot of the cumulative totals of ampule shipments, and also the numbers of -100 and -20 mesh samples shipped is shown in Figure 1. It can be seen that the number of ampules shipped increases in a generally linear fashion at a rate of about 3000 per year. In mid 1987 a number of samples were shipped and appear to have been used in programs until mid 1988 when a more uniform series of orders began. The slope of the plot is consistent to about mid 1991. The slope then decreases through mid 1992, and may be decreasing again. An examination of the relative numbers indicates a greater interest in the finer -100 mesh and smaller sized samples used for the small scale experiments.

An examination of the most popular samples as shown in Figure 2 indicates that the Illinois #6 (IL) is most requested, indicating an interest in the samples with high sulfur content. The second most requested sample, Wyodak (WY), is reactive, large reserves are available at relatively low cost, and is of interest for syn-

thetic fuel production. The other samples in decreasing order of requests are: Beulah-Zap lignite (ND), Pittsburgh (PITT), Upper Freeport (UF) and Pocahontas #3 (POC). Not shown, and less requested are the Blind Canyon and Lewiston-Stockton.

The Illinois Basin Coal Sample Program (IBCSP)

The goal of this program is to provide reproducible samples of various Illinois Basin coals. The program was initiated in 1983 and currently provides samples of 12 different lots of coal. Most of the lots are mine-washed coals. Samples are available in two sizes, a nominal 1-pound sample (8 mesh by zero particle size) and a nominal 20 pound sample (3/8" by zero) that are 1/256th and 1/16th riffled splits of a barrel of coal, respectively. Samples are provided free of charge to most researchers on request. The ICCI reserves the right to limit the quantities. Distribution of samples from nearly depleted lots is restricted to previous users. Two distinguishing characteristics of the IBCSP are the large sizes of the samples relative to other programs and the focus on Illinois Basin coals.

The time the coal is exposed to air while processing is as short as practical, but the samples (IBC-105 excepted) show minor amounts of sulfatic sulfur and traces of elemental sulfur that are products of air oxidation. Lots are stored under a nitrogen atmosphere to enable users to obtain samples for several years without significant exposure to air.

Analytical historical data and user data are also available. These data include results of semiannual tests of Btu, FSI, forms of sulfur, and chlorine contents, proximate and ultimate analyses and the names, addresses, project titles and research objectives of users of each lot are available. Two hundred investigators made a total of 688 requests and received 2100 samples totaling 25,500 pounds in the ten years of operation through August 1993. Most investigators have requested more than one coal and many have received several shipments. All told, 96 of the investigators were from Illinois, 97 from other states, and 7 from outside the United States; 105 of them were from academic laboratories, 49 from industrial laboratories and 46 from government laboratories. The origins of the 688 requests were: Illinois, 393; other states, 277; outside the United States, 18. The distribution of requests was 327 academic, 250 governmental, and 111 industrial.

The pattern of the distribution for the ten years of operation shows the activity peaked in 1988-90 (Figure 3). Reasons include a peak of activity on laboratory-scale, coal cleaning projects funded by the Illinois Coal Cleaning Institute, Carterville, Illinois. Scale-up of successful projects required quantities larger than those offered by the IBCSP. The program assisted a number of researchers in making arrangements for multi-ton quantities of coal directly from the mines. The pattern of distribution for eight of the 12 lots by year is shown in Figure 4. Not shown are IBC-105, a lot prepared by Argonne National Laboratory from an a block of Illinois #6 coal adjacent to that used in the Premium Coal Sample Program; IBC-107, an $^{34}S/^{32}S$ isotopically characterized Herrin (Illinois #6) recommended for researchers who wish to follow the fate of forms of sulfur in chemical reactions of coal by monitoring the ratio of sulfur isotopes in the products; IBC-108, a state-of-the-art, physically-cleaned, micron-sized blend of Herrin (#6) and Springfield (#5) coal (80% and 20% respectively) that now has a very low pyrite and ash; IBC-111, a Danville (Indiana VII) coal.

An ideal projected ten year life for each lot was not reached with IBC-103, IBC-104 and IBC-106. It was not possible to obtain the desired lot of Illinois No. 5 seam in 1983. The compromise was IBC-103, an 80:20 mixture of Illinois #5 and Illinois #6. Its inventory was purposely drawn down in 1986 by use of IBC-103 for mild gasification tests at the time requests for a typical-sulfur coal were shifted to a single-seam lot, IBC-106. Requests for a coal with forms of sulfur typical of Illinois and Indiana coals (about 50:50 pyritic and organic forms) continued high and it was necessary to plan for IBC-106 replacement before 10 years. That replacement is IBC-112. The projected interest in a run-of-mine coal was also underestimated in 1983. The 1500 pounds of IBC-104 lasted only 7 years.

The Pennsylvania State University Coal Sample Bank

Since its inception in 1967, 1457 samples have been collected for this sample bank; 1176 remain available for distribution (2). Thirty more samples will be collected over the next four years as part of the DOE (U. S. Department of Energy) Coal Sample Bank, a subset of the larger Penn State Coal Sample Bank. Samples from all coal provinces of the U. S. are available, representing a wide variety of ranks, organic and inorganic compositions, petrographic constituents and behavior in liquefaction, carbonization and combustion processes.

Typically, whole-seam channel samples of 200 to 300 kg are collected from fresh exposures in active mines. Samples are crushed to -6 mm, homogenized, and subsampled. A portion is crushed to -20 mesh and further subdivided. The typical subsample supplied to researchers is 300 g of coal at -20 mesh, available for $20.00; larger quantities of -6 mm or -25 mm (for older samples) coal are also available. Samples collected since 1989 in the DECS (Department of Energy Coal Sample) series have been packaged under argon in heat-sealed foil/polyethylene multilaminate bags which preserve initial sample properties (3). Earlier samples in the PSOC series were sealed under argon in steel cans. Analyses are performed on each sample and the resulting data comprise the Penn State Coal Data Base. Computer printouts of analytical data are available for every sample.

The most recent program of sample collection and distribution began in 1988. Since then, over 700 requests for samples and/or data printouts (usually for several samples per request) have been received from more than 250 agencies. Universities accounted for 63% of the requests, government agencies 12 %, and industry 25%. Ninety-five percent of the requests were from the U. S.

Figure 5 shows that in 5 1/2 years, 3270 kg of samples were distributed, 510 kg at -20 or -60 mesh in 300 g bags or cans and the remainder in larger quantities at larger particle sizes. Sharp jumps in the cumulative amount distributed represent occasional shipments of entire 100 kg drums of coal; the increase in May, 1992, represents distribution of 4 drums totaling 400 kg.

The trends in amounts of samples distributed over time are similar to those of the Argonne program. The highest rate of distribution occurred in the first year, followed by four years with a somewhat lower rate which nevertheless represents large quantities of coal samples distributed on a consistent basis. Although a further decrease in rate of distribution occurred late in 1992, periodic variations of 6 to 12 months duration make long term predictions from short term trends inadvisable, and very recent data indicate an increase.

The most requested samples have been those of the Pittsburgh seam (DECS-12, PSOC-1451, -1519, -1528, -1529, 1531), the Illinois #6 seam (DECS-2, PSOC-1493), and the Wyodak (Smith-Roland) seam (DECS-8, PSOC-1520). Recently, U. S. Department of Energy research projects investigating the use of dispersed catalysts for liquefaction have been conducted on the Blind Canyon coal (DECS-6, -16, -17, PSOC-1503). This activity has significantly increased the demand for these samples. Figure 6 illustrates the trends in distribution of these samples. These four seams alone account for over 20% of the samples distributed since 1988, although samples of over 300 other seams with a wide variety of properties are available.

The SBN

The European Center for Coal Specimens, SBN, has collected a large number of coal samples from important mines of the world. These have been prepared in a variety of sizes. A number of these samples have been prepared with special consideration for protection from the atmosphere. A coal catalog is available which indicates source and type of sample as well as analytical information.

It has been observed that the number of requests for general samples from the main collection has been decreasing, but there is a growing interest in production of a certified series of samples dedicated to multi-laboratory research projects as are being sponsored by the European Community's and European Coal and Steel Community's research programs. There is also an interest in samples of coal fly and bottom ashes and of building materials based on secondary resources.

CONCLUSIONS

There are both similarities and differences. There are periodic periods of extensive sample orders that tend to alter some long term trends. The APCSP has seen a period of consistent shipments from late 1988 to late 1991. Since that time there has been a decline to a lower but persistent level of shipments. The most popular coals for the APCSP are the Illinois #6 and Wyodak, reflecting concerns about sulfur in coal, and converting coal into synthetic liquids. The small size of these samples may be an indicator of the level of activity in the most fundamental studies.

The pattern of the Penn State Coal Sample Bank total shipments is similar to that for the APCSP. The most popular coal is from the Pittsburgh seam reflecting interests in liquefaction of this Eastern U. S. high volatile A bituminous coal. The Illinois #6 is second most popular, followed by Wyodak and Blind Canyon seams. The intermediate size of the available samples reflects interests in both basic and somewhat larger scale work.

The IBCSP shipped the largest quantities of coal in 1987 and has shipped declining total amounts since then. The number of researchers requesting samples has declined more slowly than the quantities shipped, reflecting smaller quantities per shipment. The emphasis on coal cleaning at the time of maximum quantities reflects a change in type of work away from coal cleaning. The samples are larger than the APCSP and reflect interests in both basic and applied work.

Overall the distribution curves for the samples reflect a number of rather strong and continuing programs in coal research despite recent difficulties in funding. For all of the programs most of the requests come from academic institutions. Clearly much work is done there, primarily with government funding. Industry and government organizations make similar but fewer requests, reflecting the smaller number of organizations involved in this work. Relatively few requests come from overseas, presumably because their sponsors are outside of the U.S. These workers need to use their domestic sample sources, but want to be able to compare with well-known external samples.

In general these data indicate that researchers realize the advantages of acquiring samples from centralized sample banks. These advantages include a lower cost than would be incurred from individual sampling and preparation; availability of analyzed samples; preservation of samples and the possibility of comparing results with others who have worked on the same samples.

ACKNOWLEDGMENTS

KSV gratefully acknowledges support from the US Department of Energy, Office of Basic Energy Sciences, Chemical Sciences Division under contract no. W-31-109-ENG-38. DCG and AD acknowledge support from the U. S. Department of Energy, Pittsburgh Energy Technology Center, Liquid Fuels Division. CWK acknowledges that the IBCSP has been sponsored by the Illinois Department of Energy and Natural Resources through its Coal Development Board and Illinois Clean Coal Institute, and by the State of Indiana through the Indiana Energy Development Board (IEB) and the Indiana Geological Survey (IGS).

REFERENCES

1. Vorres, K. S.; Energy Fuels **1990** 4 420-426

2. Glick, D. C.; Davis, A. Org. Geochem. **1991** 17 421-430

Figure 4.

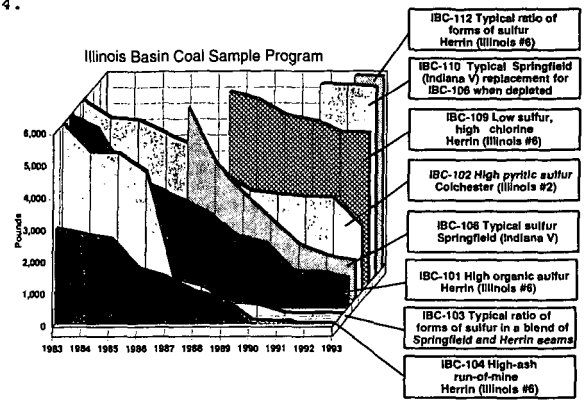

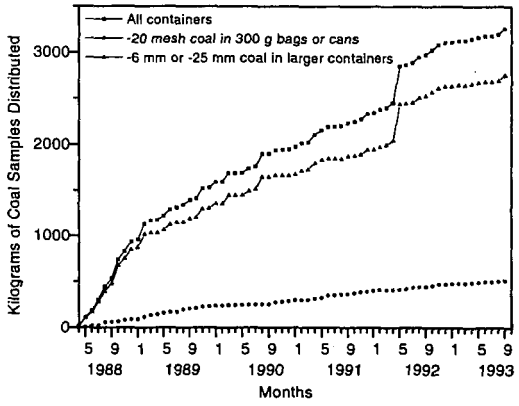

Figure 5. Cumulative weights of samples distributed from the Penn State Coal Sample Bank, -20 mesh (cans and small bags) and -6 mm or -25 mm (buckets, drums and large bags)

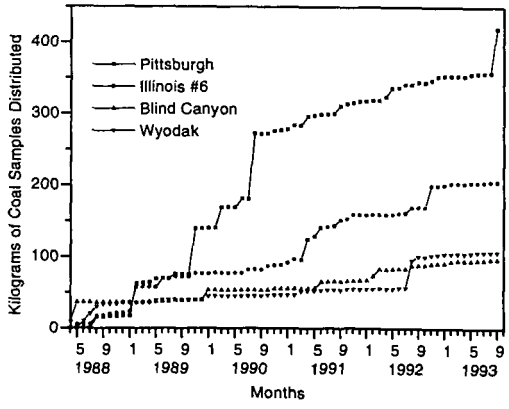

Figure 6. Cumulative weights of most frequently requested samples (Pittsburgh, Illinois #6, Blind Canyon and Wyodak seams) distributed from the Penn State Coal Sample Bank

3. Glick, D. C.; Mitchell, G. D.; Davis, A., Am. Chem. Soc., Fuel Chem. Prepr. **1991** 36:3 861-868

4. Harvey, R. D.; Kruse, C. W. **1988.** The Illinois Basin Coal Sample Program: Status and Sample Characterization. J. Coal Quality, 7 (4) 109-113. Illinois State Geological Survey Reprint Series 1989-A.

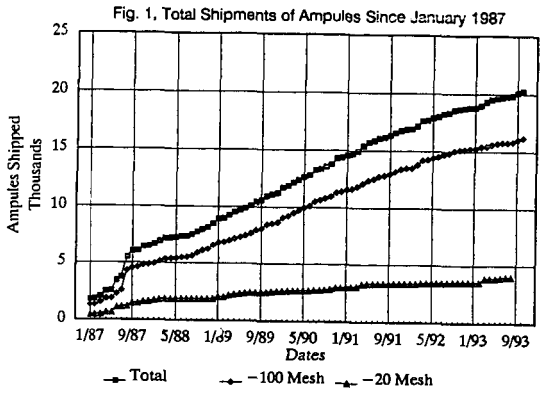

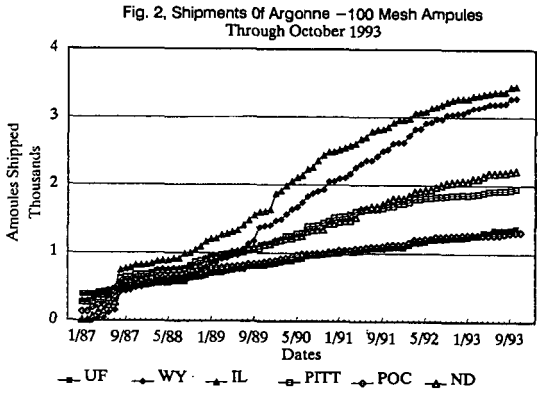

Figure 3.

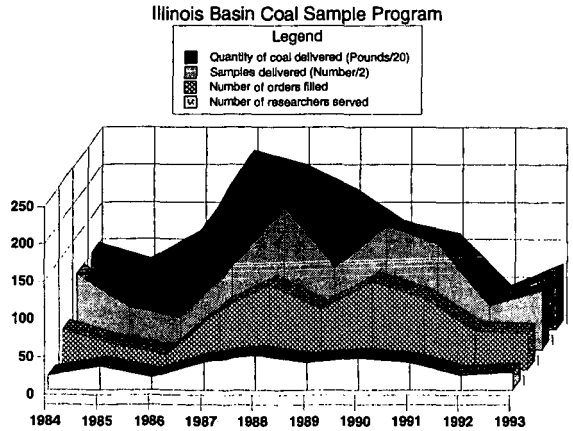

COALIFICATION OF LIGNIN TO FORM VITRINITE: A NEW STRUCTURAL TEMPLATE BASED ON AN HELICAL STRUCTURE.

Patrick G. Hatcher[1]
and
Jean-Loup Faulon[2]

[1] Fuel Science Program
The Pennsylvania State University
University Park, PA 16802

[2]Fuel Science Department
Sandia National Laboratories
Albuquerque, NM 87185

Keywords: vitrinite, coal structure, lignin, molecular modeling

INTRODUCTION

The structural evolution of vitrinite has been previously studied in our group through detailed characterization of coalified wood which spans the entire coalification range (1-6). The use of coalified logs was demonstrated to be especially useful as it removes the superposed problem of maceral scale heterogenieties from the problem of identifying fundamental transformations which delineate the coal's chemical structural evolution. The net result of these detailed studies using ^{13}C NMR and pyrolysis/gas chromatography/ mass spectrometric (py/gc/ms) methods is the identification of several key chemical structural transformations which typify the coalification of woody material into high volatile bituminous coal. By comparisons of the chemical compositions of wood at various stages of coalification, one can infer specific reactions responsible for coalification.

Although, the coalification series represents a continuum of parallel and serial processes; several principle stages of coalification are clearly evident. The initial, biochemical, stage of coalification is characterized by a complete loss in hemicellulose, a significant reduction in cellulose, and selective preservation ,with minimal alteration, of lignin derived material (2, 7). Early diagenetic changes accompanying the transformation from brown coal into lignite result in a near complete removal of cellulose and some modification of the lignin, a macromolecular material composed of methoxyphenols with a polyhydroxypropanol side-chain as basic building blocks. These modifications are, dominantly, rearrangement of alkyl-aryl ether bond that links the methoxyphenols together to yield methoxyphenols linked by an aryl-alkyl bond between the structural units, as well as some demethylation of methoxy groups yielding catechol-like structures (4). The transformation of coalified wood from lignite through the subbituminous rank range to high volatile C rank bituminous coal is characterized by transformations which result in complete demethylation of methoxyphenols to catechols and a subsequent reduction of the catechol-like structures, presumably through reaction, to form phenol-like structures (6, 8, 9). The focus of this paper is to review our current understanding of the evidence for these aforementioned chemical transformations and to present these reactions within the context of a new three-dimensional helical model that has been developed for lignin (10).

PEATIFICATION

It was made especially clear from studies of fresh wood and peatified wood (1, 7, 9) that cellulosic components of wood, the ones contributing more than 60% of the structure, essentially are mineralized or degraded and lost within a short span of time geologically. Thus, the cellulosic components do not play a significant role in the structural make-up of coalified wood. The lignin, however, is selectively preserved in a relatively unaltered state during peatification and is the substance which eventually forms the coalified wood's vitrinitic component.

Perhaps the most astounding aspect of this degradative process is the selectivity and structural precision with which it occurs. Essentially all of the major mass component of wood, the cellulose, is lost. One might infer that tremendous physical destruction ensues; however, peatified wood remarkably retains its morphology. This can clearly be seen in SEM photomicrographs of degraded wood in peat (11). Delicate wood structures such as bordered pits and cell wall tracheids appear physically intact even though all the cellulose has been degraded. Apparently, the wood has been degraded by bacteria which use extracellular enzymes to enable destruction of the cellulosic materials. This process apparently does not involve physical maceration.

Framed within the context of the helical model of lignin, the degradation of cellulose affects the three-dimensional extention of the helical chain if one considers the cellulose microfibrils on wood to be hydrogen bonded or even covalently bonded to the cellulose (10, 11). The pitch of the helix under such circumstances can be viewed to at a low angle relative to the axial dimension, depending upon how many hydrogen or covalent bonds are formed with the cellulose. In the middle lamellar region of wood cells, the general depletion of cellulose renders lignin helices with

high angle pitches. In the secondary cell wall, the high amount of cellulose provides many bonding sites, allowing the helix to be extended at a low angle pitch.

The loss of the cellulose backbone allows collapse of the helix to its most condensed configuration. This condensed configuration brings into relatively close proximity some important reaction centers for reactions that have been postulated to occur during coalification (11).

COALIFICATION TO BROWN COAL AND LIGNITE

The lignin which survives this initial degradative process relatively unscathed, is eventually altered over the course of geological time as wood in peat is buried in sedimentary systems. We know this from studies of coalified wood in brown coals and lignites (3, 4, 8, 9). By comparing the chemistries of peatified wood, mainly lignin, with brown coal or lignitic woods of the same family (e.g., gymnosperms, angiosperms), we can decipher reactions which might be responsible for observed changes. We certainly can identify the nature of chemical changes which occurred. These are depicted in Figure 1.

Perhaps the most chemically and microbiologically labile bond in lignin is the bond linking the methoxyphenolic aromatic monomers together, the β-O-4 bond. Evidence that this bond is cleaved during coalification was provided by Hatcher (3), from an examination of the NMR spectra of brown coal woods. If we consider that all such bonds in lignin are broken and the fact that approximately 60% of the bonds in lignin are of this type, then we might expect the lignin, or the peatified wood, to be completely macerated because rupture of this bond would release molecular fragments which are likely to be soluble in water. Examination of SEM photomicrographs of brown coal wood in which such bond ruptures have occurred shows that physical disruption of the wood anatomy does not occur to any great extent . Delicate structures such as bordered pits would not physically survive a maceration. Also, the SEM photos do not provide any evidence for dissolution or even partial dissolution of cell walls. This must imply that another reaction maintains the macromolecular integrity of the lignin.

The reaction most likely responsible for maintaining structural integrity must be one which allows connectivity between methoxyphenolic structures in lignin. Thus, we must maintain some bond between the aromatic units. Alkylation following β-O-4 bond rupture is the likely reaction. Botto (12) has shown that such an alkylation is possible when lignin labeled at the β carbon is subjected to artificial coalification in the presence of clays. In essence, the rupture of the β-O-4 bond releases a carbocation, the β carbon on the sidechain, which is a good electrophile and will attack positions on the aromatic ring of adjacent phenolic structures which are susceptible to electrophilic substitution (e.g., the C-5 predominantly). The most likely aromatic ring to be alkylated is the one from which the β-O-4 bond rupture occurred. The rupture of the β-O-4 bond would produce a phenol which would likely activate the C-5 site to alkylation. Evidence that such a reaction occurs in brown coal wood comes from the NMR data which show increased aromatic ring substitution (2, 4). Dipolar dephasing NMR studies indicate that brown coal wood samples have fewer protons per ring than their respective counterparts in peat, indicating that, on the average, one of the ring sites has become covalently bound to an atom other than hydrogen. The NMR data also indicate that the additional substituent atom is not an oxygen but a carbon atom. It is clear that the data all point to the fact that cleavage of the β-O-4 bond during coalification of the lignin in peatified wood leads to a alkylation of an adjacent ring by the resulting carbocation, and this overall process leads to a maintenance of the physical integrity of the wood.

To maintain this integrity observed unambiguously from SEM data it is necessary that the above reaction occur without much structural rearrangement of the lignin. In other words, the reaction must proceed rapidly and must occur at a relatively proximal site to the β-O-4 cleavage. If one considers a lignin model as one which is random in the connectivity between methoxyphenolic units (13, 14), then the likelyhood that structural order will be maintained with the above-mentioned transformation is minimal. In a random model, distances between aromatic reaction centers are variable and some significant physical disruptions will ensue if the carbocations formed from β-O-4 bond rupture have to link up with aromatic centers which are more than just local.

The recently proposed ordered model for lignin (10) would overcome this problem. The order is believed to derive from the fact that the methoxyphenolic units linked by the β-O-4 bonds in lignin exist in an helical conformation. With such a configuration, cleavage of this bond releases a carbocation which is in relatively close proximity to the C-5 site on the aromatic ring. The alkylation of this site causes minimum disruption of the helical order as a β-C-5 bond is formed. Thus, we might also expect minimum disruption of the physical integrity of the sample, consistent with what is observed in brown coal wood.

Another important coalification reaction which is observed to occur through the lignite stage of coalification is the cleavage of other aryl-O bonds in lignin. The specific bonds are those of

DIVISION OF FUEL CHEMISTRY, AMERICAN CHEMICAL SOCIETY

FEDERAL I.D. 52 6054150

Make Check Payable in U. S. Dollars
to: Division of Fuel Chemistry, ACS
MAIL PAYMENT TO:
Professor Gerald P. Huffman
Room 233, Mining & Minerals Resources Bldg.
University of Kentucky
Lexington, KY 40506-0107

For Publication Information and Orders contact:
Professor John C. Crelling
Director of Preprint Subscriptions
ACS Division of Fuel Chemistry
Department of Geology
Southern Illinois University at Carbondale
Carbondale, Illinois 62901-4324

Bill To: DIVISION OF FUEL CHEMISTRY
M. D. SCHLESINGER
4766 WALLINGFORD STREET
PITTSBURGH PA 15213

Ship To: DIVISION OF FUEL CHEMISTRY
M. D. SCHLESINGER
4766 WALLINGFORD STREET
PITTSBURGH PA 15213

Original
BALANCE DUE: 0.00

Date	Invoice
2 Feb 94	94018

PO Number	Terms	Rep	Ship Date	Ship Via	F.O.B.	Project
	NO CHARGE		18 Feb 94	US MAIL		

Quantity	Item Code	Description	Price Each	Amount
1	1-1	VOLUME 39, NUMBER 1	0.00	0.00
1	1-2	VOLUME 39, NUMBER 2	0.00	0.00
NO CHARGE. DIVISION OF FUEL CHEMISTRY, ACS			TOTAL:	0.00

methoxyl groups attached to the aromatic ring. Both NMR and py/gc/ms data show that this is happening (2, 9). The chemical degradative data of Ohta and Venkatesan (8) also show this reaction. All these studies indicate that the loss of methoxyl is through a demethylation process whereby the bond between the methyl carbons and the oxygen attached to the ring is cleaved. The molecular modeling studies show that the helical configuration is not affected by such a reaction (11). The resulting structure of the coal contains a phenol where there once was a methoxyl group, and the structure is now said to have one similar to that of catechols, if one considers that the cleavage of the β-O-4 bond has already occurred.

Additional changes in lignin structure are more subtle, but somewhat evident from NMR data. In lignin and peatified wood, the sidechains are hydroxylated at both the α and γ sites. Loss of hydroxyl groups from the sidechains is another reaction resulting from coalification of the lignin. NMR resonances attributable to these hydroxyls diminish substantially during coalification through to the rank of subbituminous coal. Simple loss of the sidechain units by a pyrolytic process would explain the loss of these resonances, but this would lead to a significant increase in aromaticity. Because aromaticities of coalified wood samples do not increase over the course of the observed loss of hydroxyls, it is likely that simple reduction of the hydroxyls to alkyl groups is the preferred pathway. This would shift the NMR resonances into the alkyl region of the spectra and preserve carbon aromaticities. Such a reaction would also be consistent with the physical structural data, because reduction of hydroxyls would maintain the presumed helical conformation and would cause minimum disruption of the helical macromolecular structure. Pyrolytic loss of the sidechain carbons would likely macerate the structures beyond recognition. Clearly, to preserve physical integrity to the rank of brown coal or even lignite, the side chains must not be lost.

The eventual structural model which can be drafted based on the helical lignin template and altered by the coalification processes mentioned above is shown in Figure 2. It is difficult to display and to describe all the features of such a model in two dimensional space, but one can discern readily that an helical configuration is apparent, even though some significant chemical changes have ensued.

COALIFICATION TO SUBBITUMINOUS AND BITUMINOUS COAL

The transformations of brown coal and lignitic woods to higher rank involve some significant changes in chemical structure. This is perhaps the primary cause for the change in physical morphology often observed as coal becomes more lustrous and the virtrinite becomes more homogeneous.This transfromation has often been referred to as gelification (15). The wood cells have become deformed significantly, presumable due to increased burial pressure, and some cells actually become annealed to a homogeneous mass.

While structures in brown coal and lignite are dominated by the catechol-like rings arranged in an helical conformation perhaps, the major components of subbituminous and bituminous woods are phenol-like structures. Evidence for the transformation of catechol-like structures to phenol-like structures as shown in Figure 3 comes from both NMR and py/gc/ms data (4, 6). The NMR data clearly indicate a loss of aryl-O carbon. In lignite, aryl-O carbons account for approximately 2 of the six aromatic carbons on the ring, whereas in subbituminous and bituminous coal, only 1 of six aromatic carbons is an aryl-O carbon. Pyrolysis data demonstrate the same observation, with lignitic wood samples being rich in catechols and subbituminous wood samples being rich only in phenols and alkylated phenols. Elemental data show that a significant diminution of oxygen content can explain these tranformations.

Coalification to the rank of high-volatile bituminous coal leads to further reductions in oxygen contents for coalified wood. Considering the fact that the amounts of aryl-O do not change significantly, it is likely that the changes imply a further condensation of phenols to aryl ethers or dibenzofuran-like structures as shown in Figure 4 (6). The py/gc/ms data confirm this as more alkylbenzenes and dibenzofurans are observed. The alkylbenzenes in pyrolyzates could arise from thermal cracking of dibenzofuran or diaryl ethers during flash pyrolysis. Also, the increased quantities of condensed aromatic rings, naphthalenes and fluorenes, in pyrolyzates suggests that aromatic ring condensation is occurring. It is likely that this condensation will disrupt the helical structure proposed. At this time we have little to offer in the way of a mechanism for this condensation. Aromaticity of coalified wood appears to increase at this rank (2), suggesting that one possible route for the formation of condensed rings is ring closure and aromatization of the alkyl sidechains. Further studies are needed to verify such a pathway.

Perhaps the next most apparent difference between woods coalified to the rank of subbituminous / bituminous coal and those at the rank of lignite or lower rank is the lack of oxygenated alkyl structures (i.e., hydroxyls or alkyl ethers). The NMR data for subbituminous and bituminous coalified woods show essentially baseline in this region of the spectra, evidence that such functional groups are not significant. Thus what were originally hydroxylated lignin sidechains have been altered. As discussed above, it is most likely that the lignin-derived hydroxyl groups have been reduced rather than lost by pyrolysis of the sidechain. The reduction of hydroxyls is essentially complete at the rank of subbituminous coal.

Consequently, the structural composition of subbituminous coal is that of a lignin structure which has lost its methoxyl groups (via demethylation and dehydroxylation) and all its hydroxyls and alkyl ethers. Presumably, all these reactions can occur with minimal disruption of the three dimensional helical network inherited from lignin. Indeed, some semblance of cellular morphology still remains at the rank of subbituminous coal (11). Pressure and temperature begin to combine at these and higher ranks to have a significant effect on physical morphology of wood. Thus, it becomes less clear whether loss of morphology is purely a physical or chemical phenomenon or both. With such a disruption in the macromolecular structure of wood brought on by the formation of condensed ring systems, it seems reasonable that cellular morphology which persists well up to the rank of bituminous coal begins to degrade into a homogeneous glassy appearance with little semblance of cell wall boundaries at ranks of bituminous coal or higher.

The helical structure is less apparent for wood coalified to bituminous coal (Figure 5) because some significant disruptions of the helix are induced by the reactions at this rank level. Condensations of phenols to diaryl ethers and dibenzofurans are primarily responsible for these disruptions of the helix which are likely to be manifested by physical disruptions in the coalified wood.

REFERENCES

1. Hatcher, P.G., Breger, I.A., Earl, W.L., *Organic Geochemistry*, 3,49, 1981.
2. Hatcher, P.G., *Energy and Fuels*, **2**, 48, 1988.
3. Hatcher, P.G., Lerch, H.E., III, and Verheyen, T.V., *Int. J. Coal Geol.*, **13**, 65, 1989.
4. Hatcher, P. G., *Organic Geochemistry*, **16**, 959, 1990.
5. Hatcher, P.G., Lerch, H.E., III, Kotra, R.K., and Verheyen, T.V., *Fuel*, **67**, 1069, 1988.
6. Hatcher, P. G., Faulon, J.-L., Wenzel, K. A. and Cody, G. D., *Energy & Fuels*, **6**, 813, 1992
7. Hedges, J.J., Cowie, G.L., Ertel, J.R., Barbour, R.J., and Hatcher, P.G., *Geochimica et Cosmochimica Acta*, **49**, 701, 1985.
8. Ohta, K. and Venkatesan, M. I., *Energy & Fuels*, **6**, 271, 1992.
9. Stout, S. A., Boon, J. J. and Spackman, W.,*Geochim. Cosmochim. Acta* , **52**, 405, 1988.
10. Faulon, J. L.and Hatcher, P. G., *Energy & Fuels* (in press).
11. Hatcher, P. G., Wenzel, K. A. and Faulon, J.-L., Preprints, American Chemical Society Fuel Division, **38**, 1270, 1993.
12. Botto, R. E. *Energy & Fuels* **1**, 228, 1987.
13. Adler E., *Wood Sci. Technol.* **11**, 169, 1977.
14. Aimz H., *Angew. Chem Int. Ed. Engl.* **13**, 313, 1974.
15. Stach, E., Taylor, G. H., Mackowski, M-Th., Chandra, D., Teichmüller, M. and Teichmüller, R. *Stach's Texbook of Coal Petrology*, Gebrüder Borntrüger, Berlin, 428pp.

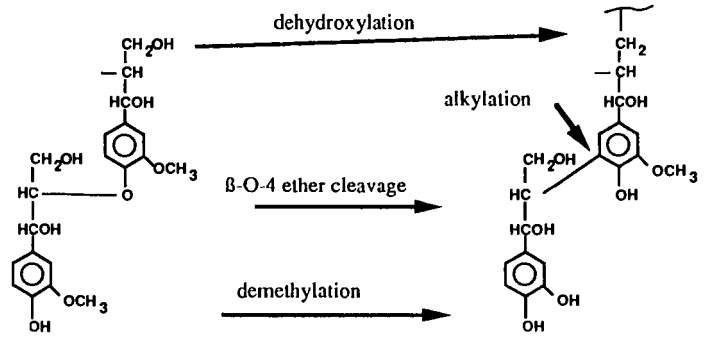

Figure 1. Reactions responsible for the transformation of lignin in peatified gymnospermous wood to brown coal and lignitic wood.

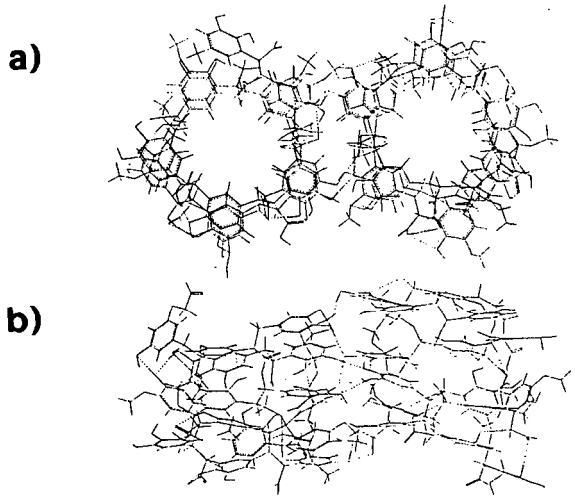

Figure 2. Two dimensional projections of the three dimensional helical model for brown coal and lignitic gymnospermous wood. a) Plan view of the structure and b) elevation view.

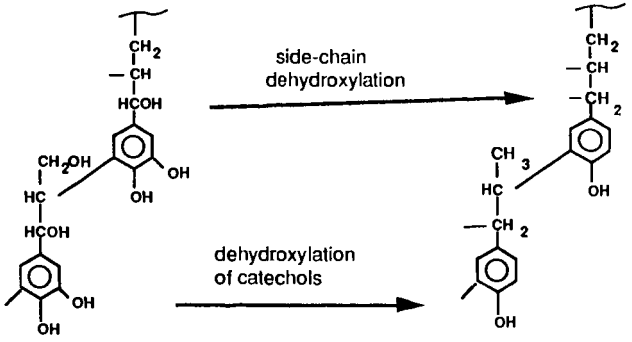

Figure 3. Reactions proposed for the transformation of lignitic gymnospermous wood to subbituminous coal wood.

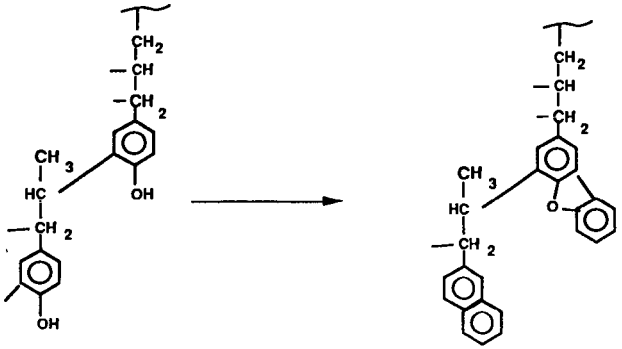

Figure 4. Reactions proposed for the transformation of subbituminous wood to bituminous wood.

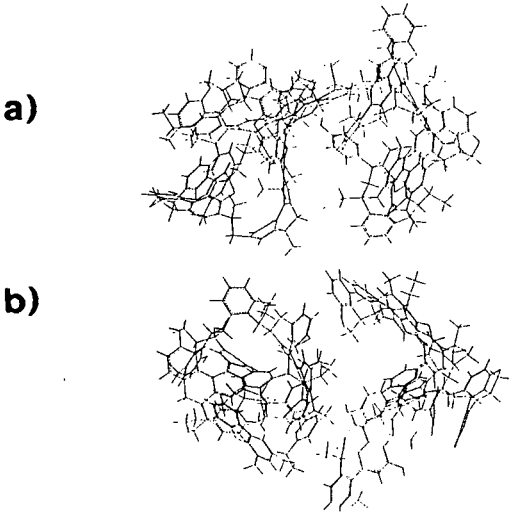

Figure 5. Structural model for bituminous coalified wood built from the helical lignin template and showing a) plan and b) elevation views of the three dimensional structure which has been energy minimized by methods outlined in Faulon and Hatcher ().

REVIEW OF SOME RECENT RESEARCH ON THE COMBUSTION PROPERTIES OF COAL MACERALS

John C. Crelling
Department of Geology
Southern Illinois University
Carbondale, IL 62901 USA

K. Mark Thomas
Northern Carbon Research Laboratories
University of Newcastle upon Tyne
Newcastle upon Tyne, NE1 7RU, United Kingdom

Keywords: Macerals, Coal Combustion, Reactivity

INTRODUCTION

The work reviewed here deals with combustion studies on coal macerals, the individual plant derived substances that make up coal, and lithotypes which are associations of macerals. Studies on these components are important for two reasons. One is that broad industrial experience in pulverized fuel combustion has shown that independently of both coal rank and ash type and content, maceral composition has a significant effect on combustion. A Gondwana coal with an high inertinite content will burn differently from a similar rank Illinois Basin coal dominated by vitrinite. The particle size in pulverized fuel combustion is 70% < 75 micrometers. This is a size range where the particles are becoming very heterogeneous and can cover the broad range of maceral and lithotype properties. This may be a factor in carbon burn-out which is especially important in low "NOx" burners. The other reason is that the bulk of the work done on coal combustion has dealt with whole coals only and is, thus, not very informative on maceral effects.

The major difficulty in carrying out maceral and lithotype combustion work is obtaining well characterized samples. Lithotypes must be obtained in the field and usually require some further processing or cleaning up. The collection of large quantities (greater than a kilogram) is sometimes very difficult. While some vitrinite and fusinite maceral-enriched fractions can be hand-picked, the most reliable way of obtaining good concentrates of maceral groups and single macerals is by Density Gradient Centrifugation (DGC) [1-6]. For example, a typical density profile for a vitrinite-rich Herrin No. 6 coal from the Illinois Basin has a main peak in the center of the profile that represents the vitrinite group macerals while the lower and higher density tails respectively represent the liptinite and inertinite maceral groups. To get concentrates of these maceral groups, the sample is further centrifuged at two petrographically determined cut points at the maceral group boundaries. To get concentrates of single macerals, the separated maceral group samples are further subdivided in a similar manner. An easier way to get the single maceral concentrates is to separate lithotypes collected in the field. A typical example of the density profile of a fusain lithotype has two main peaks that are natural concentrations of semifusinite (lower density) and fusinite (higher density). Fractions taken from the center portion of each peak prove to be very homogeneous semifusinite and fusinite.

In using DGC techniques to obtain samples for combustion studies, three factors which need to be considered are the possible effects of the CsCl separation medium, the particle size vs. maceral liberation problem, and the representativeness of the single maceral concentrates. Although the trace amounts of the alkali metal salt (CsCl) that remain on the samples after washing might be expected to act as a catalyst during combustion, no significant effects have been found in combustion experiments [7]. In experiments dealing with pulverized boiler fuel, the particle size is still too coarse to liberate most of the liptinite and some inertinite macerals, and the product will, therefore, contain a large number of mixed phase particles. In the case of the inertinite macerals, this problem can be greatly reduced by using fusain lithotype samples as the feed. In regard to the question of how well the maceral samples represent a pulverized fuel that may have a significant proportion of mixed phase particles, it was found in a series of coal combustion profile experiments [7] that the individual maceral group profiles could be proportionally combined to match the combustion profile of the whole coal sample.

COAL COMBUSTION PROFILE EXPERIMENTS

Maceral group concentrates from a rank series of Oklahoma coals were used in a set of experiments in which the samples were combusted in air in a TGA at a heating rate of 15°C per minute [7]. Compared to the whole coals, the maceral concentrates showed similar rank trends e.g., the temperatures of combustion onset, maximum combustion rate, 50% burn-off, and char burn-out all increased with rank, but were more reproducible, more linear, and less variable. Of the maceral groups the vitrinite began combustion at a slightly higher temperature than the other macerals, but it burned significantly faster and more intensely. Semifusinite temperatures, excluding combustion onset, were generally higher and the maximum rate of weight loss was lower than that of the coexisting vitrinite. The few sporinite samples that were studied were initially more reactive than the other macerals, but they became less so at higher temperatures. They had the highest char burn-out temperatures and the lowest maximum rate of weight loss. It should also be noted that the variation in combustion properties due to maceral effects are of the same order of magnitude as the rank effect. This observation confirms earlier work [8].

COAL AND CHAR EXPERIMENTS

In another recent set of experiments the combustion properties of a channel sample of the Herrin No. 6 coal, its selected lithotypes, single maceral concentrates, and associated chars were studied [9-10]. The chars were made in an Entrained Flow Reactor at 1000°C in a nitrogen atmosphere at heating rates comparable to pulverized fuel conditions (10^4 to 10^5 °C $second^{-1}$). The chars were then combusted in a TGA in an atmosphere of 80% argon and 20% oxygen and the combustion gases were analyzed in a mass spectrometer.

The results of ultimate analyses show that compared to the whole coal channel sample the DGC vitrinite had slightly less carbon and about half the sulfur content, while the DGC fusinite had slightly more carbon and about two-thirds less hydrogen and nitrogen. In the corresponding chars, the nitrogen increased by almost one-third in the vitrinite and by about two-thirds in the fusinite.

The morphology of the chars were strikingly different. The extremes were the uniform open thin-walled cenospheres of the DGC vitrinite and the totally unfused and unchanged forms of the fusinite. The semifusinite showed a mix of thick-walled open cenospheres, thick-walled honeycombed cenospheres, and unfused particles. The char from the whole coal showed a proportional mix of all these forms.

The differences in reactivity (rate of weight loss) in temperature programmed experiments are also striking. While the DGC vitrinite is just slightly more reactive than the whole coal which has about 85% vitrinite, the DGC fusinite was only about half as reactive. The DGC semifusinite is intermediate between these two extremes. Thus, there can be a wide variation in reactivity between different coal particles from the same sample.

The gas evolution profiles of these samples also show some strong similarities and differences. The temperature programmed TGA runs of the chars all show a dominant CO_2 peak with a lower intensity CO peak of the same shape and position (see Figure 1. a,b,c) The SO_2 release is bimodal with a peak before the start of CO_2 evolution related to inorganic sulfur and one just after the CO_2 maximum related to organic sulfur. The peak of nitrogen evolution consistently occurs well after the main CO_2 peak although there is a lower temperature shoulder suggesting two release mechanisms or two types of nitrogen functionality. Work on model compounds of nitrogen suggests that the pyrrolic and pyridinic functionally may be responsible [11-12]. The results on the combustion of the coal samples were generally similar except for a low temperature shoulder in all the curves representing volatile release (Figure 2. a,b,c).

The biggest differences between the vitrinite and fusinite DGC maceral profiles were that both the vitrinite coal and char were more reactive than the fusinite. For example, the temperature of 50% and 100% burnout for the vitrinite coal samples were 443°C and 549°C respectively, while for the fusinite they were 558°C and 705°C. For the chars the same temperatures for the DGC vitrinite were 489°C and 565°C respectively, while for the fusinite they were

557°C and 720°C. However, a higher proportion of the inherent nitrogen in the fusinite was converted to NO. For example, in the coal combustion the ratio of NO/N for the DGC vitrinite was 0.19 while for the fusinite it was 0.29. The same figures for the char combustion were 0.08 for the vitrinite and 0.19 for the fusinite.

This variation in conversion of fuel nitrogen to nitric oxide can be explained by differences in reactivity leading to varying degrees of NO reduction on the carbon. A higher percentage of the nitrogen content in the fusinite maceral is converted to nitric oxide. Thus, while the nitrogen contents of the macerals decrease in the order: vitrinite > semifusinite > fusinite, the conversion of the coal and char nitrogen to NO shows the reverse order. Therefore, there appears to be a compensation effect whereby the amount of NO evolved from the macerals is similar.

REFERENCES CITED

1. Dyrkacz, G.R. and Horowitz, P.E. Fuel 1982, 60, 3
2. Dyrkacz, G.R., Bloomquist, C.A.A. Ruscic, L., and Horowitz, E.P. Fuel 1984, 1166
3. Dyrkacz, G.R., Bloomquist, C.A.A., Ruscic, L. and Horowitz, E.P. 1984, in Chemistry and Characterization of Coal Macerals, eds. R.R. Winans and J.C. Crelling, American Chemical Society Symposium Series 252. Washington D.C., 67-77
4. Dyrkacz, G.R., Bloomquist, C.A.A. and Soloman, P.R. Fuel 1984, 63, 536
5. Karas, J., Pugmire, R.J., Woolfenden, W., Grant, D.M. and Blair, S. International Journal of Coal Geology 1985, 5 315
6. Crelling, John C., Ironmaking Proceedings-AIME, 1988, 43, 351
7. Crelling, John C., Hippo, Edwin J., Woerner, Bruce A., and West Jr., David P., Fuel, 1992, 71, 151
8. Crelling, J.C., Skorupska, N.M. and Marsh, H. Fuel 1988, 67, 781
9. Crelling, John C., Thomas, K. Mark, and Marsh, Harry, Fuel, 1993, 72, 339
10. Hindmarsh, Christopher J., Wang, Wanxing, Thomas, K. Mark, and Crelling, John C., Fuel, (in press)
11. Wang, W. and Thomas, K. M., Fuel, 1992, 71, 871
12. Spracklin, C. J., Stanczyk, K., Thomas, K.M., Marsh, H., Edwards, I. A. S., and Skorupska, N.M., Proceedings of the 1990 International Carbon Conference, 1990, p.330

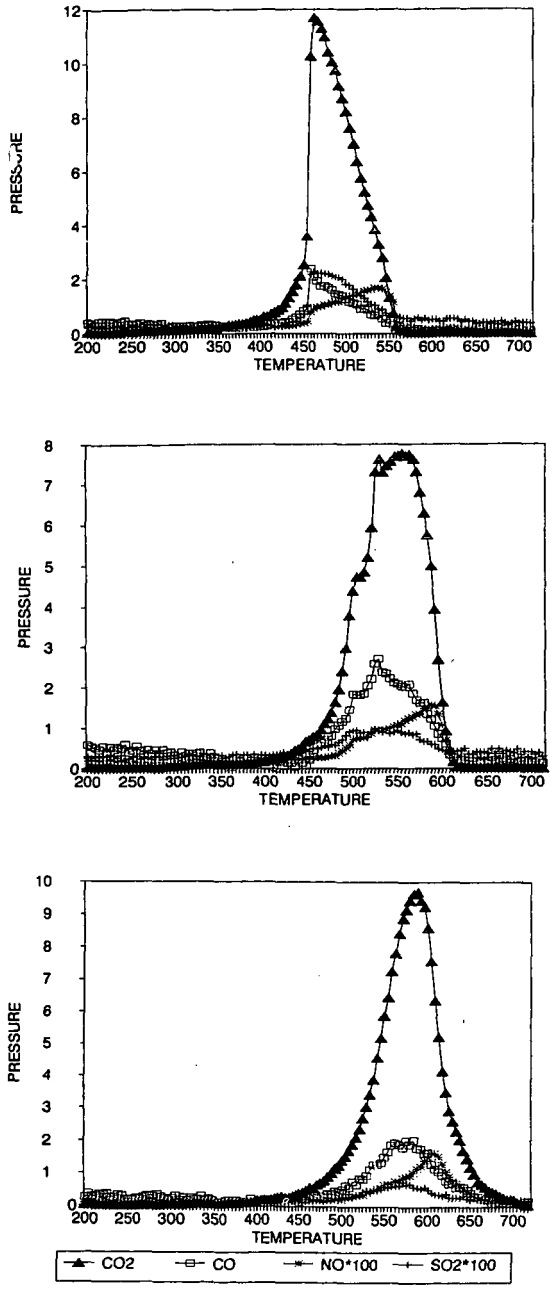

FIGURE 1. Gas evolution profiles of maceral chars combusted in an atmosphere of 80% Argon and 20% Oxygen, 1a (top) vitrinite, 1b (middle) semifusinite, 1c (bottom) fusinite. Note the shift in the peaks from top to bottom indicating decreasing reactivity.

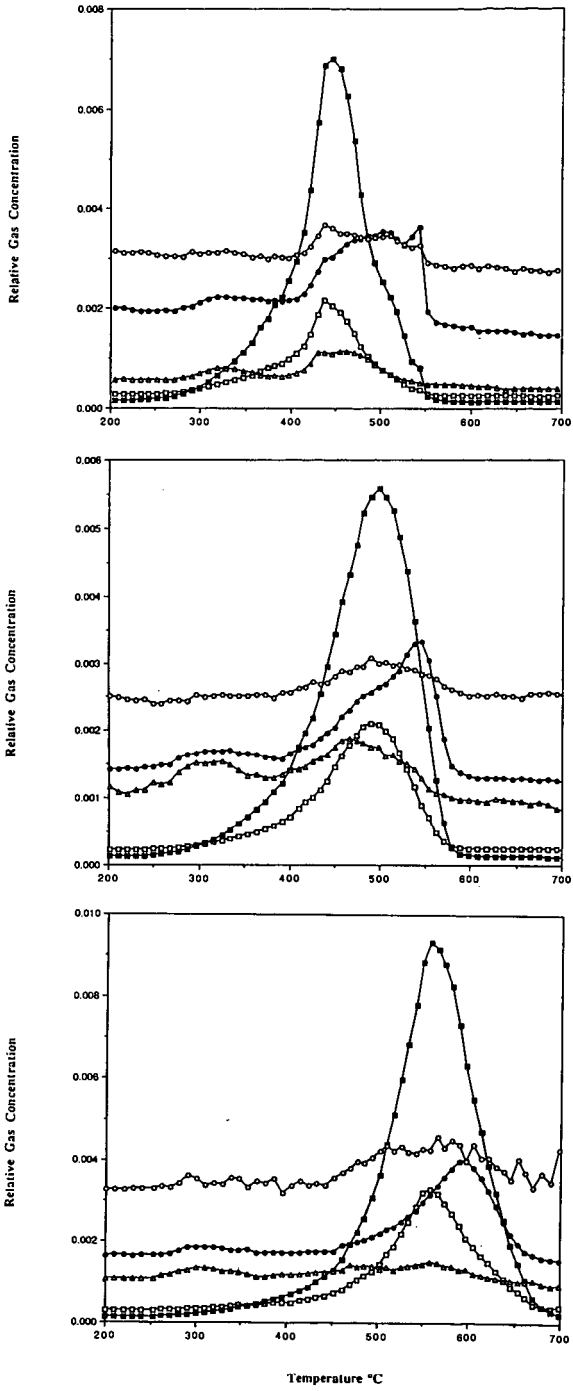

FIGURE 2. Gas evolution profiles of coal macerals combusted in an atmosphere of 80% Argon and 20% Oxygen, 1a (top) vitrinite, 1b (middle) semifusinite, 1c (bottom) fusinite. Note the shift in the peaks from top to bottom indicating decreasing reactivity. KEY: (□) CO, (■) CO_2, (●) NO x100, (△) HCN x100, (○) N_{2+}^{+2} x70.

APPLICATIONS OF MOLECULAR MODELING IN COAL RESEARCH

Gary A. Carlson and Jean-loup Faulon
Fuel Science Department
Sandia National Laboratories
Albuquerque, N.M. 87185-0710

Keywords: molecular modeling, computer modeling, coal structure

Over the past several years, molecular modeling has been applied to study various characteristics of coal molecular structures. Powerful workstations coupled with molecular force-field-based software packages have been used to study coal and coal-related molecules. Early work involved determination of the minimum-energy three-dimensional conformations of various published coal structures (Given, Wiser, Solomon and Shinn), and the dominant role of van der Waals and hydrogen bonding forces in defining the energy-minimized structures. These studies have been extended to explore various physical properties of coal structures, including density, microporosity, surface area, and fractal dimension. Other studies have related structural characteristics to cross-link density and have explored small molecule interactions with coal. Finally, recent studies using a structural elucidation (molecular builder) technique have constructed statistically diverse coal structures based on quantitative and qualitative data on coal and its decomposition products. This technique is also being applied to study coalification processes based on postulated coalification chemistry.

The three-dimensional molecular structure of coal is of considerable interest because of the relationship between structure and reactivity (especially as related to coal liquefaction). Recently, a new technique, computer-aided molecular design (CAMD), or computer-aided molecular modeling (hereafter called simply molecular modeling), has been developed and used to study the structural characteristics of complex molecular systems (1). Initially used to aid in the design of pharmaceutical molecules, the technique is now being applied in many fields such as biochemistry, materials science, polymer science, and fuel science. In the area of coal research, molecular modeling has been used to study coal and coal-related molecules and the interactions of coal with solvents and other molecular species. This paper reviews the use of the molecular modeling technique for this latter application.

The molecular modeling methods used for most coal-related studies are molecular mechanics and molecular dynamics calculations. These use a classical force field approximation to simulate the interactions of atoms within and between molecules (2). With these techniques, the minimum-energy three-dimensional structures of molecules can be determined, as well as a number of other physical properties. There are a number of commercial software packages that include energy-minimization capabilities based on force field calculations, coupled with graphical interfaces for visualization of molecules in three dimensions. These packages are described in the various papers that form the basis for this review, and will not be discussed in more detail here.

The earliest use of molecular modeling for fossil fuel applications that the authors are aware of was a structural elucidation study by Oka, Chang and Gavalas in the 1970s directed at coal-derived compounds (3). Their method used analytical data to determine appropriate combinations of structural groups that were then combined to build molecules. Ten years later, Robinson published a study of heavy coal liquids (4), in which the three-dimensional structures were explored but not the energetics. Soon after, Faulon and coworkers (5) constructed molecular representations of kerogen macromolecules, utilizing a structural elucidation technique to build the macromolecules.

The first use of molecular modeling to study coal structures was by Carlson and Granoff (6, 7), who studied a series of previously-postulated bituminous coal structures (Given, Wiser, Solomon and Shinn) and compared their minimum energy structures, physical densities and hydrogen bond interactions. Good agreement with

experimental data was obtained for density and hydrogen bonding. Carlson also explored the specific interactions that define the tertiary structure of coal (hydrogen bonding and van der Waals interactions), finding that the much weaker (but ubiquitous) van der Waals interactions actually dominated the energy-minimization driving force for coals of bituminous rank (8, 9). A method of calculating porosities as well as physical densities from the computer modeling data utilizing a grid system was presented (9), and microporosities were determined for the coal structures studied.

Carlson also addressed the concept of coal as a three-dimensionally cross-linked (network) solid, attempting to compare results with the experimental and theoretical relationships found between coal cross-link density and degree of solvent swelling (10). Previous coal molecular models (Given, Shinn, etc.) did not include cross-linking explicitly. In unpublished work (11), Carlson found that structures constructed with widely-varying cross-link densities showed no significant variations in energy, physical density or microporosity, suggesting that cross-links were not important sources of rigidity in coal structures.

In 1992, Faulon *et al.* published an extension of his original molecular builder program (12), and applied the method to build representative structures for vitrinite from bituminous coal (13, 14). In this work, the analytical data on which the structures were based were derived from elemental analysis, NMR studies and flash pyrolysis/gc/ms data from coalified wood of bituminous rank. It was found that constraints had to be introduced into the builder program to develop models with reasonable energy and physical properties (the builder had to be constrained to generate models with the maximum number of new five and six membered rings--i.e., hydroaromatic structures); otherwise, the energies were much too high, and the degree of cross-linking was excessive. In extensions of this work (15, 16), Faulon *et al.* showed that, although the number of possible coal structures that could be generated from analytical data was very high (over 300,000 for a structure of 650 total atoms), a statistical sampling of 15 structures was sufficient to provide representative results for vitrinite macerals of bituminous coal. Minimized energies, physical densities and micropore volumes for the 15 structures were essentially the same, within the statistical uncertainty. Since the cross-link densities of the 15 structures varied ten-fold, but the physical characteristics of the structures did not appreciably change, these results confirmed the previous observations by Carlson (11) that cross-link density is not a strong driver for rigidity in coal structures.

Faulon and coworkers have extended the post-modeling analysis of three-dimensional coal molecular structures, exploring porosity, surface area and fractal dimension at a molecular level for vitrinite maceral models. Results consistent with experimental measurements of microporosity and CO_2 and N_2 surface areas have been obtained. Additionally, fractal dimensions of 2.7 for coal structures, in agreement with experiment, were observed (17).

Hatcher and Faulon have also used the builder methodology to study the coalification process (18), beginning with a lignin structure and proceeding stepwise through brown coal, to lignite coal, to subbituminous coal and finally to bituminous coal structure. At each step appropriate chemical transformations of the molecular structure were used and computer results were matched to experimental data. In this study and a more extensive companion study (19), it was determined that the most probable tertiary structure for lignin in wood, as well as for isolated lignin following degradation of the cellulosic component of wood, is a helical structure.

Recently, Nakamura, Murata *et al.*, have developed a new method to simulate the physical density of coal structures using molecular modeling (20-22). The method, which involves utilizing the periodic boundary conditions available in certain modeling packages, allows a coal macromolecule to be replicated in adjacent physical locations and thus to interact with its replicates. By shrinking the size of the periodic boundaries, it is possible to estimate the optimal packing arrangement for the structure, and from this, the density. The technique has been used to study model polymers and simulated structures of four Japanese coals of varying carbon content (72-87%). The densities determined for the coal structures to date are somewhat lower (4-20%) than experimental values. For one of the coals, several

structural modifications were made in the links between molecular clusters and the effects on density determined (23). In contrast to the studies referenced earlier, cross-linked structures were found to have a significant influence (reduction of ~10%) on density.

Takanohashi *et al.* have investigated the association of coal soluble constituents using molecular modeling (24). Molecules typical of pyridine soluble and pyridine insoluble fractions were simulated and found to form relatively stable three-dimensional structures, held together by non-covalent interactions, perhaps similar to the structures and interactions in the parent coal.

Kumagai and coworkers have studied the interactions of a lignite molecular model with water molecules (25). By adding water to the lignite structure before and after energy minimization, they were able to simulate the native coal-water interactions as well as the heat of desorption of water from the lignite and the tendency of the lignite structures not to reverse the conformational changes that occurred upon drying.

In other rather different applications of molecular modeling, Vorpagel and Lavin utilized molecular mechanics calculations to explore the most stable geometric arrangements of associated polynuclear aromatic hydrocarbons (26). These studies, with a focus on the behavior of pitches, could have relevance to the stacking of polynuclear aromatic structures within coal structures as well. In another study, Budzinski *et al.* modeled the enthalpies of formation of alkylnaphthalenes using several modeling methods (27). These results are cited because of the similarity of the studied molecules to components of coal structure. Finally, as the power of available computers grows, the application of semi-empirical and even quantum mechanical methods to coal research has become more practical. For example, Ades and coworkers have recently used a molecular orbital method to study cleavage mechanisms of model compounds related to direct coal liquefaction (28). Currently, Li *et al.* are studying small molecule adsorption on nanocluster metal catalysts utilizing density functional quantum mechanical methods adapted to massively parallel computers (29). It appears likely that within the next few years, significant advances in catalysis modeling will be made utilizing these powerful new techniques.

In summary, molecular modeling has become a valuable technique for the investigation of the three-dimensional conformations and physical properties of coal molecular structures, coal-small molecule interactions and coal soluble constituents. Modeling results generally agree with experimental results, and provide additional insight beyond that from experiments alone. With the advent of new high-speed massively parallel computers, it will be possible to model significantly larger macromolecular structures, as well as to begin to utilize quantum chemical methods more effectively.

References

1. Bajorath, J.; Kraut, J.; Li, Z.; Kitson, D. H.; Hagler, A. T., *Proc. Natl. Acad. Sci* **1991**, *88*, 6423-6426.
2. Fruhbeis, H.; Klein, R.; Wallmeir, H., *Angew. Chem. Intl. Ed. Engl.* **1987**, *26*, 403-418.
3. Oka, M.; Chang, H.; Gavalas, G. R., *Fuel* **1977**, *56*, 3-8.
4. Robinson, K. K., *Proc. Electric Power Res. Inst. Conf. on Coal Structure* **1987**, 3.1-3.11.
5. Faulon, J. L.; Vandenbroucke, M.; Drappier, J. M.; Behar, F.; Romero, M., *Adv. Org. Geochem.* **1990**, *16*, 981-993.
6. Carlson, G. A.; Granoff, B., *Am. Chem. Soc. Div. Fuel Chem. Preprints* **1989**, *34(3)*, 780-786.
7. Carlson, G. A.; Granoff, B., "Modeling of Coal Structure Using Computer-Aided Molecular Design," Coal Science II, Ed. H. H. Schobert, K. D. Bartle and L. J. Lynch, *ACS Symposium Series* **1991**, *461*, 159-170.
8. Carlson, G. A., *Am. Chem. Soc. Div. Fuel Chem. Preprints* **1991**, *36(1)*, 398-404.
9. Carlson, G. A., *Energy and Fuels* **1992**, *6*, 771-778.

10. Carlson, G. A., *Proc. 1991 Intl. Conf. Coal Science* **1991**, 24-27.
11. Carlson, G. A., unpublished work (1992).
12. Faulon, J. L., *J. Chem. Info. Comput. Sci.* **1992**, *32*, 338-348.
13. Faulon, J. L.; Hatcher, P. G.; Wenzel, K. A., *Am. Chem. Soc. Div. Fuel Chem. Preprints* **1992**, *37(2)*, 900-907.
14. Faulon, J. L.; Hatcher, P. G.; Carlson, G. A.: Wenzel, K. A., *Fuel Processing Technology* **1993**, *34*, 277-293.
15. Faulon, J. L.; Carlson, G. A.; Mathews, J. P.; Hatcher, P. G., *Am. Chem. Soc. Div. Fuel Chem. Preprints* **1993**, *38(4)*, 1275-1280.
16. Faulon, J. L.; Carlson, G. A.; Hatcher, P. G., "Statistical Models for Bituminous Coal: A Three-Dimensional Evaluation of Structural and Physical Properties Based on Computer-Generated Structures," to be published in Energy and Fuels, 1994.
17. Faulon, J. L.; Mathews, J. P.; Carlson, G. A.; Hatcher, P. G., "Correlation between Microporosity and Fractal Dimension of Bituminous Coal Based on Computer, Generated Models," unpublished data (1993).
18. Hatcher, P. G.; Wenzel, K. A.; Faulon, J. L.,. *Am. Chem. Soc. Div. Fuel Chem. Preprints* **1993**, *38(4)*, 1270-1274.
19. Faulon, J. L.; Carlson, G. A.; Hatcher, P. G., "A Three-Dimensional Model for Lignocellulose," unpublished data (1993).
20. Nakamura, K.; Murata, S.; Nomura, M., *Energy & Fuels* **1993**, *7*, 347-350.
21. Murata, S.; Nomura, M.; Nakamura, K.; Kumagai, H.; Sanada, Y., *Energy & Fuels* **1993**, *7*, 469-472.
22. Nakamura, K.; Murata, S.; Nomura, M.; Kumagai, H.; Sanada, Y., *Proc. 7th Intl. Conf. Coal Science* **1993**, *I*, 385-388.
23. Dong, T; Murata, S.; Miura, M.; Nomura, M.; Nakamura, K., "Computer-Aided Molecular Design Study of Coal Model Molecules. 3. Density Simulation for Model Structures of Bituminous Akabira Coal," unpublished data (1993).
24. Takanohashi, M.; Iino, M.; Nakamura, K.; Murata, S.; Nomura, M., *Proc. 7th Intl. Conf. Coal Science* **1993**, *II*, 593-596.
25. Kumagai, H.; Nakamura, K.; Sasaki, M.; Yoneda, J.; Sanada, Y., *Proc. 7th Intl. Conf. Coal Science* **1993**, *I*, 136-139.
26. Vorpagel, E. R.; Lavin, J. G., *Carbon* **1992**, *7*, 1033-1040.
27. Budzinski, H.; Garrigues, P., *Energy & Fuels* **1993**, *7*, 505-511.
28. Ades, H. F.; Companion, A. L.; Subbaswamy, K. R., *J. Phys. Chem.* **1991**, *95*, 6502-6507.
29. Li, Y. S., unpublished data (1993).

Acknowledgements Funding was provided by the U. S. Department of Energy at Sandia National laboratories under contract DE-AC04-94AL85000.

THE ROLE OF MODEL COMPOUND STUDIES IN COAL RESEARCH

A. C. Buchanan, III and Phillip F. Britt
Chemical and Analytical Sciences Division
Oak Ridge National Laboratory
P. O. Box 2008
Oak Ridge, Tennessee 37831-6197

Keywords: Model compounds, retrogressive, interfaces, hydrogen transfer

INTRODUCTION

The extraordinarily complex chemical and physical structure of coals continues to present coal scientists with major challenges in advancing the base of scientific knowledge required for the development of substantially improved coal utilization technologies. As a consequence, model compound studies play a foundational role in advancing coal science. Model compounds are employed in studies for: (a) determination of kinetic and mechanistic information relevant to coal pyrolysis and liquefaction chemistry, and to computational modeling of these processes; (b) development of new catalysts for coal conversion or upgrading of coal-derived liquids; (c) development and benchmarking of various spectroscopic methods for analysis of coal structure and constitution by NMR, FTIR, mass spectrometry, X-ray techniques (XPS,XANES), etc.; and, (d) exploration and development of new chemical reactions for coal such as depolymerization under mild conditions, selective heteroatom removal, etc.

The choice of a model compound should not be prescribed, and the rational for the selection can vary with the goal of the research. In general, compounds are selected as substructures, or surrogates for a range of related substructures, in coal. The goal of these studies is to understand the behavior of a well-defined chemical system. Once a system is precisely understood then complexities found in coal can be added systematically, such as restricted mass transport, functional group interactions, medium and interfacial effects, etc. Whereas most early studies of model compounds involved simple molecular systems in homogeneous phases, current model compound studies include a substantial contribution from more complicated systems such as reporter molecules in multiphase media under coal conversion conditions[1], chemically and isotopically labeled coal derivatives[2], silica-immobilized organics[3-5], and polymers[6-9].

The breadth of use of model compounds in coal research precludes a thorough examination in this report. Instead, we will focus on the use of model compound studies to reveal kinetic and mechanistic details underlying coal pyrolysis and liquefaction. We will limit our examination of this topic to the presentation of four areas that we feel are prominent in current research, and that will continue to be significant in the near future. The aim is to illustrate where model compound studies can and do contribute to coal research, along with the presentation of an occasional brief example. The topics are arbitrarily categorized and, clearly, there exists a substantial degree of overlap among them.

Model Compounds Containing Heteroatoms

There has been substantial progress in obtaining detailed knowledge of the thermal chemistry of hydrocarbon models including aromatics, alkylaromatics, α,ω-diarylalkanes, and hydroaromatics, which has recently been reviewed by Poutsma[10-11] and Stein[12]. The depth of our understanding for molecules containing heteroatoms (O, S, N) is not as advanced (for example, $PhSCH_2Ph$ vs. the well-understood $PhCH_2CH_2Ph$)[11]. Recent mass spectrometry studies by Winans and coworkers have demonstrated the abundance of heteroatom-containing molecules in coals, macerals, and extracts.[13] For example, it is well-known that oxygen functionalities are particularly abundant in low rank coals and lignites. Furthermore, oxygen-containing functional groups have been implicated in the difficulty found in processing low rank coals.[14] A more detailed understanding of the chemistry of oxygen-containing model compounds is needed.

We have recently reinvestigated the thermolysis of phenethyl phenyl ether ($PhCH_2CH_2OPh$, PPE),[15] which is the simplest model for the β-aryl ether units that are

key constituents of lignin and which are also present in low-rank coals. This research has revealed a previously undetected reaction pathway that accounts for ca. 25% of the conversion of PPE, and which may account for some of the products previously observed in the pyrolyses of lignins. The standard chain propagation steps for free radical decomposition of PPE (Eqs. 1 & 2) must now be augmented by the chain propagation steps shown in Eqs. 3-5, which includes a step involving a neophyl-like rearrangement for an aliphatic radical α to oxygen prior to β-scission (Eq. 4).

$$PhCH_2CH_2OPh + PhO\bullet \rightarrow PhCH\bullet CH_2OPh + PhOH \quad (1)$$

$$PhCH\bullet CH_2OPh \rightarrow PhCH{=}CH_2 + PhO\bullet \quad (2)$$

$$PhCH_2CH_2OPh + PhO\bullet \rightarrow PhCH_2CH\bullet OPh + PhOH \quad (3)$$

$$PhCH_2CH\bullet OPh \rightleftharpoons PhCH_2CH(Ph)O\bullet \rightarrow PhCHO + PhCH_2\bullet \quad (4)$$

$$PhCH_2CH_2OPh + PhCH_2\bullet \rightarrow PhCH\bullet CH_2OPh + PhCH_2CH\bullet OPh + PhCH_3 \quad (5)$$

We are in the process of examining substituent effects (relevant to lignin substructures) on the thermolysis of PPE. Our initial findings indicate that the additional reaction pathway is general, but that the selectivity for this pathway (and the rate of decomposition of PPE) is sensitive to the substitution pattern.

This research also revealed a general need for better defined rate constants and Arrhenius parameters for many of the individual reaction steps, which are important in unraveling reaction mechanisms, global reaction kinetics, and substituent effects for complex reactions. This data can be very difficult to extract from complex reactions such as observed for PPE, particularly when secondary reactions become important at low conversions. Franz and coworkers, for example, have been able to design experiments to directly measure such absolute rate data for the β-scission of $PhCH\bullet CH(CH_3)OPh$[16], which provides key information relevant to Eq. 2 above. A particularly visible gap in our knowledge is the lack of absolute rate constants and Arrhenius parameters for hydrogen abstractions by phenoxy (and other aryloxy) radicals. Given the apparent importance of such reaction steps in the processing of lignins and low rank coals, kinetic information of this type would be very valuable.

The effect of a heteroatom substituent on a thermolysis reaction is not always easy to predict, and the results can range from subtle to dramatic. For example, we have found that pyrolysis of p-$Me_3SiOPh(CH_2)_3Ph$ proceeds similarly to $Ph(CH_2)_3Ph$ with little influence of the oxygen substituent on the reaction.[4] Similarly, m-$HOPhCH_2Ph$ is stable at 400°C as is the unsubstituted analog, $PhCH_2Ph$.[17] On the other hand, McMillen and coworkers have shown that o- and p-$HOPhCH_2Ph$ decay readily at 400°C, because an initial enol-keto tautomerization generates an intermediate with a thermally labile bond.[17] The presence of the ortho-hydroxy group in guaiacol (o-$HOPhOCH_3$) has been shown to decrease the O-C bond dissociation energy of the methoxy group by 7 kcal/mol, suggesting that hydrogen bonding interactions are important in the radical formed.[18] Finally, thermolysis of 1-naphthol has been shown to proceed by C-C ring coupling prior to condensation (loss of water),[19] while 1,3-dihydroxynaphthalene undergoes condensation first.[20] These few selected examples illustrate that there is much work to be done to understand the impact of oxygen in thermal reaction chemistry related to coal conversion, and a similar status exists for sulfur- and nitrogen-containing organic structures.

Retrogressive Reaction Pathways

The majority of previous model compound studies have been designed to learn about the cleavage of bonds during coal pyrolysis and liquefaction, and ways of altering reaction media and conditions to promote these reactions. There is now considerable interest in learning more about bond forming reactions and the conditions where they become kinetically competitive. Of particular interest are processes that form more refractory bonds since these reactions are the essence of retrogressive chemistry in coal processing. Malhotra and McMillen have discussed this chemistry with respect to hydrogen transfer reactions in a recent review.[21]

A current topic is the retrogressive chemistry that is prominent in the processing of low rank coals. This chemistry has been documented most completely by Solomon,

Serio, and coworkers who have proposed that the formation of new crosslinks in the coal network is associated with the loss of CO_2 and water from oxygen-containing functional groups. A recent review of this pyrolysis research has been published.[22] These authors have also obtained substantial information recently on the effects of demineralization, aqueous pretreatments, introduction of ion-exchanged catalysts, etc. on the liquefaction behavior of low rank coals, techniques which are designed to reduce retrogressive reactions.[23] However, a clear definition of the actual chemical reactions underlying these processes remains elusive. Ring coupling following decarboxylation of acids has been presumed to be involved. However, there is surprisingly little relevant information available in the literature on such reactions, and McMillen and coworkers have recently shown that, under liquefaction conditions, decarboxylation of model aromatic carboxylic acids is not accompanied by significant ring coupling.[24] Hence, if CO_2 evolution is a signature of the cross-linking event, additional studies are required to determine the nature of the cross-linking reactions associated with decarboxylation. We have recently initiated a project to prepare polymeric model systems containing carboxylic acids to examine the impact of a polymeric network on the thermolysis chemistry.[25] The diffusional constraints imposed by such a polymer system may alter the reactivity pattern for the decarboxylation process, as we have occasionally observed previously in the pyrolysis pathways for silica-immobilized model compounds.

There are other types of retrogressive reactions that may be involved in coal processing that need to be studied in more detail. These include ring growth through a sequence of cyclization and aromatization, and radical recombinations and skeletal rearrangements that form strong bonds.[21] We have found that restricted mass transport (induced by immobilization on silica) promotes retrogressive reactions for bibenzyl by both skeletal rearrangement (to $PhCH(CH_3)Ph$) and ring growth (to phenanthrene).[3] We recently found that a similar rearrangement process appears to occur at 300°C for the structurally related silica-immobilized phenyl benzyl sulfide ($\approx PhSCH_2Ph$), which accounts for 10-15% of the reaction. This process converts a

$$\approx PhSCH_2Ph \rightarrow \approx PhCH(SH)Ph \rightarrow \approx PhCH_2Ph \ (+ H_2S) \qquad (6)$$

very labile linkage into a much more refractory diphenylmethane-type linkage. Our current hypothesis is that Eqs. 7-8 are the key chain propagation steps in this

$$\approx PhSCH\bullet Ph \rightleftharpoons \approx PhCH(S\bullet)Ph \qquad (7)$$

$$\approx PhCH(S\bullet)Ph + \approx PhSCH_2Ph \rightarrow \approx PhCH(SH)Ph + \approx PhSCH\bullet Ph \qquad (8)$$

process analogous to bibenzyl. The sulfur to carbon neophyl-like rearrangement for the fluid-phase analog of Eq. 7 has recently been directly observed by Alnajjar and Franz.[26] Coal science would benefit from an improved molecular level understanding of retrogressive reaction types, and the impact that coal physical properties and coal processing media may have on them.

Interfacial Chemistry

Coal is of course not a homogeneous material. It is a complex, heterogeneous solid that includes interdispersed mineral matter. Yet knowledge of organic-mineral matter interactions, and how they effect the reactivity of coal is only rudimentary. There is also growing evidence that water can play a significant role in affecting the course of chemical reactions during coal processing, which needs to be investigated in more detail.[23] A more complete description of coal reactivity under pyrolysis or liquefaction conditions requires a better molecular level understanding of the effect of minerals on coal reactivity in the solid state. Clays such as montmorillonite, for example, are known to be effective catalysts for organic reactions. They have also been proposed as key catalysts for the thermal alteration of lignin during the coalification process.[27] This suggests that catalytic interactions at the solid-solid interface are important. Recently, we were able to demonstrate that montmorillonite, and other small particle size silica-aluminas, can induce acid-catalyzed reactions in the solid state for several silica-immobilized model compounds including phenethyl phenyl ether.[28]

The catalytic liquefaction of coal constitutes a truly multiphase system, involving solid coal and catalyst, hydrogen gas, and a hydrogen donor "solvent", where interfacial interactions are obviously important. Recently Malhotra and McMillen have

summarized the potential role of the reaction medium in transferring hydrogen atom activity from the catalyst to the coal reactive site.[21] A very active area of research on coal conversion is the search for new nanoscale dispersed catalysts, which could improve the direct interaction of solid coal particles with catalyst.[29] Only recently has evidence begun to emerge that such solid state interactions might be important in affecting the outcome of coal conversion. For example, Bockrath and coworkers used a pulse-flow microreactor to show that organic hydrogen in coal can be exchanged with D_2 gas at low temperatures as a result of MoS_2 catalyst-coal interactions.[30] In collaboration with Snape and coworkers, we have made a preliminary investigation of the catalyzed hydrocracking of silica-immobilized diphenylmethane in the solid state using temperature programmed reduction (TPR) under high pressures of hydrogen with mass spectrometric detection of volatile products.[31] We gained evidence, from the substantially lowered temperatures for benzene and toluene evolution, that a dispersed sulfided Mo catalyst can significantly promote the hydrogenolysis reaction (Eq. 9) in the solid state. The degree to which coal conversion can be modified

$$2(\approx PhCH_2Ph)\cdot + 2H_2 \rightarrow \approx PhH + PhCH_3 + \approx PhCH_3 + PhH \qquad (9)$$

by dispersed catalysts, and the factors controlling such interactions, have only begun to be explored and are a frontier area for model compound research.

Hydrogen Transfer Chemistry

Despite the longstanding interest and the wealth of information available, improved knowledge of the mechanisms of hydrogen transfer remains a crucial area for the attention of model compound researchers. Hydrogen transfer reactions are important in both bond breaking and bond forming reactions. Of particular current interest are medium effects (solvent systems, catalysts, restricted mass transport, etc.) on hydrogen transfer processes. An array of hydrogen transfer steps have been invoked as being involved including hydrogen abstraction by radicals, transfer of free hydrogen atoms, reverse radical disproportionation (RRD), and radical hydrogen transfer (RHT). RHT involves hydrogen transfer from a cyclohexadienyl-type carrier radical to a substrate in a single step, and has gained significant attention in recent coal and model compound studies.[21,32] However, contrary opinions on the importance of RHT have been recently presented.[33] The exact details aside, it appears that the presence of polycyclic aromatic hydrocarbons in solvent systems can mediate hydrogenolysis activity in coal liquefaction. Given the importance of controlling hydrogen utilization in the development of economically competitive coal utilization technologies, additional model compound research in this area is needed.

We have been actively investigating the effects of restricted mass transport, which may be important in coal chemistry, on thermolysis reactions through the study of silica-immobilized model compounds.[3-5] By employing two-component surfaces, one can begin to explore the effects of diffusionally constrained environments on hydrogen transfer processes. We have acquired evidence that a mechanism involving rapid serial hydrogen transfer steps on the surface can provide an alternative, non diffusional pathway for free-radical centers to "migrate" as illustrated below.[34]

$$\approx PhCH\cdot R^1 + \approx PhCH_2Ph \rightleftharpoons \approx PhCH_2R^1 + \approx PhCH\cdot Ph \qquad (10)$$

$$\approx PhCH\cdot Ph + \approx PhCH_2R^2 \rightleftharpoons \approx PhCH_2Ph + \approx PhCH\cdot R^2 \qquad (11)$$

Moreover, we have recently found that the retrogressive radical chain rearrangement path for silica-immobilized bibenzyl (analogous to Eqs. 7-8 above) is more effectively inhibited by naphthalene spacers (hydrogen transfer barricades) than by hydrogen donor spacers such as tetralin (radical relay centers).[35] These results have important implications for the transfer of reactive sites in the cross-linked network structure of coal which must be explored in more detail.

Summary

Model compound studies have made and continue to make important contributions in advancing coal science, ranging from determination of quantitative kinetic information for elementary reaction steps to unravelling the effects of restricted diffusion or interfacial phenomena on chemical processes. Constant interactions between model compound and coal researchers will enhance the prospects that the model compound

researcher is performing work of relevance to coal science, and that the coal researcher is employing the appropriate scientific basis in interpretation of coal results. Research that reveals new information on the chemical reactions associated with heteroatom-containing model compounds, retrogressive reaction pathways, organic-mineral interactions and other interfacial effects, and details of hydrogen transfer processes is of particular current interest.

Acknowledgement

This research was sponsored by the Division of Chemical Sciences, Office of Basic Energy Sciences, U.S. Department of Energy, under Contract DE-AC05-840R21400 with Martin Marietta Energy Systems, Inc.

References

1. Bockrath, B. C.; Schroeder, K. T.; Smith, M. R. Energy and Fuels **1989**, *3*, 268.
2. Stock, L. M. Acc. Chem. Res. **1989**, *22*, 427.
3. Buchanan, III, A. C.; Dunstan, T. D. J.; Douglas, E. C.; Poutsma, M. L. J. Am. Chem. Soc. **1986**, *108*, 7703.
4. Buchanan, III, A. C.; Biggs, C. A. J. Org. Chem. **1989**, *54*, 517.
5. Britt, P. F.; Buchanan, III, A. C. J. Org. Chem. **1991**, *56*, 6132.
6. Malhotra, R.; McMillen, D. F.; Tse, D. S.; St.John, G. A. Energy Fuels **1989**, *3*, 465.
7. McMillen, D. F.; Satyam, A.; Malhotra, R. Proc., 7th Int. Conf. Coal Sci., Banff, Alberta, Canada, **1993**, Vol. II, *163*.
8. Squire, K. R.; Solomon, P. R.; Carangelo, R. M.; DiTaranto, M. B. Fuel **1986**, *65*, 833.
9. Winans, R. E.; Hayatsu, R.; Squires, T. G.; Carrado, K. A.; Botto, R. E. Prepr. Pap.-Am. Chem. Soc., Div. Fuel Chem. **1990**, *35(2)*, 423.
10. Poutsma, M. L. Energy Fuels **1990**, *4*, 113.
11. Poutsma, M. L. "A Review of Thermolysis Studies of Model Compounds Relevant to Processing of Coal," Oak Ridge National Laboratory, ORNL/TM-10637, November, 1987.
12. Stein, S. E. Acc. Chem. Res. **1991**, *24*, 350.
13. Winans, R. E. "Mass Spectrometric Studies of Coals and Coal Macerals," In Advances In Coal Spectrocsopy, Muezelaar, H. L. C., Ed.; Plenum Press: New York, **1992**, 255.
14. Solomon, P. R.; Serio, M. A.; Despande, G. V.; Kroo, E. Energy Fuels **1990**, *4*, 42.
15. Britt, P. F.; Buchanan, III, A. C.; Hitsman, V. M. Proc., 6th Int. Conf. Coal Sci., Newcastle-upon-Tyne, United Kingdom, **1991**, 207
16. Autrey, S. T.; Alnajjar, M. S.; Nelson, D. A.; Franz, J. A. J. Org. Chem. **1991**, *56*, 2197.
17. McMillen, D. F.; Ogier, W. C.; Ross, D. S. J. Org. Chem. **1981**, *46*, 3322.
18. Suryan, M. M.; Kafafi, S. A.; Stein, S. E. J. Am. Chem. Soc. **1989**, *111*, 1423.
19. Poutsma, M. L.; Dyer, C. W. J. Org. Chem. **1982**, *47*, 3367.
20. McMillen, D. F.; Chang, S. -J.; Nigenda, S. E.; Malhotra, R. Prepr. Pap.-Am. Chem. Soc., Div. Fuel Chem. **1985**, *30(4)*, 414.
21. Malhotra, R.; McMillen, D. F. Energy Fuels **1993**, *7*, 227.
22. Solomon, P. R.; Fletcher, T. H.; Pugmire, R. J. Fuel **1993**, *72*, 587.
23. Serio, M. A.; Kroo, E.; Charpenay, S.; Solomon, P. R. Prepr. Pap.-Am. Chem. Soc., Div. Fuel Chem. **1993**, *38(3)*, 1021.
24. Manion, J. A.; McMillen, D. F.; Malhotra, R. Prepr. Pap.-Am. Chem. Soc., Div. Fuel Chem. **1992**, *37(4)*, 1720.
25. Britt, P. F.; Buchanan, III, A. C. Proc., 7th Int. Conf. Coal Sci., Banff, Alberta, Canada, **1993**, Vol. II, 297.
26. Alnajjar, M. S.; Franz, J. A. J. Am. Chem. Soc. **1992**, *114*, 1052.
27. Hayatsu, R.; McBeth, R. L.; Scott, R. G.; Botto, R. E.; Winans, R. E. Org. Geochem. **1984**, *6*, 463.
28. Buchanan, III, A. C.; Britt, P. F.; Thomas, K. B.; Biggs, C. A. Energy Fuels **1993**, *7*, 373.
29. Derbyshire, F. J. Energy Fuels **1989**, 3, 273.
30. Bockrath, B. C.; Finseth, D. H.; Hough, M. R. Fuel **1992**, *71*, 767.
31. Mitchell, S. C.; Lafferty, C. J.; Garcia, R.; Snape, C. E.; Buchanan, III, A. C.; Britt, P. F.; Klavetter, E. Energy Fuels **1993**, *7*, 331.
32. Smith, C. M.; Savage, P. E. Energy Fuels **1992**, *6*, 195.
33. Autrey, S. T.; Camaioni, D. M.; Ferris, K. F.; Franz, J. A. Proc., 7th Int. Conf. Coal Sci., Banff, Alberta, Canada, **1993**, Vol. I, 336.
34. Buchanan, III, A. C.; Britt, P. F.; Biggs, C. A. Energy Fuels **1990**, *4*, 415.
35. Buchanan, III, A. C.; Britt, P. F.; Thomas, K. B. Proc., 7th Int. Conf. Coal Sci., Banff, Alberta, Canada, **1993**, Vol. I, 627.

ORGANIC STRUCTURE COMPONENTS WITHIN THE ARGONNE PREMIUM COAL SAMPLES*

Randall E. Winans
Chemistry Division, Building 200
Argonne National Laboratory
Argonne, IL 60439

Keywords: Coal Structure, Heteroatoms, Argonne Premium Coals

INTRODUCTION

The nature of the major organic molecular types that make up the structures in the Argonne Premium Coals will be discussed. Data derived using a number of approaches from the literature and from our laboratory will be included to assemble statistical models for these coals. The nature and distribution of the heteroatoms will be emphasized. In addition, deficiencies in our information such as quantitation of linkages between stable clusters will be examined.

Elucidation of the important structural features in coals has been facilitated by the availability of the Argonne Premium Coal Samples. For the first time, differences between techniques and labs using the same techniques cannot be attributed to differences in the coal sample. Also, the method of storage of the samples, sealed in glass, ensures that studies started today can be compared to studies done on these samples a number of years ago. These samples are with one exception, vitrinite rich, and the discussion in this paper will focus on the organic structures in vitrinites. It is fairly clear that a majority of vitrinite is derived from lignin.[1,2] While the nature of the starting material is important in studying the "structure" of coal, there are ambiguities in our understanding of the structure of lignins.[3] The nature of the monomers is fairly well known, but it is not totally clear how they combine to make the biopolymer. Given the complexity of the starting materials, the severe reaction conditions, and the insolubility of the finished product, one can only hope to develop a statistical picture of coal structure. However, such a picture can be very useful in the development of new technology for coal utilization.

One objective of this paper is to examine what we now know about the structural features of the Argonne coals using information derived from a number of complementary approaches. The second objective is to determine what other information would be useful to better define a statistical picture of coal structure. It should be noted that the literature cited in this paper is not complete but is only representative. The broad topic of physical structure will not be discussed in this study.

Of all the direct techniques used to examine the Argonne Coals, solid ^{13}C NMR is the most popular.[4-5] A round-robin study focusing on the determination of aromaticity, involving thirteen groups, resulted in a book with a summary of all the results presented in the final chapter.[4] In addition, EPR studies are presented in this compilation. Both XPS[6] and XANES[6,7] have been used to speciate the main sulfur groups. This work has recently been reviewed.[8] Also recently, nitrogen compounds have been investigated by XPS.[9]

Most indirect methods use thermolysis to release smaller molecules, which can then be individually detected. These results are rich in information but are thought to be quantitatively less reliable than direct techniques. Various mass spectrometric methods are the most popular and those applied to the Argonne coals are listed in Table 1. Also, TG-FTIR has been used to quantify thermally released gases and tars. [17]

Table 1

Mass Spectrometric Techniques used to analyze the Argonne Premium Coals.

Ionization	Instrument	Resolution	Reference
Low voltage EI	Quadrupole	Low	10
Field Ionization	Sector	Low	11, 12
Fast Atom Bombardment	Sector	Low	13
Desorption Chemical Ionization	Sector	High	14
Desorption EI	Sector	High	15
TGA - LVEI	Quadrupole	Low	10
Laser Desorption	Time-of-flight	Low	16

The use of coal extracts simplify some of the problems in coal structure studies and are being used by a number of researchers.[5,14,15,16] Some exotic solvent mixtures result in very high yields for some of the coals. In addition, chemical modification such as alkylation has been used in studies of these coals.

EXPERIMENTAL

The preparation and properties of the samples have been described.[18] The Desorption Electron Impact High Resolution Mass Spectrometry (DEIHRMS) experiments were performed using an HRMS EI source modified to take a desorption chemical ionization probe.[15] With this probe the sample is desorbed and pyrolysed directly in the source of the mass spectrometer which reduces the likelihood of secondary reactions such as recombinations and aromatizations. The pyridine extractions have been described elsewhere.[14]

RESULTS AND DISCUSSIONS

Aromatic Structures. The fraction of aromatic carbons in the Argonne Premium coals have been determined by NMR and it is apparent that the single pulse excitation is the best approach.[4] Molecular weight determinations are not nearly so well defined. Mass spectrometry of volatile extracts or pyrolysis products should provide fairly good numbers. However, the results are very technique dependent. If one examines all of the methods in Table 1 being applied to the same sample, the following trend for average molecular weight results are: lvEI/Quad < DEI < DCI = LD < FAB < FI. The differences can be contributed to a combination of fragmentation, ionization technique sensitivity, mass analysis sensitivity, and secondary reactions. Even with these problems several trends are normally observed. Average molecular weight normally increases with rank specifically for aromatic molecules. With aliphatic molecules the trends depend on the biomarker content and types in the coal. The average molecular weights are relatively low, normally between 300 and 500. However, these methods will observe larger molecules if they exist.

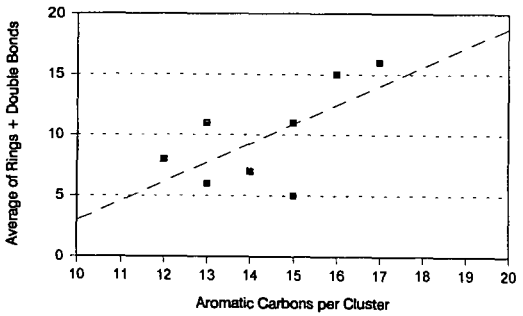

Figure 1. Correlation of aromatic carbons from NMR[5] with hyrogen deficiencies from HRMS[15] data derived from extracts of the Argonne Premium Coals.

HRMS results can be compared to NMR results for the extracts which are shown in Figure 1. Considering the assumptions and

errors from both techniques, the correlation is quite good. The lignite is the most obvious outlier, but the yields from extraction were much different. A demineralized lignite which gave a greater yield was used in the MS experiment. The MS data shows a smooth increasing average size, while the NMR shows similar trends with a few discontinuities. The important result of all these studies is that the structures are not dominated by large polycyclic aromatic compounds.

Heteroatoms. Because of their large abundance, heteroatoms must dominate the chemistry of most coals. Figure 2 shows the average number of heteroatoms per aromatic carbon. Even for the high rank coals, the heteroatom content is significant, but they are likely to be involved as links. This is especially true for oxygen, as can be seen in Figure 3 which shows the amount of ethers or furans present, estimated from three different techniques. The methylation data is incomplete, but the available numbers agree very well with the HRMS estimates. A similar trend is seen for NMR results, but the numbers are much lower which is attributed to difficulties in separating overlapping resonances. All three approaches agree for the Pocahontas coal. The nature of this coal has been thoroughly discussed in a recent paper [19]. The most inconsistent results are for the lignite which has also been observed in the NMR study of extracts.[5] In summary, phenols derived from lignin dominate in the lower rank coals, while furans and ethers may be major links in the higher rank coals.

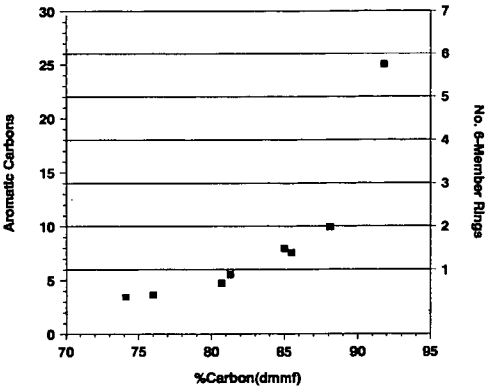

Figure 2. Number of aromatic carbons per heteroatom for the Argonne Premium Coals.

From XANES, XPS, DEIHRMS, and TG-FTIR it is apparent that coals contain a significant amount of aliphatic sulfur. Data from all four techniques have been averaged and the result is shown in Figure 4. Although not shown here, a significant finding is that the indirect, thermal techniques agree very well with the direct methods. Also, there is a very distinct rank dependence with aliphatic sulfur becoming a very minor fraction in the high rank coals.

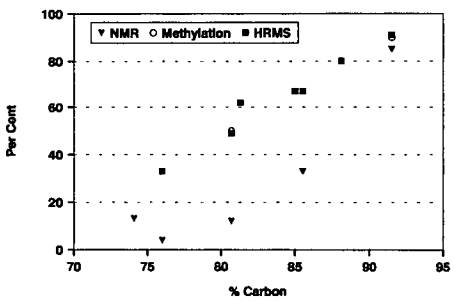

Figure 3. Estimates of the amounts of oxygen species as ethers or furans in the Argonne Premium Coals.

Nitrogen is found as pyrolic, pyridinic and quaternary by XPS with no evidence for free amines. Pyrolic content varies between

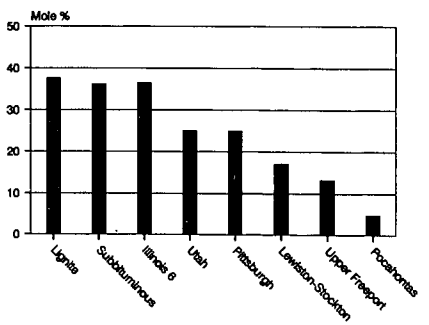

Figure 4. Averages of all available aliphatic sulfur data.

55% and 65% with little rank dependence while quaternary decreases with increasing rank. This species is probably protonated pyridinic nitrogen. DEIHRMS indicates that a significant amount of the nitrogen compounds contain an additional heteroatom. This is not surprising if one considers the data in Figure 2.

Linkages. Generally, it is thought that aliphatics such as ethylene make up the links between aromatic clusters in coals. However, the evidence for this is not compelling. Biaryl links are thought to be important in the Pocahontas coal and could be significant contributers in many of the >85% carbon bituminous coals. Biaryl and methylene links also tend to be more thermodynamically stable as is shown in the series below.

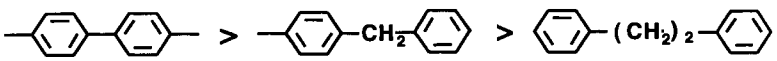

Oxygen functionalities likely play an important role in linkages, especially in higher rank coals. The decreasing oxygen content is compensated for by an increasing percentage of ethers and furans and an increase in aromatic cluster size. More information is needed to quantitate the distribution of linkages which is critical to an understanding of coal reactivity.

SUMMARY

Several key features are evident from examining the data from the Argonne coals. First, the aromatic clusters are not very large. Second, heteroatoms are associated with a majority of the clusters. Finally, we need more quantitative information on the links between clusters.

ACKNOWLEDGEMENT

This work was performed under the auspices of the Office of Basic Energy Sciences, Division of Chemical Sciences, U. S. Department of Energy, under contract number W-31-109-ENG-38.

REFERENCES

1. Hayatsu, R.; Botto, R. E.; Scott, R. G.; McBeth. R. L.; Winans, R. E. *Fuel* **1986**, *65*, 821.
2. Hatcher, P. G.; Faulon, J. L.; Wenzel, K. A.; Cody, G. D. *Energy Fuels* **1992**, *6*, 813.
3. *Lignin: Properties and Materials;* Glasser, W. G.; Sarkanen, S., Eds; American Chemical Society: Washington D.C., 1989.
4. *Magnetic Resonance of Carbonaceous Solids*; Botto, R. E.; Sanada, Y., Eds.; American Chemical Society: Washington D.C., 1993.
5. Fletcher, T. H.; Bai, S.; Pugmire, R. J.; Solum, M. S.; Wood, S.; Grant, D. M. *Energy Fuels* **1993**, *7*, 734.
6. George, G. N.; Gorbaty, M. L. ; Kelemen, S. R.; Sansone, M. *Energy Fuels*, **1991**, *5*, 93.
7. Huffman, G. P.; Mitra, S.; Huggins, F. E.; Shah, N.; Vaidya, S.; Lu, F. *Energy Fuels* **1991**, *5*, 574.
8. *Organic Sulfur in Coal*, Davidson R.; IEA Coal Research: London, 1993.
9. Kelemen, S. R.; Gorbaty, M. L.; Vaughn, S. N.; Kwiatek, P.J. *Prepr. Pap. - Am. Chem. Soc., Div. Fuel Chem.* **1993**, *38*(2), 384.
10. Yun, Y.; Meuzelaar, H. L. C.; Simmleit, N.; Schulten, H-R. *Energy Fuels*, **1991**, *5*, 22
11. Malhotra, R.; McMillen, D. F.; Huestis, D. L. *Prepr. Pap. - Am. Chem. Soc., Div. Fuel Chem.* **1991**, *36*(3), 1252.
12. Simmleit, N.; Schulten, H-R.; Yun, Y.; Meuzelaar, H.L.C. in *Advances in Coal Spectroscopy*, Meuzelaar, H. L.C., Ed.; Plenum Press: N.Y. 1992, 295.
13. Winans, R. E. *J. Anal. Appl. Pyrolysis*, **1991**. *120*, 1.
14. Winans, R. E.; McBeth, R. L.; Hunt, J. L.; Melnikov, P. E. *Proceeding, 1991 International Conf. Coal Sci.* **1991**, 44.
15. Winans, R. E.; McBeth, R. L. ; Melnikov, P.E., Botto, R.E. *1993 International Conf. Coal Sci.* **1993**, 515.
16. Hunt, J. E.; Lykee, K. R.; Winans, R. E. *Prepr. Pap - Am. Chem. Soc. Div. Fuel Chem.* **1991**, *36*(3), 1325.
17. Bassilakis, R.; Zhao, Y.; Solomon, P. R.; Serio, M. A. *Energy Fuels* **1993**, *7*, 710.
18. Vorres, K. S. *Energy Fuels* **1990**, *4*. 420.
19. Stock, L. M.; Muntean, J. V. *Energy Fuels* **1993**, *7*, 704.

Organic Oxygen and Nitrogen Transformations During Pyrolysis of Coal

S. R. Kelemen, M. L. Gorbaty and P. J. Kwiatek
Exxon Research and Engineering Co.
Annandale, NJ 08801, USA

Keywords: Argonne Premium Coals, Oxygen, Nitrogen

Abstract

The chemical changes in organically bound oxygen and nitrogen forms have been studied using X-ray Photoelectron Spectroscopy (XPS) following mild pyrolysis of Argonne Premium coal. The evolution of CO_2, CO and H_2O during pyrolysis was quantified and their appearance was associated with the loss of hydroxyl and carboxyl functional groups present in coal. There is a corresponding loss of quaternary nitrogen species upon pyrolysis. This loss of quaternary nitrogen species is interpreted to result from broken associations between pyridinic nitrogen and hydroxyl groups from either carboxylic acids or aromatic hydroxyl moieties.

I. Introduction

During the pyrolysis, hydropyrolysis and liquefaction of coal the thermolysis of labile chemical bonds is thought to initiate a complex series of reactions that can lead to either hydrogen addition reactions and lower molecular weight products or retrograde cross-linking reactions and heavier products [1-4]. The chemical reactions of organic oxygen functionalities initially present in coal have been implicated as important factors. However, there exists little detailed information about the transformations that take place early during coal conversion. The present work focuses on the chemical changes of organically bound oxygen and nitrogen forms in coal structure prior to the evolution of liquid-like products during coal pyrolysis.

II. Experimental

X-Ray Photoelectron Spectroscopy was used to speciate and characterize the organic oxygen and nitrogen functional group distributions. An energy correction was made to the spectra due to sample charging based on a carbon (1s) peak position of 284.8 eV. The amount of organic oxygen was determined relative to carbon from the total area of the XPS peaks after accounting for inorganic contributions to the oxygen (1s) and sulfur (2p) peak intensities [5-7]. The inelastic background and shake-up emission features to the carbon (1s) spectra were subtracted prior to curve resolution [8]. The details of the carbon (1s) and nitrogen (1s) curve resolution process appear elsewhere [5,6,8,9]. Argonne Premium coals were used in this study [10]. Pyrolysis experiments were done in helium. The details of the pyrolysis reactor have been described previously [5]. Briefly, a linear (0.5 deg/sec) heat-up period from 160 to 400°C was followed by isothermal reaction at 400°C for 5 min. Analysis of the accumulated gas composition following the heat-up and isothermal period was made by GC analysis using a thermal conductivity detector.

III. Results and Discussion

During the early stages of coal pyrolysis a substantial amount CO, CO_2 H_2O and other light gaseous products are formed. The amount of these gaseous products have been quantified. Table I shows the results of gas analyses following pyrolysis at 400°C for 5 min. The results are expressed as molecules per 100 carbons initially present in each coal sample. Included in Table I is the total amount of oxygen that can be accounted for by these gaseous products. For the lower rank coals the loss of oxygen is greater than for higher rank coals.

XPS has been used to follow the corresponding changes in total organic oxygen in the coal chars. Table II shows the results expressed as atoms of oxygen per 100 carbons initially present. Included in Table II are the corresponding results of the XPS analysis of fresh Argonne premium coals. All coals show a decrease in the level of organic oxygen upon pyrolysis but the effect is most evident with lower rank coal.

There are well known problems associated with different techniques for establishing the level of total organic oxygen and different oxygen functionalities present in coal. Fast neutron activation analysis (FNAA) for oxygen analysis [11,12] followed by correction for inorganic forms has been attempted as an alternate to ASTM oxygen-by-difference estimates and similar modified "by difference" formulas. Indirect chemical methods have been combined with these by-difference determinations for total oxygen to provide functional group information [13, 20, 21]. These results have been compared to indirect pyrolysis attempts at organic oxygen analysis [13, 22]. ^{13}C NMR analysis of Argonne Premium coal has yielded insight into the kinds of organic functionalities present [14]. XPS has also been used to evaluate organic oxygen [5, 15-19].

With the emergence of more reliable methods for determining XPS shake-up and inelastic loss processes, the XPS carbon (1s) line shape can provide quantitative information about the kinds of organic oxygen functionalities initially present in coal [8]. XPS was used in the present work to determine the kinds of organic oxygen functionalities initially present in Argonne Premium coals and those that remain after pyrolysis. Figure 1 shows the XPS carbon (1s) spectrum following background subtraction of the initial Wyodak. Included in this figure are the results of a curve resolution analysis. For the starting Wyodak coal, the main peak is due to unoxidized carbon. There is also a strong peak due to carbon with a single bond to oxygen. Carbonyl and carboxyl peaks show up with less intensity. After pyrolysis, only singly bonded carbon oxygen functionalities are observed and with less relative intensity to unoxidized carbon species. The digital results of the detailed XPS analysis for oxygen functionality for Wyodak and the other Argonne Premium coals are shown in Table II. Low rank coals contain much more carbonyl and carboxyl species. After pyrolysis, low rank coals show a loss of carboxyl and carbonyl species. For low rank coals, much of the lost carboxyl and carbonyl oxygen functionalities can be accounted for in the evolution of light gaseous products. The loss of hydroxyls, mostly from acid functional groups, is thought to occur and explains the appearance of H_2O as a major pyrolysis product of low rank coal.

The changes in the XPS nitrogen (1s) line shape following mild pyrolysis of Argonne Premium coal have been studied. These results are shown in Table III. In contrast to oxygen, the total level of nitrogen remains nearly constant relative to carbon after pyrolysis [9]. The retention of nitrogen in the pyrolysis char is expected, based on lack of gaseous evolution of nitrogen containing pyrolysis products. The results of curve resolution analysis of the nitrogen (1s) spectra for fresh Argonne Premium coals have been previously reported [9] and these results are included in Table III for comparison. In all cases the level of quaternary nitrogen decreases upon pyrolysis, while a corresponding increase in pyridinic nitrogen is observed. The level of pyrrolic nitrogen remains almost constant. These observations, taken together with the results for organic oxygen, suggest that the quaternary nitrogen species are pyridinic forms associated with hydroxyls and that the association is broken as a result of thermal reactions [9].

IV. References

1) Wiser, W. H., *Fuel*, **1969**, 47, 475.

2) Gorin, E, Chemistry of Coal Utilization; Wiley Interscience: N. Y. 1981 Supp. Vol. 2, Chapter 27.

3) Whitehurst, D. D.; Mitchell, T. O.; Farcasiu, M., Coal Liquefaction; Academic Press: NY 1980.

4) Neavel, R. C., *Fuel* **1976**, 55, 237.

5) Kelemen, S. R.; Freund, H., *Energy & Fuels*, **1989**, 3, 498: **1990**, 4, 165.

6) Kelemen, S. R.; George, G. N.; Gorbaty, M. L., *Fuel*, **1990**, 69, 939.

7) Kelemen, S. R.; Gorbaty, M. L.; George, G. N.; Kwiatek, P. J., *Energy & Fuels*, **1991**, 5, 720.

8) Kelemen, S. R.; Rose, K. D.; Kwiatek, P. J., *App. Surface Science*, **1993**, 64, 167.

9) Kelemen, S. R.; Gorbaty, M. L.; Vaughn, S. N.; Kwiatek, P. J., *Prepr. Pap. ACS Fuel Div.*, **1993**, 38, 384.

10) Vorres, K. S., *Energy & Fuels*, **1990**, 4, 420.

11) Ehmann, W. D.; Koppenall, D. W.; Hamrin Jr., C. E.; Jones, W. C.; Prasad, M. N.; Tian, W. Z., *Fuel*, **1986**, 65, 1563.

12) Mahajan, O. P., *Fuel*, **1985**, 64, 973.

13) Jung, B.; Stachel, S. J.; Calkins, W. H., *Prep. Pap. ACS Fuel Div.*, **1991**, 36, 869.

14) Solum, M. S.; Pugmire, R. J.; Grant, D. M., *Energy & Fuels*, **1989**, 3, 187.

15) Clark, D. T.; Wilson, R., *Fuel*, **1983**, 62, 1034.

16) Grint, A.; Perry, D. L., *Fuel*, **1983**, 1029.

17) Wu, M. M.; Robbins, G. A.; Winschel, R. A.; Burke, F. P., *Energy & Fuels*, **1988**, 2, 150.

18) Gonzalez-Elope, A. R.; Martinez-Alonso, A.; Tascon, J. M. D., *Surf. Inter. Anal.*, **1988**, 12, 565.

19) Weitzsacker, C. L.; Gardella Jr., J. A., *Anal. Chem.*, **1992**, 64, 1068.

20) Liotta, R.; *Am. Chem. Soc.*, **1981**, 103, 1735.

21) Liotta, R.; *Fuel*, **1981**, 60, 453.

22) Winans, R. E.; McBeth, R. L.; Meinikov, P. E.; Botto, R. E., *Proc. 7th Int. Conf. Coal Sci. Vol. II*, **1993**, 515.

Table I

	Molecules Per 100 Initial Carbons				
Coal	**CH_4**	**CO_2**	**H_2O**	**CO**	**Total Oxygen in These Gases**
Beulah Zap	0.26	1.58	4.07	0.21	7.44
Wyodak	0.20	0.84	3.30	0.40	5.38
Illinois #6	0.40	0.32	0.56	0.05	1.25
Blind Canyon	0.33	0.22	0.54	0.08	1.06
Pittsburgh #8	0.44	0.56	0.34	<0.05	1.46
Lewiston	0.46	0.11	0.19	<0.05	0.41
Upper Freeport	0.09	0.06	0.12	<0.05	0.24
Pocahontas	0.05	0.05	0.10	<0.05	0.20

Table II

Coal		Atoms Per 100 Initial Carbons			
		Total Org. Oxygen	-O	C=O	O-C=O
Beulah Zap	Fresh	18.8	11.2	1.4	6.2
	Char	10.7	9.2	0.5	1.0
Wyodak	Fresh	16.9	10.4	1.3	5.2
	Char	10.8	9.3	0.5	1.0
Illinois #6	Fresh	10.9	9.9	0.4	0.6
	Char	8.2	8.2	0.0	0.0
Blind Canyon	Fresh	10.0	9.6	0.4	0.0
	Char	8.5	8.5	0.0	0.0
Pittsburgh #8	Fresh	7.8	6.8	0.9	0.0
	Char	6.2	6.2	0.0	0.0
Lewiston	Fresh	8.0	6.8	1.2	0.0
	Char	6.5	6.5	0.0	0.0
Upper Freeport	Fresh	4.5	3.9	0.6	0.0
	Char	3.8	3.8	0.0	0.0
Pocahontas	Fresh	3.2	3.2	0.0	0.0
	Char	3.0	3.0	0.0	0.0

Table III

Coal		XPS Mole Percent (± 3.0)		
		Pyridinic	Pyrrolic	Quaternary
Beulah Zap	Fresh	26	58	16
	Char	29	60	11
Wyodak	Fresh	25	60	15
	Char	30	61	9
Illinois #6	Fresh	26	62	12
	Char	30	63	7
Blind Canyon	Fresh	31	55	14
	Char	39	57	4
Pittsburgh #8	Fresh	32	61	7
	Char	35	63	2
Lewiston	Fresh	31	60	9
	Char	34	63	3
Upper Freeport	Fresh	28	65	7
	Char	35	63	2
Pocahontas	Fresh	33	64	3
	Char	34	65	1

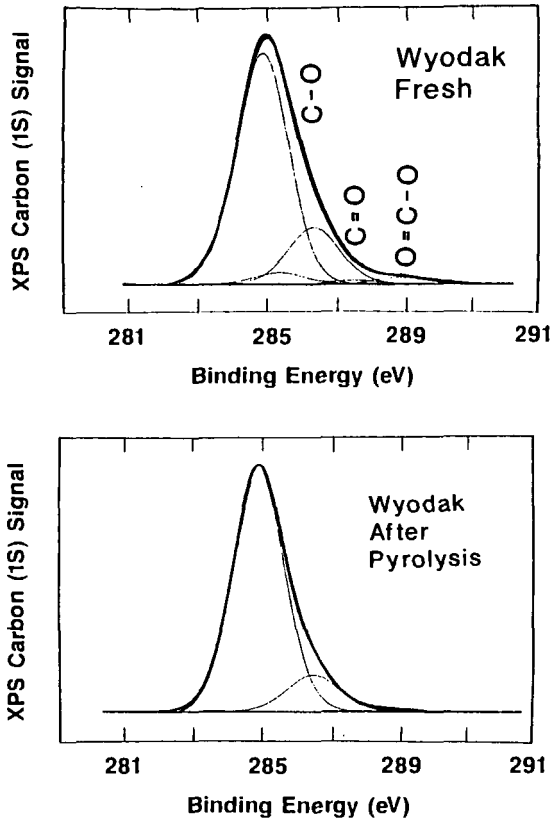

Figure 1

Top) XPS carbon (1s) spectrum of fresh Wyodak coal after background subtraction. Included in the figure are the results of the curve resolution analysis. Bottom) XPS carbon (1s) spectrum after background subtraction of Wyodak coal pyrolyzed at 400 Celcius. Included in the figure are the results of curve resolution analysis.

ROLE OF ON-LINE MASS SPECTROMETRY FOR STUDYING THE STRUCTURE/REACTIVITY RELATIONSHIPS AND CONVERSION PROCESSES OF COAL

Henk L.C. Meuzelaar, Center for Micro Analysis & Reaction Chemistry
University of Utah, Salt Lake City, UT 84112

KEYWORDS: on-line mass spectrometry techniques; coal structure/reactivity studies; coal conversion process monitoring

INTRODUCTION

Less than two decades ago a typical mass spectrometer was an extremely expensive and delicate instrument that would completely take up a moderately sized laboratory room. Few coal scientists or engineers had access to such an instrument and even fewer mass spectrometrists were willing to "contaminate" their instrument with something as complex and dirty as coal and its tar. Against this historic background it is nothing less than amazing that as early as 1966 Vastola et al. [1] at Penn State University, using a finely focussed ruby laser and a time of flight (TOF) mass spectrometer, already carried out laser pyrolysis experiments on coal samples inside the ion source. Their example was soon followed by Joy et al., [2]. However, since Vastola's experiment was too far ahead of the state-of-the-art in signal processing electronics it would take more than 15 years before his group was able to obtain reproducible pyrolysis mass spectrometry (Py-MS) patterns from a series of PSOC coal samples [3].

In the meantime, the same coal samples had already been studied by Curie-point pyrolysis mass spectrometry (Py-MS) in our own laboratory [4] as part of a series of 104 Rocky Mountain Province coals. The latter study demonstrated the reproducibility of carefully designed, dedicated Py-MS instruments, as well as the power of multivariate statistical analysis techniques, for reducing the voluminous MS data and bringing out the most significant chemical components and trends.

Already during the late seventies and early eighties several organic geochemistry groups, e.g., at the Technical University Delft (DeLeeuw et al. [5]) at Chevron (Gallegos [6]) and at the University of Bartlesville (Philp et al. [7]) had started to use pyrolysis-gas chromatography/mass spectrometry to characterize a broad range of different coals and coal macerals. Yet another promising instrumental approach, namely thermogravimetry (TG) in direct combination with MS (also reported by Gallegos [6]) was being developed further by Szekely's laboratory in Budapest [8] followed by the development of a vacuum TG/MS system in our own laboratory (Yun [9]). In the mid eighties further advances in TG/MS techniques were reported by Ohrbaeh and Kettrup [10] using a commercially available molecular beam type interface. Most recently, a homebuilt TG/MS system based on similar principles was successfully tested in our own laboratory [11]. Finally, the promising results of the various TG/MS combinations prompted us to pursue more sophisticated analytical configurations such as TG/IR/MS [12] and TG/GC/MS [13], with the latter method eventually being adapted to on-line analysis of high pressure reactions, as reported by Kui et al. [14].

In the mid eighties, Schulten's laboratory in West Germany started pursuing an entirely different approach involving direct probe type pyrolysis of coal directly in the ion source of a high resolution magnetic sector MS system with field ionization (FI) and field desorption (FD) capabilities [15]. Related FIMS work was reported at SRI by Malhotra et al. [16]. That a wealth of information on coal conversion processes and reaction products could also be obtained by high resolution MS in combination with other ionization methods, such as low voltage electron ionization (LVEI) and fast atom bombardment (FAB) was elegantly demonstrated by Winans et al. [17] at Argonne National Laboratory. Last year, a collaborative comparison between different desorption/ionization methods capable of producing ion signals up to several thousand Dalton was performed by two different research groups [18]. Barely was their report submitted or one of the authors (Herod, et al.) published several articles raising the upper mass limit of detected ion species to 4,000 and 270,000 Dalton for FAB [19] and matrix assisted laser desorption/ionization (MALDI [20]), respectively.

Obviously, high mass MS techniques are presently a hot topic in coal science. However, in order to keep the scope of this article within the limitations posed by the ACS Fuel Chemistry Division preprint format, only techniques and applications of MS methods involving direct coupling to micro-scale or upscale coal conversion reactors will be discussed.

METHODOLOGY

Figure 1 depicts six basic configurations that have found application in coal science and technology. Sequentially progressing from configuration I to configuration VI we notice an increasing spatial and temporal separation between reaction and ionization zones. Configurations I-III involve vacuum pyrolysis. However, whereas in configuration I reaction and ionization zones overlap more or less completely, configurations II and III require some vapor transport mechanism. Configurations IV and V feature (near)ambient pressure reactors whereas configuration VI depicts a high pressure reactor. The degree of separation between reaction and ionization regions in configurations IV and V progresses from a molecular beam or leak type inlet (IV) to a capillary transfer line or full fledged chromatographic column (V). The final configuration (VI) shows a high pressure reactor region with a two stage coupling (involving an intermediate ambient pressure step) to the mass spectrometer vacuum.

Configuration I - Integral Pyrolysis/Ionization Zones - Examples include the LAMMA (Laser Microprobe Mass Analyzer) experiments (Dutta and Talmi [21]) and the pyrolysis field desorption MS studies (Schulten [22]) reported in 1982. Also some of the early laser ionization MS experiments reported by Vastola et al. [23] and Joy et al. [2] fall into this category. More recently, FAB studies were described by Winans et al. [24] and by Herod et al. [19] whereas laser desorption/ionization experiments were reported by Herod et al. [25] and by John et al. [20]. Generally speaking, the interpretation of the results obtained by the integral degradation/desorption/ionization methods have two things in common: (1) very large ions (ranging from 10^3 to over 10^5 Daltons) are observed, and (2) chemical interpretation of the results has not yet been very successful.

Configuration II - Direct Probe Inlets - Much of the published on-line MS work falls under this broad category, which includes direct probe Py-FIMS, as well as Curie-point Py-MS and vacuum TG/MS studies. Also, the newer work reported by Vastola's group, involving LVEIMS of neutral laser pyrolysis products, falls under this category. As shown in Figure 2 results obtained by the various techniques can be surprisingly similar in spite of the large differences in pyrolysis, ionization and mass spectrometry methods used. This demonstrates that the underlying pyrolysis chemistry is quite constant and that a satisfactory degree of interlaboratory reproducibility is attainable when operating under chemically controlled, conditions (as is readily achievable in Configuration II experiments). Among these techniques, the pyrolysis field ionization MS results reported by the German [26] and US groups [16] stand out with regard to mass range covered (up to approx. 1200 amu) and the absenee of confusing fragmentation processes such as produced by conventional (70 eV) electron ionization. However, the upper mass range limit in Py-FIMS is determined by vapor transport limitations and ion transmission characteristics of the mass spectrometer. Remarkably similar spectra can be obtained by electron ionization at 12 eV, as reported by Taghizadeh et al. [27] and Yun et al. [28] and illustrated in Figure 2. As illustrated in Figure 3, the work performed with configuration II instruments has distinguished itself with regard to the application of advanced data reduction and pattern recognition methods [4, 29], especially when combined with time- and temperature-resolved MS data [30, 31].

Configuration III - Vacuum Manifold Inlets - The use of vacuum manifold type transfer lines between pyrolysis and ionization regions is generally the result of MS instruments equipped with batch (vapor) inlets being adapted to pyrolysis studies. Some of the work reported by Winans et al. [32] and by Burnham et al. [33] falls into this category. Also, Curie-point Py-MS studies using a so-called "expansion chamber" [34,35] could be included here. With properly heated, inactivated lines and short residence times results of vacuum manifold type inlets may become "nearly indistinguishable from category II direct probe inlet results. However, the risk of desorption losses and/or secondary reactions requires careful attention to experimental procedures.

Configuration IV - Molecular Beam Type Interfaces - The commercial TG/MS system used by Ohrbach and Kettrupp [10] has an inlet consisting of two nested quartz tubes with carefully aligned centerline pinholes, affording direct access of volatile products into the ion source of a quadrupole mass spectrometer. Nonetheless, the largest coal pyrolysis product ions reported by these authors appear to consist of relatively low MW phenols. A more recent inlet of this type developed by Nie et al. [11] features special flow arrangements designed to minimize condensation losses and the low voltage EI MS patterns obtained closely resemble the corresponding Py-FIMS profiles produced with configuration II type inlets, with peak intensities well into the m/z 400-500 range.

Configuration V - Transfer Line and GC Column Interfaces - Configurations falling into this category feature a narrow bore capillary transfer line which may or may not function as a GC column, depending on temperature and sample injection method used. A broad variety of Py-GC/MS type inlets have been used to study the organic geochemistry of coal and coal macerals

[36]. Closely related is the so-called transfer line GC (TLGC) interface between reaction and pyrolysis zone described by Maswadeh et al [37] for CO_2 laser pyrolysis studies of single coal particles (see GC/MS profiles in Figure 4). Furthermore, the capillary TG/MS interface used by Blaszo et al. [8] and the TG/IR/MS interface reported by our laboratory [12] could be included here, as well as the recent ruby laser Py-GC/MS studies reported by Greenwood et al. [38].

Configuration VI - High Pressure Transfer Line GC Interfaces - Most recently, Kiu et al. [14] described a two stage TLGC interface between a high pressure PG system and a quadrupole mass spectrometer permitting on-line monitoring of high pressure (hydro) pyrolysis reactions in coal under thermally and catalytically controlled conditions. Currently, work is underway in our laboratory to extend this approach to high pressure liquid flow-through reactors [39], thus permitting monitoring of coal hydroliquefaction processes, as illustrated in Figure 5.

APPLICATIONS

Fortunately, the bewildering array of techniques described appears to conceal a limited number of experimental objectives, namely: (A) elucidation of coal composition and structure as well as structure/reactivity relationships; (B) mechanistic and kinetic studies of coal reactions and (C) optimization of coal conversion processes as well as a characterization of conversion products.

(A) Structural Characterization - This includes many of the organic geochemistry studies using type V (Py-GC/MS) inlet configurations as well as the type I desorption/ionization experiments by means of laser, fast atom bombardment or field desorption techniques. Most recently John et al. reported the "identification" of molecular masses up to 270,000 Dalton by Matrix-Assisted laser desorption MS [20]. Major contributions in this areas have also been made by direct probe type (Configuration II) pyrolysis FIMS and HRFIMS studies and by the vacuum manifold (Configuration III) type HREIMS work shown in Figure 6. It can be stated without exaggeration that our current understanding of the molecular composition and structure of coal and its structure/reactivity relationships, however incomplete, depends more strongly on mass spectrometry than on any other analytical methodology.

(B) Reaction Mechanisms and Kinetics - Particularly informative are the time- and temperature-resolved pyrolysis MS studies performed with category II (see Figure 7) as well as IV type experiments which combine the ability to detect labile, reactive species while permitting quantitative analysis of rates and yields. Combined thermogravimetry/mass spectrometry methods are especially well suited for such studies since knowledge of the precise weight loss rates and yields without knowing the chemical identity of the reactive species involved, and *vice versa*, does not fulfill the elementary criteria for kinetic and mechanistic studies. Nevertheless, useful information has been contributed by type III (e.g., HRMS) and type IV (e.g., laser Py-GC/MS) configurations, whereas type VI (high pressure TLGC/MS) methods are starting to open up a whole new field of study for catalytic reaction mechanisms and kinetics.

(C) Conversion Process and Product Characterization - Field Ionization MS techniques have gained an especially strong reputation in this area, although it should be pointed out that measurable vapor pressures are a strict requirement. Completely nonvolatile conversion products can only be analyzed by means of category I desorption/ionization techniques, although generally in an off-line mode. Sufficiently volatile conversion products can, of course, be analyzed by category V (or VI) on-line GC/MS techniques. Due to the availability of MS reference libraries containing over 200,000 standard spectra GC/MS techniques are likely to remain unparalleled in their ability to provide positive chemical identification of compounds in complex mixtures. For dynamic processes type IV molecular beam inlets offer a superior solution. However, if positive chemical identification is required short column "transfer line" GC methods may be the best compromise.

ACKNOWLEDGEMENTS

This work was sponsored by the Advanced Combustion Engineering Research Center (funds for this Center are received from the National Science Foundation, the State of Utah, 23 industrial participants and the U.S. Department of Energy) and by the Consortium for Fossil Fuel Liquefaction Science (DOE grant no. UKRF-4-23576-90-10).

REFERENCES

1. Vastola, F.J., et al. in *Advances in Organic Geochemistry*, 1966, 427.
2. Joy, W.K., et al., *Nature*, 217, 1968, 641.
3. McGahan, L.J., M.S. Thesis, Penn State University, May 1983.
4. Meuzelaar, H.L.C., et al. *Fuel*, 63(5), 1984, 640.

5. Van Graas, G., et al., in *Advances in Organic Geochemistry*, 1979, 485.
6. Gallegos, E.J., in *Analytical Chemistry of Liquid Fuel Sources, Advances in Chemistry*, #170, 1978, ACS (publ.), Washington D.C., 13.
7. Philp, R.P., et al., *J. Anal. Appl. Pyroly.*, 4, 1982, 143.
8. Blaszo, M., et al., *J. Anal. Appl. Pyroly.*, 8 1985, 255.
9. Yun, Y., et al., *ACS Preprints, Div. Fuel Chem.*, 33(3), 1988, 75.
10. Ohrbach, K.-H., et al., *J. Anal. Appl. Pyroly.*, 8, (1985), 195.
11. Nie, X. et al., *ACS Preprints, Div. Fuel Chem.*, 1994, San Diego, in press.
12. Dworzanski, J., et al., *ACS Preprints, Div. Fuel Chem.*, 37(2), 1992, 424.
13. McClennen, W.H., *Anal. Chem.*, 65, 1993, 2819.
14. Lui, K, X. et al., *ACS Preprints, Div. Fuel Chem.*, 1994, San Diego, in press.
15. Schulten, H.-R., Marzec, A., *Fuel*, 65, 1986, 855.
16. Malhotra, R., et al., *ACS Preprints, Div. Fuel Chem.*, 36(3), 1991, 1252.
17. Winans, W.E., in *Advances in Coal Spectroscopy*, 1992, Plenum Press, N.Y., 255.
18. Herod, A.A., et al., *Fuel*, 72, 1993, 31.
19. Herod, A.A., et al., Fuel, 72, 1993, 1317.
20. John, P., et al., *Rapid Comm. Mass Spectrom.*, 7, 1993, 795.
21. Dutta, R.K., Talmi, Y., *Fuel*, 61, 1982, 1241.
22. Schulten, H.-R., *Fuel*, 61, 1982, 670.
23. Vastola, F.J., et al., in *Spectrometry of Fuels*, 1970, Plenum Press, N.Y., 29.
24. Winans, R.E., *J. Anal. Appl. Pyroly.*, 20, 1991, 1.
25. Herod, A.A., *J. Chem. Soc., Chem. Commun.*, 9, 1993, 767.
26. Schulten, H.-R., et al., *Energy & Fuels*, 6, 1992, 103.
27. Taghizadeh, K., et al., *Fuel Processing Tech.*, 26, 1990, 181.
28. Yun, Y., Meuzelaar, H.L.C., *Energy & Fuels*, 5, 1991, 22.
29. Meuzelaar, H.L.C., et al., in *Computer-Enhanced Analytical Spectroscopy*, III, 1992, Plenum Press, N.Y.
30. Chakravarty, T., et al., *Energy & Fuels*, 2, 1988, 400.
31. Simmleit, N., et al., in *Advances in Coal Spectroscopy*, 1992, Plenum Press, N.Y., 295.
32. Winans, R.E., et al., *ACS Preprints, Div. Fuel Chem.*, 33(3), 1988, 85.
33. Burnham, A.K., et al., *Energy & Fuels*, 3, 1989, 42.
34. Tromp, P.J.J., et al., in *New Trends in Coal Science*, 1988, 241.
35. Meuzelaar, H.L.C., et al., *Curie-point Pyrolysis Mass Spectrometry of Recent and Fossil Biomaterials; Compendium and Atlas*, 1982, Elsevier, Amsterdam.
36. Vastola, F.J., McGahan, L.J., *Fuel*, 66, 1987, 886.
37. Maswadeh, W., et al., *Energy & Fuels*, 7, 1993, 1006.
38. Greenwood, P.F., *Anal. Chem.*, 65, 1993, 1937.
39. Gibbins, J.R., Kandiyoti, R., *Fuel*, 70, 1991, 909.
40. Maswadeh, W., et al., *ACS Preprints, Div. Fuel Chem.*, 37(2), 1992, 699.
41. Nie, X., et al., *ACS Preprints, Div. Fuel Chem.*, 38(4), 1993, 1147.
42. Yun, Y., et al., in *Advances in Coal Spectroscopy*, 1992, Plenum Press, N.Y., 275.

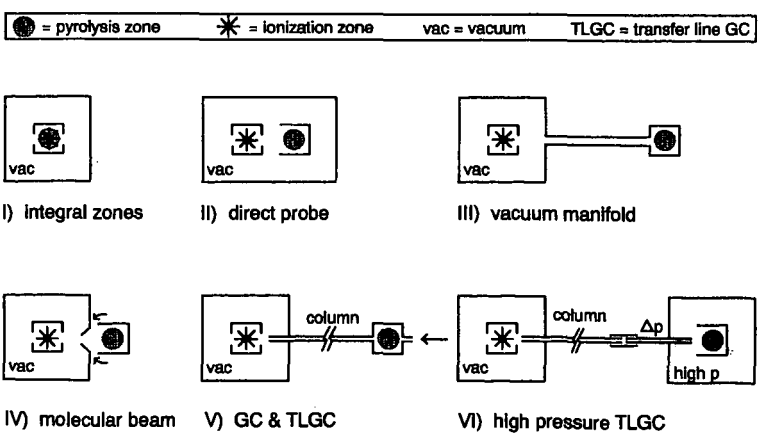

Figure 1. Schematic representation of six different pyrolysis mass spectrometry interface configurations ordered according to degree of separation between pyrolysis and ionization zones.

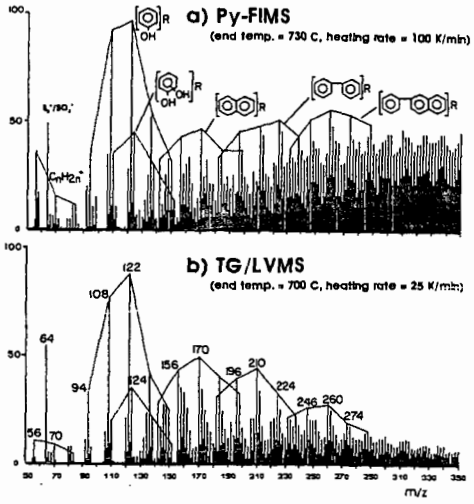

Figure 2. Comparison of mass pyrograms of hvAb Pittsburgh #8 coal obtained by (a) direct probe (100 μg sample) Py-FIMS and (b) vacuum thermogravimetry (5 mg sample) in combination with low voltage (12 eV) EIMS (from ref. 28).

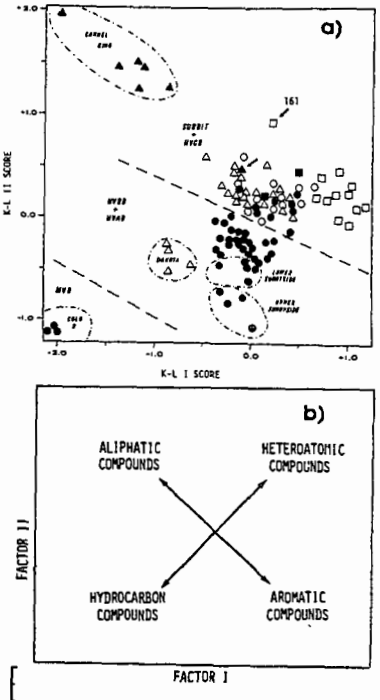

Figure 3. (a) Karhunen-Loeve ("factor") score plot for Curie-point pyrolysis mass spectra from 104 Rocky Mountain Province coals showing spontaneous separation by rank and depositional effects; (b) Chemical interpretation of the observed clustering trends (from ref. 4).

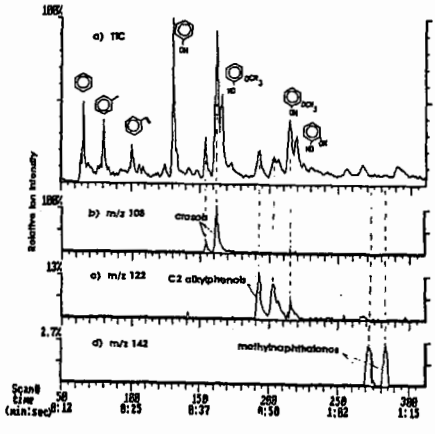

Figure 4. Typical CO_2 laser pyrolysis GC/MS profile of a 100 μm dia Beulah Zap lignite particle at 20 msec pulse duration showing effective GC separation within approx. 70 sec as well as dominant hydroxy-and methoxy-aromatic signals typical of low rank coal (from ref. 40).

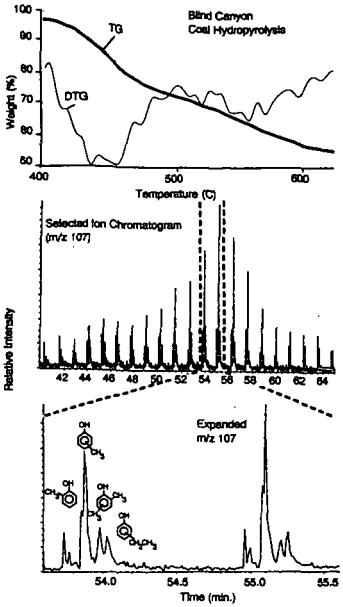

Figure 5. TG/GC/MS profiles of a 50 mg hvAb Blind Canyon coal sample in H_2 at 900 psi obtained at a heating rate of 10 K/min, demonstrating feasibility of on-line GC/MS monitoring of high pressure coal conversion reactions (from ref. 41).

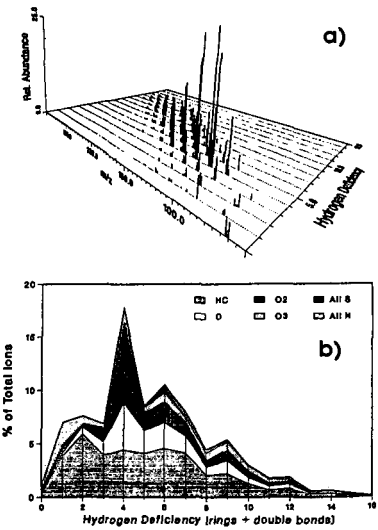

Figure 6. (a) Peaks containing one, two, or three oxygens from Py-HRMS of APCS #8 lignite; (b) area chart of the distribution of heteroatoms for the same coal (from ref. 17).

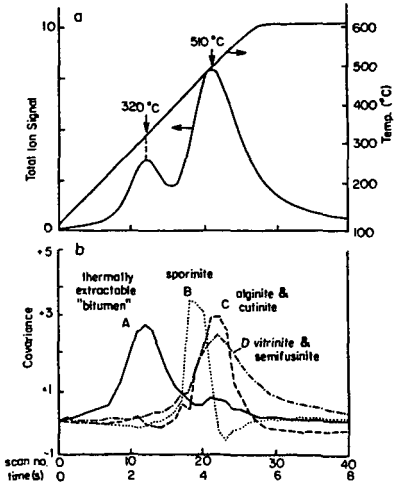

Figure 7. Time-resolved Curie-point pyrolysis MS profiles of a Pittsburgh #8 coal showing "deconvolution" of the total ion signal profile (a) into components A-D (b) by means of factor analysis techniques (from ref. 42).

THE MEASUREMENT OF ^{13}C CHEMICAL SHIFT TENSORS IN COMPLEX POLYCYCLIC AROMATIC COMPOUNDS AND COALS BY AN EXTREMELY SLOW SPINNING MAS EXPERIMENT

R.J. Pugmire*, J.Z. Hu+#, D.W. Alderman+, A.M. Orendt+, C. Ye#, and D.M. Grant+
Departments of Chemistry+ and Chemical and Fuels Engineering*, University of Utah, Salt Lake City, Utah 84112 USA
Wuhan Institute of Physics#, the Chinese Academy of Sciences, P.O. Box 71010, Wuhan 430071, China

NMR, Chemical Shift Anisotropy, Coal

INTRODUCTION

The ^{13}C CP/MAS experiment has proven to be a powerful technique for obtaining high resolution spectra in complex solids such as coal (1). MAS narrows the chemical shift anisotropy (CSA) to its isotropic shift when the sample spinning speed is greater than the anisotropy. While the isotropic chemical shift is useful in characterizing chemical structure, the principal values of the chemical shift tensor provide even more information. These principal values are available from the powder pattern obtained from a stationary or slowly spinning sample. Unfortunately, the overlap of many broad powder patters in a complex solid often prevents the measurement of the individual principal values.

In an effort to address this problem of spectral overlap, many 2D techniques have been developed to simultaneously obtain the dispersion by isotropic shift, such as produced by MAS, in one dimension and the tensorial information as separate powder patterns in the second dimension (2-6). A very successful technique is the slow spinning modification of the magic angle hopping experiment (2) recently proposed by Gan (5), which we call the Magic Angle Turning (MAT) experiment (6). This experiment has a number of advantages over earlier 2D methods. The use of very slow spinning speeds (<50 Hz) favors the quantitative polarization of all carbons and allows the use of a large volume sample rotor resulting in a typical 2D spectrum acquisition requiring less than 24 hours. The mechanical device for slow spinning is very stable and high resolution in the isotropic chemical shift dimension can be easily obtained. The MAT experiment could be done on a suitably stable MAS probe. The only disadvantage of the original MAT experiment is that data acquisition starts right after the last pulse, causing distortion in the evolution dimension (the second dimension) even if a delay as short as 20μs is used.

In this paper, a triple-echo MAT sequence, previously described (6,7), is employed which improves the 2D baseline. Two additional experiments, using short contact times and dipolar dephasing techniques, are also employed to further separate the powder patterns of protonated and nonprotonated carbons in complex compounds. Experimental results on representative model compounds as well as coals are presented in this paper.

EXPERIMENTAL DETAILS

The experiments were performed on a Varian VXR-200 NMR spectrometer. A large-sample-volume slow-spinning MAS probe was constructed for the experiment. The probe holds approximately 5 cm^3 of sample and has a very stable sample spinning rate ranging from 20 to 300 Hz. A spinning rate of 44 HZ was used for the experiments discussed below. 1,2,3-trimethoxybenzene (TMB) and 2,3,-dimethylnaphthalene were used as received from Aldrich and the coal samples were obtained from Argonne Premium Coal Sample Bank.

RESULTS AND DISCUSSION

The triple-echo and dipolar dephased MAT sequences are given in Fig. 1. The 2D spectrum obtained in this manner and plotted in a square has the bands inclined relative to the acquisition dimension axis at an angle $\arctan(\omega_2/(3\omega_1))$, where ω_1 and ω_2 are the evolution and acquisition spectral widths, respectively. In order to obtain a 2D spectrum whose projection along one axis gives the isotropic shift spectrum, these data must be sheared through the inclination angle. For all experiments reported in this paper, the evolution-time increments are chosen to be three times the acquisition dwell times, so that the spectral widths for the acquisition dimensions are three times those for the evolution dimensions. This results in 2D spectra with bands inclined at an

angle of arctan(1) = 45°. After a 45° shearing operation, the isotropic shift spectrum is obtained from the projection on one axis, while the powder patterns are taken as the perpendicular slices at the isotropic shift positions. The resultant contour plot spectrum of 1,2,3-trimethoxybenzene (TMB) is shown in Fig. 2. The resolution achieved for the isotropic chemical shift dimension is about 1 ppm, as illustrated in Fig. 2, where the resonance for M_1 and M_3, separated by 1 ppm, are resolved (8). The flat baseline in the isotropic shift projection of Fig. 2 indicates the quality of the 2D baseline achieved, which is essential for the quantitative measurement of the aromaticity (f_a) of coal. The individual powder patterns, from which the principal values of the chemical shift tensor can be extracted, are displayed in Fig. 3.

Results from a triple-echo MAT spectrum of 2,3-dimethylnapthalene (2,3-DMN) are given in Fig. 4 and Table 1. The methyl carbon isotropic shift at 21 ppm is well-separated from those of the ring carbons, and is easily assigned. Assignment of the closely-spaced aromatic carbon shifts is more difficult. An expansion of the aromatic region of the MAT isotropic-shift projection and a similar portion of the MAS spectrum are shown in Figure 4(a). These spectra are interpreted as showing isotropic shift peaks at 124 ppm, 128 ppm, 133 ppm, and 134 ppm. The 128 ppm peak has double intensity, but it is no wider than the single intensity peak at 124 ppm, indicating that two pairs of chemically equivalent carbons have virtually identical isotropic shifts in the solid. A dipolar-dephasing MAS spectrum (not shown) indicates that the nonprotonated carbons are those with isotropic shifts of 133 ppm and 134 ppm. A tentative assignment of the aromatic carbons can be made by assuming that the order of the solid isotropic shifts is the same as that in solution. The chemical shift assignments for 2,3-DMN in solution reported by Wilson and Stothers (9) are given in Table 1. On the basis of the isotropic shift order the 124 ppm shift is assigned to $C_{6,7}$, the 133 ppm shift to $C_{4a,8a}$, and the 134 ppm shift to $C_{2,3}$. These assignments are consistent with the dipolar-dephasing MAS data. The isotropic shifts of $C_{1,4}$ and $C_{5,8}$ have moved together in the solid to form the double-intensity peak at 128 ppm. Assignment of $C_{1,4}$ and $C_{5,8}$ requires examination of the principal values of the tensors and the details for the assignments of all carbons are given in reference 6. The important point of note from the example of 2,3,DMN is that the triple-echo MAT experiment provides sufficient resolution to deconvolute overlapping tensor principal values.

The combination of triple-echo MAT, dipolar dephasing triple-echo MAT, and short-contact-time triple-echo MAT experiments can be used as a basic technique for extracting ^{13}C tensor information in complex powdered solids, *e.g.* coal. The flat 2D baseplanes produced by these modified sequences and the quantitative cross polarization of the MAT technique are especially important to this application. Shown in Figure 5(a) is the 2D contour plot of a spectrum of Pocahontas coal obtained with the triple-echo MAT pulse sequence; the projection onto the isotropic shift axis is given in Figure 5(b). The aromaticity (f_a) obtained by a volume integration of the spectrum in the aliphatic and aromatic regions is 0.86, in good agreement with the value of 0.86 obtained by a variable contact time of ^{13}C MAS experiment at a field of 2.35T (1). Pocahontas coal powder pattern slices are shown in Figure 6. The normal triple-echo MAT powder pattern at an isotropic shift of 20 ppm in Figure 6(a) corresponds to methyl carbons on aromatic rings. The dipolar dephasing triple-echo MAT powder pattern at 139 ppm in Figure 6(e) arises from the substituted aromatic carbons, some of which cluster in the 135-139 ppm range. Figure 6(b) shows the normal triple-echo MAT powder pattern from the overlapping protonated and nonprotonated aromatic carbons at 124 ppm. These overlapping patterns are successfully separated in Figures 6(c) and 6(d) by the short contact time and the dipolar dephasing experiments, respectively, into patterns characteristic of protonated and nonprotonated (bridgehead) carbons. Nonprotonated and protonated structural types can thus be distinguished in coal by these MAT techniques. The principal values of the tensors for different types of carbons obtained by measuring the shift at the peaks and half-heights of the breakpoints are given in Table 2. The principal values are in good agreement with those obtained by a 1D variable-angle spinning experiment (10). The extraction of the methyl powder pattern, difficult to see in a coal by any other technique, further demonstrates the power of the MAT experiment.

With the MAT experiment we have examined a number of anthracite coal as well as the coals from the Argonne Premium Sample Bank.

It is clear that a great deal of information is available in the experimental data and we are evaluating methods for analysis of the principal value data. The quantitative aspects of the MAT experiment on coals in portrayed in Fig. 7. The triple-echo MAT values of aromaticity correlate closely with those reported by Solum (1). A careful analysis of the quantitative nature of the experiment will be pursued in the future.

CONCLUSIONS

The data presented in this study demonstrate that the Magic Angle Turning experiment enables the measurement of ^{13}C principal values in complex powdered solids by separating tensor powder patterns according to their isotropic shifts. Furthermore, the principal values of different types of tensors are recognizable even when the isotropic shifts overlap. The triple-echo MAT experiment produces 2D spectra with flat baseplanes which are well-adapted to quantitative analysis. Protonated and nonprotonated carbons may be separated by the short-contact-time and dipolar-dephasing variants of the triple-echo MAT experiment. The major problems associated with obtaining MAS spectra at high fields, the very high spinning speeds required to suppress or separate sidebands and the consequent difficulty in uniformly polarizing all spins, are eliminated by the MAT experiment. The triple-echo MAT experiment effectively suppresses spinning sidebands at low rotation frequencies, and the slowly rotating sample appears to promote the polarization of all spins. To date, none of the experiments performed in this laboratory on a wide range of model compounds exhibit recognizable magic angle holes. The MAT experiments described above are particularly promising for the investigation of complex solids such as coal at high fields. Hence, it appears that the MAT experiment will be very useful in the study of a wide range of complex materials. A particular advantage is found in the relatively high resolution features of the experiment. In the isotropic chemical shift dimension the spectral resolution is comparable to that of a traditional CP/MAS experiment, while the uncertainty in the principal values in the powder pattern projections is estimated at ±2 ppm.

ACKNOWLEDGMENTS

This work was supported by the Pittsburgh Energy Technology Center through the Consortium for Fossil Fuel Liquefaction Science (Contract number DE-FC22-89PC89852) and by the Department of Energy Basic Energy Sciences (Contract number DE-FG02-86ER13510). The assistance of Yi Jin Jiang in building the probe and Dennis Edwards in constructing the optic sensor for detecting the rotation frequency is greatly appreciated. Julion Facelli and Mark Solum are gratefully acknowledged for their helpful discussions. Zhehong Gan, who invented the original MAT experiment, is particularly acknowledged for his cooperation.

REFERENCES

1. Solum, M.S., Pugmire, R.J., and Grant, D.M., Energy & Fuel, 1989, **3**, 187.
2. Bax, A., Szeverenyi, N.M., and Maciel, G.E., J. Magn. Reson., 1983, **52**, 147.
3. Maciel, G.E., Szeverenyi, N.M., and Sardashti, M., J. Magn. Reson., 1984, **64**, 365.
4. Kolbert, A.C. and Griffin, R.G., Chem. Phys. Lett., 1990, **166**, 87.
5. Gan, Z., J. Am. Chem. Soc., 1992, **114**, 8307.
6. Hu, J.Z., Orendt, A.M., Alderman, D.W., Pugmire, R.J., Ye, C., and Grant, D.M., submitted for publication.
7. Pugmire, R.J., Hu, J.Z., Alderman, D.W., Orendt, A.M., Ye, C., and Grant, D.M., Proceedings, 7th International Conference on Coal Science, Sept. 12-17, 1993, Banff, Alberta, Canada, p. 485.
8. Hu, J.Z., Alderman, D.W., Ye, C.,Pugmire, R.J., and Grant, D.M., Magn. Reson., 1993, **105**, 82.
9. N.K. Wilson and J.B. Strothers, J. Magn. Reson, 1974, **15**, 31.
10. Orendt, A.M., Solum, M.S., Sethi, N.K., Pugmire, R.J., and Grant, D.M., Advances in Coal Spectroscopy, Meuzelaar, H.L.C., Editor, Plenum Press, 1992, page 250.
11. Sherwood, M.H., Farelli, J.C., Alderman, D.W., and Grant, D.M., J. Am. Chem. Soc., 1991, **113**, 750.

Table 1.
Carbon-13 Chemical Shift Tensors in 2,3-Dimethylnaphthalene and Naphthalene.

Carbon	δ_{11}	δ_{22}	δ_{33}	$\delta_{iso.}$	$\delta_{sol.}$[b]
2,3-Dimethylnaphthalene[c]					
Methyl	30	25	8	21	20.1
$C_{1,4}$	218[d]	132	34	128	127.3
$C_{2,3}$	232	157	14	134	135.2
$C_{5,8}$	222[d]	142	20	128	126.7
$C_{6,7}$	225	135	11	124	124.8
$C_{4a,8a}$	207	197	-4	133	132.3
Naphthalene[e]					
C_1, C_4	224.7, 223.9	140.3, 145.6	22.8, 20.4	129.6	127.7
C_2, C_3	227.6, 227.6	139.3, 138.2	11.1, 10.4	125.7	125.6
C_{4a}	208.5	202.2	-5.9	134.9	133.3

a. Shift obtained from isotropic projection and MAS spectrum.
b. Solution shifts from Reference 9.

c. Solid shifts in ppm from TMS. Estimated error in solid data is ±2 ppm. The shifts are referenced via the methyl carbon of hexamethylbenzene at 17.3 ppm from TMS.
d. Calculated from δ_{22}, δ_{33}, and $\delta_{isotropic}$.

e. Solid shifts taken from Reference 11; the single crystal environment exhibits C_i symmetry and has two values for the alpha and beta carbons.

Table 2. ^{13}C chemical shift tensors in Pocahontas coal.[a]

Carbon type	δ_1 1	δ_2 2	δ_3 3	$\delta_{ave.}$	$\delta_{iso.}$
Methyl	35	22	5	20.7	20.3
Protonated	223	131	20	124.7	126.7
Nonprotonated	197	184	-8	124.3	124.0
Substituted	228	163	32	141.0	139.4

a. Shifts in ppm from TMS referenced via methyl carbon of hexamethylbenzene at 17.3 ppm from TMS.
b. Average of three principal value shifts.
c. Chemical shift of slice used.

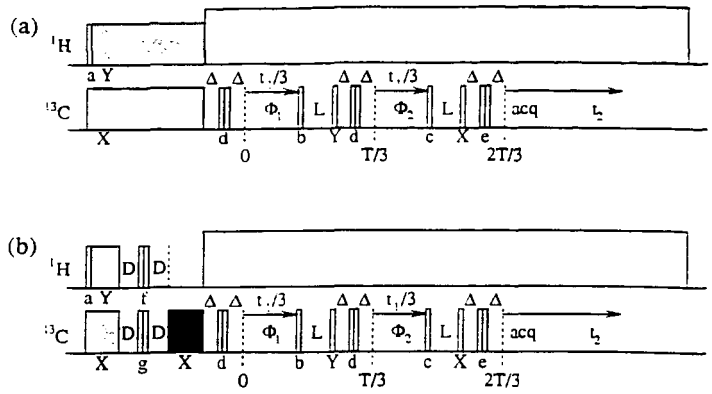

Figure 1. Pulse sequences for the 2D MAT experiments. 90° pulses are represented by single rectangles; two adjacent rectangles denote a 180° pulse. The cross-polarization pulses are shaded. The time T is an integral number of rotor periods (excluding a multiple of three rotor periods). The magnetization precesses in the transverse plane during the periods labeled f_1 and f_2, and is along the longitudinal axis during the periods labeled L.
(a) Normal triple-echo MAT pulse sequence. Δ is an echo delay time determined by the probe ring-down and receiver recovery time. The character above each pulse indicates the entry in the phase cycle table (reference 6) which gives the phase of the pulse.
(b) Dipolar dephasing triple-echo MAT pulse sequence. The spin-lock pulse is darkened. The character above each pulse indicates the entry in the phase cycle table (reference 6) which gives the phase of the pulse.

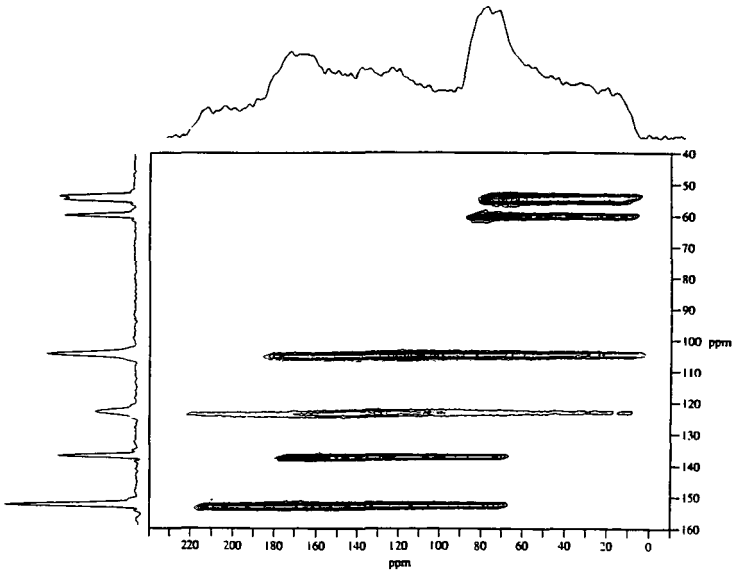

Figure 2. Contour plot of the central portion of the 1,2,3,-TMB 2D spectrum obtained by shearing the spectrum by 45°. The contour interval is 4% of the maximum peak height. The position of the breakpoints and peaks in the bands are given correctly by the ppm scale on the horizontal acquisition dimension axis. The isotropic shifts of the carbons can be read from ppm scale on the vertical axis. A 1.5 ppm Gaussian line broadening was applied in both dimensions, except that the isotropic shift projection was prepared from a 2D spectrum with no line broadening.

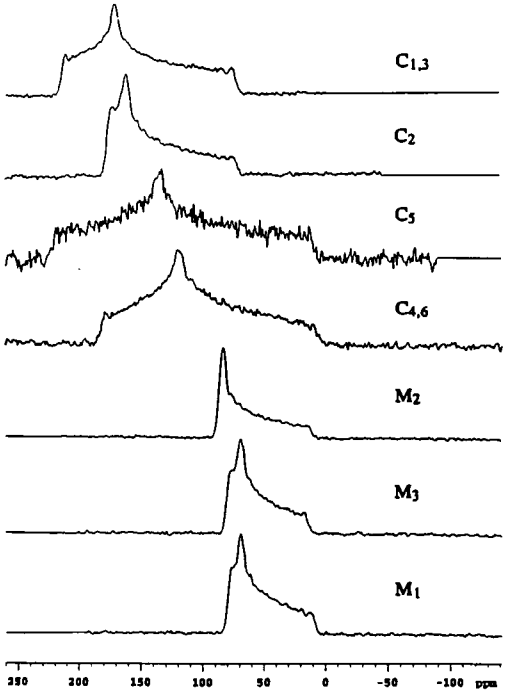

Figure 3. 1,2,3,-TMB powder patterns from slices of the triple-echo MAT 2D spectrum in Figure 2.

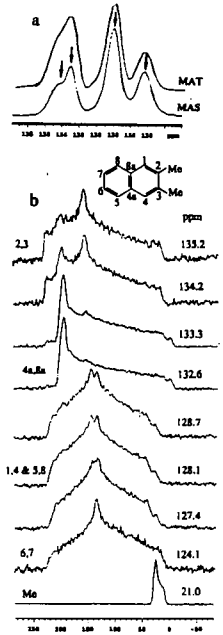

Figure 4. (a) The projection along the isotropic shift dimension and the CP/MAS spectrum of the aromatic carbons of 2,3-DMN with the isotropic shifts of the resolved resonances highlighted. (b) Powder pattern slices taken from normal triple-echo MAT spectrum of 2,3-DMN at indicated values of the isotropic chemical shift. The spectrum was obtained using a 4 ms contact time, spectral widths of $\omega_2=3\omega_1=32000$ Hz, a 12 s recycle delay, 32 scans for both real and imaginary FIDs, 120 evolution increments with a 93.75 μs increment time, and 26 hours total experimental time.

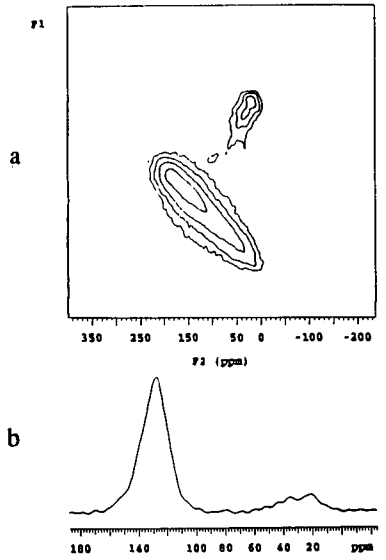

Figure 5. Pocahontas coal triple-echo MAT spectra.
(a) 2D spectrum obtained using a sample rotation rate of 4412.025 Hz, a Δ of 60 μs, a contact time of 2 ms, a recycle delay of 2 s, an acquisition dwell time of 31.25 μs, a t_1 increment of 93.75 μs, and 25 t_1 increments. Data was acquired for 512 scans in the real data set and 512 scans in the imaginary data set for a total measuring time of approximately 8 hr. A 2 ppm full-width-at-half-maximum Gaussian line broadening was applied in both dimensions.
(b) Projection of the 2D spectrum in (a) onto the isotropic shift axis.

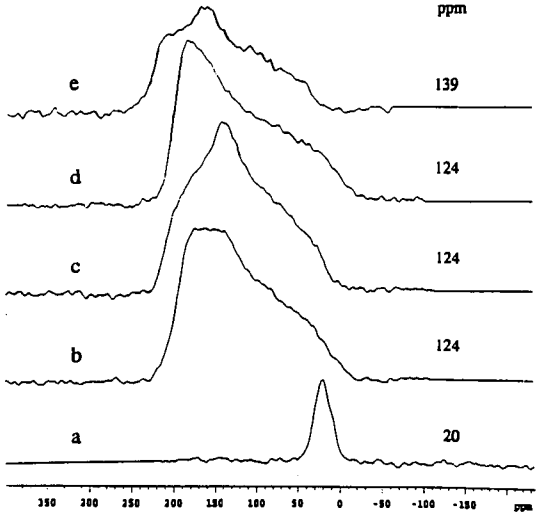

Figure 6. Pocahontas coal triple-echo MAT spectrum slices at selected isotropic shift values.
(a) Normal triple-echo MAT spectrum slice showing the allphatic carbons centered at 20 ppm;
(b) Normal triple-echo MAT spectrum slice showing the overlapping protonated and nonprotonated (bridgehead) carbons centered at 124.0 ppm.
(c) 50 μs contact time triple-echo MAT spectrum slice showing the protonated carbons centered at 124 ppm.
(d) Dipolar dephasing triple-echo MAT spectrum slice with D = 30 μs and a spin lock pulse of 1.5 ms showing the nonprotonated carbons centered at 124 ppm.
(e) Dipolar dephasing triple-echo MAT spectrum slice with D = 30 μs and a spin lock pulse of 1.5 MS showing the nonprotonated carbons centered at 139 ppm.

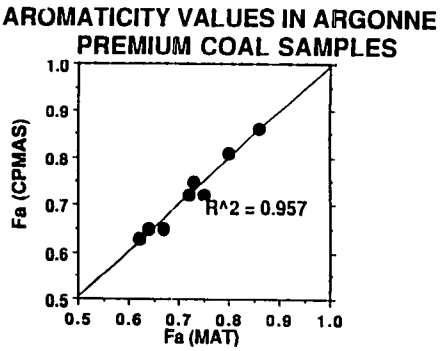

Figure 7. Comparison of the carbon aromaticity values (fa) for the Argonne Premium Coals as determined by the variable contact time CP/MAS technique (reference 1) and the triple echo MAT technique.

CURRENT STATUS OF FTIR IN THE ANALYSIS OF COAL STRUCTURE

Paul Painter, Maria Sobkowiak, Shahrzad Heidary and Michael Coleman
Polymer Science Program
Penn State University
University Park, PA 16802

INTRODUCTION

Infrared spectroscopy has been a basic "workhorse" technique for coal characterization since the pioneering work of Brown nearly 40 years ago (1). The optical and data handling advantages of FTIR have allowed various advances, such as the introduction of "hyphenated" techniques (GC-FTIR, IR-Microscopy, etc.) and novel sampling methods (diffuse reflection, photo-acoustic measurement, etc.), but most of the problems in coal structural analysis remain the same; the quantitative determination of various functional groups in coal and how the concentration of these groups varies with, for example, oxidation or liquefaction.

In a short article of this type justice cannot be done to the range and scope of work reported by various groups. Accordingly, we will concentrate our attention on just one problem, but a problem that is of central importance in the analysis of coal structure; the determination of the aliphatic and aromatic CH content of coal and coal derived material.

THE NATURE OF THE PROBLEM AND THE CURRENT STATE OF THE ART

Unlike nmr, band intensities in the infrared spectrum do not give a direct measure of the proportions of the functional groups giving rise to those bands. For spectra obtained in transmission the relationship depends on absorptivities or absorption coefficients through a Beers law relationship. Accordingly, it is the determination of these absorption coefficients for coal that is the central problem in applying FTIR to the analysis of coal structure. There are essentially three methods that in the past have been used to obtain these parameters;

1) calibration using model compounds

2) studies of solvent extracts, where calibration is provided by proton nmr measurements of the same samples.

3) equating band intensities to elemental hydrogen content and solving the simultaneous equations that can be written for a set of samples.

In one form or another all of these methods were used by the scientists who pioneered spectroscopic studies of coal (1-9), but most recent studies have used methods 2 and 3 to determine absorption coefficients. We will review this work first and in the following section indicate how some new work with polymeric models may contribute to solving various problems.

The seminal work on the application of FTIR to the quantitative measurement of the aromatic and aliphatic CH content of coals was performed by Solomon (10) and Solomon and co-workers (11-13). They employed the third calibration method listed above, setting up a set of simultaneous equations for a set of coals and coal derived materials, where the hydrogen contents determined by elemental analysis are equated to the OH and CH contents through equations involving band intensities and absorptivities. The principle problem with this approach is the ill-conditioned nature of the equations, which can result (depending on the sample set) in a range of almost equally valid solutions (14-16). In their most recent studies, Solomon and Carangelo (13) addressed this difficulty and obtained better defined solutions by broadening the range of their sample set. However, it is possible that the methodology used in this work introduces a systematic error, which we will discuss below.

In our studies we have employed a different methodology to that used by Solomon and co-workers. Our approach follows the general lines described in some older work (15), where absorption coefficients were determined by characterizing pyridine soluble coal extracts. The aromatic and aliphatic CH content of these materials can be established independently using proton nmr measurements. Naturally, if the extracts have a different average structure to the parent coal, then this procedure will not be of much use. This is only a problem with low rank coals, however. (See reference 17).

In early work (14) we studied only eleven samples. This is clearly inadequate if we are to accurately determine variations with rank, petrography, geological history, etc. Accordingly, in a recent study we characterized the extracts obtained from a very broad range of coals (17). The initial set of samples consists of 44 North American coals and 17 Polish coals. The use of such a large sample set has also allowed us to examine the effectiveness of various sample preparation

techniques (e.g., KBr pellets vs. diffuse reflectance) and methodologies. Space does not allow us to present the details of this work here, but our conclusion can be grouped into six separate areas;

1. Our first set of conclusions deals with sampling and curve revolving methodology. First, because relatively small amounts of material are required for analysis (1-2 mg), variations due to the inhomogeneous nature of coal are important. It is therefore necessary to average the results of a number of KBr pellets ($\geq$5) in order to obtain consistent results. Second, in applying curve resolving methods to the stretching region of the spectrum, allowance must be made for the different band shapes of the aromatic and aliphatic modes. Ignoring this factor leads predominantly to errors in the determination of the areas of the aromatic modes, the much more intense aliphatic modes are barely affected.

2. The absorption coefficients determined for the stretching modes vary not only with rank, the values for bituminous coals being distinctly different to those obtained for lignites and sub-bituminous coals, but also with the origin of the coal. We believe this is a particularly important result and to illustrate the type of data we obtained we have reproduced in figure 1 values of the ratio's of the intensities of the aromatic and phatialic CH stretching modes plotted against the ratio of aromatic to aliphatic CH content of the coal extracts determined by proton nmr. When the bituminous coals in our sample set are considered together then there is clearly a band of values, but when separated according to origin (U.S. Interior and Eastern Province Coals, U.S. Rocky mountain coals and Polish coals), good straight line correlations are obtained. The slopes of the lines are different, however, which translates into a difference in the ratio of the absorption coefficients (aromatic CH/aliphatic CH). Because the lines are straight is it reasonable to conclude that these absorption coefficients, which represent an average over the functional groups present, do not vary *within* each sample set. Variations in the relative proportion of such groups, and hence the average absorption coefficient, appear to be more significant between bituminous samples of different origin. [Also, an equivalent plot obtained for lignites and sub-bituminous coals has a very different slope to those shown in figure 1].

3. We have also demonstrated (see reference 17) that the use of the aromatic out-of-plane region of the spectrum (900-700 cm^{-1}) must introduce a systematic error due to the presence of aliphatic rocking modes. This error depends on the absorption coefficient of such vibrations relative to the aromatic out-of-plane modes, but its size remains unknown at this point. This is important in that even thought we have successfully obtained absorption coefficients for the stretching modes (see figure 1), the measurement of the area of the aromatic CH band is particularly prone to error because of its weak intensity. Measurements based on the out-of-plane modes are much easier to make and alleviate many problems associated with curve resolving the stretching modes. We will return to this point in the following section as we believe there is a set of experiments that can be performed that will allow us to assess the extent of any error in using the area of the bands between 900 and 700 cm^{-1}. Preliminary experiments indicate that any error may be extremely small.

4. Similarities in the spectra and other considerations lead us to conclude that absorption coefficients for the pyridine extracts of bituminous coals can be applied to their parent material. This is not so for lignite and sub-bituminous coals, however, as the extracts are far more aliphatic than their parent material and appear to have very different absorption coefficients. A different procedure will have to be devised in order to determine absorption coefficients for these coals.

5. We have also characterized all of our samples using diffuse reflectance sampling methods. This technique is much easier to use and superficially less demanding than the preparation of KBr pellets and if we could establish appropriate procedures it would allow FTIR to be applied to coal characterization in a much more routine fashion. Unfortunately, the plots of the ratio of the intensities of the aromatic to aliphatic CH stretching modes show considerably more scatter than the equivalent plots for KBr pellets. The diffuse reflectance results are shown in figure 2. In part, this scatter may reflect a fundamental problem in the diffuse reflectance technique, in that weaker modes appear to be selectively enhanced in intensity (relative to absorption measurements) and this, in turn, depends on things such as packing (in the sampling cup) that are not easily controlled or reproducible.

6. Finally, how consistent are the results that have been obtained using different methodologies? The older work (compare refs 10-12 and 14-16) displayed some distinct differences, but there has been a remarkable convergence of values of the absorption coefficients obtained in more recent studies. Solomon and Carangelo(13) reported values for the absorption coefficients of the aliphatic CH stretching mode, a_{al}^{st}, and out-of-plane bending modes, a_{ar}^{op} of 744 and 684, respectively, for a Pittsburgh seam coal. These values are in remarkably good agreement with those reported in our work (17) for US bituminous coals from the Eastern and Interior Provinces (764 and 665, respectively, ref. 17). This agreement is truly extraordinary, considering the different methodologies employed in these studies. Clearly, as far as the stretching modes and the 900-700 cm^{-1} region of the spectrum are concerned, the procedures used to prepare KBr pellets, measure band areas, etc. must be producing equivalent results. Furthermore, the absorption coefficients determined for extracts by calibration with proton nmr.

are apparently also in agreement with the results of the procedure applied to whole coals and char, indicating an equivalence in structure. There remains the question of the extent of the error that is introduced by the rocking modes that also appear in the 900-700 cm^{-1} region of the spectrum, and this is where some new work sheds some light.

PHENOLIC RESINS AS MODELS FOR COAL

In order to determine the extent of any contribution of CH_2 aliphatic rocking modes to the bands between 900 and 700 cm^{-1} we have embarked on a study of various phenolic resins. Essentially, our plan is to prepare resins where the phenolic rings are protonated and the methylene linkages are deuterated (i.e., - CD_2-) and resins where this labeling is reversed. We have synthesized the first models and it appears from preliminary spectra that methylene vibrations contribute negligibly to the 900 - 700 cm^{-1} region of the spectrum. This work will be completed in the next two months and a more complete discussion presented at the conference. The synthesis of these resins has also opened up what might become a new and intriguing area of study involving the near infrared region of the spectrum, and we will conclude this paper with a brief discussion of these initial results.

The near infrared region (~9000 - 4000 cm^{-1}) of the spectrum of coals (and many other materials) has not been studied in great detail, but appears to be very sensitive to aromatic and aliphatic CH content (because these modes are overtones and combinations and are a result of a breakdown of quantum mechanical selection rules, they usually involve vibrations of protons, which are "light" and therefore more likely to be anharmonic). A comparison of the spectrum of an all-protonated and CD_2 linked resin is shown in figure 3. Coal has a similar spectrum, but with additional bands probably due to CH_3 species as illustrated in figure 4. It is particularly interesting that the modes between about 6300 cm^{-1} and 5500 cm^{-1} have a band near 6000 cm^{-1} which can be assigned to an overtone of aromatic CH stretching vibrations, that is much more intense than the aliphatic modes near 5700 cm^{-1}, reversing the intensity ratio of the fundamentals. This may prove to be very useful in quantitative work.

CONCLUSIONS

The development of FTIR techniques for the quantitative determination of the functional groups present in coal has advanced considerably in the past few years. There has been particular progress in the measurement of aliphatic and aromatic CH content, with a pleasing convergence in the values of the absorption coefficients obtained by different groups using different methodologies. It appears that the use of phenolic resins as models should enable us to "sort out" the remaining problems and also allow band assignments in the near IR region of the spectrum, thus opening up a new means of analysis.

ACKNOWLEDGMENT

We gratefully acknowledge the support of the Office of Basic Energy Sciences, Division of Chemical Sciences, Department of Energy, under Grant no. DE-FG02-86ER 13537.

REFERENCES

1. Brown, J. K., p. 744, J. Chem. Soc., 1955.
2. Brown, J. K. and Ladner, W. R. Fuel, 1960, 39, 87.
3. von Tschamler, V. H. and de Ruiter, E., Grenst. - Chem., 1962, 43, 16.
4. Durie, R. A. and Sternhell, S., Aust. J. Chem., 1959, 12, 205.
5. Durie, R. A., Schewchyk, Y. and Sternhell, S., Fuel, 1966, 45, 99.
6. Fujii, S., Fuel, 1963, 42, 17, and 341.
7. Retcofsky, H. L. and Friedel, R. A., Fuel, 1968, 47, 487.
8. Retcofsky, H. L., Applied Spectroscopy, 1977, 31, 116.
9. Retcofsky, H. L. and Friedel, R. A. in "Spectrometry of Fuels" Editor, R. A. Friedel, Plenum Press, 1070, Chapter 6.
10. Solomon, P. R., Prepr. Pap.-Am. Chem. Soc. Div. Fuel Chem., 1979 24 (2), 185.
11. Solomon, P. R., and Carangelo, R. M. Fuel, 1982, 61, 663.
12. Solomon, P. R., Hamblen, D. G., and Carangelo, R. M., ACS Symp. Ser, 1982, 205, 77.
13. Solomon, P. R. and Carangelo, R.M., Fuel, 1988, 67, 949.
14. Sobkowiak, M., Riesser, B., Painter, P. C., and Given, P. H. Fuel 1984, 63, 1245.
15. Riesser, B., Starsinic, M., Squires, E., Davis A., and Painter, P. Fuel, 1984, 63, 1253.
16. Painter, P. C. Starsinic, M., and Coleman, M. M. in Fourier Transform Infrared Spectroscopy, 1985, Vol. 4, 169.
17. Sobkowiak, M. and Painter, P. C. Fuel 1992, 71, 1105.

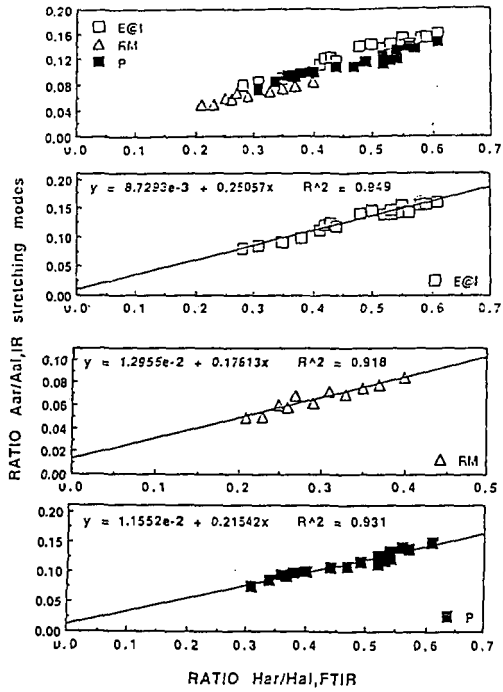

Figure 1. Plots of the ratio of the areas of the aromatic to phatialic CH stretching modes of KBr pellets of coal to aliphatic hydrogen determined by proton nmr.

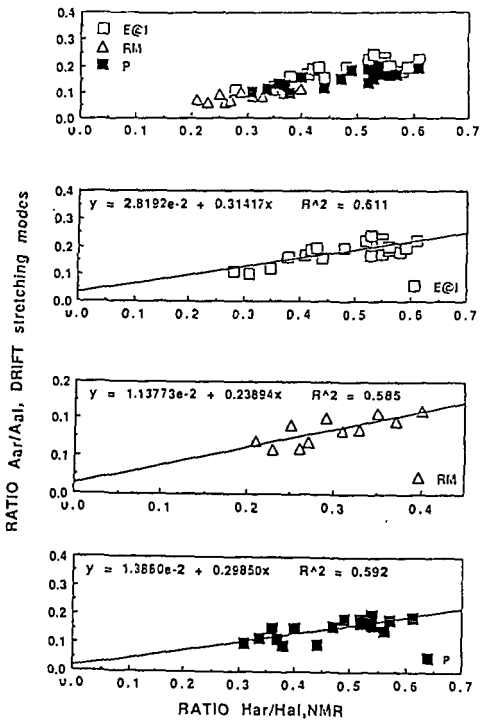

Figure 2. The same plots as Figure 1, but with the spectra of the extracts obtained by diffuse reflectance.

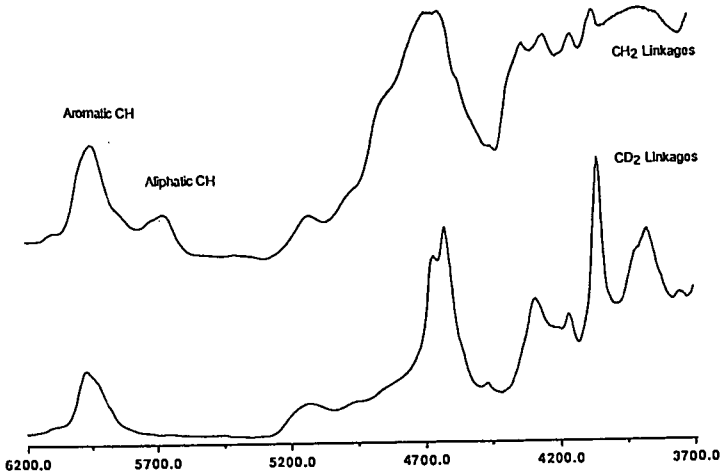

Figure 3. Near infrared spectrum of phenolic resins where the aromatic group are connected by CH_2 linkages (top) and CD_2 linkages (bottom).

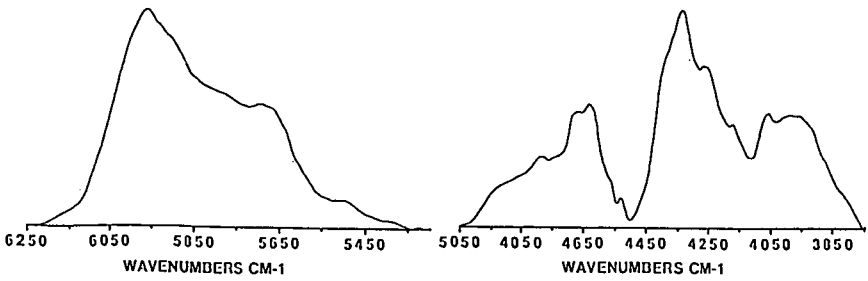

Figure 4. Near infrared spectrum of a coal extract.

POROSITY OF APCS COALS: THE ACCESSIBLE NATURE OF COAL IN THE PRESENCE OF SWELLING SOLVENTS

Lowell D. Kispert, David Tucker and Wojciech Sady
Department of Chemistry
University of Alabama
Tuscaloosa, Alabama 35487-0336

KEYWORDS: Coal, Porosity, Swelling Solvents, Accessibility

ABSTRACT

A review will be given of the current status of spectroscopic techniques used to study the porous structure of coal with emphasis placed on the recent application of the EPR spin probe method to the study of Argonne Premium Coal Samples (APCS). The spin probe method has provided valuable insight into micropore size and shape characteristics during the swelling process. This technique also proved to be sensitive to changes in the coal structure brought about by variations in swelling solvent polarity, swelling temperature and other modifications of experimental conditions during the swelling process. Successive experiments showed that monitoring the accessibility of spin probes to the pore structure of coal could be used to follow the physical and chemical changes in coal during the weathering process, and to distinguish between the effects of dehydration and oxidation for periods as short as 30 seconds. Some of the results of long term weathering for periods upto six months of exposure to air will be discussed.

INTRODUCTION

The porous structure of coal has been of concern for many decades. Catalysis in the conversion of coal is generally related to the surface area available to the catalyst. Since most of the surface area of coal lies in the micropore structure of the coal, the determination of this structure and its effect on catalyst accessibility are important in coal conversion.[1,2] The most popular and versatile method for determination of the porous structure of coal is the gas adsorption method. Although this method provides more information than Hg porosimetry or other physical methods, it does have some severe limitations.[3] Several studies have given contradictory data and it has been shown that micropore volumes can vary by more than an order of magnitude when different gases are used.[4] This leads naturally to spectroscopic or imaging methods.

SANS, SAXS and light scattering: In the mid 1980's, methods using small angle neutron diffraction and small angle x-ray diffraction were used with success to characterize the shape and size of the micropores in Illinois # 6 coal.[6-11] It was determined from these studies that the micropores in low-ranked coal had elongated cylindrical shapes which had diameters of about 5.2A. More recently, SAXS has been used to study the pore structure during fluid extraction.[5] It was shown that micropore dilation was an irreversible process, whereas swelling of the macropore system was a reversible process.[5] In 1981, Kalliat et. al. used small angle x-ray scattering to show that there were three classes of pore systems in coal.[6] These results were somewhat consistent with adsorption data interpretation at that time. Small angle x-ray scattering was used later on by Setek et. al. in 1983 to determine the micropore structure of brown coal.[7] SAXS has also been used by Nemmers et. al. in 1990 to study the porous structure of coal during fluid extraction.[5] During various stages of fluid extraction of coal with THF, small angle x-ray scattering experiments showed that the extensive micropore structure formed during fluid exposure played a key role in the interaction between the fluid and the coal matrix needed for substantial extraction yields.[5] It was determined by Tricker et. al. in 1983 that small angle neutron scattering could be used to effectively determine pore size distributions in various ranked coals.[9] They felt that since the data obtained were substantiated by gas adsorption techniques, SANS could be used to probe coal porosity under circumstances where gas adsorption techniques were either severely limited or not possible.[9] Likewise, in 1983, Kaiser and Gethner also used small angle neutron scattering to study pore distributions and pore accessibility in coal.[10] It was determined that D_2O was not able to penetrate uniformly through dried coals.[10] Later, in 1986, Gethner used SANS to determine the void structure of Illinois #6 coal.[3] He determined that the microvoid volumes were elongated and possessed a well defined circular crossection of about 25A.[3] Also by comparison of aqueous and non-aqueous solutions, it was determined that the surface of the microvoid volume was primarily aliphatic.[3] In 1987, Gethner used SANS and a combination of light scattering and absorption measurements to show that coal is a continuous distribution of voids rather than a well defined, discrete pore distribution, and to separate chemical changes from physical changes in coal during treatment and reactions.[11]

SEM and imaging techniques: Another technique used recently involves SEM analysis during liquid metal infiltration to provide direct imaging of the micropore system.[12] In 1991, Cody and Davis were able to directly image the pore space available to liquid metal (Wood's alloy) in a variety of coal ranks using SEM analysis.[12] They determined that the pores in the lowest rank coal were roughly cylindrical in shape, but that they constituted a rough particle surface and not an interconnected cylindrical pore network.[12] Pore space available to liquid metals in bituminous and higher ranked coals appeared to be made up entirely of microcracks.[12] Around this time, magnetic resonance imaging was also used to study pore structures during swelling.[13] It was shown that coal swells anisotropically; that is, solvents enter the bedding planes and thus the solvent is not distributed uniformly in the coal structure.[13]

NMR spin lattice relaxation and proton NMR

Glaves et. al. showed in 1988, that pore size distributions could be derived by deconvoluting measurements of the NMR relaxation spectra and applying a model to the pore fluid behavior.[14]

Xe129 NMR: Recently, Xe129 NMR studies have been used to determine average micropore volumes and diameters.[15,16] Xe-129 NMR was used in 1990 by Wernet et. al. to determine average micropore diameters in Illinois #6 bituminous coal.[15] After performing Xe-129 NMR experiments on spherocarb, which gave results very close to the manufacturer's specifications of microporosity, they found that the average micropore diameter of Illinois #6 coal was 5.2 Å.[15] More recently, in 1991, Tsiao and Botto use this technique to determine the average micropore size of APCS coals and to investigate the effect of weathering on the average micropore size of coals.[16] This information was then used to develop a model to approximate pore sizes and pore size swelling chacteristics.[16]

EPR spin probe method: Finally, a technique using EPR to follow the inclusion of molecular probes in the micropore structure has been used to determine pore size and shape characteristics of a range of coals during the swelling process.[17,18-23] This technique has also been used to follow changes in the micropore structure during weathering, oxidation, dehydration and short term oxidation.[24,26-30] The EPR spin probe method was first used to study coal by Silbernagel et. al. in 1981.[17] Later, in 1985, Wuu and Kispert expanded this technique to determine micropore size distributions in coal during swelling.[18] This EPR spin probe technique was further developed in this lab to study micropore size distributions and acid / base character of various ranked coals.[19-21] More recently, changes in pore structure and wall chemistry of APCS coals upon swelling at different temperatures and with solvents of various polarities were determined by following the retention characteristics of the coals.[22,23] The results showed that as the polarity of the solvent was increased, the shape of the micropores changed from spherical to cylindrical.[22,23] Additional studies employing EPR spin probe techniques were performed on the breaking up of the hydrogen bonding between bedding planes.[24] To gain insight into the accessible nature of the covalently cross-linked materials during swelling, the EPR spin probe method was used during the swelling of polystyrene-divinylbenzene copolymers which were cross-linked covalently to various extents (2% to 12%).[25] The study showed that hydrogen bonding in coal has a much greater impact than % cross-linking on the micropore structure and swelling character of coal. Despite this, significant amounts of guest molecules could be intercalated into the copolymer structure, even though the copolymers were relatively non-porous.[25] The effect of weathering on the structure and molecular accessibility of spin probes in coal was studied using the EPR spin probe technique.[26] It was shown that after seven days of exposure to air, coals of most ranks exhibited significant changes in spin probe retention.[26] The lower ranked coals (Beulah Zap and Wyodak Anderson), were observed to undergo structural collapse which precluded retention of even the smallest probes, while medium ranked coals actually exhibited improved retention.[26] A detailed analysis of the data collected from the swelling of coals oxidized in a moisture free environment was completed to differentiate between oxidation and the weathering process.[27,28] Eight vacuum dried APCS coals were oxidized in a pure O_2 environment and weathered in air, and the effects of oxidation alone on coal structure were determine by the intercalation of EPR spin probes.[27,28] It was shown that the removal of water was primarily responsible for the structural collapse observed in low ranked coals and for the increase in retention of polar spin probes in medium ranked coals.[27] Coals oxidized in a pure oxygen environment showed an increase in retention by as much as a factor of five.[28] Even the higher ranked coals showed significant retention of polar spin probes after four days of exposure to oxygen.[28] Studies of short term exposure of Illinois #6 to dry Argon and Oxygen were accomplished using the EPR spin probe technique.[29] It was determined that exposure to a dry gas could affect dramatic changes in the coal structure in as little as 30 seconds.[29] Currently, more detailed analyses of the effects of long term weathering for as long as six months have been carried out and will be discussed further in this paper.

EXPERIMENTAL

Samples of eight APCS coals (Beulah Zap, Wyodak Anderson, Blind Canyon, Illinois #6, Lewis Stockton, Pittsburgh #8, Upper Freeport and Poccahontas #3, defined previously[30]) were stored in vials which were exposed to the air but protected from dust or other contaminants during the period of exposure. During the weathering period, the samples were agitated each day to insure complete exposure of the coal to the air. At various points during the weathering period of six months, samples were swelled in one millimolar solutions of each spin probe in the swelling solvents toluene and pyridine. The spin probes used for this study are shown in Figure 1, VI (3-carboxy-2,2,5,5-tetramethylpyrrolidine-1-oxyl), VII (TEMPAMINE) and VIII (TEMPO). 30 mg of each coal was mixed with 2mLs of the pyridine or toluene spin probe solution. The mixture was then stirred for 18 hours so that the swelling would reach an equilibrium. The coal was then filtered and vacuum dried for 2 hours. After this the samples were washed with cyclohexane, a non-swelling solvent, to remove any spin probes on the surface or any spin probes not trapped in the coal structure. The samples were again vacuum dried and then sealed in the evacuated EPR tubes. The concentration of spins in each sample was calculated from the EPR spectra as previously described.[19]

RESULTS AND DISCUSSION

The concentration of spin probe VII retained in weathered APCS coals after swelling is shown as a function of rank and days of oxidation in Figure 2. The front edge at zero days of oxidation represents the retention of spin probe VII in fresh coals as a function of rank. Since toluene does not swell coal to a large extent, the data represents changes in structure and active site functionality during the weathering process which facilitate or inhibit interaction and retention of the polar amino spin probe. It can be seen at b_0 that the retention of fresh Beulah Zap (74.05% carbon dmmf) is about 2800 x 10^{15} spins per gram. This concentration drops to about 1000 x 10^{15} spins per gram after 7 days of weathering. By comparing these data with the retention of spin probe VIII, it has been previously determined that this decrease is caused by a physical collapse of the structure brought about by water removal.[26] After 14 days of weathering, shown at b_{14}, Beulah Zap does not show much change. However, extending the weathering period out to 36 days and even further to 64 days shows a continuing drop in spin probe retention indicated at b_{36} and b_{64}. There is a slight increase as the period of exposure to air reaches 114 days, shown at b_{114}, but essentially the following changes are relatively small compared to the weathering period. It has been shown previously during exposure to pure oxygen in a dry environment, that oxidative changes in Beulah Zap will reopen the structure to polar spin probes. This clearly is not the case during exposure to air, and it can be inferred from this data that the presence of moisture in the air inhibits oxidation in Beulah Zap lignite.

The retention character of Illinois #6 (80.73% carbon dmmf) can be similarly tracked on the three dimensional plot shown in Figure 2. The retention of spin probe VII in fresh Illinois #6 is about 750 x 10^{15} spins per gram as shown at i_0. An increase in retention is observed after 7 days of exposure shown at i_7 to about 2800 x 10^{15} spins per gram. This is followed at 14 days of exposure by a decrease in retention to about 1200 x 10^{15} spins per gram indicated at i_{14}. At 36 days of exposure, the retention of the spin probe is increased to 2300 x 10^{15} spins per gram as shown by i_{36}. It seems that an equilibrium is reached at 36 days, for further weathering has little effect on spin probe retention shown at i_{64}, i_{114} and i_{180}. The initial increase in spin probe retention in Illinois #6 is attributed to removal of water from active sites with minimal collapse of the physical structure. Since the water loss in Illinois #6 has not reached an equilibrium by 14 days,[27] it can be asserted that a partial collapse inhibits the retention of spin probes at this point. The changes which bring about the increase in retention at 36 days must be primarily due to oxidative changes in the coal structure since the water loss has reached an equilibrium by this point.

It can be seen in Figure 2 that higher ranked coals are also affected by the weathering process. Fresh Upper Freeport coal (88.08% carbon dmmf) exhibits almost no retention of spin probe VII, as shown at u_0. As the coal is weathered for 7 days, an increase in retention is observed, shown at u_7. This increase reaches over an order of magnitude as the weathering period is extended to 14 days at u_{14}. This represents the maximum retention of Upper Freeport coal, for a decrease in retention is observed at 36 days and no further changes are observed after this. Like Illinois #6, the accessibility of Upper Freeport coal seems to reach an equilibrium at 36 days of exposure to air.

A two dimensional plot of the retention of spin probe VII is shown in Figure 3 for Beulah Zap, Illinois #6 and Upper Freeport coals. It can be more easily seen in this plot that little change is affected after a weathering period of 36 days. However the same is not true for Wyodak

Anderson (76.04% carbon dmmf), Blind Canyon (81.32% carbon dmmf) and Lewis Stockton (85.47% carbon dmmf) coals (shown in Figure 4), which undergo changes throughout the 6 month weathering period studied. This would indicate that oxidation does continue throughout this period. Some comparison to data collected for long term weathering of coals swelled in pyridine might provide additional insight into this process.

CONCLUSION

It has been shown through the study of the collapse of the Beulah Zap structure, that the presence of moisture in air can inhibit oxidational changes. The structure of Illinois #6 is made much more accessible by long term weathering, and very little change of the structure is observed by monitoring the amino spin probe. Even the higher ranked coals are made more accessible during the weathering process, although this accessibility reaches a maximum after 14 days for Upper Freeport coal. Many of the coals do not exhibit continuing changes in retention of spin probe VII after 36 days.

ACKNOWLEDGMENT

This work was supported by the U.S. Department of Energy, University Coal Grant Program, Grant No. DE-FG22-93PC93202.

REFERENCES

1. Markova, K.; Radev, G.; Kostova, N. *Khim. Tverd. Topl. (Moscow)*, **1992**, *3*, 20-22
2. Itoh, M.; Demurs, A.; Oda, H.; Yokokawa, C. *Coal Sci. Technol., 11th (Int. Conf. Coal Sci., 1987)* **1987**, 527-530
3. Larsen, J. W.; Wernett, P. C. *Energy and Fuels* **1988**, *2(5)*, 719-720
4. Larsen, J. W.; Wernett, P. C. *Prepr. Pap. Am. Chem. Soc., Div. Fuel Chem.* **1992**, *37(2)*, 849-855
5. Nemmers, S.; Horne, D. K.; Bale, H. D. *J. Appl. Phys.* **1990**, *68(7)*, 3178-3186
6. Kalliat, M.; Kwak, C. Y.; Schmidt, P. W. *ACS Symp. Ser., 169 (New Approaches Coal Chem.)* **1981**, 3-22
7. Setek, M.; Wagonfeld, H. K.; Stacy, W. O.; Kiss, L. T. *Fuel*, **1983**, *62(4)*, 480-482
8. Gethner, J. S. *J. Appl. Phys.*, **1986**, *59(4)*, 1068-1085
9. Tricker, M. J.; Grint, A.; Audley, G. J.; Church, S. M.; Rainy, V. S.; Wright, C. J. *Fuel* **1983**, *62(9)*, 1092-1096
10. Kaiser, H.; Gethner, J. S. *Proc.-Inter. Conf. Coal Sci.* **1983**, 300-303
11. Gethner, J. S. *Prepr. Pap. Am. Chem. Soc., Div. Fuel Chem.* **1987**, *32(1)*, 239-246
12. Cody, G. D.; Davis, A. *Energy and Fuels* **1991**, *5(6)*, 776-781
13. Cody, G. D.; Larsen, J. W.; Siskin, M. *Energy and Fuels* **1988**, *2*, 340
14. Glaves, C. L.; Davis, P. J.;Gallegos, D. P.; Smith D. M. *Energy and Fuels* **1988**, *2(5)*, 662-668
15. Wernett, P. C.;Larsen, J. W.;Yamada, O.; Yue, H. J. *Energy and Fuels* **1990**, *4(4)*, 412-413
16. Tsiao, C.; Botto, R. E. *Energy and Fuels* **1991**, *5(1)*, 87-92
17. Silbernagel, B. G.; Ebert, L. B.; Schlosberg, R. H.; Long R. B. *Adv. Chem. Ser.* **1981**, *192*, 23-35
18. Wuu, S. K.; Kispert, L. D. *Fuel* **1985**, *64*, 1681-1686
19. Goslar, J.; Kispert, L. D. *Energy and Fuels* **1989**, *3*, 589-594
20. Goslar, J.; Cooray, L. S.; Kispert, L. D. *Fuel* **1989**, *68*, 1402-1407
21. Goslar, J.; Kispert, L. D. *Fuel* **1990**, *69*, 564-569
22. Spears, D. R.; Kispert, L. D.; Piekara-Sady, L. *Fuel* **1992**, *71*, 1003-1014
23. Spears, D. R.; Sady, W.; Kispert, L. D. *Prepr. Pap. Am. Chem. Soc., Div. Fuel Chem.* **1991**, *36*, 1277
24. Spears, D. R.; Sady, W.; Kispert, L. D. *Fuel* **1993**, *72*, 1225-1233
25. Spears, D. R.; Sady, W.; Tucker, D.; Kispert, L. D. *Energy and Fuels* In Press
26. Sady, W.; Kispert, L. D.; Spears, D. R. *Prepr. Pap. Am. Chem. Soc., Div. Fuel Chem.* **1992**, *37*, 1151
27. Sady, W.; Tucker, D.; Kispert, L. D.; Spears, D. R. *Prepr. Pap. Am. Chem. Soc., Div. Fuel Chem.* **1993**, *38*, 1323
28. Tucker, D.; Kispert, L. D. *Prepr. Pap. Am. Chem. Soc., Div. Fuel Chem.* **1993**, *38*, 1330
29. Tucker, D.; Kispert, L. D. *Prepr. Pap. Am. Chem. Soc., Div. Fuel Chem.* **1993**, *38*, 1335
30. Vorres, K. S. *Energy and Fuels* **1990**, *4*, 420-426

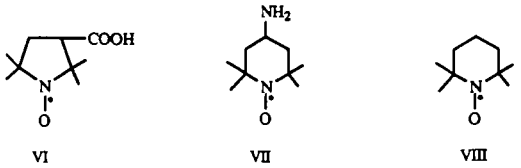

Figure 1. Spin probes VI, VII, and VIII.

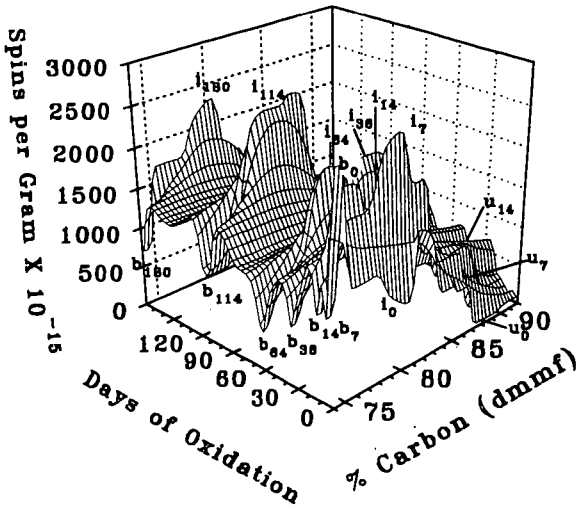

Fig.2 Spin probe VII concentration in fresh APCS coals weathered in air and swelled in toluene.

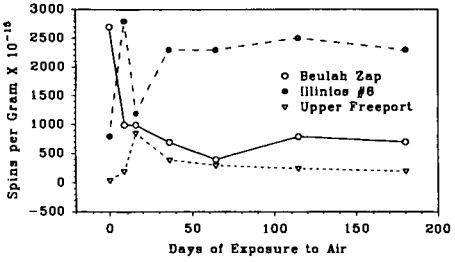

Fig.3 Spin probe VII concentration in fresh APCS Beulah Zap, Illinios #6 and Upper Freeport coals weathered in air and swelled in toluene

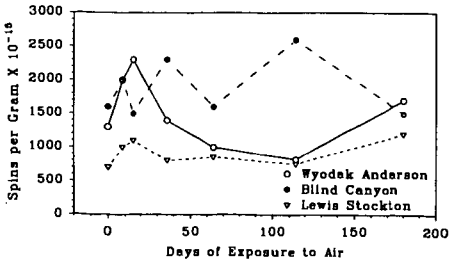

Fig.4 Spin probe VII concentration in fresh APCS Wyodak Anderson, Blind Canyon and Lewis Stockton coals weathered in air and swelled in toluene

NMR Imaging of Heterogeneous Coal Macromolecular Networks

George D. Cody, David C. French and Robert E. Botto

Chemistry Division, Argonne National Laboratory, 9700 So. Cass Ave.
Argonne, IL 60439

Keywords: Microscopy, NMR, Coal

Introduction

Over the past few years, we have been developing new NMR imaging strategies for probing the chemical and physical structure of coal. Early experiments focused on proton NMR imaging techniques for spatially resolving individual macerals within a solid coal specimen.[1] Distinction of individual macerals was achieved by taking advantage of differences in proton density or in spin-lattice relaxation rates, which were shown to vary significantly between the two maceral types. With the implementation of multipulse proton line narrowing in the presence of large static magnetic field gradients, together with back-projection reconstruction NMR imaging methods [2], we were able to image and distinguish macroscopic resinite and vitrinite regions within a 2-mm x 2-mm x 1.4-mm specimen of Utah Blind Canyon (APCS No. 6) coal to an in-plane resolution of about 150 μm.

More recent efforts have focused on obtaining information concerning solvent accessibility in coals and maceral domains by proton NMR imaging of mobile proton distributions resulting from solvent swelling.[3] Imaging in the presence of deuterated solvents illuminated proton distributions of mobile phases within the coal macromolecular structure preferentially. Images with resolutions of 40 to 80 μm were obtained using protic solvents, and showed the presence of different macerals, mineral cleats, and microfractures. Regions which differed with regard to pyridine accessibility were also contrasted in the images. We also were prompted by the initial investigation to elucidate the details of transport behavior of pyridine into coal during swelling. In that study,[4] time-resolved proton NMR images of pyridine penetrating a homogeneous sample of high volatile bituminous A rank vitrain (APCS No. 4) that had been pre-extracted with pyridine were used to descibe the uptake behavior. In addition to coal swelling in pyridine, we investigated transient state imaging results from three polymer-solvent systems for comparison: polyethylmethacrylate swollen in methanol, polymethylsilicone swollen in hexafluorobenzene, and isobutyl rubber swollen in toluene. A model for case II transport in coals was described.

The purpose of this presentation is to review these earlier studies and to provide an overview of the present and future applications of NMR imaging for coal structure determination.

Results and Discussion

Solvent Swelling Studies.

Since the early work of Sanada and Honda, solvent swelling has been employed to probe the physical structure of coal.[5] The swelling behavior of bituminous coals in solvents such as pyridine has been used to assess different strengths or types of secondary interactions which determine the macromolecular structure of coal.[5-9] These include weak interactions of less than ~15 kcal mol^{-1}, such as hydrogen bonding, van der Waals interactions, weak complexes, and π–electron intermolecular interactions.[10-12] The secondary interactions which can be broken by one solvent may be unaffected by a different solvent. A high degree of secondary interactions imparts rigidity to the macromolecular structure in coals, whereas disruption of these secondary interactions by a good swelling solvent mobilizes the structure. Pyridine has been found to effectively relax all of the secondary interactions in coal, leaving only covalent bonds intact.[10,11] It is known that the chemical heterogeneity of coal leads to anisotropic swelling.[12] Coal swelling has been found to be greater perpendicular to the bedding plane than parallel to it.[13] Cracking at mineral–organic interfaces is also expected due to differential swelling of the organic matrix relative to mineral matter.

Important information concerning solvent accessibility to the pore structure and maceral domains in coals also may be obtained by imaging mobile proton distributions resulting from solvent swelling. Images of coals swollen with perdeuterated solvents can be used to map mobile phases in the coal macromolecular structure, while images obtained with protic solvents map distributions of the ingressed solvent.

Here, we discuss the results from two different three–dimensional (3D) NMR imaging techniques for spatially mapping mobile proton distributions in coals that have been swollen with pyridine–d_5 or pyridine. Three–dimensional back–projection techniques

employing a 3D Radon transform inversion reconstruction algorithm were used to map mobile proton distributions on the basis of T_1 (spin–lattice relaxation time) differences. Contrast based on differences in T_2 (spin–spin relaxation time) was achieved employing 3D gradient recalled echo (GRE) pulse sequence for data acquisition, and image reconstruction by 3D Fourier transform (FT). Both techniques display proton distributions of mobile phases within the solid preferentially. Images with resolutions of 40 to 80 microns show the presence of different macerals, mineral cleats, microfractures, and the distribution of mobile macromolecular phases in solvent swollen coals. Regions which differ with regard to pyridine accessibility are also contrasted in the images.

The proton NMR spectrum of a specimen of Utah Blind Canyon coal swollen with pyridine–d_5 showed three distinct proton resonances. There was a broad resonance (*ca.* 27 kHz) arising from rigid protons, and there were two considerably narrower resonance lines discernable as aromatic and aliphatic signals arising from protons in environments of high molecular mobility. Analysis of the broad and narrow components revealed that 14% of the protons are found in regions of high mobility. The fraction aromaticity of mobile phase protons calculated from line simulation was 0.45 compared to a value of 0.24, obtained from proton CRAMPS analysis of the dried coal. The estimated contribution to the total proton signal from residual protons in the pyridine–d_5 was less than 0.1%, while the observed f_a^H increased nearly two–fold as a result of swelling. Clearly, there is a substantial enhancement in the amount of motionally narrowed aromatic proton signal due to swelling.

The 3D surface–rendered NMR image of the Utah coal swollen with pyridine–d_5 was a good representation of the general topology of the actual specimen. For example, a dark feature was found which is known to be a macroscopic crack from solvent swelling the coal. Other dark features on the surface were derived from regions where rigid macromolecular proton signal is suppressed by employing a short relaxation delay; the magnetization of the rigid phase is saturated due to the longer T_1 of these protons.

An 80–micron thin section (slice) through the 3D radon reconstruction showed image contrast from the same sources affecting the 3D surface–rendering. Mobile proton phases resulting from relaxation of the secondary interactions in the coal by swelling with pyridine–d_5 appear bright. Void spaces or mineral deposits which lack protons appear dark. In addition to regions of low proton density, regions of the rigid macromolecular network with long T_1's in the coal appear dark due to the T_1 saturation effects.

The ^1H single–pulse NMR spectrum of pyridine-swollen Lewiston–Stockton coal exhibited a single resonance from the pyridine protons exclusively, whose linewidth was 424 Hz. The ^1H linewidth of pyridine in the Utah coal was 340 Hz. The T_1 of pyridine protons in both samples was measured by progressive saturation, and a value of approximately 1.3 ms was obtained. The baseline–to–baseline projection width of the Lewiston–Stockton coal recorded with the GRE pulse sequence and the phase–encoding gradients off was 11.2 kHz, and that of the Utah coal was 13.5 kHz. The pyridine natural linewidths and baseline–to–baseline projection widths, along with the $1mm^3$ specimen sizes, afforded an in–plane resolution of 50 and 40 microns, respectively, for the two coals.

The 3D surface–rendered GRE images of the Utah and Lewiston–Stockton pyridine swollen coals exhibited bright features resulting from regions in the coals which contain a high density of mobile pyridine; dark areas resulted from regions which are inaccesible to the solvent. Photographs of the Utah and Lewiston–Stockton coal showed a close correspondence between the shape of the coal specimens and the surface–rendered GRE image geometries. Also, features devoid of pyridine such as pits, cracks, and gouges appeared magnified in the images. The vertical feature on the front face of the 3D surface–rendering of the Lewiston–Stockton specimen showed a microscopic structure contiguous with the surface of the specimen which is inaccessible to pyridine. The photograph showed that this is a solid region in the coal rather than a void space.

Slices of the interior of the Lewiston–Stockton coal show the presence of contrasting horizontal bands in the *xy*–plane similar to the lamellar structures visible in the photograph of the coal. A dark vertical feature was seen which corresponds to the same region which appears as a void in the 3D surface–rendering, and indicated that this interior structure runs through the object to its surface. Since the photograph shows that this area of the specimen is solid, the dark structure in the images is clearly a region of low pyridine accessibility rather than a void space. When the coal was swollen with pyridine, the secondary interactions binding strata within the specimen were relaxed. Contrasting bands in the images showed that differential swelling in the bedding plane has produced microfractures and regions with greater or lesser pyridine accessibility.

This preliminary investigation has shown that 3D NMR imaging is a promising tool for studying solvent swelling of coals. This non–destructive technique revealed rich microscopic detail concerning the penetration and accessibility of a solvent into the interior of coal specimens. Further development of this technique also presents the possibility for visualization and analysis of the dynamics of the coal swelling process which can be used to elucidate coal physical structure. In addition, several preparatory pulse sequences prior to the imaging experiment may be employed for the quantitative characterization of NMR relaxation phenomena and solvent diffusion in coals. Image contrast produced by differences in the mobility of the macromolecular network in the coal will be compared with image contrast produced by differences in solvent accessibility in the same specimen. Coal

specimens with known petrography will be utilized and correlated with NMR images obtained using multiple–pulse proton decoupling methods prior to the solvent swelling measurements.

Solvent Transport Studies

Significant insight into the character of solvent transport has been obtained through time-resolved, direct imaging of concentration gradients during solvent uptake. Early on, optical microscopic methods revealed that solvent transport in some macromolecular networks did not conform to Fickian kinetics.[14] Specifically, these systems exhibited steep-gradient solvent fronts which propagate into a sample at a constant velocity, much like a shock wave; such behavior has been called case II transport to distinguish it from Fickian transport.

Case II transport is not restricted to synthetic polymers. Biopolymers and geopolymers such as cellulose and bituminous coals, for example, also exhibit case II transport behavior under suitable conditions.[10,14,15] All that is required for case II transport is that the dry network exist initially in a glassy state and that the penetrating solvent is capable of suppressing T_g.

Given the interesting physical behavior of glassy networks near their glass transition, the search for a theoretical basis for non-Fickian behavior has been irresistible for both experimentalists and theorists. To date, numerous theories abound.[16-24] While the specific approaches to this problem vary from one model to another, universally they rely on the generality that case II behavior results from coupled solvent diffusion and network relaxation.[25,26] There are several rigorous approaches which quantify case II transport in terms of a relatively small set of physically based dynamic parameters.[19-24] These models tend to be valid only for very small displacements from equilibrium, because linear behavior of the governing equations is required in order to obtain an analytical solution. Large scale departures from equilibrium conditions requires that the concentration dependence on each of the dynamic parameters be considered explicitly. This has resulted in a complicated data analysis, stemming from a many-fold expansion of the parameter set and, consequently, an increase in the total number of degrees of freedom of the model.

Many, if not most, applications involving solvent-macromolecular systems are far from equilibrium. In the present paper, the essential characteristics of case II transport are exploited for the purpose of reducing the dynamic parameter set size, in order to simplify quantification under conditions far from equilibrium, e.g., the situation of solvent transport following immersion of a dry macromolecular network into a solvent reservoir. Case II transport of methanol in polyethylmethacrylate (PEMA) and pyridine in coal is explored and compared with Fickian transport of toluene in polybutadiene rubber (PBD) and hexafluorobenzene in polymethylsilicone (PMS) using magnetic resonance microscopy and optical microscopy.

The characteristic relaxation times for each solvent-network system were established at full dilation using a standard inversion-recovery pulse sequence to derive T_1, and a Hahn spin-echo pulse sequence to derive T_2. It is acknowledged that in protonated solvent systems, contributions to the signal intensity can arise from both the protons in the solvent and protons associated with the mobile network. Analysis of the NMR spectral and dynamic characteristics of these swollen networks in deuterated solvents reveals that, in general, only a minor contribution to the total signal intensity results from the mobile network protons. This contribution is significant, however, in the case of PBD in toluene. No signal is detectable from the rigidly bound protons in the glassy regions of PEMA or coal due to severe dipolar broadening (linewidth > 20 kHz) in the rigid solid. Obviously, in the case of ^{19}F imaging of solvent transport into polymethylsilicone, signal is derived from the solvent exclusively.

In the present experiments, two-dimensional (2D) images are sufficient to elucidate the fundamental aspects of the transport phenomena. In order to ensure that the transport process was also two dimensional, the upper and lower sample surfaces were protected from solvent infiltration by glass cover slips which restricted the flow of solvent to cross only the exposed faces of each sample. Each sample is rectangular with initial dimensions on the order of 1-2 x 1-2 x 1 mm. The experimental protocol involved immersing the sample in the solvent for a period of time, removing it from the solvent bath, acquiring an image, and re-immersing it. During the imaging stage the sample was placed in cell with "plugs" such that the free volume within the cell was minimized. It was anticipated that this would reduce the amount of desorption over the duration of the imaging.

In order to obtain sufficiently high quality images, given the dynamic behavior of the three protonated solvent/macromolecule systems, it was necessary to acquire 24 (128 point) transients with a recycle delay of 200 ms for each of 128 phase-encoded gradient positions using a standard imaging spin-echo pulse sequence.[27] This yielded reasonably high quality 2D images, with a resolution on the order of 70 μm, which was obtained over intervals of approximately 10 min. Typically a 64-kHz spectral width was chosen, establishing an echo time on the order of 0.5 ms. In the case of ^{19}F imaging, a longer T_1 and an inherently lower sensitivity of the nucleus necessitated the acquisition of 32 scans per phase encoded position and a recycle delay of 500 ms; this resulted in a time interval on the order of 30 min to obtain a quality image. It is clear that during the time that the images are acquired some

spatial averaging does take place. However, in all cases, the entire uptake process takes between 3 to 4 hrs, and therefore, it is assumed that the averaging is relatively minor.

A 2D ^{19}F image projection of a specimen of polymethylsilicone swelling in hexafluorobenzene, observed at some intermediate time, exhibited a shallow concentration gradient into the core of the specimen. The 2D image of polyethylmethacrylate in methanol was strikingly different; in this case a sharp front was observed with a nearly constant solvent concentration behind the front.

Magnetic resonance imaging data in the form of 1D slices, reconstructed from the center of the 2D image projections, revealed sequential cross-sections through PBD dilated in toluene; a sizable contribution to the image intensity arose from the protons associated with the rubbery PBD itself. Superimposed on this was the additional signal due to the solvent. Clearly evident, however, were the smooth, exponential, solvent gradients directed into the core of the sample, indicating a Fickian transport mechanism. Fickian transport was also revealed in the case of the fluorinated solvent in PMS. Smooth solvent gradients were clearly evident despite the lower signal-to-noise ratios obtained in the ^{19}F images.

The character of transport was drastically different for PEMA swollen in methanol. The presence of a sharp solvent front and solvent absent core clearly indicated case II transport. This behavior is typical of many acrylate polymers swollen in a variety of solvents, and it has been detected previously by NMR imaging techniques.[28-30] The imaging results gave some indication of a sigmoidal solvent front similar to that derived numerically , and suggested that the NMR images might be used to help constrain values of the solvent activity. Pyridine transport in coal also exhibited case II behavior, whose signature was revealed by sharp solvent fronts moving into the sample. The situation was complicated by the formation of a crack on the left side of the lower most cross-section, which destroyed the symmetry of the solvent fronts. The formation of cracks accompanying case II transport is not unusual, nor unexpected, considering the magnitude of the strain gradients along the solvent front.

The measured front velocities were constant for both the PEMA and the bituminous coal, consistent with case II transport. There was some concern that a degree of spatial uncertainty or blurring may occur during evolution of the front within the imaging interval, leading to an apparent reduction in the gradient of the solvent front. Furthermore, distortions in image intensity due to T_2 effects were expected to add some further degree of uncertainty. The accuracy of the magnitudes of the front velocities derived from magnetic resonance imaging, however, are not subject to these effects. Hence, the velocities provide a valuable and quantitative constraint for the parameterization of the uptake data.

Direct measurement of linear dilation accompanying swelling is a simple means to quantify the overall swelling behavior of rubbery networks.[31,32] Linear dilation behavior for PBD and PMS were consistent with Fickian transport in rubbery networks. Given the uptake data, it was trivial to derive a mass-fixed diffusion coefficient through linear fitting of the experimental data. The generation of a curve for Fickian transport, in the present case, requires solving the two-dimensional diffusion equation and integrating this solution with respect to time. Fitting of the dilation data results in values of $D_R = 2.5 \times 10^{-6}$ cm^2/s and 1.1×10^{-6} cm^2/s for PBD-toluene and PMS-hexafluorobenzene, respectively. These relatively large values of D_R reflect the high degree of inter- and intra-molecular mobility of these networks, which explains the rapidity with which the rubbery systems respond to applied stresses that are osmotic in nature.

In the case of solvent transport in systems undergoing a glass transition, or case II transport, we have defined the uptake behavior using three parameters: a characteristic cooperative diffusion coefficient, D_C, governing dilation of the network; a molecular relaxation rate constant, β, which is given by the relationship $\beta = K_{os}/\eta_l$, where η_l is the bulk viscosity and K_{os} is the osmotic modulus; and a critical solvent concentration, C^*, above which there is a transformation of the network from a glass to a rubber. However, there are several degrees of freedom associated with the present model of case II transport. Without constraints on the magnitude of C^* or β, it is not possible to uniquely define the three transport parameters. In the present case the dilation data for both PEMA and bituminous coal were fitted to characteristic case II curves, using β as a floating variable while C^* was independently constrained. The final constraint used was the solvent front velocity, v, obtained from magnetic resonance imaging.

A relationship between C^* and solvent concentration was established by relating the change in free volume of the solvent-polymer system to contributions from the respective free volumes of polymer and solvent taken independently. Essentially linear T_g suppression with concentration is observed at low solvent concentrations, $\Delta T = -kC_S$, where $\Delta T = T_{g,supp.} - T_{g,dry}$, k is typically in the range of 200 - 500 °K for a variety of solvents, and C_S is the volume fraction of the solvent. Recalling that T_g of PEMA is only 308 °K, the value of C_S, accordingly, is anticipated to be very small. Using a lower value of k, we calculate $C_S = 0.05$, yielding $C^* = 0.17$. Bituminous coal is reported to have its T_g on the order of 650 to 700 °K, suggesting that C_S of pyridine must be very high. Indeed, calculations along these lines have indicated that C_S (calculated) actually exceeds the equilibrium C_S associated with coal dilated at room temperature at a solvent activity of 1.0.[33] On the basis of this analysis, it would appear that pyridine is not capable of suppressing coal's T_g to less than room temperature, which is inconsistent with the present results. Recent experimental results derived from incremental solvent sorption isotherm experiments on bituminous coal,

however, clearly indicate the presence of a glass transition at solvent activities less than 1.0, yielding a magnitude of C^* on the order of 0.65.[34]

The gross dilation behavior of both samples was clearly case II with an unambiguous sigmoidal uptake profile . The essential character of the present model for case II transport processes is revealed when comparing the swelling kinetics of these two glassy networks. Both samples are essentially the same size, with uptake occurring over essentially the same interval of time. The glassy diffusion coefficients for the two samples are also very similar in magnitude. The coal's network relaxation rate following the glass transition, however, is almost 15 times larger than that of PEMA. It is the relative magnitudes of the critical concentration parameter, C^*, which compensates for this disparity in the relaxation dynamics and results in comparable overall uptake times. For the case of PEMA swollen in methanol, C^* is relatively small. In the present model, network relaxation at the glass transition drives diffusion; all other things remaining equal, the sooner relaxation occurs the faster transport evolves.

Comparing all four samples, the nearly two order of magnitude difference in diffusion coefficients between the Fickian and case II systems is compensated by the lack of any phase-transition induced, network relaxation in the Fickian systems. Generally, these results confirm assertions made by authors of one of the earliest papers on the applications of magnetic resonance imaging to diffusion in glassy polymers;[28] i.e., it is the presence of the phase transition which drives the overall diffusion process.

Acknowledgement

This work was performed under the auspices of the Office of Basic Energy Sciences, Division of Chemical Sciences, U. S. Department of Energy, under contract number W-31-109-ENG-38.

References

1. Dieckman, S. L.; Gopalsami, N.; Botto, R. E. *Energy & Fuels* **1990**, *4*, 417.
2. Grangeat, P.; Hatchadourian, G.; Le Masson, P.; Sire, P. *Logicial Radon, Notice Descriptive Des Algorithmes Ef Des Programmes* 1990, Version 2.1 du 13–04–1990, LETI/DSYS/SETI/90–180 PS: Grenoble, 1990.
3. French, D. C.; Dieckman, S. L.; Botto, R. E. *Energy & Fuels* **1993**, *7*, 90.
4. Cody, G. D.; Botto, R. E. *Energy & Fuels*, **1993**, *7*, 561.
5. Sanada, Y.; Honda, H. *Fuel* **1966**, *45*, 295.
6. Green, T.; Kovac, J.; Brenner, D.; Larsen, J. W. *Coal Structure*; Meyers, R. A., Ed.; Academic Press: New York, 1982; Chapter 6.
7. Nelson, J. R.; Mahajan, O. P.; Walker, Jr., P. L. *Fuel* **1980**, *59*, 831.
8. Peppas, N. A.; Lucht, L. M. *Chem. Eng. Commun.* **1984**, *30*, 291.
9. Suuberg, E. M.; Lee, D.; Larsen, J. W. *Fuel* **1985**, *64*, 1668.
10. Brenner, D. *Fuel* **1985**, *64*, 167.
11. Quinga, E. M. A.; Larsen, J. W. In *New Trends in Coal Science*; Yurum, Y., Ed.; HRT NATO ASI Series 244; Kluwer Academic Publishers: Boston, 1988.
12. Quinga, E. M.; Larsen, J. W. *Energy Fuels* **1987**, *1*, 300.
13. Brenner, D. *Fuel* **1984**, *63*, 1324.
14. Alfrey, T. E.; Gurnee, E. F.; Lloyd, W. G., *J. Polym. Sci*, **1966**, *12*, 249.
15. Maffei, P.; Kiéné, L.; Canet, D., *Macromolecules*, **1992**, *25*, 7114.
16. Enscore, D. J.; Hopfenberg, H. B.; Stannett, V. T. *Polymer*, **1977**, *18*, 793.
17. Jou, D.; Camacho, J.; Grmela, G. *Macromolecule*, **1991**, *24*, 3597.
18. Thomas, N. L.; Windle, A. H. *Polymer*, **1982**, *23*, 529
19. Vrentas, J. S.; Duda, J. L. *J. Polym. Sci, Polym. Phys. Ed.*, **1977**, *15*, 403.
20. Jackle, J.; Frisch, H. L. *J. Poly. Sci. Polymer Phys. Ed.*, **1985**, *23*, 675.
21. Durning, C. J. *J. Poly. Sci. Polymer Phys.* Ed. **1985**, *23*, 1831.
22. Durning, C. J.; Tabor, M. *Macromolecules*, **1986**, *19*, 2220.
23. Neogi, P. *AiChE Journal*, **1983**, *29*, 829.
24. Neogi, P. *AiChE Journal*, **1983**, *29*, 833
25. Hopfenberg, H. B.; Frisch, H. L., *J. Polym. Sci, Part B*, **1969**, *7*, 405
26. Vrentas, J. S.; Duda, J. L. *AIChE J.*, **1975**, *21*, 894.
27. Callaghan, P. T. *Principles of Nuclear Magnetic Resonance Microscopy*, Oxford Science Publications, Clarendon Press, Oxford 1991
28. Mareci T. H.; Dønstrup, M.; Rigamonti, A. *J. Mol. Liquids*, **1988**, *38*, 185
29. Weisenberger, L. A.; Koenig, J. L. *Macromolecules*, **1990**, *23*, 2445
30. Mansfield, P.; Bowtell, R.; Blackband, S. *J. Magn. Res.*, **1992**, *99*, 507
31. Tanaka, T. ; Fillmore, D.J. *J. Chem. Phys.*, 1979, *70*, 1214.
32. Landau, L. D.; Lifshitz, E. M. *Theory of Elasticity* ,Pergamon Press, New York, NY, 1959.
33. Lucht, L. M.; Larsen, J. M.; Peppas, N. A. *Energy & Fuels* **1987**, *1*, 56.
34. Green, T., *personal communication.*

STATUS OF COAL RESEARCH: SOLVENT EXTRACTION

David H. Buchanan
Department of Chemistry
Eastern Illinois University
Charleston, IL 61920-3244

Keywords: Coal, Solvent Extraction, Swelling

INTRODUCTION

The early history of solvent extraction in coal research has been reviewed by Van Krevelen. *(1)* From the beginning, solvent extraction has been used to isolate and characterize both soluble and insoluble coal fractions. The recent studies covered in this report fall into four broad areas: 1) Improvement in extraction yields or selectivity; 2) Correlation of solvent swelling and extraction behavior to structural models for the insoluble organic portion of coal; 3) Analyses of extracts to identify and perhaps quantify organic compounds in the raw coal and 4) Use of solvent extraction to predict or influence coal behavior in some other process such as liquefaction. To cover this active area in a brief Preprint, references were chosen to illustrate both the current status of the field and cite related studies.

The availability of the pristine Argonne Premium Coal Samples *(2)* has led to a significant improvement in the reproducibility of solvent extraction as an analytical tool. In 1984, Triolo and Child cautioned that solvent extraction may be an inherently unreproducible process. *(3)* Based on studies of how weathering affects solvent extraction, that was a fair statement at the time. *(4)* With the improvements and standardization of solvent extraction practices developed since then, it is now possible to obtain reproducible and reliable information from the solvent extraction of coal.

EXPERIMENTAL

Protection of pristine coal samples and solvent extracts from air is necessary if colloid-free extract solutions are to be isolated. *(4)* Solvents must be of high purity if large volumes are to be concentrated by evaporation or distillation for product isolation. Soxhlet extraction, stirring -100 mesh coal with a large volume of solvent for several days or ultrasonic irradiation for 30-90 minutes at room temperature have all been reported to give the same extract yield for a given solvent/coal combination. *(4)(5)(6)(7)* Complete separation of extract from insoluble residue requires either membrane filtration (Nylon or Teflon of 0.45 m pore size, pre-filter needed if colloids are present) or centrifugation at 24,000g or greater. Removal of hydrocarbon solvents such as toluene from extract and residue can be accomplished by drying to constant weight at elevated temperature and reduced pressure (100°, 0.1 Torr). Removal of nitrogen containing solvents requires washing with specific solvents such as 80% methanol/water for pyridine or DMF *(4)* or acetone/water for N-methyl-2-pyrrolidinone (NMP) *(6)* before vacuum drying.

DISCUSSION

1) Improvement in yield or selectivity. "Solvent Extract" is an operational definition for material isolated from the complex and inhomogeneous mixture which is coal. Unless the separation process is specified, including filter pore size or centrifugation clearing factor, the material isolated is not well defined and may not be the same as that isolated by other workers. This is especially true for coals subject to weathering. We showed that insoluble colloids were present in polar solvent extracts of Argonne coals which were exposed to air during or after extraction. The colloids passed ordinary filter paper or fritted glass funnels but were removed by 0.45 m membrane filtration or ultracentrifugation. *(4)* Weathered coals are less prone to colloid formation, presumably because the reactive material is no longer present. Additional insight into the effect of weathering and moisture removal on the accessibility of coals to solvents was given by Kispert using intercalation of epr spin probes. *(8)* Even brief air exposure caused measurable changes in the retention of polar probes by Ill. No. 6 coal. Most workers dry coal before extraction in order to determine extract yields and material balances; however this may collapse pore structure in low-rank coals and produce other changes in high-rank coals. Even drying at 100° can induce cross-linking reactions in low-rank coals which reduce pyridine swellability. *(9)*

Pyridine is a good solvent for many coals and has been extensively studied. Selected extraction data for the Argonne Premium Coals are given in Table 1. All material balances are 94-102% and the lab to lab variation in yield is typical of recent studies. Pyridine cannot be completely removed from coal or extracts by heating, either under reduced pressure or in a flow of nitrogen. In our experience, 80% methanol/water washing followed by vacuum drying is the most effective method to remove pyridine or DMF in terms of minimizing the time and volume of wash solvent used - which minimizes chances for air oxidation or loss of slightly soluble minerals. This wash solvent has a high heat of wetting for coal surfaces.*(10)* Trace amounts of either DMF or pyridine can be detected by FT-IR spectroscopy*(4)* and the human nose is quite sensitive to traces of pyridine on coal fractions.

Efforts to increase extraction yields include Liotta's addition of $(n\text{-}Bu)_4NOH$ in methanol for ultrasonic pyridine extraction of several coals.*(11)* For Argonne coal 301 the yield increased from 28 to 70% only when the good swelling agent, $(n\text{-}Bu)_4NOH$ in methanol, was present. Our results on the effect of acid demineralization on pyridine extraction yields of Argonne coals 201, 301, 401 and 801 are shown in Figure 1. The increase in yield for low-rank coals may be, in part, the effect of converting carboxylic acid salts into pyridine soluble acids. Our preliminary results on the effect of demineralization on toluene extraction yields for Ill. No. 6 coals show that, although the absolute yield is much smaller, the relative increase after demineralization is greater than with pyridine. This is consistent with the view that, given enough time for mass transport, a good swelling solvent such as pyridine can remove soluble material by diffusion through the organic matrix but a poorly swelling solvent such as toluene removes material only *via* the interconnected pore network, portions of which may be blocked by minerals.

Iino used CS_2/NMP mixed solvent, with and without ultrasonic irradiation, to remove from 30-66% by weight of soluble material from 29 of the 59 coals they studied.*(6)* Results for the Argonne coals are also listed in Table 1. Based on analyses of coals, extracts and residues as well as extraction of separated macerals, they suggest a synergistic effect due to the good solvent and swelling character of the NMP and high diffusibility of the CS_2. Morgan has recently reported that KOH or NaOH added to NMP or DMF extractions of South African and the Argonne coals gave extracts containing up to 80% of the carbon from the feed coals.*(12)* However, from the information given, the absence of colloids or material balances cannot be be determined. Other strong base treatments of pyridine extract residues also lead to high total yields of extract at modest temperatures.*(13)*

Supercritical solvent extraction has been used by several groups to study coal porosity*(14)* or to remove organic*(15)* or elemental sulfur*(16)* from coal, either as a prototype desulfurization process or as an analytical method. For the isolation of analytical samples for GC or HPLC analyses the method is quick and equipment requirements modest.*(17)*

2) Correlation of solvent swelling and extraction with structure. Solvent extraction is often used to prepare the insoluble residue for solvent swelling studies which are used to infer structural information by reference to the literature on solvent swelling of cross-linked polymers. Access to this active field can be gained from recent papers by Green,*(18)* Iino,*(19)* Larsen,*(20)* Nishioka,*(21)* Painter*(22)* and Snape.*(23)* Current work shows that brief heating of coals with solvents in which they are not soluble, such as water or chlorobenzene, causes irreversible changes in swelling and extraction yields with good solvents (defined as those such as pyridine which swell and extract coal to the greatest extent.) The suggestion that new cross-links such as hydrogen bonds have been established*(19)* has been criticized by Painter who notes that hydrogen bonds are dynamic and cannot serve as true cross-links as do the covalent bonds in cross-linked polymers.*(22)* Physical association with strong concentration and temperature dependence is suggested as a better representation than a cross-linked network for the insoluble portion of most coals.*(21)* The implications for coal liquefaction if this model is substantiated are profound.

3) Analyses of Extracts. Modern size exclusion chromatography (SEC) is a powerful method for determining molecular weight

distributions of mixtures. Because coal fractions usually contain both polar and non-polar molecules, interpretation of SEC data is difficult. Advantages and problems with THF *(24)*, NMP *(25)* and pyridine *(26)* as SEC mobile phases for coal fractions are discussed in the references cited. Solvents which prevent self-association of coal molecules (pyridine, DMF, NMP) give more realistic molecular weights but limit the choice of SEC detectors. The common refractive index detector over-estimates the contribution of oxygen rich species such as phenols and gives average molecular weights which are too high unless calibrated with appropriate compounds. Changes in SEC molecular size distributions find use in studies of the progress of coal liquefaction and other processes. A novel recent use is the screening of microorganisms which bio-degrade coal. *(27)*

Among the methods which have the possibility for identification of specific compounds in solvent extracts, GC/MS has been the most studied. For this purpose, solvents such as benzene/methanol *(28)* have the advantage of extracting only molecules which can be volatilized in a typical GC or MS inlet and thus need no fractionation before analysis. In contrast, during FIMS analysis of the toluene insoluble portion of a pyridine extract, only 34% of the sample was volatilized. *(4)* A disadvantage to non-polar solvents is that potentially soluble molecules may not be accessible to the solvent and their absence may bias the conclusions drawn. To avoid this problem, chromatographic fractionation of pyridine extracts is often used to isolate fractions which can be analyzed by mass spectroscopy. In the usual methods, elution from a silica gel *(29)* or alumina column *(5)(30)* produces increasingly polar coal extract fractions which may be further fractionated on other supports for specific analyses. A typical application is the study of terpenoid biomarkers in coal to better understand the progress of the coalification process. *(31)(5)*

Solvent extraction is often used to prepare samples for IR, NMR, X-ray and other analyses, the results of which are discussed by other speakers at this Symposium. Elemental sulfur in coal can be determined by perchloroethylene (PCE) extraction followed by HPLC analysis *(32)* or GC analysis of supercritical extracts. *(15)*

4) Solvent extraction as related to other processes. Pretreatment of coals with solvents prior to liquefaction often leads to increased yields of desirable products, lower conversion temperatures or both. Studies utilizing both very polar *(33)* and non-polar solvents *(34)* illustrate the complexity of the effects in that both swelling and non-swelling solvents can improve liquefaction depending on the process and coal used. Recent work using chlorobenzene *(35)* appears to support the view that, since solvents which disrupt molecular aggregates without bond cleavage increase liquefaction conversions, physical association is an important structural feature in coal. *(21)*

Removal of noxious elements such as sulfur by simple solvent extraction of coal is an attractive idea. However the claim that PCE extraction removes organic sulfur in a coal desulfurization process is controversial. ASTM organic sulfur reductions of up to 40% following PCE extraction have been reported, *(36)* however the effect appears to be due to removal of elemental sulfur ("organic sulfur" by ASTM) produced by pyrite oxidation. *(37)*

SUMMARY

With careful attention to anerobic conditions and clarification of solutions, solvent extraction of coal is a useful, reproducible technique for coal science. Studies of the extraction process itself and the related solvent swelling provide important insights into coal matrix structure while analyses of the extracts provide increasingly detailed information about the chemical species present in both extract and raw coal.

ACKNOWLEDGEMENTS

In addition to those cited, experimental work at EIU was carried out by Cindy Ludwig, Stanislav Kalembasa and Yunsong Tong. Funding was provided, in part, by the Illinois Department of Energy and Natural Resources through the Illinois Clean Coal Institute (formerly CRSC) and by the US DOE (Grant Number DE-PC22-92PC 92521). The opinions and conclusion expressed herein are those of the author and do not necessarily reflect the views of IDENR, ICCI and the DOE.

REFERENCES

(1) Van Krevelen, D.W. "Coal: Typology-Chemistry-Physics-Constitution", Elsevier, Amsterdam; (1981); Chapter 10.

(2) Vorres, K.S. *Energy Fuels* **1990**, 4, 420-426.

(3) Triolo, R.; Child, H.R. *Fuel* **1984**, 63, 275.

(4) a) Buchanan, D.H.; Warfel, L.C.; Mai, W.; Lucas, D. *Prepr. Pap.-Am. Chem. Soc., Div. Fuel Chem.* **1987**, 32(1), 146-153. b) Buchanan, D.H.; Osborne, K.R.; Warfel, L.C.; Mai, W.; Lucas, D. *Energy Fuels* **1988**, 2, 163-170.

(5) Chang, H.K.; Bartle, K.D.; Markides, K.E.; Lee, M.L. in "Advances in Coal Spectroscopy", H.L.C. Meuzelaar, Ed.; Plenum Press, New York, (1992), Chap. 7.

(6) a) Iino, M.; Takanohashi, T.; Ohsuga, H.; Toga, K. *Fuel* **1988**, 67, 1639-1647. b) Takanohashi, T.; Iino, M. *Energy Fuels* **1990**, 4, 452-455. c) Takanohashi, T.; Ohkawa, T.; Yanagida, T.; Iino, M. *Fuel* **1993**, 72, 51-55.

(7) Pugmire, R.J.; Solum, M.S.; Bai, S.; Fletcher, T.H.; Woods, S.; Grant, D.M. *Prepr. Pap.-Am. Chem. Soc., Div. Fuel Chem.* **1993**, 38(2), 647-654.

(8) a) Tucker, D.; Kispert, L.; Sady, W. *Prepr. Pap.-Am. Chem. Soc., Div. Fuel Chem.* **1993**, 38(4), 1330-34. b) Tucker, D.; Kispert, L. *Prepr. Pap.-Am. Chem. Soc., Div. Fuel Chem.* **1993**, 38(4), 1335-1340.

(9) Suuberg, E. M.; Otake, Y.; Yun, Y.; Deevi, S.C. *Energy Fuels* **1993**, 7, 384-392.

(10) Wightman, J.P.; Glanville, J.B.; Hollenhead, J.B.; Phillips, K.M.; Tisa, K.N. *Prepr. Pap.-Am. Chem. Soc., Div., Fuel Chem.* **1987**, 32(1), 205.

(11) Matturro, M.G.; Liotta, R.; Reynolds, R.P. *Energy Fuels* **1990**, 4, 346-351.

(12) Morgan, D.L. *Prepr. Pap.-Am. Chem. Soc., Div. Fuel Chem.* **1992**, 37(4), 1996-2001.

(13) Winans, R.E.; McBeth, R.L.; Hunt, J.E. *Prepr. Pap.-Am. Chem. Soc., Div. Fuel Chem.* **1993**, 38(2), 561-564 and references therein.

(14) Olson, E.S.; Diehl, J.W.; Horne, D.K.; Bale, H.D. *Prepr. Pap.-Am. Chem. Soc., Div. Fuel Chem.* **1988**, 33(4), 826-831.

(15) a) Yurum, Y.; Ozyoruk, H.; Altuntas, N.; Gulce, H. *Energy Fuels* **1993**, 7, 620-624. b) Muchmore, C.B.; Chen, J.W.; Kent, A.C.; Tempelmeyer, K.E. *Prepr. Pap.-Am. Chem. Soc., Div. Fuel Chem.* **1985**, 30(2), 24-34.

(16) Louie, P.K.K.; Timpe, R.C.; Hawthorne, S.B.; Miller, D.J. *Fuel* **1993**, 72, 225-231.

(17) Hawthorne, S.B. *Anal. Chem.* **1990**, 62, 633A-642A.

(18) Green, T.K.; Selby, T.D. *Prepr. Pap.-Am. Chem. Soc., Div. Fuel Chem.* **1993**, 38(4), 1316-1322.

(19) Fujiwara, M.; Ohsuga, H.; Takanohashi, T.; Iino, M. *Energy Fuels*, **1992**, 6, 859-862.

(20) Larsen, J.W.; Mohammadi, M. *Energy Fuels* **1990**, 4, 107.

(21) a) Nishioka, M. *Fuel* **1992**, 71, 941-948. b) Nishioka, M. *Fuel* **1993**, 72, 997, 1001, 1011.

(22) Painter, P. *Energy Fuels* **1992**, 6, 863-864.

(23) McArthur, C.A.; Hall, P.J.; MacKinnon, A.J.; Snape, C.E. *Prepr. Pap.-Am. Chem. Soc., Div. Fuel Chem.* **1993**, 38(4), 1290-1296.

(24) Bartle, K.D.; Mills, D.G.; Mulligan, M.J.; Amaechina, I.O.; Taylor, N. *Anal. Chem.* **1986**, 58, 2403-2408.

(25) Lafleur, A.L.; Nakagawa, Y, *Fuel* **1989**, 68, 741-752.

(26) Buchanan, D.H.; Warfel, L.C.; Bailey, S.; Lucas, D. *Energy Fuels* **1988**, 2, 32-36.

(27) Polman, J.K.; Quigley, D.R. *Energy Fuels* **1991**, 5, 352-353.

(28) Neill, P.H.; Xia, Y.j; Winans, R.E. *Prepr. Pap.-Am. Chem. Soc., Div. Fuel Chem.* **1989** 34(3), 745-751.

(29) Farcasiu, M. *Fuel*, **1977**, 56, 9.

(30) Later, D.W.; Lee, M.L.; Bartle, K.D.; Kong, R.C.; Vassilaros, D.L. *Anal. Chem.* **1982**, 53 1612.

(31) Hayatsu, R.; McBeht, R.L.; Neill, P.H.; Winans, R.E. *Energy Fuels* **1990**, 4, 456-463.

(32) Buchanan, D.H.; Coombs, K.J.; Murphy, P.M.; Chaven, C. *Energy Fuels* **1993**, 7, 219-221.

(33) Joseph, J.T. *Fuel* **1991**, 70, 179; 459.

(34) Larsen, J.E.; Hall, P.J. *Energy Fuels* **1991**, 5, 228.

(35) McArthur, C.A.; Hall, P.J.; Snape, C.E. *Prepr. Pap.-Am. Chem. Soc., Div. Fuel Chem.* **1993**, 38(2), 565-570.

(36) a) Lee, S.; Kesavan, S.K.; Lee, B.G.; Ghosh, A.; Kulik, C.J. *Fuel Sci. Technol. Int.* **1989**, 1, 443-468. b) Atwood, G.A.; Leehe, H.H. *Coal Prep.* **1991**, 11, 77-86.

(37) a) Hackley, K.C.; Buchanan, D.H.; Coombs, K.; Chaven, C.; Kruse, C.W. *Fuel Process. Technol.* **1990**, 24 431-436. b) Chou, M.-I.M.; Lytle, J.M.; Ruch, R.R.; Kruse, C.W.; Chaven, C.; Buchanan, D.H. *Prepr. Pap.-Am. Chem. Soc., Div. Fuel Chem.* **1992**, 37(4), 2002-2009.

TABLE 1. Solvent Extraction Yields of Argonne Premium Coals

APCS #	% C MAF[a]	Wt % Toluene[b]	Wt % Pyridine[b]	Wt % Pyridine[c]	Wt % Pyridine[d]	Wt % CS_2/NMP[e]
801	73		2.9	3.1	3.1	2.3
201	75	2.3	7.1	7.4	6.2	9.9
301	78	7.0	25.8	27.5	27.9	33.1
601	81				32.1	33.6
401	83	5.8	29.7	29.8	26.5	39.0
701	83				14.7	27.1
101	86	0.6	20.9	6.9	14.9	59.4
501	91	0.4	1.2	0.8	0.5	2.8

a Ref. 2; *b* This work; *c* Ref. 5; *d* Ref. 7; *e* Ref. 6.

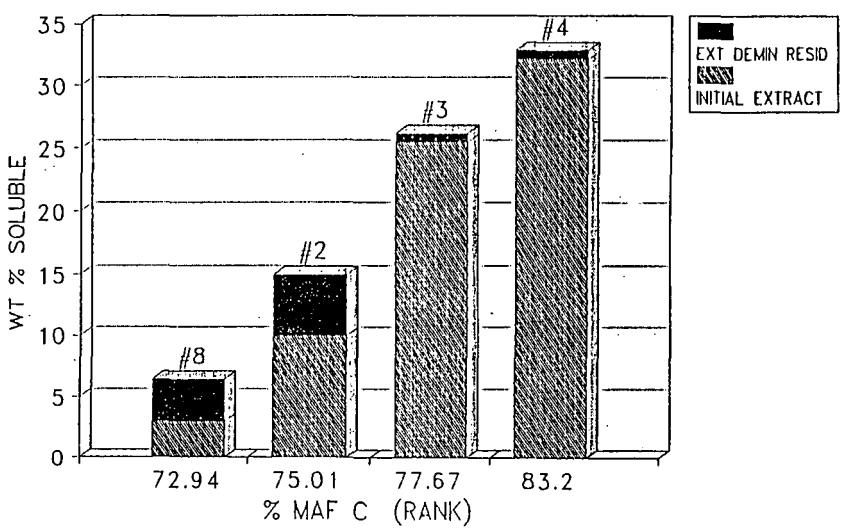

Figure 1. Yields of additional pyridine soluble material extracted from the demineralized, pyridine-insoluble residues of four Argonne Premium coals as a function of coal rank.

PROGRESS IN COAL PYROLYSIS RESEARCH

Peter R. Solomon and Michael A. Serio
Advanced Fuel Research, Inc.
87 Church Street
East Hartford, CT 06108

KEYWORDS: Pyrolysis, Coal, Crosslinking

INTRODUCTION

This paper considers some of the recent progress in both the improved understanding and the identification of areas uncertainty with regard to coal pyrolysis, rates, and mechanisms. The paper addressed two questions:

- what are the controlling chemical factors in coal pyrolysis?
- what are the controlling physical factors in coal pyrolysis?

The factors considered are summarized in Table 1. The problem of answering the questions is that multiple chemical reactions occur whose results depend on how the reactants are bound in the coal macromolecular network. Species-selective transport of the reactants and products further complicate the interpretations. In what follows, we have tried to focus on topics where answers are needed or where significant new progress is being made.

TABLE 1

FACTORS WHICH CONTROL COAL PYROLYSIS

CHEMICAL	PHYSICAL
Bond Breaking Reactions	Tar Vaporization
Retrogressive / Crosslinking Reactions	Viscosity
Effects of Cations	Network Effects
Effects of H_2O	
Effects of O_2	
Network Effects	

Chemical Factors

Bond Breaking - The bond breaking reactions can be separated into two broad categories, those which release small molecular side groups attached to the macromolecular network and those which break bonds holding the network together to form a collection of fragments called metaplast. Study of the former category is easier because, in this case, reactions of a limited number of identifiable functional groups lead (without significant mass transfer limitations) to the production of a limited number of identifiable gas species. The chemistry has been organized into global reactions of functional groups to form specific products.

Study of the latter category of reactions is particularly complicated because: i) the reactants are large, heterogeneous and often insoluble; ii) multiple reactions are generally required to free a product, and iii) removal of products from the reacting metaplast is subject to mass transfer limitations. Global rates can be determined for the overall reactions.

In general, all reaction rates need to be represented by a distribution of reaction parameters about an average (e.g., a Gaussian distribution of activation energies) because of the heterogeneous chemical nature of coals. While much progress has been made in describing the classes of reactions and measuring global rates, a quantitative description of the detailed chemistry of pyrolysis is not yet possible. This objective remains as an important goal.

Of particular interest is the systematic rank dependence of the reaction rates (the rates for all reactions decrease with increasing rank) which has recently been reported (1-3). These experiments were performed at several low heating rates where the temperature of coal particles can be accurately determined and hence the rates accurately measured. Experiments at high heating rates, in which coal particle temperatures are measured (4-9), indicate that extrapolation of the rates measured at low heating rates to high heating rates is reasonable. In addition, some progress has been made in considering higher rank coals to be the results of nature's pyrolysis of lower rank coals in the coal bed over millions of years. These analyses employ pyrolysis rates extrapolated to the lower bed temperatures (6,10,11). For some pyrolysis products, nature's removal of the higher reaction rate part of the distribution can explain the systematic shift in the average rate with rank. This is illustrated in Figure 1 which compares the water evolution curves during pyrolysis of several Argonne coals with predictions for Zap lignite after a simulated maturation at various temperatures.

Crosslinking - Crosslinking reactions are particularly hard to identify because the products are insoluble. Crude measurements can be made of "crosslink density" without identification of the specific crosslinking bond. Such measurements are made by solvent swelling (12) or carbon NMR (9,13). In addition, measurements of the mobile phase by proton NMR (14,15) or by solvent extraction (16) provide data on the variation in the concentration of mobile molecules as they are formed or linked into the network.

The results from pyrolysis studies at heating rates between 0.5 and 1000 K/sec show that crosslinking is rank dependent, with lignites crosslinking at lower temperatures than bituminous coals (17,18). Crosslinking in lignites occurs prior to tar evolution and the rapid loss of weight and aliphatic hydrogen. Crosslinking in high volatile bituminous coals occurs at temperatures slightly higher than the temperature for maximum tar evolution, weight loss, and aliphatic hydrogen loss.

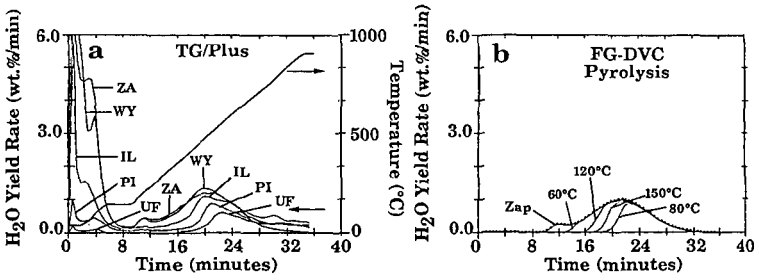

Figure 1. Evolution of H_2O from Five Argonne Premium Coals: (a) Pyrolyzed at 30 K min^{-1}; (b) Predicted for Slow Pyrolysis (geological ageing) at Different Temperatures followed by Pyrolysis at 30 K min^{-1}. ZA, Beulah Zap Lignite; Wy, Wyodak Anderson Subbituminous; IL, Illinois No. 6 HVB, PI, Pittsburgh No. 8 HVB; UF, Upper Freeport MVB. (from Ref. 6).

Studies correlating the crosslink density with other pyrolysis reactions have identified a connection between low temperature crosslinking and CO_2 (and possibly H_2O evolution). These low temperature crosslinking reactions are also related to a loss of carbonyl and hydroxyl functional groups in the coal (17), which is consistent with a loss of carboxyl groups. Similarly, a correlation exists between moderate temperature crosslinking and CH_4 evolution, and high temperature condensation of the macromolecular network and H_2 evolution (17,18).

As in the case of bond breaking reactions, global pathways and rates have been identified for crosslinking reactions but the detailed chemistry is still an important target for study.

Effects of Cations - Crosslinking has also been observed to be influenced by the presence of alkali metals, whose removal increases pyrolysis tar yields (19-22). These results would indicate that the role of carboxyl groups, as indicated above, is important, but it is the carboxylate (cation exchanged carboxyls) which are the key agents in retrogressive reactions for low rank coals. The role of calcium in reducing liquefaction yields from low rank coals has been suggested in previous work by Mochida et al. (23) and Joseph and Forrai (24). It is also consistent with work which shows an effect of calcium on reducing pyrolysis tar yields (19-22). The role of calcium may be to provide a nascent crosslink site in the coal by allowing coordination of groups like carboxyl and hydroxyl which are prone to such reactions. Otherwise, these sites would be more likely to coordinate with water (through hydrogen bonding) then with each other.

Effects of H_2O - The presence of water appears to have a profound effect on the course of pyrolysis. Effects of water during pyrolysis have been studied by Lewen (25) and Monthioux and Landais (26). The impact of water is illustrated in Figure 2 modified from Ref. 26.

The figure presents the atomic H/C ratio as a function of O/C ratio for several pyrolysis experiments. For the line labeled path 1, the pyrolysis system is open and pyrolysis products escape the pyrolysis vessel as they are formed. For these experiments, both oxygen and hydrogen are lost in comparable amounts as pyrolysis proceeds. For path 2, the pyrolysis system is closed. Pyrolysis products fill the pyrolysis vessel and can re-react with the pyrolyzing char. The result is a reduction in the loss of hydrogen and an increase in the loss of oxygen. For path 3, the system is confined to minimize any space into which pyrolysis products can escape. Under these conditions, the loss of hydrogen is further retarded, while the loss of oxygen is accelerated. The path taken by the char is now similar to nature's maturation sequence shown by the shaded band in Fig. 2 for coals from the same bed. The interpretation of these results, as well as the other hydrous pyrolysis experiments suggests that the presence of water due to the confinement of the system results in significant changes in the pyrolysis chemistry. Since the loss of oxygen functional groups is desirable to improve liquid yields from

pyrolysis and liquefaction, and since it is one of the dominant mechanisms in the maturation of coal, understanding and controlling these reactions involving H_2O is an important target.

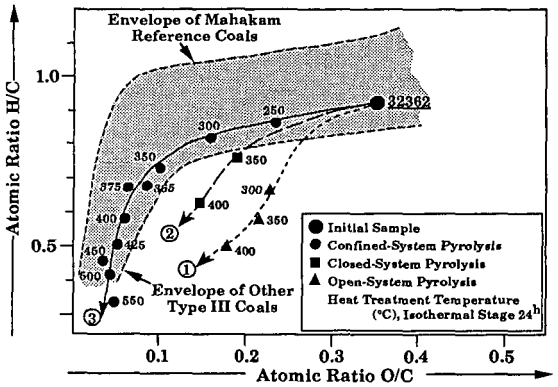

Figure 2. Influence of Confinement Conditions on Elemental Composition of Pyrolysis Chars (from Ref. 26).

Oxygen - The effect of oxygen on coal pyrolysis is most often exhibited through weathering. Low temperature oxidation of the coal results in reduced yields of tar and liquids as well as reduced fluidity. A feature of coal oxidation is that often a very small amount of oxygen added to the coal can cause significant effects in subsequent pyrolysis and liquefaction. Why oxidation has such a profound effect may be a result of changes in the network geometry as discussed in the next section.

Network Effects - Recognizing the macromolecular network nature of coal, a number of network models have been developed (27-30). These models assume the network to be made of thermally stable aromatic ring clusters connected by less stable bridges. When the network is heated, random cleavage of the less stable bridges leads to a collection of network fragments called the metaplast. The molecular weight distribution has been computed using chain statistics (31,32), percolation theory (6,29,30), and Monte Carlo methods (6,27,28). The lightest fraction of the metaplast can vaporize to form tar. Somewhat heavier molecules can be extracted. The heaviest molecules, which are mobile but are not easily extracted, and the extractable molecules provide the coal's fluidity. What is important about the network models is the effect of the network geometry (i.e., whether it is a chain-like or fish-net-like) on the products of pyrolysis. This effect is illustrated in Fig. 3 (from Ref. 6) which presents the molecular weight distribution of network fragments as a function of the average number of bridges per cluster, σ, for two geometries represented by the coordination number, $1 + \sigma$. The coordination number is the maximum number of bridge attachments per cluster. The figure presents results for $\sigma + 1 = 2.2$ (Fig. 3a) which is chain-like (1 extra bridge or crosslink every

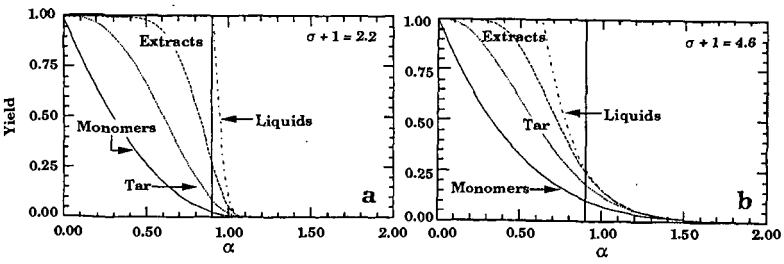

Figure 3. Percolation Theory Predictions for Macromolecular Network Fragment Molecular Weight Distribution as a Function of the Average Number of Attachments per Ring Cluster, σ. For a) $\sigma + 1 = 2.2$; b) $\sigma + 1 = 4.6$ (from Ref. 6). Monomers are all Single Clusters. Tar Consists of Monomers, Dimers, and Trimers. Extracts Consist of Molecules up to 10-nmers and Liquids Consist of Molecules up to 100-nmers.

5th cluster) and $\sigma + 1 = 4.6$ (Fig. 3b) which is fish-net-like. As can be seen, the molecular weight distributions are quite different. In Fig. 3a there is nearly an even distribution of all molecular sizes, while in Fig. 3b the small molecules are favored. The former case would represent the highly fluid char of high volatile bituminous coal, while the latter would represent a non-softening (thermosetting) lignite or subbituminous coal. The importance of low temperature crosslinking events in low-rank coals or in oxidized high rank coals is that the network coordination number is increased. A few added crosslinks does not have a strong influence on the bond breaking chemistry, but rather changes the product distribution through its influence on the network geometry.

Physical Factors:

Tar Vaporization - The tar fraction in pyrolysis consists of molecules heavy enough to condense at room temperature. The source for this material is the small unattached "molecular" fraction of the network plus small molecular fragments produced by pyrolysis. The removal of these molecules is controlled by mass transfer including: vaporization, diffusion, and convective transport. The removal process is in competition with the repolymerization process. Recent models suggest that the tars reach their equilibrium vapor pressure (or close to it) in the light gases produced in pyrolysis and are transported through the char primarily by convection through the pores or by bubble motion (6,28,33,34).

Fluidity - The fluidity of coal as it is heated is typically measured with a Geissler plastometer. High to medium volatile bituminous coals exhibit the highest fluidities. As temperature increases, measurable fluidity appears at a temperature of 350°C. The initial fluidity is reversible and is attributed to physical melting (35). As temperature increases, fluidity increases due to irreversible bridge breaking reactions and then decreases due to crosslinking (36). Low temperature crosslinking in low rank coals can prevent the onset of any observable fluidity.

Models relate fluidity to the amount of the liquid or mobile phase (16,36-38) which can be predicted from network models (6,27-30,35). Experiments which measure the liquid content or mobile phase (14-16) all show similar temperatures for the onset, peak and disappearance of the coal fluidity (6).

Network Effects - The physical effects (tar formation, solvent interactions, and fluidity) are related to the molecular weight distribution of small molecules in the coal, the network fragments forming the metaplast during pyrolysis, and the bonding forces holding these molecules together. Thus, the effect of the network is important because of the effect of network geometry on the molecular weight distribution (see Fig. 3). Low temperature crosslinking in low rank coals leads to a high effective coordination number and hence low amounts of tar and extracts and low fluidity. The lack of such crosslinking in bituminous coals leads to high yields of extracts and tars and high fluidity. Thus, the application of macromolecular network models appears to unify many observations of coal pyrolysis including tar formation, extract formation, metaplast formation, fluidity, and solvent swelling behavior.

CONCLUSION

The progress during the past ten years of research in coal science has resulted in the maturation of many new experimental techniques to follow coal conversion chemistry including NMR, XPS, XANES, FT-IR, ESR, TG-FTIR, solvent swelling, solvent extraction, and MS. These techniques have been used on coals, chars, tars, extracts, model compounds, and model polymers containing natural and isotopically labeled compounds to follow the chemistry in a variety of coal conversion experiments. The results have led to a new understanding of bridge breaking and crosslinking and their variations induced by solvents, catalysts, water, and oxygen. The results have also led to new macromolecular network models of coal pyrolysis and liquefaction. Such models provide a vastly improved global understanding of coal conversion behavior, but detailed understanding of the controlling reactions has not yet been achieved. Such detailed understanding and the resulting strategies for controlling the conversion behavior is the central challenge of coal science in the future.

ACKNOWLEDGEMENTS

Much of the work performed by the authors was supported by the Morgantown Energy Technology Center of the Department of Energy under Contract No. DE-AC21-86MC23075.

REFERENCES

1. Burnham, A.K., Oh, M.S., Crawford, R.W., and Samoun, A.M., Energy & Fuels, **3**, 42, (1989).
2. Solomon, P.R., Serio, M.A., Carangelo, R.M., Bassilakis, R., Gravel, D., Baillargeon, M., Baudais, F., and Vail, G., Energy & Fuels, **4**, (3), 319, (1990).
3. Serio, M.A., Solomon, P.R., Charpenay, S., Yu, Z.Z., and Bassilakis, R., ACS Div of Fuel Chem. Preprints, **35**, (3), 808, (1990).

4. Solomon, P.R., Serio, M.A., and Markham, J.R., Kinetics of Coal Pyrolysis, Int. Conference on Coal Science Proceedings, IEA, Tokyo, Japan, p. 575, (October 23-27, 1989).
5. Serio, M.A., Hamblen, D.G., Markham, J.R., Solomon, P.R., Energy and Fuel, **1**, 138, (1987).
6. Solomon, P.R., Hamblen, D.G., Serio, M.A., Yu, Z.Z., and Charpenay, S., Fuel, **72**, 469, (1993).
7. Fletcher, T.H., Combust. Sci. and Tech., **63**, 89, (1989).
8. Fletcher, T.H., "Time-Resolved Particle Temperature Measurements and Mass Loss Measurements of a Bituminous Coal during Devolatilization", Combustion and Flame, **78**, 223, (1989).
9. Fletcher, T.H., Solum, M.S., Grant. D.M., and Pugmire, R.J., Energy and Fuels, **6**, 643, (1992).
10. Braun, R.L., Burnham,. A.K., and Reynolds, J.G., Energy and Fuel, **6**, 468, (1992).
11. Solomon, P.R., Serio, M.A., Carangelo, R.M., Bassilakis, R., Yu, Z.Z., Charpenay, S., and Whelan, J., J. Anal. and Appl. Pyrol., **19**, 1-14, (1991).
12. Green, T.K., Kovac, J., and Larsen, J.W., Fuel, **63**, 935, (1984).
13. Solomon, P.R., Charpenay, S., Yu, Z.Z., Serio, M.A., Kroo, E., Solum, M.S., and Pugmire, R.J.,"Changes During Coal Pyrolysis: Experiment and Theory", presented at the 1991 Int. Conf. on Coal Science, New Castle, England, (Sept. 1991).
14. Marzec, A., Jurkiewicz, A., and Pislewski, N., Fuel, **62**, 996, (1983).
15. Lynch, L.J., Webster, D.S., Sakurovs, R., Barton, W.A., and Maher, T.P., Fuel, **67**, 579, (1988).
16. Fong, W.S., Peters, W.A., and Howard, J.B., Fuel, **65**, 251, (1986).
17. Solomon, P.R., Serio, M.A, Deshpande, G.V., and Kroo, E., Energy and Fuels, **4**, 42, (1990).
18. Suuberg, E.M., Lee, D., and Larsen, J.W., Fuel, **64**, 1668, (1985).
19. Tyler, R.J. and Schafer, H.N.S., Fuel, **59**, 487, (1980).
20. Morgan, M.E. and Jenkins, Fuel, **65**, 764, (1986).
21. Serio, M.A., Kroo, E., Teng., H., Solomon, P.R., ACS Div. of Fuel Chem. Preprints, **38** (2), 577 (1993).
22. Wornat, M.J. and Nelson, P.F., Energy and Fuel, **6** (2), (1992).
23. Mochida, I., et al., Fuel **62**, 659, (1983).
24. Joseph, J.T. and Forrai, T.R., Fuel **71**, 75 (1992).
25. Lewen, M.D., in Organic Geochemistry, (M.H. Engel and S.A. Macko, Eds.), Plenum Press, NY, Chapter 24, to be published.
26. Monthioux, M. and Landais, P., Energy and Fuels, **2**, 794, (1988).
27. Gavalas, G.R., Coal Pyrolysis, Elsevier, NY, p. 51 (1982).
28. Solomon, P.R., Hamblen, D.G., Carangelo, R.M., Serio, M.A., and Deshpande, G.V., Energy and Fuel, **2**, 405, (1988).
29. Grant, D.M., Pugmire, R.J., Fletcher, T.H., and Kerstein, A.R., Energy and Fuels, **3** 175, (1989).
30. Niksa, S. and Kerstein, A.R., Fuel, **66**, 1389, (1987).
31. Solomon, P.R. and King, H.H., Fuel, **63**, 1302, (1984).
32. Niksa, S., and Kerstein, A.R., Combustion and Flame, **66**, 95, (1986); see also Energy and Fuels, **5**, 647, (1991).
33. Solomon, P.R., Hamblen, D.G., Carangelo, R.M., Serio, M.A. and Deshpande, G.V., Combustion and Flame, **71**, 137, (1988).
34. Niksa, S., AIChE J. **34**, (5), 790, (1988).
35. Waters, P.L.,Fuel **41**, 3, (1962).
36. Solomon, P.R., Best, P.E., Yu, Z.Z., and Charpenay, S., Energy & Fuel, **6**, 143, (1992).
37. Fong, W.S., Khalil, Y.F., Peters, W.A., and Howard, J.B. Fuel, **65**, 195, (1986).
38. Oh, M.S., "Softening Coal Pyrolysis", Ph.D. Thesis, Massachusetts Institute of Technology, (1985).

PROGRESS TOWARD THE DESULFURIZATION OF ORGANIC COAL MOLECULES

Leon M. Stock
Chemistry Division, Building 200
Argonne National Laboratory
Argonne, IL 60439

Keywords: Organic Desulfurization

Introduction

The broad occurrence of sulfur in coal greatly reduces its economic potential, and it is well recognized that the selective removal of the sulfur that is covalently bonded in organic coal molecules constitutes the key challenge for technology. This brief article concerns the character of the organic sulfur compounds, and strategies for the removal of these substances.

The Organic Sulfur Compounds in Bituminous Coals

There is general agreement (1,2) that sulfur was introduced into coal through secondary reactions of the organic plant materials with inorganic sulfur compounds, and that these substances, which were produced by the microbiological reduction of sulfate ions, reacted with coal precursors in a variety of chemical processes including ionic and free radical substitution and addition reactions. Virtually every model compound experiment that has been performed between a plausible sulfur reagent and an organic substrate has successfully introduced sulfur into the organic matrix. Inasmuch as the natural processes occurred in a variety of different environments, the exact reaction pathways are difficult to define. However, it is evident that the amount of sulfur introduced into the coal precursors and retained in the coal varies significantly.

It has been recognized for a long time that heterocyclic sulfur compounds including thiophenes, benzothiophenes, dibenzothiophenes and other heterocycles and their alkylated derivatives, particularly the methylated compounds, are present in fossil fuels. In addition, many kerogens and the less mature coals have considerable amounts of aliphatic sulfur compounds. Although some workers in this field have been rather slow to accept this view, previous investigations by Attar (3), and Calkins (4) and the recent work of de Leeuw and his coworkers (5,6) on kerogens, and also of Gorbaty (7,8), and Huffman (9,10) and their coworkers on coals has demonstrated that these aliphatic materials are clearly present. Indeed, the aliphatic sulfidic sulfur content of the Argonne Premium Coal Samples increases systematically and the thiophenic sulfur content decreases systematically as the maturity of the coal decreases. The Argonne Premium Sample of lignite contains 30 to 40% aliphatic sulfidic sulfur, but the low volatile, much higher ranking bituminous coal sample contains only 3 to 15% aliphatic sulfidic sulfur (7,8,9,10). Presumably, natural thermal and hydrolylic processes convert the aliphatic sulfur compounds into thiophenic derivatives as the coals mature. The X-ray work and even more recent mass spectroscopic investigations are in good accord with the view that rather high levels of sulfidic sulfur can exist in low rank American coals (7-10,11).

Even more important Winans and White and their associates (11,12,13) have shown that many American coals and high sulfur, low rank coals from Europe such as the Rasa subbituminous coal examined by White and his research group (13) have many molecules with more than one heteroatom. This feature of the chemistry is especially relevant in desulfurization reactions when it is coupled with the concept that these lower ranking coals appear to be dominated by molecules with only one, two, and three rings (14).

In summary, the sulfur rich subbituminous and bituminous coals, of which the coals of the Illinois Basin are often described as representative, are heteroatom rich substances with a broad variety of sulfur compounds bonded to sp3 as well as to sp2 carbon atoms and many of the molecules that contain sulfur also contain oxygen atoms. Unfortunately, virtually all of the work on compound speciation has been qualitative, the few quantitative investigations (15) indicate that only a very small fraction of the organic sulfur compounds have actually been defined.

Desulfurization Methods

New methods of the desulfurization of solid coals have been investigated in several laboratories. This work on coal contrasts with the generally well known strategies for the desulfurization of fossil petroleum materials. Molecules that are freely soluble in oils can generally be desulfurized through catalytic hydrogenation reactions involving catalysts that are based upon molybdenum sulfide (16). This chemistry is illustrated by the coprocessing of subbituminous and bituminous coals with petroleum resids. These catalytic reactions enable high coal and asphaltene conversions with the formation of pentane-soluble products in good yield (17). The pentane-soluble oils that are produced in these reactions are virtually free of oxygen, and have rather low concentrations of sulfur and nitrogen. Specifically, the coprocessing of Illinois No. 6 coal and Lloydminster resid provides a product spectrum in which 80% of the sulfur atoms and 40% of the nitrogen atoms have been removed; the oil that is produced contains 1.2% sulfur and 0.4% nitrogen compared to more than 4% sulfur in the resid and coal that were used as the starting fossil materials (17).

An array of other chemical strategies have been studied for the elimination of the organic sulfur from solid coal. Vigorous basic hydrolysis with molten hydroxides has been investigated in some detail (18). The approach requires very severe conditions for effective organic desulfurization, and as a consequence, many workers in the field have sought much lower severity reactions that might accomplish the goal of selective sulfur elimination without comprising the carbon content of the coal or the heat value of the product. One of the key problems that emerged in the early investigations was the fact that of pyritic, organic, and elemental sulfur simultaneously occur in coals that have been exposed to the atmosphere. The elemental sulfur arises from the air oxidation of pyrite and may be reported as organic sulfur as a consequence of the usual analytical scheme. Unfortunately, this complexity can lead to some confusion in the assessment of desulfurization strategies. One solution to this problem is the removal of pyrite and elemental sufur from samples prior to research on organic desulfurization. Both oxidative and reductive procedures are available. We found that the reaction with lithium aluminum hydride, was convenient, quantitative, and, more important, was essentially free of byproduct formation (19). It is much easier to interpret the results of desulfurization experiments when these pyrite-free coals or other very low pyrite macerals or kerogens are used as the starting materials.

Our research for new approaches for selective organic desulfurization has been successful, and the primary goal has been realized in principal, but the chemistry cannot as yet be practically applied.

It seems pertinent to mention some of the strategies that have been considered. Acid-promoted hydrolysis reactions have received some attention. In one approach, we attempted to intercept and selectively to hydrolyze hemithioketal intermediates, but the experiments with coals yielded disencouraging results (20). We also examined thermal methods and thermal methods coupled with sulfur capture by metals as well as strategies based on organonickel compounds.

However, we placed most of our effort on single electron transfer reactions. Our ideas were based on the concept that the carbon-sulfur bond strengths in anion radicals would be greatly diminished when these substances were reduced to anion radicals, and on the fact, which has been known for many years, that single electron transfer reactions can eliminate sulfur from heterocyclic and aromatic molecules under quite mild reaction conditions. Investigations of these single electron transfer reactions for pure compounds and representative bituminous coal have been very encouraging and some coals can be almost completely desulfurized in such reactions (21,22). For example, the sulfur content of pyrite-free Illinois No. 6 coal could be reduced by SET chemistry to about 1.1% sulfur under quite mild conditions (21,22).

The study revealed that some sulfidic sulfur compounds in the Illinois coals resisted desulfurization by this SET strategy (22). We then considered the use of strong bases which might be more effective for aliphatic desulfurization (23), even though they are not usually effective for the removal of heterocyclic molecules. These basic reactions had to be carried out near 100°C, and the Illinois coals experienced extensive desulfurization. When the SET and base reactions were carried out sequentially, the organic sulfur content was reduced to about 0.7 wt%. Subsequent work has demonstrated that the remaining sulfur compounds have fragile carbon-sulfur bonds that are readily cleaved. Thus, we have demonstrated that chemical reagents can quite selectively remove or alter the properties of the organic sulfur compounds in coal under rather mild conditions and that these reactions can be performed without detrimental losses of material or heat content. The technological challenge remains to implement this chemistry by practical means.

References

1. Smith, J. W.; Batts, B. D. *Geochimica et Cosmochimica Acta*, **1974**, *38*, 121.
2. Chou, C. L. In *Geochemistry of Sulfur in Fossil Fuels* , Orr, W. L.; White, C. M., Eds.; *ACS Symposium Series , 429*, American Chemical Society: Washington, D.C., Chapter 2.
3. Attar, A., In *Analytical Methods for Coal and Coal Products*, Karr, C. Ed.; *Academic Press*, New York, **1979**.
4. Calkins, W. H. *Energy and Fuels*, **1987**, *1*, 59.
5. Sinninghe Damsté, J. S.; Eglinton, T. I.; DeLeeuw, J. W.; Schenck, P. A. *Geochim. Cosmochim. Acta* **1989**, *53*, 873.
6. Sinninghe Damsté, J. S. *Organically-Bound Sulphur in the Geosphere: A Molecular Approach*, Offsetdrukkerij Kanters B. V.: Alblasserdan, The Netherlands, **1988**.
7. George, B. N.; Gorbaty, M. L.; Kelemen, S. R.; Sansone, M. *Energy and Fuels*, **1991**, *5*, 93.
8. Calkins, W. H.; Torres-Ordonez, R. J.; Jung, B.; Gorbaty, M. L.; George, G. N.; Kelemen, S. R. *Energy and Fuels*, **1992**, *6*, 411.
9. Huffman, G. P.; Huggins, F. E.; Mitra, S.; Shah, N.; Pugmire, R. J.; Davis, B.; Lytle, F. W.; Greegor, R. B. *Energy and Fuels*, **1989**, *3*, 200.
10. Huffman, G. P.; Huggins, F. E.; Shah, N.; Lu, F.; Zhao, J. *Preprint Pap., Fuel Chem. Div., Am. Chem. Soc.*, **1993**, *38(2)*, 369.
11. Winans, R. E.; Neill, P. H. *Multiple-Heteroatom-Containing Sulfur Compounds in a High Sulfur Coal*, In *Geochemistry of Sulfur in Fossil Fuels*, Orr, W. L.; White, C. M. Eds., *ACS Symposium Series, 429*, American Chemical Society: Washington, D.C., Chapter 15.
12. Winans, R. E.; Melnikov, P. E.; Dyrkacz, G. R.; Bloomquist, C. A. A. *Preprint Pap. Fuel Chem. Div., Am. Chem. Soc.*, **1993**, *38(2)*, 375.
13. White, C. M. ; Douglas, L. J.; Anderson, R. R.; Schmidt, C. E.; Gray, R. J. In *Geochemistry of Sulfur in Fossil Fuels*; Orr, W. L.; White, C. M., Eds.; *ACS Symposium Series 429*, American Chemical Society: Washington, D.C., Chapter 16.
14. Winans, R. E. *Mass Spectrometric Studies of Coals and Coal Macerals*, In *Advances in Coal Spectroscopy*, Plenum Press: New York and London, **1992**, Chapter 11.
15. Nishioka, M. *Energy and Fuel*, **1988**, *2*, 214.
16. Gates, B. C.; Katzer, J. R. Schuit, G. C. A. *Hydrodesulfurization.* In *Chemistry of Catalytic Processes*, McGraw-Hill Book Co.: New York, **1979**, Chapter 5.
17. Nafsis, D. A.; Humbach, M. J.; Gatsis, J. G. Coal Liquefaction Coprocessing, *Final Report*, DOE/PC/70002-T6, **1988**.
18. Meyers, R. A.; McClanthan, L. C.; Hart, W. D. Proc. Pittsburgh Coal Conf., **1985**, 112.
19. Westgate, L. M.; Anderson, T. F. *Anal. Chem.*, **1982**, *54*, 2136.
20. Wolny, R.; Stock, L. M. *The Protodesulfurization of Naphthalene Thiols and Sulfides.* In *New Trends in Coal Chemistry*, Y. Yurum, Ed., Kluwer Academic Publishers, **1988**, 287.
21. Chatterjee, K.; Wolny, R.; Stock, L. M. *Energy and Fuels*, **1990**, *4*, 402.
22. Stock, L. M.; Chatterjee, K. *Preprint Pap., Fuel Chem. Div., Am. Chem. Soc.*, **1993**, *38(2)*, 379.
23. Chatterjee, K.; Stock, L. M. *Energy and Fuels*, **1991**, *5*, 704.

XAFS STUDIES OF COAL

G.P. Huffman, F.E. Huggins, N. Shah, F. Lu, and J. Zhao
CFFLS, 233 Mining & Minerals Res. Bldg., University of Kentucky,
Lexington, KY 40506-0107

Keywords: XAFS, sulfur, trace elements, calcium, chlorine, potassium

INTRODUCTION

Over the past 10 years, x-ray absorption fine structure (XAFS) spectroscopy has been extensively applied to a variety of problems in coal science. The current paper will review those applications. Because of the fact that XAFS spectroscopy focuses on only one element at a time, it is ideally suited to examining the structure of individual elements in highly heterogeneous materials like coal and its derivatives. We will briefly review XAFS studies of S, Ca, K, Cl, and several trace elements(As, Cr, etc.) in coal. Applications of XAFS in studies of coal combustion, liquefaction, and gasification will be discussed, with emphasis on in situ studies.

EXPERIMENTAL METHOD

The experimental procedure for obtaining high quality XAFS spectra from various elements in coal is discussed in detail in the references. Briefly, the x-ray beam emitted tangentially from a synchrotron is converted into a high-intensity, monochromatic x-ray beam using a double crystal monochromator. This x-ray beam is then collimated and directed onto the sample to be studied. The monochromator crystals are then turned through a range of Bragg angle in such a manner as to sweep the x-ray energy through the x-ray photoelectric absorption edge(usually the K-edge, occasionally the L-edge) of the element of interest. The x-ray absorption spectrum is measured either by detecting the x-rays that pass through a thin sample without being absorbed, or by detecting the fluorescent x-rays that are emitted by the element of interest after photoelectric absorption of the incident x-rays takes place. Variations on the experiment, such as in situ spectroscopy at elevated temperatures, the use of specialized detectors, etc., are discussed in the references.

The spectra are broken into two regions for detailed computer analysis: the x-ray absorption near edge structure(XANES) region and the extended x-ray absorption fine structure(EXAFS) region. The XANES consists of a series of peaks derived from inner-shell photoelectron transitions to vacant bound levels and scattering resonances. It can be deconvoluted to yield definitive information about the types of electronic bonding present. The EXAFS region can be subjected to a Fourier transform analysis procedure which yields radial distribution functions that are processed to derive information about the local atomic environment; i.e., the type, number, and interatomic distances of neighboring atoms.

RESULTS

The principal results obtained for a number of different elements of interest in several areas of coal science are briefly summarized below. Topics of current and future interest are also discussed.

Calcium

One of the earliest coal-related XAFS studies conducted was an investigation of calcium in coal.[1,2] It was demonstrated that XAFS spectroscopy detected two major types of calcium: that contained in calcite in bituminous coals, and that bound to oxygen anions in carboxyl groups in lignites and subbituminous coals. The radial distribution functions derived from the XAFS spectra indicated that the carboxyl bound calcium is molecularly dispersed through the macerals.

In situ studies of the carboxyl-bound calcium in lignite were carried out during pyrolysis in He and gasification in CO_2 and He-O_2 at temperatures up to 500 °C.[3-5] Only small changes were observed in the calcium spectra, indicating that the calcium undergoes relatively little agglomeration and retains its nearest neighbor oxygen environment with relatively little change under these conditions. Pyrolysis at higher

temperatures (800-1000 °C) causes agglomeration of the calcium to form CaO, which exhibits a distinctive radial distribution function.

During combustion, calcium is rapidly transformed to CaO, which can either react with aluminosilicates to form a Ca-containing aluminosilicate slag, or with SO_2 to form $CaSO_4$. XAFS studies combined with other characterization research have demonstrated that these reactions play an important role in slagging and fouling during coal combustion.[6,7]

Potassium

Potassium occurs almost exclusively in bituminous coals in the form of illite, which exhibits a very distinctive XANES spectrum.[8] Under combustion conditions, the illite melts and contributes significantly to ash deposition problems during combustion.[7,9]

In situ XAFS studies of the pyrolysis and gasification reactions of potassium ion-exchanged into lignite have been carried out.[5] The ion-exchanged, carboxyl-bound potassium exhibits little change up to 500 °C in He, but converts rapidly to K_2CO_3 when O_2 is admitted into the hot cell.

Chlorine

The authors have recently completed an XAFS investigation of chlorine in a wide variety of coals.[10,11] Chlorine XANES spectra for coals of rank higher than subbituminous are closely similar regardless of chlorine content, rank, and geographic origin, indicating one major mode of occurrence. The evidence indicates that this mode of occurrence is chloride anions in moisture anchored to the surfaces of micropores in coal by organic ionic complexes, such as quaternary amine groups and alkali carboxyl groups. It would appear that the observation of NaCl and other inorganic chlorides is an artifact resulting from precipitation of solid chlorides upon release of moisture from the coal during size reduction and storage.

Sulfur

Extensive XAFS research has been conducted on sulfur in coal in recent years.[12-18] It is no exaggeration to say that, as a result of this work, analysis of sulfur XANES spectra has become widely recognized as the best method yet developed for the non-destructive, in situ characterization of the organic sulfur functional forms in coal. Sulfur K-edge XANES can distinguish and quantify with an accuracy of ~±5-10% the amounts of the following major forms of sulfur: thiophene, sulfide, disulfide, elemental sulfur, sulfoxide, sulfone, sulfate, pyrite, and pyrrhotite. S K-edge XANES has been used to study the reactions of sulfur during pyrolysis[16] and desulfurization[17,18].

Recently, it has been demonstrated that sulfur L-edge XANES spectroscopy also has great potential for quantification of sulfur functional forms.[19,20] The L-edge XANES spectra appear to have better resolution for different sulfur groups than the K-edge spectra. However, the technique is considerably more difficult experimentally, and much model compound calibration work remains to be done. Nevertheless, a preliminary comparison of sulfur K-edge and L-edge results for the analysis of sulfur forms in Mequinenza lignite gave reasonable results.[21]

An excellent review of the XANES methods and other methods of characterizing sulfur in coal has recently been written by Davidson.[22]

Trace Elements

Recently, by using an array detector with 13 germanium detection elements, it has been possible to obtain quality XAFS spectra of several critical trace elements in coal.[23,24] The primary work to date has been on arsenic and chromium. High quality spectra were obtained at concentration levels as low as 10 ppm. The principal observation of interest for chromium is that there appears to little if any(<5% of the total) Cr^{+6} present in either the coals or the combustion ashes investigated to date. Only Cr^{+3} is observed. In coal, the form of chromium has been tentatively identified as chromium hydroxide. For arsenic, it is found that most of the arsenic in fresh coals is contained as As in pyrite. In only one coal(Pittsburgh #8, DECS-12) was arsenopyrite observed. Arsenic was also present, however, in all of the coals studied

as arsenate(As(V)). The amount of arsenate was observed to increase fairly rapidly as a result of oxidation under ambient conditions, becoming the dominant form of arsenic present after ~6 months.

Current and Future Research

XAFS spectroscopy has proven to be an excellent method for investigating the structures of the many important elements in coal. Research currently underway or planned for the future that is expected to yield significant results is summarized briefly below.

1. Nitrogen XANES spectroscopy may prove to be as informative as sulfur XANES spectroscopy. Initial studies by Mitra-Kirtley et al.[25] look quite promising.
2. XAFS studies of trace elements will undoubtedly increase. Investigation of the reactions of As and Cr during combustion, cleaning or other processes are in progress, and several additional trace elements will be studied.
3. In situ studies under more severe conditions will be emphasized in future research. These include in situ studies of the reactions of such elements as Fe, Ca, K, and S during coal combustion, and studies of liquefaction catalysts at high temperatures and hydrogen pressures.
4. Carbon XANES has recently been shown to have promise in the area of imaging. Using a highly collimated beam, Botto and his co-workers[26] have succeeded in imaging macerals in coal by bracketing the characteristic XANES peaks from aromatic and aliphatic carbon and scanning a thin sample.

It appears that this highly versatile technique will continue to have many applications in coal science for years to come.

ACKNOWLEDGEMENT

This work has been supported by the office of Exploratory Research at the Electric Power Research Institute under contract RP-8001, by the U.S. Department of Energy under several contracts, and by the Gas Research Institute.

REFERENCES

1. F. E. Huggins, G. P. Huffman, F. W. Lytle, and R. B. Greegor, Proceedings of the 1983 International Conference on Coal Science, Pittsburgh; PA; pp. 679-682 (International Energy Agency, 1983).
2. G. P. Huffman and F. E. Huggins, ACS Symposium Series No. 264, pp. 159-174, Chemistry of Low-Rank Coals, Ed., H. H. Schobert, Amer. Chem. Soc., 1984.
3. G. P. Huffman, F. E. Huggins, R. G. Jenkins, F. W. Lytle, and R. B. Greegor, Fuel 65, 1339-1344 (1986).
4. F. E. Huggins, N. Shah, G. P. Huffman, R. G. Jenkins, F. W. Lytle, and R. B. Greegor, Fuel, 67, 938-941 (1988).
5. F. E. Huggins, N. Shah, G. P. Huffman, R. G. Jenkins, F. W. Lytle, and R. B. Greegor, Fuel, 67, 1662-7 (1988).
6. G. P. Huffman, F. E. Huggins, A. A. Levasseur, J. Durant, F. W. Lytle, R. B. Greegor, and Arun Mehta, Fuel, 68, 238-242 (1989).
7. G. P. Huffman, F. E. Huggins, and N. Shah, Progress in Energy and Combustion Science, 16. #4, 293-302 (1990)
8. G. P. Huffman, F. E. Huggins, R. A. Shoenberger, J. S. Walker, R. B. Greegor, and F. W. Lytle, Fuel 65, 621-632 (1986).
9. S. Srinivasachar, J. J. Helble, A. A. Boni, G. P. Huffman, F. E.Huggins, and N. Shah, Progress in Energy and Combustion Science, 16, #4, 243-252 (1990).
10. F. E. Huggins and G. P. Huffman, "An XAFS Investigation of the Form-of-Occurrence of Chlorine in U.S. Coal," Chlorine in Coal, First International Conference, Ed., J. Stringer, Vol.17, Coal Science and Technology, Elsevier, **1991**, pp.45-58.
11. F. E. Huggins and G. P. Huffman, "Chlorine in Coal: An XAFS Spectroscopic Investigation," **1993**, Fuel, submitted.
12. G.N. George and M.L. Gorbaty, **1989**, J. Am. Chem. Soc., *111*, 3182.

13. S.R. Kelemen, M.L. Gorbaty, G.N. George, **1990**, Fuel, *69*, 939.
14. G.N. George, M.L. Gorbaty, and S.R. Kelemen, **1991**, Energy & Fuels, *5*, 93.
15. G.P. Huffman, S. Mitra, F.E. Huggins, N. Shah, S. Vaidya, and F. Lu, **1991**, Energy & Fuels, *5*, 574-581.
16. M. Mehdi Taghiei, F.E. Huggins, N. Shah, and G.P. Huffman, Energy & Fuels, **1992**, *6*, 293-300.
17. F.E. Huggins, S.V. Vaidya, N. Shah, and G.P. Huffman, Fuel Processing Technology, in press.
18. G. Huffman, N. Shah, F. Huggins, L. Stock, K. Chatterjee, J. Kilbane, M. Chou, and D. Buchanan, "Sulfur Speciation of Desulfurized Coals by XANES Spectroscopy", submitted to Fuel; preprint version published in Amer. Chem. Soc. Div. of Fuel Chem. Preprints, **1992**, *37(3)*, 1094-1102.
19. M. Kasrai, J.R. Brown, G.M. Bancroft, K.H. Tan, and J.M. Chen, **1990**, Fuel, *69*, 411-414.
20. J.R. Brown, M. Kasrai, G.M. Bancroft, K.H. Tan, and J.M. Chen, **1992**, Fuel, *71*, 649-653.
21. C.M. White et al., "A Study of Mequinenza Lignite," **1993**, Fuel, in press.
22. R.M. Davidson, Organic Sulphur in Coal, **1993**, IEA Coal Research, London.
23. F.E. Huggins, N. Shah, J. Zhao, F. Lu, and G.P. Huffman, Energy & Fuels, **7**, 482-489.
24. G.P. Huffman, F.E. Huggins, N. Shah, and J. Zhao, "Speciation of Critical Trace Elements in Coal and Combustion Ash by XAFS Spectroscopy," International Trace Elements Workshop, Scottsdale, AR, April, 1993; to be published in Fuel Processing Technology.
25. S. Mitra-Kirtley, O.C. Mullins, J. Branthaver, J. Van Elp and S.P. Cramer, **1993**, Amer. Chem. Soc., Div. Fuel Chem. Preprints, *38(3)*, 762-768.
26. R.E. Botto, reported during a presentation at the 7th ICCS Conference, Banff, Canada, 1993.

STATUS OF COAL ASH BEHAVIOR RESEARCH

Steven A. Benson, Everett A. Sondreal, and John P. Hurley
Energy & Environmental Research Center
PO Box 9018
Grand Forks, ND 58202-9018

Keywords: Coal, Combustion, Gasification, Inorganic Species, Ash Deposition

INTRODUCTION

The inorganic impurities in coal are converted to ash during combustion and gasification. The problems associated with ash in combustion and gasification systems include deposition on refractory and heat-transfer surfaces, corrosion and erosion of system parts, fine particulate that is difficult to collect, and maintaining slag flow in slagging systems. An overview of ash formation and deposition in utility boilers was performed by Benson and others (1993).

In recent years, significant advances have been made in understanding and predicting the behavior of ash in combustion and gasification systems. These predictions are based on a detailed knowledge of ash formation and deposition mechanisms that have been obtained through bench-, pilot-, and full-scale testing. The mechanisms have been elucidated through the use of advanced methods of coal and coal ash analysis. These techniques are based on scanning electron microscopy and microprobe analysis to determine both the chemical and physical characteristics of coal minerals, fly ash, agglomerates, and deposits. Several methods to predict ash behavior are being developed, including advanced indices and phenomenological models. The analytical methods and predictive methodologies have been described in detail by Benson and others (1993).

This paper summarizes Energy & Environmental Research Center (EERC) work that has been accomplished on ash-related research pertaining to coal-fired utility boiler and provides a brief overview of ash issues related to emerging and advanced technologies that utilize coal. Much of the discussion focuses on the behavior of ash produced from lower-ranked coals, such as lignites and subbituminous from the U.S.

ASH FORMATION

Depending upon the severity of the process, the inorganic impurities can go through significant physical and chemical transformations. Physical transformations involved in high-temperature suspension- or entrainment-type combustion and gasification systems include 1) selective elemental vaporization and subsequent reaction/condensation to form surface coatings or homogeneous fine particulates, 2) coalescence of mineral grains within hot reactive char particles, 3) char fragmentation and partial coalescence of included minerals, 4) shedding of particles from the char surface, 5) fragmentation or fusion of liberated mineral grains, 6) convective transport of volatile species within and between char/mineral particles, and 7) formation of thin-walled ash spheres known as cenospheres. The typical result of these interactions is an ash having a multimodal size distribution, including larger particles that resemble the inorganic constituents in the parent coal and a very fine submicron fractionate resulting from condensation and fragmentation. Some liberated minerals with high melting temperatures, such as quartz (SiO_2), are carried through a reactor in their original angular form. However, at high temperatures, the bulk of the total inorganic content, made up of silicate and aluminosilicate particles, in dynamic association with other condensed or fused phases, will tend to form molten glassy spheres.

The extent to which different elements initially vaporize and subsequently remain in the vapor state depends on their original association in the coal, the process temperature, and the gas composition (e.g., oxidizing or reducing, water vapor concentration, HCl concentration). In general, alkaline earth elements (Ca, Mg) will tend to remain primarily in a condensed form. Silica and alumina can only be volatilized as suboxides in a reducing atmosphere, causing their vapor or submicron fume to play a very minor role in combustion systems, but possibly a significant role in gasification. The fraction of potassium originally present in illite-type clays tends to be retained in the bulk aluminosilicate ash, as evidenced by the high temperatures (up to 1350°C) required to revolatilize potassium from combustion fly ash (Sondreal, Gronhovd, and Severson, 1985). All available evidence indicates that the sodium in low-rank coal (along with the organically associated potassium) is substantially vaporized and subsequently distributed throughout a reactor system, primarily as a surface coating on ash particles or as discrete particles (with enrichment in finer particle-size fractions), but also as a persistent vapor under certain conditions of concern in advanced power systems.

Reactions of organically associated alkali and alkaline earth elements are initiated by the decomposition of carboxylates to form carbonates between 400° and 600°C (Stewart, Stinespring, and Davidovits, 1982). At higher temperatures, the carbonates are believed to decompose to metal oxides that are subsequently reduced to metal vapor by carbon monoxide or char. In a quadrupole mass spectrometry profile of a laboratory-pulverized lignite–air flame, vapor-phase sodium atoms appeared first, followed by vapor-phase sodium hydroxide

(Greene and O'Donnell, 1987). Quenched sampling of an entrained flow combustion reactor operated on Montana lignite indicated that up to 80% of the coal sodium was vaporized and converted to a submicron fume at 1900 K (1627°C, 2961°F) (Neville and Sarofim, 1985). Up to 20% of the magnesium and a small percentage of the calcium were vaporized (Quann and Sarofim, 1986).

Thermal reaction products from discrete mineral grains in low-rank coals produced by laboratory ashing (oxidation in air) at temperatures between 250° and 1300°C include the major x-ray diffraction (XRD) groupings (Falcone and Schobert, 1986; Falcone, Schobert, Rindt, and Braun, 1984). Laboratory thermogravimetric analysis (TGA) and differential thermal analysis (DTA) have also been used to study phase transformations as a function of temperature (O'Gorman and Walker, 1973). With heating in air, clays first lose their absorbed interlayer water between 50° and 150°C. Gypsum ($CaSO_4 \cdot 2H_2O$) dehydrates in this same temperature range, first to bassanite ($CaSO_4 \cdot \frac{1}{2}H_2O$) and then to anhydride ($CaSO_4$) at 180°C. Clay structures are further dehydrated and collapsed by loss of hydroxyl water between about 350° and 600°C, with attending substitution of cations derived from carboxylates, carbonates, oxides, and sulfates into the structure. The oxidation of pyrite (FeS) to produce iron oxides occurs between 325° and 620°C, and calcite ($CaCO_3$) decomposes to calcium oxide between 700° and 830°C. Quartz is stable up to 1000°C. Various glassy and amorphous phases are observed at 1300°C. The amorphous glass and liquid phases have special importance as bonding agents in high-temperature sintered deposits. In crystalline materials the structural units observed for some of the common silicate systems typical of many lower-rank coal deposits are summarized in Table 1.

The crystallization behavior of ashes and slags can provide insight into the temperature at which the deposit or fly ash formed. In addition, crystallization from a liquid phase changes the composition of the residual liquid and that influences its physical properties. This is extremely important in determining slag viscosity. The temperature of critical viscosity, T_{cv}, is the temperature when crystallization from the liquid phase occurs. This crystallization causes the flow characteristics to go from a Newtonian liquid to a non-Newtonian liquid.

Sulfates also contribute to the formation of deposits in combustion systems. The sulfate phases form as a result of the reaction of SO_3 with alkali and alkaline earth elements such as sodium and calcium, respectively. Sulfates are formed primarily by vaporization and condensation processes. During combustion, sulfur oxides form primarily from the oxidation of sulfides and organic sulfur in the flame. At the high temperatures in a flame, sulfur dioxide forms first followed by the formation of sulfur trioxide. At lower temperatures, equilibrium favors the formation of SO_3. Sulfur oxides can interact with the surface of fly ash particles. It has been shown that the maximum amount of reaction occurs between sulfur oxides and ash at approximately 560°C and is dependent upon the quantity of alkali and alkaline earth oxides in the ash. The exact way alkali and alkaline earth sulfates form in combustors appears to be poorly understood. It is assumed that the alkali elements volatilize in the flame and are converted to oxides. The alkali oxide then reacts with SO_2 and O_2 or SO_3 to form sulfates. It has been postulated that sulfates form in the gas stream and condense on the surfaces of materials such as fly ash particles or boiler steel surfaces. Another possible path for the reaction is on the surface of entrained fly ash particles where an alkali layer (NaOH) is first deposited and the subsequent sulfur oxide interaction.

ASH DEPOSITION AND AGGLOMERATION

Pulverized Coal Combustion

Ash deposition mechanisms in pulverized coal combustion systems have been extensively investigated by the EERC under sponsorship of industry consortia (Benson and others, 1988, 1992; Hurley and others, 1992). At the microscopic level observable by scanning electron microscope point count (SEMPC) techniques developed at the EERC, ash deposits in combustion systems are shown to be caused by sodium-rich glass/liquid cementing phases and recrystallized alkaline earth aluminosilicates at temperatures above about 1900°F (1038°C) and by low melting sulfate-rich phases that bond deposits at lower temperatures. Sodium enrichment of the aluminosilicate-based amorphous phase is the foremost cause of the low liquid-phase viscosity and sintering that characterize severe fouling at higher temperatures. This type of ash deposition has been successfully modeled by a viscous flow sintering mechanism, where the growth and strength of the deposit are directly related to the amount of the liquid phase and inversely proportional to its viscosity.

At temperatures below 1900°F (1038°C), the thermodynamic equilibrium shifts to allow sulfation of alkali and alkaline earths, leading to several modes of ash deposition when high-calcium coals are burned in pc-fired boilers. Laboratory strength tests and SEM observations indicate that calcium sulfate crystals form an interlinked lattice that imparts strength over periods of 1 to 10 days, with more rapid strength development occurring at higher temperatures up to 1850°F (1010°C), at higher ratios of total alkali to silica ($[Na_2O + K_2O + MgO + CaO]/SiO_2$), and with more uniform diffusion of SO_2 through the deposit. Deposits formed on leading edge tube banks just below 1900°F rapidly become sulfated and hard. Tubes downstream of this screening action are coated with calcium-rich enamel-like deposits that are hard upon deposition and formed from particles smaller than about 3 μm. Loose powdery deposits formed on the downstream side of tubes, by ash particles smaller than

10 μm being trapped in gas eddies behind the tubes, are somewhat stronger at higher gas velocities and correspondingly smaller, affected particle sizes. A low-temperature engineering algorithm of deposition risk (LEADER) has been developed at the EERC to predict low-temperature deposition.

Fluidized-Bed Combustion

The FBC process consists of two subprocesses: a) the fluidization of solids, by which solid particles/granules are suspended in an upward flowing stream of gas and b) the combustion process, in which fuel particles are burned to sustain temperature. The solids in FBCs are typically fuel ash, bed material, sorbent used to control pollutants, and reaction products formed by sulfur capture and other sorbent–coal interactions. FBC systems operated at atmospheric pressure are classified as atmospheric fluidized-bed combustors (AFBCs), which usually also denotes low fluidization velocities resulting in a bubbling bed. Circulating fluidized-bed combustors (CFBCs) operate at fluidization velocities approximately 7 to 8 times higher. At these velocities, the rising gas entrains the bed materials; the resulting bed consists of a turbulent cloud of solids that fills the combustion chamber. A portion of the bed material is continuously carried out with the offgas and recirculated back to the combustion chamber. Pressurized fluidized-bed combustion (PFBC) systems are similar to AFBCs, but operate under pressure. The compressed air used contains more oxygen per unit volume and, therefore, sustains a higher intensity of combustion, allowing for the design of smaller combustors. The other principal advantage of the PFBC is the increased conversion efficiency (coal-to-electricity) that can be achieved by passing the hot, pressurized combustion gases through both a gas turbine and a waste-heat boiler serving a steam turbine to extract more usable energy in a combined cycle system.

Although FBCs typically operate at low temperatures (1450° to 1700°F), evidence from pilot, industrial, and utility boilers indicates that certain ash components have the potential to cause ash-related problems. These problems can manifest themselves as agglomeration and sintering of the bed material or as deposition on the heat exchanger tube surfaces.

Agglomeration, sintering, and deposition have all been observed in a number of operational FBCs (Steen and Imsdahl, 1989; Makansi, 1988; Miller, 1988; Mann and others, 1992). Analytical results of samples from these various units indicate that the material that forms the initial layers on the bed material, in the case of agglomeration, and on tube surfaces, in the case of deposition, is the result of the presence and behavior of sodium- and potassium-rich calcium sulfates. The sodium, potassium, and sulfur are readily volatilized during combustion and condense on the cooler surfaces. Calcium released from the coal during combustion also reacts with the sulfate matrix. This sulfate matrix may be molten at the operating temperatures of the fluid bed and serve to glue particles together in the form of agglomerates or form thicker deposits. The sulfate matrix sinters over time to form a strongly bonded deposit.

Certain requirements are necessary for these phenomena to occur. The fuel must contain alkali or alkaline earth elements that can be liberated during combustion. Organically bound elements are typically liberated during combustion and have been shown to be the major precursors to in-bed tube deposition and agglomeration. In addition, competing reactions with other coal mineral components can reduce the alkali availability. The fate of these potential deposit- and agglomerate-forming minerals will ultimately influence the extent of deposition and agglomeration. Therefore, it is important to understand the nature of the mineral matter in the original coal so that improvements can be made in the prediction of FBC performance.

Bed material agglomeration is the process which causes relatively small bed particles to stick together, forming larger masses of material. Coal ash reacting with bed material forms the substance which acts as the "glue" in agglomeration. These ash-related interactions occur under normal FBC-operating conditions and include the formation of low melting eutectics between sodium-, potassium-, calcium-, and sulfate-rich components and, possibly, some solid-solid reactions. Agglomeration can also occur as a result of localized hot spots of bed material, where temperatures in the FBC system can exceed the typical 1700°F limit. Temperatures capable of melting various ash species can be attained even during relatively stable operation of the FBC.

A very fine-grained coal ash matrix deposited on in-bed superheat surfaces has been noted in both pilot facilities and utility-scale systems. This deposition is related to the coal ash chemistry and has been observed in stations operating with a bed temperature as low as 1450°F, despite the high erosive forces of bed material in a bubbling fluid bed. The mechanism of adherence and growth appears to be via a molten sulfate matrix, due to the fluxing action of alkali.

Coal Gasification

In coal gasification systems, the coal is converted to a combustible gas, volatiles, char, and ash/slag. Coal gasification has been technically and economically feasible for many years. Commercial gasifiers differ widely in the way in which they produce ash, and either a dry ash, an agglomerated ash, or slag may result. The Lurgi and other fixed-bed gasifiers

operate by passing air or oxygen and steam under pressure up through a bed of coal, which is fed to the top of the bed through a lock hopper. Coal and char move to the bottom as they are gasified, and the dry ash is removed through a bottom grate. Alternatively, a fixed-bed gasifier can be designed to operate at high temperatures, producing a bottom slag that is tapped through a hearth, i.e., the British Gas Lurgi (BGL) process. Fluidized-bed gasifiers, including the U.S. Kellogg Rust Westinghouse (KRW) and Institute of Gas Technology (IGT) processes and the German Winkler process, operate in a gasification mode using steam and air or oxygen in a fashion resembling PFBC. Either dry ash or a fused agglomerated ash may be produced depending on the design, operating temperatures, and the fusion temperature of the ash. Entrained flow gasifiers, including Dow, Texaco, and Shell designs, all operate at very high temperatures and produce a vitreous slag. Integrated gasification combined cycle (IGCC) systems directly link these various types of gasifiers with a gas turbine/steam turbine cycle to achieve high conversion efficiency.

In a dry ash fixed-bed gasifier or grate-type combustor, bed temperatures are maintained below the fusion temperature of the ash, and the bulk of the ash along with a substantial part of the coalesced vapor and liquid species are consolidated in the grate discharge. In very high-temperature slagging gasifiers and combustors, all of the physical transformations described are operative, but the consolidation of ash and slag depends on reactor configuration. In a fixed-bed slagging reactor (e.g., the BGL gasifier), virtually all of the inorganic reaction products are recaptured in the relatively cool descending fuel bed and consolidated into the slag discharge. In an entrained flow reactor (e.g., Texaco, Dow, and Shell gasifiers or cyclone-type combustors), slag is partially separated by impingement or cyclonic action while a (potentially small) fraction is carried forward with the hot gas.

The chemical, mineralogical, and physical characteristics of gasifier ash have been investigated (Eklund, 1986; McCarthy and others, 1985; Stevenson and Larson, 1985; Hassett and others, 1985), and the characteristics of ash produced from the Shell pilot-scale testing (Mahagaokar and others, 1990) and Texaco testing (EPRI, 1990) have been reported. Slag/ash samples have been characterized from eight gasifiers (Eklund, 1986). The types of materials examined included coarse ash or slag and cyclone dust. The materials were found to be nonhazardous, but the physical characteristics and chemical compositions varied significantly as a function of process configuration, operation, coal feed composition, and coal handling. The elemental compositions of the slags produced in gasification systems were similar to the bottom ash from conventional coal combustion systems (Turner and Lowry, 1983). The bulk compositions of cyclone dust samples were found to be similar to conventional coal combustion fly ash (Wetzel and others, 1982). The mineralogical examination of slags (McCarthy and others, 1985) indicated that many of the same high-temperature silicate minerals are present in the slag samples along with reduced iron-bearing compounds. The key difference in coal gasification ash and slag compared to combustion ash is the lack of sulfur. Sulfur is present in small quantities in the ash, usually in the form of a sulfide. In addition, the other ash species in the system may also be in reduced form. The entrained-flow slagging gasifiers recycle all fly ash back to the vitreous slag. Slag samples produced in the Shell process (Mahagaokar and others, 1990) were shown to be depleted in several trace elements. The fine fly slag contained carbon and a higher level of trace metals.

Slagging Combustors and Direct-Fired Gas Turbines

A pressurized slagging combustor coupled with hot-gas cleaning is a potentially simple system for producing hot gas for a gas turbine combined cycle. The major problems encountered in using coal directly as a gas turbine fuel are due to the inorganic components in the fuel. Direct-fired slagging combustors offer potential capital cost savings for coal-fired combined cycle systems, but only if the hot gases generated can either be used directly or economically cleaned to remove particulates, sulfur, and alkalies. A slagging combustor direct-fired gas turbine system is being tested and so is a three-stage slagging combustor (Lecren and others, 1992). The ash by-products produced from these systems are a vitreous slag and the particulate collected in collection devices. Slagging combustors retrofit to a package boiler (Zauderer and Fleming, 1991) were able to produce a vitreous slag with relatively high ash retention. The fly ash produced was chemically and physically similar to typical pulverized coal fly ash. The fine particulates generated from volatilized inorganic components or organically associated inorganics in low-rank coals would be expected to reduce the percentage of total ash that could be removed in the slag cyclone or impactor alone, thereby adding to the need for a barrier filter. High-alkali coals would likely require alkali gettering. In reference to controlling sulfur along with slag, the reported high levels (up to 90%) of nonequilibrium sulfur captured on limestone in the reducing section of a slag combustor have, in fact, provided no more than about 50% sulfur control overall, even with rapid slag removal, owing to reemission of sulfur at high temperature under more fuel-lean conditions (Diehl and others, 1992). Sulfides that may occur in reduced slag would pose problems in either use or disposal, possibly requiring subsequent oxidative treatment. Calcium sulfide produces poisonous and odoriferous hydrogen sulfide on contact with water.

Externally Fired Combined Cycle Systems

Externally fired combined cycle systems, based on currently available gas turbine technology supporting a turbine inlet temperature of 2500°C when using air as the working fluid, offer potential efficiencies of 47% to 50%, fired either on coal alone or on a combination of coal and

natural gas. Accordingly, DOE is vigorously pursuing a system development program, Combustion 2000, based on high-temperature coal-fired air heaters using advanced ceramic materials such as high-density silicon carbides (SiC) and SiC–alumina blends. Lead contractors for Combustion 2000 are United Technologies (Seery, 1993) and Foster Wheeler (FW) (Shenker and McKinsey, 1992), with a separate program being pursued by Hague International (Vandervort and Orozco, 1992). The generic system configuration includes a high-temperature advanced furnace consisting of the combustor, slag screen, radiant and convective air heaters, and a heat recovery steam generator, together with the gas turbine/steam turbine combined cycle power system and conventional SO_x and particulate control modules. The FW system uses a series of three air heaters fired on coal char, pyrolysis gas, and natural gas. Low NO_x emissions in these various systems would be achieved by combustion controls, using staging (rich–lean) or aerodynamically controlled mixing. Combustion 2000 aims at commercial demonstration by 1999 of an ultraclean system for achieving a minimum efficiency of 47% operating on a wide range of coals. The characteristics of the ash and slag from these systems will likely be similar to those found in conventional combustion systems. Higher carbon contents may be found in the ash owing to the low-NO_x combustion technologies under consideration.

SLAG AND ALKALI ATTACK ON CERAMIC MATERIALS

Candidate ceramic materials used in hot particulate filters and heat exchangers are subject to corrosive attack by molten slag and alkali vapor, augmented by other agents including sulfur oxides, sulfides, chlorides, hydrogen, steam, carbon monoxide, char, and ceramics impurities. Failures of ceramic filters in short-term tests conducted to date, up to about 1000 hours, are attributed primarily to mechanical flaws in design or manufacturing; long-term reliability over a desired service life of 10,000 hours will be largely determined by stability to chemical attack. Candidate materials include both oxides, such as mullite, alumina, and cordierite, and non-oxides, such as silicon carbide and silicon nitride, in various bonded matrices. Extensive research is continuing to understand the synergistic interaction of chemical, thermal, and mechanical failure mechanisms (Alvin and others, 1991; Vass and others, 1990). The corrosive mechanisms which have special relevance to low-rank coals are those involving alkali vapors and low-viscosity basic slags.

Alkali attack on aluminosilicates such as mullite occurs by formation of low melting alkali–silica glassy phases on surfaces and in grain boundaries, involving the same types of chemical reactions as occur in ash deposition; resistance to alkali attack is increased by increasing alumina content up to about 60%. Silicon carbide and silicon nitride materials suffer alkali attack when the protective surface layer of silica resulting from passive oxidation during manufacture and later use is converted to an alkali–silica glassy phase, exposing the unprotected SiC and Si_3N_4 surface to further oxidation and alkali attack. In other contributing mechanisms, hydrogen and steam can cause silica volatilization in reduced (SiO) or oxidized (H_2SiO_4) states, and the decomposition of carbon monoxide to carbon at 400° to 700°C can lead to the chemical reduction of iron oxide impurities in ceramics, triggering iron-based catalytic disintegration reactions. These various mechanisms are strongly temperature-dependent, but all are significant at or above the 1600°F (871°C) maximum operating temperature of first-generation ceramic filters and at the 2000°–2500°F (about 1100°–1400°C) temperatures of structural or insulating refractories used in direct coal-fired turbine combustors and heat exchangers for externally fired combined cycle systems. The phase changes resulting from chemical attack together with thermal cycling lead to volume expansion, cracking, spalling, viscous creep, loss of mechanical strength, and eventual structural disintegration. Susceptibility to progressive corrosive attack can be critically influenced by the viscosity of the melts and coal–ash slags on refractory surfaces. Chemically basic slags from some low-rank coals exhibit a rapid reduction in viscosity over a relatively narrow range of temperature increase. Tests at Oak Ridge National Laboratory on heat exchanger ceramics at temperatures up to 2260°F (1238°C) (Ferber and Tennery, 1981) indicated that the most corrosion-resistant (silicon carbide) material survived 500 hours of exposure without degradation under a dry acidic slag, but was severely attacked by a runny basic slag. However, differences in the reported corrosion resistance of various ceramics suggest that subtle differences in the slag composition may play an important role that is unexplained by the currently available data or theory.

SUMMARY AND CONCLUSIONS

The advances made over the past several years in understanding ash behavior in coal utilization systems have been made possible as a result of more detailed and better analysis of coal and ash materials. These advanced techniques are able to quantitatively determine the chemical and physical characteristics of the inorganic components in coal and ash (fly ash and deposits) on a microscopic scale. Many of the mechanisms of ash formation, ash deposition, and ash collection in pulverized coal combustion systems are more clearly understood as a result of these new data. This understanding is leading to the development of better methods of predicting ash behavior in pulverized coal combustion systems. Currently, these same methods are being applied to emerging and advanced coal utilization technologies.

REFERENCES

Alvin, M.A.; Lippert, T.E.; Lane, J.E. "Assessment of Porous Ceramic Materials for Hot Gas Filtration Applications," *Ceramic Bulletin* **1991**, *70* (9), 1491.

Benson, S.A.; Jones, M.L.; Harb, J.N. "Ash Formation and Deposition," In *Fundamentals of Coal Combustion for Clean and Efficient Use*; Smoot, L.D. Ed.; Elsevier: Amsterdam, 1993; pp 299–373.

Benson, S.A. et al. "Project Sodium Final Technical Report: Follow-On Work to the Original Evaluation of Sodium Effects in Low-Rank Coal Combustion Systems," EERC publication, 1992.

Benson, S.A. et al. "Project Sodium," final technical report; Energy and Mineral Research Center, University of North Dakota, 1988.

Diehl, R.C. et al. "Development of a Slagging Combustor for a Direct-Coal-Fired Combined Cycle," *In* Proceedings of the 9th Annual International Pittsburgh Coal Conference; Oct. 12–16, 1992, pp 322–327.

Eklund, A.G. "Coal Gasification Environmental Data Summary: Solid Wastes and Tar By-Products," EPA/600/7-86/015c, April 1986.

Electric Power Research Institute. "Cool Water Coal Gasification Program," final report; EPRI GS-6806, Project 1459, 1990.

Falcone, S.K.; Schobert, H.H. "Mineral Transformations During Ashing of Selected Low-Rank Coals," In *Mineral Matter and Ash in Coal*; Vorres, K.S. Ed.; ACS Symposium Series No. 301, 1986; pp 114-127.

Falcone, S.K.; Schobert, H.H.; Rindt, D.K.; Braun, S. "Mineral Transformations During Ashing and Slagging of Selected Low-Rank Coals," *Prepr. Pap.—Am. Chem. Soc., Div. Fuel Chem.* **1984**, *29* (4), 76-83.

Ferber, M.K; Tennery, V.J. "Evaluation of Tabular Ceramic Heat Exchanger Materials in Basic Coal Ash from Coal-Oil Mixture Combustion," ORNL/TM-8385, 1981.

Greene, F.T.; O'Donnell, J.E. "Investigation of the Mechanisms of Ash Deposit Formation from Low-Rank Coal Combustion," DOE/FC/10287-2416, 1987.

Hassett, D.J.; McCarthy, G.J.; Henke, K.R.; Korynta, E.D. "Characterization of a Lignite Ash from the METC Gasifier III: Correlations with Leaching Behavior and Mineralogy," In *Fly Ash and Coal Conversion By-Products: Characterization, Utilization, and Disposal I.*; McCarthy, G.J.; Lauf, R.J., Eds.; Materials Research Society, Pittsburgh, PA, 1985.

Hurley, J.P.; Benson, S.A.; Erickson, T.A.; Allan, S.E.; Bieber, J.A. "Project Calcium, Final Report," EERC publication, 1992.

Lecren, R.T.; Stephenson, M.D.; Cowell, L.H.; Wen, C.S.; Galica, M.A. "Mineral Matter Management in Solar's Coal-Fueled Gas Turbine," In *Inorganic Transformations and Deposition During Combustion*; Benson, S.A., Ed.; ASME: New York, 1992.

Mahagaokar, U.; Krewinghous, A.B.; Kiszka, M.B. "Shell Coal Gasification Project: Gasification of Six Diverse Coals," EPRI report; GS-7051s, 1990.

Makansi, J., "Users Pause, Designers Wrestle with Fluid-Bed-Boiler Scaleup," *Power* **1988**, July.

Mann, M.D.; Galbreath, K.C.; Kalmanovitch, D.P. "The Role of Ash Chemistry and Operating Parameters on Ash Agglomeration and Deposition in FBC Systems," In *Inorganic Transformations and Deposition During Combustion*; Benson, S.A., Ed.; ASME: New York, 1992.

McCarthy, G.J.; Keller, L.P.; Stevenson, R.J.; Galbreath, K.C.; Steinwand, A.L. "Characterization of a Lignite Ash from the METC Gasifier I. Mineralogy," *In* Proceedings of the Fly Ash and Coal Conversion By-Products: Characterization, Utilization, and Disposal I Symposium; McCarthy, G.J.; Lauf, R.J., Eds.; Materials Research Society, Pittsburgh, PA, 1985.

Miller, J.R. "Operating Experience on a 19-MW CFBC," 1988 Seminar on Fluidized-Bed Combustion Technology for Utility Applications, Volume 1: Atmospheric Fluidized-Bed Combustion, Palo Alto, CA, May 1988.

Neville, M.; Sarofim, A.F. "The Fate of Sodium During Pulverized Coal Combustion," *Fuel* **1985**, *64*, 38–390.

O'Gorman, J.V.; Walker, P.L. "Thermal Behaviour of Mineral Fractions Separated from Selected American Coals," *Fuel* **1973**, *52*, 71–79.

Quann, R.J.; Sarofim, A.F. "A Scanning Electron Microscopy Study of the Transformations of Organically Bound Metals During Lignite Combustion," *Fuel* **1986**, *65*, 40–46.

Seery, D.J. "Combustion 2000: Burning Coal in the Twenty-First Century," Prepared for the 1993 Low-Rank Symposium, May 1993, 8 p.

Shenker, J.; McKinsey, R. "Development of a Coal-Fired, Combined-Cycle Power Generation System with a Pyrolysis Gas and Char-Fired High-Temperature Furnace," *In* Proceedings of the Pittsburgh Coal Conference; 1992, p 670.

Sondreal, E.A.; Gronhovd, G.H.; Severson, D.E. "Alkali Metals in Low-Rank Coals," Coal Energy Technology Consultants, Grand Forks, ND, 1985.

Steen, D.; Imsdahl, B. "Montana-Dakota Utilities Company Bubbling Fluid-Bed Retrofit O Original Performance," *In* Proceedings of the 1989 International Conference on Fluidized Bed Combustion; Manaker, Arnold, Ed., San Francisco, CA, pp 793–800, May 1989.

Stevenson, R.J.; Larson, R.A. "Characterization of a Lignite Ash from the METC Gasifier II. Scanning Electron Microscopy," *In* Proceedings of the Fly Ash and Coal Conversion By-Products: Characterization, Utilization, and Disposal I. Symposium; McCarthy, G.J.; Lauf, R.J., Eds.; Materials Research Society, Pittsburgh, PA, 1985.

Stewart, G.W.; Stinespring, G.W.; Davidovits, P. "The Fate of Alkalies in Coal Combustion," *Prepr. Pap.—Am. Chem. Soc., Div. Fuel Chem.* **1982**, 27 (1), 138–144.

Turner, R.R.; Lowry, P.D. "Comparison of Solid Wastes from Coal Combustion and Pilot Coal Gasification Plants," Performed by Oak Ridge National Laboratory for EPRI under EA-2867, Feb. 1983.

Vandervort, C.L.; Orozco, N.J. "Development Status of a Utility-Scale Externally Fired Combined Cycle," *In* Proceedings of the 9th Annual International Pittsburgh Coal Conference; Oct. 12–16, 1992, pp 316–321.

Vass, R.J.; Brown, N.R.; Brown, J.J., Jr. "Corrosion and Degradation of Ceramic Particulate Filters in Coal Combustion Environments," In *Ceramic Transactions: Corrosion and Corrosive Degradation of Ceramics*; 1990; Vol. 10, pp 411–423.

Wetzel, R.E.; Crawford, R.W.; Yee, W.C. "Environmental Aspects of the GKT Coal Gasification Process," *In* Proceedings of the Environmental Aspects of Fuel Conversion Technology-VI Symposium; EPA-600/9-82-017, PB83-128181, Aug. 1982.

Zauderer, B.; Fleming, E.S. "The Demonstration of an Advanced Cyclone Coal Combustor," final report; DOE/PC/79799-t7, Aug. 30, 1991.

TABLE 1
Crystalline Forms and Examples of Specific Crystal Species (Benson and others, 1993).

Crystalline Forms	Structural Units	Examples
Orthosilicates	$(SiO_4)^{-4}$	Fayalite - Fe_2SiO_4
Pyrosilicate	$(Si_2O_7)^{-6}$	Melilite (Gehlenite-Alkermanite) $Ca_2Al_2SiO_7$ - $Ca_2MgSi_2O_7$
Metasilicate	$(SiO_3)_n$	Pyroxenes (Diopside - Augite) $CaMgSi_2O_6$ - $Ca(Fe, Mg)Si_2O_6$
Framework Silicates	Al^{3+} replaces Si^{4+} in tetrahedra	Plagioclase (*Albite - Anorthite*) $NaAlSi_3O_8$ - $CaAl_2Si_2O_8$

A METHOD FOR COUNTING THE HYDROGEN BOND CROSS LINKS IN COAL

John W. Larsen* and Ilona Gurevich
Department of Chemistry
Lehigh University
Bethlehem, Pennsylvania 18015

Keywords: Coal, Macromolecular Structure, Hydrogen Bonding, Solvent Swelling

ABSTRACT

A method has been developed which is able to count the number of hydrogen bond crosslinks in coals. The method consists of swelling the coal in non-polar solvents to which small amounts of a good hydrogen bond acceptor have been added. In an entropy controlled process, the hydrogen bond acceptor selectively interacts with those hydroxyl groups which are participating in hydrogen bond crosslinks. This results in a rapid decrease in the effective cross link density of the coals, rapid uptake of the non-polar solvent, and a rapid increase in the swelling. The resulting "titration curve" readily yields an estimate of the number of hydrogen bond crosslinks in the coal.

INTRODUCTION

We begin by discussing the interactions of a good hydrogen bond acceptor, for example pyridine, with hydroxyl groups in coals. For the sake of simplicity, we shall assume in our idealized experiment that all of the hydroxyl groups are phenolic. This is not necessary in the real system, it just makes the explanation easier to follow. We divide the hydroxyl groups in coals into three types. Free hydroxyls which are not participating in any hydrogen bond, hydroxyls which are hydrogen bonded but within the cluster or to a nearby molecule such that the hydrogen bond is not a crosslink, and hydrogen bonds between different macromolecular units such that the hydrogen bond is a non-covalent crosslink in the system.

We now inquire into the selectivity of a hydrogen bond acceptor for the three different types of hydroxyl groups. In thermodynamic terms; for which hydroxyl group is the free energy (ΔG) of interaction with pyridine most favorable. To do this, in a gedankin experiment we envision two extreme situations. Consider first the one in which the enthalpy dominates. That is, ΔH for hydrogen bonding will be much larger than $T\Delta S$ and control the situation. In this case, the pyridine will selectively hydrogen bond to the free hydroxyls. The reasons for this are straightforward. The heat of hydrogen bond formation between pyridine and phenol is -7.5 kcal/mole (exothermic).[1] If the pyridine interacts with a hydroxyl group which is already hydrogen bonded, then the heat of its interaction will be reduced by the enthalpy of the existing hydrogen bond. A 2.8 kcal/mole hydrogen bond existing in the coal would lead

to a 100 to 1 preference of the pyridine for the free hydroxyls, given constant entropy. A plot of solvent swelling as a function of the pyridine concentration in the non-polar solvent would start almost flat as the free hydroxyls are saturated with pyridine while the cross-link density of the coal remains constant. Once all of the free hydroxyls have been bonded, the hydrogen bond cross links in the coal would be broken by pyridine thus reducing the cross-link density of the coal and leading to a very rapid increase in solvent swelling. The result is a curve which is initially nearly independent of pyridine concentration but which then rises sharply at some higher pyridine concentration.

The next situation to consider is that of entropy control, where the $T\Delta S$ term is much larger than the ΔH term. If pyridine hydrogen bonds to a free hydroxyl or to a hydroxyl which is hydrogen bonded but not a crosslink, there will be a net loss of transnational entropy of the pyridine. The overall entropy change will be modestly unfavorable. If the pyridine breaks a hydrogen bond crosslink, the two macromolecular chain segments which were pinned together by the hydrogen bond are now free from each other and can adopt many more configurations. This provides a potentially large and favorable entropy term. It is this configurational entropy which is responsible for the elastic restoring force in rubbers.[2] It can be quite large. In this case, the pyridine driven by the favorable and dominant entropy change would first interact with the cross-linking hydroxyls in the coal to destroy the crosslinks, and only when these had been saturated would it interact with the other two classes of hydroxyls. The prediction here is that a plot of swelling versus pyridine concentration would show an initial very steep rise eventually almost leveling off as all of the crosslinks are broken. A further and striking prediction is that this swelling behavior will be independent of the hydrogen bond acceptor used. The driving force for the selectivity is the increase in configurational entropy of the coal which occurs when the hydrogen bond cross link is broken. This is independent of the solvent used to break the hydrogen bond. Thus, over an as yet undetermined range of hydrogen bond acceptor strengths, the selectivity for the cross-linking hydroxyls will be independent of the hydrogen bond acceptor. This would not be the case in an enthalpy controlled process.

Our data for Illinois No. 6 coal swollen with pyridine in toluene and THF in toluene are shown in Figures 1 and 2. It is clear from these figures that the predictions of an entropy controlled selective "titration" of the hydroxyl crosslinks in coal are followed. Superposition of the two plots reveals essentially identical behavior by both hydrogen bond acceptors in spite of a 1.7 kcal/mole difference in their heats of hydrogen bonding with phenol.[1] Extension of this technique to other materials and other interactions is underway.

ACKNOWLEDGEMENTS

We are grateful to the U. S. Department of Energy for support of this work.

REFERENCES

1. Arnett, E. M.; Joris, L.; Mitchell, E.; Murty, T.S. S. R.; Gorric, T.M.; Schleyer, P v.R. J. Am. Chem. Soc. **1970**, 92, 2365-2377.
2. Treloar, L.R.G. The Physics of Rubber Elasticity, 3rd Ed; Oxford University Press: New York, 1975.

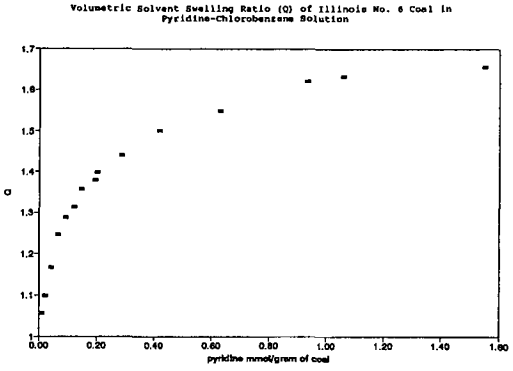

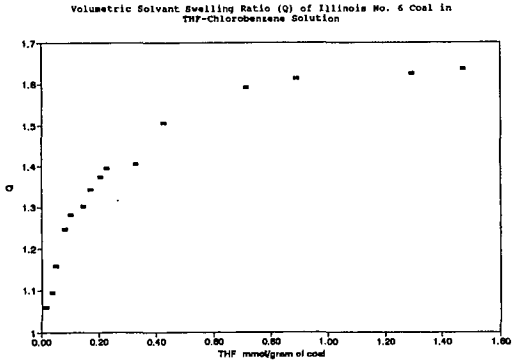

ANALYSIS OF WILSONVILLE LOW RANK COAL LIQUEFACTION DATA

Glenn Munkvold, Anthony M. Valente, Donald C. Cronauer
Amoco Oil Company
P. O. Box 3011
Naperville, IL 60566

Keywords: Coal liquefaction, Low rank coal, Wilsonville

ABSTRACT

The use of both dispersed and supported catalysts for the liquefaction of low rank coals in the Wilsonville, AL facility has been evaluated using a statistical approach. This analysis was undertaken to identify the most important operating variables and their effects upon coal conversion and product distributions. The preferred two-stage configuration for the liquefaction of low rank coal consists of a slurry first-stage reactor followed by an ebullated-bed second stage reactor. The presence of a dispersed catalyst promotes the initial liquefaction steps. An ebullated-bed second stage resctor is effective for hydrocracking the coal-derived products and hydrogenating a stream to be recycled as liquefaction solvent. The effect of process configuration upon coal conversion and product distributions is significant.

INTRODUCTION AND BACKGROUND

The principal goal of this study of Wilsonville low rank coal conversion data was to identify the primary operating variables and their effects upon conversion and product distributions. The goals of Wilsonville operation with low rank coal were to demonstrate operation with increasing yields, to provide an overall design concept, and to evaluate different coals. A total of 41 run periods was made with several low rank coals over a wide range of conditions. Only those periods that were lined-out were included in this study. In addition, the runs were not carried out using a statistical approach, so there may be some confounding of reaults.

The Department of Energy Advanced Two-Stage Coal Liquefaction Facility was located in Wilsonville, Alabama. The Wilsonville pilot plant was run by Southern Company Services (SCS) with funding by the United States Department of Energy (DOE), the Electric Power Research Institute (EPRI), and Amoco Corporation. The unit capacity was about 6 tons of coal per day. Only the recent runs with low rank coals using the close-coupled, integrated two-stage liquefaction (CC-ITSL) mode with and without interstage separation with "ashy recycle" are discussed herein. "Ashy recycle" refers to the recycle of a portion of the mineral matter and unconverted coal with the recycle solvent to the feed tank and first reactor. Solids separation was achieved using a Kerr-McGee ROSE-SR℠ unit. A description of the process has been reported.[1]

Four low rank coals were considered in this data analysis (three Wyoming subbituminous coals and a Texas lignite).

Consideration was made for differences in catalyst bed configurations. The pilot plant had two reactors. The reactor volumes were varied (50, 75, or 100%), and an ebullated supported-catalyst bed was used in none, one, or both reactors. In this paper, a "thermal" stage (T) indicates that no supported catalyst was used; however, the feed to the stage included red mud (an iron ore with limited catalyst activity). A "catalytic" stage (C) refers to the use of an ebullated-bed reactor. A "soluble catalyst" stage (S) refers to the use of a oil-soluble catalyst precursor. Combinations were used; for example, a T/C mode indicates that the first reactor was thermal and the second was catalytic. In addition, when a soluble catalyst precursor was added to the feed, it would be carried into the second stage. When the second stage was catalytic, the designation was S/C. Each of these modes called for different reactor temperatures, and because of the lack of experimental design, reactor temperatures were confounded with reactor configuration.

The data analysis was based on t-tests of the primary dependent variables grouped by reactor mode (T/C, C/C, C/T, S/T, and S/C). The primary aasumptions were that differences between the coals were minimal and any effects of temperature, hydrogen partial pressure, and reactor volumes were lumped into the mode distinction.

SUMMARY OF WILSONVILLE LOW RANK LIQUEFACTION RUNS

Overall coal conversion ranged between 87 and 95% (all yields and conversions were calculated on a moisture-ash-free basis: MAF). The average of the statistical group was 92.2%. This conversion was calculated as the MAF portion of the feed coal that was converted to creosote soluble materials. The conversion of the organic portion of the feed coal to total products other than solids recovered from the ROSE-SR unit was reported as 100%-energy rejection. This energy rejection included unconverted coal plus any heavy materials carried along with the solids in the reject stream from the ROSE-SR unit. Energy rejections ranged from about 9 to 24% with an average of 19%. This rejected energy isn't really lost in that the stream could be gasified along with additional coal to generate needed hydrogen and heat for the process.

The yield of distillable liquids (C_4+distillate) averaged 54.7% with a range of about 47 to 57%. That of resid (material boiling above 1000°F) was about 5.5% with a range of 0 to 13%. It was regarded that the resid could have been further converted to distillate by being recycled to extinction in a commercial facility; therefore, the overall yield of liquids was projected to be about 60% with a maximum approaching 65%. The yields of light hydrocarbons (C_1-C_3) was sizeable with a range of 4.2 to 14.2% MAF. The average was 8.3% based on total MAF coal feed; this average calculated on a basis of coal converted to C_4+distillate was 15.2%.

Hydrogen consumption is a significant factor in determining the cost of coal conversion to liquids. In the ideal case, all hydrogen should be consumed in generating distillate liquids. However, light hydrocarbon gases are generated and hetero-atom reduction (deoxygenation, desulfurization, and denitrogenation) add to hydrogen consumption. The level of hydrogen consumption in these low rank coal runs averaged 5.4% on an MAF coal feed basis (9.9% on a basis of coal conversion to C_4+distillate). The range of hydrogen consumption was 4.3 to 7.7% MAF.

STATISTICAL ANALYSIS OF WILSONVILLE RESULTS

Designations and Definitions of Variables:

The following measures of yield/quality (with units in square brackets) were considered in this statistical evaluation:

1. Overall coal conversion [wt% MAF coal],
2. Energy rejection [ratio of combustibles in the ROSE-SR reject stream, "ash concentrate," to that of the feed coal, given as %],
3. Resid+unconverted coal conversion [wt% MAF feed],
4. Individual distillate fraction yields [wt% MAF coal],
5. Overall resid (1000°F+) yield [wt% MAF coal],
6. Hydrogen yield/consumption [wt% MAF coal], and
7. Hydrogen efficiency [C4+ distillate/hydrogen consumed].

Table 1 summarizes the averages of the nominally independent variables for each of the modes considered. Note that temperatures for the soluble catalyst runs were higher in both stages than for the other run periods.

Overall Coal Conversion (wt% MAF):

Figure 1 shows coal conversion as a function of operating mode. The highest level of coal conversion was achieved in the C/C mode. The C/T mode has very poor conversion compared to the other modes. Significant differences exist between C/C and C/T, C/C and S/C, and C/T and S/T modes. Conversion is improved by either switching to the soluble catalyst in the first stage or adding supported catalyst in the second stage.

Energy Rejection:

Reactor operating mode has little effect on energy rejection as shown in Figure 2. The best (lowest) level of energy rejection was achieved in the C/C mode; this is consistent with this mode having the highest level of coal conversion. Only the difference between soluble catalyst and supported catalyst when using supported catalyst in the second stage is significant at 90% confidence.

(Resid+Unconverted Coal) Conversion (Wt% MAF feed):

Figure 3 summarizes the resid + UC conversion data. Significant differences exist between C/C and C/T, C/C and S/C, S/C and S/T, and C/T and S/T modes. Highest conversions again occur in C/C mode. This would be anticipated considering that an active, supported catalyst was used in both stages.

Overall C1-C3 Yield (wt% MAF coal):

Figure 4 shows C1-C3 yield as a function of operating mode. The lowest gas yield was that of the C/T mode periods. The highest yield of light hydrocarbon gases occurred in the C/C mode. This mode generated more light gases than the S/C mode in spite of having much lower temperatures (826/681° vs. 841/810°F).

Overall C4+ Total Yield (wt% MAF coal):

Figure 5 shows C4+ total yield as a function of operating mode. None of the differences are significant at 90% confidence (note the scale is expanded). While the operating mode has no significant effect on C4+ total yield, it is interesting that the pattern of C4+ yields is similar to that of the C1-C3 yields as first stage and second stage modes are changed.

Overall Resid (1000°F+) Yield (wt% MAF coal):

Figure 6 shows resid (1000°F+) yield as a function of operating mode. None of the primary comparisons is statistically significant. The lowest yields occurred when operating in the S/C and C/C modes (averaging about 4%) while the averages of those of the other modes were in the range of 5% to 6%.

Overall Hydrogen Consumption (Wt% MAF coal):

Figure 7 shows hydrogen consumption as a function of operating mode. Significant differences exist between T/C and C/C, C/C and S/C, C/T and S/T, C/C and C/T, and S/C and S/T modes. Using supported catalyst in both stages consumes the most hydrogen, and the substitution of soluble catalyst for supported catalyst in the first stage resulted in reduced hydrogen consumption. It is interesting to note, however, that while the C/C mode consumes the most hydrogen, it is least efficient in putting that hydrogen into the distillate product.

CONCLUSIONS AND OBSERVATIONS

It is concluded that when liquefying low rank coals in a close-coupled, two-stage system similar to that at Wilsonville, the second stage should use supported catalyst in an ebullated bed configuration. The first stage should be catalytic, but the differences between soluble and supported catalysts are not particularly pronounced. (The use of a soluble catalyst was effective in limiting operating problems not discussed herein.) Operation with a supported catalyst in both stages generates more light oil fractions, but wastes hydrogen by making more light gases. Operation using a soluble precursor in the first stage makes more efficient use of hydrogen, but a slightly heavier product is generated.

ACKNOWLEDGMENTS

The authors are indebted to Drs. R. E. Lumpkin, A. Basu, and N. C. Stewart for their aid in the field of coal liquefaction and numerous individuals at DOE and Southern Company Services who participated in the operation of the Wilsonville facility.

REFERENCES

1. Lamb, C. W., Nalithan, R. V., Johnson, T. W., PREPRINTS: Am. Chem. Soc., Div. Fuel. Chem., 1986, 24, 1091.

Table I. Variable Averages by Operating Mode

		Operating Mode				
Variable	All runs	C/T	C/C	T/C	S/T	S/C
CoalConc	29.2	30.1	32.7	30.4	24.7	29.8
Vol1	62.5	75	100	63.889	50	50
Temp1	832	784	826	837	836	841
SpRate1	33.8	28.6	23.9	31.4	37.6	46.9
Vol2	63.971	100	100	62.5	50	50
Temp2	774	792	681	760	809	810
SpRate2	33.3	21.4	23.9	31.7	37.6	46.9

1. Coal Concentration in Feed Slurry [wt% MF], *CoalConc* - Coal concentration in the feed is defined as the concentration of coal on a MF basis in the slurry that is fed to the first reactor.

2. Relative Reactor Volume [%], *Vol 1 or Vol 2.* - Total liquid volume as a percent of full reactor volume.

3. Reactor Temperature [°F], *Temp1, Temp2* - Individual reactor temperatures are designated as the average temperature over the length of the reactor.

4. Space Rate [%], *SpRate1, SpRate2* - Space rate is calculated as the lb/hr feed rate of MF coal per ft^3 of single reactor volume and reported as a ratio to a standard value.

Figure 1

Coal Conversion as a Function of Operating Mode

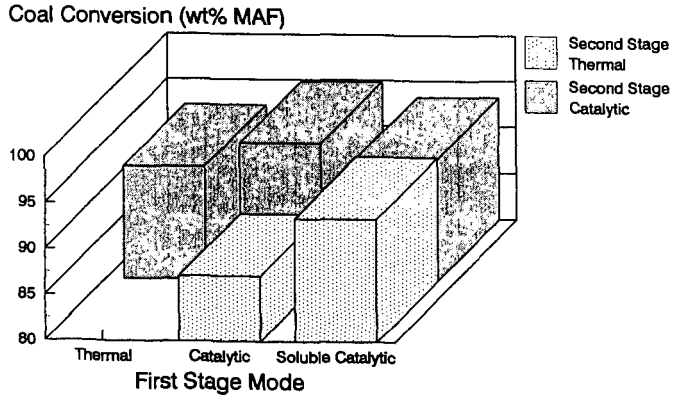

Figure 2

Energy Rejection as a Function of Operating Mode

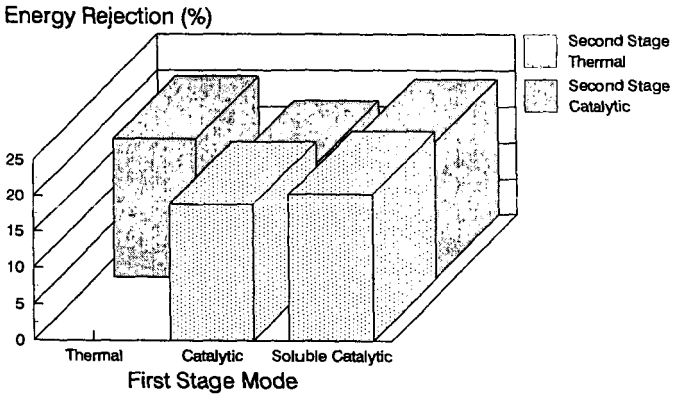

Figure 3

Resid+UC Conversion as a Function of Operating Mode

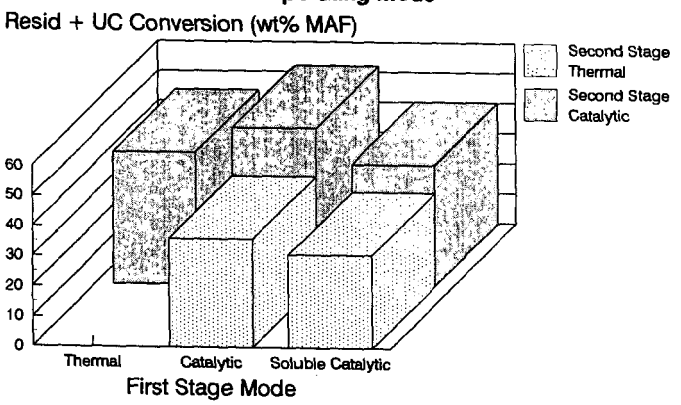

Figure 4

Overall C1-C3 Yield as a Function of Operating Mode

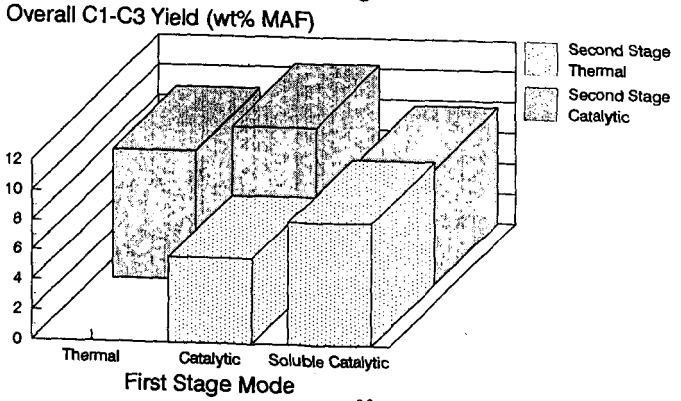

Figure 5

Overall C4+ Total Yield as a Function of Operating Mode

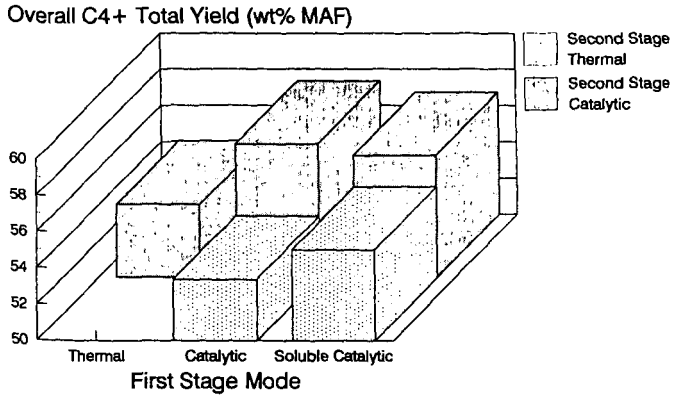

Figure 6

Overall Resid Yield as a Function of Operating Mode

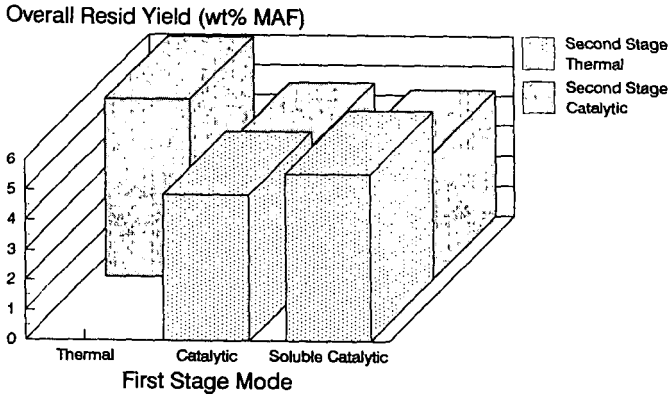

Figure 7

Overall Hydrogen Consumption as a Function of Operating Mode

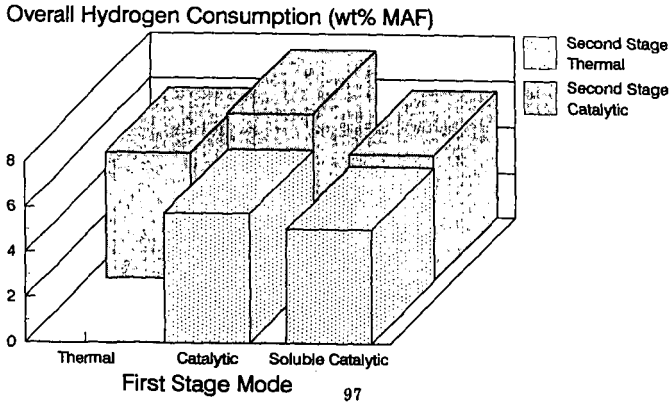

Progress in Donor Assisted Coal Liquefaction : Hydroaromatic Compound Formation

R.J. Kottenstette and H.P. Stephens
Process Research Department Sandia National Laboratories
P.O. Box 5800
Albuquerque, New Mexico 87185-0709

Keywords: Hydrogen Donor, Coal liquefaction, Fluoranthene

Introduction

The role of hydrogen donor compounds in coal liquefaction has been extensively investigated since the mid 1960's using model compounds and process derived hydrogen donor solvents[1-4]. Our recent research [5] and that of other investigators [4] have shown that two model compounds in particular have great efficacy in solvating low rank coals. 1,2,3,10b tetrahydrofluoranthene (H_4Fl) and 1,2,3,6,7,8 hexahydropyrene (H_6Py) have been used to dissolve Wyodak coal to > 95% soluble material as measured by tetrahydrofuran (THF). Although these hydrogen donors are very effective, they may not be found in any significant concentrations in actual liquefaction process recycle solvents. Therefore, studies with process derived recycle materials are necessary to understand donor solvent chemistry. The objective of this paper is to present results of solvent hydrogenation experiments using heavy distillate solvents produced during testing at the Wilsonville Advanced Coal Liquefaction Test Facility. We evaluated the impact of hydrogenation conditions upon hydrogen donor formation in process derived distillates and compared these process derived solvents with the highly effective H_4Fl and H_6Py donors in coal liquefaction tests. This paper presents data on reaction conditions used for distillate hydrotreating and subsequent coal liquefaction, with an aim toward understanding the relationship between reaction conditions and donor solvent quality in recycle distillates.

Experimental

To evaluate distillate hydrotreating conditions, tests were performed with a laboratory-scale trickle-bed reactor. Coal liquefaction tests were performed with the hydrogenated distillates and model compounds to evaluate solvent quality. Proton NMR spectroscopy was used to evaluate distillate solvent quality by measuring hydroaromatic content.

Materials- Wyodak subbituminous coal was used as -100 mesh from the Argonne Premium Coal Sample Bank. Fluoranthene, H_6Py, and n-hexadecane with a 99% purity were purchased from the Aldrich Chemical Company. H_4Fl was produced by hydrogenating fluoranthene with the trickle-bed reactor at 260°C followed by separation from the hydrogenated mixture with a spinning band distillation column (Perkin Elmer 19" adiabatic); the final H_4Fl purity was ~96%. Dewaxed heavy distillate was prepared and supplied by Consol from the V1074 process stream (B.P. 650-1050°F) at the Wilsonville Advanced Coal Liquefaction Test Facility (Run 262/Wyodak coal feed).

Apparatus- Heavy distillate solvent was hydrogenated in a microflow reactor consisting of 0.5" O.D., 0.37" I.D. type 316 stainless steel tube that was enclosed in a convectively heated oven. The reactor tube was packed with the NiMo/Alumina catalyst, which was activated with H_2S in hydrogen. Heavy distillate feed was pumped into the reactor with an Eldex A-30 liquid chromatography pump and hydrogen was metered into the microflow reactor with a Brooks 5850 flowmeter. Gases and liquids were separated at high pressure, and liquids were periodically sampled from the product receiver vessel. Constant pressure was maintained with a Circle Seal BPR-7A back pressure regulator. Hydrotreating temperature was 320°C or 360°C, hydrogen pressure was 7 MPa (1000 psig), hydrogen flow was 330 sccm H_2/ccm distillate, and typical volume liquid hourly space velocities were ~$1hr^{-1}$. Proton NMR spectroscopy was performed on the hydrogenated heavy distillate with a 200.13 megahertz Bruker instrument after dissolution in chloroform according to the method of Winschel et al [6].

Coal liquefaction tests using microautoclave batch reactors [7] were performed to evaluate donor solvent quality. Hydrogenated solvent was tested in either of two microautoclaves (40 cc or 22 cc total gas volume) consisting of a Swagelok tubing tee which was heated in a fluidized sand bath while being shaken horizontally at 200 cycles per minute. The larger microautoclave has a slurry capacity of approximately 8cc while the smaller microautoclave has a slurry capacity of 2cc.

Procedure - After the heavy distillate was hydrogenated with the microflow reactor, proton NMR analyses were used to evaluate hydroaromatic content and coal liquefaction tests were performed to measure coal conversion with the distillates. Heavy distillate solvents representing various

hydrotreating conditions or H_6Py or H_4Fl were weighed into the microautoclave reactor with as-received coal. The microautoclaves were sealed and pressurized with 2.1 MPa (300 psig) nitrogen before reaction, fastened to the shaker and immersed in the fluidized sand bath. The microautoclaves were heated to reaction temperature until the desired time at temperature elapsed, and then cooled and depressurized. Gases were collected and the microautoclave was dismantled to recover the reaction products. The gas samples were analyzed for hydrogen, carbon monoxide, carbon dioxide and C_1-C_2 hydrocarbons using a Carle series 400 Gas Chromatograph. Liquid and solids were recovered from the reactor with THF; THF insolubles were determined by pressure filtration. After the THF filtrate was roto-evaporated to remove most of the THF, pentane was added to these samples to precipitate the preasphaltene/asphaltene material. The product was pressure filtered to remove pentane insolubles which were dried and weighed. Coal conversion was calculated on a dry mineral matter free (dmmf) basis.

Results and Discussion

Solvent hydrogenation - Hydrogen donor compounds are produced in recycle solvents by hydrogenating aromatic compounds in the catalytic stage of a two-stage liquefaction process or in a separate hydrotreating reactor. One measure of the effectiveness of this hydrogenation is the concentration of hydroaromatic compounds in the product oil. To illustrate this point fluoranthene was hydrogenated in a trickle-bed reactor at different temperatures. As can be seen in Figure 1, fluoranthene is readily hydrogenated to >80% of the desirable H_4Fl at 250°C, but is hydrogenated to $H_{10}Fl$ and more extensively hydrogenated fluoranthene compounds at 300°C. These results illustrate that polynuclear aromatic hydrocarbons can be "overhydrogenated" to form alicyclic compounds which are poor hydrogen donors. Process solvents can be overhydrogenated in the same way and often become enriched in saturated material. Figure 2 presents the results of proton NMR analyses of heavy distillate samples hydrotreated at 360°C and shows that alkyl hydrogens, which make poor hydrogen donors, are more abundant, at the lower space velocities (0.7-0.9 hr^{-1}) than at the higher space velocity (1.1hr^{-1}). However, hydroaromatic hydrogen (cyclic α+β) concentrations remain constant or are only slightly increased. Thus the content of hydroaromatic compounds can be controlled by the solvent residence time in the hydrogenation reactor. The accumulation of paraffinic material is somewhat process dependent in that different processes and feedstocks accumulate different amounts of these non-donor compounds [8]. Results from proton NMR analyses of several process derived distillate solvents are shown in Figure 3. Solvent A is a sample of V1074 heavy distillate that had been dewaxed by Consol. The dewaxed heavy distillate has been enriched in aromatic (from 15% to 22%) and hydroaromatic hydrogen (from 30% to 36%) compared to the original heavy distillate[9]. Sample B is a sample of Distillate A that was hydrogenated at 320°C with the trickle-bed reactor. This hydrogenation increased the hydroaromatic hydrogen concentration from 35.8% to 39.2%. Sample C is a sample of a pasting solvent from the Lummus process using Illinois #6 coal [8,10], and exhibits a higher aromatic character than the Wilsonvillle distillate. For comparison purposes a sample of H_6Py was analyzed by the proton NMR method and included in the figure. The hydroaromatic cyclic α protons account for 50% of the H_6Py hydrogen and because of proton assignments, some cyclic β protons in H_6Py report to the alkyl designation. In any event, results in Figure 3 give a realistic picture of what can be expected from a recycle distillate in terms of hydrogen donor content, with H_6Py being an upper bound with nearly 2.9% donatable hydrogen. Most recycle distillates have significantly more alkyl hydrogen, however, than pure donors such as H_6Py and H_4Fl as liquefaction experiments attest.

Coal liquefaction tests - Coal conversion experiments were performed to test the ability of the hydrogenated distillate or model compounds to liquefy coal. The tests were performed non-catalytically to evaluate the effectiveness of the solvents for coal conversion. Coal conversions for the model compound liquefaction tests are presented in Tables 1 and 2 along with the results from high resolution gas chromatography (HRGC) analyses for solvent recovery and amount of donor remaining. "Solvent recovery" is the sum of hydrogenated and dehydrogenated solvent compounds, while "donor remaining" is the amount of the original donor compound remaining in the product. Table 1 shows that coal conversion was >94% for all tests with H_4Fl. HRGC analyses indicate that solvent recovery (% of initial solvent) decreases from 98% at 10 minutes to 73% at 60 minutes of reaction. The HRGC analyses show that the balance of the solvent is present as lower molecular weight cracked products. This observation is consistent with previous reports of disappearance of fluoranthene compounds from coal liquefaction recycle streams[2]. Table 2 presents the results of coal liquefaction tests using H_6Py as the donor solvent. Coal conversion was greater than 92% for all of the 450°C runs. Solvent recoveries were also lower at the more severe conditions due to solvent cracking but the effect was not nearly as notable as for H_4Fl. In general, H_4Fl and H_6Py are excellent hydrogen donors, which carry approximately 2-3% donatable hydrogen by weight and readily liquefy Wyodak coal. However, severe processing (long residence times at high temperatures) incurs solvent losses due to cracking.

Table 3 presents the results of coal liquefaction with the process solvents shown in Figure 3. Coal conversions were about 10% lower than similar experiments with H_4Fl. The increased alkyl nature of the heavy distillates as compared with the pure hydrogen donor compound (Figure 3) would explain the lower conversions. More notable however, are the pentane solubility analyses of products using Sample A (unhydrogenated) and Sample B (hydrogenated) V1074 samples. Experiments with Sample A gave a negative seven percent pentane soluble yield indicating solvent adduction using Wyodak coal. Reaction at 425°C showed still further decreases in pentane soluble material (-31%) with the unhydrogenated distillate A, indicating that the solvent hydrogen was insufficient for preventing solvent adduction.

Conclusions

Because they contain an overburden of saturated compounds, and therefore are unable to accept hydrogen to form higher concentrations of hydroaromatic compounds, hydrogenated process derived heavy distillate samples, in general, have less donatable hydrogen than pure hydrogen donor model compounds. However, processing steps such as dewaxing and carefully controlling hydrotreating conditions can significantly improve donor solvent content of the distillates. Model compounds such as H_4Fl and H_6Py are known to be excellent hydrogen donors, having two and three percent donor hydrogen by weight. Liquefaction tests with these compounds have shown high (>95%) conversion, yet illustrated that severe processing can reduce desirable solvent qualities by solvent cracking. Our experiments with model donor and heavy distillate solvents confirm that solvent hydrogen is very effective for coal liquefaction and appears to minimize solvent adduction reactions during coal thermolysis. Progress in coal liquefaction using donor hydrogen will occur by optimizing processing conditions to generate and maintain hydroaromatic species in the recycle distillate. Such processing conditions would consist of, but not be limited to, selective paraffin cracking, proper temperature, pressure and residence time for solvent hydrogenation and ensuring aromaticity of the solvent fed to a recycle hydrotreater.

Acknowledgments

We gratefully acknowledge Consol Inc. for providing the dewaxed heavy distillate. This work was supported by the U.S. Department of Energy at Sandia National Laboratories under contract DE-AC04-94AL8500.

References

1) Ruberto, R. G. , Cronauer, D. C. , Jewell D. M. , Seshadri, K. S. *Fuel* 1977, **56**, 17.

2) Kuhlman, E. J. , Jung, D. Y. , Guptill, R. P. ,Dyke, C. A. , Zang, H. K. *Fuel* 1985, **64**, 1552.

3) Bien, C. N. , Luttin, K. P. , Smith, B. E. , White, N. , *Energy and Fuels* 1988, **2**, 807.

4) Mochida, I. , Takayama, A. , Sakata, R. , Sakanishi, K. *Energy and Fuels* 1990, **4**, 398.

5) Kottenstette, R. J. , Stephens, H. P. , Preprints of Papers, Amer. Chem. Soc. Div. Fuel Chem. 1993, **38(2)**, 534.

6) Winschel, R. A. , Robbins, G. A. , Burke, F. P. , *Fuel* 1986, **65**, 526.

7) Kottenstette, R. J. , Sandia National Laboratories Report SAND82-2495, 6 (1983).

8) Burke, F. P. , Winschel, R. A. , Robbins, G. A. , Coal Liquefaction Process Solvent Characterization and Evaluation. DOE/PC 70018-70, September 1989.

9) Winschel, R. A. , Lancet, M. S. , Robbins, G. A. , Burke, F. P. , Kottenstette, R. J. , Stephens, H. P. , Proceedings of the 1993 International Conference on Coal Science, Vol. 2, 279.

10) Gupta, A., Peluso, M., Schiffer, A., Greene, M., "The Development of Lummus Crest Inc. Integrated Two-Stage Coal Liquefaction Process: Enhanced ITSL Configuration", Proceedings of the DOE Direct Liquefaction Contractors' Review Meeting, 1985, Pittsburgh, PA.

Figure 1. Concentration of Hydrogenated Fluoranthene Component in Hydrotreated Model Compound Mixture

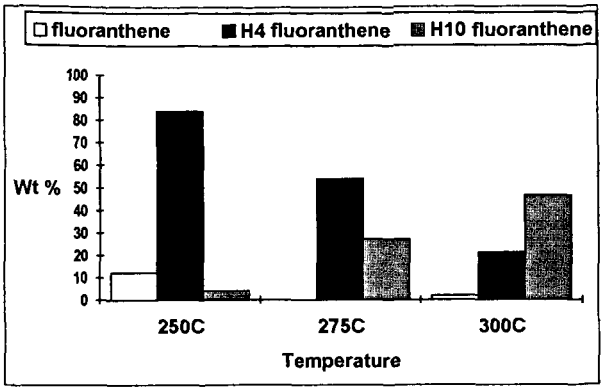

Figure 2. Effect of Increased Hydrotreater Feed Rate upon Proton Distribution in Heavy Distillate.

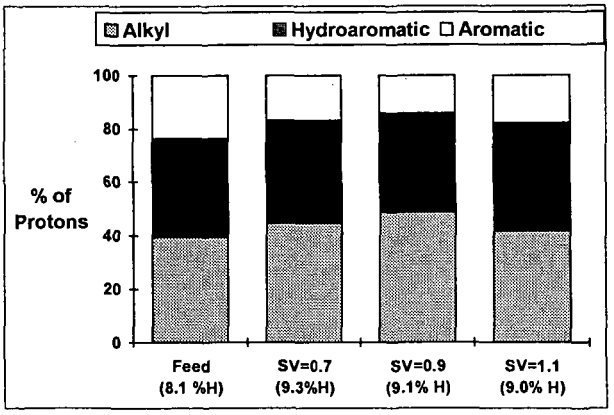

Figure 3. Proton Distributions for Heavy Distillate Solvents and Hexahydropyrene

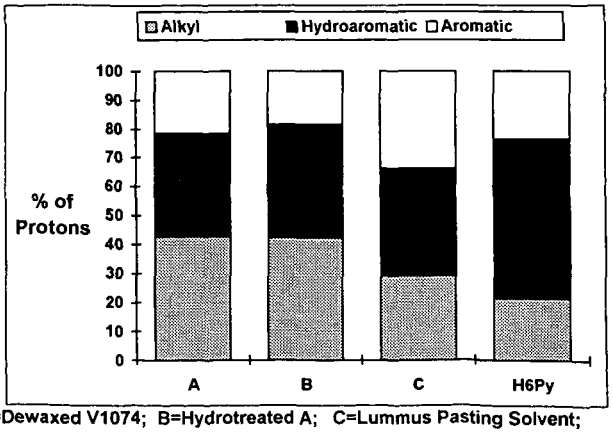

A=Dewaxed V1074; B=Hydrotreated A; C=Lummus Pasting Solvent;

Table 1. Wyodak Coal Liquefaction Results for 1,2,3,10b Tetrahydrofluoranthene. Solvent to Coal Ratio 2:1

Time (min)	Temperature °C	THF conversion (%dmmf)	Donor remaining (wt%)	Solvent recovery (wt%)
10	450	94	48	98
20	450	96	26	91
40	450	97	14	80
60	450	98	8	73

Table 2. Wyodak Coal Liquefaction Results for 1,2,3,6,7,8 Hexahydropyrene. Solvent to Coal Ratio 1.3:1

Time (min)	Temperature °C	THF conversion (%dmmf)	Donor remaining (wt%)	Solvent recovery (wt%)
10	450	93	58	100
20	450	97	49	98
40	450	96	35	92
60	450	95	26	87

Table 3. Wyodak Coal Liquefaction Results for Heavy Distillate Solvents. Solvent to Coal Ratio 2:1

Time (min)	Solvent	Temperature °C	THF conversion (%dmmf)	% Pentane soluble yield
20	H4FI	400	73	ND
40	H4FI	400	79	ND
30	B	400	68	19
30	A	400	68	-7
30	B	425	81	10
30	A	425	75	-31

Coal Conversion = (dmmf coal in - iom out)/(dmmf coal in); Pentane (c5) soluble yield was calculated as (dmmf coal in - iom - c5 insol- gas make)/(dmmf coal in).

EFFECT OF TEMPERATURE ON FUNCTIONALITY CHANGES DURING COAL LIQUEFACTION

J. T. Joseph, D. C. Cronauer, N. H. Rosenbaum
Amoco Oil Company, Research and Development Department
P. O. Box 3011, Naperville, IL 60566

A. Davis
Department of Materials Science and Engineering
The Pennsylvania State University
University Park, PA 16802

Keywords: Liquefaction, functional groups, FTIR analysis

INTRODUCTION

This paper discusses characterization of solids from the liquefaction of Black Thunder subbituminous coal using Wilsonville coal-derived solvents with and without dispersed molybdenum-containing catalyst precursors. The overall goals of the present investigation are to investigate low cost subbituminous coal liquefaction concepts using dispersed catalysts and to evaluate low temperature, short contact coal pretreatment to decompose carboxylic acids.

EXPERIMENTAL

A sample of Black Thunder subbituminous coal was used for the present investigation. The coal was pulverized under N_2 and screened to pass 100 mesh. The liquefaction solvents were coal-derived liquids obtained from the Wilsonville Advanced Coal Liquefaction Facility from runs made with Black Thunder subbituminous coal. Elemental analyses of the coal and solvent samples on a dry basis are given in Table I.

The liquefaction runs were made in a 300 cc, stirred tank single-stage continuous feed unit at temperatures of 316-449°C and space times of 14-30 minutes. The space time was calculated by dividing the reactor volume by the volumetric feed rate. The lower temperature runs (316 to 371°C) were carried out with Solvent A, a solvent blend consisting of 40 wt% ROSE®-SR resid and 60 wt% V-1074 vacuum bottoms (343-538°C). The higher temperature (399-449°C) runs were made Solvent B, which consisted of only V-1074 vacuum bottoms. Neither solvent had any THF insoluble materials to start with. After a line-out operating period, product slurry samples were extracted with tetrahydrofuran (THF). The residue was dried in a N_2 swept vacuum oven at ~60°C. Coal conversion was calculated on a moisture-ash-free (MAF) basis as the difference between weights of the feed coal and THF insoluble residue.

Infrared Spectroscopic Analysis of Liquefaction Residues: The THF insoluble residues in KBr pellets were analyzed by quantitative FTIR spectra on a Mattson Cygnus 100 FTIR spectrometer with a MCT detector. Sample preparation and spectral acquisition were performed in an inert atmosphere to prevent moisture absorption and air oxidation of the sample. Transmission FTIR spectra were obtained at 4 cm^{-1} resolution using 1000 averaged scans. The following data manipulations were performed on the FTIR spectra: 1) mild smoothing to eliminate spectral fringing, 2) spectral subtraction of the H-bonded water spectrum to eliminate the absorbance band near 1630 cm^{-1} due to the bending vibration of water absorbed or chemically bound to the sample or KBr, 3) a baseline correction in the 1500-1750 cm^{-1} region that consisted of overlapped bands of carbonyl and aromatic functional groups, and 4) curve fitting (Curvefit in Spectra Calc Software of Galactic Industries) to fit spectra to individual line shapes (Gaussian/Lorentzian profile.)

All FTIR intensities were normalized to the weight of the starting coal sample, to reflect the concentration of each functional group present in the residue on a starting material basis. This method of weighting is only qualitative, because the soluble portion and the residue do not have the same distribution of functional groups.

RESULTS AND DISCUSSION

Coal Conversion. Coal conversion to THF solubles in the thermal and catalytic liquefaction runs is summarized in Figure 1. At 399 and 427°C catalyst addition caused 2 - 5% increase in the THF solubles. At 441 and 449°C this difference increased to ~8%. The THF insoluble fraction is considered to be "unconverted coal"; however, previously dissolved coal-derived components that have undergone retrogressive coking reactions also may become insoluble in THF.

Elemental Composition of THF Insolubles. The H/C and O/C ratios of the THF insolubles from both non-catalytic and catalytic runs are summarized in Table II. These results follow expected trends with increasing liquefaction temperature. The H/C ratios of the 316 and 329°C THF insolubles were marginally higher than that of the feed coal. This is presumably due to some incorporation of the solvent into the coal solids. With the start of liquefaction, the H/C ratio decreased with increasing temperature and coal conversion. The O/C ratio also decreased as temperature increased.

Petrographic Examination of Unconverted Coal. A visual separation of the unconverted coal from coke can be achieved by petrographic analysis. Selected results of the microscopic examination of samples of raw coal and THF insolubles are presented in III. In summary, the resinous liptinite was completely converted as reaction temperature increased, the vitrinite and semi-inertinite macerals were progressively converted, and the inertinite underwent little conversion and was concentrated in the THF insolubles. Vitroplast (coke) formation was high at 449°C.

FTIR Characterization of THF Insoluble Fractions. The functional groups that were studied included aliphatic C-H, carboxyls, and ethers. The weighted FTIR intensities of these functional groups were plotted on an arbitrary scale against liquefaction temperature in Figures 2-7. Hydroxyl groups were not analyzed because of the difficulty in quantifying the O-H stretching bands due to the interference from moisture.

Aliphatic C-H: For most organic compounds, the aliphatic C-H bond stretching bands can be found in the 2890-2970 cm^{-1} region[1,2]. Although the liquefaction residue is highly aromatic, the aromatic C-H bonds are less abundant than the aliphatic C-H bonds because of the preponderance of multinuclear aromatic structures present in the residue[2]. The weighted intensities of the absorption bands in the range of 2800-3000 cm^{-1} for non-catalytic and catalytic residues are plotted against reaction temperature in Figures 2 and 3, respectively. The data indicate that for the non-catalytic residue, the C-H intensity stays the same up to 371°C and then slowly decreases. For the catalytic residue, the C-H intensity of the residue increases after the liquefaction at 343°C and then decreases at a faster rate than the non-catalytic residue. Both catalytic and non-catalytic liquefaction at 449°C produces similar residues, indicating a maximum coal conversion at that temperature. It appears that the soluble catalyst assists hydrogenation at lower temperatures and dehydrogenation at higher temperatures. Therefore, attention should be given to the appropriate temperature range when selecting the most beneficial coal liquefaction catalysts.

Carboxylate Groups: The weighted intensities of aliphatic acids (1675-1725 cm^{-1}), aromatic acids (1645-1665 cm^{-1}), and carboxylate anions (1534-1560 cm^{-1}) in non-catalytic and catalytic residues are plotted against reaction temperature in Figures 4 and 5, respectively. These data indicate that the aliphatic acids decompose much more rapidly than the other two types, and the levels of decomposition in both the non-catalytic and catalytic runs are essentially the same. This observation is consistent with published data[2]. It is also known that the shorter the aliphatic chain, the faster the carboxyl group decarboxylates[3]. Therefore, it appears that Black Thunder coal may not contain significant quantities of long chain fatty acids.

While aliphatic acids begin to decarboxylate at lower temperatures, in the absence of a catalyst, aromatic acid content decreases significantly only above 399°C. It has been reported that thermally, aromatic acids decarboxylate easily if there are activating groups present on the aromatic ring.[4,5] For example, a hydroxyl group in the *ortho* position can stabilize the carboxylate activated complex by hydrogen bonding and thus enhance the rate of decarboxylation. The results of the non-catalytic liquefaction runs indicate that the Black Thunder aromatic acids do not contain suitable activating groups for facile decarboxylation. However, the dispersed catalyst assists decarboxylation of the aromatic acids even at 343°C.

It appears that the carboxylate ions are virtually unaffected in the non-catalytic runs. However, in the presence of the catalyst, the carboxylate concentration decreases slowly with temperature and substantial decarboxylation occurs at 449°C.

In short, during non-catalytic liquefaction only the aliphatic acids decarboxylate significantly. In contrast, decarboxylation of all three carboxylate types are enhanced by the dispersed molybdenum catalyst.

Ether and Hydroxyl Groups: Identification of ether groups from the infrared spectra of complex organic molecules is notoriously difficult because the characteristic bands (1100-1300 cm^{-1}) of these groups appear in the midst of absorbance bands of many other groups, especially those of water and hydroxyl groups. (Because the samples were dried under nitrogen and the KBr pellets were handled in a dry atmosphere, the amount of moisture present in the test samples is assumed to be negligible compared to that of the hydroxyl groups.)

For this discussion, the absorption band centered at the 1100 cm^{-1} (1140-1065 cm^{-1}) is considered to be due to the ether groups, the bands in the range of 1065-1020 cm^{-1} (peaking at 1040 cm^{-1}) are assigned to both ethers and hydroxyls, and the bands in the range of 1020-990 cm^{-1} (peaking at 1010 cm^{-1}) are assigned to substituted furans - possibly dibenzofurans[6,7] and to alcohols β to an aromatic ring[7,8]. Several layered silicates also have strong bands in this region[9,10]. However, because of the small amount of mineral matter present in the starting coal, the contribution from the silicates is not considered predominant.

The ether group intensities in the non-catalytic and catalytic residues are plotted against liquefaction temperature in Figures 6 and 7, respectively. For the non-catalytic runs, the ether band intensity at 1100 cm^{-1} increases with temperature above 343°C. This is a clear indication of the formation of ether bonds as the liquefaction severity is increased. Most likely the ether bonds are of diaryl type

and could be formed by condensation of phenolic groups with other phenolic groups or with aromatic structures. The diaryl ether bonds are thermally very stable, and their formation indicates significant retrogressive reactions during uncatalyzed coal liquefaction above 399°C.

The 1040 cm^{-1} band shows a slight increase in intensity in the residue from the 399°C reaction, but decreases with further increases in temperature. The high intensity of this band at lower temperatures is probably due to the formation of hydroxyl groups (alcohols or phenols) by the hydrolysis of ethers. These hydroxyl groups disappear by hydrogenation at higher temperatures and therefore, their intensities are reduced.

The ether and hydroxyl group intensities of the residues from the catalytic runs show a significantly different pattern from that of the residues from the non-catalytic runs. The changes in the 1100 cm^{-1} band intensity with temperature for the catalytic runs are much less marked than those for the non-catalytic runs. In contrast, the intensity of the ether band at 1040 cm^{-1} approximately doubled with a temperature increase from 316 to 343°C, and it subsequently decreased with increase in temperature, indicating substantially different reactions in the catalytic and non-catalytic runs. The overall effect of the catalyst is to reduce in the ether/hydroxyl group concentration in the residue.

The behavior of the 1010 cm^{-1} band also differs in the presence of the catalyst. The intensity of this band, which may be due mainly to dibenzofurans and hydroxyls β to an aromatic ring, increases significantly above 399°C. Above 399°C, the contribution to this band could be primarily from dibenzofurans. Since the curves for the 1040 cm^{-1} and the 1010 cm^{-1} band intersect slightly above 399°C, it is tempting to conclude that at this temperature, the hydroxyl groups may be effectively converted to the dibenzofurans in the presence of the catalyst. Quantitative measurement of hydroxyl and dibenzofuran groups is necessary to confirm this hypothesis.

CONCLUSIONS

The following conclusions are drawn from the characterization of THF insolubles generated from the liquefaction of Black Thunder subbituminous coal using a short contact time, single-stage, continuous flow reactor: Dispersed molybdenum catalyst precursor enhances the dissolution of coal to THF solubles by 3 to 8% depending upon reaction temperature. It assists hydrogenation at lower temperatures and dehydrogenation at higher temperatures. The addition of the catalyst also serves to decrease the level of ether/hydroxyl groups left in the residue.

Aliphatic acids decompose much more rapidly than the other types of acids, and the level of their decomposition is not influenced by the presence or absence of the catalyst. The aromatic acids and carboxylate ions do not undergo facile thermal decarboxylation. The dispersed molybdenum catalyst facilitates decarboxylation of all carboxylate groups.

A number of retrogressive reactions occur during coal liquefaction above 427°C. This is confirmed by the presence of a high concentrations level of vitroplast and dibenzofuran type structures in the THF insoluble residues.

REFERENCES

1. Bellamy, L. J. *The Infra-red Spectra of Complex Molecules, Volume 1*, Chapman and Hall, London, 1975.
2. Solomon, P. R., Miknis, F. P. *Fuel*, **1980**, *59*, 893.
3. Seshadri, K. S., Young, D. C., Cronauer, D. C. *Fuel*, **1985**, *64*, 22.
4. Bredig, G., Balcom, R. W. *Chem. Ber.*, **1908**, *41*, 740.
5. Clark, L. W. in *The Chemistry of Carboxylic Acids and Esters*, Patai, S. Ed; Interscience-Publishers, London, 1969, *Chapter 12.*
6. Clark, L. W. *J. Phys. Chem.*, **1963**, *67*, 2831.
7. Pouchert, C. J. *The Aldrich Library of FT-IR Spectra, Volume I*, Aldrich Chemical Company, Milwaukee, 1985.
8. Clark, L. W. *J. Phys. Chem.*, **1965**, *69*, 3565,
9. Socretes, G. *Infrared Characteristic Group Frequencies*, John Wiley & Sons, New York, 1980.
10. Farmer, V. C. in *The Infra-red Spectra of Minerals*, Mineralogical Society, London, 1974, *Chapter 15.*

TABLE I

ELEMENTAL ANALYSES OF COAL AND SOLVENTS

	Coal	Solvent A	Solvent B
Elemental Analyses, Wt% (Dry basis)			
Carbon	69.60	89.56	87.23
Hydrogen	5.01	8.26	9.68
Nitrogen	1.07	0.80	0.53
Oxygen (diff)	17.14	1.33	2.52
Sulfur	0.46	0.05	0.04
Ash	6.72	0.0	0.0

TABLE II

CHANGES IN THE ATOMIC RATIOS OF LIQUEFACTION RESIDUE FROM BLACK THUNDER COAL WITH TEMPERATURE

Temperature(C)	Conversion,wt%		H/C		O/C	
	n-c	c	n-c	c	n-c	c
316	4.8	-	0.85	-	0.17	-
329	9.3	-	0.84	-	0.17	-
343	6.5	16.5	0.81	0.91	0.14	0.21
357	16.5	-	0.80	-	0.15	-
371	24.2	35.8	0.79	0.89	0.14	0.19
399	52.5	57.9	0.79	0.87	0.17	0.18
427	63.1	73.3	0.77	0.87	0.15	0.18
441	72.9	-	0.74	-	0.11	-
449	72.9	81.2	0.68	0.77	0.09	0.14

n-c = non-catalytic; c = catalytic

TABLE III

PETROGRAPHIC ANALYSIS OF BLACK THUNDER COAL AND LIQUEFACTION RESIDUES

	Coal	399°C Residue	449°C Residue
THF Insolubles, wt%	99	42	19
Maceral Distribution, wt%			
Huminite(vitrinite)	82	78	39
Liptinite	3	1	0
Semi-inertinite	7	6	8
Inertinite	5	10	26
Vitroplast	3	5	27

Figure 1.
Coal Conversion to THF Solubles

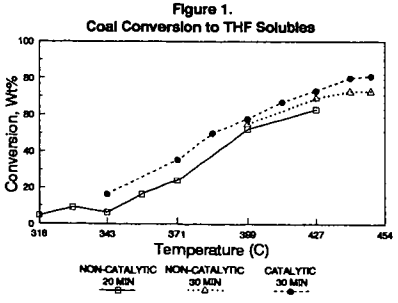

Figure 2.

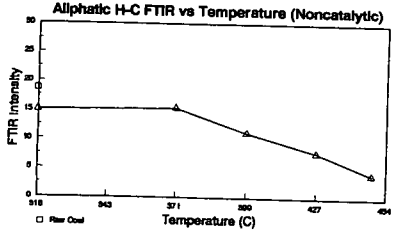

Figure 3.

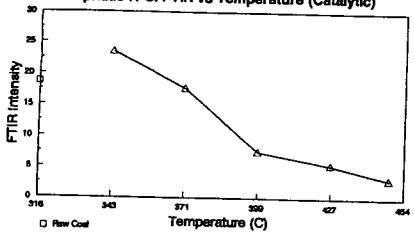

Figure 4

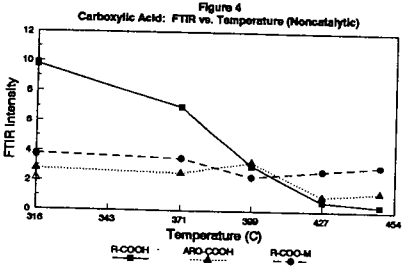

Figure 5

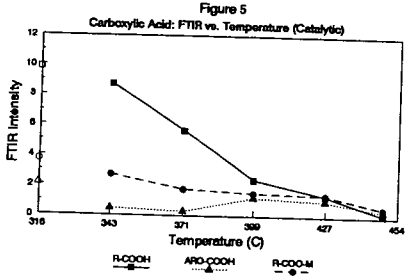

Figure 6

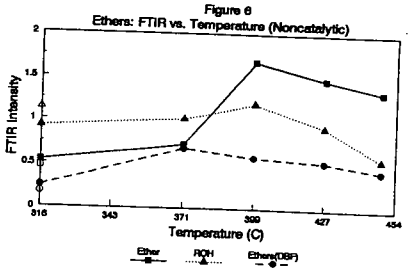

Figure 7

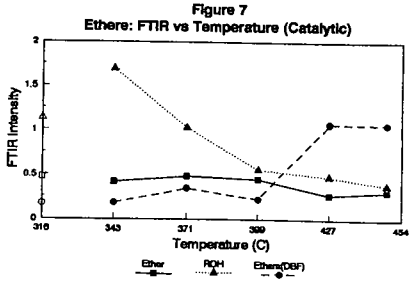

CHEMICAL STRUCTURE CHANGES OF COAL, CHAR, AND TAR DURING DEVOLATILIZATION

Thomas H. Fletcher† and Ronald J. Pugmire‡

†Chemical Engineering Dept., Brigham Young University, Provo, UT 84602
‡Dept. of Chemical and Fuels Engineering, The University of Utah, Salt Lake City, UT 84112

Keywords: coal, pyrolysis, ^{13}C NMR

Introduction

Enormous progress has been made in coal pyrolysis research during the last decade. Models of coal devolatilization have progressed from simple rate expressions based on total mass release[1, 2] to empirical relationships based on the elemental composition of the parent coal[3] to models that attempt to describe the macromolecular network of the coal.[4-6] Measurements of particle temperature during devolatilization have eliminated much of the controversy regarding overall rates of devolatilization.[7-10] In the last several years, advancements in chemical analysis techniques have allowed quantitative investigations of the chemical structure of both coal and its pyrolysis products, including the nature of the resulting char. A prominent research goal is to accurately predict the rates, yields, and products of devolatilization from measurements of the parent coal structure. This goal necessitates modeling the reaction processes on the molecular scale, with activation energies that relate to chemical bond breaking rather than release of products from the coal. ^{13}C and ^{1}H NMR spectroscopy have proven particularly useful in obtaining average values of chemical structure features of coal, char, and tar.[11-14] This paper reviews experimental data regarding chemical structure features of coal, char, and tar during rapid devolatilization, and how these data have impacted the development and input parameters for devolatilization models. In particular, the relationship between pyridine extract yields and extract yields predicted purely from NMR chemical structure data is discussed.

Parent Coal Structure

Coal consists of a macromolecular structure of fused aromatic rings connected by non-aromatic bridges and loops. Although measurement of carbon aromaticity in coals has been possible for a number of years, more detailed quantification of chemical features of coal structure has become possible in the last five years. Advanced solid state ^{13}C NMR techniques (CP/MAS and dipolar dephasing), combined with carbon counting, have been used to determine the chemical structure features of the Argonne Premium Coals.[11, 15] In addition to carbon aromaticity (f_a), the distinction between aromatic carbons with and without attachments (such as hydrogen, carbon, or oxygen) is measured. A correlation was made to determine the average number of aromatic carbons per fused aromatic cluster assuming circular rather than linear catenation.[11] The specification of the number of aromatic carbons per cluster (C_{cl}) provides the basis for the determination of many interesting chemical structure features. Probably one of the most useful quantities is the number of attachments per aromatic cluster, referred to as the coordination number (σ+1), which is determined from the number of alkylated (f_a^S) and phenolic (f_a^P) attachments to aromatic carbons, as follows:

$$\sigma + 1 = \frac{(f_a^P + f_a^S) C_c}{f_a} \qquad (1)$$

In addition to the total number of attachments per cluster, it is possible to determine the fraction of total carbons in methyl and methoxy groups. This quantity identifies methyl groups, which, to a first approximation, are considered to be the only chain terminators. This allows quantification of the total attachments per cluster into chains that terminate (i.e., attachments with methyl groups, referred to as side chains) and chains that connect to other aromatic clusters (referred to as bridges and loops). Since this is a carbon counting method, there may be some discrepancy in that oxygen bridges are not counted. The fraction of attachments that are bridges between clusters (p) is determined as follows:

$$p = \frac{f_a^P + f_a^S - f_{al}^*}{f_a^P + f_a^S} \qquad (2)$$

and (1-p) is the fraction of attachments that are side chains. Orendt, et al.[15] showed that the coordination number varies from 3.9 to 5.6 for the Argonne premium coals, while the fraction of attachments existing as bridges and loops (p_o) ranged from 0.49 to 0.74. This means that on average, each aromatic cluster is connected to other aromatic clusters at p(σ+1) or 2.5 to 3.6 points. In contrast, a long chain-like polymer with no crosslinks contains 2.0 connecting bridges

per aromatic cluster. In general, the more crosslinks per aromatic cluster (i.e., as the coordination number increases beyond 2.0), the harder it is for a material to thermally decompose.

Once the number of aromatic carbons per cluster and the number of total attachments per cluster are determined, the average cluster molecular weight (M_{cl}, including side chains and one-half the bridges and loops) can be determined using the elemental carbon composition (x_C) and the molecular weight of carbon (M_C):[4, 11]

$$M_{cl} = \frac{C_{cl} M_C}{f_{a'} x_C} \tag{3}$$

This corresponds to the size of the average monomer unit in the coal macromolecule. The average molecular weight of a side chain (M_δ) can also be determined:

$$M_\delta = \frac{M_{cl} - C_{cl} M_C}{\sigma + 1} \tag{4}$$

Values of cluster molecular weights (M_{cl}) in parent coals determined using this method range from 270 to 410 amu, with no clear trend with coal rank. Side chain molecular weight (M_δ) show a clear trend with coal rank, ranging from 12 amu for the high rank coals to 52 for the low rank coals (see Fig. 1). These average values of M_δ roughly correspond to methyl groups (15 amu) and carboxylic acid groups (45 amu), respectively. It must be remembered, however, that these values represent weighted average of many types of attachments.

Structure of Pyrolysis Products (Chars and Tars)

Char and tar samples were obtained as a function of residence time in a devolatilization experiment (1250 K, 2 x 10^4 K/s in nitrogen) and just subsequent to devolatilization in a laminar flame-fired experiment (1500 K, 5 x 10^4 K/s).[14] Quantitative measurements of chemical structure were performed on the coals and chars using the ^{13}C NMR techniques described above. Results show that the chemical structures of fully-devolatilized chars are very similar, even though a wide diversity is seen in the parent coal structures. For example, the average cluster molecular weights of the fully-pyrolyzed chars span a range of only 50 amu, in contrast to the span of 150 amu observed in the parent coals. Side chain molecular weights of the fully-pyrolyzed chars span a narrow range from 11 to 18 amu, which contrasts even more with the parent coal data (see Fig. 1). The change in side chain molecular weight is most dramatic for the low rank coals, corresponding to the release of large amounts of aliphatic material as light gases. The similarity in chemical structure of fully-devolatilized coal chars suggests that differences in measured heterogeneous char reactivities may be influenced primarily by physical structure.[14]

Use of Chemical Structure Features in Devolatilization Models

The use of statistics applied to polymer chains was applied to coal devolatilization by Niksa and Kerstein.[16] Devolatilization models have evolved to use network structures that represent coal as aromatic clusters connected by labile bridge material.[4-6] A summary of these three models was recently published.[17] A non-linear relationship exists between the number of intact labile bridges and the amount of clusters disconnected from the "infinite" lattice structure.[18] Closed-form solutions have been formulated to relate the breakup of the lattice structure to the bridge population and the initial characteristics of the lattice. Both straight chain lattices[5] and Bethe lattices[6, 18] have been used to represent the coal macromolecular structure.

The three coal devolatilization models utilize the chemical structure features available from solid-state NMR analyses in different ways. All of the models use or reference the number of aromatic carbons per cluster (i.e., $MW_{cluster}$). The number of attachments per cluster (σ+1) are used directly in the CPD and FG-DVC models, but straight chains are used in FLASHCHAIN. The molecular weight per side chain (MW_δ) is used directly in the CPD model, and directly impacts the light gas yield. In the FG-DVC model, the light gas species evolution is specified based on empirical fits of light gas yields in TG-FTIR experiments, and therefore does not link the light gas evolution directly to the lattice structure of the parent coal. In FLASHCHAIN, the molecular weights of the bridge material are much larger than the NMR data, and a correction factor is used to specify the final molecular weight of the light gas.

The direct use of NMR data to specify the coal-dependent parameters is illustrated in Fig. 2, which compares predicted tar and total volatiles yields for sixteen coals during devolatilization at heating rates from 1 to 10,000 K/s agree with measured values.[14] For most coals, no adjustable parameters were used to tune the predictions to match the yields. However, one adjustable parameter was used for lignite to represent early crosslinking, while this same parameter was adjusted to represent stable bi-aryl bridges in high rank coals (i.e., lv bituminous). In these predictions, the total gas yield was calculated without the use of yield factors from previous pyrolysis experiments.

The initial fraction of the labile bridges that are intact specifies the connectivity of the lattice. The initial lattice is generally not fully connected, and a certain amount of free or

disconnected material is predicted by the lattice statistics. This material is generally thought to correspond to the solvent extracts from unreacted coals. However, there seems to be a discrepancy between the amount of "extracts" predicted by using the solid state NMR data and measured pyridine extract yields. Figure 3 shows pyridine extract yields from the Argonne Premium coals measured by Fletcher, et al.[19] Also shown are the predicted amounts of unattached material (i.e., extract) based on a Bethe lattice with coordination number and fraction of intact bridges taken directly from NMR measurements using the CPD model. The measured pyridine extract yields are as high as 26% for the Pittsburgh #8 coal, while the predicted yields for this coal are significantly lower.

Possible reasons for the lack of agreement between measured pyridine extracts and predictions based on NMR structural data are:

(i) errors in the NMR measurements and their interpretation
(ii) the use of average NMR structural data rather than distributions
(iii) the use of Bethe lattices as approximations of coal molecular structure
(iv) the representation of the extract and the residue by the same lattice structure, even though they are chemically different

Of these hypotheses, (iv) seems to be the most rationale explanation for the disagreement shown in Fig. 3. For example, the total number of attachments per cluster (σ+1) determined by ^{13}C NMR in the pyridine extracts is an average of 15% lower than in the corresponding residue, as shown in Fig. 4 for the Argonne Premium coals.[19] The number of aromatic carbons per cluster in the pyridine extracts is also consistently lower than in the corresponding residues, and the result is lower molecular weights per cluster in the extracts (Fig. 5). The number of bridges and loops per cluster is also lower in the extracts than in the residues, although the molecular weight per side chain in the extracts is similar to that in the corresponding residues. The differences in average chemical structure features between the extracts and residues seems to confirm hypothesis (iv) above; the extract is chemically different from the residue and should not be treated with the same lattice structure. These results obviously have the most impact for those coals with high pyridine extract yields.

Conclusion

Coal pyrolysis research has progressed to the point that measurements of the chemical structure features of parent coals is useful in current devolatilization models. Chemical structure features of particular importance to modeling efforts seem to be the number of aromatic carbons per cluster, the number of attachments per cluster, and the total molecular weight per cluster (including attachments). Most current models are able to describe tar and gas yields as a function of time, temperature, heating rate, coal type, and pressure, although the network models of devolatilization appear to have the closest ties with coal structure. However, the models selectively use chemical structure information in order to attain agreement with measured tar and gas yields, while other pertinent data are ignored. One such example is that the models use as input parameters either measured pyridine extract yields *or* the fraction of intact connecting bridges. Chemical structure features of pyridine extracts do not match those of the corresponding residue, suggesting that models should treat extracts as a different chemical than the coal. The challenge for the models is to reduce the number of empirical parameters by using chemical structure information.

Acknowledgments

This work was sponsored by the Advanced Combustion Engineering Research Center at Brigham Young University and the University of Utah. Funds for this center are received from the National Science Foundation, the State of Utah, 31 industrial participants, and the U. S. Department of Energy. The authors also acknowledge the contributions of Dave Grant and Mark Solum at the University of Utah who were key participants in much of the work reviewed here.

References

1. Anthony, D. B., J. B. Howard, H. C. Hottel and H. P. Meissner *15th Symposium (International) on Combustion*; The Combustion Institute, Pittsburgh, PA: **1974**; pp 1303-1317.
2. Kobayashi, H., J. B. Howard and A. F. Sarofim *16th Symposium (International) on Combustion*; The Combustion Institute, Pittsburgh, PA: **1976**; pp 411-425.
3. Ko, G. H., D. M. Sanchez, W. A. Peters and J. B. Howard *22nd Symposium (International) on Combustion*; The Combustion Institute, Pittsburgh, PA: **1988**; pp 115-124.
4. Fletcher, T. H., A. R. Kerstein, R. J. Pugmire and D. M. Grant *Energy and Fuels* **1992**, *6*, 414.
5. Niksa, S. *Energy and Fuels* **1991**, *5*, 673-683.

6. Solomon, P. R., D. G. Hamblen, R. M. Carangelo, M. A. Serio and G. V. Deshpande *Energy and Fuels* **1988**, *2*, 405-422.
7. Solomon, P. R., M. R. Serio, R. M. Carangelo and J. R. Markham *Fuel* **1986**, *65*, 182-193.
8. Fletcher, T. H. *Combustion Science and Technology* **1989**, *63*, 89.
9. Fletcher, T. H. *Combustion and Flame* **1989**, *78*, 223.
10. Solomon, P. R., T. H. Fletcher and R. J. Pugmire *Fuel* **1993**, *72*, 587-597.
11. Solum, M. S., R. J. Pugmire and D. M. Grant *Energy and Fuels* **1989**, *3*, 187.
12. Fletcher, T. H., M. S. Solum, D. M. Grant, S. Critchfield and R. J. Pugmire *23rd Symposium (International) on Combustion*; The Combustion Institute, Pittsburgh, PA: **1990**; pp 1231.
13. Pugmire, R. J., M. S. Solum, D. M. Grant, S. Critchfield and T. H. Fletcher *Fuel* **1991**, *70*, 414.
14. Fletcher, T. H., M. S. Solum, D. M. Grant and R. J. Pugmire *Energy and Fuels* **1992**, *6*, 643-650.
15. Orendt, A. M., M. S. Solum, N. K. Sethi, R. J. Pugmire and D. M. Grant In *Advances in Coal Spectroscopy*; H. L. C. Meuzelaar, Ed.; Plenum Press: New York, **1992**; pp 215-254.
16. Niksa, S. and A. R. Kerstein *Combustion and Flame* **1986**, *66*, 95-109.
17. Smith, K. L., L. D. Smoot and T. H. Fletcher In *Fundamentals of Coal Combustion for Clean and Efficient Use*; L. D. Smoot, Ed.; Elsevier: New York, **1993**; pp 131-298.
18. Grant, D. M., R. J. Pugmire, T. H. Fletcher and A. R. Kerstein *Energy and Fuels* **1989**, *3*, 175-186.
19. Fletcher, T. H., S. Bai, R. J. Pugmire, M. S. Solum, S. Wood and D. M. Grant *Energy and Fuels* **1993**, *7*, 734-742.

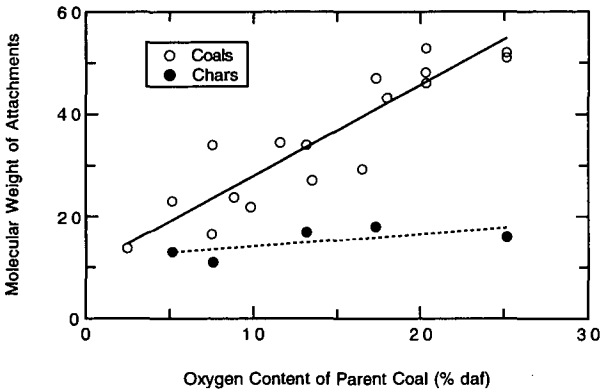

Figure 1. Average molecular weight of side chains attached to aromatic clusters in unreacted coals and fully-devolatilized chars. Oxygen content of the parent coal is used as a rank indicator. Lines represent linear correlations of the data (see Fletcher et al.[14])

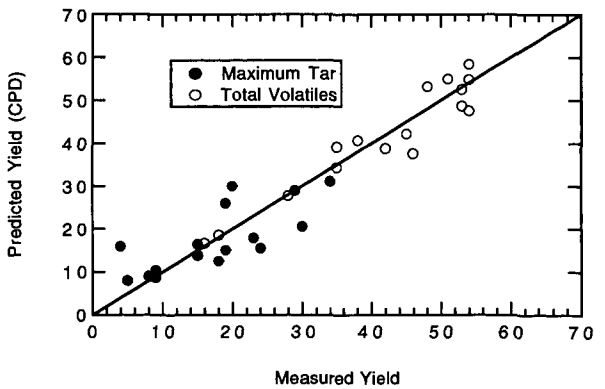

Figure 2. Comparison of predicted tar and total volatiles yields from NMR structural data versus measurements. Data are from sixteen coals during pyrolysis over a range of heating rates (see Fletcher et al.[4])

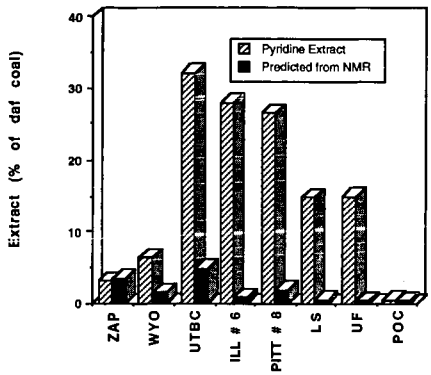

Figure 3. Measured pyridine extract yields compared with predictions of unconnected fragments in a Bethe lattice using ^{13}C NMR characterizations of average chemical structure (see Fletcher, et al.[19]).

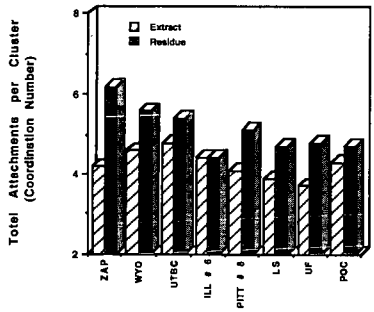

Figure 4. Coordination numbers (σ+1) determined from ^{13}C NMR analyses of pyridine extractions of the Argonne premium coals (see Fletcher, et al.[19]).

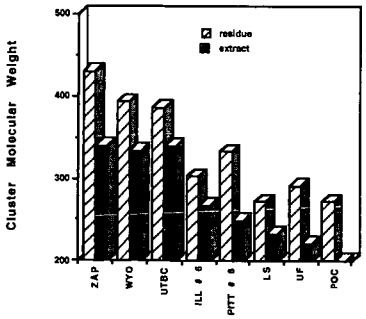

Figure 5. Average molecular weight per cluster determined from ^{13}C NMR analyses of pyridine extractions of the Argonne premium coals (data from Fletcher, et al.[19]).

THE PRODUCTION OF MATERIALS AND CHEMICALS FROM COAL

Frank Derbyshire, Marit Jagtoyen, You Qing Fei, and Geoff Kimber

**University of Kentucky Center for Applied Energy Research,
3572 Iron Works Pike, Lexington KY 40511-8433**

Keywords: Coal, Chemicals, Carbon Materials

Introduction

When coal came to prominence as a fuel during the Industrial Revolution, there developed, in parallel, its use for the production of materials and chemicals. By-product liquids and gases from coal carbonization processes became the basic raw materials for the organic chemical industry, and the production of metallurgical coke from coal was essential to the development of steel manufacture. Coal tar constituents were used for the industrial syntheses of dyes, perfumes, explosives, flavorings, and medicines. Processes were also developed for the conversion of coal to gas and liquid fuels. Gases from coal carbonization and coke production were used for illumination as long ago as the late eighteenth century. By the 1930s direct and indirect liquefaction technologies became available for the substantial conversion of coals to liquid fuels and chemicals. Subsequently, the advent of readily available petroleum and natural gas, and the decline of the steel industry, reduced dependence on coal as a resource for the production of chemicals and materials.

For the last several decades, the availability of coal tar chemicals has depended on the production of metallurgical coke, which in turn is tied to the fortunes of the steel industry. In recent times, coke manufacture has been severely cut back, due to reduced demand for steel, which is facing competition from alternative materials, principally engineering polymers, and to improvements in steel-making technology that have reduced the amount of coke required to produce pig iron. In the US, the coke rate, or tons of coke needed to produce a ton of pig iron, has decreased from 0.75 in 1960, to 0.58 in 1978, while elsewhere rates are as low as 0.4, and new technologies completely obviate the use of coke (Song and Schobert, 1993a). In the 1970s, coal liquefaction processes seemed on the point of commercialization, and would have provided new sources of coal liquids for chemical use, as well as fulfilling the principal intended function of producing alternate fuels. Because of the low price of petroleum crude, this prospect is unlikely to come to fruition in the immediate future, due to the question of economic viability, albeit not technical feasibility. The combination of these and other factors has contributed to sharpening the focus on the use of coal for the production of heat and power, and lessening or eclipsing its possible use as a starting point for other processes. To illustrate this, in the US in 1991, approximately 80 percent of the coal produced was consumed by utilities.

However, coal tars still continue to make an important contribution to the demand for aromatic chemicals. According to Song and Schobert (1993a), metallurgical coke production in 1987 generated 15-17 million tons of coal tar and 5 million tons of benzol as by-products. The worldwide consumption of BTX is about 25 million tons and 5 million tons for two- to four-ring aromatics. Coal liquids accounted for 15 -25% of the demand for BTX and about 95% of the demand for polycondensed aromatics and heterocyclics. Other important products of coal tar distillation are phenolics (creosote), feedstocks for carbon black manufacture (Donnet and others, 1993), and pitch that is used as a binder and source for materials such as carbon fibers and needle cokes.

In the US, coal is by far the largest indigenous fossil fuel resource. At the same time, petroleum imports now account for over 50 percent of total consumption, and domestic petroleum and natural gas reserves are limited. Similar situations prevail in other industrialized nations. Consequently, there is a considerable incentive to explore the expanded uses of coal, both as a fuel and as a materials source. In either case, there are also contingent needs and challenges to develop environmentally acceptable manufacturing processes.

Over the last few years, there has been a growing or revived interest in the non-fuel uses of coal, as evidenced by symposia at national meetings, and publications in scientific journals (ACS, 1992; ACS, 1993; Pitts Coal Conf., 1993; EOSS, 1993; Fuel Proc Technology Special Issue, 1993). Optimistically, one would hope that this is driven by a sense of scientific and technical relevance, rather than a new gimmick in the endless quest for research funds. There certainly appear to be some compelling reasons to re-evaluate the utility of coal as a source of non-fuel products. Research and development in Japan has provided a leading example of how this can be accomplished. The development of alternative uses for coal could lead to the diversification of resource use, and new industries. Further, the ability to utilize by-products or process streams for non-fuel applications could also assist the economics of coal utilization processes, and may lead to new materials. [In this context, it must be stressed that the higher the product selling price, the smaller the market, and the quantities of by-product streams that can be realistically utilized may be very limited.] For example, low-rank coals have long provided sources of wax and resin, obtained by solvent extraction (Kirk-Othmer, 1984). It has also been shown that paraffinic waxes, and

some naphthenic compounds, are produced during the liquefaction of subbituminous coals, and that they concentrate in the recycle distillate stream, reaching levels of 15-20 wt% or more. Their presence can adversely affect process solvent quality, while their removal by solvent dewaxing offers a method to improve process performance and recover potentially valuable by-product waxes (Derbyshire and others, 1993).

In addition to taking a new look at more traditional uses of coal products, there are a number of emerging technologies for which coal may be the most appropriate resource. Song and Schobert (1993a, 1993b) have discussed, at some length, the growth potential for high performance engineering polymers based on one- to four-ring aromatics, and that many of the aromatic monomers are not readily available from petroleum and could be derived, perhaps more easily, from coal. There is also a host of carbon-based products that can be obtained starting from coal. As can be seen in Table 1, these include a high proportion of advanced materials. The connection between coal and high technology materials may serve another useful purpose in dispelling the air of antiquity that is presently associated with coal science, and elevate it to a more respected status.

This paper will address the role of coal as a resource for non-fuel products. Rather than attempt a comprehensive coverage, a few selected materials, electrode coke, activated carbons, and carbon fibers, are reviewed in terms of their production, applications, and existing and future markets.

Electrode Coke

Graphite electrodes for arc-steel furnaces are generally manufactured from needle coke that is produced from selected petroleum feedstocks: one example is decant oils from fluid catalytic cracking. Feedstock properties such as high aromatic carbon content are important. During the process of delayed coking, it is critical to produce a mesophase coke with extended domain structures that will readily graphitize upon subsequent processing. The presence of heteroatoms, for example, can impede mesophase development through crosslinking reactions, resulting in an isotropic coke. The name needle coke arises from the acicular shape of the coke particles that reflects the anisotropic nature of the coke structure. The aromatic character of coals implies that they could present an attractive alternative source for the production of needle coke. In fact, highly aromatic coal tar pitch gives excellent needle cokes with developed anisotropy and low thermal expansion. The high coke yield from coal ~60 wt.% versus ~30% for petroleum makes the coke the principal product of the delayed coking process, although the properties of coal tar, and hence of the coke, are dependent on the coal coking conditions (Mochida and others, Carbon 1989).

Production

During the 1970s, the British Coal Corporation (formerly the National Coal Board) developed a process to produce a suitable substitute needle coke from coal via solvent extraction (Kimber, 1981). In this process, bituminous coal is slurried with about three times its mass of anthracene oil (itself a product of coal tar distillation), and heated to 415°C for 60 min at 0.8 MPa (autogenous pressure), when approximately 70-80% of the coal (dmmf) is solubilized. The mineral matter and undissolved coal are then separated by hot pressure filtration to afford a coal extract solution (filtrate) containing around 0.1% ash. The extract is then preheated to ~ 520°C and fed to a delayed coker. The coker overhead is recycled as solvent, and the coke is removed after water quenching the contents of the coker drum.

Laboratory tests showed that cokes with a wide range of properties could be produced, ranging from isotropic to anisotropic, depending on the coal precursor and extraction conditions. Consistent with the above-mentioned influence of heteroatoms on mesophase development, increasing coal rank and/or the severity of extraction were more conducive to the formation of anisotropic cokes (Kimber, 1977). The ability to control the properties of extracts through the selection of the coal and reaction parameters allows considerable latitude in the preparation of precursors for different end-products: as discussed later, the requirements for isotropic and mesophase pitch fibers are quite different.

The coal extraction process was scaled up to construct and operate a pilot plant, which was later used in a project to demonstrate the feasibilty of producing quality graphite electrodes from coal. Thirty tonnes of coke were produced from a medium volatile bituminous coal, and used by Anglo Great Lakes Corporation to fabricate graphite electrodes (coal tar pitch binder) that were then tested in a 25 ton steel production furnace by British Steel Corporation (Kimber, 1981).

A comparison of the properties of these electrodes with their petroleum-based equivalents predicted poor furnace performance, based upon the criteria normally considered to be important. However, the results of working trials showed that the coal-based electrodes behaved comparably: this was mainly due to their toughness - although cracks developed relatively quickly, crack propagation was inhibited. While the demonstration project confirmed the potential of coal as a materials source for electrode manufacture, the work was not continued beyond 1979. Because of limited quantities of coke, it was not possible to optimize the steps of electrode fabrication and furnace tesing, and potential clearly exists for further improvement.

Kimber and Gray (1976) also showed that there are other advantages in using coal-derived electrode coke. The evolution of heteroatoms, when carbonized coal extracts are subjected to graphitizing conditions, is quite different to that for petroleum cokes. In particular, sulfur evolution form petroleum cokes continues to elevated temperatures, when it causes expansion and cracking of the artefact (puffing). This does not occur with coal extract cokes, presumably as the organic sulfur is in a different form, leading to a stronger, denser carbon product, and eliminating the need to add iron oxide as a puffing inhibitor.

Recent work by Zondlo and others (1993) has confirmed these earlier results, showing that different graphitic products can be obtained from the same coal, depending on the conditions of extraction. Extracts obtained under hydrogenation conditions were more anisotropic than those obtained by non-hydrogenative solvent extraction. It is supposed that the former have a lower content of heteroatoms, which would reduce the propensity for crosslinking reactions upon carbonization, and allow more extensive mesophase development.

Markets

The global capacity for coke production of all types in 1992 was about 21 million tons. Needle coke production in 1992 was 1.3 million tons per annum of which approximately 10% was produced from pretreated coal tar after the removal of free carbons (quinoline insoluble substances) by anti-solvent techniques. The production of anode coke for aluminum manufacture was around 10 million tons, and the remaining coke was used as fuel, where the sulfur content allowed.

The consumption of carbon in arc-steel making is about 3.5 kg per ton of steel, and the principal criteria for needle coke quality are the carbon structure, impurity content (nitrogen and sulfur), and CTE (Coefficient of Thermal Expansion). The selling price of needle coke is about $500 per ton.

For anode coke, carbon consumption is 0.5 tons per ton of aluminum, the higher consumption because the carbon serves as a reductant. In this case, a low content of metal impurities is desired, especially of metals such as Fe, Na. The cost of anode coke corresponds to its fuel value and is around $100 per ton.

Activated Carbons

Activated carbons are materials with highly developed internal surface area and pore volume, and hence have a large capacity for adsorbing chemicals from gases or liquids. The extensive industrial use of activated carbons is related to their unique properties and low cost compared to that of possible competitive adsorbents (Baker, 1992; Derbyshire and others, 1993; Bansal and others, 1988)

Activated carbons can be synthesized from almost any carbonaceous precursor, naturally occurring or synthetic. An essential criterion is that the starting material is thermosetting, or can be so rendered during processing. Common commercial feedstocks are biomass materials such as wood, coconutshell, and nut kernels, and degraded or coalified plant matter - peat, lignite, and all ranks of coal. The properties of activated carbons can be very diverse. While they are influenced to some extent by the process route and conditions, they are predominantly determined by the precursor structure. Generally, microporous carbons (pore diameter <2 nm) are synthesised from high rank coals, or coconutshell precursors. Carbons with larger pore sizes (mesopores with 2nm <d <50nm) are synthesised from wood, peat, lignite and lower rank coals. In 1988, coals accounted for almost 30% of the raw materials for activated carbon manufacture, lignite 14%, peat, 10%, with wood at 35% and coconut shell, 10% (Bansal and others, 1988).

Production

Activated carbons are produced in the form of powders, granules, and shaped products (pellets and extrudates). Activated carbons have also been produced in fibrous form from cellulose (Audley, 1989) and pitch (see later section). There are two main routes for the synthesis of activated carbons, thermal activation or chemical activation. Thermal activation is a two-step process where the precursor is first carbonized in an inert atmosphere at temperatures from 500-700°C to produce a low surface area char. Subsequent controlled gasification or activation at 800-1000°C in steam or CO_2 greatly increases the pore volume and surface area, through volatile loss and carbon burn-off. Coconut shell, anthracite, and certain woods can be carbonized in granular form to produce hard carbons. Precursors that tend to form soft carbons must be reconstituted at some stage using a binder if strong shaped carbons are required. Bituminous coals are first pulverized and then reconstituted by briquetting under pressure, optionally with added binder. Thermoplasticity is eliminated by the promotion of crosslinking reactions, either by air oxidation, or the use of additives.

Chemical activation is normally used for lignocellulosic precursors, and consists of mixing the precursor with a chemical reagent such as H_3PO_4 or $ZnCl_2$ and heat treating in a single stage at

temperatures between 400-700°C. The reagent is then recovered in a leaching step to recover the reagent for recycle. Porosity is developed as a consequence of dehydration reactions occurring at low temperatures. Recent studies of the phosphoric acid activation of hardwood have revealed that reaction with the acid first causes shrinkage at temperatures around 150°C, which is attributed to the promotion of dehydration reactions, and there then follows a dilation of the structure, corresponding to the development of porosity (Jagtoyen and Derbyshire, 1993).

A different chemical activation process has been developed that uses KOH to produce exceptionally high surface area carbons from precursors such as bituminous coals and petroleum coke (Wennerberg and Grady, 1978; Jagtoyen and others, 1993). Activation with KOH can also be used to produce high surface area, hard extruded carbons from low-rank coals (Guy and others, 1989) or preoxidized bituminous coals (Verheyen and others, 1993). The chemical activation of viscose with Lewis acids (e.g. aluminum chloride, ferric chloride or zinc chloride) has been used to produce activates in the form of fibers or cloth (Baker, 1992).

Applications

Activated carbons are used in both liquid and gas phase applications for purification, environmental applications, chemical recovery, and catalysis. Liquid phase applications require carbons with a higher proportion of wide pores (macro- and mesoporosity) than gas phase applications, in order to reduce diffusional restrictions on the adsorption of impurities. The presence of wide pores (mesopores) also allows adsorption of large molecules such as color bodies and humic acids. Liquid phase carbons are used in both powder (typically 15 - 25 μm) and granular or shaped (0.3 - 3.0 mm) forms. Powdered carbons are normally used on a once-through basis. Their advantage over larger particles is their lower diffusional resistance to adsorption. Granular or shaped carbons are more desirable for continuous or cyclic processes, and can be removed for regeneration.

In 1987, liquid phase applications accounted for about 80% of the total activated carbon use in the USA (Goin and others, 1989). The principal uses are in potable water treatment (24%), industrial waste water treatment (17%), and the removal of color from sugars and foods (21%). Other applications include the refining of foods, beverages and cooking oils, gold recovery from low-grade ores, medical applications such as the recovery of antibiotics, vitamins and steroids from fermentation broths, the removal of blood toxins, and as catalyst supports (Goin and others, 1989, The Economics of Activated Carbon, 1990, Hassler, 1974).

Activated carbons for gas phase applications are mostly microporous and usually in a shaped or granular form. They are used for solvent recovery (26%), gasoline emission control in Evaporative Loss Control Devices (24%), air purification to remove toxic constituents and odors (18%), gas separation by pressure swing adsorption (6%), and catalysis (16%). [Percentages are figures for the USA in 1990, Chemical Economics Handbook, 1993]

Market

The world annual production of activated carbons was estimated to be in the region of 375,000 tonnes in 1990 (Baker, 1992), excluding Eastern Europe and China. About 55% of production is in powder form, 35% as granules, and the remainder as shaped carbons. The highest production capacity is in the US (40%), followed by Western Europe (30%), and Japan (20%).

The approximate selling price for granular or shaped carbons is in the region of $4.50 - 5.50/kg, while for powdered carbons it is closer to $2.00/kg. The actual price depends upon the adsorption capacity (typical surface areas fall in the range 800 to 1500 m^2g^{-1}), hardness, and whether impregnants have been added to enhance performance. Speciality carbons can be much more expensive.

Consumption is increasing by about 5 - 7% per year (Baker, 1992, Irving-Monshaw, 1990). Growth will be primarily in areas affected by environmental regulations for the improvement of air and water quality.

Isotropic and Mesophase Pitch-Based Carbon Fibers

Carbon fibers can be divided into four main types based upon polymers, rayon and polyacrylonitrile (PAN), upon pitch, or are vapor-grown, Singer (1992). The focus here is on fibers that can be produced from pitch: petroleum and coal tar pitches are used industrially (Okuda, 1982; Matsumura, 1987; Thwaites, 1992). Fibers have also been produced from coal extracts (Jorro and Ladner, 1974), and recent work has shown that continuous filaments of isotropic carbon fibers and activated carbon fibers can be produced from coal liquefaction products (Fei and others, 1993). Appropriate precursor materials could be produced from coal by several methods: solvent extraction; carbonization; hydropyrolysis; and coal liquefaction. Pitch-derived fibers can be divided into those produced from isotropic precursors, and those derived from pitch that has been pretreated to introduce a high concentration of carbonaceous mesophase. The former are low-

performance, general purpose fibers while the latter are high performance products that can be produced with high tensile strength and very high modulus. An extensive discussion of the synthesis and applications of isotropic pitch-based and mesophase pitch-based carbon fibers has been given by Edie (1990).

Production

The steps involved in the synthesis of both types of fibers are illustrated in Figure 1. In each case, care must be taken in the selection and preparation of the starting material, although the requirements are quite different, and the pretreatment required to produce mesophase fibers is much more extensive. Accurate control of process conditions is also critical to the production of isotropic and mesophase fibers. However, the end-uses of isotropic fibers also allow them to be produced by melt-blowing, which produces short blown fibers and is relatively inexpensive, while the applications of high performance fibers necessitate the production of continuous filaments.

Whether produced from mesophase or isotropic pitch, the as-formed, "green" fibers require to be stabilized to render them thermosetting before carbonization. Stabilization is normally accomplished by air oxidation, although other methods may be used (Otani, 1971). Oxidation must be initiated at temperatures below the softening point of the fibers. As this temperature is lower for isotropic fibers than mesophase fibers, the process of oxidative stabilization is much slower in the former case.

For the development of tensile strength, the fibers are carbonized at temperatures up to 1700°C, or graphitized by heat treatment at temperatures approaching 3000°C. The final fiber properties are determined by the degree of orientation of layer planes along the fiber axis, and the size and perfection of individual crystallites. The lack of orientation in the structure of isotropic fibers causes their modulus to be about 1/20 of that of mesophase fibers, while their tensile strength is around 1/3. While there is little improvement in the properties of isotropic fibers on graphitization, graphitized mesophase fibers develop very high modulus. Compared to carbonized or graphitized PAN fibers, they have higher modulus and lower tensile strength, giving advantages in applications requiring high stiffness, high electrical and thermal conductivity, low thermal expansion, and high temperature oxidation resistance, while the former are employed where high strength is required.

Applications

The costs of PAN, isotropic pitch and mesophase pitch fibers are in the region of $60, $22, and $90 per kg. The low precursor cost, lower processing costs and higher carbon yields contribute to isotropic pitch fibers being much cheaper than PAN fibers. For mesophase fibers, the additional step of mesophase formation, and higher complexity of other processing steps result in a much higher fiber price.

Low cost makes isotropic pitch fibers attractive for applications where high tensile strength or stiffness are not required. Examples include: enhancing the properties of composite friction materials for brake pads and clutches; the reinforcement of engineering plastics; ablation and thermal insulating materials; electrically conductive fillers for polymers; filter media; paper and panels; the production of hybrid yarns with other fibers; reinforcing concrete to improve flexural strength and other properties (Okuda, 1992; Soroushian and others, 1991); and as potential replacements for asbestos.

Because of their high modulus, mesophase fibers are used in aerospace structures, and the very high thermal conductivity of more recently developed fibers has opened applications for heat dissipation in areas such as high speed machinery, aircraft structures, and electronics. The cost of some of these specialized, ultra high performance fibers can be many hundreds of dollars per kg. Even for the lower cost products, their use is only readily justified in military and commercial aircraft applications and aerospace, where they can be used in materials that have performance characteristics unobtainable elsewhere. Reductions in the cost of mesophase fibers would substantially expand their applications into areas such as automotive structures.

Market

The worldwide production of all types of carbon fiber is in the region of 9000 tonnes (1993). The largest growth is in general purpose fibers which accounted for about 2500 tonnes in 1992, representing a threefold increase since 1989: projections for 1994 are over 5000 tonnes, and by the year 2000, one estimate predicts 40,000 tonnes.

In 1989-90, approximately 25% of pitch-based fibers were produced from coal tar pitch, and the remainder from petroleum pitch. At that time, the production capacity for mesophase pitch fibers was 800 tonnes, about 65% from coal tar pitch and 35% from petroleum pitch.

Activated Carbon Fibers from Pitch

In recent years, interest has developed in the activated forms of isotropic carbon fibers, where high surface areas can be produced by partial gasification in steam or other oxidizing gas (Thwaites and others, 1993, Suzuki, 1993). Carbon fibers have only been commercially available since the 1960s, and the development of activated carbon fibers has been a direct consequence of this technology.

Activated carbon fibers have novel properties that make them more attractive than other, more conventional forms (powder or large-size carbons) for certain applications (Suzuki, 1993). While porosity could be generated in most types of carbon fiber, low-modulus, isotropic pitch fibers are particularly well-suited for activation due to their unique structure in which the random packing of small crystallites allows the development of an extensive pore structure. A growing and completely different array of applications exists for the activated forms of isotropic carbon fibers (Suzuki, 1993; Mochida and others, 1991 and 1992; Foster and others, 1992; Economy and others, 1992).

High surface areas can be produced and most commercially produced fibers are microporous (< 2nm diameter pores). The narrow fiber diameter essentially eliminates mass transfer limitations, and adsorption and desorption rates are very rapid, roughly two orders of magnitude higher than for granular carbons. The fibrous form facilitates incorporation into woven and non-woven fabrics, felt, paper, and specific formed shapes. Among the possible applications, activated carbon fibers are of interest for the adsorption and recovery of organic vapors (Suzuki, 1993, Foster and others, 1992), removal of SO_x and NO_x from flue gas (Mochida and others, 1991, 1992), and for water treatment (Suzuki, 1991).

Despite the singular attributes of carbon fibers and activated carbon fibers from isotropic pitches, the potential of these materials has not yet been realized: in 1992, only 200 tons were produced in Japan (Suzuki, 1993). One reason is that production costs are still too high to attract widespread use and hence economies of scale. Lowering production costs through technological advances would help to reverse this situation, increasing the volume of sales and providing the incentive for larger scale production which would, in turn, effect further economies - a pattern that has already been realized for high performance carbon fibers. The high material costs and low yield for polymer derived fibers makes pitch a viable alternative with greater potential for reducing processing costs.

Literature

American Chemical Society (1992), Preprints Fuel Science Division, "Symposium on High Value Materials from Fossil Fuels", San Francisco, CA, April 5-10, **37**, No. 2, p. 497-619.

American Chemical Society (1993), Preprints Fuel Science Division, "Symposium on Alternate Uses for Fossil Fuels", Denver, CO, March 28-April 4, **38**, No. 2, p.400-468.

Audley, G. J.(1989), European Patent 0312 395 A2.

Baker, F. S. (1992), Kirk-Othmer Encyclopedia of Chemical Technology,John Wiley&Sons, Inc., 4th. Ed., **4**.

Bansal, R. C., Donnet, J. B. and Stoekli, F. (1988), Active Carbon, Marcel Dekker, New York.

Chemical Economics Handbook (1993)-SRI International, Menlo Park, Calif.

Derbyshire, F., Jagtoyen, M. and Thwaites, M. (1993), Active Carbons-Production and Applications, in book to be published by Butterworths.

Donnet, J. B., Bansal, R. C. and Wang, M. J. (1993), Carbon Black, Second Edition, Marcel Dekker, Inc.

Economy, J., Foster, K., Andreopoulos, A., and Jung, H. (1992), Chemtech, October, 597-603.

Edie, D. D.(1990), Carbon Fibers Filaments and Composites, Kluwer Academic Publishers, Netherlands, p. 43-72.

Eastern Oil Shale Symposium (1993), Papers presented in "Symposium on New Products and Uses of Oil Shales and Oil Sands", Lexington, KY, Nov. 17-19, 1993.

Fei, Y. Q., Derbyshire, F. , Jagtoyen, M. and Mochida, I.(1993), Paper presented at 1993 Eastern Oil Shale Symposium, Lexington, KY, Nov. 17-19.

Foster, K. L., Fuerman, R. G., Economy, J., Larson, S. M., and Rood, M. J.(1992.),

Chem. Mater., **4**, p.1068-1073.

Fuel Processing Technology (1993), Special Issue: High Value Materials from Coal, **34 (2)**.

Goin, J., von Schuller-Goetzburg, V. and Sakuma, Y.(1989), Chemical Economics Handbook-SRI International, Menlo Park, Calif.

Guy, P.J. , Verheyen, T. V. , Heng, S., Felber, M. D. and Perry, G. J.(1989), Proc. Int. Conf. Coal. Sci., p. 23.

Hassler, J. W.(1974), in Purification with Activated Carbon, 3rd. ed., Chemical Publishing Company, Inc., New York, p. 353.

Irving-Monshaw, S.(1990), Chemical Engineering, Feb., p. 43.

Jagtoyen, M. and Derbyshire, F. J. (1993),Carbon, **31**(7), p.1185.

Jagtoyen, M., Toles, C. and Derbyshire, F.(1993), Preprints Fuel Science Division, ACS meetingDenver, CO, March 28 - April 4, **38**, No.2, p. 400.

Jorro, M. A. A. and Ladner, W.R.(1974), Proc., 4th Int. Carbon-Graphite Conference, London, Sept, p. 287-303.

Kimber, G. M. , Brown, A. and Kirk, J. N.(1981), High Temperatures-High Pressures, **13**, p. 133-137.

Kimber, G. M., Proceedings 13th Carbon Conference, Irvine, CA, 1977.

Kimber, G. M. and Gray, M. D. (1976), in Petroleum Derived Carbons, **31**, p. 444-450.

Kirk-Othmer (1984), Encyclopedia of Chemical Technology, John Wiley & Sons.,3rd. ed, **24**, p. 472.

Matsumura, Y.(1987), Seikiyu Gakaishi, **30(5)**, p. 291.

Mochida, I., Hirayama, T., Kisamori, S., Kawano, S., and Fijitsu, H.(1992), Langmuir, **8** (9), p. 2290-94.

Mochida, I., Sun, Y-N., Fijitsu, H., Kisamori, S., and Kawano, S. (1991), Nippon Kagaku Kaishi (J.Chemical Society of Japan), **6**, p. 885-890.

Mochida, I., Fei, Y.Q., Korai, Y. and Fujimoto, K.(1989), Carbon, **27** (3), p. 375.

Otani, S. (1971), U.S. Patent # 3,629,379.

Okuda, K.(1992), TANSO, **155**, p. 426.

Okuda, K.(1982), Petrotech, **5(1)**, p. 37.

Pittsburgh Coal Conference (1993), Session on "Non-Fuel Use of Coal", Proceedings, September 20-24, p. 379-416.

Singer, L. S.(1992), Proc. Eighth Annual Conference on Materials Technology: Structural Carbons, Sept. 1-2, 1992, Southern Illinois University at Carbondal, Carbondale, IL 2901, USA, p. 3-32.

Song, C. and Schobert, H.H (1993a), Fuel Processing Technology, **34**, p. 157-196.

Song, C. and Schobert, H.H (1993b), Proceedings, 10th Internatl. Pittsburgh Coal Conference, September 20-24, p. 384.

Soroushian, P., Aouadi, F. and Nagi, M.(1991), ACI Materials Journal, **88**, No. 1, p. 11-18.

Suzuki, M.(1993.), Proc. 21st Biennial Carbon Conference, Buffalo, June 13 to 18.

Suzuki, M.(1991), Water Science technology, **23**, p. 1649.

The Economics of Activated Carbon (1990), 3rd. Ed., Roskill Information Services Ltd., London, p.8,9.

Thwaites, M.W., Stewart, M. L., McNeese, B. E., and Sumner, M. B.(1993), Fuel Proc. Tech., **34**, p. 137-145.

Verheyen, V., Rathbone, R., Jagtoyen, M. and Derbyshire, F. (1993), paper submitted to Carbon.

Wennerberg, A. N, Grady, T. M.(1978), United States Patent 4 082 694 .

Zondlo, J., Stansberry, P. and Stiller, A.(1993), Proceedings, 10th Pittsburgh Coal Conference, September 20-24, p. 379.

Table 1: Carbon materials based on coal-derived feedstocks (adapted from Song and Schobert, 1993a)

* Pitch-based carbon fibers
* Mesophase-based carbon fibers
* Carbon fiber reinforced plastic
* Carbon whiskers or filament
* Graphite and graphite-based materials
* Electrodes
* Composite materials
* Molecular sieving carbons
* Mesocarbon microbeads
* Activated carbons
* Activated carbon fibers
* Metallurgical cokes
* Carbon blacks
* Intercalation materials
* Elastic carbons
* Fullerenes or "bucky-balls"
* Diamond-like films

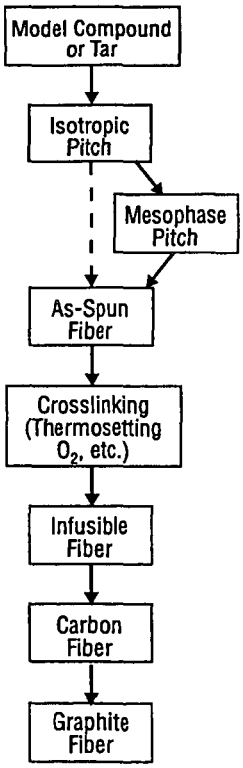

Figure 1: Preparation of isotropic and mesophase pitch carbon fibers

KINETICS OF THE REACTION OF GROUND STATE OXYGEN ATOMS WITH TRICHLORO-ETHYLENE FROM 295 TO 1127 K; COMPARISON TO OTHER O + CHLORO-ETHYLENE REACTIONS

Jasmina Hranisavljevic and Arthur Fontijn
High-Temperature Reaction Kinetics Laboratory, The Isermann Department of Chemical Engineering, Rensselaer Polytechnic Institute,Troy, NY 12180-3590

key words: chloro-ethylenes, high-temperature kinetics, oxidation

INTRODUCTION

Chlorinated hydrocarbons frequently occur in wastes and present a major pollution hazard from waste incinerators. Compounds such as chlorinated olefins are toxic and carcinogenic by themselves and their oxidation and pyrolysis products may be involved in the formation of highly toxic chloro-furans and ,-dioxins.[1-3] In order to influence the incineration process, such that hazardous emissions are reduced, kinetic models based on realistic kinetic data are needed.[1] Few measurements on individual oxidation reactions of chloro-ethylenes are available for the 700-1500 K regime of prime incineration interest. We have recently reported on the reactions of ground state oxygen atoms with monochloro-ethylene (1), 1,1-dichloro-ethylene (2) and *trans* 1,2-dichloro-ethylene (3) in the 290-1200 K range,[4] and compared these to ethylene[5]. The series is now expanded to trichloro-ethylene (4), one of the compounds most commonly encountered in municipal wastes.

It is known that below about 500 K, in O-atom olefin reactions, addition to the double bond dominates.[6] In the earlier study we found that, below about 700 K, the temperature dependences of the rate coefficients of the four reactions mentioned differ only slightly from each other. However, the magnitude of the rate coefficients was found to decrease substantially in the sequence $k_{C_2H_4}(T)>k_1(T)\approx k_2(T)>k_3(T)$, in agreement with the preferential attack of O-atoms at the site of the unsubstituted olefinic C-atom. While these trends were shown to continue at higher temperatures for the first three members of this sequence, a sharp increase was observed in $k_3(T)$ above about 700 K. It was thought that this increase may be attributed to H-atom abstraction from the weakened C-H bond. A method was developed for estimating rate coefficients, for H-abstraction from organic molecules by O-atoms, over wide temperature ranges.[4,7] The sum of the $k_{ABS}(T)$ thus obtained, and the $k_{ADD}(T)$ based on the extrapolation of a transition state theory (TST) expression for addition,[6] was shown to be in good agreement with the experimental data for reaction (3). The same type of calculations also suggested a negligible influence of abstraction on the other discussed reactions in the investigated temperature range, in agreement with the experiments.

These results, and those of a study of O-atom reactions with the four C_4H_8 butenes,[7] suggested that it is possible to predict the high temperature rate coefficients for O-atom reactions with olefins, with good accuracy, by:
i) taking a few experimental points below 500 K
ii) using those points with the Singleton and Cvetanovic TST expression[6] to obtain $k_{ADD}(T)$ over the temperature range of interest, and
iii) adding the estimated $k_{ABS}(T)$ to the $k_{ADD}(T)$to obtain the overall k(T).
In the present work we confirm the validity of this approach for the trichloro-ethylene reaction.

EXPERIMENTAL TECHNIQUE

The measurements were performed in two different HTP (high-temperature photochemistry) reactors. The older design reactor,[8] here referred to as reactor A, is shown in Fig. 1, while reactor B[9] is shown in Fig. 2. The reactant gases were introduced into the heated bath gas through cooled inlets. Ground state oxygen atoms were produced by photolysis of O_2 through a MgF_2 window, or SO_2 through a Suprasil quartz window. Flash photolysis FP was used in reactor A, while both flash photolysis and laser photolysis LP were employed in reactor B. The relative concentrations of oxygen atoms were monitored by fluorescence of the 130.2-130.6 nm resonance triplet. The source of resonance radiation was a microwave discharge flow lamp through which He flowed at 2.0 mbar. The O-atom fluorescence was monitored with a photomultiplier tube through a CaF_2 window (λ>125 nm).

The operational procedures have been previously described.[8,10,11] The experiments were carried out under pseudo-first-order conditions $[O]\ll[C_2HCl_3]$, for which the fluorescence intensity I, proportional to [O], can be written as

$$I=I_o \exp(-k_{ps1}t) + B \qquad (5).$$

Here, I_o+B is the intensity at time t=0, k_{ps1} is the pseudo-first-order rate coefficient, and B is the background due to scattered light. The values of k_{ps1} were obtained by fitting[12] the observed *ln* I *vs.* t profiles to eq. 5. In all cases exponential *ln* I *vs.* t plots were obtained, as verified by a two stage residual analysis.[13] Plots of typically five or six k_{ps1} obtained over a range of C_2HCl_3 concentrations were used to obtain rate coefficients k_4 for the temperature of the experiment; uncertainty analysis was used as previously described.[11]

RESULTS

The experimental conditions were varied over wide ranges of the flash or laser energy, total gas concentration (pressure), average gas velocity, cooled inlet to observed reaction zone distance, and residence time. Residual analyses showed the independence of the results of these implicit parameters. The rate coefficients obtained are shown in Figs. 3 and 4. There is a good agreement between the data obtained from the two reactors and from the different O-atom production arrangements, as shown in these figures. A four-parameter fit was found to give the best fit to the data:

$$k_4(295\text{-}1127\ K) = 1.1\times10^{-12} \exp(-695\ K/T) + 1.5\times10^{-9} \exp(-7508\ K/T)\ \ cm^3\ molecule^{-1}s^{-1} \quad (6).$$

As in previous work[4,7-10] the results of a covariance matrix analysis were combined[14] to determine precision limits. 2σ precision limits obtained vary from a minimum of ±3% at 393 K to a maximum of ±12% at 1127 K. Allowing, probably exaggeratedly, for ±20% systematic errors leads to corresponding accuracy limits of ±20% to ±23%. A three-parameter fit of the format $k(T) = a\ (T/K)^n \exp(-e\ K/T)$ was also attempted, but led to higher 2σ precision limits, varying from a minimum of ±6% at 541 K to a maximum of ±16% at 295 K.

There has been only one previous measurement of the O-atom trichloro-ethylene reaction. This relative room temperature measurement, as assessed in the evaluation of Cvetanovic,[15] is shown in Fig. 4. and is in good agreement with the present work.

DISCUSSION

In Fig. 5 the rate coefficient plot of reaction (4) is compared to those of the other discussed ethylenic reactions. The trends that were observed[4] are continued. Below about 700 K the plots have similar slopes, indicating that Cl-substitution does not strongly affect the activation energies. The rate coefficients of reactions (3) and (4) are approximately equal near room temperature and differ only slightly at higher temperatures. This confirms that rate coefficients do not change much with further Cl-substitution of an already mono-substituted C-atom. The sequence of rate coefficients can now be extended to read: $k_{C_2H_4}(T)>k_1(T)\approx k_2(T)>k_3(T)\approx k_4(T)$. The sharp curvature of the $k_4(T)$ plot above 700 K, similar to, but stronger than, that of $k_3(T)$, can again be attributed to H-abstraction and is shown below to be in agreement with the predictive method described in the Introduction.

The rate coefficient expression for the addition channel used is:[6]

$$k_{ADD}(T) = A\ T^{-0.5}\ [1\text{-}\exp(\text{-}1.439\ \omega/T)]^{-2} \exp(\text{-}E_o/RT) \qquad (7),$$

Here A is a temperature independent pre-exponential factor, ω is the vibrational frequency of the degenerate bending mode in the O-olefin transition state, and E_o is the energy barrier. The parameters A, ω and E_o are selected such that the best fit is obtained with the experimental values of the rate coefficients at three temperatures in the 300-500 K range. This yields:

$$k_{ADD}(295\text{-}1460) = 1.0\times10^{-11}\ (T/K)^{-0.5}\ [1\text{-}\exp(\text{-}423\ K/T)]^{-2} \exp(\text{-}729\ K/T)\ \ cm^3\ molecule^{-1}s^{-1} \quad (8)$$

The previously described method for estimating rate coefficients for H-atom abstraction[4,7] gives for O + trichloro-ethylene:

$$k_{ABS}\ (295\text{-}1460) = 2.4\times10^{-16}\ (T/K)^{1.55} \exp(\text{-}2801\ K/T)\ \ cm^3\ molecule^{-1}s^{-1} \qquad (9).$$

In Fig.6 the estimated rate coefficient values are compared to the experimental points. It may be seen that the addition channel expression alone yields at higher temperatures values lower than those measured, but that the sum of the $k_{ABS}(T)$ and $k_{ADD}(T)$ expressions again[4,7] yields good agreement with experimental results.

CONCLUSIONS

Rate coefficients for the O + trichloro-ethylene reaction have been measured for the first time above room temperature. They follow the trends estabilished for the O-atom reactions with the less substituted ethylenes and confirm the usefulness of our recently developed method for estimating high temperature rate coefficients for O-atom olefin reactions. It would appear that the method can be extended to other reactions of O-atoms with aliphatic hydrocarbons.

REFERENCES

1) Tsang, W.; *Combust. Sci. and Tech.* **1990**,*74*,99
2) Oppelt, E. T.; *J.Air Poll.Contr.Assoc.*, **1987**,*37*,558
3) Penner, S. S.; Report from NSF sponsored Workshop, **1988**, La Jolla, California
4) Hranisavljevic, J.; Adusei, G.Y.; Xun, Y.; Fontijn, A; *Combust. Sci. and Tech.*, submitted
5) Klemm, R. B.; Sutherland, J. W.; Wickramaaratchi, M. A.; Yarwood, G.; *J.Phys.Chem.* **1990**,*94*,3354
6) Singleton, D. L.; Cvetanovic, R. J.; *J.Am.Chem.Soc.* **1976**,*98*,261
7) Adusei, G.Y; Fontijn, A.; *J.Phys.Chem.*, submitted

8) Ko, T.; Marshall, P.; Fontijn, A.; *J.Phys.Chem.* **1990**,*94*,1401
9) Mahmud, K.; Kim, J. S.; Fontijn, A.; *J.Phys.Chem.* **1990**,*94*,2994
10) Marshall, P.; Ko, T.; Fontijn, A.; *J.Phys.Chem.* **1989**,*93*,1922
11) Fontijn, A.; Futerko, P. M.; in Fontijn, A. (Ed.), *Gas-Phase Metal Reactions*, North Holland, Amsterdam, 1992, Chapter 6.
12) Marshall, P.; *Comput.Chem.* **1987**,*11*,219
13) Ko, T.; Adusei, G. Y.; Fontijn, A.; *J.Phys.Chem.* **1991**,*95*,8745
14) Wentworth, W. E.; *J.Chem.Educ.* **1991**,*95*,8745
15) Cvetanovic, R. J.; *J.Phys.Chem.Ref.Data* **1987**,*16*,261

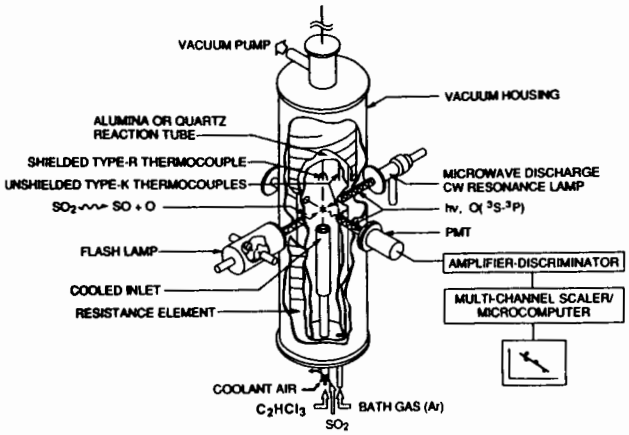

Figure 1. HTP reactor - older design (reactor A), for details see Ref. 8

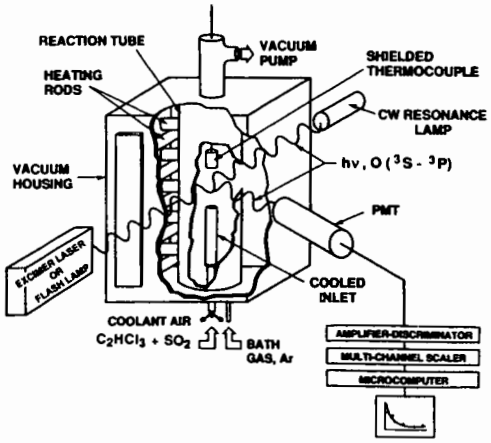

Figure 2. HTP reactor - newer design (reactor B),for details see Ref. 9

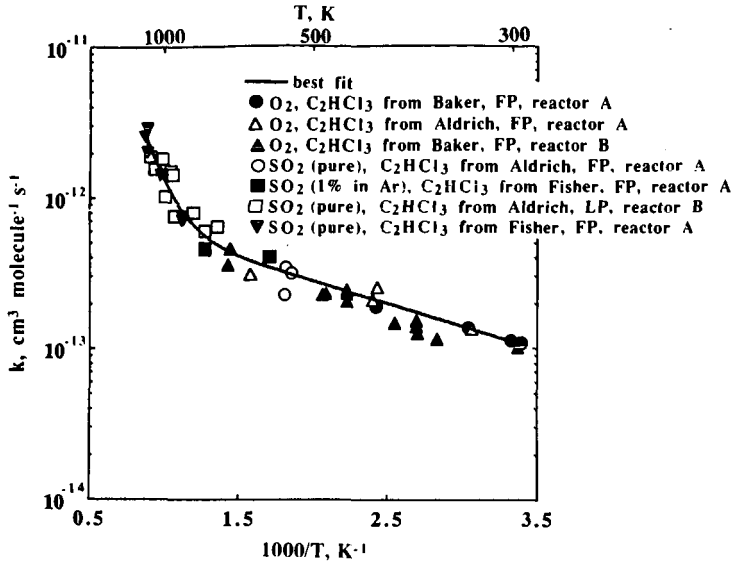

Figure 3. Summary of the rate coefficient measurements for the O + trichloro-ethylene reaction

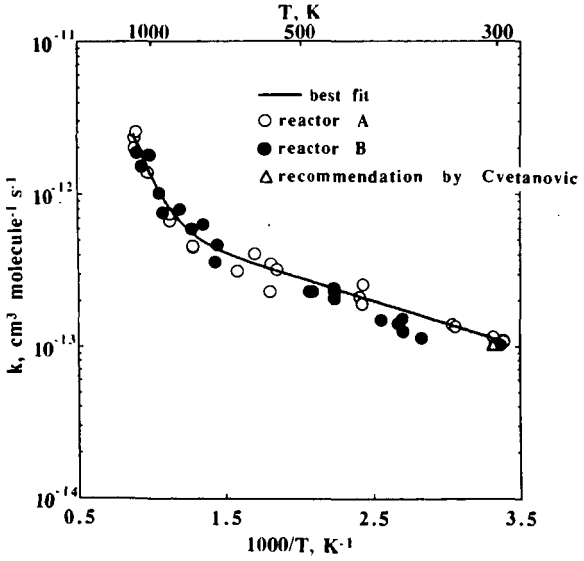

Figure 4. Rate coefficient measurements for the O + trichloro-ethylene reaction differentiated by the reactor

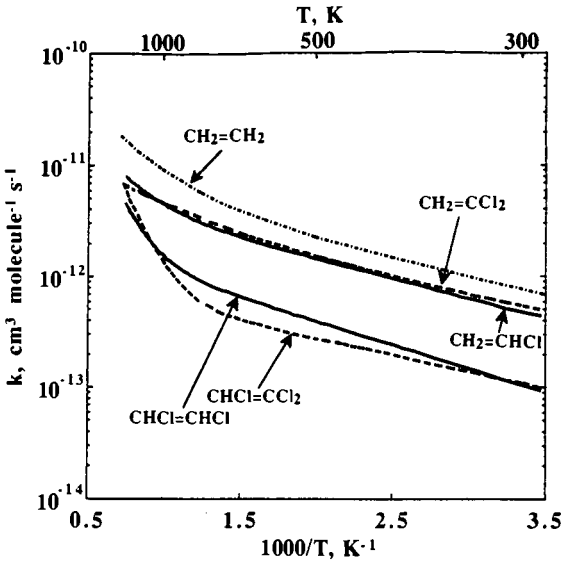

Figure 5. Comparison of ethylenic reactions

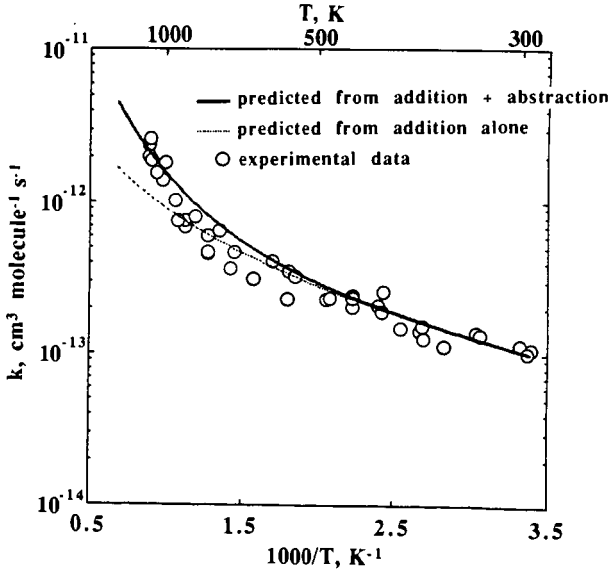

Figure 6. Comparison of the predicted and measured rate coefficients for the O + trichloro-ethylene reaction

HIGH-TEMPERATURE STUDY OF O + H_2CO → OH + HCO

Jan P. Hessler,[1] Hong Du,[2] and Paul J. Ogren[3]

[1]Chemistry Division, Argonne National Laboratory, 9700 S. Cass Ave., Argonne, Illinois 60439
[2]Present address: Physical Sciences Inc., 20 New England Business Center, Andover, Massachusetts 01810
[3]Department of Chemistry, Earlham College, Richmond, Indiana 47374

Keywords: Elementary Chemical Kinetics, Gas Phase Rate Coefficients, Formaldehyde

In our previous studies of the reactions of the methyl radical with molecular oxygen, we noticed that after the methyl radical has been consumed the reactions which control the concentration of hydroxyl are the hydroxyl-hydroxyl self reaction, the title reaction, and the reaction between hydroxyl and formaldehyde. From the long-time temporal behavior of hydroxyl we have been able to extract the rate coefficient for the title reaction over the temperature range 1580 to 2250 K. When we combine our data with the low temperature data of Klemm et al [J. Chem. Phys. 1980, 72, 1256-1264] we obtain the rate expression

$$k(T) = 2.6 \times 10^{-16} T^{1.67} \exp\{-891/T(K)\} \text{ cm}^3\text{s}^{-1}$$

This result is consistent with the earlier recommendation of Herron [J. Phys. Chem. Ref. Data 1988, 17, 967-1026] which is based on a Bond-Energy-Bond-Order calculation adjusted to agree with the experimental results at 700 K.

INTRODUCTION

The reactions of formaldehyde represent an important set of secondary reactions in the combustion of hydrocarbon fuels. Unfortunately, above 1000 K, very few rate coefficients of reactions with formaldehyde have been measured. All of these high-temperature measurements, by different groups or techniques, differ significantly. Previously, only three high-temperature shock-tube studies of the reaction of formaldehyde with atomic oxygen have been published. Izod *et al*[1] estimated a rate coefficient of 1.0×10^{-10} cm^3s^{-1} from 1400 to 2200 K, Bowman[2] deduced $8.3 \times 10^{-11}\exp\{-2300/T(K)\}$ cm^3s^{-1} from 1875 to 2240 K, and Dean *et al*[3] concluded the coefficient is $3.0 \times 10^{-11}\exp\{-1552/T(K)\}$ cm^3s^{-1} from 1905 to 3045K.

While we were measuring the primary reactions of the methyl radical with molecular oxygen we noticed that as the radical is consumed a formaldehyde molecule and a hydroxyl radical are created. This is independent of the reaction chain which produces formaldehyde. We have taken advantage of this observation to extract the rate coefficient at high temperatures for the reaction of formaldehyde with atomic oxygen from the long-time behavior of our measured profiles of the hydroxyl concentration.

EXPERIMENTAL

The experiments were performed in an ultra-high purity stainless-steel shock tube fitted with two 2"-long windows for optical observations and six pressure transducers for measurements of the shock velocity. The tube has a diameter of 25 mm and the expansion section is 1.5 m long. The methyl precursor, azomethane, was synthesized by the standard method[4] and purified by bulb-to-bulb distillation. High-purity oxygen (99.998%), xenon (99.999%), and helium (99.9999%) were purchased from commercial vendors and used as supplied. Samples were prepared manometrically in a three-liter stainless-steel mixing vessel and introduced into the shock tube from the expansion end of the tube. The purity and composition of each batch of samples were checked by mass spectrometric analysis.

The temporal dependence of the hydroxyl radical was monitored by the tunable-laser flash-absorption technique.[5] The wavelength of the doubled light from a high-resolution (0.02 cm^{-1} at 618 nm) pulsed dye laser was tuned to the $^{Q}Q_{11}(13/2)$ [$^{\Delta N}\Delta J_{F'F''}(J'')$ notation] transition of the (0,0) band of hydroxyl at 32381 cm^{-1}. An absorption profile at 2200 K is shown in figure 1.

ANALYSIS

In any analysis of a complex chemical system the reduction of experimental data is only as good as the mechanism used to describe the chemistry. A high-speed parallel-processor (Alliant Concentrix 2800) allows us to use a relatively large reaction mechanism for this description. We have constructed a reaction mechanism which contains 25 species and 89 reactions. The mechanism presented by Frenklach *et al*.[6] was used as the starting point. Most of the rate coefficients are from the recent review by Baulch *et al*.[7] The rate coefficients for the major reactions under our experimental situation are given in Table I. At high temperatures the primary reactions which remove the methyl radical and

produce formaldehyde, hydroxyl, and atomic oxygen are

H + O2 ⇔ OH + O,	(Rxn. 7)
CH3 + O2 ⇔ CH3O + O,	(Rxn. 49)
CH3 + O2 ⇔ H2CO + OH, and	(Rxn. 51)
CH3O (+M) ⇔ H2CO + H (+M).	(Rxn. 76)

Since reaction 76 is relatively fast, for every methyl radical removed a formaldehyde molecule is formed. This is independent of the relative rates of reactions 49 and 51. Also, because reaction 7 is fast a hydroxyl radical is formed for every formaldehyde molecule. Although the concentrations of formaldehyde and hydroxyl are independent of the relative rates of reactions 49 and 51, the concentration of atomic oxygen will depend upon this ratio. Therefore, this approach is only suited for the high-temperature region where the rate of reaction 49 dominates that of reaction 51. The secondary reactions which control the long-time behavior of the hydroxyl radical are

OH + OH ⇔ H2O + O,	(Rxn. 11)
H2CO + O ⇔ HCO + OH, and	(Rxn. 32)
H2CO + OH ⇔ HCO + H2O.	(Rxn. 33)

To demonstrate that we can obtain information on the rate of reaction 32 by monitoring the temporal behavior of the hydroxyl radical we used our complete reaction mechanism to perform a sensitivity analysis[8] for hydroxyl at the experimental conditions of the profile shown in figure 1. In figure 2, we plot the square of the reduced sensitivity coefficients with respect to hydroxyl. From this figure we see that immediately after the methyl radical is depleted reaction 32 determines the kinetic behavior of the hydroxyl radical. Reaction 32 produces another hydroxyl radical. Therefore, at long times the profile is controlled by reaction 11. To quantitatively determine the relative importance of each reaction[9] we integrate the squared sensitivity coefficients in figure 2 between 0 and 30 μs. From this calculation we conclude that over the initial 30 μs interval the relative weight of reaction 32 is 26%, for reaction 11 the weight is 53%. The total weight for the sum of all of the reactions which remove methyl is 9.1%. At this high temperature the relative weight for reaction 33 is only 2.7%. A relative weight of 26% is more than sufficient to extract a rate coefficient from an experimental profile. For this analysis we use the recently measured rate coefficient of Wooldridge *et al*[10] for the hydroxyl-hydroxyl self reaction and vary only the incubation time, the cross section for optical absorption, and the rate coefficient for reaction 32 to fit the experimental profiles. The result of the non-linear least-squares analysis for the profile of figure 1 is shown in figure 3.

As we change the experimental conditions to produce lower temperatures the sensitivity of hydroxyl with respect to the rate coefficient of reaction 32 becomes less important while that of reaction 33 becomes more important. By reformulating the procedure for non-linear least-squares analysis in terms of dimensionless parameters[11] we are able to estimate the relative importance of reactions 32 and 33 for each experimental profile. With this approach we have been able to determine the rate coefficient for reaction 32 from the highest temperature of 2250 K down to 1580 K. Below 1580 K the relative weight of reaction 32 is not large enough to allow us to determine its rate. The results of our non-linear least-squares reduction of the experimental profiles are summarized in Table II.

DISCUSSION

At 2000 K our results are a factor of 1.8 lower than those of Izod *et al.*, a factor of 2.1 higher than Bowman's, and a factor of 3.9 higher than those of Dean *et al*. All of the above scientists, including ourselves, have numerically integrated the set of differential equation which result from a complex reaction mechanism to deduce the rate coefficient for the O + H_2CO reaction. From our analysis we know that our *best-fit* values for the rate coefficient of reaction 32 are correlated with the value for the rate coefficient for the hydroxyl-hydroxyl self reaction. This correlation may be expressed as

$$\delta k_{32} = 0.672 \delta k_{11}$$

where δk_j is the fractional change in the rate coefficient of the j^{th} reaction. The numerical coefficient was determined by a correlation analysis[9] of the reduced sensitivity coefficients shown in figure 2. It should be obvious that similar correlations may also exist in the previous experiments. These correlations could account for the observed discrepancies. However, before precise statements about correlations can be made it is necessary to carefully compare the mechanisms used for each experiment and perform both a sensitivity and correlation analysis for each set of experimental conditions. Such a detailed discussion is beyond the scope of this preprint.

The rate coefficient for reaction 32 has been measure by Klemm *et al*[12] between 250 and 750 K. Their results along with ours are shown in figure 4. We have fit both sets of data to the general expression $\ln[k(T)] = \ln A + \beta \ln T - \Delta E/kT$ and obtain

$$\ln[k(T)] = -(35.9 \pm 3.7) + (1.67 \pm 0.47)\ln T - (891 \pm 342)/T(K)\ cm^3 s^{-1}.$$

The confidence limits are at the 95.4% or 2-σ level. These apparently large confidence limits are due to the correlation between the parameters. This correlation may be expressed by the vector

$$S_1 = 0.103\epsilon_{\ln A} + 0.281\epsilon_{\beta} - 0.382\epsilon_{\Delta E/k}$$

where the ϵ_is represent unit vectors in the 3-dimensional fractional parameter space. The physical interpretation of this vector is that if we change lnA by 10.3%, β by 28.1%, and $\Delta E/k$ by -38.2% we will move from the minimum value of χ^2 to a point on the $\Delta\chi^2$ surface which defines the 2-σ confidence limits and produces the largest change in all of the parameters. The two curves at the 2-σ confidence limit are shown by the dashed lines in figure 4.

Our analytic expression for the rate coefficient compares favorably with the recommendation of Herron,[13] $5.5 \times 10^{-17} T^{1.94} \exp\{-522/T(K)\}$ which is based upon a Bond-Energy-Bond-Order calculation adjusted to give agreement between experiment and calculation at 700 K. Our expression differs significantly with the recommendation of Baulch et al[7] of $6.85 \times 10^{-13} T^{0.57} \exp\{-1390/T(K)\}\ cm^3 s^{-1}$.

ACKNOWLEDGEMENTS

We wish to thank Chris C. Walker, an undergraduate student from Earlham College, for help with the analysis of the hydroxyl profiles. He participated in the Fall 1993 Science and Engineering Research Semester program. This program is coordinated by the Division of Education Programs. This work was performed under the auspices of the U. S. Department of Energy, Office of Basic Energy Sciences, Contract No. W-31-109-ENG-38.

REFERENCES

(1) Izod, T. P.; Kistiakowsky, G. B.; Matsuda, S. *J. Chem. Phys.* 1971, *55*, 4425-32.

(2) Bowman, C. T. *Proc. 15th Symp. (Int.) on Combust. (1975)*, pp. 869-82. Pittsburgh: Combustion Inst.

(3) Dean, A. M.; Johnson, R. L.; Steiner, D. C. *Combust. Flame* 1980, *37*, 41-62.

(4) Renaud, R.; Leitch, L. C. *Can. J. Chem.* 1954, *32*, 545-49.

(5) VonDrasek, W. A.; Okajima, S.; Kiefer, J. H.; Ogren, P. J.; Hessler, J. P. *Applied Optics* 1990, *29*, 4899-906.

(6) Frenklach, M.; Wang, H.; Rabinowitz, M. J. *Prog. Energy Combust. Sci.* 1992, *18*, 47.

(7) Baulch, D. L.; Cobos, C. J.; Cox, R. A.; Esser, C.; Frank, P.; Just, T.; Kerr, J. A.; Pilling, M. J.; Troe, J.; Walker, R. W.; Warnatz, J. *J. Phys. Chem. Ref. Data* 1992, *21*, 411-752.

(8) Lutz, A. E.; Kee, R. J.; Miller, J. A. "SENKIN: A Fortran Program for Predicting Homogeneous Gas Phase Chemical Kinetics With Sensitivity Coefficients," Sandia National Laboratories, 1989.

(9) Hessler, J. P.; Ogren, P. J. *J. Chem. Phys.* 1992, *97*, 6249-58.

(10) Wooldridge, M. S.; Hanson, R. K.; Bowman, C. T. *A Shock Tube Study of the OH + OH → H2O + O Reaction*, paper 92-93. 1992 Fall Technical Meeting, Western States Section, The Combustion Institute, 12-13 October 1992, Berkeley, CA.

(11) Hessler, J. P.; Current, D. H.; Ogren, P. J. *to be published.*

(12) Klemm, R. B.; Skolnik, E. G.; Michael, J. V. *J. Chem. Phys.* 1980, *72*, 1256-64.

(13) Herron, J. T. *J. Phys. Chem. Ref. Data* 1988, *17*, 967-1026.

Table I. Rate Coefficients for some of the reactions of the mechanism.

REACTIONS CONSIDERED	A($cm^3 s^{-1}$)	β	E/k(K)
7. H+O2<=>OH+O	1.62E-10	0.0	7474
11. OH+OH<=>H2O+O	4.00E-11	0.0	3080
32. CH2O+O<=>HCO+OH	This work		
33. CH2O+OH<=>HCO+H2O	1.25E-11	0.0	84
49. CH3+O2<=>CH3O+O	2.20E-10	0.0	15800
51. CH3+O2<=>CH2O+OH	5.50E-13	0.0	4500
76. CH3O(+M)<=>CH2O+H(+M)	1.00E+15	0.0	17223
Low pressure limit: 0.432E-09 0.0 11065.			

Table II. High-temperature rate data for O + H2CO → OH + HCO.

Mach #	P(kPa)	T(K)	t_{max}(μs)	N	rmsd(m^{-1})	k($10^{-12} cm^3 s^{-1}$)	σ(pm^2)
5.081	186.6	2251	30	271	0.55	66.8	6306
5.072	174.7	2244	60	561	0.51	88.9	5958
4.880	193.2	2100	40	373	0.58	54.3	6087
4.813	188.3	2047	62	547	0.35	69.3	4222
4.689	221.9	1956	68	617	0.61	61.3	4880
4.587	221.1	1891	33	280	0.61	27.4	5450
4.458	221.3	1797	50	438	0.41	46.3	5341
4.321	217.5	1705	58	488	0.44	22.6	5739
4.128	207.8	1580	40	311	0.37	19.0	4749

For all profiles: X_{Xe} = 0.49785, X_{C2H6N2} = 0.00015, X_{He} = 0.198, X_{O2} = 0.304

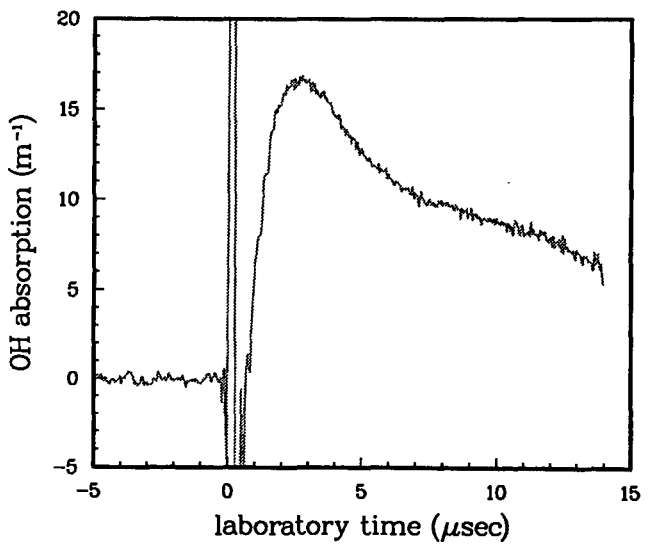

Figure 1. Absorption profile of hydroxyl at 2244 K and 174.7 k(Pa). The compression ratio, ρ_2/ρ_1, gives $t_{particle} \approx 4.07 t_{lab}$.

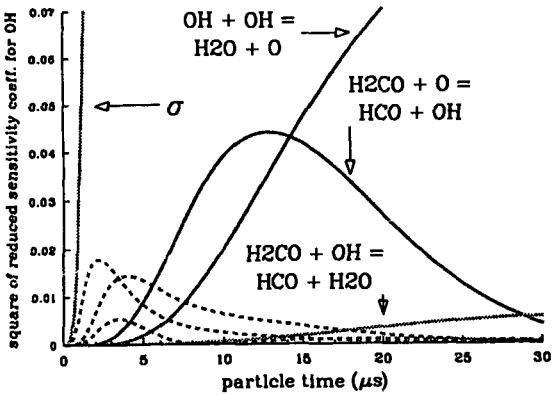

Figure 2. Square of the reduced sensitivity coefficients for the profile in figure 1.

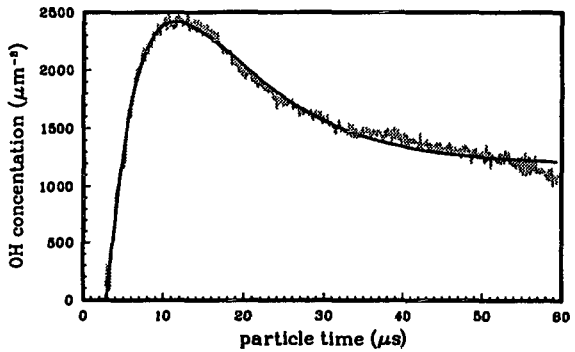

Figure 3. Non-linear least-squares fit of the profile in figure 1.

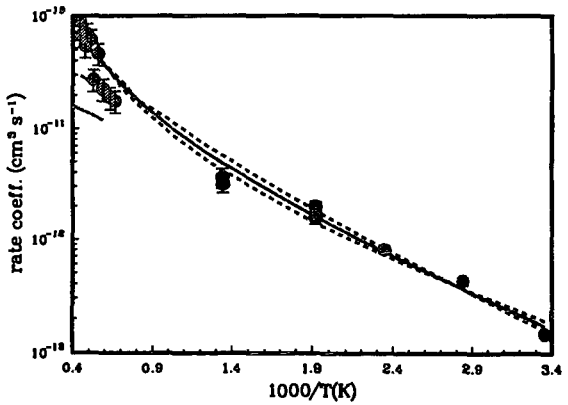

Figure 4. Rate coefficient for the O + H_2CO → OH + HCO reaction. The solid line is the best fit to the data and the dashed lines represent the 2-σ boundary.

Thermal Decomposition Studies of Chlorocarbon Molecules in a Shock Tube using the Cl-atom ARAS Method

K. P. Lim and J. V. Michael
Chemistry Division
Argonne National Laboratory
Argonne, IL 60439

Keywords: Rate constants, Shock tubes, Chlorocarbon dissociations

ABSTRACT

Because of needs for understanding the chemical kinetic mechanism in chlorocarbon molecule incineration, we have recently completed studies on the thermal decompositions of $COCl_2$, CH_3Cl, CH_2Cl_2, CCl_4, and CF_3Cl. The shock tube technique combined with atomic resonance absorption spectrometry (ARAS), as applied to Cl atoms, has been used to obtain absolute rate data for these reactions. In all cases, the decompositions are nearly in the second-order regime. Theoretical calculations, using the Troe formalism, have been performed. In these calculations, both the threshold energies for decomposition, E_0, and the energy transferred per down collision, ΔE_{down}, are varied parametrically for best fitting to the data. The latter quantity determines the collisional deactivation efficiency factor, β_c.

INTRODUCTION

This article discusses thermal decomposition results obtained with the shock tube technique for five chlorocarbon molecules. One motivation is to supply thermal rate data for understanding the chemical destruction mechanisms in incinerators for this important class of compounds. The atomic resonance absorption spectrometric (ARAS) method is used to monitor the production of Cl atoms as they form during the decompositions. The reactions studied are:

$$COCl_2 \ (+ Kr) \rightarrow COCl + Cl \ (+ Kr), \quad (1a)$$

$$\rightarrow CO + Cl_2 \ (+ Kr), \quad (1b)$$

$$CH_3Cl \ (+ Ar) \rightarrow CH_3 + Cl \ (+ Ar), \quad (2)$$

$$CH_2Cl_2 \ (+ Kr) \rightarrow CH_2Cl + Cl \ (+ Kr), \quad (3a)$$

$$\rightarrow CHCl + HCl \ (+ Kr), \quad (3b)$$

$$CCl_4 \ (+ Ar) \rightarrow CCl_3 + Cl \ (+ Ar), \quad (4)$$

$$CF_3Cl \ (+ Kr) \rightarrow CF_3 + Cl \ (+ Kr). \quad (5)$$

We have attempted to rationalize the results on these reactions with Troe type theoretical fits that are based on C—Cl bond strengths and the average energy transferred per down collision.[1-3] The results of these comparative theoretical calculations are discussed.

EXPERIMENTAL

The shock tube methods that are used in the present studies are traditional[4] and have been described in detail previously.[5-9] Therefore, only a brief description will be given here. Experiments in both incident and reflected shock waves have been carried out on these systems. In both instances, corrections for non-ideal shock wave behavior have been applied.[10] The tube has an optical path length of 9.94 cm, and the resonance radiation from a Cl-atom resonance lamp traverses the tube at a distance of 67 or 6 cm from the endplate for incident or reflected shock wave experiments, respectively.

In order to use the method, it was necessary to measure the curve-of-growth for Cl atoms. In experiments on CH_3Cl,[6] the curve-of-growth was determined; however, the results were slightly perturbed by secondary chemistry. We have checked the curve-of-growth by carrying out additional experiments with CF_3Cl where no such complications are present.[9] The results are shown in Fig. 1 where they are compared to the dashed line determined previously.[5,6] This result demonstrates that the perturbing secondary chemistry in the CH_3Cl case was adequately being described because the present agrees with the earlier result within experimental error. The line shown in the figure can be expressed in modified Beer's law form as:

$$-\ln(I/I_0) \equiv (ABS) = \sigma\ell[Cl]^{\alpha} = 4.41 \times 10^{-9}\,[Cl]^{0.581} \qquad (6)$$

when [Cl] is expressed in molecules cm^{-3}. Hence any value of $(ABS)_t$ can be converted into $[Cl]_t$ thereby giving a Cl-atom concentration profile for any experiment.

RESULTS

The thermal decomposition results were obtained at three loading pressures in either incident or reflected shock wave experiments. Bimolecular rate constant values, k/[M], were determined in each instance. The data were then plotted in Arrhenius form as shown in Figs. 2 to 7. Essentially no pressure effects could be documented in any of the cases within experimental error suggesting that the decompositions were near to the low pressure values. We then performed linear least squares analysis on the entire data base for each reactant. The results are given as equations (7) to (13) in units of cm^3 $molecule^{-1}$ s^{-1}.

Reaction (1a): $k/[Kr] = 7.24 \times 10^{-8} \exp(-30594\ K/T)$ (7)

Reaction (1b): $k/[Kr] = 7.60 \times 10^{-9} \exp(-30594\ K/T)$ (8)

Reaction (2): $k/[Ar] = 1.09 \times 10^{-8} \exp(-29325\ K/T)$ (9)

Reaction (3a): $k/[Kr] = 6.64 \times 10^{-9} \exp(-28404\ K/T)$ (10)

Reaction (3b): $k/[Kr] = 2.26 \times 10^{-8} \exp(-29007\ K/T)$ (11)

Reaction (4): $k/[Ar] = 1.19 \times 10^{-7} \exp(-25050\ K/T)$ (12)

Reaction (5): $k/[Kr] = 1.73 \times 10^{-7} \exp(-33837\ K/T)$ (13)

DISCUSSION

We have used the semi-empirical form of Troe theory[1-3] to calculate theoretical rate constants for these reactions. Since there are no potential energy surface calculations for the present cases, as described earlier,[6] the best choice of transition states are the Lennard-Jones (LJ) complexes where the LJ-distance between the combining species is taken to be the reaction coordinate, and all rotational degrees of freedom in each of the combining species are considered to be free. Using conventional transition state theory, this model will always give, as the high pressure limit for the recombination of the two species making up the complex, the collision rate constant with electronic degeneracy factors included. Hence,

$$k_{-1LJ} = (g^{\ddagger}/g_1 g_2)\, \sigma_{12}^2 \Omega(2,2)^{*}\, (8\pi kT/\mu)^{1/2} \exp(\varepsilon_{12}/kT). \qquad (14)$$

With $g^{\ddagger} = 1$, $g_1 = g_{radical} = 2$, and $g_2 = g_{Cl} = 2\,(2 + \exp(-hc(882.36\ cm^{-1})/kT))$, equation (14) has been evaluated for the various back reactions. The value for the high pressure dissociation rate constants are then calculated as $k_{\infty} = k_{-1LJ}K$ where equilibrium constants, K, have been directly calculated from molecular constants.

The theory of Troe and coworkers[1-3] has then been used to calculate the limiting low pressure rate constants, k_{sc}^{o}, which are functions of the various threshold energies, E_o. These values for k_{∞} and k_{sc}^{o}, along with the LJ model for the transition states and values for the collisional deactivation efficiency factor, β_c, can then be used to calculate values for S_K, B_K, F_{cent}, and finally, k/[M] = $k_{\infty}F_{LH}F(P_r)$ where F_{LH} is the Lindemann-Hinshelwood factor, $P_r/(1+P_r)$, and $F(P_r)$ is the broadening factor, a function of reduced pressure, $P_r = \beta_c k_{sc}^{o}[M]/k_{\infty}$. The parameter, ΔE_{down}, determines β_c. In all of the present calculations, we parametrically vary both E_o and ΔE_{down}. The final fitted theoretical results are compared to the data in Figs. 2-7.

For $COCl_2$, parametric calculations were carried out with E_o between 65.4 and 77.5 kcal $mole^{-1}$ and with respective ΔE_{down} values between 420 and 4897 cm^{-1}.[5] Mutual values, (75.5, 2553), (75.0, 2169), (74.5, 1714), or (73.75, 1574), can explain the data shown in Fig. 2; however, the best overall fit is with the third set. This threshold value implies a heat of formation for COCl that is consistent with new thermochemical data[11] within experimental error. Similar parametric calculations were carried out for CH_3Cl, again yielding a range of acceptable values which are: (81.3, 866), (80.3, 761), (79.3, 638), (78.3, 560), or (77.3, 490). The calculation for the middle set is shown in Fig. 3. Using the heat of formation for CH_3Cl given in the JANAF tables,[12] the

implied E_o value would be 82.32 kcal mole^{-1}. Since the heats of formation of Cl and CH_3 are not in doubt, the present results would suggest a (-3.0 ± 2.0) kcal mole^{-1} modification to (-15.1 ± 2.0) kcal mole^{-1} for the heat of formation of CH_3Cl at 0 K. It should be pointed out that the large ΔE_{down} value of 1600 cm^{-1}, reported earlier,[6] is mostly due to the fact that E_o was fixed at the JANAF value of 82.32 kcal mole^{-1}. Two thermal decomposition processes have to be considered in the thermal decomposition of CH_2Cl_2.[7] The one that gives Cl atoms is about one-third of the molecular elimination process. We have carried out parametric calculations on both processes. The Cl-atom process can be fitted with mutual values, (81.25, 560), (78.25, 394), and (75.25, 268) with the middle set being only slightly superior at all pressures. The best set for the molecular elimination process is (73.0, 630). These two best fits are shown in Figs. 4 and 5. Our conclusion is that the heat of formation for CH_2Cl at 0 K is (28.5 ± 3.0) kcal mole^{-1}, and this agrees with a recent evaluation.[13] Several Troe calculations have been carried out for CCl_4 using only the ARAS data from this laboratory.[8] Mutual values, (68.7, 1329), (67.7, 1049), (66.7, 735), (65.7, 560), or (64.7, 428), bracket the acceptable sets of fits. The lines shown in Fig. 6 are calculated from the middle set. Hence, the implied value for E_o is (66.7 ± 2.0) kcal mole^{-1}, and this agrees with a recent thermochemical determination for the heat of formation of CCl_3, 16.7 kcal mole^{-1}.[14] Lastly, the acceptable parametric fits for the CF_3Cl experiments[9] are: (87.0, 1049), (86.0, 857), (84.8, 700), or (84.0, 595). The best fit is with the second set implying that E_o = (86.0 ± 2.0) kcal mole^{-1}, and this calculation is shown in Fig. 7. This suggests that the heat of formation for CF_3Cl at 0 K is (-1.2 ± 2.0) kcal mole^{-1} lower than the JANAF value[12] at (-169.2 ± 2.0) kcal mole^{-1}. Therefore, the present value agrees with JANAF within experimental error. The findings from the theoretical calculations are summarized in Table 1.

In four out of the five cases, the thermochemical conclusions from the present analysis are in agreement with earlier thermochemical data. The only exception is CH_3Cl where a downward modification of 3.0 kcal mole^{-1} in the heat of formation would be more compatible with our results. Stronger thermochemical conclusions from the present results are simply not possible because, in each case, there are a number of acceptable fits spanning a range of threshold energies. In principal, this range could be narrowed if the temperature range were substantially expanded; however, with the present ARAS technique, a large increase in the temperature range is not possible. We point out that even if the temperature range was much greater, there is a strong coupling between E_o and ΔE_{down} (i. e., they are strongly correlated). Hence, an uncertain knowledge in either parameter creates a significant uncertainty in the other quantity. Troe and coworkers have given a rationale for understanding the behavior of the collisional deactivation efficiency factor, β_c, in terms of the energy loss per collision with bath gas molecules. These factors decrease with increasing temperature thereby supplying a reason for the usual observation that apparent experimental activation energies are always lower than the bond strengths of the bond being broken in a dissociation. This is a significant advance in understanding; however, it is still true that there is really no first principles theory for *a priori* calculation of these quantities.[15] Trends in β_c's (or in the ΔE_{down} values that determine them) might be discovered if the thermochemistry is known perfectly. This may be the case in hydrocarbon chemistry; however, there are still uncertainties in the chlorocarbon thermodynamic functions. We believe that this is a partial explanation for the unrelated values for ΔE_{down} in Table 1. With this state of affairs, continuing experimental studies on this type of molecule are absolutely necessary if the thermal rate behavior is desired for any reason. Theoretical calculations alone will not be predictive and therefore will not be helpful.

ACKNOWLEDGMENT

This work was supported by the U. S. Department of Energy, Office of Basic Energy Sciences, Division of Chemical Sciences, under Contract No. W-31-109-Eng-38.

REFERENCES

1. Troe, J., J. Chem. Phys. **65**, 4745 (1977); *ibid.*, 4758 (1977).
2. Troe, J., J. Phys. Chem. **83**, 114 (1979).
3. Troe, J., Ber. Bunsenges. Phys. Chem. **87**, 161 (1983).
4. Bradley, J. N., Shock Waves in Chemistry and Physics, Wiley, New York, 1962.
5. Lim, K. P., and Michael, J. V., J. Phys. Chem., in press.
6. Lim, K. P., and Michael, J. V., J. Chem. Phys. **98**, 3919 (1993).
7. Lim, K. P., and Michael, J. V., Symp. (Int.) Combust., [Proc.] **25**, submitted.
8. Michael, J. V., Lim, K. P., Kumaran, S. S., and Kiefer, J. H., J. Phys. Chem. **97**, 1914 (1993).
9. Kiefer, J. H., Sathyanarayana, R., Lim, K. P., and Michael, J. V., J. Phys. Chem., submitted.
10. Michael, J. V., and Sutherland, J. W., Int. J. Chem. Kinet. **18**, 409 (1986).
11. Nicovich, J. M., Kreutter, K. D., and Wine, P. H., J. Chem. Phys. 92, 1429 (1992).
12. Chase, M. W. Jr., Davies, C. A., Downey, J. R. Jr., Frurip, D. J., McDonald, R. A., and Syverud, A. N., J. Phys. Chem. Ref. Data **14**, Supplement No. 1 (1985).
13. Manion, J. A., and Rodgers, A. S., Thermodynamic Tables, Non-Hydrocarbons, Thermodynamics Research Center, Texas A & M University Press, College Station, TX, June 30, 1993, p. r-7250 – r-ref-7251.
14. Hudgens, J. W., Johnson, R. D. III, Timonen, R. S., Seetula, J. A., and Gutman, D., J. Phys. Chem. **95**, 4400 (1992).
15. Michael, J. V., and Lee, J. H., J. Phys. Chem. **83**, 10 (1979); Michael, J. V., ibid., 17 (1979).

Table 1. **Theoretical Results**

Reaction		ΔE_{down}/cm^{-1}	E_o/kcal mole^{-1}	Comments	Ref.
$COCl_2$ (+ Kr)	→ $COCl + Cl$ (+ Kr)	1714	74.5±1.0	75.6 implied by	11,12
CH_3Cl (+ Ar)	→ $CH_3 + Cl$ (+ Ar)	638	79.3±2.0	compared to 82.3	12
CH_2Cl_2 (+ Kr)	→ $CH_2Cl + Cl$ (+ Kr)	394	78.25±3.0	79.0 implied by	12,13
	→ $CHCl + HCl$ (+ Kr)	630	73.0±3.0	79 or 70.1, from	12 or 13
CCl_4 (+ Ar)	→ $CCl_3 + Cl$ (+ Ar)	735	66.7±2.0	67.7 implied by	12,14
CF_3Cl (+ Kr)	→ $CF_3 + Cl$ (+ Kr)	857	86.0±2.0	compared to 84.8	12

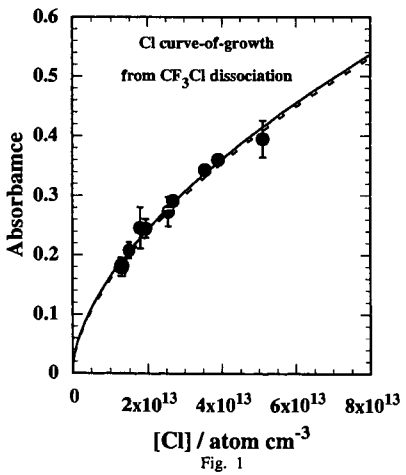

Fig. 1

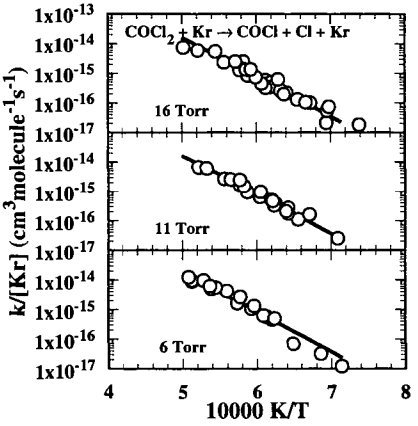

Fig. 2

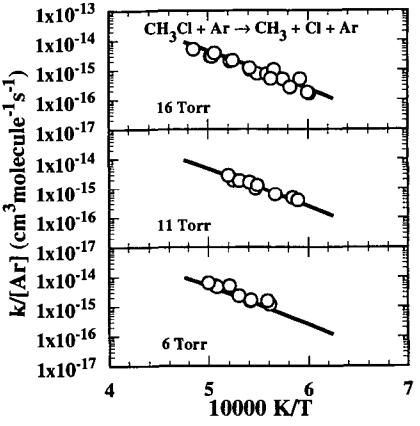

Fig. 3

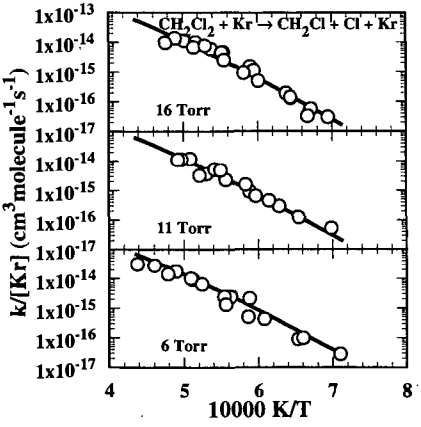

Fig. 4

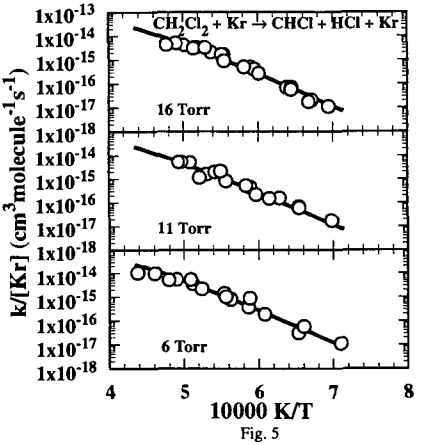

Fig. 5

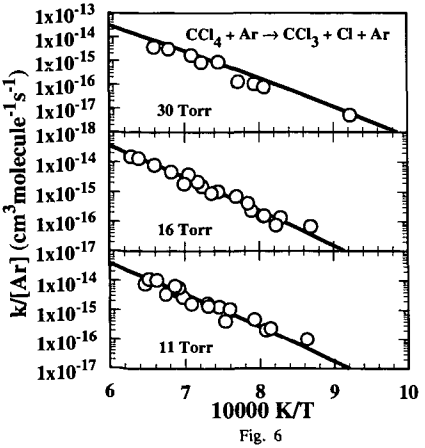

Fig. 6

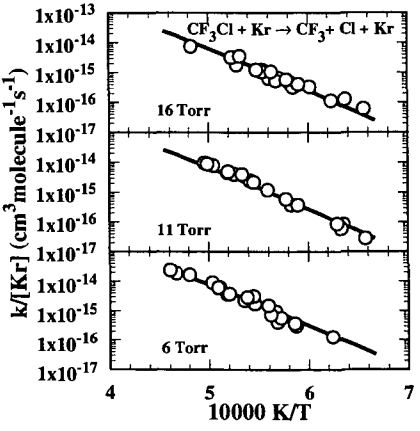

Fig. 7

SINGLE PULSE SHOCK TUBE STUDIES ON THE UNIMOLECULAR DECOMPOSITION OF LARGE UNSATURATED MOLECULES: TRANS-1-PHENYL-1-PENTENE

Wing Tsang and James A. Walker
Chemical Kinetics and Thermodynamics Division
National Institute of Standards and Technology
Gaithersburg, MD 20899

Keywords: 1-phenyl-1-pentene, decomposition, shock tube

Introduction

Decomposition kinetics represent an important component of combustion chemistry. A challenging aspect of this chemistry involves the building up, breakdown and rearrangements of large and unsaturated structures. In this paper experiments that lead to quantitative information on the thermodynamic and kinetic properties of these large unstable species will described. The aim is to provide a base of information upon which predictions can be made. Thus the concentration on single step thermal reactions. Previously, the methodology has been employed to determine unimolecular rate constants (at the high pressure limit) for the decomposition of a large variety of alkenes, alkynes and benzyl compounds. These have also led to a determination of the heat of formation of the large radicals that are formed. A summary of earlier results can be found in Table 1.

	Rate Expressions s^{-1}	Constants (1100)
1-hexene->allyl+n-propyl[1]	$8x10^{15}exp(-35600/T)$	70
->2 propene	$4x10^{12}exp(-28900/T)$	16
1-hexyne->propargy+n-propyl[1]	$8x10^{15}exp(-36300/T)$	37
->allene+propene	$5x10^{12}exp(-28400/T)$	31
phenylpentane->benzyl+n-butyl[2]	$1x10^{16}exp(-36500/T)$	39
c-hexene-2->t-hexene-2[3]	$4x10^{14}exp(-33333/T)$	37
t-1,3pentadiene- ->c-1,3pentadiene[4]	$4x10^{13}exp(-26700/T)$	287

Table 1. Earlier Data on the Decomposition of Unsaturated Compounds

The present study is concerned with a molecule that contains both aromatic and olefinic groups, trans 1-phenylpentene (TPP). Possible mechanisms for decomposition can be found in Figure 1. They involve the cleavage of the resonance weakened C-C bond (2) leading to the formation of 3-methylallyl radical and ethyl, a retroene reaction (1) that forms ethylene and allylbenzene directly and trans to cis(CPP) isomerization (3). All of these reactions have their counterparts in the simpler compounds. Some of the results are listed in Table 1. The quantitative results will bear on a number of interesting issues. In the case of trans-cis isomerization, it will be possible to determine the effect of benzyl resonance. From the rate expression for bond breaking, the activation energy will lead directly to the heat of formation of the 3-phenylallyl radical and in turn its resonance energy. The A-factor can be compared with that for reactions of the 1-olefins, thus leading to information on the effect of the addition to the phenyl group to the vinyl structure. Of particular interest will be the fate of the 3-phenylallyl radical. It can undergo beta bond scission to form phenyl allene or internal displacement to form indene. The latter is especially interesting since it represents the formation of the second ring in such systems. We have observed indene formation in the hydrogen atom induced decomposition of 1-phenylpropene and for the purposes of determining abstraction rate constants it is important to demonstrate that the conversion is quantitative. Similarly, it will be possible to determine how the rate constants for the molecular, retroene, process will be effected in the more complex environment of this molecule.

Single pulse shock tube studies have unique capabilities for

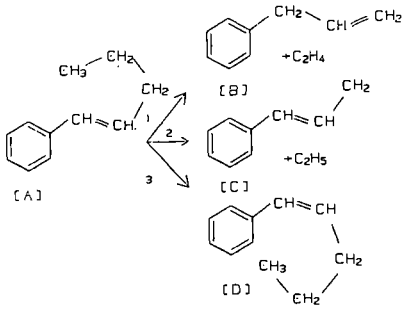

Figure 1. Mechanism for the decomposition of trans-1-phenyl-1-pentene. A=Trans-1-phenyl-1-pentene, B=Allylbenzene, C=3-phenylallyl, D=Cis-1-phenyl-1-pentene

determining the thermal decomposition properties of large organic molecules. There is no chance of surface processes. Final product analysis using gas chromatography with flame ionization detection offers the possibility of detecting all reactants and products. Multiple reaction channels can thus be quantitatively investigated. By working at dilute concentrations, in the presence of a chemical inhibitor, all chain processes can be suppressed. The high temperatures are an important factor in assuring that practically all large organic radicals are decomposed in a time scale such that only the initial and subsequent unimolecular decomposition processes can occur. This is an important aid in the interpretation of the results. The isolation of individual reactions for study means that it is possible to study a number of unimolecular decompositions simultaneously. This is the basis of the internal standard method and removes the uncertainty in the reaction temperature, an important contributing factor to errors in single pulse shock tube experiments. The general technique has been successfully used to determined the rate expression for unimolecular decomposition of many organic compounds. For bond breaking reactions, these lead directly to heats of formation of the organic radicals that are formed. It is by this technique that the first indications were obtained regarding the need for an upgrading of the then generally used heats of formation of simple alkyl radicals[5].

There have been no previous study on the decomposition of TPP. Robaugh and Stein[6] have studied in VLLP experiments the decomposition of 1-phenyl-1-butene. Assuming an A-factor of $2x10^{15}$ s^{-1}, they find an activation energy of 282 kJ/mol leading to an "extra" resonance energy in comparison to that for benzyl of 23 kJ/mol. From the data in Table 1 it can be seen that the breaking of the C-C bond in these cases are characterized by A-factor near $10^{16}s^{-1}$ and resonance energies near 45 kj/mol. The former is a factor of 3 smaller than the characteristic values for alkanes while the latter is directly reflected in the activation energy. The smaller A-factor for alkene and alkyne decomposition can be attributed to the tightened structure of the resonance stabilized radical that is formed and contrasts with the alkyl radicals formed during alkane decomposition. Overall, the unimolecular rate constants are increased by factors ranging from 20 to 30 as a result of allylic and benzyl subsitution at the present temperatures. For the 3-phenylallyl radical, the structure compared to the molecule is even tighter since two weakly hindered rotors will in the radical become torsions. At these temperatures, retroene reactions are competitive with the bond breaking reaction for the alkenes and alkynes (see Table 1) but apparently does not occur for the benzyl compounds. The recommended rate expressions for the cis<->trans isomerization demonstrate that the full value of the resonance energy is manifested in the transition state. There appears to be

surprisingly large differences in the A-factors. Nevertheless, the changes are in the proper direction.

Experimental

Experiments are carried out in a heated single pulse shock tube. The entire shock tube and the gas handling system is maintained at 100°C. This permits the introduction and withdrawal from the shock tube of quantitative mixtures of low-volatility compounds. Details of the apparatus and the procedures can be found in earlier papers[1]. Analysis is by gas chromatography with flame ionization detection. Two columns are used for the analysis. The light hydrocarbons, principally ethylene are separated with a 12 foot Poropak N[7] column operated at 50 C. For the heavier species, from C_4 on up, a wide bore 30 meter dimethylsiloxalane column in the programmed temperature mode is used for analysis. Toluene is used as the chemical inhibitor. The ratio of toluene to the TPP is maintained at 200 to 1. This guarantees that all the reactive radicals will react with toluene in preference to the TPP. Stable benzyl radicals are formed. Under the conditions of the shock tube experiments they can only recombine with itself or other radicals that are present. They have insufficient time to react with the TPP. As a result the initial unimolecular decomposition reaction is isolated for study. For the determination of rate expressions, the use of an internal standard as the reference reaction[1] (k(1-methylcylcohexene =isoprene + ethylene) = $10^{15}\exp(-33500/T)s^{-1}$) permits the calculation of the reaction temperature on the basis of the extent of reaction and the heating time (500 microsecs).

Results

The important products formed from the thermal decomposition of dilute concentrations of TPP in large excesses of toluene are listed in Table I. Also present are considerable amounts of methane and smaller quantities of ethane and ethylbenzene. These are the expected products from the hydrogen atom induced decomposition of toluene. These were not needed for the quantitative analysis of the data. Excellent mass balances are realized and it is clear that the mechanism outlined in Figure 1 fully accounts for the decomposition processes. Benzene is from the reaction of hydrogen atom with toluene and the amount that is formed is in reasonable agreement from that which would have been predicted on the basis of earlier determinations of hydrogen atom attack on toluene. Note that the benzene formed is a measure of all the hydrogen that can be formed in the reactive system. This can include impurities or small quantities from the decomposition of toluene, the inhibitor itself. Ethylene is formed from the decomposition of the ethyl radical and directly from the retroene reaction. From the allylbenzene yields, it is apparent that the latter is only a minor reaction channel. Unfortunately allylbenzene is present as an impurity in the reaction mixture.

Table 2: Typical Product Distribution from the Decomposition of 100 ppm Phenyl-1-Pentene in 2% Toluene at 2 atm. pressure

Compounds	Temperature(K) % yield		
	1057	1080	1149
ethylene	2.7	4.9	27.3
benzene	1.7	3.0	17.2
allylbenzene		.62	1.3
indene	2.2	4.3	24.5
cis-phenyl-1-pentene	4.4	6.6	13.1
trans-phenyl-1-pentene	93.9	88.2	60.4

Thus it proved impossible to make a high accuracy determination of the rate expression of the retroene reaction. Nevertheless it is interesting that, as required, the sum of the allylbenzene and indene concentration is close to that of the ethylene found. Indene and the cis isomer are the major large reaction products.

The former is more important at high extent of reaction. The satisfactory mass balance indicates that all the 3-phenylallyl radical formed is converted into indene. Further confirmation is offered by the absence of any of the phenyl butenes, the expected product from the addition of methyl radicals to 3-phenylallyl. This radical should exist in the cis and trans conformation and it is only from the cis isomerization that indene can be formed. The present results demonstrate that under high temperature conditions this isomerization must be quite rapid. No phenyl allene is detected. Beta bond cleavage is not competitive with internal displacement. This is not surprising since it is expected that the activation energy for the ejection of a beta hydrogen bond in this system will have an activation energy of 260 kJ/mol.

A small uncertainty is introduced into the quantitative interpretation of the results in terms of bond breaking by the simultaneous conversion of TPP to the cis-isomer with the bond breaking reaction. The cis-isomer can of course also undergo the retro-ene and bond breaking reactions. At the high temperatures of these experiments the properties of the cis and trans isomers are very similar. It should be possible to speak of a single average entity. Furthermore, the concentration of the cis compound is never more than 20% of the trans species. On this basis and using the relation k = log (1 - X *indene/$(TPP)_i$)/X * t where t is the residence time of about 500 microseconds and X = 1+ allylbenzene/indene and represents the contribution from the retroene channel, an Arrhenius plot of the data can be found in Figure 1. This leads to the following rate expression for the bond breaking reaction $k(TPP\rightarrow 3\text{-phenylallyl+ethyl})=4\times10^{15}\exp(-34010/RT)s^{-1}$ over the temperature range of 1000-1180 K. and at a pressure of argon of approximately 2 atms.

As noted earlier, accurate determination of the concentration of allylbenzene is made difficult by its presence as an impurity. The consequence is that it is necessary to subtract two numbers. Thus as can be seen in Figure 1, the data show considerable scatter. The rate expression that is obtained $k(1\text{-PP}\rightarrow\text{allylbenzene} + C_2H_4)= 1.9\times10^{11}\exp(-25640/T)s^{-1}$ has parameters that are much lower than that listed above. Nevertheless, it is probably not an accident that at 1100 K the rate constant is 14 s^{-1} or very close to the value for hexene decomposition to form two propene. It is suspected that the expression in Table 1 is more likely to be the correct one.

From the yields of cis-1-phenylpentene (CPP), the rate expression for trans->cis isomerization can be obtained. The rate relation is $k_3=\log(1(CPP/TPP_i)(1+K_{eq})\exp(k_1+k_2)t)/(1+K_{eq})t=k_3$ where $K_{eq}=k_3/k_{-3}$ and is derived from the observed convergence of the ratio of the trans and cis compounds as the temperature is increased. This ratio, 3.9 implies the greater stability of the trans compounds and is contrary to the published results for the analogous phenylpropenes[9]. An Arrhenius plot of the results can also be found in Figure 1. This leads to the rate expression $1.5\times10^{13}\exp(-27400/T)s^{-1}$.

Discussion

The experimental rate constants are only slightly larger than that determined by Robaugh and Stein. Since their study involves the ejection of a methyl group instead an ethyl the differences should be somewhat larger. It is suspected that the discrepencies are about a factor of 1.5 to 2. High pressure rate constants are not directly determined from VLPP studies and this type of differences may arise from the extrapolational procedure.

Assuming that combination rate constants involving 3-phenylallyl and ethyl radical have no temperature dependence, the enthalpy of reaction at 1100 K is 291 kj/mol. From known thermodynamics[8] this is equivalent to a resonance energy of the 3-phenylallyl radical of 66±6 kj/mol and can be compared with that for allyl and benzyl of about 50±4 kj/mol[1]. The heat of formation of the 3-phenylallyl radical is 228±6 kj/mol. The A-factor is an

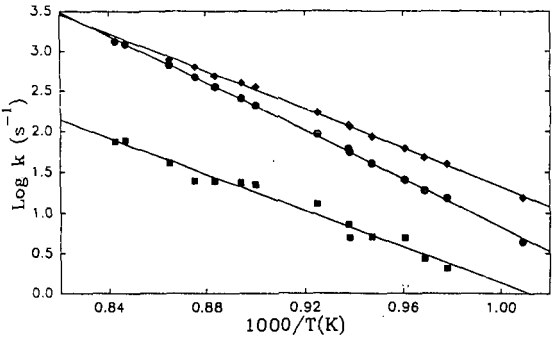

Figure 2: Arrhenius Plots for the Decomposition of t-1-phenylpentene to form 3-phenylallyl+C_2H_5, (●); cis-1-phenylpentene, (◆); and allylbenzene + C_2H_4, (■).

order of magnitude and half an order of magnitude lower than those for alkanes and alkenes, respectively and is consistent with the very stiff radical (no free rotors) that is formed. At lower temperatures rRate constants for cis isomerization are larger than that for bond cleavage. They are consistent with an activation energy that feels the full effect of the benzyl resonance energy. The retroene reaction is slower than for bond cleavage. It appears that phenyl substitution does not have much effect on on the rate constants. The satisfactory mass balance also means that there are no other processes that make contributions to the decomposition process as the molecular complexity is increased.

The formation of indene from 3-methylallyl must involve an internal addition followed by the displacement of the hydrogen atom. This is an endothermic process. From the heat of formation of 3-methylallyl and indene[9] the enthalpy of reaction is 63 kj/mol. When this is coupled with the estimated barrier for addition of hydrogen to indene leading to the breaking of the olefinic ring structure one obtains an overall barrier for cyclization of 89 kj/mol. This barrier is made up of a barrier to addition and then that for ejection of hydrogen. An actual rate expression could be derived if there are reliable values for the entropies of indene. In its absence, a typical value of the A-factor, $10^{11}s^{-1}$, coupled with the barrier for cyclization will lead to rate constants near 0.5 microseconds at 1100 K. Quantitative conversion to indene must occur.

References

1. Tsang, W., "Comparative Rate Single Pulse Shock Tube in the Thermal Stability of Polyatomic Molecules," Shock Tubes in Chemistry, A. Lifshitz ed., Marcel Dekker, pg. 59, 1981.
2. Walker, J. A. and Tsang, W., J. Phys. Chem.,94, 3324, 1990
3. Bauer, S. H., Yadava, B. P. and Jeffers, P., J. Phys. Chem., 76, 770, 1974
4. Marley, W. N. and Jeffers, P., J. Phys. Chem., 79, 2085, 1975
5. Tsang, W., J. Amer. Chem. Soc., 2873, 1985
6. Robaugh, D. A. and Stein S. E., J. Amer. Chem. Soc., 108, 3224, 1985
7. Certain commercial materials and equipment are identified in this paper in order to specify adequately the experimental procedure.In no case does such identification imply recommendation of endorsement by the national Bureau of Standards, nor does it imply that the material or equipment is necessarily the best available for the purpose.
8. Stull, D. R., Westrum, E. F., and Sinke, G. C., "The Chemical Thermodynamics of Organic Compounds" John Wiley and Sons, New York, 1969.
9. Cox, J. D. and Pilcher, G. "Thermochemistry of Organic and Organo-Metallic Compounds", Academic Press, New York, 1970

FLUORINATED HYDROCARBON FLAME SUPPRESSION CHEMISTRY

D. Burgess, Jr., W. Tsang, and M.R. Zachariah
Chemical Science and Technology Laboratory
National Institute of Standards and Technology
Gaithersburg, MD 20899
and
P.R. Westmoreland
Department of Chemical Engineering
University of Massachusetts
Amherst, MA 01003

Keywords:Combustion Chemistry;Reaction Mechanism;Flame Inhibition

ABSTRACT
A comprehensive, detailed chemical kinetic mechanism was developed for fluorinated hydrocarbon destruction and flame suppression. Existing fluorinated hydrocarbon thermochemistry and kinetics were compiled and evaluated. For species where no/incomplete thermochemistry was available, this data was calculated through application of ab initio molecular orbital theory. Group additivity values were determined consistent with experimental and ab initio data. For reactions where no or limited kinetics was available, this data was estimated by analogy to hydrocarbon reactions, by using empirical relationships from other fluorinated hydrocarbon reactions, by ab initio transition state calculations, and by application of RRKM and QRRK methods. The chemistry was modeled considering different transport conditions (plug flow, premixed flame, opposed flow diffusion flame) and using different fuels (methane, ethylene), equivalence ratios, agents (fluoromethanes, fluoroethanes) and agent concentrations. An overview of this work is presented.

INTRODUCTION

During the past year a major effort was conducted at NIST to rate potential replacements (FCs, HFCs, HCFs) for Halon 1301 (CF_3Br). Halon 1301 has been widely used as a chemical extinguisher in sensitive/critical environments where it is necessary to use fire suppressants that are clean (minimal residue & reactivity), non-toxic, and non-conductive. These environments include aircraft, nuclear reactors, computer rooms, and libraries. Halon 1301 has all of these desirable properties and is extremely effective for fire suppression. Unfortunately, it is also extremely effective for depleting stratospheric ozone (attenuates damaging UV radiation from the sun). Consequently, production and use of Halon 1301 and other high ODP chemicals are being banned on a worldwide level.

The chemical kinetic modeling work presented here is a small part of larger, short term intensive program at NIST evaluating potential replacements for Halon 1301 for the U.S. Air Force, Navy, Army and Federal Aviation Administration. The modeling effort complemented the many experimental measurements in the overall NIST program characterizing the effectiveness of various potential replacements. Our work focused on agent chemistry. However, there are also many physical effects relating to mass and heat transport processes. Many of these issues were addressed by other work in the overall project. This included measurements of PVT properties, discharge dynamics, dispersion mechanics, as well as measurements of extinction effectiveness for more realistic geometries than can be modeled. In our work, we attempted to consider indirectly these physical effects in order to provide a framework for transfer of the results of our simulations to more realistic conditions.

FLUORINATED HYDROCARBON SYSTEM

The major objective of this work was to provide a chemical basis for rationalizing the relative degree of effectiveness of each candidate agent. In order to accomplish this objective, it was necessary to develop a chemical mechanism based on elementary reaction steps for their destruction, their participation in and influence on hydrocarbon flame chemistry, as well as prediction of potential by-products of incomplete combustion. The focus of this work was restricted to chemistry involving only fluoromethanes and fluoroethanes. This included both agents specifically considered in the overall NIST project as replacements (CH_2F_2, CF_3-CH_2F, CF_3-CHF_2, CF_3-CF_3), as well as all other possible fluoromethanes and fluoroethanes. The chlorine-substituted (CHF_2Cl, CF_3-CHF_2Cl) and larger fluorinated hydrocarbon (C_3F_8, C_3F_7H, C_4F_{10}, cyclo-C_4H_8) candidates were not considered in our study because they would significantly increase the complexity of the chemistry. However, the effectiveness of each can be estimated to some degree by analogy to

other agents that were studied using qualitative trends observed and a fundamental understanding of the chemistry.

The complete set of fluoromethanes and fluoroethanes were studied for two basic reasons.

First, when the four considered candidate agents decompose in the flame, they generate a pool of fluorinated hydrocarbon stable species and radicals, which results in the formation of many other fluoromethanes and fluoroethanes. Consequently, in order to adequately describe the decomposition of these four agents (and resultant chemistry), it is necessary to describe the chemistry of all intermediates and products that are created, including most of the other fluoromethanes and fluoroethanes. For example, the lowest energy and primary decomposition pathway for one of the agents, CF_3-CF_3, involves dissociation of the C-C bond to form (two) CF_3 radicals. The CF_3 radicals then react with methyl radicals (CH_3), which are present in significant concentrations in hydrocarbon flames. This radical-radical combination has two channels whose relative importance depend upon temperature. These channels result in the formation of both a fluoroethylene, CH_2=CF_2 (and HF), and another fluoroethane, CH_3-CF_3. In order to correctly predict flame products, the magnitude and rate of heat release in the flame, and ultimately the effectiveness of the added agent, it is also necessary to correctly describe the decomposition of these additional stable fluorinated hydrocarbon species (CH_3-CF_3, CH_2=CF_2). When one considers decomposition channels for these molecules, other reaction channels for CF_3, and relevant chemistry for other candidates, most of the fluoromethanes and fluoromethanes must also be considered.

Second, since there was no directly related experimental work, it was imperative to provide a level of self-consistency by considering a range of modeling parameters, including a variety of reactor/flame geometries, fuels, and (potential) agents. This provided a level of confidence and some validation of the qualitative trends that we observed. Quantitative prediction of the absolute or even relative effectiveness of the specific agents will require benchmarking of the simulations with experimental measurements. It is anticipated that this will be done in the near future.

SPECIES THERMOCHEMISTRY

A large comprehensive reaction set or "mechanism" for fluorinated hydrocarbon chemistry was constructed including C_1 and C_2 stable and radical hydrocarbon species, as well as partially oxidized fluorinated hydrocarbons. Existing thermochemical data was compiled and evaluated. A number of general sources were used [1-5], as were compilations/evaluations [6,7] and individual sources [8-11] for fluorinated hydrocarbons. Where little or no data existed for species of interest (most radicals), we estimated that thermochemistry using either empirical methods (e.g. group additivity) or through applications of ab initio molecular orbital theory. In all cases (experimental, empirical, ab initio), an effort was made to use thermochemistry consistent with data for all species.

Standard hydrogen/oxygen and hydrocarbon thermochemistry was used, most of which can be found in the JANAF tables [2], as can data for F, F_2, and HF. FO•, FOO•, FOF, and HOF species were initially considered, but later excluded, because their concentrations were found to be negligible in the high temperature hydrocarbon flames.

Thermochemical data for the fluoromethanes (CH_3F, CH_2F_2, CHF_3, CF_4) can be found in the JANAF tables [2] and has also been reexamined more recently [12]. Thermochemical data for the perfluoromethyl radical (•CF_3) can be found in the JANAF tables. Reliable, experimentally derived heats of formation for the other fluoromethyl radicals (•CH_2F, •CHF_2) and a more recent value for •CF_3 can be found in other evaluated sources [9,11,13]. Ab initio calculations of thermochemical data [14-16] for the fluoromethanes and fluoromethyls are consistent with the experimentally derived values. In this work we employed thermochemical data for the fluoromethylenes (:CHF, :CF_2) from the JANAF tables. However, there is some uncertainty (±10-20 kJ/mol) in heats of formation for these important species. Furthermore, there have been recent measurements and evaluations [8,10,17,18] and ab initio calculations [14,15] that need to be evaluated. Thermochemical data for CHF=O, CF_2=O, •CF=O, and •CF can be found in the JANAF tables. However, there is some uncertainty (±10-20 kJ/mol) in the heats of formation for CHF=O and •CF=O as their heats of formation were calculated using average

bond dissociation energies from other compounds. Our ab initio calculations [15] of thermochemistry for these carbonyl fluorides are consistent with the indirect, experimentally derived values. However, given the uncertainty in all of the data, further mechanism refinement will require critical evaluation of these data.

Experimentally derived thermodynamic properties for six fluoroethanes have been compiled and critically evaluated [6]. Data for other fluoroethanes can be found in the DIPPR compilation [5]. There are experimentally derived thermochemical data [8] for only a few fluoroethyl radicals (CH_3-CH_2•, CF_3-CH_2•, CF_3-CF_2•). However, thermochemistry for all fluoroethyl radicals have been calculated using ab initio molecular orbital theory by Tschuikow-Roux et al [19] and for a few fluoroethyl radicals by other workers [14-16]. For consistency, we have used the Tschuikow-Roux et al values. Experimentally derived thermochemistry is available for CF_2=CF_2 in the JANAF tables [2] and for CH_2=CHF and CH_2=CF_2 in the DIPPR compilation [5]. For the other fluoroethylenes: CHF=CHF(E), CHF=CHF(Z), CHF=CF_2, we relied upon ab initio calculations [14]. We are not aware of any experimentally derived thermochemistry for fluorovinyl radicals and, consequently, used our ab initio calculated values [15]. Further mechanism refinement would involve benchmarking ab initio calculations with the experimental data (using bond and group additivity methods) to provide a consistent set of data for the fluoroethanes, -ethyls, -ethylenes, and -vinyls.

REACTION SET DEVELOPMENT

The literature on reaction kinetics for fluorinated hydrocarbons was compiled, reviewed, and evaluated. A large part of our work is based on the pioneering work of Biordi et al [20] and Westbrook [21]. Due to the limited nature of this paper, the reaction set that we developed can only be outlined here. Many of the rate constants can be found in the NIST Chemical Kinetics Database [22].

Utilizing species identified as potentially important, we constructed a grid of possible reactions. Existing chemical rate data involving these fluorinated species were then compiled and evaluated. Where rate data was available over a limited temperature range or at different pressures (for unimolecular or chemically activated steps), RRKM and QRRK methods were used to estimate the rate constant temperature (and pressure) dependence and to predict relative rates where multiple product channels were possible. Where no rate data were available for potential reactions, the rate constants were estimated by analogy to hydrocarbons or substituted hydrocarbons. The rate constant prefactors were adjusted for reaction path degeneracy and activation energies were adjusted empirically based on relative heats of reaction or bond energies.

Initially, upper limits were used for estimated rate constants. If as a result of simulation under a variety of conditions, it was observed that a specific reaction contributed to the chemistry and its rate constant was an upper limit estimate, then its value was reexamined and possibly refined. For important contributing reactions, where no good analogy was available, where significant uncertainty existed in the barrier (generally reactions with tight transition states and modest-to-large barriers), or where energetically similar product channels were possible, ab initio methods were used to calculate the geometries and energies of the transition states. RRKM methods were then applied to obtain the temperature (and pressure) dependence of the rate constant.

CONTRIBUTING REACTIONS

The hydrocarbon and hydrogen/oxygen reaction subsets of the mechanism were derived from the Miller/Bowman mechanism [23]. This reaction subset consists of about 30 species and 140 reactions. A number of species important in fuel rich flames (e.g. C_2H) were eliminated from the mechanism. A number of species important in fuel lean flames (e.g. CH_3OH) were added using kinetics from other validated mechanisms [20]. Rate constants for a few reactions (e.g. CH_3+OH) were also adjusted to provide correct fall-off and product channel ratios. The hydrogen/oxygen/fluorine reaction subset consists of only 3 species and about 8 reactions, although many more were initially considered. Three reactions were determined to be most important: combination of H and F atoms to form HF and H atom abstractions from H_2 and H_2O by F radicals.

The C_1 reaction subset consists of about 15 species and 200 reactions. Both thermally- and chemically-activated fluoromethane decompositions are included (e.g. CH_2F_2 => :CHF + HF and •CHF_2 + H

=> :CHF + HF). Fluoromethane decompositions via abstraction of H atoms by H, O, and OH radicals were also considered with abstractions by OH and H the major decomposition pathways. The fluoromethyls produced here were destroyed by several pathways whose relative importance were sensitive to conditions: reactions with H radicals, CH_3 radicals, and oxygen-containing species (O_2, O, OH). The products of the latter reactions consist of carbonyl fluorides (i.e. CF_2O, CHF=O, •CF=O) and HF or other elimination products (e.g. $•CHF_2$ + OH => CHF=O + HF). It was seen almost exclusively that any reaction channel with an HF product was the dominant channel. The fluoromethylenes (:CHF, $:CF_2$) were largely created by combination of fluoromethyls and H radicals via chemically-activated fluoromethanes (and HF elimination). The fluoromethylenes were predominantly destroyed similarly by combination with H radicals via chemically-activated fluoromethylenes (and HF elimination creating •CH and •CF). •CF radicals created here were largely consumed by reactions with H_2O and O_2 resulting in CHF=O and •CF=O formation.

Typical reaction pathways for the decomposition of two potential agents, CH_2F_2 and CHF_3, are shown in Figure 1.

The C_2 reaction subset consisted of about 40 species and 400 reactions. Due to the limited nature of this paper, this reaction set cannot be described here in detail. Briefly, the fluoroethane destruction pathways (like fluoromethanes) consist of thermally- and chemically-activated decompositions and H atom abstraction reactions. Fluoroethyl radicals can react with H radicals (like fluoromethyls) creating fluoroethylenes (via chemically activated fluoroethanes and HF elimination). Fluoroethyl radicals can also react with oxygen-containing species (O_2, O, OH) resulting in the formation of oxidized fragments (e.g. CF_3-CF_2• + O => $•CF_3$ + CF_2=O). Fluoroethylenes (produced from thermally- and chemically-activated fluoroethane decompositions) are predominantly destroyed via reaction with O radicals resulting in the formation of oxidized fragments (e.g. CH_2=CF_2 + O => •CH=O + $•CHF_2$). Fluoroethylenes are also destroyed to a lesser degree through H atom abstraction by radicals such as OH, resulting in formation of fluorovinyl radicals (e.g. CH_2=CF_2 + OH => CF_2=CH• + H_2O). Fluorovinyl radicals (like fluoromethyl and fluoroethyl radicals) are destroyed via reactions with H radicals, as well as with oxygen-containing species. However, it was observed that the fluorovinyl radicals established a dynamic equilibrium with the parent fluoroethylenes, irrespective of the specific creation and destruction pathways.

PREMIXED FLAME CALCULATIONS

Adiabatic, freely-propagating, premixed flame calculations [25] were performed utilizing the reaction mechanism briefly outlined above. Typically, fuel lean CH_4/air conditions were modeled in order to be most sensitive to flame speed changes and (in a practical sense) since agents are added to the air supply. More realistic would be to simulate agent effects in a diffusion flame. We have performed a few opposed flow diffusion flame calculations; however, those results are preliminary and ongoing.

A summary of the effects on adiabatic flame temperature and speed are shown in Figure 2 for addition of a variety of "agents" to a CH_4/air flame (equivalence ratio of 0.65). In addition to potential fluorinated hydrocarbon agents: CF_4, CHF_3, CH_2F_2, CF_3-CF_3, CF_3-CF_2H, and CF_3-CFH_2, other species were added to investigate the effect of heat capacity and heat release on flame speed changes. These reference "agents" include N_2, H_2O, CO_2, HF, and CH_4. In order to correct for differences in heat capacities for the different "agents", the amount of added "agent" was normalized to an equivalent amount of N_2, adjusting for relative heat capacities at 1500K. For example, addition of 1% CF_4 (with C_p=105 J/mol/K) would be roughly equivalent to addition of 3% N_2 (with C_p=35 J/mol/K). Using heat capacities at other temperatures (1000-2000K) had little impact on the relative normalized mole fractions.

In Figure 2a, it can be seen that the effect of the various agents on flame temperature can be bracketed by addition of inert molecules (N_2, H_2O, CO_2, HF), where there is decrease in flame temperature, and by addition of more fuel (CH_4), where there is an increase in flame temperature. The decrease in flame temperature upon addition of the inerts is due to dilution and increased heat capacity of the mixture. The increase in flame temperature upon addition of more fuel is due to increased heat release as the mixture becomes more rich. Addition of agents which are more fuel-

like results in a larger increase in flame temperature. All of the fluorinated hydrocarbons are fuels since they all eventually decompose, burn, and form CO_2, H_2O, and HF (liberating heat). At one extreme is CF_4, very little of which decomposes in the flame, and consequently, there is only a small increase in flame temperature relative to addition of inerts. On the other extreme is CH_2F_2, which completely burns forming highly exothermic products CO_2 and HF. In Figure 2b, a range of effects on flame speed for the various added agents can be observed. For the inert molecules and the nearly inert fluorinated hydrocarbons (CF_4, CF_3-CF_3), a decrease in flame speed is observed consistent with dilution of the mixture. On the other extreme, for CH_4 (the fuel) and CH_2F_2 (a slightly poorer fuel), an increase in flame speed is observed.

Of the various agents considered, only CHF_3 was seen to have any chemical effect in flame suppression. Figure 2 shows that although there is an increase in flame temperature upon CHF_3 addition, there is also a decrease in flame speed relative to inert molecule addition. Inspection of reaction pathways for CHF_3 and other agents (see Figure 1) reveals that a significant amount of decomposed CHF_3 results in the formation of the relatively unreactive perfluoro-compound carbonyl fluoride (CF_2=O). Decomposition of CF_2=O occurs only very slowly via reaction with either H radicals (H addition + HF elimination) or with H_2O (through a hot fluoroformic intermediate). For all other agents, this CF_2=O bottleneck is avoided.

SUMMARY

These simulations are consistent with qualitative trends observed in experimental measurements of agent effectiveness in the work by others in other parts of the overall project at NIST. In order to quantitatively predict agent effectiveness, experimental validation of the mechanism will be necessary and is currently underway.

REFERENCES

1. D.R. Stull, E.F. Westrum, Jr., and G.C. Sinke, The Chemical Thermodynamics of Organic Compounds, John Wiley, NY, 1969.
2. D.R. Stull and H. Prophet, JANAF Thermochemical Tables, NSRDS-NBS 37, 1971.
3. J.B. Pedley, R.D. Naylor, and S.P. Kirby, Thermochemical Data of Organic Compounds, Chapman and Hall, NY, 1986.
4. A.S. Rodgers, TRC Thermodynamics Tables, Texas A&M University, College Station, TX, 1989.
5. T.E. Daubert and R.P. Danner, DIPPR Data Compilation of Pure Compound Properties, NIST Standard Reference Data, 1985.
6. S.S. Chen, A.S. Rodgers, J. Chao, R.C. Wilhoit, and B.J. Zwolinski, J. Phys. Chem. Ref. Data 4, 441 (1975).
7. S.A. Kudchadker and A.P. Kudchadker, J. Phys. Chem. Ref. Data 7, 1285 (1978).
8. A.S. Rodgers, ACS Symp. Ser. 66, 296 (1978).
9. D.F. McMillen and D.M. Golden, Ann. Rev. Phys. Chem. 33, 493 (1982).
10. S.G. Lias, Z. Karpas, and J. F. Liebman, J. Am. Chem. Soc. 107, 6089 (1985).
11. W. Tsang, J. Phys. Chem. 90, 414 (1986).
12. A.S. Rodgers, J. Chao, R.C. Wilhoit, and B.J. Zwolinski, J. Phys. Chem. Ref. Data 3, 117 (1974).
13. J.M. Pickard & A.S. Rodgers, Int.J. Chem. Kinet. 15,569(1983).
14. C.F. Melius, private communication, 1992.
15. M.R. Zachariah, unpublished results, 1993.
16. M.R. Nyden, private communication, 1993.
17. D.S. Hsu, M.E. Umstead & M.C. Lin, ACS Symp.Ser.66,128(1978).
18. G.O. Pritchard, W.B. Nilsson, and B. Kirtman, Int. J. Chem. Kinet. 16, 1637 (1984).
19. Y. Chen, A. Rauk, and E. Tschuikow-Roux, J. Chem. Phys. 94, 7299 (1991); and prior references.
20. J.C. Biordi, C.P. Lazzara, and J.F. Papp, J. Phys. Chem. 82, 125 (1978).
21. C.K. Westbrook, Combust. Sci. Technol. 34, 201 (1983).
22. W.G. Mallard, F. Westley, J.T. Herron, R.F. Hampson, and D.H. Frizzel, NIST Chemical Kinetics Database, NIST Standard Reference Data, Gaithersburg, MD, 1993.
23. J.A. Miller and C.T. Bowman, Prog. Energy Comb. Sci. 15, 287 (1989).
24. C.K. Westbrook and F.L. Dryer, Combust. Sci. Technol. 20, 125 (1979).
25. R.J. Kee, J.F. Grcar, M.D. Smooke, and J.A. Miller, A Fortran Program for Modeling Steady Laminar One-Dimensional Premixed Flames, SAND85-8240, Sandia National Laboratories, 1985.

FIGURE 1. Typical Reaction Pathways for CH_2F_2 and CHF_3

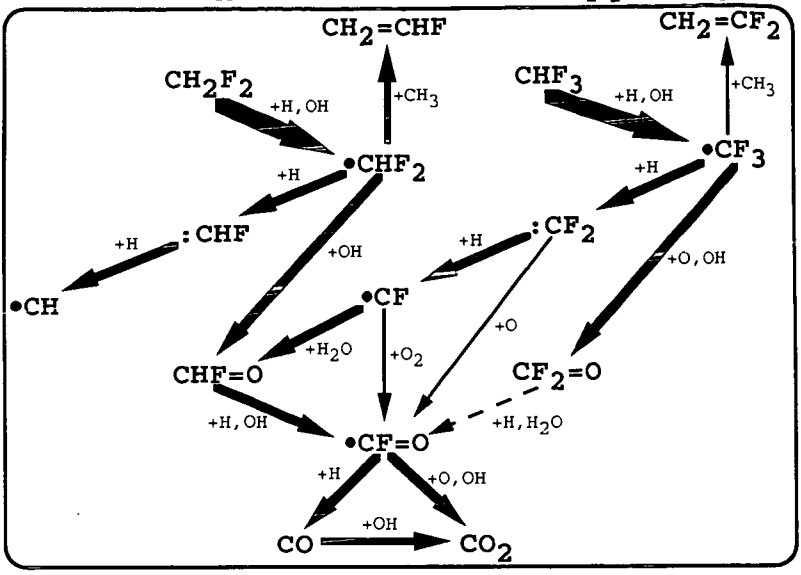

FIGURE 2. Effect of Agents on Flame Temperature and Speed

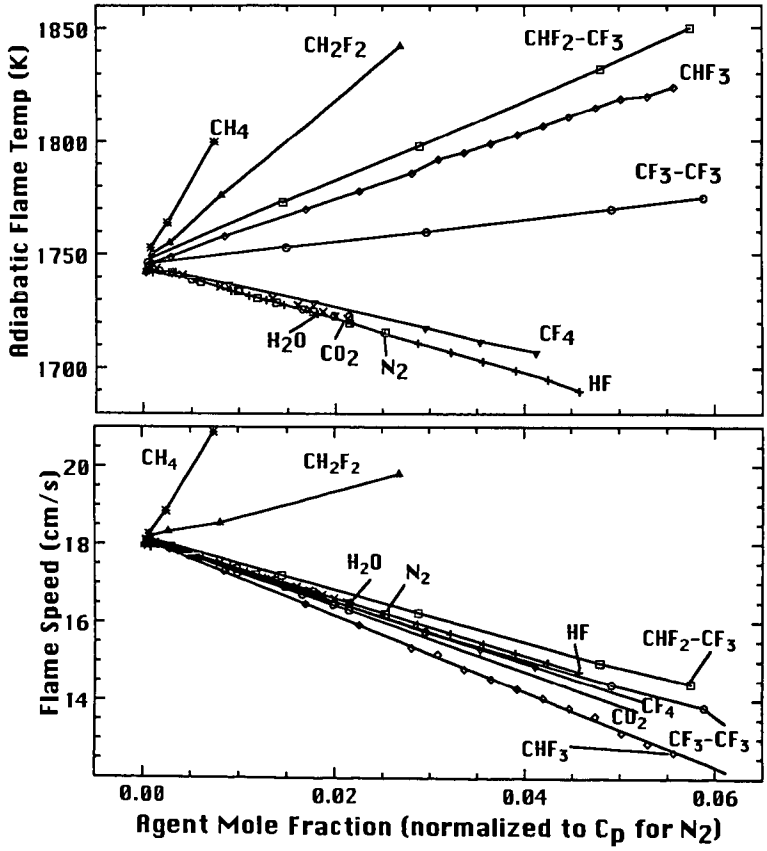

FORMATION OF AROMATIC COMPOUNDS AND SOOT IN FLAMES

R.P. Lindstedt and G. Skevis
Mechanical Engineering Department,
Imperial College of Science, Technology and Medicine,
Exhibition Road, London SW7 2BX, UK.

Keywords: Soot Formation, PAH Formation in Flames, HACA Sequence

ABSTRACT

The formation of aromatic compounds such as toluene, naphthalene and phenylacetylene is discussed in the context of soot nucleation in flames. Detailed kinetic reaction steps have been reviewed and a reaction mechanism has been constructed. It is shown that good quantitative agreement between computations and measurements can be obtained for minor aromatic compounds in premixed benzene flames with the notable exception of naphthalene. Benzene flames have been preferred on the grounds that the uncertainties associated with the formation of the first ring can be avoided and as a detailed reaction mechanism for benzene oxidation has recently been proposed. Special attention has been given to species and processes, such as the *HACA* sequence, which are generally considered essential to the soot nucleation process.

INTRODUCTION

To develop a predictive capability for the formation of *PAH* and soot in laminar and turbulent flames is of fundamental scientific and practical interest. For diffusion flames with C_1-C_3 fuels it has been shown [1] that predictions of soot are insensitive to the exact nature of the nucleation process for a wide range of conditions. For example, an *ad hoc* approximation assigning a C_{60} shell as a typical particle size where mass growth becomes dominant over nucleation, has been shown [1] to be satisfactory, provided that nucleation occurs close to the correct location in the flame structure. By contrast, it is reasonable to expect that in premixed flames the dynamics of the nucleation process becomes more important due to shorter time scales. Thus while the use of benzene [1], or even ethyne [2], as indicative species has been shown to be satisfactory in diffusion flame environments, this situation is unlikely to prevail for premixed or partially premixed combustion. Furthermore, many practical fuels, e.g. kerosene, contains a spectrum of aromatic fuel components. Clearly, for these cases current simplified approaches require refinement. The most obvious way of introducing improved descriptions of soot nucleation leads to the introduction of reaction steps for the formation of the second and subsequent aromatic rings. Modelling of the formation of the second ring requires accurate predictions of the underlying flame structure. For benzene flames this has proved difficult in the past. However, recently a benzene oxidation mechanism has been proposed [3] which gives good quantitative agreement for the flame features of relevance to the present study.

CHEMISTRY

Uncertainties have long prevailed regarding the benzene formation steps in flames burning C_1-C_4 fuels. For methane flames it appears clear that the predominant path passes via

$$C_3H_3 + C_3H_3 = l\text{-}C_6H_5 + H \qquad (1)$$

with the subsequent cyclization of the linear C_6H_5 species [3,4]. The situation for higher hydrocarbons is not as firmly established. However, there is some evidence [5] to suggest that reactions via the C_4 chain become competitive for ethyne flames.

$$C_2H_2 + nC_4H_3 = l\text{-}C_6H_5 \qquad (2)$$

$$C_2H_2 + nC_4H_5 = l\text{-}C_6H_5 + H_2 \qquad (3)$$

To by-pass the uncertainty associated with the formation reactions for the first ring the present work considers benzene flames. The reaction mechanism used is that proposed by Lindstedt and Skevis [3] which has been shown to predict the MBMS data by Bittner and Howard [6] well.

The reaction sequence adopted for toluene, phenyl-acetylene and naphthalene (the second ring) formation is outlined below. Toluene is produced by methyl radical attack on the benzene ring according to

$$C_6H_5 + CH_3 = C_7H_8 \qquad (-4)$$

$$C_6H_6 + CH_3 = C_7H_8 + H \qquad (-5)$$

Toluene subsequently undergoes H atom attack on the side chain to form the benzyl radical

$$C_7H_8 + H = C_7H_7 + H_2 \qquad (6)$$

The benzyl radical further dissociates by ring opening either to cyclopentadiene and acetylene or to vinylacetylene and the propargyl radical thus feeding into the C_5 and C_4 chains respectively. Both reactions are assumed to be uni-molecular

$$C_7H_7 = c\text{-}C_5H_5 + C_2H_2 \qquad (7)$$

$$C_7H_7 = C_4H_4 + C_3H_3 \qquad (8)$$

The phenylacetylene mechanism used here is adopted from the work of Herzler and Frank [7] who obtained data in a shock tube at temperatures in the range 1500 - 1900 K. Phenylacetylene is formed by direct C_2H_2 attack on the benzene ring via

$$C_6H_5 + C_2H_2 = C_8H_6 + H \quad (-9)$$

Phenylacetylene may subsequently undergo aryl H atom abstraction giving ethynylphenylene.

$$C_8H_6 + H = C_8H_5 + H_2 \quad (10)$$

Styrene formation was also considered and postulated to occur via vinyl radical attack on the benzene.

$$C_6H_5 + C_2H_3 = C_8H_8 \quad (-11)$$

The plausibility of naphthalene formation via the building blocks of the *HACA* sequence [8,9] is here investigated further. In the $C_{10}H_8$ formation sequence ethynylphenylene undergoes a further acetylene attack *on the free site* thus forming a di-substituted aromatic compound which subsequently isomerises to naphthyl radical. Naphthalene is then formed by a second H attack on the ring.

$$C_8H_5 + C_2H_2 = C_6H_4C_2H_2C_2H \quad (12)$$

$$C_6H_4C_2H_2C_2H = C_{10}H_7 \quad (13)$$

$$C_{10}H_7 + H = C_{10}H_8 \quad (14)$$

The above mechanism may readily be written in a generalised form for the formation of higher *PAH* [8] and soot. For the latter only the equivalent of reaction *(10)* is treated as reversible while reactions *(12)* and *(13)* are written in a slightly different form. Table 1 provides a listing of the most important reactions and rate coefficients in the present mechanism. The thermodynamic data was mainly obtained from the *CHEMKIN* database [10]. Toluene and naphthalene were assigned ΔH_f values of 12 kcal/mole and 36 kcal/mole respectively, while the heat of formation of the benzyl radical was set at 51.9 kcal/mole. Styrene was assigned a heat of formation of 35.5 kcal/mole. The heats of formation of phenylacetylene, 78.2 kcal/mole, and ethynylphenylene, 133.6 kcal/mole, were adopted from the work of Herzler and Frank [7]. For $C_6H_4C_2H_2C_2H$ the heat of formation was adopted from Frenklach et al [19]. Group additivity [11] was employed to estimate thermodynamic data for species not found in the literature.

RESULTS AND DISCUSSION

The first flame considered in this study was the rich, laminar, low-pressure 21.8% C_6H_6, 68.2% O_2, 10% Ar flame studied by McKinnon [12]. The flame was assumed to be burner stabilised and the experimental temperature profile was imposed on the calculations. However, it was found necessary to shift the temperature profile by 2 mm with respect to the species concentration profiles in order to account for probe effects. Profiles of the major species are shown in Figures 1 and 2. Clearly, major species are predicted well and the benzene consumption rate is matched. Also the model gives excellent agreement for acetylene and methane concentration levels as shown in Figure 3. The second flame considered was the rich, laminar, near-sooting 13.5% C_6H_6, 56.5% O_2, 30% Ar flame of Bittner and Howard [6], which has been studied extensively elsewhere [3]. Predictions of toluene and phenylacetylene levels are within a factor of 2 or better as shown in Figure 4. Computations using a lower heat of formation for C_8H_6 - 75.2 kcal/mole as suggested in [10] leads to equally acceptable phenylacetylene levels. Good agreement, again within a factor of 2, was also observed for styrene levels in the flame. Toluene and phenylacetylene profiles are also shown in Figure 5 for the 14.8% C_6H_6, 55.2% O_2, 30% Ar flame studied by McKinnon [12]. The agreement is again acceptable. Naphthalene chemistry is important because it provides the first step for *PAH* mass growth in flames. Initial computations using the above sequence [8,9] led to severe under-prediction of $C_{10}H_8$ levels - by a factor of 15 or more. In order to partially resolve the issue, the reaction sequence was retained but reactions *(12)* and *(14)* were postulated to proceed with a collision efficiency of 5%. This led to an increase of naphthalene levels by a factor of 3, as shown in Figure 6. Even assigning a collision efficiency of 1, unreasonable for a gas phase reaction, results in under-predictions by a factor of 4. Given the accuracy of predictions of other minor aromatic species this is of concern for quantitative predictions of soot nucleation based on the above reaction sequence.

CONCLUSIONS

It has been shown that good agreement between measurements and predictions may be obtained for small aromatic compounds in benzene flames and that consequently improved soot nucleation models may be developed. However, it has also been shown that significant uncertainties surround the reaction sequence for the second aromatic ring. It appears that either the reaction rates in the formation sequence [9] have to be assigned collision efficiencies similar to those used for soot mass growth [8] or that the whole mechanism for second ring formation has to be refined. For gas phase reactions the latter is clearly preferable. This may involve distinguishing between active sites, accounting for steric effects, incorporating attacks by a variety of radicals and exploring supplementary reaction paths.

ACKNOWLEDGEMENT

The Authors Gratefully Acknowledge the Financial Support of British Gas plc.

REFERENCES

[1] Lindstedt, R.P., in *Mechanisms and Models of Soot Formation* (H. Bockhorn, Ed.), Springer-Verlag, To Appear.

[2] Leung, K.M., Lindstedt, R.P. and Jones, W.P., Combustion and Flame 87, p.289 (1989)

[3] Lindstedt, R.P. and Skevis, G., Submitted to the *Twenty-Fifth Symposium (International on Combustion)* Nov. 1993

[4] Leung, K.M. and Lindstedt, R.P., Comb. and Flame, To Appear.

[5] Vovelle, Ch., Delfau, J.-L. and Doute, Ch., Proc. of Anglo-German Comb. Symp., Cambridge 1993, p. 148.

[6] Bittner, J.D. and Howard, J.B., *Eighteenth Symposium (International) on Combustion,* The Combustion Institute, 1980, p.1105

[7] Herzler, J. and Frank, P., in *Mechanisms and Models of Soot Formation* (H.Bockhorn, Ed.), Springer-Verlag, To Appear.

[8] Frenklach, M. and Wang, H., *Twenty-third Symposium (International) on Combustion,* The Combustion Institute, 1990, p.1559

[9] Frenklach, M. and Warnatz, J., *Comb. Sci. and Tech.* 51:265 (1987)

[10] Kee, R.J., Rupley, F.M. and Miller, J.A., *The CHEMKIN Thermodynamic Database,* Sandia National Laboratories Report No. SAND87-8215, 1987

[11] Benson, S.W., *Thermochemical Kinetics,* Wiley, New York, 1976

[12] McKinnon, J.T., Jr., *Ph.D. Thesis,* Chemical Engineering Department, MIT, 1989

[13] Miller, J.A. and Melius, C.F., *Combust.Flame.* 91:21 (1992)

[14] Westmoreland, P.R., Dean, A.M., Howard, J.B. and Longwell, J.P., *J. Phys. Chem.* 93:8171 (1989)

[15] Emdee, J.L., Brezinsky, K. and Glassman, I., *J.Phys.Chem.* 96:2151 (1992)

[16] Braun-Unkhoff, M., Frank, P. and Just, Th., *Twenty-second Symposium (International) on Combustion,* The Combustion Institute, 1988, p.1053

[17] Brouwer, L.D., Muller-Markgraf, M. and Troe, J., *J. Phys. Chem.*, 92:4905 (1988)

[18] Colket III, M.B., Seery, D.J. and Palmer, H.B., *Combust.Flame.*, 75:343 (1989)

[19] Frenklach, M., Clary, D.W. and Yuan, T., Gardiner, W.C., Jr and Stein, S.E., *Comb. Sci. and Tech. 50,* p. 79 (1986)

Table 1. Reaction Mechanism Rate Coefficients in the Form k= $AT^n exp(-Ea/RT)$. Units are kmole, cubic metres, seconds, Kelvin and KJ/mole

Reaction	A	n	Ea	Reference
$C_3H_3 + C_3H_3 \rightarrow l\text{-}C_6H_5 + H$	3.00e10	0.00	0.00	13
$l\text{-}C_6H_5 \rightarrow n\text{-}C_4H_3 + C_2H_2$	1.00e14	0.00	163.72	3
$n\text{-}C_4H_5 + C_2H_2 \rightarrow C_6H_6 + H$	1.90e04	1.47	20.54	14
$C_7H_8 \rightarrow C_6H_5 + CH_3$	1.14e15	0.00	417.56	15
$C_7H_8 + H \rightarrow C_6H_6 + CH_3$	1.20e10	0.00	21.54	15
$C_7H_8 + H \rightarrow C_7H_7 + H_2$	5.00e11	0.00	52.30	16
$C_7H_7 \rightarrow c\text{-}C_5H_5 + C_2H_2$	1.66e10	0.00	187.00	17
$C_7H_7 \rightarrow C_4H_4 + C_3H_3$	2.00e15	0.00	349.60	17
$C_8H_6 + H \rightarrow C_6H_5 + C_2H_2$	2.00e11	0.00	40.58	7
$C_8H_6 + H \rightarrow C_8H_5 + H_2$	4.00e10	0.00	40.58	7
$C_6H_5 + C_2H_2 \rightarrow C_8H_8$	5.01e09	0.00	0.00	18
$C_8H_5 + C_2H_2 \rightarrow C_6H_4C_2H_2C_2H$	2.00e11	0.00	0.00	9, pw
$C_6H_4C_2H_2C_2H \rightarrow C_{10}H_7$	1.00e10	0.00	0.00	9
$C_{10}H_7 + H \rightarrow C_{10}H_8$	5.00e11	0.00	0.00	9, pw

Figure 1 - Comparison between computed (lines) and experimental (points) profiles for C6H6, H2 and H2O
Experimental data are from McKinnon [12]

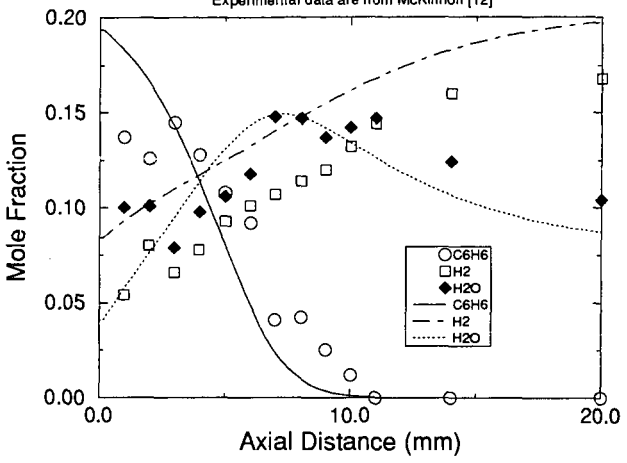

Figure 2 - Comparison between computed (lines) and experimental (points) profiles for O2, CO and CO2
Experimental data are from McKinnon [12]

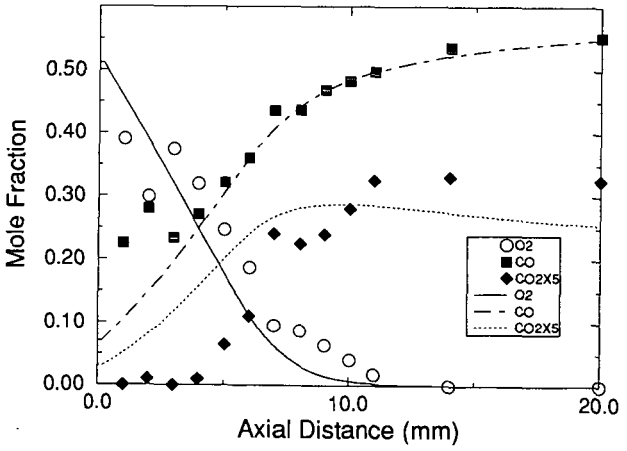

Figure 3 - Comparison between computed (lines) and experimental (points) profiles for C2H2 and CH4
Experimental data are from McKinnon [12]

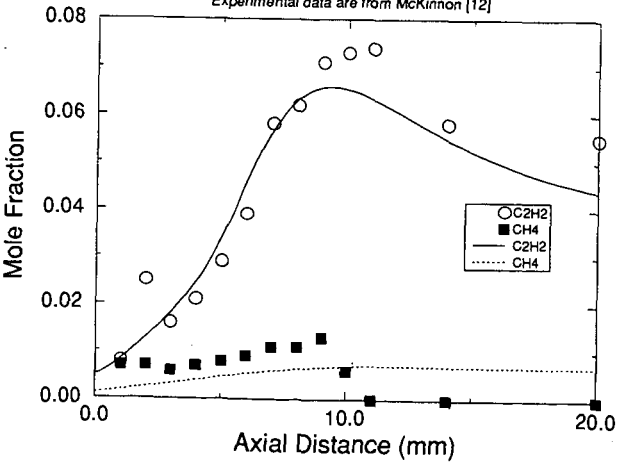

Figure 4 - Comparison between computed (lines) and experimental (points) profiles for C7H8 and C8H6
Experimental data are from Bittner and Howard [6]

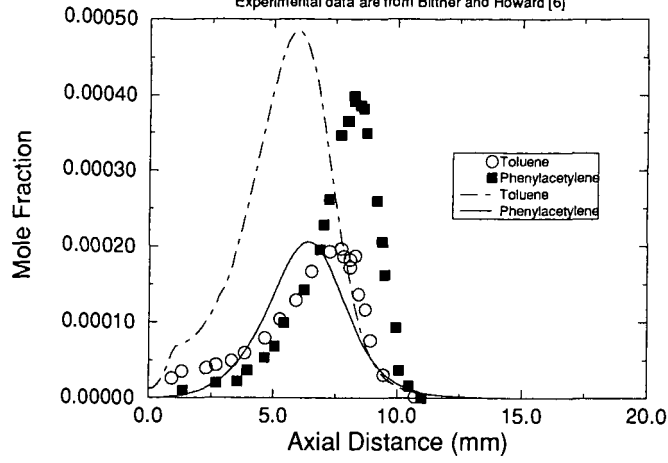

Figure 5 - Comparison between computed (lines) and experimental (points) profiles for C7H8 and C8H6
Experimental data are from McKinnon [12]

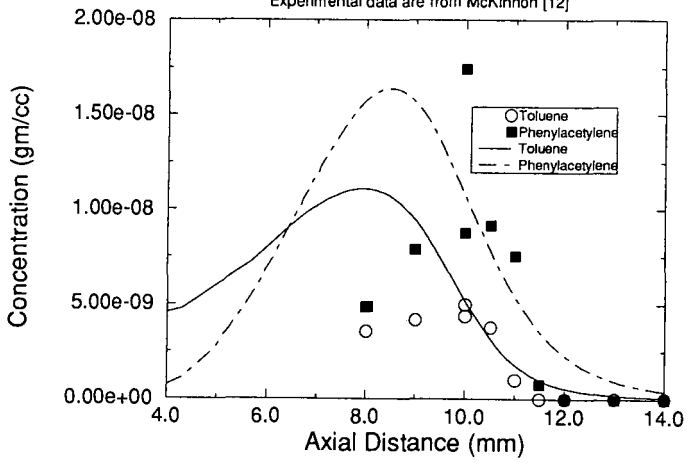

Figure 6 - Comparison between computed (lines) and experimental (points) profiles for C10H8
Experimental data are from Bittner and Howard [6]

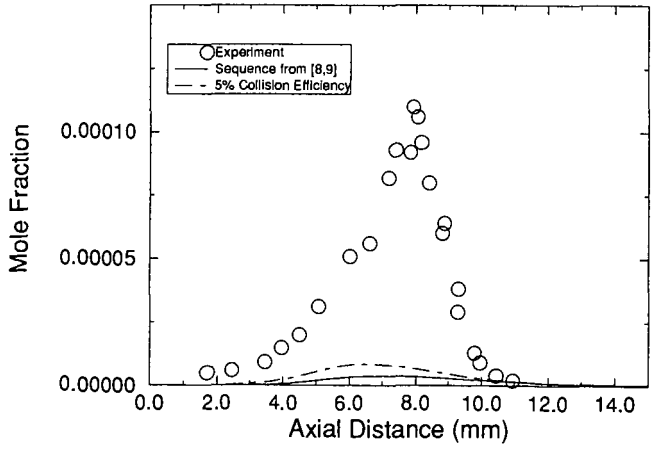

ENHANCED SOOT FORMATION IN FLICKERING CH_4/AIR DIFFUSION FLAMES

Christopher R. Shaddix, Joel E. Harrington, and Kermit C. Smyth
Building and Fire Research Laboratory
National Institute of Standards and Technology
Gaithersburg, MD 20899

ABSTRACT

Optical methods are used to examine soot production in a co-flowing, axisymmetric CH_4/air diffusion flame in which the fuel flow rate is acoustically forced to create a time-varying flowfield. For a particular forcing condition in which tip clipping occurs (0.75 V loudspeaker excitation), elastic scattering of vertically polarized light from the soot particles increases by nearly an order of magnitude with respect to that observed for a steady flame with the same mean fuel flow rate. Peak soot volume fractions, as measured by time-resolved laser extinction/tomography at 632.8 and 454.5 nm and calibrated laser-induced incandescence (LII), show a factor of 4–5 enhancement in this flickering flame. A Mie analysis suggests that most of the enhanced soot production results from the formation of larger particles in the time-varying flowfield.

Keywords: soot formation, laser diagnostics, laminar diffusion flames

INTRODUCTION

A critical assumption in applying chemical models developed in laminar flames to turbulent combustion is that the limited combinations of residence times, temperature histories, local stoichiometries, and strain rates sampled in laboratory-scale steady laminar flames are sufficient to quantitatively describe chemical processes in turbulent environments. In order to critically evaluate the validity of this assumption, an experimental facility for performing optical measurements in time-varying, laminar diffusion flames has been developed at NIST [1].

Under a wide variety of conditions, axisymmetric diffusion flames and pool fires exhibit a natural flickering behavior, with a frequency dependence on the fuel tube or pool diameter expressed as $f \sim 1.5/(D)^{1/2}$ (for f in Hz and D in meters) [2,3]. Previous researchers have found that this flickering tendency may be locked near the natural flicker frequency by applying a small periodic perturbation to the fuel flow [4–7]. In the present investigation optical diagnostics are phase-locked to a sinusoidal variation of the fuel flow velocity at the 10 Hz repetition rate of a Nd^{3+}:YAG laser, allowing phase-specific measurements.

In a preliminary study of OH· laser-induced fluorescence and elastic scattering from soot in steady and time-varying CH_4/air diffusion flames, it was found that the scattering intensity in the time-varying flame was significantly greater than that observed for the steady (i.e., unforced) flame with the same mean fuel and air flow rates [1]. In order to better quantify the observed soot enhancement for a forcing condition in which flame tip clipping occurs, we have applied laser light extinction and laser-induced incandescence (LII) to determine the soot volume fraction fields in these CH_4/air flames. In addition, laser energy-corrected imaging of soot scattering in the steady and flickering flames has been performed using vertically polarized incident light, supplementing previous measurements using horizontal polarization [1]. The OH· fluorescence and soot scattering fields for the flickering flame studied here and its steady counterpart are shown in Fig. 1, to aid in the interpretation of the experimental results to follow.

EXPERIMENTAL METHODS

Figure 2 shows a schematic diagram of the burner and phase-locked imaging setup, which has been described in detail previously [1]. A coannular axisymmetric burner with a 1.1 cm diameter fuel tube surrounded by a 10.2 cm air annulus supports an unconfined laminar flame. The mean methane cold flow velocity and air coflow are 7.9 cm/s for both the steady and forced flames; the steady flame has a visible height of 79 mm. A loudspeaker attached to the fuel plenum locks the frequency of the flickering flame to the 10.13 Hz repetition rate of the Nd^{3+}:YAG pumped dye laser system. The flickering flame data presented here were taken with 0.75 V peak-to-peak sine wave forcing, which is an intermediate excitation amplitude of those studied earlier [1].

Laser Extinction

Laser light extinction has traditionally been used to measure soot volume fraction. However, both absorption from large molecules, such as polycyclic aromatic hydrocarbons (PAH), and soot scattering interfere with the signal from soot absorption. For the CH_4/air flames studied here, soot scattering should represent a minor portion of the extinction, since the primary soot particles are small [8] and the extent of soot agglomeration in our relatively short residence time flames is expected to be limited. On the other hand, the contribution of molecular absorption to the measured extinction is of concern, particularly at low soot loadings. Consequently, extinction measurements were performed using the longest wavelength cw laser readily available in our laboratory (632.8 nm - HeNe). In most cases extinction was also measured using a shorter wavelength laser source (454.5 nm - Ar^+), where molecular absorption is expected to be much stronger [9].

In order to perform accurate extinction measurements in these lightly sooting flames, a laser power stabilizer was used to reduce the noise in the input laser beams to ~ 0.1%, allowing measurement of extinction levels as small as 0.01% after averaging. The line-of-sight nature of extinction necessitates data collection along multiple chords and subsequent tomographic inversion to yield locally resolved values of extinction. To obtain acceptable signal-to-noise, 200 consecutive time records of the amplified photodiode output were averaged using a digital oscilloscope. Extinction records were obtained for radial chords spaced by 0.25 mm across the width of the flames and were tomographically inverted with a 3-point Abel routine as implemented by Dasch [10]. For the time records in the flickering flame a Pascal-encoded version of Dasch's routine [11] was employed to yield phase-specific extinction profiles.

Laser-Induced Incandescence

Laser-induced incandescence (LII) has recently been developed as an alternative method for both relative [12,13] and quantitative [14] measurement of soot volume fraction. We employed LII as a second means of quantifying the soot volume fraction in both the steady and flickering CH_4/air flames, in order to identify possible contributions from molecular absorption to the measured extinction and to avoid noise difficulties in the extinction signal which arose from flame wobble at heights above 60 mm in the flickering flame. For the LII measurement the fundamental dye laser beam at 560 nm was focused with a 300 mm focal length lens at the center of the flame. In order to minimize signal variations with shot-to-shot laser energy fluctuations, the LII data were obtained at sufficiently high energies ($\sim 7 \times 10^8$ W/cm^2) to lie well within the plateau region where the LII signal varies little with laser energy [13,14]. Single-shot, 1-D line images were recorded on the ICCD camera, with a glass filter providing a detection bandwidth of 300–480 nm. To improve the signal-to-noise, 10 consecutive frames were collected at each height and averaged after verifying that the peak signal levels were consistent from frame to frame. Higher in the flickering flame the consecutive images often displayed side-to-side flame wobble. In these instances the LII frames were aligned radially and aberrant profiles were discarded (typically 2–3 out of 10, from H = 60 mm to H = 110 mm) before averaging. Flame luminosity signals were ~ 10 times weaker than the LII signals and were accounted for by taking a duplicate set of line images without laser light and subtracting these from the LII images. Further experimental details of the extinction and LII measurements are given in Ref. 15.

Soot Scattering

Scattering measurements were made with the same basic experimental setup and data collection procedure used for the earlier OH· and soot imaging, in which dye laser light at 567 nm was frequency doubled to 283.50 nm [1]. To image scattering from vertically polarized light, a variable retardation plate (Babinet-Soleil compensator) rotated the incident beam to a vertical polarization relative to the detection axis. Shot-to-shot spatial profiles of the laser energy were recorded via on-camera imaging of a reflection from the incident laser sheet (see Fig. 2).

RESULTS

The soot volume fraction was calculated from the tomographically inverted extinction measurements using the Lambert-Beer transmissivity law and the Mie extinction formula in the Rayleigh limit [16–18]. An index of refraction $\tilde{m} = 1.57\text{-}0.56i$ was used for both HeNe and Ar^+ wavelengths in order to make direct comparisons with the results of Santoro and coworkers [18,19]. Figure 3 shows the symmetrized (averaged about the centerline), steady flame HeNe results; the maximum soot volume fraction is $3.2 (\pm 0.3) \times 10^{-7}$ at H = 60 mm above the fuel tube exit. Above H = 30 mm in the steady flame, peak soot volume fractions determined from the Ar^+ measurements are greater than the HeNe results by ~ 5–10%, which is within the 15% uncertainty estimated for the extinction measurements. Lower in the flame and along the inner edge of the soot profile, Ar^+ extinction yields a significantly larger soot volume fraction than HeNe extinction, consistent with the expectation of greater absorption by PAH in these regions [18,20,21]. Figure 3 also includes the comparison of symmetrized LII signals with the extinction-determined soot volume fractions in the steady methane flame. The peak HeNe soot volume fraction at H = 50 mm was used to calibrate the LII signal, since at this height and radial location one expects the smallest relative contribution of molecular absorption to the observed extinction [20]. The similarity in location and magnitude of the peak values of the extinction and LII results at different heights indicates that the LII signal closely follows the soot volume fraction. Differences in the two signals towards the center of the profiles may be due to significant molecular absorption at 632.8 nm at these locations, as well as the increased error in the tomographic inversion procedure towards the flame centerline [10].

In Fig. 4 the tomographically inverted, time-resolved HeNe extinction data for the flickering flame are shown at H = 40 mm. The soot volume fraction fields higher in the flame are qualitatively similar, with a decreasing time duration of measurable extinction and greater "rippling" noise in the reconstructed annular soot layer. This noise arises from side-to-side flame wobble during the data collection process. The largest instantaneous soot volume fraction (f_v) is $1.3 (\pm 0.3) \times 10^{-6}$, observed at H = 120 mm; this value is four times greater than the maximum f_v in the corresponding steady flame. Ar^+ extinction measurements were completed only to H = 100 mm in the flickering flame and yield somewhat greater (~ 30%) soot volume fractions than the HeNe extinction. Fig. 5 presents the area-integrated and time-averaged (for the flickering flame) soot volume fraction measurements as a function of height. The area under the HeNe flickering flame curve, a volumetric measure of the soot in the flame, is four times greater than its steady counterpart. This figure also shows the consistently larger Ar^+ signals in the flickering flame (up to H = 100 mm) and the convergence of the Ar^+ measurement

with the HeNe result higher in the steady flame. As in the steady flame, the increased Ar^+ signals are attributed to enhanced PAH absorption.

LII signals were measured in the flickering flame up to H = 110 mm for the ten phase angles shown in Fig. 1. The maximum signal gives a soot volume fraction of 1.5 ($\pm$ 0.2) x 10^{-6} at H = 110 mm (80% phase), which is 5 times larger than that observed in the steady flame. Figure 6 shows the symmetrized LII signals compared with the extinction-derived soot volume fraction for 50% phase. Above H = 60 mm in the flickering flame the extinction-derived profiles are generally wider and shorter than their LII counterparts, consistent with the observed flame wobble and the time-averaged nature of the extinction measurement at each radial chord.

For vertically polarized incident light the maximum local soot scattering intensity in the flickering flame is ~ 8 times greater than that measured in the corresponding steady flame and occurs in the annular soot region of the clipped-off flame for phases of 80 and 90%. At the same locations the enhancement in peak scattering of horizontally polarized light is approximately a factor of 20. Flame tip burnout is complete at about 17 cm in the flickering flame, so it is certainly possible that even greater soot scattering intensities would be found at heights above the current limit for imaging of 13.4 cm.

Uncertainties quoted are one standard deviation, derived from signal variations in repeat measurements of scattering and LII; random errors in the extinction measurements are estimated from noise in the profiles. Calibration of LII in the steady flame may lead to small systematic errors for the time-varying flame results, due to changes in soot particle morphology. Long time-scale movements of the flames remain as a possible source of unquantified error.

DISCUSSION

The dramatic enhancement in soot formation observed when a steady CH_4/air flame is induced to flicker may provide a demanding test of the ability of recently formulated integrated soot models [e.g., 22–25] to accurately predict soot formation and oxidation rates in complex combusting flowfields. Changes in residence times, temperatures, and/or local stoichiometries are most likely responsible for the increased soot production, but differences in these variables have not been determined in these flames. Rayleigh and Mie analyses have been conducted on our scattering and soot volume fraction data in order to estimate the mean soot particle sizes and number densities as a useful first step in elucidating why soot production is enhanced in the flickering flames.

The vertically polarized scattering measurements were indirectly calibrated [15] by comparison with the data of Richardson and Santoro in the same nominal flame [19]. Rayleigh and Mie theory calculations were then performed on the calibrated LII and scattering signals using a FORTRAN code with the Mie-solution subroutine (BHMIE) given by Bohren and Huffman [26]. Number densities were calculated assuming a monodisperse size distribution at each measuring location. An index of refraction of 1.57-0.56i was used both to calibrate the LII signals to the HeNe extinction results in the steady flame and for the Mie analysis of the scattering at 283.5 nm. Calculations with other values for the index of refraction show similar trends.

Table I presents only a small subset of the calculated results: the soot volume fraction, particle diameter, and number densities are given at the point of maximum soot scattering for each measurement height in the steady flame and in the flickering flame at 50% phase. In lieu of velocity measurements, the contour of maximum scattering is used as a rough guide to the time history of soot particles in the steady flame. The Mie diameters in the steady CH_4/air flame increase up to H = 50 mm, and the calculated number densities decrease slightly as soot particle mass growth occurs, possibly reflecting the effect of soot particle agglomeration. The larger number densities at H = 60 mm and H = 70 mm in the steady flame may result from soot particle inception towards the centerline of the flame, or may also arise from the failure of the monodisperse Mie analysis to account for the high degree of polydispersion in the particle field anticipated at these locations (due to primary particle or agglomerate breakup during oxidation). At 50% phase in the flickering flame the derived soot particle diameter increases monotonically with height, while the number densities remain roughly constant until oxidation occurs at the top of the flame. In examining these results, however, recall that any given phase is a snap-shot in the time-history of the flickering flame. The Mie results shown in Table I, when combined with similar trends for all but the greatest heights of the flickering flame, show that particle number densities remain near 2-3 x 10^9/cm^3 through both the steady and flickering flames, whereas the effective particle diameters increase from a maximum of ~60 nm in the steady flame to ~90 nm in the flickering flame (using $\widetilde{m}$ = 1.57-0.56i). The extent of particle size increase shown here should not be over interpreted, since the particle size parameters ($x = \pi D/\lambda$) in the flickering flame are large (~1) and the deviation between agglomerate and Rayleigh or Mie analysis increases with increasing size parameter [27,28].

We thank Chris Cromer for loaning us the laser power stabilizer and George Mulholland and Robert Santoro for insightful discussion of soot formation processes and diagnostic techniques, particularly with regard to the calibration of LII signals.

REFERENCES

1. Smyth, K.C., Harrington, J.E., Johnsson, E.L., and Pitts, W.M., *Combust. Flame* 95:229-239 (1993).
2. Hamins, A., Yang, J.C., and Kashiwagi, T., *Twenty-Fourth Symposium (International) on Combustion*, The Combustion Institute, Pittsburgh, 1992, pp. 1695-1702.
3. Cetegen, B.M., and Ahmed, T.A., *Combust. Flame* 93:157-184 (1993).
4. Strawa, A.W., and Cantwell, B.J., *Phys. Fluids* 28, 2317-2320 (1985).

5. Lewis, G.S., Cantwell, B.J., Vandsburger, U., and Bowman, C.T., *Twenty-Second Symposium (International) on Combustion*, The Combustion Institute, Pittsburgh, 1988, pp. 515-522.
6. Pearson, I.G., and Proctor, D., in *Experimental Heat Transfer, Fluid Mechanics, and Thermodynamics 1991* (J.F. Keffer, R.K. Shah, and E.N. Ganic, eds.), Elsevier Science, 1991, pp. 316-322.
7. Vandsburger, U., Seitzman, J.M., and Hanson, R.K., *Combust. Sci. and Tech.* 59:455-461 (1988).
8. Puri, R., Santoro, R.J., and Smyth, K.C., *Combust. Flame*, in press.
9. Miller, J.H., Mallard, W.G., and Smyth, K.C., *Combust. Flame* 47:205-214 (1982).
10. Dasch, C.J., *Applied Optics* 31:1146-1152 (1992).
11. We thank J. Houston Miller for providing us with the base Pascal algorithm required to tomographically invert extinction records in time or frequency.
12. Dec, J.E., zur Loye, A.O., and Siebers, D.L., *SAE Technical Papers Series* SAE-910224, Society of Automotive Engineers, PA, 1991.
13. Tait, N.P., and Greenhalgh, D.A., *Proceedings of the "Optical Methods and Data Processing in Heat Transfer and Fluid Flow" Conference*, London, April 1992.
14. Quay, B., Lee, T.-W., and Santoro, R.J., *Combust. Flame*, in press.
15. Shaddix, C.R., Harrington, J.E., and Smyth, K.C., submitted to *25th Symposium (International) on Combustion*.
16. Kerker, M., *The Scattering of Light*, Academic Press, New York, 1969, pp. 31-39.
17. D'Alessio, A., in *Particulate Carbon: Formation During Combustion* (D.C. Siegla and G.W. Smith, Eds.), Plenum, New York, 1981, pp. 207-259.
18. Santoro, R.J., Semerjian, H.G., and Dobbins, R.A., *Combust. Flame* 51:203-218 (1983).
19. Richardson, T.F., and Santoro, R.J., private communication, 1993.
20. Prado, G., Garo, A., Ko, A., and Sarofim, A., *Twentieth Symposium (International) on Combustion*, The Combustion Institute, Pittsburgh, 1984, pp. 989-996.
21. Smyth, K.C., Miller, J.H., Dorfman, R.C., Mallard, W.G., and Santoro, R.J., *Combust. Flame* 62:157-181 (1985).
22. Syed, K.J., Stewart, C.D., and Moss, J.B., *Twenty-Third Symposium (International) on Combust-ion*, The Combustion Institute, Pittsburgh, 1990, pp. 1533-1541.
23. Leung, K.M., Lindstedt, R.P., and Jones, W.P., *Combust. Flame* 87:289-305 (1991).
24. Honnery, D.R., and Kent, J.H., *Twenty-Fourth Symposium (International) on Combustion*, The Combustion Institute, Pittsburgh, 1992, pp. 1041-1047.
25. Villasenor, R., and Kennedy, I.M., *Twenty-Fourth Symposium (International) on Combustion*, The Combustion Institute, Pittsburgh, 1992, pp. 1023-1030.
26. Bohren, C.F., and Huffman, D.R., *Absorption and Scattering of Light by Small Particles*, John Wiley & Sons, New York, 1983, pp. 477-482.
27. Charalampopoulos, T.T., and Chang, H., *Combust. Flame* 87:89-99 (1991).
28. Mountain, R.D., and Mulholland, G.W., *Langmuir* 4:1321-1326 (1988).

Table I: Mie Analysis of Soot Field Along Contour of Maximum Qvv

Height Above Burner	Steady Flame			Flickering Flame (50% phase)		
(mm)	f_v (10^{-7})	D (nm)	N (10^9/cc)	f_v (10^{-7})	D (nm)	N (10^9/cc)
30	0.7 (0.2[a])	39 (5[b])	2.4 (1.3)	0.4 (0.1)	34 (4)	2.0 (1.4)
40	2.2 (0.4)	57 (6)	2.2 (1.1)	1.0 (0.2)	50 (6)	1.5 (0.9)
50	2.3 (0.3)	62 (6)	1.9 (0.8)	2.1 (0.2)	53 (5)	2.7 (1.0)
60	2.2 (0.4)	49 (5)	3.5 (1.8)	3.6 (0.3)	68 (5)	2.2 (0.7)
70	2.0 (0.5)	50 (7)	3.1 (2.2)	6.4 (0.5)	80 (6)	2.4 (0.7)
80				8.1 (0.5)	86 (6)	2.5 (0.7)
90				0.8 (0.2)	85 (11)	0.3 (0.2)

[a] One standard deviation uncertainty estimates.

[b] Diameter and number density uncertainties are the result of propagating volume fraction and scattering error estimates through Rayleigh analysis. These uncertainties agree well with the variation in Mie results over the range of uncertainty in f_v and Q_{vv}.

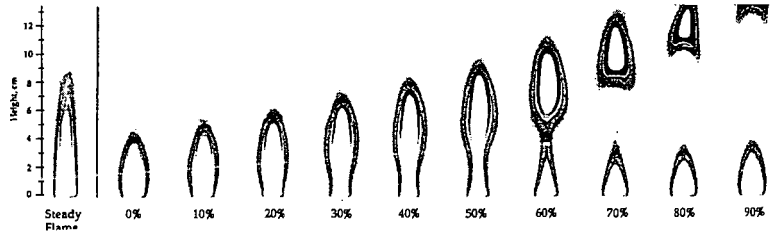

Figure 1. Laser energy-corrected OH• laser-induced fluorescence and soot scattering images in a steady and time-varying laminar CH_4/air diffusion flame using horizontally polarized light at 283.55 nm. The visible flame height of the steady flame is 79 mm above the fuel tube exit, which is located 1 mm above the bottom of the images. For the flickering flame, ten equally spaced phase increments are shown, corresponding to a time interval of 10 ms; zero phase is arbitrary. The OH• fluorescence signals have not been corrected for local quenching rates and hence serve as a convenient, qualitative marker of the high-temperature reaction zone. For the full-height images presented here, 5 single-shot images (3.2 cm high) have been overlapped to compensate for reduced signal-to-noise at the upper and lower edges of the incident laser sheet. Several of the stacked images shown have been shifted slightly from side-to-side to compensate for flame wobble at higher flame locations.

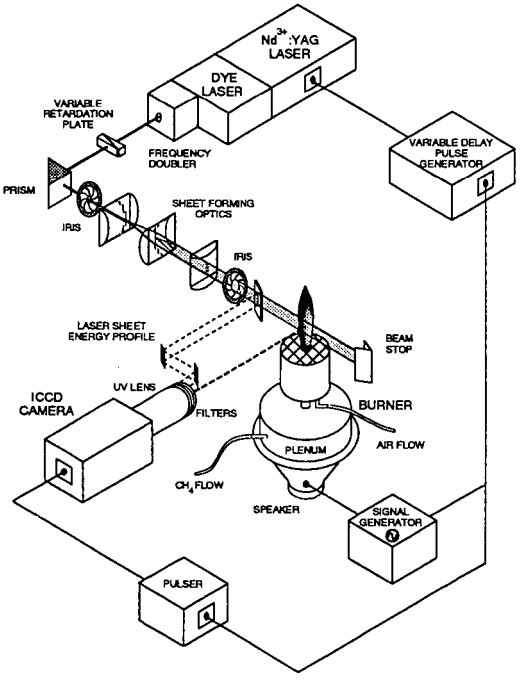

Figure 2. Experimental set-up for 1- or 2-D imaging of axisymmetric diffusion flames which are acoustically excited and phase-locked to the pulsed dye laser system operating at 10.13 Hz. For the laser-induced incandescence experiment, the frequency doubler and sheet-forming optics are removed, and a 300 mm focal length lens is used to focus the beam at the center of the flame. Images are recorded using an intensified charge-coupled device (ICCD) camera.

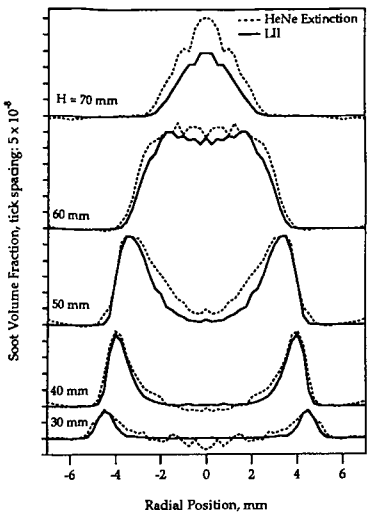

Figure 3. Soot volume fraction from symmetrized HeNe laser extinction (632.8 nm) and laser-induced incandescence (LII) signals at a series of heights in the steady CH_4 / air diffusion flame.

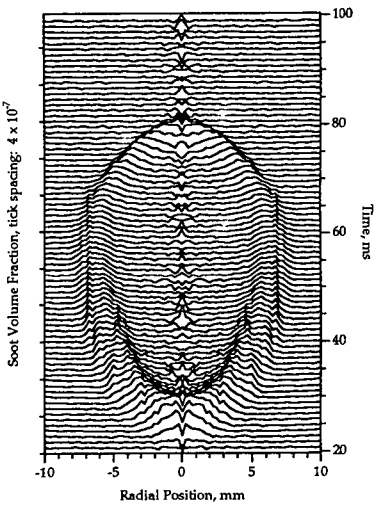

Figure 4. Time evolution of the soot volume fraction field at H = 40 mm in the flickering CH_4 / air diffusion flame (0.75 V loudspeaker excitation). Each line shown is separated by 1 ms in time and staggered by 6×10^{-8} in soot volume fraction. Time progresses from the bottom to the top of the figure, showing first the arrival of soot, the widening of the soot profile into an annular structure as time increases, the convergence of the soot profile to the centerline, and finally its disappearance as the bottom of the clipped-off portion of the flame passes above H = 40 mm.

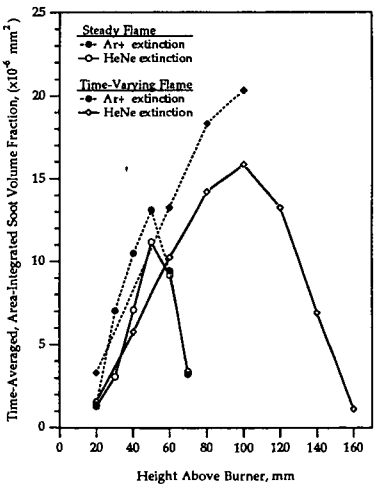

Figure 5. Area-integrated soot volume fraction from symmetrized HeNe (632.8 nm) and Ar^+ (454.5 nm) laser extinction measurements at a series of heights in CH_4 / air diffusion flames. The flickering flame measurements are expressed as time averages over a full cycle period. The area under the steady flame HeNe curve is 3.4×10^{-4} mm^3; that under the flickering flame is 1.3×10^{-3} mm^3.

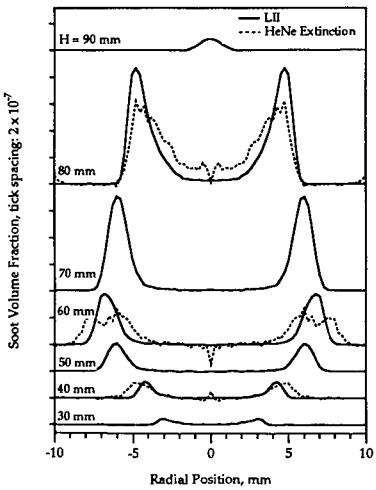

Figure 6. Laser-induced incandescence (LII) signals, interpeted as soot volume fraction, at a series of heights in the flickering CH_4 / air diffusion flame at 50% phase. Time-resolved, tomographically inverted HeNe extinction data are also shown at heights of 40, 60, and 80 mm above the burner.

REACTIONS OF ^{1}:CX_2 DURING CHLOROFLUOROCARBON PYROLYSIS

John J. DiFelice and Edward R. Ritter
Department of Chemical Engineering
Villanova University
Villanova, PA 19085

Keywords: fluorocarbon pyrolysis, difluoromethylene, chlorodifluoromethane

INTRODUCTION

Singlet carbenes are reactive intermediates which behave in a fashion quite different from radicals. In hydrocarbon and hydrochlorocarbon systems, radicals and radical chemistry typically dominate. However, in chlorofluorocarbon (CFC) and hydrochlorofluorocarbon (HCFC) systems, formation of perhalogenated singlet carbenes (^{1}:CX_2) has been observed (DiFelice and Ritter, 1993; Westmoreland, 1993). While radicals undergo abstraction reactions and addition to double bonds, singlet carbenes can insert into single bonds. Singlet carbenes are species which have two paired nonbonded electrons; since paired electrons have opposite spin, singlet carbenes can insert into single bonds (March, 1992). Triplet carbenes , in contrast, contain unpaired electrons and behave essentially like radicals. Formation of perhalogenated triplet carbenes (^{3}:CX_2) is less favorable in CFC and HCFC systems since the :CX_2 singlet state is as much as 56 kcal/mol lower in energy than the triplet state (Melius, 1993).

The insertion of ^{1}:CX_2 into single bonds makes CFC and HCFC pyrolytic chemistry unique and interesting. However, There have been few studies on the combustion and pyrolysis chemistry of these compounds. Most experimental studies of CFCs and HCFCs are at conditions relevant to stratospheric ozone depletion (NIST, 1991a). These conditions are typically at much lower pressure and temperature than those encountered during incineration or pyrolysis. Recent combustion studies by Naegli, et.al. (1991) and Tokuhashi, et.al. (1990) demonstrate the need for further research on the incinerability and pyrolysis chemistry of these species. These studies focused on CF_2Cl_2 (Freon-12) and CHF_2Cl (Freon-22). They demonstrated that these species can be broken down in an incineration environment, and that significant quantities of by-products (PICs) are formed. These by-products have been neither completely classified, nor quantified.

Previous work (Ritter, 1993 and DiFelice and Ritter, 1993) has focused on the thermal reactions of CF_2Cl-$CFCl_2$ (Freon-113) and CHF_2Cl under pyrolytic conditions in helium and helium/hydrogen mixtures. These studies have characterized the pyrolysis under inert and reducing conditions. Studies have shown that formation and reaction of perhalogenated singlet carbenes (^{1}:CX_2) are important during CHF_2Cl pyrolysis, while they are of questionable importance during CF_2Cl-$CFCl_2$ pyrolysis. The significance of various carbene insertion reactions are important for the mechanistic modeling of CHF_2Cl pyrolysis. Determination of their significance would also give insight into the CF_2Cl-$CFCl_2$ pyrolytic system. The carbene insertion reactions investigated include insertion into carbon-hydrogen (C-H) bonds and carbon-halogen (C-X) bonds. Other CFCs studied during the investigation include CF_2Cl_2 (Freon-12), CF_3Cl (Freon-13), and C_2HF_4Cl (Freon-124).

EXPERIMENTAL

The experimental flow tube reactor consists of a quartz or alumina flow tube which passes through a 6 zone electrically heated tube furnace (see Figure 1). Typical reaction times range from 0.05 to 2 seconds with temperatures from 773 - 1098 K. In atmospheric pressure flow tube reactors, there is always the concern for significant wall reactions. Ritter et.al. (1990) observed significant differences between experimentally determined rate constants for chlorobenzene decomposition when carried out in 0.4 and 1.0 cm id reactor tubes. However, they observed little difference between decomposition rates in 1.0 and 1.6 cm id reactors. In these studies 1.6 and 2 cm i.d. reactors are used to reduce the importance of possible surface reactions. Quartz flow tubes can be used for lower temperatures (less than 775°C), however, alumina is required at higher temperatures due to the rapid degradation of quartz by fluorides. The reactor operates isobarically near 1 atm total pressure. Liquid reagents such as CF_2Cl-$CFCl_2$ or $CHCl_3$ (chloroform) are admitted to the reactor by sparging helium gas through the liquid held at 0°C in an ice point impinger. Gaseous CFCs enter directly through calibrated rotameters. Calibration of the reactor temperature is performed using a 1/8" diameter Type-K thermocouple probe. This probe is moved axially to obtain the temperature of the reactor.

Helium is allowed to flow through the reactor to minimize radiation error from the furnace wall by cooling the bare-bead junction to the temperature of the gas.

Samples are drawn through a cold surface water cooled sampling probe by use of a vacuum pump. Gas leaving the probe passes through a heated line to a six port gas sampling valve equipped with a 1 mL sample volume for on-line analysis using GC/FID. Reactant and stable products are quantified using a GOW MAC model 750 P GC with dual flame ionization detectors. Gas chromatographic separations are carried out using a packed column Graphpac 60/80 mesh with 5% Flurocol (Supelco) or Carbopac with 5% Krytox (Alltech) which give excellent separation for complex mixtures of hydrocarbons, fluorocarbons, and CFCs. Accurate calibration of FID responses for parent CFCs are obtained by using a reactor bypass. GC/MS analyses are performed off-line for product identification. After initial identification, product responses are calibrated using standards prepared from the pure materials which are obtained from PCR Chemicals Inc, Gainesville, Fl. Standards are prepared to determine GC response factors.

HCl and HF produced are quantified by diverting the total reactor effluent through a 2 stage impinger containing standardized NaOH solution and an appropriate indicator dye. Cl^- and F^- concentrations are measured directly using ion selective electrodes (Fisher Scientific). The electrodes are calibrated using standardized Cl^- and F^- solutions prepared at pH similar to the samples. All standards and samples contain the total ionic strength adjuster appropriate to the halide which is being measured. These measurements give total F^- and Cl^- only and do not speciate between halogen and hydrogen halide gases. They are used to check material balance on halogens.

RESULTS AND DISCUSSION

Results from CHF_2Cl pyrolysis in helium at 2 seconds reaction time suggest that CHF_2Cl conversion primarily follows first order kinetics at low temperatures (773 - 898K) via unimolecular HCl elimination:

$$CHF_2Cl \longrightarrow {}^1{:}CF_2 + HCl$$

The major products of the pyrolysis in helium include perfluoroethylene (C_2F_4, the most abundant product), perfluoropropene (C_3F_6), octafluorocyclobutane (C_4F_8), and chlorotrifluoroethylene (C_2F_3Cl). Perfluoroethylene is formed by ${}^1{:}CF_2$ combination, C_4F_8 by dimerization of C_2F_4, and C_2F_3Cl by recombination of ${}^1{:}CF_2$ and ${}^1{:}CFCl$.

$$2\ {}^1{:}CF_2 \longrightarrow C_2F_4$$
$$2\ C_2F_4 \longrightarrow C_4F_8$$
$${}^1{:}CF_2 + {}^1{:}CFCl \longrightarrow C_2F_3Cl$$

The product C_2F_3Cl is observed at temperatures only above 898K, suggesting either some degree of HF elimination from CHF_2Cl occurs at higher temperatures

$$CHF_2Cl \longrightarrow {}^1{:}CFCl + HF$$

or that ${}^1{:}CF_2$ inserts into CHF_2Cl followed by α,β HF elimination from the adduct:

$$CHF_2Cl + {}^1{:}CF_2 \longrightarrow \{CHF_2\text{-}CF_2Cl\}^* \longrightarrow C_2F_3Cl + HF$$

Perfluoropropene (C_3F_6) most likely results from reaction of ${}^1{:}CF_2$ and C_2F_4.. Although carbenes are believed to add to double bonds to form cyclopropanes (March, 1992), perfluorocyclopropane (cyC_3F_6) is not observed. This suggests that rapid isomerization to the perfluoropropene occurs, or some other mechanism is responsible for the production of this species.

The elimination of HCl from CHF_2Cl represents the lowest dissociation channel. However, at higher temperatures (above 898K) it becomes apparent that conversion of CHF_2Cl moves away from first order kinetics. When a first order assumption is applied over the entire temperature range (773 - 1023K), an Arrhenius plot yields an activation energy of 43 kcal/mol. This energy barrier, however, is lower than the Δ H of the reaction based upon the H_f of ${}^1{:}CF_2$ used by Paulino and Squire (1991). This suggests that there is a shift in reaction mechanism at higher temperatures.

The addition of H_2 to the CHF_2Cl pyrolytic system was found to inhibit CHF_2Cl at 2 seconds reaction time and over the same temperature range (see Figure 2). This observation was surprising since the addition of H_2 greatly increased conversion in other CFC and chlorocarbon systems which have been studied (Ritter, 1993; Won and Bozzelli; Ritter et. al. (1990); Bozzelli and Ho, 1992). Difluoromethane (CH_2F_2) was identified as a major product during pyrolysis in H_2. Difluoromethane is the only energetically favorable product from ^{1}:CF_2 insertion into H_2. Figure 2 shows the formation of CH_2F_2 at 2 seconds reaction time as a function of temperature in the H_2 system. The temperature 873K represents a point of dramatic increase in the production of CH_2F_2 as well as the point of departure of the H_2 and helium systems. This suggests that the decreased conversion in the H_2 system is due to the much faster reaction of ^{1}:CF_2 with H_2.

$$^1\text{:}CF_2 + H_2 \longrightarrow CH_2F_2$$

It then follows that ^{1}:CF_2 insertion into the C-H bond of CHF_2Cl becomes an important decomposition route under inert conditions at temperatures greater than 898K. The removal of this reaction pathway inhibits CHF_2Cl conversion when H_2 is present.

At high temperatures, the two reactions which are reponsible for CHF_2Cl loss are

$$\begin{aligned} CHF_2Cl &\longrightarrow {}^1\text{:}CF_2 + HCl \\ CHF_2Cl + {}^1\text{:}CF_2 &\longrightarrow \{CHF_2\text{-}CF_2Cl\}^* \longrightarrow C_2F_4 + HCl \\ &\qquad\qquad\qquad\qquad\quad \longrightarrow C_2F_3Cl + HF \end{aligned}$$

As shown in Figure 3, ^{1}:CF_2 insertion into CHF_2Cl may produce C_2F_4 via rapid α,β HCl elimination (low energy product channel). Since C_2F_4 is believed to be formed primarily by ^{1}:CF_2 combination, and insertion will likely result in the same product, no direct evidence of insertion could be observed. Therefore experiments were performed to investigate the role of ^{1}:CX_2 insertion.

Insertion into C-H

Pyrolysis of C_2HF_4Cl

A stable homologue of CHF_2Cl, C_2HF_4Cl (chloro-1,2,2,2-tetrafluoroethane), was chosen to investigate ^{1}:CF_2 insertion because it would result in a product which is distinguishable from carbene recombination. Insertion of ^{1}:CF_2 into the C-H bond of C_2HF_4Cl and subsequent α,β HCl elimination would produce C_3F_6, which is distinguishable from the ^{1}:CF_2 combination product C_2F_4. When pyrolyzed without a ^{1}:CF_2 source in helium at 973K and 2 seconds reaction time, only 13% conversion of C_2HF_4Cl was observed, with no significant C_3F_6 production. However, when pyrolyzed in the presence of CHF_2Cl at a ratio of 2:1, greater than 30% conversion of C_2HF_4Cl was observed. In addition, a 250% increase in the C_3F_6 production was observed over that produced during CHF_2Cl pyrolysis alone. These results are consistent with ^{1}:CF_2 insertion into the C-H bond followed by rapid α,β HCl elimination from the adduct to give C_3F_6.

Insertion into C-X

Pyrolysis of $CF_2Cl\text{-}CFCl_2$ in Helium

Thermodynamically, elimination of ^{1}:CCl_2 from a C-F bond in $CF_2Cl\text{-}CFCl_2$ is a low energy decomposition path (Ritter, 1993), however the energy barrier is not known. Dichlorocarbene (^{1}:CCl2) insertion into CF_3Cl was investigated by pyrolyzing chloroform ($CHCl_3$) in the presence of CF_3Cl at 2 seconds reaction time and 923-973K in helium. Chloroform was used as a ^{1}:CCl_2 source. Insertion of ^{1}:CCl_2 into C-F or C-Cl bonds in CF_3Cl would determine if the reverse reaction (carbene elimination) occurs based on microreversibility. Products of the insertion would be $CF_2Cl\text{-}CFCl_2$ and $CF_3\text{-}CCl_3$ (Freon-113a). Neither species, however, was produced during the pyrolysis. This result suggests that carbene insertion into C-X bonds has a substantial energy barrier.

Pyrolysis of CF_2Cl_2 in Helium

CHF_2Cl was pyrolyzed with CF_2Cl_2 to gain further insight into carbene insertion into C-X bonds. CF_2Cl_2 is much more stable than CHF_2Cl at temperatures above 898K - it dissociates primarily by the loss of chlorine atom (a higher energy route). The experiments were performed in helium at 2 seconds reaction time and at two different temperatures. When pyrolyzed without a ^{1}:CF_2 source at 923K and 973K, conversion of CF_2Cl_2 was not observed. Addition of CHF_2Cl to the system (as a ^{1}:CF_2 source) did not result in increased conversion at

923K. Results obtained at 973K, however, show a noticeable increase in CF_2Cl_2 conversion. This result suggests that ^{1}:CF_2 plays a role in CF_2Cl_2 conversion, under these conditions. This system is currently being investigated in more detail.

CONCLUSION

Insertion of ^{1}:CF_2 into C-H bonds appears to be important during the pyrolysis of CHF_2Cl and mixtures of CHF_2Cl and C_2HF_4Cl at temperatures greater than 898K. Addition of H_2 to the CHF_2Cl pyrolytic system inhibits conversion by scavenging ^{1}:CF_2 by reaction with H_2. Dichlorocarbene isertion into C-X appears to be an unfavorable reaction based upon experiments involving $CHCl_3$ and CF_3Cl. Similar reactions involving CF_2Cl_2 are curently being.

REFERENCES

Buravtsev, N.N, Grigor'ev, A.S., and Kolbanovskii, Y.A. (1989) Kinet. Catal.,

DiFelice, J.J. and Ritter, E.R. (1993), presented at the Fall Technical Meeting of the Combustion Institute (Eastern States Section), Princeton, NJ, Oct. 1993.

Ho, W., Yu, Q., and Bozzelli, J (1992), Comb. Sci. and Tech, 85, 22.

March, Jerry (1992), Advanced Organic Chemistry, 2nd ed., John Wiley & Sons, NY.

Melius, Carl F.(1993), BAC-MP4 Heats of Formation and Free Energies.

Naglei, D.W., Robledo, R.C., and Erwin, J.(1991), Western States Combustion Institute Meeting, Los Angeles, CA, Paper No. 91-60.

NIST (1991) Chemical Kinetics Database Version 3.0, NIST Standard Reference Database 17, 1991.

Paulino, J.A. and Squires (1991), R.R., J. Am. Chem. Soc., 113, 5573-5580.

Ritter, E.R., Bozzelli, J.W., and Dean (1990), A.M, J. Phys. Chem., 94, 2493.

Ritter, E.R. (1993), Submitted to Combustion Science and Technology, (accepted, in press, 1994).

Tokuashi, K., Urano, Y., Horiguchi, S. and Kondo, S.,(1990) Combustion Science and Technology, 72, 117-129.

Won, Y. S. and Bozzelli, J. W. (1992), Combust. Sci. and Tech., 85, 345.

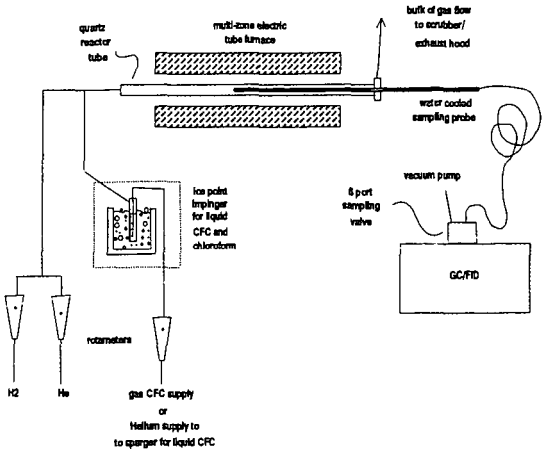

Figure 1. EXPERIMENTAL APPARATUS

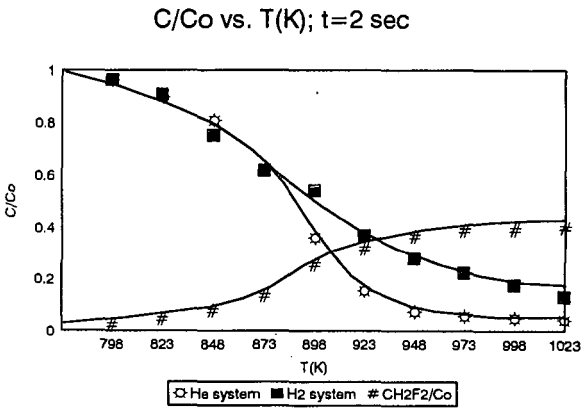

Figure 2. CHF_2Cl PYROLYSIS IN HE AND H_2

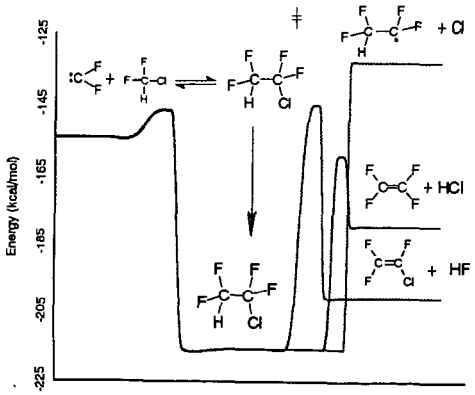

Figure 3. ^{1}:CF_2 INSERTION INTO CHF_2Cl

LAMINAR FLAMELETS, CONSERVED SCALARS, AND NON-UNITY LEWIS NUMBERS: WHAT DOES THIS HAVE TO DO WITH CHEMISTRY?

J. Houston Miller and Michael A.T. Marro
Department of Chemistry
The George Washington University
Washington, DC 20052

and

Mitchell Smooke
Department of Mechanical Engineering
Yale University
New Haven, CN

Keywords: conserved scalar, flamelet, combustion model

Abstract

In general, computation of laminar flame structure involves the simultaneous solution of the conservation equations for mass, energy, momentum, and chemical species. It has been proposed and confirmed in numerous experiments that flame species concentrations can be considered as functions of a conserved scalar (a quantity such as elemental mass fraction, that has no chemical source term). One such conserved scalar is the mixture fraction which is normalized to be zero in the air stream and one in the fuel stream. This allows the species conservation equations to be rewritten as a function of the mixture fraction (itself a conserved scalar) which significantly simplifies the calculation of flame structure. Despite the widespread acceptance that the conserved scalar description of diffusion flame structure has found in the combustion community, there has been surprisingly little effort expended in the development of a detailed evaluation of how well it actually works. In this presentation we compare the results of a "full" transport and chemical calculation performed by Smooke with the predictions of the conserved scalar approach. Our results show that the conserved scalar approach works because some species' concentrations are *not* dependent only on mixture fraction.

Introduction

The use of the laminar flamelet concept endures as an important tool in the analysis of turbulent combustion systems. In this technique, the occurrence of flamelet structures is determined probablistically and then combined with structural information derived from either laminar flame calculations or experiments[1,2,3,4]. A central criticism of the use of these laminar flamelet libraries to model turbulent systems centers on the interaction of small scale turbulent structures with flamelet structures.

In general, computation of laminar flame structure involves the simultaneous solution of the conservation equations for mass, energy, momentum and species. The latter may be solved in the Shvab-Zeldovich form[5] as (Equation 1):

$$L(Yi) \equiv \rho \frac{\partial Y_i}{\partial} + \rho V \cdot \nabla Y_i - \nabla \cdot (\rho D_i \nabla Y_i) = w_i$$

where Y_i is the mass fraction of species i, w_i is the chemical production rate of species i, ρ is the total gas density, V is the convective velocity, and D_i is the molecular diffusivity.

Chemical elements (such as i = C, H, or O) are conserved throughout the chemical reaction mechanism ($L(Z_i) = 0$). Linear combinations of elemental abundances, such as the mixture fraction, ξ, will also be conserved. Here we adopt Bilger's[6] formulation of mixture fraction in terms of conserved scalars representing relative elemental concentrations for the fuel and oxidant streams in terms of atomic masses for C, H, and O and their mass fractions.

It has been previously shown[6] that flame species concentrations are only functions of ξ. This observation, combined with the assumption of equal diffusivities of all flame species, allows the species conservation equation (Eq. 1) to be rewritten as a function of the mixture fraction. The net chemical production rate for a species then can be written as (Equation 2):

$$w_i = -\left(\frac{1}{2}\right) \cdot \rho \chi \cdot \left(\frac{\partial^2 Y_i}{\partial \xi^2}\right)$$

with the instantaneous scalar dissipation rate, χ, defined as (Equation 3):

$$\chi = 2D \cdot (\nabla \xi^2)$$

It has been postulated that concentrations will depend exclusively on mixture fraction when chemical times are short with respect to transport times (i.e., large Domkohler number). It has been shown that this condition is not met for species whose chemistry of formation is slow[7,8]. It has also been suggested that a second independent variable may be required to determine concentrations even for species whose chemistry is fast, and the scalar dissipation rate has been suggested as that variable[9,10,11]. When a species' concentration is determined mostly by its mixture fraction dependence, molecular diffusion will occur preferentially along paths of the steepest mixture fraction gradients in space (Figure 1). We refer to these paths as diffusive trajectories in this paper.

Despite the widespread acceptance that the conserved scalar description of diffusion flame structure has found in the combustion community for the description of turbulent flame structure, there has been surprisingly little effort expended in the development of a detailed evaluation of how well it actually works[12,13]. In this paper we analyze the validity of the conserved scalar approach to the analysis of laminar flame structures. Using the results of a flame structure calculation which has recently been reported[12], we evaluate the magnitude of the net chemical production rate, w_i, using Eq. 2 above and compare it to rates calculated from contributions of specific reactions in the flame code. The agreement between these two methods provides a test of the conserved scalar approach.

Flame Structure Calculations

The chemical structure of an unconfined, co-flowing, axisymmetric CH_4/air diffusion flame was computed with detailed transport and finite rate chemistry. C1 and C2 chemistry were included in a reaction mechanism which involved 83 reversible reactions and 26 species. Details of the calculation have been presented previously, and are summarized briefly below. The fuel was introduced into the flame through an inner tube of radius 0.2 cm and the coflow air through a concentric 5.0 cm diameter outer tube. The results of this flame calculation have been compared with an extensive data base of species concentrations and temperatures collected in a Wolfhard-Parker laminar diffusion flame. Concentration profiles of most flame species agree well for the calculations and the experiments. From calculated species concentrations, temperatures and their positions, ξ and χ can be calculated[12].

Figure 1 shows contours of mixture fraction in the calculated flame. Also shown are a number of diffusive trajectories through the flame. As stated earlier, these trajectories originate in the fuel rich regions of the flame and follow mixture fraction from rich to lean flame regions along pathways of the steepest gradient of ξ. As the data in this figure illustrate the mixture fraction gradients along these different vary dramatically, with those which cross the stoichiometric contour near the base of the flame having significantly steeper gradients than those that cross higher in the flame (for example the centerline trajectory).

Figure 2 illustrates the range of mixture fractions and scalar dissipation rates which are observed throughout the computed flame. This data show that at the stoichiometric surface (ξ=0.055) the value of the scalar dissipation rate (χ_{ST}) varies dramatically, from nearly 0 up to 5 s^{-1}. Extinction occurs in methane/air flames[7] at χ_{ST}= 12 s^{-1}. Since the data shown in this figure include only locations as low as 0.64 mm above the burner surface, it is reasonable to expect that extinction occurs at lower flame heights.

Figure 3 shows concentrations of methane plotted as a function of mixture fraction for computational nodes throughout the flame. Except for positions very low in the flame, methane concentrations collapse onto a single curve when plotted in this way. Figure 4 shows a similar data presentation for hydrogen atom concentrations. In contrast to the data for methane, the peak shape as well as the peak location shows a dependence on flame location with data low in the flame having larger peak concentrations that occur at lower (leaner) mixture fractions.

Conserved Scalar Rates

Mass fractions of methane, Y_{CH4}, were calculated and plotted against mixture fraction along each of the chosen trajectories of Figure 1. For these trajectories the dependence of Y_{CH4} on ξ is largely independent of the trajectory chosen. These curves were numerically differentiated, and combined with local scalar dissipation rates to calculate the net production rate of methane

throughout the flame using Eq. 2. For this calculation we adopt Smooke's formulation for the diffusion coefficient[14].

Figure 5 shows the results for all except the richest flame regions (for $\xi > 0.2$, w_i rapidly approaches zero). Notice the sharp increase in CH_4 consumption near the stoichiometric surface. Because the methane concentrations show a common dependence on mixture fraction (Fig. 3), the magnitude of the conserved scalar rates is determined by the magnitude of the scalar dissipation rate which is largest near the base of the flame.

Chemical Rates

Of the 83 reactions in the mechanism used by Smooke six include methane as a reactant or product. The net rate of methane formation can be evaluated at each location in the flame by summing the contributions of these reactions. Figure 6 shows the dependence of these net rates on mixture fraction along the three diffusive trajectories. As the data in Figs 5 and 6 show, there is good agreement between rates calculated using the conserved scalar approach and that from an evaluation of the rate law. The six reactions that involve methane in the mechanism include it's abstraction reaction with hydrogen atoms. The data in Fig. 4 show that hydrogen atom concentrations, like the scalar dissipation rate, show a strong dependence on flame position with larger concentrations low in the flame.

Net chemical production rates for hydrogen atoms using the conserved scalar approach do not agree with those calculated using the hydrogen rate law in the mechanism. This result might have been anticipated given the non-collapse of the concentration versus mixture fraction data shown in Fig. 4.

Conclusions

In this paper we have compared the results of a "full" transport and chemical calculation performed by Smooke with the predictions of the conserved scalar approach. Our results show that the conserved scalar approach works because some species' concentrations are *not* dependent only on mixture fraction. For the latter species, the net chemical rates can not be evaluated from conserved scalar expressions. The current effort in this project focuses on the cause for the hydrogen atom concentration dependence on flame location. One possibility for this relationship is the fast diffusion velocity that exists for hydrogen atoms near the base of the flame because of its steep concentration gradients. For this species, transport times are short and of the same magnitude as chemical times. It is interesting to conjecture that this fast transport may be cast quantitatively as a dependence of concentration on scalar dissipation rates as has been proposed for flamelet modeling of turbulent combustion.

References

1. Williams, F.A. *Turbulent Mixing in Non-Reactive and Reactive Flow*; Plenum: New York, **1975**, 198.
2. Peters, N. *Twenty-First Symposium (International) on Combustion*; The Combustion Institute: Pittsburgh, **1986**, 1231.
3. Bilger, R.W. *Twenty-Second Symposium (International) on Combustion*; The Combustion Institute: Pittsburgh, **1988**, 475.
4. Hermanson, J.C.; Vranos, A. *Combust. Sci. and Tech.*; **1991**, *75*, 339.
5. Williams, F.A. *Combustion Theory*; Addison-Wesley: Reading, MA, **1965**.
6. Bilger, R.W. *Combust. and Flame*; **1977**, *30*, 277.
7. Smyth, K.C.; Taylor, P.H. *Chem. Phys. Lett.*; **1985**, *122*, 518.
8. Miller, J.H. *Twenty-Fourth Symposium (International) on Combustion*; The Combustion Institute: Pittsburgh, **1992**, 131.
9. Drake, M.C. *Twenty-First Symposium (International) on Combustion*; The Combustion Institute: Pittsburgh, **1986**, 1579.
10. Seshadri, K.; Maußß, F.; Peters, N.; Warnatz. J *Twenty-Third Symposium (International) on Combustion*; The Combustion Institute: Pittsburgh, **1990**, 559.
11. Peters, N.; Kee, R.J. *Combust. and Flame*; **1987**, *68*, 17.
12. Norton, T.S.; Smyth, K.C.; Miller, J.H.; Smooke, M.D. *Combust. Sci. and Tech.*; **1993**, *90*, 1.
13. Smooke, M.D.; Lin, P.; Lam, J.K.; Long, M.B. *Twenty-Third Symposium (International) on Combustion*; The Combustion Institute: Pittsburgh, **1990**, 575.
14. Smooke, M.D.; Giovangigli, V. *Reduced Kinetic Mechanisms and Asymptotic Approximations for Methane-Air Flames*; Lecture Notes in Physics, Springer-Verlag: Berlin, **1991**, *384*, 1.

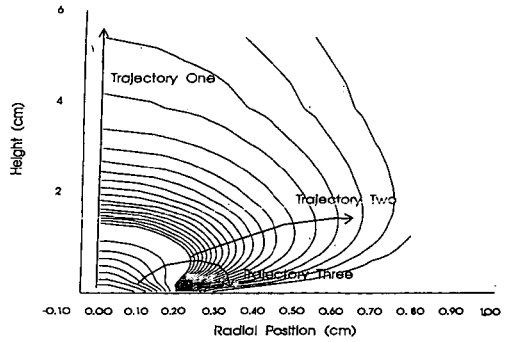

Figure One: Pictoral representation of the diffusive trajectories chosen across contours of mixture fraction, ξ.

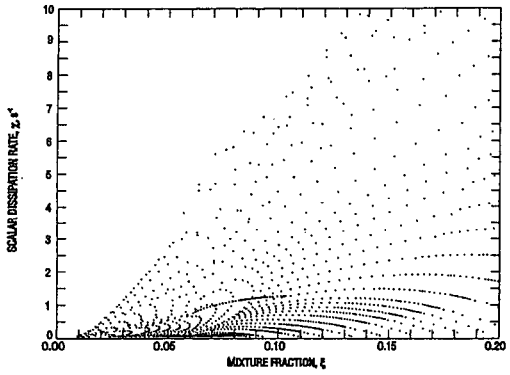

Figure Two: Plot of scalar dissipation rate, χ, versus mixture fraction, ξ. Values move from low to high in the flame from top to bottom.

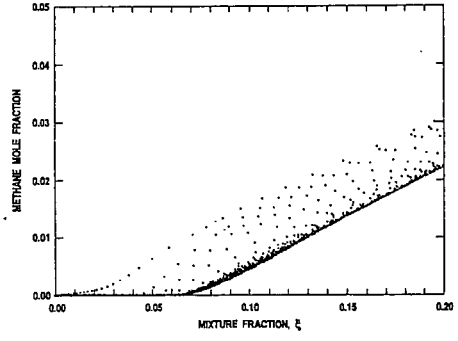

Figure Three: Plot of CH_4 mole fraction versus mixture fraction, ξ. (Positions low in the flame are on the left).

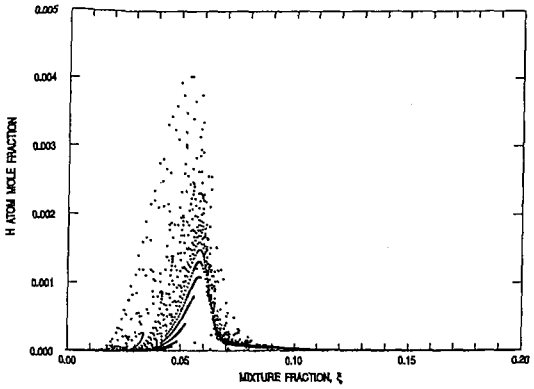

Figure Four: Plot of H atom mole fraction versus mixture fraction, ξ. (Values move from low to high in the flame from top to bottom).

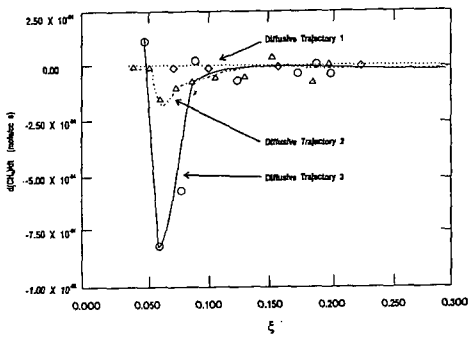

Figure Five: Conserved Scalar predicted rates of CH_4 production versus mixture fraction, ξ, along the diffusive trajectories chosen.

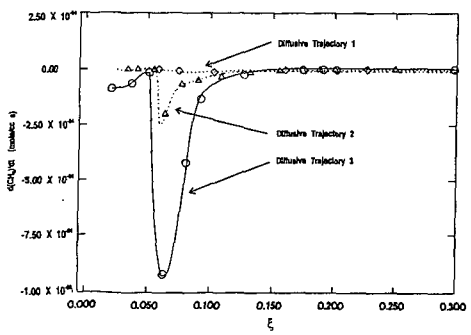

Figure Six: Chemical rate of CH_4 formation versus mixture fraction, ξ, along the chosen diffusive trajectories.

COMPUTER MODELING OF CHLORINE-CATALYZED INHIBITION REACTIONS IN C_2H_4/H_2/AIR/Cl_2 OXIDATION

C.R. Casias and J. Thomas McKinnon
Department of Chemical Engineering and Petroleum Refining
Colorado School of Mines
Golden, CO, 80401

Keywords: Chlorinated hydrocarbons, oxidation, chlorine inhibition

INTRODUCTION

This paper pertains to research currently underway in the area of chlorinated hydrocarbon combustion. The effects on combustion of chlorinated hydrocarbons or in the presence of chlorine is of practical importance, particularly as related to the incineration of hazardous wastes consisting of organic material containing chlorinated hydrocarbons. Overall, this effort has been undertaken in order to obtain a better understanding at the microscopic level of the oxidation process relating to free radical branching and inhibition of free radical branching. Additionally, this effort may provide insight for a better understanding of the conditions resulting in flame blow-out.

The effects on the concentration of free radicals such as H and OH in the presence of Cl have been previously studied by others. The principal reaction for the production of free radicals is given as

$$H + O_2 \Leftrightarrow OH + O \qquad \textit{(Rxn 1)}$$

In the presence of chlorine, this reaction is generally considered to become inhibited by a reduced H atom concentration as a result of the formation of molecular hydrogen through the following net reaction,

$$H + H \Leftrightarrow H_2 \qquad \textit{(Rxn 2)}$$

The actual route through which H_2 is formed will vary depending on the temperature and concentration of species present. A generalized kinetic model for catalyzed recombination of H atoms (Westbrook, 1982) considers a cycle of reactions to result in the above net reaction. This cycle consists of the following reactions,

$$\begin{aligned} H + RX &\Leftrightarrow HX + R\cdot \\ R\cdot + X_2 &\Leftrightarrow RX + X \\ H + HX &\Leftrightarrow H_2 + X \\ X + X + M &\Leftrightarrow X_2 + M \end{aligned}$$

where X represents the halogen atom and R· represents methyl, ethyl, or vinyl radicals.

This cycle of reactions will be of significance in recombining H atoms when the rates on each of the reactions are of the same relative order and particularly when no reaction significantly inhibits the ability of another reaction to proceed. For instance, if the first reaction of the cycle is limiting, the importance of following reactions dependent on the free radical R will be greatly reduced. Thus, the net recombination reaction must be rigorously analyzed by evaluation of each of the individual reactions involved in the cycle. These types of analyses are currently underway and preliminary findings are presented.

Additionally, conditions for blow-out are being assessed in order to establish the mechanism leading to this phenomena. The difficulty in assessing this is due primarily to the interdependency of temperature and the reaction mechanisms contributing to the rate of change of free radicals.

MODELING APPROACH

This study focuses on computer simulation predictions of the effects on ethylene oxidation by the introduction of chlorine in concentrations of less than 0.005 initial mole fraction, and under lean fuel conditions. Ethylene, being a hydrogen lean fuel, will produce a lower concentration of H atoms and changes in the concentration should therefore be more apparent.

The computational analysis was conducted using the Sandia CHEMKIN (Kee et al, 1989) and Perfectly-Stirred Reactor (PSR) (Glarborg et al,1990) codes running on an IBM RISC 6000 computer. Calculations were performed adiabatically whereby inlet gas temperature and the mixture composition were specified.

The thermochemical data were acquired primarily from a Sandia National Laboratories report (Kee et al, 1992), although some estimations were conducted based on group additivity theory (Benson, 1976). The detailed chemical kinetic reaction mechanism consisting of 189 reversible and 77 irreversible elementary reactions was used. These elementary reactions were compiled from three different sources and account for the chlorinated hydrocarbon chemistry of trichloroethane (Chang and Senkan, 1986), inclusion of HCl and Cl_2 inhibiting reaction mechanisms (Westbrook et al, 1977), and premixed CH_3Cl/CH_4/air flames employing enhanced third-body effectivities (Lee et al, 1993).

For the adiabatic configuration, the fuel equivalence ratio of ethylene was approximately 0.75. The inlet temperature was set at 1650 K and chlorine was introduced in the form of Cl_2. To minimize the deviations of the inlet mole fractions of fuel and air, an initial mole fraction for H_2 of approximately 0.02 was included, and as the inlet mole fraction of Cl_2 was increased, the H_2 mole fraction was correspondingly decreased. The Cl_2 mole fraction was varied from 0.000 to 0.020; however, the primary region of interest was below 0.005 mole fraction Cl_2. The residence time was varied throughout the region of no conversion of C_2H_4 at the initial time to a time where the conversion was greater than 0.90. The residence time was increased as specified and then reduced to a time less than the time required for blow-out to occur. At the blow-out time, sensitivity analysis were conducted for the purpose of evaluating the dominant reactions at this point.

RESULTS

Results for exit mole fraction versus residence time are plotted in Figures 1 through 4 for varying inlet concentrations of Cl_2. These results agree with general expectations in that as the Cl_2 concentration is increased from 0.0025 to 0.01 mole fraction, the ignition and blow-out residence times increase. Below a value of 0.0025, the results from computer modelling indicate that ignition will not occur. This prediction also agrees with expectations since the more reactive Cl_2 possesses a greater tendency than H_2 to interact with other species in the reactor, particularly at lower temperatures.

At the point just prior to blow-out, sensitivity analyses were conducted. Species evaluated included H, OH, O and H_2. The most significant reactions were the free radical chain branching reactions

$$H + O_2 \Leftrightarrow OH + O \qquad \textit{(Rxn 3)}$$
$$O + H_2 \Leftrightarrow OH + H \qquad \textit{(Rxn 4)}$$

Since the concentrations of the free radicals decreased as the Cl_2 concentration increased, this result is evidence that Cl_2 plays a role in the removal of OH and H radicals. In conjunction with Westbrook's findings, one mode of chlorine-catalyzed recombination consistent with the results obtained in this analysis would include the following reactions,

$$H + CL_2 \Leftrightarrow HCl + CL \qquad \textit{(Rxn 5)}$$
$$HCl + H \Leftrightarrow H_2 + CL \qquad \textit{(Rxn 6)}$$

where the net reaction would yield,

$$H + H + CL_2 \Leftrightarrow H_2 + Cl + Cl. \qquad \textit{(Rxn 7)}$$

Reactions 5 and 6 were among the more significant reactions as indicated from the sensitivity analysis. Preliminary assessment of the possibility of this pathway has included the evaluation of the forward and reverse rate constants and rates. Continued investigations will include in-depth analysis kinetics of this particular pathway as well as investigation into other possible pathways. Other such pathways under investigation include the set of reactions

$$HCl + H \Leftrightarrow H_2 + CL \qquad \textit{(Rxn 6)}$$
$$Cl + H \Leftrightarrow HCl \qquad \textit{(Rxn 8)}$$

and

$$HCl + H \Leftrightarrow H_2 + CL \qquad \textit{(Rxn 6)}$$
$$Cl + OH \Leftrightarrow HCl + O \qquad \textit{(Rxn 9)}$$
$$O + HO_2 \Leftrightarrow O_2 + OH \qquad \textit{(Rxn 10)}$$

where the net reaction results in H atom recombination. The rates for these sets of reactions are being evaluated at various temperatures and species concentrations to determine their relative order and role in H atom recombination.

ACKNOWLEDGEMENT

This work is supported by the National Science Foundation National Young Investigation Program (Grant Number CTS-9258149)

REFERENCES

Benson, S.W., *Thermochemical Kinetics*, (1976), 2nd. Ed., John Wiley & Sons, New York.

Chang, Wen-Donq, and Senkan, Selim M., Detailed Chemical Kinetic Modelling of Fuel-Rich C_2HCl_3/O2/Ar Flames, (1989), *Environ. Sci. Technol.*, **23**, 442-450.

Glarborg, P., Kee, R.L., Grcar, J.F., and Miller, J.A., (1990),"PSR: A FORTRAN Program for Modeling Well-Stirred Reactors", Sandia National Laboratories, SAND86-8209.

Kee, R.J., Rupley, F.M., and Miller, J.A., :The Chemkin Thermodynamic Data Base", (1992), Sandia National Laboratories, SAND-8215B

Kee, R.J., Rupley, F.M., and Miller, J.A., (1989), "Chemkin-II: A Fortran Chemical Kinetics Package for the Analysis of Gas-Phase Chemical Kinetics", Sandia National Laboratories, SAND89-8009.

Lee, K.Y., Yang, M.H., and Puri, I.K., (1993), Numerical Simulation of Stoichiometric Premixed Flames Burning CH_3Cl/CH_4/Air Mixtures at Atmospheric Pressure with a Full and Short Mechanism and Comparison of the Flame Speeds with Experimental Results, *Combust. Flame*, **92**, 419-439.

Westbrook, C.K., (1982), Inhibition of Hydrocarbon Oxidation in Laminar Flames and Detonations by Halogenated Compounds, *Nineteenth Symp. (IntN'L) on Comb.*, The Combustion Institute, 127-141.

Westbrook, C.K., Creighton, J. Lund, and Dryer, F.L., (1977), A Numerical Model of Chemical Kinetics of Combustion is a Turbulent Flow Reactor., *J. Phys. Chem.*, **81**, 2542.

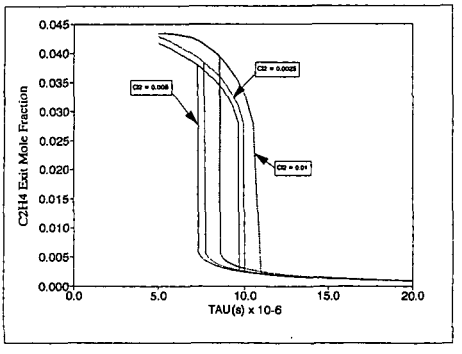

Figure 1. Ethylene Oxidation: Exit mole fraction of ethylene in a perfectly-stirred reactor for initial Cl_2 inlet mole fractions of 0.0025, 0.005, and 0.01.

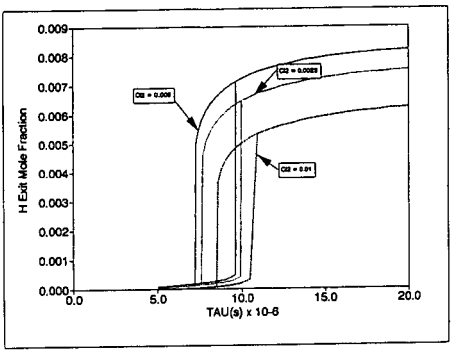

Figure 2. Ethylene Oxidation: Exit mole fraction of H in a perfectly-stirred reactor for initial Cl_2 inlet mole fractions of 0.0025, 0.005, and 0.01.

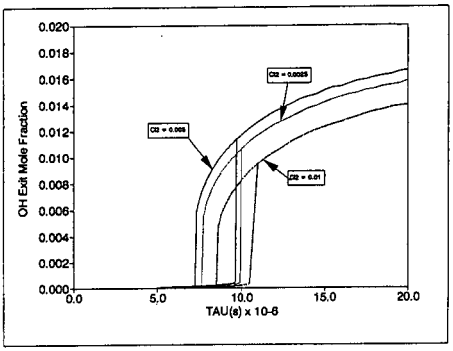

Figure 3. Ethylene Oxidation: Exit mole fraction of OH in a perfectly-stirred reactor for initial Cl_2 inlet mole fractions of 0.0025, 0.005, and 0.01.

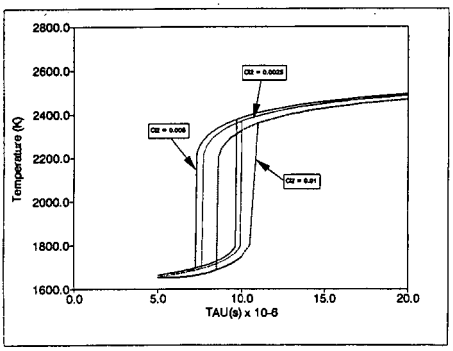

Figure 4. Ethylene Oxidation: Temperature profile in a perfectly-stirred reactor for initial Cl_2 inlet mole fractions of 0.0025, 0.005, and 0.01.

NUMERICAL CALCULATION OF SOOT FORMATION IN PREMIXED HYDROCARBON FLAMES

Fabian Mauss and Henning Bockhorn
Fachbereich Chemie, Universität Kaiserslautern
Erwin Schrödingerstraße, 67663 Kaiserslautern, Germany

Keeywords: Soot formation, numerical simulation, hydrocarbon flames

Abstract

Numerical calculations including a chemical model for soot formation have been performed for premixed burner stabilized ethene-air flames at 0.1 and 1.0 MPa that have been investigated experimentally by Wagner et al. The maximum temperatures in the flames have been varied in the experiments by changing the mass flow rates of the mixture. In accordance with the experimental data the numerical calculations predict a bell shaped dependence of the final soot volume fraction on the maximum flame temperature.

The dependence of the final soot volume fraction on pressure between 0.1 and 1.0 MPa is calculated to be proportional $p^{1.5}$ to p^2. This is slightly weeker than found experimentally in the experiments of Wagner et al. It is concluded that the pressure dependence of some gasphase reaction rates, in particular that for the formation of benzene and the PAH growth has to be validated.

Introduction

In sooting hydrocarbon flames fuel molecules are converted within few milliseconds into carbonaceous particles containing millions of carbon atoms. It is known that the formation of soot is mainly determined by particle inception, by coagulation of primary soot particles to larger aggregates, and by heterogeneous reactions of soot particles with the surrounding gasphase. Much progress has been made in understanding these processes, however, a number of problems are yet unsolved [1-4].

Phenomenologically, the final soot volume fraction f_v^∞ in premixed flames—that is the soot volume fraction attained shortly after the reacton zone—depends for a given fuel on pressure, mixture, composition and temperature. From numerous experimental work, e.g. [5-9] it is known that in a pressure range from 0.1 to 1.0 MPa the final soot volume fraction varies with the square of pressure. The temperature dependence of the final soot volume fraction reveals a bell shaped form, whereas the dependence on mixture composition may be given as $f_v^\infty \sim \left[(\mathrm{C/O}) - (\mathrm{C/O})_{sooting\,limit}\right]^n$ with $2.5 \le n \le 3$, cf. [8].

The formation of soot in premixed flames is dominated by heterogeneous surface growth reactions, see e.g. [10,11]. Ethyne has been found to be the most likely chemical " growth specie", because ethyne is the most abundant hydrocarbon species in the soot forming region of premixed flames.

A mechanistic interpretation of surface growth reactions has been introduced by Frenklach [12]. Analogously to the planar growth of polycyclic aromatic hydrocarbons, surface growth of soot particles is, on the per-site basis, explained by a radical hydrogen abstraction carbon addition (HACA) mechanism. In addition oxidation of soot particles by OH and O_2 has been taken into account.

In the following the over-all temperature and pressure dependence of the final soot volume fraction is explained in terms of chemical reactions between gasphase compounds and the soot surface. This concept basicly contains the competing processes in soot formation by surface reactions: carbon addition by adding ethyne and oxidation by oxygen and OH. Presuming a different temperature dependence of the three processes, the picture of the temperature dependence of the soot volume fraction is—in principle—understandable.

Model for soot formation

The model for soot formation that has been integrated into a numerical code for one-dimensional flat premixed flames, cf. [14], has been developed from the one discussed above. The PAH growth has been formulated with the help of fast polymerisation reactions [14] reducing the number of equations to be solved and the numerical effort.It should be emphasized that detailed models of the kind below depend essentially upon the quality of kinetic parameters and the knowledge of the reaction channels for the reactions of the species involved. Furthermore, it should be mentioned that these models reproduce only phenomena connected with the formation of the bulk of soot. Many phenomena, e.g the formation of high molecular tarry structures that are observed in an early stage of soot formation or the "fine structure" of soot are not covered by these models.

The model is essentially subdivided into three parts — gas phase chemistry, polymerisation of PAH and formation and growth of soot particles.

The gas phase chemistry up to the first aromatic ring is calculated with the help of a detailed mechanism provided by Warnatz [15], consisting of about 250 elementary reactions between 52 chemical species. The first aromatic ring, viz. benzene, is formed via the reaction $C_3H_3 + C_3H_3 \rightleftharpoons c - C_6H_6$. The calculation of the growth reactions of benzene to small PAH follows the mechanism suggested by Frenklach and Warnatz [16]. Following Frenklach [17], the further growth of PAH is assumed to be a polymerisation process.

Within each polymerisation stage two aromatic rings are added to a given PAH. Each step from PAH to PAH involves several chemical reactions. The detailed growth and oxidation mechanism used for the calculations presented here is given below.

1.a	$P_{i,1}$	+ H	$\overset{k_{1a,f}}{\underset{k_{1a,r}}{\rightleftharpoons}}$	$P_{i,2}$	+ H_2
1.b	$P_{i,1}$	+ OH	$\overset{k_{1b,f}}{\underset{k_{1b,r}}{\rightleftharpoons}}$	$P_{i,2}$	+ H_2O
1.c	$P_{i,1}$	+ O	$\overset{k_{1c,f}}{\underset{k_{1c,r}}{\rightleftharpoons}}$	$P_{i,2}$	+ OH
2.	$P_{i,2}$	+ H	$\overset{k_{2,f}}{\underset{}{\rightleftharpoons}}$	$P_{i,1}$	
3.	$P_{i,2}$	+ C_2H_2	$\overset{k_{3,f}}{\underset{k_{3,r}}{\rightleftharpoons}}$	$P_{i,3}$	+ H
4.a	$P_{i,3}$	+ H	$\overset{k_{4a,f}}{\underset{k_{4a,r}}{\rightleftharpoons}}$	$P_{i,4}$	+ H_2
5.	$P_{i,4}$	+ H	$\overset{k_{5,f}}{\underset{}{\rightleftharpoons}}$	$P_{i,3}$	
6.	$P_{i,4}$	+ C_2H_2	$\overset{k_{6,f}}{\underset{k_{6,r}}{\rightleftharpoons}}$	$P_{i,5}$	
7.	$P_{i,5}$	+ C_2H_2	$\overset{k_{7,f}}{\underset{k_{7,r}}{\rightleftharpoons}}$	$P_{i+1,1}$	+ H
8.a	$P_{i,6}$	+ H	$\overset{k_{8a,f}}{\underset{k_{8a,r}}{\rightleftharpoons}}$	$P_{i,5}$	+ H_2
9.	$P_{i,5}$	+ H	$\overset{k_{9,f}}{\underset{k_{9,r}}{\rightleftharpoons}}$	$P_{i,6}$	
10.a	$P_{i,6}$	+ OH	$\overset{k_{10a,f}}{\underset{k_{10a,r}}{\rightleftharpoons}}$	$P_{i,3}$	+ CHO + CH_2
10.b	$P_{i,3}$	+ OH	$\overset{k_{10b,f}}{\underset{k_{10b,r}}{\rightleftharpoons}}$	$P_{i,1}$	+ CHCO
10.c	$P_{i,1}$	+ OH	$\overset{k_{10c,f}}{\underset{k_{10c,r}}{\rightleftharpoons}}$	$P_{i-1,6}$	+ CHCO
11.a	$P_{i,5}$	+ O_2	$\overset{k_{11a,f}}{\underset{k_{11a,r}}{\rightleftharpoons}}$	$P_{i,3}$	+ 2 CO
11.b	$P_{i,4}$	+ O_2	$\overset{k_{11b,f}}{\underset{k_{11b,r}}{\rightleftharpoons}}$	$P_{i,2}$	+ 2 CO
11.c	$P_{i,2}$	+ O_2	$\overset{k_{11a,f}}{\underset{k_{11a,r}}{\rightleftharpoons}}$	$P_{i-1,5}$	+ 2 CO

The growth mechanism is initiated by an H-abstraction step due to the attack of H, O and OH via reactions 1a–1c. The radicalic site of $P_{i,2}$ may be deactivated by the H-addition (reaction 2) or by the revers of reactions 1a-1c. Ethyne is taken up at the radicalic site of $P_{i,2}$ via reaction 3. The repetition of this reaction sequence (reactions 4-6) leads to the closure of an aromatic ring. Because $P_{i,5}$ has a radicalic site, ethyne may be added again and an other ring closure occurs (reaction 7). This second ring closure leads to the next polymerisation stage, where the reaction sequence is repeated. In analogy to the radical sites of $P_{i,2}$ and $P_{i,4}$ the radical site of $P_{i,5}$ can be deactivated by H-addition (reaction 9) or by the revers of reactions 8a-8c. PAH may be oxidized by reactions with OH (10.a-c) and t PAH with a radicalic site may be oxidized by reactions with O_2 (11.a-c).

The formulated reaction sequence is one possible reaction sequences leading to PAH-growth involving six-membered rings. Five-membered rings can be included by similar reaction sequences involving a larger number of intermediates without affecting, however, the basic ideas of the following approach.

Differently from the approach of Frenklach the growth of the PAH is assumed to be a fast polymerisation process. It follows that each PAH is in quasi steady state and that the concentrations of PAH can be calculated from an algebraic system of equations. Details of this analysis are given in [14].

The pathways to soot from PAH are particle inception and condensation of PAH on the surface of the soot particles. Both pathways are assumed to follow Smoluchowski's coagulation equations in the free molecular regime [12,18]. The equations are also used to calculate the coagulation of soot particles.

The heterogeneous surface growth and oxidation of soot particles follow the mechanism given below:

1.a	$C_{soot,i}H$	+ H	$\overset{k_{1a,f}}{\underset{k_{1a,r}}{\rightleftharpoons}}$	$C^*_{soot,i}$	+ H_2
1.b	$C_{soot,i}H$	+ OH	$\overset{k_{1b,f}}{\underset{k_{1b,r}}{\rightleftharpoons}}$	$C^*_{soot,i}$	+ H_2O
2.	$C^*_{soot,i}$	+ H	$\overset{k_{2,f}}{\underset{}{\rightleftharpoons}}$	$C_{soot,i}H$	
3.a	$C^*_{soot,i}$	+ C_2H_2	$\overset{k_{3a,f}}{\underset{}{\rightleftharpoons}}$	$C_{soot,i}C_2H_2$	
3.b	$C_{soot,i}C_2H_2$		$\overset{k_{3b,f}}{\underset{k_{3b,r}}{\rightleftharpoons}}$	$C_{soot,i+1}H$	+ H
4.a	$C^*_{soot,i}$	+ O_2	$\overset{k_{4a,f}}{\underset{}{\rightleftharpoons}}$	$C^*_{soot,i-1}$	+ 2 CO
4.b	$C_{soot,i}C_2H_2$	+ O_2	$\overset{k_{4b,f}}{\underset{}{\rightleftharpoons}}$	$C^*_{soot,i}$	+ 2 CHO
5.	$C_{soot,i}H$	+ OH	$\overset{k_{5,f}}{\underset{}{\rightleftharpoons}}$	$C^*_{soot,i-1}$	+ CH + CHO

The mechanism is modified compared with the one introduced by Frenklach [12]. The reverse of reaction 1.b accounts for the radicaicl site consuming influence of H_2O. Reaction 3 consists of two reactions—carbon addition, ring closure—, because it has been found recently that the reverse of reaction 3 accounts for the limitation of surface growth at high temperatures [19]. The more detailed analysis here shows, that the reverse of reaction 3.a is responsible for this effect, while reaction 3.b is approximately irreversible. If—in analogy to Frenklachs formulation and the planar PAH growth—$\chi(C^*_{soot,i})$ and $\chi(C_{soot,i}C_2H_2)$ are replaced by the assumption of quasi stationarity, the appearance rate of soot can be expressed as follows. We first introduce a factor accounting for the progress of soot growth.

$$f3a = \frac{k_{3b,f}}{k_{3b,f} + k_{3a,b} + k_{4b}[O_2]} \tag{1}$$

If the ring closure via reaction $k_{3b,f}$ is fast compared with the radicalic site consuming and oxidation reactions then $f3a = 1$. If the radicalic site consuming and oxidation reactions are fast then $f3a = 0$. With this definition we write

$$\chi(C^*_{soot,i}) = \frac{k_{1a,f}[H] + k_{1b,f}[OH] + k_{3b,b}[H](1 - f3a)}{k_{1a,b}[H_2] + k_{1b,b}[H_2O] + k_2[H] + k_{3a,f}[C_2H_2]f3a} \cdot \chi(C_{soot,i}) \tag{2}$$

$$\chi(C_{soot,i}C_2H_2) = \frac{k_{3a,f}[C_2H_2]}{k_{3b,f} + k_{3a,b} + k_{4b}[O_2]} \cdot \chi(C^*_{soot,i}) + \frac{k_{3b,b}[H]}{k_{3b,f} + k_{3a,b} + k_{4b}[O_2]} \cdot \chi(C_{soot,i}) \tag{3}$$

$$\frac{df_v}{dt} = (k_{3a,f}[C_2H_2]f3a \cdot \chi(C^*_{soot,i}) - (k_{3b,b}[H](1 - f3a) + [OH]k_5) \cdot \chi(C_{soot,i})) \cdot S \tag{4}$$

In the soot forming limit $f3a = 1$). In the radicalic site consuming limit, $f3a = 0$ the growth of soot is limited at high temperature because of the high activation energy of reaction $k_{3a,b}$.

The algebraic formulation of this model leads to an infinite number of partial differential equations for the number density of soot particles which is reduced to a limited number by using the method of moments (method 2 in [18]). Thermophoretical transport and size dependent diffusion of soot particles has been considered. The system of equations is solved numerically employing a Newton Method

Results and Discussion

Burner stabilized flat premixed ethene-air flames (C/O = 0.72) that have been investigated experimentally by Wagner et al. [8,20] have been numerically simulated at 0.1 and 1.0 MPa. The maximum flame temperature in the experiment has been varied by varying the mass flow rate of the unburnt mixture.

The temperature and soot volume fraction profiles of an ethene-air flame (C/O = 0.72) with a cold gas flow velocity of 4.5 cm/s are given in Fig.1. The soot volume fraction (cm^3_{soot}/cm^3_{gas}) is density related. Therefore, we have normalized the profile to a temperature of 1400 K. This is also demonstrated in Fig.1. It is obvious from this figure, that the final soot volume fraction is attained at a height of 35 mm above the burner. At larger heights the soot volume fraction increases with decreasing temperature and the normalized soot volume fraction remains constant. The agreement between calculated and measured data is reasonably good.

The calculated final soot volume fractions of all investigated flames at 0.1 MPa are shown in Fig. 2 in dependence on the flame temperature at 10 mm height above the burner. The final soot volume fraction: is given in the the normalized form. We prefer the normalized soot volume fraction, because this definition is not dependent on the shape of the temperature profile. The comparison of the model prediction with experimental data from Refs.[8,20] reveal that the calculations reproduce the soot volume fraction quitc well at high flame temperatures. At lowcr flame temperatures the agreement between measured and calculated soot volume fractions is reasonable. In summary, the over-all dependence of soot formation on flame temperature can be understood with the help of the detailed chemistry soot model.

Most of the rate coefficients of reactions concerning the formation and growth of PAH or soot are unknown and have to be estimated from comparable gasphase reactions by analogy. However, the above discussed results clearly point out that within the framework of the presently available information the soot volume fraction can be predicred reasonably in terms of chemical reactions between gasphase compounds and the soot surface.

In addition to the calculations above the temperature dependence of soot formation in ethene/air flames at 1.0 MPa has been calculated. This is shown in Fig.3. It can be seen, that the model again predicts a bell shaped dependence of the soot volume fraction on flame temperature. However, the pressure dependence of the prediction as well as the temperature dependence at the higher pressure is weeker than found in the experiment [8]. The presssure

dependence of the final soot volume fraction is calculated to be proportional to p^2 at high flame tempeatures. With decreasing flame temperature the pressure dependence reduces to proportional to $p^{1.5}$. A similar week pressure dependence has been found experimentally [9] at pressures larger than 1.0 MPa where the final soot volume fraction varies linearly with pressure. We conclude that the decreasing pressure dependence of the soot volume fraction with increasing pressure is overestimated by the model used in this investigation. We note that the linear increase of the density related soot volume fraction just refers to the linear increase of the density with pressure. An analysis of the numerical results indicates, that the increasing partial pressure of H_2 is responsible for the limited rate of soot formation at high pressure. The increasing partial pressure of H_2 reduces the number of radicalic sites on the surface of the soot particles via the revers of reaction (1.a,s).

Conclusions

A model that encompasses two pathways to soot from PAH, particle inception and condensation of PAH on the surface of the soot particles and that describes surface growth of soot similarly to the planar growth of PAH is employed to predict temperature and pressure dependence of soot formation in premixed ethene-air flames.

Within the framework of this model the experimentally measured final soot volume fraction and its temperature and pressure dependence are well reproduced.

Acknowledgement

This research was partially supported by the commission of the European Communities, the Swedish National Board for Technical Development (STU) and the Joint Research Committee of european car manufacturer (Fiat, Peugeot SA, Renault, Volkswagen and Volvo) within the IDEA programs.

References

1 Haynes, B.S. and Wagner, H.Gg.: Prog. Energy Combust. Sci. 7, p. 229 (1981).

2 Glassman, I.: Twenty-Second Symposium (International) on Combustion, p. 295, The Combustion Institute, 1988.

3 Howard, J.B.: Twenty-Third Symposium (International) on Combustion, p. 1107, The Combustion Institute, 1990.

4 Haynes, B.S. and Wagner, H.Gg.: Z. Phys. Chem. N.F. 133, p. 201, (1982).

5 Baumgärtner, L., Jander, H. and Wagner, H.Gg.: Ber. Bunsenges. Phys. Chemie 87, p. 1077, (1983).

6 Mätzing, H. and Wagner, H.Gg.: Twenty-First Symposium (International) on Combustion, P. 1047, The Combustion Institute, 1986.

7 Böhm, H., Hesse, D., Jander, H., Lüers, B., Pietscher, J., Wagner, H.Gg. and Weiss, M.: Twenty-Second Symposium (International) on Combustion, P. 403, The Combustion Institute, 1988.

8 Bönig, M., Feldermann, Chr., Jander, H., Lüers, B., Rudolph, G. and Wagner, H.Gg.: Twenty-Tird Symposium (International) on Combustion, P. 1581, The Combustion Institute, 1990.

9 Böhm, H., Feldermann, Ch., Heidermann, Th., Jander, H., Rudolf, G. and Wagner, H.Gg.: Twenty-Fourth Symposium (International) on Combustion, P. 991, The Combustion Institute, 1992.

10 Bockhorn, H., Fetting, F., Wannemacher, G. and Heddrich, A.: Twentieth Symposium (International) on Combustion, p. 879, The Combustion Institute, 1985.

11 Bockhorn, H., Fetting, F., Wannemacher, G. and Heddrich, A.: Ber. Bunsenges. Phys. Chemie 91, p. 819, (1987).

12 Frenklach, M. and Wang, H.: Twenty-Third Symposium (International) on Combustion, p. 559, The Combustion Institute, 1990.

13 Markatou, P., Wang, H. and Frenklach, M.: Combust. Flame 93, p. 467 (1993)

14 Mauss,F., Trilken,B. and Peters,N. in: Mechanisms and Models of Soot Formation, Bockhorn,H. (ed.); Springer Verlag, in press.

15 Warnatz, J. and Chevalier, C. in: Combustion Chemistry 2nd edition, Gardiner, W.C.jr.(ed.); Springer Verlag, in press.

16 Frenklach,M., Warnatz,J.: Combust. Sci. and Tech., 51, p. 265 (1987).

17 Frenklach,M.: Chemical Engineering Science, Vol. 40, No. 10, p. 1843 (1985).

STAGED COMBUSTION OF CHLORINE- AND NITROGEN-CONTAINING HYDROCARBONS FOR THE MINIMIZATION OF NO_X AND PIC's

Fuhe Mao and Robert B. Barat
Dept. of Chemical Engineering, Chemistry, and Environmental Science
New Jersey Institute of Technology
Newark, NJ 07102

Keywords: combustion, nitrogen oxides, chlorinated hydrocarbons

This paper describes our current research in the area of staged combustion, wherein the overall fuel-lean system is divided into a fuel-rich (oxidant lean) first stage followed by a fuel-lean (oxidant rich) second stage. The first stage of our turbulent flow combustor is a jet-stirred, backmixed zone which can be modeled as a perfectly stirred reactor (PSR) under most conditions. The effluent from this zone enters a linear flow zone which can be modeled as a plug flow reactor (PFR). Industrial turbulent combustors, incinerators, and afterburners which employ a central fuel nozzle and swirled concentric air for flame stabilization can often be modeled with this sequence (Beer and Chigier, 1983).

This work utilizes an atmospheric pressure toroidal jet-stirred / linear flow two stage sequential combustor shown in Figure 1. The primary zone (torus) was first described by Nenniger et al., 1984. Premixed fuel gas and air are introduced at sub-sonic velocities into the torus around its outer circumference. The off-radial jets entrain the swirling bulk gas, causing a highly turbulent, backmixed condition. Residence times are typically 5-10 milliseconds in this 250 milliliter primary zone. The hot, reactive gases exit the torus, passing over a flow straightener into the secondary (linear) stage. Additional gases, typically air/O_2/steam in this work, are injected at this point. Second stage residence times are on the order of 20 milliseconds in this 30 centimeter long secondary zone. Stable species gas samples are withdrawn through two water-cooled probes. At present, all fuels are input to the reactor as gases. The primary fuel is C_2H_4. Fuel-bound chlorine and nitrogen sources simulating hazardous wastes are CH_3Cl and CH_3NH_2, respectively. A schematic of the entire facility is presented in Figure 2.

When CH_3Cl is burned, the sample gas is scrubbed of HCl in a gas-water countercurrent flow packed tower. The column is sufficiently oversized that effectively 100% HCl recovery from the inlet sample gas stream is achieved. The liquid effluent contacts chloride ion selective and reference electrodes used for HCl quantification.

The sample gas stream passes successively through a chilled bath for water vapor condensation, a droplet knockout, and a metal bellows pump, which provides the suction for sample withdrawal and the pressure head for sample passage to the various analyzers. The metered pump outlet sample gas is then split, with a portion flowing to O_2, CO, and CO_2 continuous emission analyzers and a gas chromatograph. The gas chromatograph is equipped columns for separation of light hydrocarbons and chlorocarbons, CO, and CO_2. The columns elute onto thermal conductivity and flame ionization detectors. The remainder of the sample gas passes through a gas drier, then flows to Total Hydrocarbon and NO_X analyzers.

There are three segments to the modeling of this combustor: elementary reaction mechanism, reactor simulation, and rate-of-production analyses. The first and second represent a major simplification of the turbulent fluid mechanics in favor of an emphasis on detailed chemistry. A favorable comparison of the experimental data and model predictions justifies the use of the third segment, which identifies the important chemical pathways.

For the experimental cases considered in this work, the reaction mechanism for the combustion of C_1/C_2 hydrocarbons and CH_3Cl is taken from Ho et al., 1992. The mechanism for CH_3NH_2 combustion and NO_x chemistry is taken from Miller and Bowman (1989), Sun et al. (1987), and Beer et al. (1981). Generated from the mechanism is ω_k, the net molar rate of production by reaction of species k, which is used in the reactor simulation equations.

The jet-stirred zone can be modeled under most conditions as a PSR, with the following governing species balance equations:

$$M(Y_k - Y_{ko}) = \omega_k W_k V \qquad (1)$$

where M = mass flow rate, Y_k = mass fraction of species k (total of K species), W_k = molecular weight of k, and ω_k = net molar rate of production by reaction of k, V = reactor volume, and subscript o represents the feed condition. The linear flow zone can be modeled as a PFR, with the following governing species balance equations:

$$\frac{dY_k}{dt} = \frac{\omega_k W_k}{\rho} \qquad (2)$$

where t = reaction (residence) time and ρ = mass density.

The mechanism is incorporated into a PSR+PFR reactor simulation program (driver code) which accesses the *CHEMKIN* package (Kee and Miller, 1986). The input to this driver includes composition, temperature, and mass rate of the PSR feed and post-PSR injection, reactor pressure, PSR volume and measured temperature, and PFR residence time and measured temperatures. Our driver program includes options to request net rate-of-production information for selected species to construct the chemical pathways involving reactants, intermediates, and products.

A series of runs were made to examine the effects of full staging on NO levels. A fuel-lean (equivalence ratio[1] ϕ = 0.86) baseline was established. The feed to the primary stage was sequentially increased (ϕ = 0.86 to 1.43) while the temperature was kept constant at 1760 K. The molar ratio of CH_3NH_2 to C_2H_4 in the feed was maintained at 0.058. For each fuel-rich PSR feed, air was injected into the secondary stage so as to achieve an overall combustor ϕ of 0.86. All concentrations reported for the PFR have been corrected upward for the dilution effect of the injected air.

[1] ϕ = $[\text{fuel/air}]_{\text{actual}}/[\text{fuel/air}]_{\text{stoichiometric}}$

Measured temperature profiles for these runs are given in Figure 3. The PFR temperatures either decrease or increase along its length depending on the degree of additional combustion occurring. At higher primary stage ϕ values, the heat produced in the second stage more than overcomes sensible losses. The experimental operability advantage of these losses is now clear.

Figure 4 presents measured and model-predicted NO levels for these runs in the PSR. The highest levels occur for the fuel-lean feeds. As the primary stage ϕ increases, the NO concentration drops dramatically. However, as expected, the CO level increases with a drop in CO_2, as shown in Figures 5 and 6 respectively. The injection of the secondary air, though, enhances CO conversion. Figure 7 dramatically illustrates that a minimum in NO at the PFR outlet exists for a PSR feed ϕ of 1.35. Though the 700 ppm level is twice the 350 ppm PSR concentration, it is still much lower than the PFR outlet NO level of 1800 ppm for the all fuel-lean base case (ϕ = 0.86).

Preliminary results have been obtained on the simultaneous staged combustion of $C_2H_4/CH_3Cl/CH_3NH_2$. The feed CH_3NH_2/C_2H_4 ratio, primary stage ϕ, and overall ϕ were kept constant, while the feed CH_3Cl/C_2H_4 ratio was varied. Increasing the CH_3Cl loading results in a drop in NO concentration (Figure 8), which cannot be explained by the negligible drop in reactor temperature profiles as the chlorine content increases. Rate-of-production analysis will be used to identify the responsible chemical pathways.

ACKNOWLEDGEMENT

The authors would like to thank the Hazardous Substances Management Research Center and the National Science Foundation for their financial support of this work.

REFERENCES

Beer, J. M. and Chigier, N. A., Combustion Aerodynamics, Krieger Publishing, Malabar, FL (1983).

Beer, J. M., Jacques, M. T., Farmayan, W., and Taylor, B. R., *18th Symposium (Int.) on Combustion,* The Combustion Institute, Pittsburgh, PA, p. 101 (1981).

Kee, R. J. and Miller, J., Sandia National Laboratories Report, SAND86-8841, Livermore, CA (1986).

Miller, J. and Bowman, C., *Progress in Energy and Combustion Science,* vol. 15, p. 287 (1989).

Nenniger, J. E., Chomiak, J., Kridiotis, A., Longwell, J. P., and Sarofim, A. F., *20th Symposium (Int.) on Combustion,* The Combustion Institute, Pittsburgh, PA (1984).

Sun, W. H., Longwell, J. P., and Sarofim, A. F., 193th National Meeting of the American Chemical Society (1987).

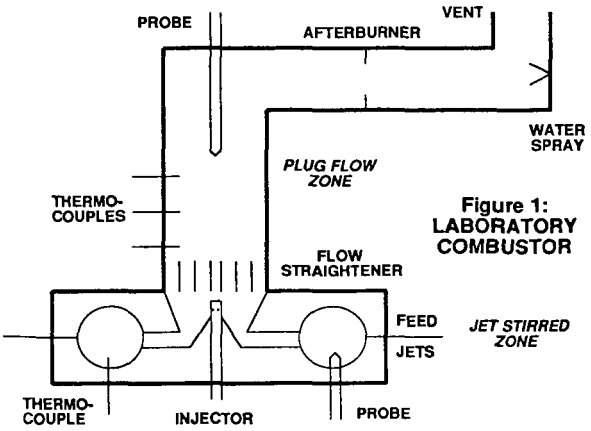

Figure 1: LABORATORY COMBUSTOR

Figure 2: STAGED COMBUSTION FACILITY

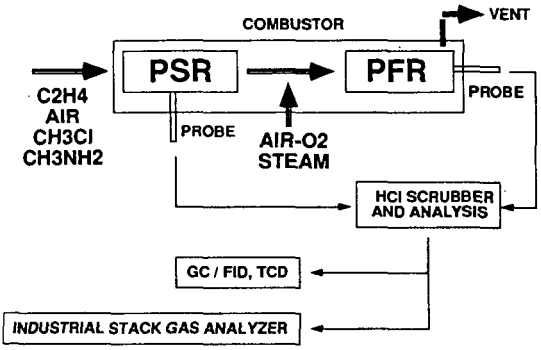

FIGURE 3

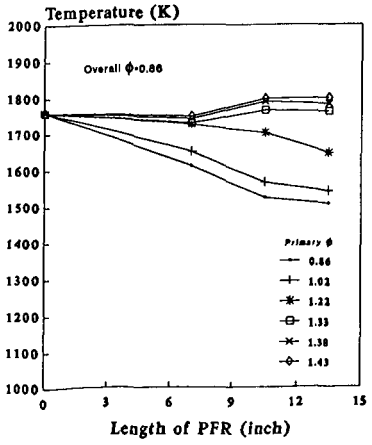

FIGURE 4

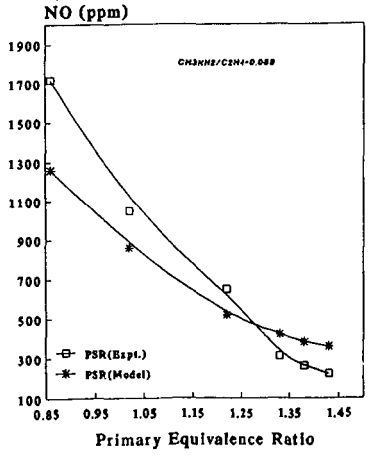

emissive factors less than 0.3 (9). Figure 3 compares the combustion reactivities of the suite of residual carbon samples to those of various laboratory-generated chars in the early-to-intermediate stages of combustion (20 - 60% char carbon conversion). To facilitate direct comparison, char combustion rates are presented at a common oxygen concentration of 6% and a gas temperature of 1500 K. The laboratory char data in Fig. 3 includes a set of previously published oxidation rates for a suite of ten U.S. coals of various rank (4). Char reactivity is seen to be a strong function of rank, represented here by the dry, ash-free carbon content of the parent coal. At any given rank the residual carbon samples are much less reactive than the laboratory chars by factors of 2 to 7. Also, in each case where chars were available from the same parent coal, the residual carbon samples are seen to be much less reactive (see Fig. 2). The residual carbon materials were also found to be significantly less reactive than the laboratory-generated chars in 7% oxygen at 500 - 700 °C, as determined by thermal gravimetric analysis.

Physicochemical properties: Carbon dioxide surface areas of the residual carbon sample investigated here range from 93 to 188 m^2/g-organic-matter (on a dry, ash-free basis) and are roughly comparable to the areas of laboratory chars in the early and middle stages of combustion (8). The residual carbon samples have hydrogen to carbon ratios of 0.2 and 1.2 wt-% and oxygen to carbon ratios of 2 - 6 wt-%, also comparable to those of a variety of laboratory-generated chars in the intermediate stages of combustion (8).

Carbon structure: Fig. 4 shows two selected micrographs (HRTEMs); one of Illinois #6 char in the intermediate stages of combustion, after 72 msec residence time and a carbon conversion of approximately 45%, and one of Illinois #6 residual carbon. The images represent typical structures based on examination of at least ten fields for each sample. Individual graphitic layers are easily discernible in the images, often in parallel groupings with the nominal interlayer spacing characteristic of graphitic carbon, 0.34 nm. Curved structures are present in both images, as has been observed for other carbon materials (11). Indeed, there is evidence that curved structures are thermodynamically favored for graphitic carbon units below a certain size — flat graphitic layers of small size would necessarily possess high-energy dangling bonds at the edges (11). Fig. 4 clearly shows that the residual carbon samples possess a higher degree of crystalline order than the laboratory-generated chars at 72 msec residence time. The residual carbon sample in Fig. 4b shows numerous crystallites with stacking depths of 3 - 5 nm, or approximately 10 graphitic layers, and dimensions parallel to the basal planes of up to 10 nm.

DISCUSSION AND CONCLUSIONS

Despite the complexity of the boiler environment and the wide variety of boiler operating conditions and fuels examined here, the residual carbon samples, as a class of materials, exhibit consistent and unique properties. Particularly noteworthy is their low combustion reactivity relative to laboratory-generated chars in the early-to-intermediate stages of combustion. Here we attempt to relate the low reactivities to some measurable physicochemical property or properties of the residual carbon samples. In general, the high-temperature reactivity of a carbon material to oxygen is determined by 1) the amount of internal surface area available for reaction, 2) the pore structure which provides access to the particle interior, 3) the degree encapsulation of carbon by mineral matter, 4) the intrinsic reactivity of the internal surfaces, governed by the chemistry and crystalline structure of the organic matrix and by the catalytic action, if any, of inorganic impurities [12]. The material characterizations performed provide some information on each of these factors and suggest that factor 4 is the likely explanation for the low reactivity of residual carbon.

High resolution TEM shows that residual carbon can possess a much higher degree of crystalline order than the laboratory-generated chars. The observed increase in order is likely the result of thermally induced lattice rearrangement (pregraphitization), possibly promoted by the oxidative removal of carbon. The importance of pregraphitization or "thermal annealing" on char reactivity has been noted by a number of researchers [13,14] A recent study [15] has shown that a similar degree of turbostratic crystalline order in developed in coal chars over the coarse of 100 msec of combustion at particle temperatures of 1800 K. Pregraphitization and oxidation have similar time constants and thus occur to a large extent simultaneously under the conditions relevant to pulverized coal combustion. Because increased crystalline order in carbons is generally accompanied by a loss of reactivity due to a reduction in the number of reactive edge sites and basal plane defects, the low combustion reactivity of the residual carbon samples is not surprising.

Finally, we should consider what the residual carbon properties and reactivities may tell us about the combustion process in pulverized coal fired boilers. The boiler environment appears to induce significant crystalline order in chars, thereby reducing their oxidation reactivity relative to the chars formed in the laboratory. The primary differences between the two environments are (1) the much longer residence times in the boiler (approx. 1 sec vs. 70 msec), which leads both to more severe heat treatment and much higher extents of oxidation (> 99% vs. 20-60%) and (2) differences in peak particle temperature (1800 - 2400 K in boilers [16] vs. 1800 - 1900 K in the laboratory. The reactivity differences may also be influenced by differences in particle heating rates, although these are believed to be roughly similar in the two environments. The bulk of the residual carbon has been severely heat treated and oxidized — it is not a fraction of the feed that has bypassed high temperature regions due to poor mixing. Recent studies [8] have shown that subjecting the laboratory chars to further combustion to high conversions (> 80%), leads to loss of reactivity and near-extinction of the oxidation reaction. Low reactivities have thus been observed for highly reacted, highly heat-treated residues from both laboratory and commercial-scale combustors. This result implies that char combustion cannot be accurately modeled assuming a reactivity that is

phenomenon affecting the latter stages of combustion, and accounting for deactivation may be key to making more accurate predictions of unburned carbon levels in fly ash.

REFERENCES

1. Field, M. A. *Combustion and Flame* 1970 14 237
2. Smith I. W. *Combustion and Flame* 1971 17 303
3. Essenhigh R. H., in *Chemistry of Coal Utilization, Second Supp. Vol.* (M.A. Elliott ed.) John Wiley and Sons Inc., 1981
4. Hurt, R. H. and Mitchell R. E. *24th International Symposium on Combustion*, The Combustion Institute, Pittsburgh, PA, pp. 1243 - 1250, 1992
5. Walsh, P. M., Xie, J., Douglas, R. E., Battista, J. J., and Zawadzki, E. A. "Unburned Carbon Loss from Pulverized Coal Combustion," submitted to Fuel (1993).
6. Nandi, B. N., Brown, T. D., and Lee, G. K., *Fuel* 56 125 (1977).
7. Shibaoka, M. *Fuel* 64:263-269 (1985).
8. Hurt, R. H., Davis, K. A., and Hardesty, D. R. "Impact of Coal Quality on Coal Char Combustion, Final Report to EPRI". Sandia Technical Report June 1993
9. Mitchell R. E. *22nd International Symposium Combustion*, The Combustion Institute, p. 69, 1988.
10. Hurt, R. H. "Reactivity Distributions and Extinction Phenomena in Coal Char Combustion" submitted to *Energy and Fuels*, March 1993.
11. Ugarte, D. *Nature* 1992 359 707
12. Hecker, W. C., McDonald, K. M., Reade, W., Swensen, M. R., and Cope, R. F. *Twenty-Fou (International) Symposium on Combustion*, The Combustion Institute, Pittsburgh, 1992, pp. 12 1231.
13. Smith, I. W., and Tyler, R. J., *Fuel* 51:312-321 (1972).
14. Suuberg, E. M. in *Fundamental Issues in Control of Carbon Gasification Reactivity*, Kluwer Academic Publishers, 1991, pp. 269-305.
15. Davis, K. A., Hurt, R. H., Yang, N. Y. C., and Headley, T. H., "Evolution of Char Chemistry Crystallinity, and Ultrafine Structure during Pulverized Coal Combustion," submitted to the *Twe Fifth (International) Symposium on Combustion,* 1993.
16. Fletcher, T. H. personal communication, 1993.

ACKNOWLEDGMENTS

Financial support for this work is provided by the EPRI Office of Exploratory and Applied Research and the U.S. DOE Pittsburgh Energy Technology Center's Direct Utilization Advanced Research and Technology Development Program. The authors wish to acknowledge Hardarshan Valia of Inland Steel, Bruce Dyas of New England Power, John Sorge of Southern Company Services, and Donald Bull of Northern Indiana Public Service Co. for technical discussions and/or sample donation. The technical contributions of James Ross and Richard Yee are gratefully acknowledged.

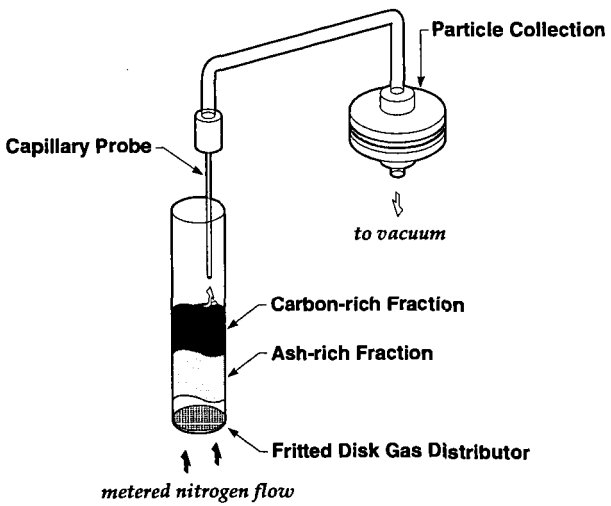

Figure 1. Residual carbon extraction by incipient fluidization.

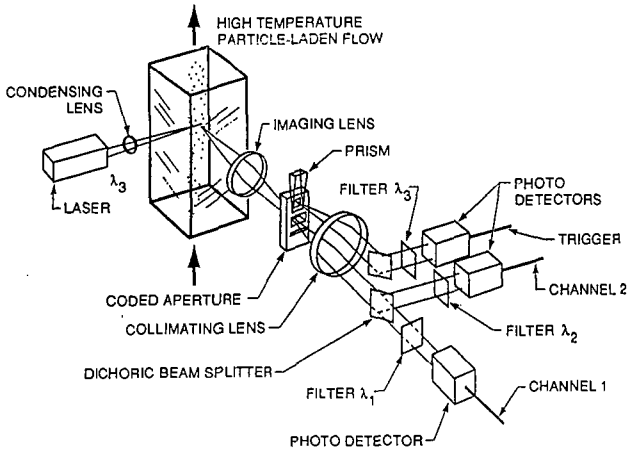

Fig. 2 The laminar flow reactor and optical diagnostic used for in situ measurement of particle size, temperature, velocity, and emissive factor.

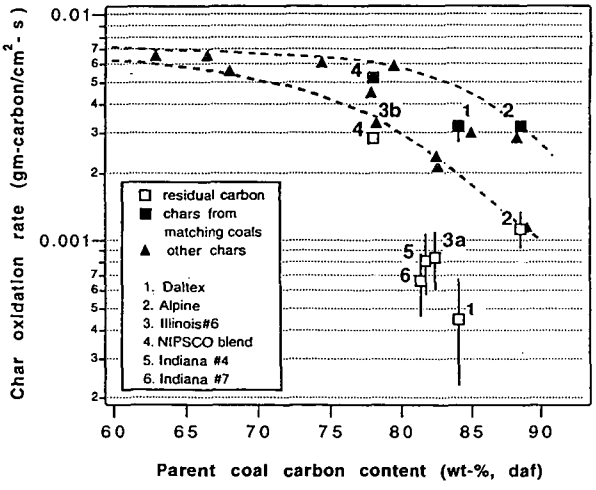

Figure 3 Combustion rates of various chars and residual carbon samples as a function of the carbon content of the parent coal. Gas temperature 1500 K; oxygen concentration 6 mol-%. Dashed curves indicate the range of reactivities observed for laboratory-generated chars at low-to-intermediate carbon conversion. Samples 3a and 3b both originate from Illinois #6 coals, but from two separate sources.

a.

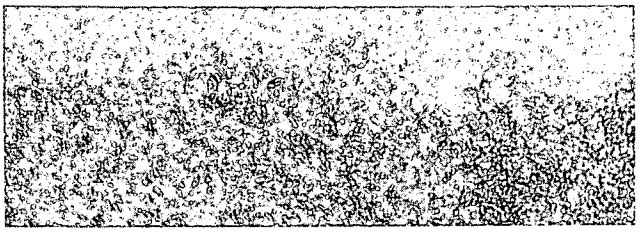

b.

Figure 4 High-resolution transmission electron fringe images of Illinois #6 chars with different combustion histories. a) char samples from Sandia's high-temperature entrained flow reactor after 72 msec of combustion in 12 mole-% oxygen, b) residual carbon from commercial-scale pulverized-coal fired boiler. Magnification 2,000,000x.

FLAME STRUCTURE OF SANDWICH SYSTEMS BASED ON AMMONIUM PERCHLORATE, HMX AND POLYBUTADIENE RUBBER STUDIED BY PROBE MASS-SPECTROMETRY AND MODELING.

A.A. Chernov, V.M. Shvartsberg, N.E. Ermolin, O.P. Korobeinichev, V.M. Fomin
Institute of Chemical Kinetics and Combustion
Siberian Branch Russia Academy of Science,
630090 Novosibirsk, Russia

Keywords: chemistry of combustion, solid propellant, mass-spectrometry, modeling

ABSTRACT

The structure of subatmospheric flames of sandwich-type systems consisting of alternating laminae of ammonium perchlorate (AP) or HMX and "base" (polymerized mixture of fine-grained AP and polybutadiene binder) has been studied. The burning surface shape as well as the profiles of concentrations for 17 stable components and of temperature for three crosssections corresponding to the middle of "base" lamina, and to the interface between the laminae have been determined. The hypothesis assuming the existence of three types of flames in sandwiches has been verified experimentally. A concentration gradient of fuel components has been observed at the burning surface of the oxidizer, directed towards the burning surface. Multizone structures and step-by-step mechanisms of reactions in AP and HMX flames have been confirmed. A numerical study for the flame structure of sandwich system based on AP and "base" have been carried out. A simplified set of equations obtained from a complete Navier-Stokes set with the limiting transition M ->0 have been used in order to construct a solution. Satisfactory agreement between calculated and experimental data on flame structure have been obtained.

INTRODUCTION

An important role in the combustion process for mixed solid fuel (MSF) is played by microflames caused by heterogeneous distribution of the oxidizing agent in the fuel-binder. The dependence of combustion rate on particle fineness and the effect of microflames on the formation of local thermal and diffusion flows point to the necessity of studying the local structure of flames. MSF consist of coarse-grained AP (particle size several hundred micrometers), the space between the particles being filled with the "base" - the mixture composed of a fuel-binder and fine-grained AP (particle size from a few micrometers to a few tens of micrometers) . Therefore, oxidizer - "base" sandwiches should be the best models for composite systems. Such sandwiches, however, have been considered only by Price and co workers / 1 /.The other studies performed hitherto dealt with sandwiches consisting of alternating laminae of oxidizer and fuel - binder. There are no published works on combustion of HMX - based sandwiches. The aim of this work was to study chemical and thermal structure of flame for sandwiches on the basis of AP or HMX and the "base" consisting of AP (<50 mkm) and carboxy terminated polibutadiene (CTPB).

EXPERIMENTAL

The sandwiches consisted as a rule of five alternating laminae: three AP (or HMX) laminae and two "base" laminae. An AP-based (system 1) was made of pressed AP plates (density 1.85 g/cm-3 , thickness 1.3 mm) and the laminae (thickness 1.0 mm) of polymer "base" - the mixture of fine - grained AP (particle size < 50 mkm) and CTPB in a 4:3 ratio. The mixed "base" laminae were prepared by polymerization in Teflon arrays at 100 `C for 24 hours. The sandwich samples were 4.8×6×10 mm. An HMX-based sandwich (system 2) was made of 1 mm thick HMX laminae (mixture of fine-grained AP and CTPB in a 73:27 ratio) . The sandwich dimensions were 4.2×6×12 mm.

Thermal structure of the flames was studied using thermocouples (tungsten- rhenium wires 30 and 50 mkm in diameter) embedded in propellant samples. Chemical structure of flame was analyzed by mass-spectrometric probing described elsewhere (2). Quartz cones: 15-20 mkm sampling orifice, 0.45 for system 1 and 0.15 for system 2 external tip diameters, 40-50 grad. interior angular openings. Systems 1 and 2 were examined in helium flow at pressures of 0.03 MPa and 0.053 MPa,burning rates 0.3 mm/s and 0.65 mm/s,respectively. In order to study the structure of burning surface and the shape of oxidizer and "base" laminae, the samples were quenched using rapid depressurization. At low pressures AP-lamina and HMX-lamina protrudes above "base" lamina approximately by 0.5 lamina thickness and has the shape close to a circle segment. At 4 MPa the "base" and AP laminae have similar V-shaped profiles.

SET OF EQUATIONS. METHOD OF SOLUTION

Flow at a MSF combustion surface is defined by Mach numbers of <0.003 and Reynolds numbers of 10-200 . A simplified set of equations obtained from a complete Navier-Stokes set with the limiting transition M -> 0 have been used in order to construct a solution. Thermal and diffusion flows are specified in accordance with (3). In (3). In the present studies in order to construct a solution a splitting method (4) combined with the method of artificial compressibility is used. On the basis of the calculations performed (5) a kinetic mechanism including 58 elementary stages and 35 components is separated.

RESULTS

The following components have been found out in the sandwich flames: H_2, NH_3, H_2O, C_2H_2, HCN, CO, N_2, NO, HCL, CO_2, N_2O, NO_2, CLOH, O_2, C_4H_6, CLO_2, CL_2, $HCLO_4$, whose mole fractions and temperature profiles are shown in figs. 1-2. Analysis of the data obtained testifies to the fact that there are two zones in the flame of sandwich-type system 1 in the cross section corresponding to the middle of AP lamina (fig.1a). The first zone adjoining the burning surface of AP is a narrow (about 0.2 mm) AP flame zone wherein ammonia is oxidized by HCLO4 and CLO_2 to yield NO, O_2,and other substances. In the second, more wide (about 3 mm) zone, O_2 and NO are consumed. Oxygen and nitric oxide are consumed in oxidation reaction of carbon monoxide with CO_2 and N_2 formation; HCN, C_2H_2 and H_2 are oxidized slowly. The experiments have shown that at the distances from sample surface longer than 5 mm CO and N_2 concentrations do not change. It should be noted that the fuel components, i.e. products of "base" destruction, HCN and $C2H_2$ penetrated right up to the oxidizer surface due to diffusion: there is a concentration gradient of the components, directed to the burning surface. These products can react with AP, that may be an additional source of heat release on the burning surface. On the other hand, the probability of such an interaction is confirmed by the work reported by Inami et al. (6), wherein AP decomposition in the presence of gaseous propylene has been studied.

Data on flame structure for system 1 in the crosssection corresponding to the middle of a "base" lamina (fig.1b) also indicate that there are two zones: a narrow (0.3 mm) zone of the oxidation of butadiene (fuel-binder destruction product) by CLO_2 and HCLO4 with formation of carbon monoxide and other substances and a wide (2-3mm) zone of consumption of ammonia, carbon monoxide, HCLO and accumulation of other substances due to their diffusion from the oxidizer lamina. Inhibition of ammonia oxidation in the presence of butadiene is observed.

Fig.2a shows profiles of mole fractions and temperature in flame of sandwich system 2 in the cross section corresponding to the middle of an HMX lamina. Chemical structure of the flame in this cross section is identical to the chemical structure of pure HMX flame at 0.1 MPa (7). Two zones may be distinguished. The first one is a narrow (of 0.2-0.3 mm width) zone of NO_2 and CH_2O consumption and accumulation of nitric oxide and other substances. The second, more wide (2-3 mm), zone is that of the oxidation of cyanic hydrogen by nitric oxide. As shown by Cohen et al. (8). the reaction of HCN with NO plays the principal role in the high temperature zone of HMX flame. The circularity of laminar system flame (HMX lamina) lies in the fact that cyanic hydrogen is oxidized by nitric oxide incompletely.This may by accounted for by thermal interaction between the laminae. The flame of HMX lamina transfers some heat of "base" flame, the temperature decreases (as compared to adiabatic temperature for HMX), and the rate of the HCN + NO reaction decreases. On the other hand, HMX lamina in the condensed phase receives a portion of the "base" laminaheat and HMX becomes able to burn steadily at 0.053 MPa (at this pressure pure HMX burns unsteadily). The data obtained on HMX flame structure confirm the mechanism adopted by Bizot et al. (9) in the model for HMX combustion and are consistent with data reported by Kubota and co workers (10). The main reaction in the zone adjacent to the HMX burning surface and responsible for the heat transfer to the condensed phase is seemingly the reaction between NO_2 and CH_2O and not the decomposition reaction of HMX vapors, as it was assumed earlier (8, 11).

RESULTS OF CALCULATION

Fig 3 shows results of computer simulation of AP-based sandwich flame (system 1) at=0.03 MPa: profiles of mole fractions H_2, HCN, $C2H_2$, the shape of combustion surface between the central layer AP (Z=1.2) and the central layer "base" (Z=0) together with field of velocity (standardized to 1.5 m/sec), the isoline of HCN concentration and temperature. Calculations were carried out for plane-parallel and asymmetrically flows on curvilinear grids with a number of nodes 20×20, condensed in regions of higher gradients.Blowing mixture from the combustion surface takes a direction on the normal to the surface. At the combustion surface depending on the pressure, the values of temperature, rate, and molar fractions of components Ai are prescribed. At low pressures Ai corresponds to the experiment, and at high pressures to rough extrapolation of data for combustion of AP and a layered system. At the lower and upper boundary of the calculation region conditions are prescribed, and at the outlet conditions are extrapolated. The temperature of the combustion surface in calculations is prescribed by the

relationship $T=673+30\times(1+\cos(\pi(1-Z/1.2))$ and it equals the experimental temperature with Z=0 and Z=1.2 mm. In both calculations and the experiment a broad mixing layer is observed washing the combustion surface, although there is no total mixing in the region with right-hand boundary X= 3 mm. The reaction occurs in kinetic region, and the temperature field in sections X= const (see Fig.3) levels out the concentration fields more intensely. Good agreement of calculations and the experiment is observed. The value for thermal flow over normal to the combustion surface is provided below (W/m^2): 1×10^5(Z=1.2), 2×10^5 (Z=0.55), 3×10^5 (Z=0).The ratio of this flow to similar flow for a plane combustion surface reaches a maximum value of 2.4 at Z=1.2 mm. At high pressures the difference in thermal flows of the combustion for plane -parallel and asymmetries flows does not exceed 3%. The point with the maximum value of thermal flow shifts in the direction of oxidizing agent.

REFERENCES

1. Price E.W., Sambamurthi J.K. et al., Comb. and Flame, 63, 381 (1986).
2. Ermolin N.E., Korobeinichev O.P., Tereschenco A.G., Fomin V.M., Comb., Explos. and Shock Waves, 1, 18, 36 (1982).
3. Ermolin N.E., Korobeinichev O.P.,et al., Khim. Fiz.,N12,p.1711(1982).
4. Kovenya V.M. and Yanenko N.N., The Spiltting Method in Problems of Gas Dynamics (in Russian), Nauka,Novosibirsk (1981).
5. Korobeinichev O.P.,Chernov A.A.,et al., Fiz. Gorenia Vzryva,26,3,46(1990)
6. Inami S.H., Ragapakse Y.H., Wise H. Comb. and Flame, 17, 189 (1971)
7. Korobeinichev O.P.,et al.,Comb. Explos. and Schock Waves, 20,3,282(1984).
8. Cohen N.S.,Lo G.A.,Crowley L.H. AIAA-Journal, 23, 2, 276 (1985).
9. Bizot A.,Bekstead W.M.. A model for HMX propellant combustion. Paper at the 3-rd Int. Seminar of Flame Structure, Alma-Ata, 1989.
10. Kubota N.,Sakamoto S., Propellants, Explosives, Pyrotechnics, 14, 6(1989).
11. Ben-Reuven M.,Caveny L.H. AIAA-Journal, 19, 10, 1276 (1981).

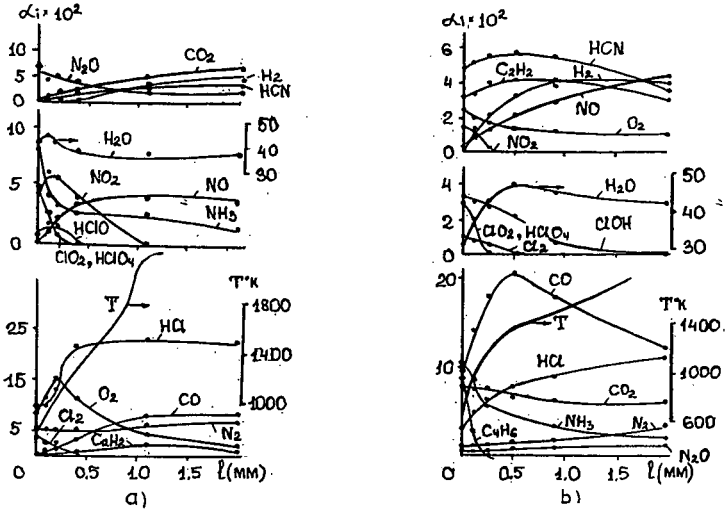

Fig.1. Mole fractions of combustion products and temperature profiles in the AP-based sandwich (system 1) flame obtained by mass-spectrometr probing in the transection corresponding the middle of : a) AP lamina b) "base" lamina

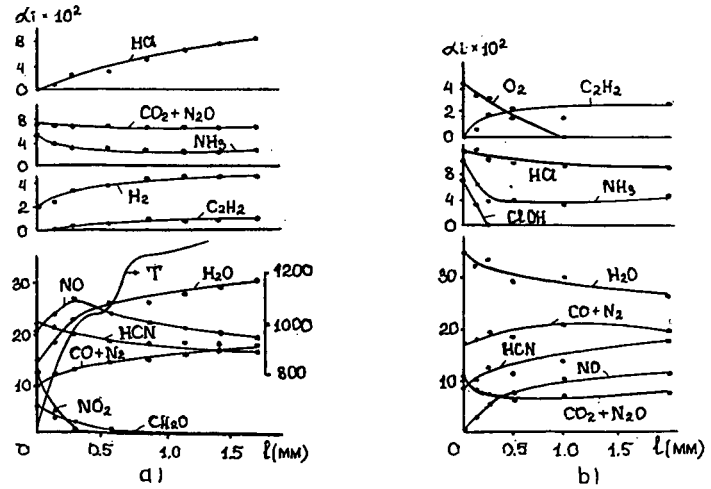

Fig.2. Experimental date of probing HMX-based sandwich flame : a)HMX lamina , b) "base" lamina

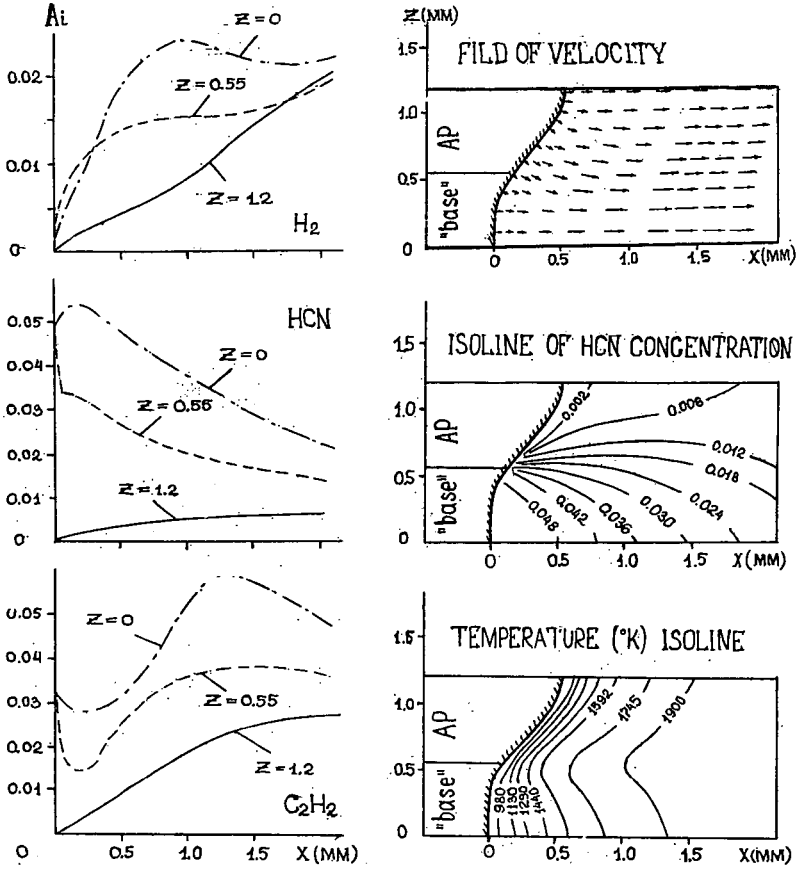

Fig.3. Results of computer simulation of AP-based sandwich flame (system 1) at P=0.03 MPa

MASS-SPECTROMETRIC INVESTIGATION OF THE STRUCTURE OF A STOICHIOMETRIC $H_2/O_2/Ar$ FLAME DOPED WITH TRIMETYLPHOSPHATE AND N-TRIBUTYLPHOSPHATE

O.P. Korobeinichev, A.A. Chernov, V.M. Shvartsberg
Institute of Chemical Kinetics and Combustion
Siberian Branch Russia Academy of Sciences,
Novosibirsk,630090 Russia

Keywords: chemistry of combustion, waste incineration, mass spectrometry

ABSTRACT

Molecular beam mass-spectrometry was used to study the structure of a stabilized premixed H_2 / O_2 / Ar (25.4% / 12.7% / 61.9%) flame without and with additives (0.034% TMP-trimethylphosphate or TBP-tributylphosphate) at 80 torr (burner temperature: 85°C). The behavior of the TMP, TBP in flames and reactions leading to their destruction in flames have been studied. The promoting effect of the additive on the flame was observed, i.e. in the presence of the additive the combustion zone considerably decreases. Mass-spectrometric analysis of the species sampled from different flame zones, performed under soft ionization (at low ionization energies), was used to identify the intermediate and end products of the reactions destroying TMP in the flame, to measure the concentration profiles of some components in the flame related to these reactions. The data obtained testify that the primary products of the reaction of TMP destruction are either dimethylphosphate or dimethylphosphite or both of them. CH_3OH, CH_2O, CH_3O and the compound, the mass-spectrum of which contains the peak with m/e=80 (possibly, CH_5O_2P) were recorded as intermediates. The zone of TBP reacting in the flame is a bit narrower than that of TMP. Butene was registered as intermediate in an $H_2/O_2/Ar$ flame doped with TBP. The distributions of mass peak intensities with m/e=64 (HPO_2^+), 63 (PO_2^+), 48 (HPO^+), 47 (PO^+) in flames, characterizing the corresponding phosphorous containing components of the $H_xP_yO_z$ type were measured. The data obtained indicate the following sequence of the transformations of these components in flame:

$$HPO_2 , PO_2 \Rightarrow PO$$

The possible mechanisms of TMP and TBP transformations in the $H_2/O_2/Ar$ flame are discussed.

INTRODUCTION

The combustion of organophosphorus substances (OPS) is of a great interest in connection with the disposal of toxic and hazardous chemical wastes and other undesirable substances that frequently contain these classes of compounds. One of the most promising techniques for the disposal of wastes is their incineration which provides a high destruction degree of toxic and hazardous substances. However, for better reliability and control over these processes one should know the details of the mechanism of their combustion and especially their chemistry. One of the typical representatives of the class of toxic OPS is the class of alkylophosphates. On the one hand, some of these are industrial wastes (e.g. tri-n-butylphosphate is the product of uranium ore treatment). On the other hand, these can be the models for studying the problems of the incineration of pesticides and the components of a chemical weapon. The chemistry of OPS combustion is practically not understood. The interest in the behavior of phosphorous containing substances in flames is not limited by the problem of their destruction. These substances (e.g. trimethylphosphate, phosphine) can play the role of inhibitors or promoters of the combustion process. These questions were the object of studies in references 1, 2, and 3. The aim of the present paper is to study 1) the behavior of trimethhylphosphate (TMP) and n-tributylphosphate (BP) as the simplest representatives of OPS in a well-studied flame of $H_2/O_2/Ar$ stabilized at low pressure on a flat burner and 2) the chemistry of reactions leading to the destruction of TMP in a flame by identifying intermediate and end products (including atoms and radicals) by their mass-spectra, measuring the concentrations and concentration profiles of initial, intermediate and end products. This could be the basis for developing the model of TMP combustion as one of the simplest OPS.

EXPERIMENTAL

The premixed $H_2/O_2/Ar$ (25,4/12,7/61,9) flames of a stoichiometric composition without additives and with TMP (0.034%) or TBP (0.04%) were stabilized at 80 Torr on a flat Spolding-Botha burner[4] 24 mm in diameter a brass disc with about 250 holes with diameter 0.7 mm each. The total consumption of the gas mixture was 65 cm/s (NTP). With such a burner, the flames at 80 Torr are sufficiently one-dimensional. A quartz cone, 15 mm high ,with an apex angle of 40 degrees, and a 0,17 mm diameter orifice, the width of walls at the top 0,15 mm was used. The probe was coupled with the flange of stainless steel cooled with water. TMP was

supplied by a peristaltic pump or chromatographic syringe to the evaporator into the flow of preliminary mixed and heated to 85°C combustible mixture. Further the mixture passed to the burner. The temperature of the evaporator and the burner was kept equal to 85°C (in the case of TMP) or 150°C (in the case of TBP) with the help of a thermostat. Flame temperature was measured using a platinum - platinum with 10% rhodium microthermocouple weld of wires with a diameter of 50 microns and covered with a layer 10 microns thick. The thermocouple shoulder was 10 mm. The correction for radiation losses was introduced into the readings of the thermocouple. A molecular beam sampling technique coupled to a quadrupole mass-spectrometer was used for analysis of species and measurement of their concentrations in the flame.

The mass-spectrometric setup with molecular-beam sampling is partially described in reference 5. Synchronous detecting was used to record the modulated component of the molecular beam under ion-counting conditions. The modulation frequency was 12,5 Hz. The mass-spectrometer was supplied by an ion source with a small spread of electrons in energies (± 0.1eV) which allowed us to work at low ionization energies close to the ionization potentials of atoms, radicals and molecules. The number of accumulations was 80-400. The concentrations of stable species are determined by direct calibration at ambient temperature by a procedure reported by Peeters and Mahnen[6]. The uncertainty in the stable species concentration is estimated as ± 10%.

RESULTS

The probe is known to perturb the flame. In this case the lines of equal concentrations near the probe tip shift relative to the unperturbed flame. The value of this shift can be estimated from the formula[7] $Z=0.4\ D_o A_o(1/2)$, where D_o is the diameter of probe orifice; A_o is the sampling degree depending on the volumetric rate of sampling and the rate of the flow. For the flame described and the probe used, Z=0,65 mm. Although this value is small compared to the width of the combustion zone (2-3 mm), in the represented data this shift was taken into account. In the profiles of measured concentrations the origin of coordinates along the abscissa was put at the distance of 0,65 mm from the burner surface. Figures 1-3 show the data of the study of the structure of the above mentioned flames.

The data in Figure 1 are the experimentally measured profiles of temperature and concentrations of H_2, O_2, H_2O, and TMP in the flames with and without TMP. Figure 1 shows also TBP concentration profile in H_2/O_2/Ar flame, doped with TBP. It is seen that small additions of TMP promote combustion process causing an appreciable decrease in the combustion zone width. The zone of TMP reacting is about 1,5 mm and is a bit narrower than that of oxygen and hydrogen in the flame. The same effect of promotion in the H_2/O_2/Ar flame was observed at the addition of TBP. The zone of TBP reacting is a bit narrower than that of TMP. The chemistry of TMP transformations in the flame was studied by measurements of the profiles of peak intensities of masses related to the possible intermediate and end products of TMP transformations at low ionization energies close to the ionization potentials of these products. Several such products have been found. Figure 2 gives the profiles of mass peak intensities with m/e=32 (CH_3OH^+), 31 (CH_3O^+), 30 (CH_2O^+) and 140 (TMP^+) and 110 ($C_2H_7O_3P^+$) in the flame. These were measured for different U. The peak with m/e=110 is present in the TMP mass-spectrum as a fragmentary ion $C_2H_7O_3P^+$ with the appearance potential 11,9 ± 0.2eV[8]. With U=11.6 eV there is practically no contribution to the 110 peak of the fragmentary ion upon TMP ionization. So the m/e=110 peak intensity characterizes the concentration profile of the intermediate products resulting from TMP reacting. Such product can be represented either by DMP (dimethylphosphate $(CH_3O)_2P(O)H$) or DMP* (dimethylphosphite $(CH_3O)_2POH$) or their mixture. The possible reactions that can lead to the formation of DMP are the following:

$$(CH_3O)_3PO + H \Rightarrow (CH_3O)_2P(O)H + CH_3O$$
$$(CH_3O)_3PO \Rightarrow (CH_3O)_2P(O)H + CH_2O$$

Preferable is the first one. The reaction of DMP isomerization leading to the formation of dimethylphosphite can proceed in parallel. This can, probably, account for the existence of the two maxima on the curve of ($C_2H_7O_3^+$). CH_3OH^+ and O_2^+ contribute to the peak with m/e=32. The contribution of O_2^+ was taken into account by measuring the peak with m/e=34 (oxygen isotope).

In the profile of peak intensity with m/e=32 in Figure 2 the contribution of O_2^+ ion is subtracted. This profile thus characterizes the concentration profile of CH_3OH. The CH_3OH formation can be explained by the reaction:

$$CH_3O + H_2 \text{ --> } CH_3OH + H$$

Because the intensity of this peak with m/e=31 (CH_3O) was measured with ionization energy

U=11,6 eV which is less than the potential of the appearance of this peak (PA=12,6 eV) in the mass-spectrum of CH_3OH, the profile of CH_3O^+ intensity in Figure 2 characterizes the concentration profile of CH_3O radical. The profile of the m/e=30 peak intensity characterizes the concentration profile of CH_2O, because the intensity of this peak was measured for an ionization energy U=16,5 eV, almost equal to the potential of CH_2O^+ ion appearance in the spectrum of CH_3OH (AP=16,3 eV). Note also the spatial separation of the concentration profiles of CH_3OH and CH_2O is pointing to the sequence of transformations upon CH_3OH oxidation in the flame.

Figure 3 presents the profiles of mass peak intensities with m/e=80 ($CH_3O_2P^+$, HPO_3^+), 64 (HPO_2^+), 63(PO_2^+), 48 (HPO^+) and 47 (PO^+) with U=13,1eV in the flame. Analyzing the behavior of these peaks in the flame, it is assumed that the contributions to the peak with m/e=47 of the PO^+ fragmentary ion, forming from PO_2, HPO_2, and HPO ionization, are rather small. Therefore the profiles of the intensities of mass peaks with m/e=47 and 64 characterize the concentration profiles of PO and HPO_2. The maximum in the profile of peak intensity with m/e=80 is in the range between two maxima in the peak intensity profile with m/e=110 which can be attributed to the formation of CH_5O_2P product due to DMP reaction or the reaction of DMP* with hydrogen atom. The behavior of the profiles of mass peak intensities with m/e=64, 63, 48, and 47 points to the following sequence of $H_xP_yO_z$ compound transformations in the flame:

$$HPO_2, PO_2 \Rightarrow PO$$

The errors in the measurements of the intensities of mass peaks in Figures 2 and 3 are: m/e=140 ±3%; m/e=110, 30, 32 ±10-20%; m/e= 47, 48, 63, 64 ±20%; and m/e= 31, 80 ±50%. The promoting effect of TMP on H_2/O_2 combustion can be explained as in reference 3 by the influence of phosphorous oxides on the reaction of H and OH recombination:

$$H + PO_2 \Rightarrow HOPO$$
$$OH + H_2 \Rightarrow H_2O + H$$
$$H + HOPO \Rightarrow H_2 + PO_2 .$$

REFERENCES

1. Hastie,J.W.; Bonnell,D.W. *Molecular Chemistry of Inhibited Combustion Systems*, National Bureau of Standards Report No. NBSIR, **1980**, 80-2169.
2. Hastie,J.W. *J. Res. N.B.S. Sect.A.*, **1973**, *77*, 733.
3. Twarowski,A. *Combust. and Flame*, **1993**, *94*, 91-107.
4. Botha, J.P.; Spalding, D.B. *Proc. R.. Soc. Lond. A 225*, **1954**, 71-96.
5. Amosov,K.A.; Kuibida,L.V.; Korobeinichev,O.P.; Bol'shova, T.A. *Flame Structure* (Ed. O.P. Korobeinichev) Novosibirsk: Nauka S.B., **1991**, *1*, 93.
6. Peeters,J.; Mahnen,G. *Fourteenth Symposium (International) on Combustion*, The Combustion Institute: Pittsburgh, **1973**, 133-146.
7. Korobeinichev, O.P.; Tereschenko, A.G.; Emel'yanov,I.D.; Rudnitskii, A.L.; Fedorov, S.Yn.; Kuibida, L.V.; Lotov, V.V. *Fiz. Goreniya Vzryva*, **1985**, *21*, 5, 22-28.
8. Bafus, D.A.; Gallegos,E.J.; Kiser, R.W. *J. Phys. Chem.*, **1966**, *70*, 8, 2614-2619.

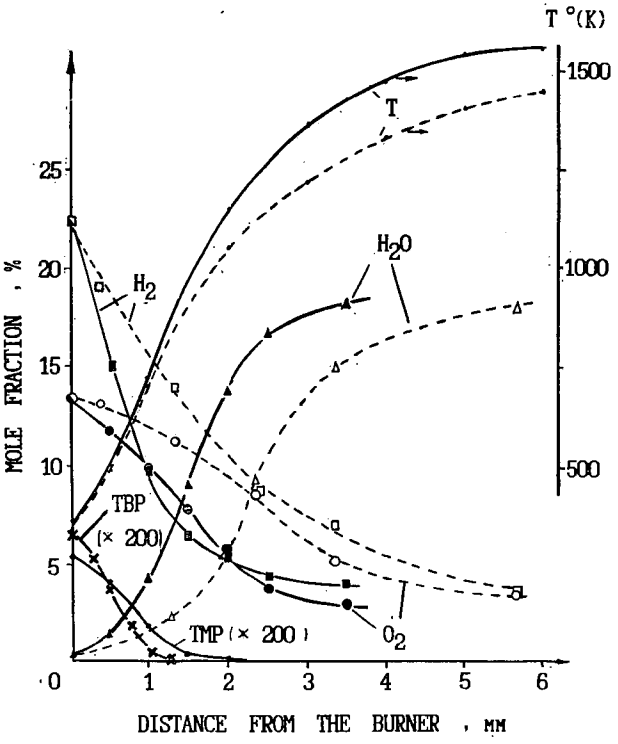

Fig. 1 The profiles of temperature and concentrations of components in H2/O2/Ar flame without additions:T,H2, O2, H2O - dotted lines; and with additions of TMP:T,H2, O2, H2O, TMP and with addition of TBP; TBP - solid lines.

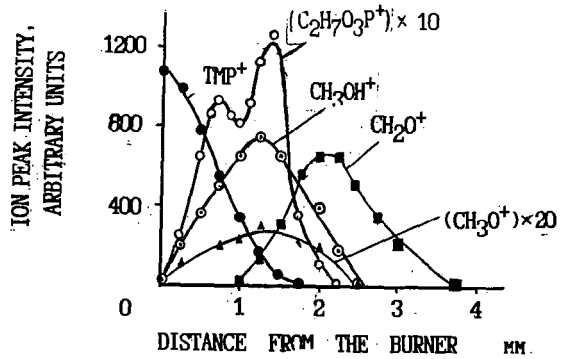

Fig. 2 The profiles of the intensities of mass peaks in the H2/O2/Ar flame with TMP additive with: m/e=32 (CH3OH+), U=13.1eV; m/e=140 (TMP+), U=13.1eV; m/e=31(CH3O+), U=11.6eV; m/e=30 (CH2O), U=16.5eV ; m/e=110(C2H7O3P+),U=11.6 eV

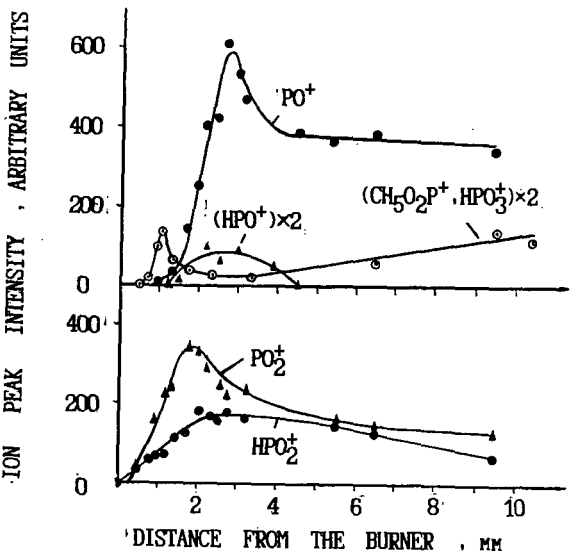

Fig. 3 The profiles of the intensities of mass peaks in the H2/O2/Ar flame with TMP additive with: m/e=47(PO+),48(HPO+), 63(PO2+), 64(HPO2+), 80(HPO3+, CH5O2P+). U=13.1eV.

thought to arise from the cyclized carbon attached to the exocyclic methylene (carbon 8). The peaks resonating at 127ppm and 138ppm in the spectrum of the Yallourn resinite have been assigned to the protonated (carbon 12) and quaternary (carbon 13) carbons of the side chain double bond by chemical shift comparisons with model compounds (27-28) and by previously reported dipolar dephasing experiments (12). Relative peak areas for each resonance in the olefinic region as well as the total olefinic carbon content of the spectra indicate that the total olefinic content, in a 20 carbon structural unit, progressively decreases from approximately 4 carbons per monomer in the spectrum of the Yallourn resinite to approximately 2 carbons per monomer in the spectrum of the Brunner resinite. As the thermal maturation of the resinite increases, there is a decrease of nearly 50% for the olefinic carbons in the samples being studied. This loss corresponds to the transformation of diterpenoids containing two double bonds (polycommunic acid units) to diterpenoids having only one double bond.

Integration of the carboxylic acid resonances, peaks at 186ppm and 181ppm, of the spectra of the Yallourn and Morwell resinites and 186ppm, 181ppm and 177ppm for the spectrum of the Brunner resinite, yielded values of 0.8, 0.7, and 0.5 carbons per monomer, respectively. As the degree of maturation increases, there appears to be a decrease in intensity of the peaks resonating at 186ppm and 181ppm with an additional resonance in the carboxyl region centered around 177ppm visible in the spectrum of the Brunner resinite. The broad peak resonating between 201ppm and 210ppm in the spectra of the Morwell and Brunner resinites has been assigned to ketones resulting from oxidation (18).

The intramolecular cyclization of the exocyclic methylene to form a mono-unsaturated C ring (Figure 2), is entirely consistent with pyrolysis and NMR data. The positioning of the double bond between carbons 8 and 17 (of the communic acid monomer) will stabilize the B and C rings thus making cleavage of the A ring rather than the B or C rings the more likely site of pyrolysis. The compound(s) expected to dominate the pyrolysis of a polymeric tricyclic acid (as described above) are alkyl naphthalenes and alkyl hydronaphthalenes. With this information, the combined results of the quantitative NMR data and py/gc/ms data, it is possible to rule out proposed mechanisms of maturation other than that of intramolecular cyclization which appears to correlate with all the chemical data.

SESQUITERPENOID-TYPE RESINITES

The general consensus regarding the structure of sesquiterpenoid resinites is that the maceral exists as two fractions. One fraction consists of a high molecular weight (HMW) polymer proposed to be that of polycadinene (PC)(30) and the second fraction is composed of low molecular weight compounds shown by gas chromatography/ mass spectrometry (GC/MS) to be dimers and trimers of cadinene and functionalized triterpenoids (30-32).

In this report, we will discuss the results of a series of experiments which were carried out in an effort to characterize the polymeric fraction of an immature resin, a precursor to sequiterpenoid-based resinites. By examining the structure of polycadinene from a young resin such as a Dammar resin, we would be able to compare these structural characteristics with those of more mature resinites such as that described from the Blind Canyon coal (33-34). From this comparison the chemical changes that accompany the maturation process can be identified thus further aiding in the structural identification of the Blind Canyon coal's resinite maceral.

The Dammar resin was chosen due to its availability in a relatively pure form. In addition, this particular resin is extremely soluble in $CDCl_3$. Solubility in $CDCl_3$ was an important consideration, since NMR was chosen as the primary structural tool for this study. NMR techniques, which include one- and two-dimensional NMR spectra, were used in this study to determine the consistency of the structure of a high molecular weight methanol insoluble fraction of the Dammar resin (the polycadinene biopolymer as suggested by van Aarssen et al.(30)) with that of a theoretical polycadinene polymer and to propose possible chemical alterations induced during catagenesis.

The resin selected for this study is a commercially available Dammar resin purchased from Aldrich Chemical Co. The Dammar resin was first dissolved in 50 mL of hexane then approximately 5 mL of methanol was added to precipitate the polymer as a white powder following the procedure described by van Aarssen et. al. (30). The powder was then separated by centrifugation and washed with methanol. The methanol was evaporated and replaced with approximately 0.6 mL of $CDCl_3$, a solvent suitable for NMR spectroscopy.

The high resolution liquid ^1H and ^{13}C NMR experiments were performed on a Bruker AMX-360 spectrometer equipped with a 5mm inverse-detected probe. The one-dimensional single pulse ^1H and ^{13}C experiments were carried out using a 30^0 flip angle. The ^{13}C distortionless polarization transfer (DEPT) experiments were carried out using 45^0 (3.3 µs), 90^0 (6.6 µs), and 135^0 (16.5 µs) ^{13}C read pulses, respectively. A solid state ^{13}C CPMAS spectrum was obtained on a Chemagnetics M-100 NMR spectrometer. The pertinent parameters are found elsewhere (33). A two-dimentional high resolution liquid experiment COSY (homonuclear correlation) with a 45^0

read pulse was performed on the HMW fraction isolated from the Dammar resin using a standard Bruker experiment.

Elemental analyses of the methanol insoluble fraction of the extant Dammar resin as well as previously reported data for resinite from the Blind Canyon coal can be seen in Table 1. Included in Table 1 are the calculated oxygen and hydrogen weight percentages of a pure polycadinene polymer (structure shown in Figure 4), which has the monomeric formula $C_{15}H_{26}$, and the monomeric formula of the HMW Dammar polymer. It can be infered from this table that the polymeric constituent of the Dammar resin does not differ significantly from that of the Blind Canyon resinite. Also evident in this table are the considerable differences between the polymer isolated from the extant Dammar resin and that of a pure polymer composed solely of cadinene monomers. The Dammar PC elemental data suggests the presence of approximately one oxygen atom for every two cadinene monomers (assuming 15 carbons per monomer) and two less hydrogen atoms than the cadinene's 26.

^{13}C NMR was used to identify the functional groups and substitution patterns of the carbons present in the polycadinene fraction of the Dammar resin. Figure 5a-d shows high resolution ^{13}C NMR spectra of the polycadinene from Dammar resin in $CDCl_3$. Figure 5a is a quantitative decoupled ^{13}C NMR spectrum, while Figures 5b-d are the ^{13}C distortionless polarization transfer (DEPT) used to aid in assigning carbon substitution. The aliphatic region of the spectrum (0 ppm to 60 ppm) is extremely complex and contains a number of sharp signals far greater than what can be anticipated for pure polycadinene. The olefinic region of the spectrum (120 ppm to 140 ppm) is not as complex, however, but it is still not consistent with the structure of a pure cadinene monomer. In cadinene, there are two olefinic carbons with one being a tertiary carbon and the other a quaternary carbon. The spectrum shows at least four peaks.

The spectra shown in Figures 5b-d are the three ^{13}C DEPT experiments (45^o, 90^o, and 135^o). From these spectra and the spectrum in Figure 5a, the functional group assignments can be made. Chemical shift analysis of the spectrum in Figure 5a is used as a preliminary means of assigning carbon substitution, while the DEPT spectra provide a means of sorting or spectrally editing the signals. For example, the DEPT 45^o spectrum contains CH_3, CH_2, and CH carbons with the most intense signals emanating from the CH_2 carbons. The DEPT 90^o spectrum contains only CH carbons, and the DEPT 135^o spectrum contains positive signals from the CH and CH_3 carbons, but negative signals from the CH_2 carbons. Thus when the results from the three DEPT specta are combined all the protonated carbons can be assigned. The non protonated carbons are assigned by difference from the ^{13}C broadband decoupled spectrum.

To further aid in the structural elucidation of the Dammar HMW resin polymer, two dimensional (2D) NMR data was obtained. 2D-NMR is capable of correlating and spreading out NMR spectral data thus providing a means of confirming one dimensional spectral assignments while at the same time providing structural information concerning molecular connectivity. The 1H-1H correlation spectrum (COSY) for the HMW fraction of the Dammar resin is shown in Figure 6. From the two dimensional NMR spectrum it is possible to determine the association of protons in the one dimensional spectrum.

It is clear from the detailed NMR studies presented here that the HMW polymer isolated from Dammar resin is not purely polycadinene. By examination of the olefinic region, we observe at least four peaks indicating four different environments where only two would be expected in a pure polymer of polycadinene. Integration of these peaks indicates that approximately 1.5 olefins are present per 15-carbon unit, and we would expect 2 such carbons in the pure polymer. The aliphatic region contains many more peaks than would be expected for pure polycadinene. These results suggest that the polymer from Dammar resin is not represented by a pure polycadinene structure. We suggest that the general structural makeup of the polymer is similar to the polycadinene structure but that only two of three units contain olefinic carbons, the other is fully saturated. In addition, on average the olefinic carbons in two units containing such carbons are not at the same site in the structure. This would account for four peaks being present in the NMR spectra. The structure shown in Figure 4 depicts our model for polycadinene structures which comprise sesquiterpenoid resins.

References

1. Dyrkacz, G. R., Horwitz, E. P., *Fuel*, **61**, 3, 1982.
2. Dyrkacz, G. R., Bloomquist, C. A. A., and Ruscio, L., *Fuel*, **63**, 1367, 1984.
3. Greenwood, P. F., Zhang, E., Vastola, F. J. and Hatcher, P. G., *Anal. Chem.*, **65**, 1937, 1993.
4. Stout, S. A. and Hall, K. J., *J. Anal. Appl. Pyrol.*, **21**, 195, 1990

5 Stout, S. A., Boon, J. J. and Spackman, W., *Geochim. Cosmochim. Acta*, **52**, 405, 1988.
6 Hatcher, P. G., *Organic Geochemistry*, **16**, 959, 1990.
7. Faulon, J. L.and Hatcher, P. G., *Energy & Fuels* (in press).
8. Hatcher, P. G., Wenzel, K. A. and Faulon, J.-L., Preprints, American Chemical Society Fuel Division, **38**, 1270, 1993.
9. Langenheim, J. H. *Science*, **163**, 1157, 1969.
10. Brooks, J. D. and Stevens, J. R., *Fuel*, **46**, 13, 1967.
11. Cunningham A., Gay, I. D., Oehschlanger, A. C., and Langenheim, J. H., *Phytochem*, **22(4)**, 965, 1983.
12. Wilson, M. A., Collin, P. J., Vassallo, A. M., and Russel, N. J., *Org. Geochem.*, **7(2)**, 161, 1984.
13. Anderson, K. A., Botto, R. E., Dyrkacz, G. R., Hayatsu R., and Winans, R. E., *Fuel*, **69**, 934, 1990.
14. Thomas, B. R., *Organic Geochemistry - Methods and Results, Springer-Verlag*, 599-618, 1969.
15. Carman, R. M., Cowley, D. E., and Marty, R. A., *Aust. J. Chem.*, **23**, 1655, 1970.
16. Beck, C. W., *Appl. Spec. Rev.*, **22(1)**, 57, 1986.
17. Vassallo, A. M., Liu, Y. L., Pang, L. S. K., and Wilson, M. A., *Fuel*, **70**, 635, 1991.
18. Wilson, M. A., Hanna J. V., Cole-Clarke, P. A., Greenwood, P. F., and Willett, G. D., *Fuel*, **71**, 1097, 1992.
19. Wilson, M. A., Hanna J. V., Cole-Clarke, P. A., Willet G. D., and Greenwood, P. F., *Org. Geochem.*, **18(4)**, 555, 1992.
20. Anderson, K. B., Winans R. E., and Botto R. E., *Org. Geochem.*, **18(6)**, 829, 1992.
21. Challinor, J. M., *J. Anal. Appl. Pyrol.*, **16**, 323, 1989.
22. Nobes, E. D., *Trans. R. Soc. South Aust.*, **46**, 528, 1992.
23. Suggate, R. P., *N.Z.J. Sci. Technol.*, **B31(4)**, 1, 1950.
24. Grimalt J. O., Simoneit, B. R. T., Hatcher, P. G., and Nissenbaum A., *Org. Geochem.*, **13**, 677, 1988.
25. van Aarssen, B. K. G., and Deleeuw, J. W., *Am. Chem. Soc. Div. Fuel Chem. Prepr.*, **36(2)**, 774, 1991.
26. van Aarssen, B. K. G., and Deleeuw, J. W., *Geochem. Cosmochim, Acta.*, submitted for publication, 1992.
27. Clifford, D. J., and Hatcher, P. G., *Org. Geochem.*, submitted for publication, 1993.
28. Wenkert, E., and Buckwalter, B. L., *J. Am. Chem. Soc.*, **94(12)**, 4367, 1972.
29. Lambert, J. B., and Frye, J. S., *Science*, **217**, 55, 1982.
30. van Aarssen, B. G. K., Cox, H. C., Hoogendoorn, P., and de Leeuw, J. W., *Geochem. Cosmochim. Acta.*, **54**, 3021, 1991.
31. Crelling, J. C., Pugmire, R. J., Meuzelaar, H. L. C., McClennen, W. H., Huai, H. and Daras, J., *Energy & Fuels*, **5**, 688, 1991.
32. Meuzelaar, H. L. C, Huai, H., Lo, R. and Dworzanski, J. P., *Fuel Proc. Technol.*, **28**, 119, 1991.
33. Clifford, D. J., Hou, L., Bortiatynski, J. M. and Hatcher, P. G., Technical Progress Report February - 1993, Prepared for the U.S. DOE under Contract No. DE-FG22-92PC92104.
34. Hou L., Clifford, D. J., Bortiatynski, J. M., and Hatcher, P. G., Technical Progress Report October - 1993, Prepared for the U.S. DOE under Contract No. DE-FG22-92PC92104.

Table 1 . Ultimate analysis (DMMF) of the HMW fraction from a Dammar resin, the resinite from a Blind Canyon coal sample, and pure polycadinene.

Sample	% C	% H	% O	Monomeric Formula
HMW polymer (Dammar)	84.2	11	4.8	$C_{15}H_{24}O_{0.65}$
Whole resinite (DECS16)	86.2	10.4	3.4	
Polycadinene (pure polymer)	87.3	12.7	0	$C_{15}H_{26}$

*Obtained by difference.

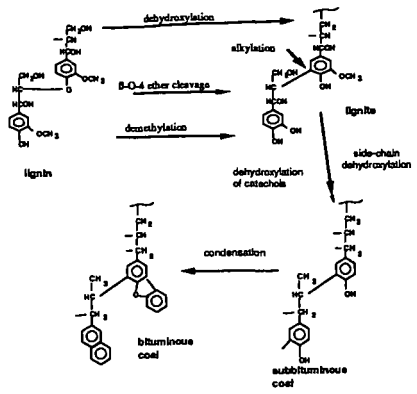

Figure 1. Sequence of reactions proposed for the coalification of lignin in wood to coalified wood of the rank of bituminous coal.

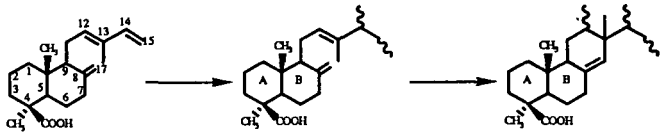

Figure 2: Polymerization of communic acid to *trans* -14,15-polycommunic acid followed by the intamolecular cyclization of carbons 17 and 13.

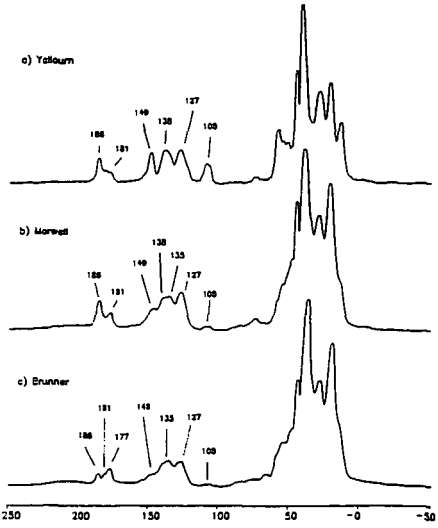

Figure 3: ^{13}C CPMAS NMR of diterpenoid resinites.

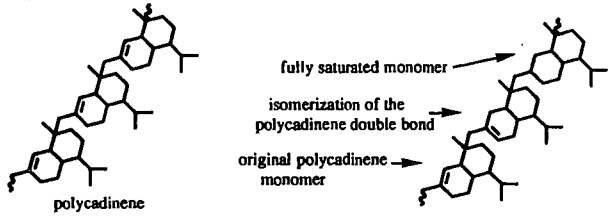

Figure 4: Polycadinene polymer and polymer containing possible transformations of the cadinene monomers.

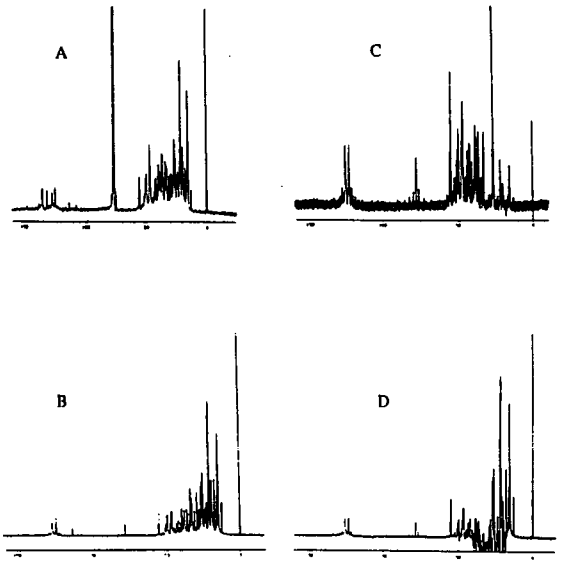

Figure 5: ^{13}C broadband decoupled (A), 45° DEPT (B), 90° DEPT (C), and 135° DEPT (D) NMR spectra of HMW fraction of Dammar resin in $CDCl_3$.

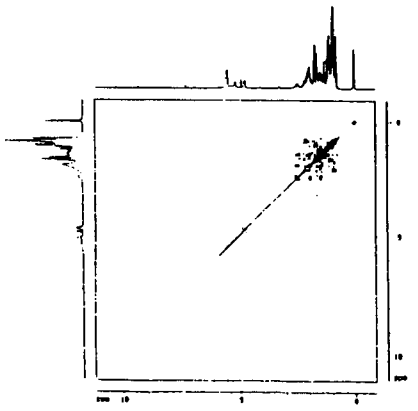

Figure 6: ^{1}H-^{1}H correlation spectrum (COSY 45°) of the high molecular weight fraction of the Dammar resin in $CDCl_3$.

Scanning Transmision X-ray Microscopy: A New "Looking Glass" into Coal Chemical Structure

Robert E. Botto and George D. Cody

Chemistry Division, Argonne National Laboratory, 9700 So. Cass Ave.
Argonne, IL 60439

Keywords: Microscopy, X-ray, Coal

Introduction

Since the early observations by Thiessen[1] and later by Stach,[2] who first recognized coal to be an extremely heterogeneous substance having distinguishable components that could be readily observed only with a microscope, the discipline of coal petrography has had enormous impact on the entire field of coal science. Following the realization that coal is composed of widely diverse, yet totally recognizable fossilized plant materials that have been converted into one or more macerals during coalification, coal chemists began to study the isolated maceral constituents individually. Characterization of their properties revealed that these individual constituents had chemistries as rich and diverse as the mozaic textures that had been seen for macerals microscopically, and as a result, a new level of understanding of the chemistry of coal has been attained.

Notwithstanding the enormous strides that have been made in the chemical characterization of macerals, facilitated primarily by the aid of elegant separation methods,[3] there has been no direct correlation of the optical textures observed under a microscope with maceral chemistry. Moreover, an important issue still to be resolved is whether the macerals themselves are chemically homogeneous or whether there is heterogeneity on a still smaller scale.

In this paper we report, for the first time, the use of scanning transmission x-ray microscopy (STXM) to spatially map the chemistry of aromatic and aliphatic carbon functionalities in coal to a resolution of less than 0.1 μm. In addition, localized x-ray absorption spectroscopy recorded at the carbon K absorption edge have facilitated analysis of the variations in fundamental chemistry at maceral interfaces and within maceral boundaries.

Results and Discussion

Measurements were performed at the National Synchrotron Light Source at Brookhaven National Laboratory using the soft x-ray microscope facility (line X1A).[4,5] The wavelength of the x-ray beam was selected by a spherical-grating monochromator having a bandwidth of 6 pm for a 180-μm exit slit; this corresponds to an energy band width of 0.7 eV at a photon energy of about 290 eV. The specimens were mechanically scanned under computer control, and transmitted x-rays were detected by a gas flow counter. The microscope was enclosed in a helium atmosphere and was separated from the beamline vacuum by a 120-nm silicon nitride membrane. Coal specimens were ultramicrotomed to a thickness of approximately 200 nm for analysis.

Images of three distinct regions within a microtomed thin section of hvA Pittsburgh bituminous coal (APCS No. 4) recorded at photon energies of 285.5 eV (left column) and 288.1 eV (right column) are shown in Figure 1. Chemical contrast can clearly be discerned between image pairs taken at the two energies, and this chemical specificity can be related to differences in x-ray absorption near-edge structure (XANES) cross sections of sp^2- and sp^3-carbon functional groups. Other features seen in the images may be due to variations in sample thickness or to regions of matter with different densities; however, these can easily be distinguished from chemical variations by the lack of contrast reversal between image pairs.

Two fundamental types of features can be readily distinguished within the top pair of micrographs shown in Figure 1. The narrow feature running from the top left to lower right portion of the image exhibits high absorptivity at 288.1 eV (sp^3-absorption band) and correspondingly little absorptivity at 285.5 eV (sp^2-absorption band). This response is typical of highly aliphatic material, and taken together with the morphology of this feature, suggests that it may be the maceral cutinite embedded within a more highly aromatic, or vitrinite, matrix. The diagonal stripes that traverse the image in the opposite direction show no contrast reversal, hence are likely to be scoring marks made by the microtome blade.

The middle two micrographs contain structures that exhibit somewhat different behavior. Two large elliptical bodies are evident which show lower absorptivity in the 285.5 eV image than the surrounding material; however, very little image contrast is observed at an energy of 288.1 eV. The contrast seen in the image recorded at the sp^2 absorption energy suggests that the elliptical bodies contain more highly aliphatic material than the surrounding regions, and given this difference in chemistry, lack of contrast in the sp^3 image implies that these domains contain less dense material as well. The morphology and chemistry suggests that these ellipitical regions are microspores. Within the upper microspore, a small x-ray

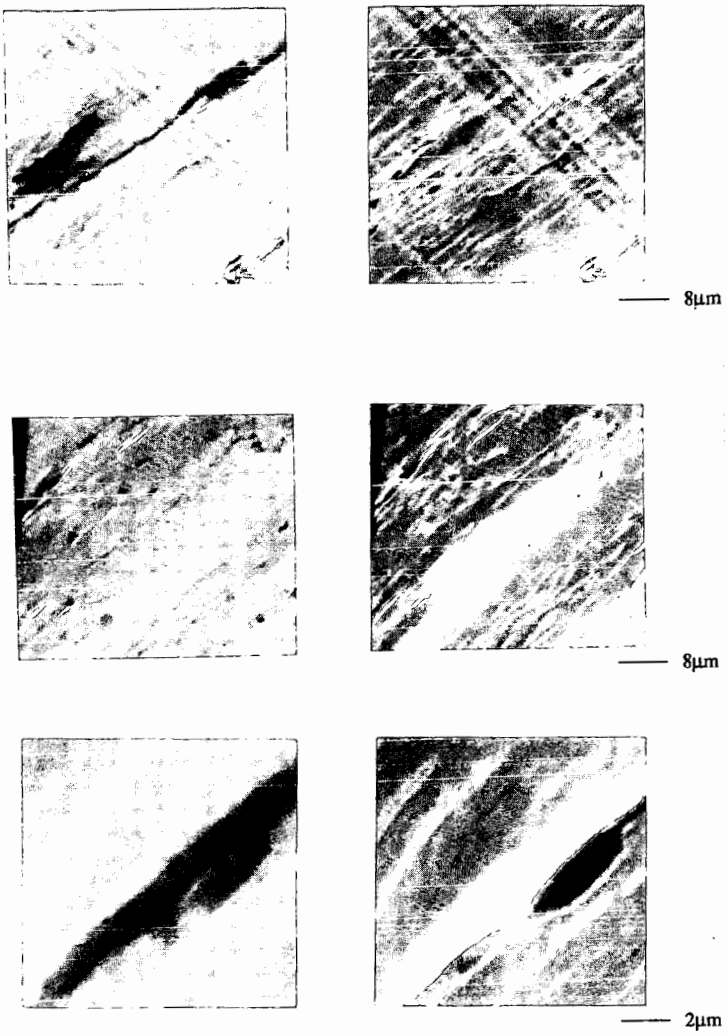

Figure 1. Scanning transmission x-ray micrographs of three regions within a 200-nm microtomed section of hvA Pittsburgh bituminous coal (APCS No. 4) recorded at photon energies of 285.5 eV (sp^2 absorption) and 288.1 eV (sp^3 absorption) at the carbon K-edge.

transparent region is observed whose sp^3-absorption image contrast is reversed, clearly demonstrating intramaceral heterogeneity. Other aliphatic structures are also observed in the lower portion of the micrograph. The morphology of the thin sinuous feature at the lower right is suggestive of the maceral, cutinite. Bright features clearly visible at both energies are cracks which formed as a result of microtoming the sample.

The lower two micrographs represent an expanded view of a cutinite band similar to that represented in the first images above. The cusp found near the center provides additional support for the assignment that this maceral is cutinite. The dark pod that appears at the right of the cutinite band exhibits high absorptivity at both energies; upon careful inspection, several similar structures may be identified in the top pair of micrographs as well.

In order to elucidate the chemistry of the features seen in the lower micrographs, microfocus XANES spectra were taken at various points within individual structures. Figure 2 shows XANES spectra that were taken within regions of the cutinite band, the dark pod and surrounding vitrinite. It should be noted that the spectra are not totally quantitative, especially at the higher energies, due to high absorptivity of the specimens. These effects

also limit chemical contrast in images taken at the higher energy. The cutinite spectrum exhibits a strong absorption at 288.1 eV and a relatively weak absorption centered at 285.5 eV, which is consistent with its aliphatic nature. On the other hand, XANES spectra of the dark pod and surrounding vitrinite show intense sp^2 absorptions. The relative intensity ratios between sp^2- and sp^3- absorption bands in both spectra are also remarkably similar. This implies that the unknown pod structure must be composed of a denser material but is similar in chemical composition to the surrounding vitrinite.

Reflected light microscopic (ROM) analysis of the same sample using standard immersion oil techniques lends support to the assignment of vitrinite, cutinite, and microspores by STXM. Vitrinite and cutinite macerals are abundant in this coal; however, the assignment of microspores is somewhat more tenuous. ROM reveals some microspore structures having elliptical cross-sections with dimensions in the micron range. Moreover, no other potential candidates in this size range and with these morphologies were observed. Consequently, the assignment of microspores to the aliphatic entities shown in the middle micrographs is certainly reasonable.

The ability of STXM to map the chemical composition to this resolution has provided rich detail into the chemical and physical heterogeneity of a coal (APCS No. 4) regarded as being reasonably homogeneous , i.e., containing about 85% vitrinite. However, the variety of textures seen are not limited to those presented in this preliminary report. Vitrinite regions having subtle chemical differences, morphologically different exinite bodies, and microfine mineral particles and veins have also been observed and will be discussed. Recent studies toward the characterization of other Argonne Premium coals and results extending present capibilities to include STXM at the oxygen and calcium K-absorption edges will also be discussed.

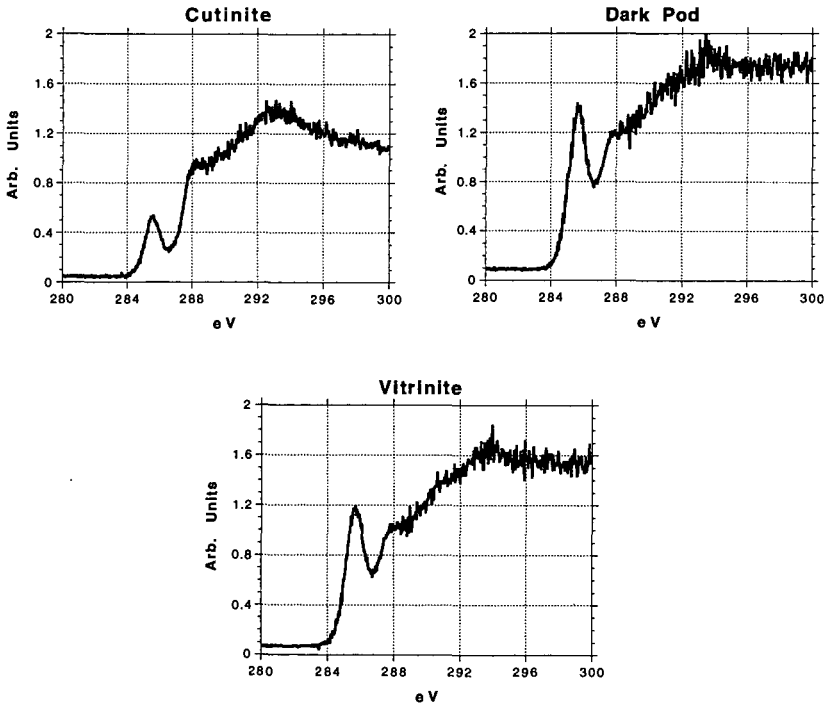

Figure 2. Carbon K-edge XANES spectra of selected regions within (A) the cutinite band, (B) the dark pod and (C) surrounding vitrinite that are identified (see text) in the lower micrographs of Figure 1.

Acknowlwedgment

We express our gratitude to Nester J. Zaluzec and Russell E. Cook of the Materials and Components Technology Division at Argonne for their advice and help in the preparation of some of the samples, to Susan Wirick and Chris Jacobsen of the Department of Physics at SUNY Stony Brook for their help with data acquisition, conversion and transfer, and to the staff of the Coal Petrology Laboratory at Penn State University for their help with ROM. Support of this work from the Office of Basic Energy Sciences, Division of Chemical Sciences, U. S. Department of Energy is gratefully aknowledged. This work was performed at the National Synchrotron Light Source, which is supported by the Department of Energy, Office of Basic Energy Sciences.

References

1. Thiessen, R. *Bur. Mines Bull.* **1920,** *117,* 296 pp.
2. Stach, E. *Lehrbuch der Kohlenpetrographie* **1935,** Borntraeger, Berlin.
3. Dyrkacz, G. R. ; Horwitz, E. P. *Fuel* **1982,** *61* , 3.
4. Kirz, J.; Ade, H.; Jacobsen C.; Ko C-H; Lindaas, S.; Williams S.; Zhang, X. *AAPPS Bull.* **1992,** *2,* 15.
5. Ade, H.; Zhang, X.; Cameron, S.; Costello, C.; Kirz, J.; Williams, S. *Science* **1992,** *258,* 972.

TARGETING SINGLE COAL MACERALS WITH DENSITY GRADIENT CENTRIFUGATION EXPERIMENTS

John C. Crelling
Department of Geology
Southern Illinois University
Carbondale, IL 62901 USA

INTRODUCTION

Since density gradient centrifugation (DGC) techniques were introduced into coal science a little over ten years ago, continuous work has been done to separate and characterize coal macerals [1-11]. To date, good separations of the liptinite, vitrinite, and inertinite maceral groups have been reported, as have separations of individual maceral types including, sporinite, resinite, cutinite, vitrinite, pseudovitrinite, semifusinite and fusinite from coal and of alginite, sporinite, and amorphous kerogen from petroleum source rocks. Most of the separations have been verified both petrographically and chemically. Chemical analysis including chromatography and spectroscopy of these separated materials show them to have diverse bulk chemistry and chemical structures. Most recently, reactivity and combustion studies on separations of both maceral groups and single macerals have shown significant differences between them. The results of all of these studies have shown the extreme heterogeneity of coal and has improved our ability to predict the behavior of coal in any process of interest.

TARGETING SINGLE MACERALS

To obtain separations of single coal macerals from a particular coal, coal maceral groups (liptinite, vitrinite, and inertinite) must first be concentrated. The common procedure is to do an initial two gram DGC run to obtain a density profile. Two grams is the maximum sample capacity of the standard two liter centrifuge bowl and usually provides enough material to give a useful density profile, if the macerals are well liberated. The normal procedure is to reduce the coal sample to micrometer size to get reasonable liberation and a minimum of mixed phase particles. From the density profile, two density cut-points are chosen, one at the liptinite/vitrinite boundary and one at the vitrinite/inertinite boundary as illustrated in Figure 1. While these cut-points can be determined by inspection, a superior technique is to do the determination by petrographic methods including white light and fluorescence analysis. Any cut-point determinations not verified by petrography are immediately open to question. Once the cut-points are in hand, quantities of the various maceral groups are concentrated by centrifugation at the chosen densities serially. It should be noted that for some research, the separations of these maceral groups are sufficient and further subdivision is not required. However, the results of such research must indicate that maceral groups and not single macerals were used.

When the separation of single coal macerals is desired, two gram quantities of the maceral group concentrates are again processed in a DGC run over the appropriate but limited density range, e.g. 1.00 g/mL to the liptinite/vitrinite cut-point for the liptinite maceral group. Such density profiles of the maceral groups usually reveal structure that indicates the presence of a number of single macerals such as cutinite, resinite, and sporinite in the liptinite group.

SPECIAL TECHNIQUES FOR SEPARATING SINGLE MACERALS

There are a number of techniques that facilitate the separation of single macerals from coal. The three most useful are cryogenic treatment, demineralization, and semicontinuous centrifugation. While the usual techniques of micronization using a fluid energy mill or a jet mill will reduce the particle size of a sample to the micrometer range, some multiphase particles often persist. These can be reduced by immersing the sample in liquid nitrogen to freeze it and then rapidly thawing it out at room temperature. With this treatment, the multiphase particles tend to fracture along maceral boundaries. This process can be repeated with or without regrinding to achieve maximum liberation of the macerals.

Demineralization with HCl to eliminate carbonates and HF to eliminate silicates will both increase the yield of a DGC separation and increase the purity of a given density fraction by reducing mixed maceral/mineral phases. However, mineral sulfides

especially pyrite and mineral oxides will not be removed by this acid treatment. If any significant amounts of these minerals are present, a preliminary sink/float separation at a density of about 1.7 g/mL has been found to improve the DGC separation. In cases where pyrite is extremely fine-grained and well dispersed, separation results can be unsatisfactory.

When the target macerals are not very abundant and more than milligram to gram quantities are needed, semicontinuous centrifugation can be used. This technique has been well described [12-13] and allows kilograms of sample to be processed per day. Because it operates at only a single density per run, sequential runs are necessary to concentrate a target maceral.

DISCRIMINATING SAMPLE SELECTION

The techniques described above will usually achieve successful separations on most coals, however, much higher yields and much shorter processing times are possible, if there are no constraints on the choice of the original sample, i.e. the target maceral is specified and not its source [14-16]. While most coals are composed of 50 to 90% vitrinite as shown in the density profile in Figure 1, some coals particularly the Permian Gondwana coals of the southern hemisphere are dominated by inertinite macerals. The density profile of such a coal from South Africa is as shown in Figure 2. It has an inertinite content of over 70% and is clearly an excellent choice for inertinite maceral separation. Other humic coals have higher than normal contents of specific macerals, such as the resinite rich coals from the western U.S. (see Figure 3). Sapropelic coals are dominated by sporinite (cannel coal), alginite (boghead coal) and bituminite, and thus make good candidates for the separation of these macerals. Although these coal types are not abundant, they are ubiquitous. The density profiles of a typical boghead coal along with two different cannel coals are given in Figures 4, 5, and 6 respectively. When appropriate whole coals cannot be found, selected layers in particular coal seams can sometimes be used. The layers, called lithotypes, are specific associations of macerals that can be quite different from the average composition of the whole coal seam. A common lithotype and the easiest to collect is fusain. It is composed of inertinite macerals, mainly semifusinite and fusinite. An example is shown in Figure 7. The two main peaks are natural concentrations of semifusinite (lower density) and fusinite (higher density). The vitrain lithotype is a natural concentration of vitrinite. It can be hand-picked with only moderate effort. As shown in Figure 8, it gives a density profile that shows only vitrinite. Figure 9 shows a monomaceralic boghead coal that shows only alginite.

REFERENCES CITED

1. Dyrkacz, G.; Bloomquist, C.; Horwitz, P.; Sep. Sci and Tech. 1981, 16, No. 10, 1571
2. Dyrkacz, G.; Horwitz, P.; Fuel 1982, 61, 3
3. Dyrkacz, G.; Bloomquist, C.; Ruscic, L,; Horwitz, P.; in "Chemistry and Characterization of Coal Macerals"; Winans, R. and Crelling J., Eds.; ACS Symp Ser. 252: Washington D.C., 1984, 65
4. Dyrkacz, G.; Bloomquist, C.; Ruscic, L.; Fuel 1984, 63, 1166
5. Dyrkacz, G.; Bloomquist, C.; Solomon, P.; Fuel 1984, 63, 536
6. King, H.; Dyrkacz, G.; Winans, R.; Fuel 1984, 63, 341
7. Karas, J.; Pugmire, R.; Woolfenden, W.; Grant, D.; Blair, S.; Int. Jour. Coal Geol. 1985, 5, 315
8. Crelling, J.; Ironmaking Proc. A.I.M.E., 1988, 47, 351.
9. Crelling, J.; Proc. Inter. Conf. Coal Sci. -IEA, in Coal Science and Technology II, Elsevier, Amsterdam: 1987, 119
10. Crelling, J.; Skorupska, N.; Marsh, H.; Fuel 1988, 67, 781
11. Crelling, J.; Pugmire, R.; Meuzelaar, H.; McClennen, H.; Karas, J.; Energy and Fuels, 5, 668
12. Dyrkacz, G. R. and Bloomquist, C. A. A.; Energy and Fuels 1992, 6, 374
13. Dyrkacz, Gary R.; Bloomquist, C. A. A.; and Ruscic, Ljiljana; Energy and Fuels 1992, 6, 357
14. Skorupska, N.M.; Sanyal, A.; Hesselman, G. J.; Crelling, J.C., Edwards, I. A. S.; and Marsh, H.; Proc. Inter. Conf. Coal Sci.-IEA, in Coal Science and Technology II, Elsevier, Amsterdam: 1987, 119.
15. Crelling, John C.; Hippo, Edwin J.; Woerner, Bruce A.; and West Jr., David P.; Fuel, 1992, 71, 151
16. Crelling, John C.; Thomas, K. Mark; and Marsh, Harry; Fuel, 1993, 72, 339

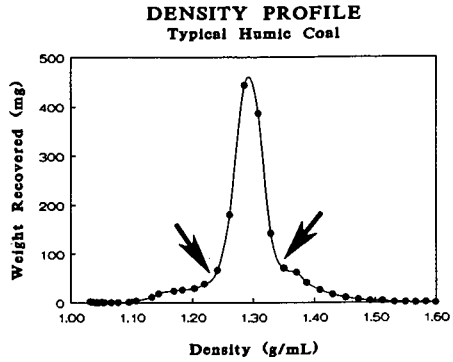

Figure 1. A typical density profile of an humic coal. The main peak represents the vitrinite group macerals, the low density shoulder represents the liptinite group, and the high density shoulder represents the inertinite group. The arrows indicate typical cut-points between the macerals groups.

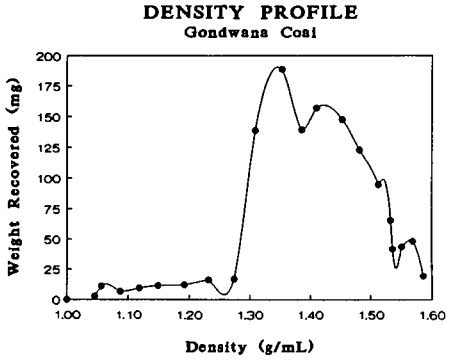

Figure 2. A typical density profile of an inertinite rich Gondwana coal. While the highest peak represents vitrinite the bulk of the sample is inertinite group macerals on the high density side of the vitrinite.

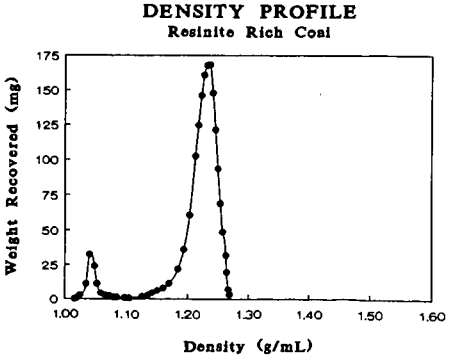

Figure 3. A density profile of a resinite rich coal from the western U.S. The major peak is the vitrinite maceral group, but the smaller very low density peak is resinite.

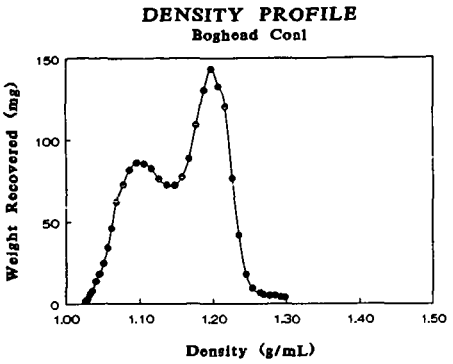

Figure 4. A density profile of a boghead coal. The main peak represents the amorphous kerogen (bituminite?) matrix and the well defined low density peak is alginite.

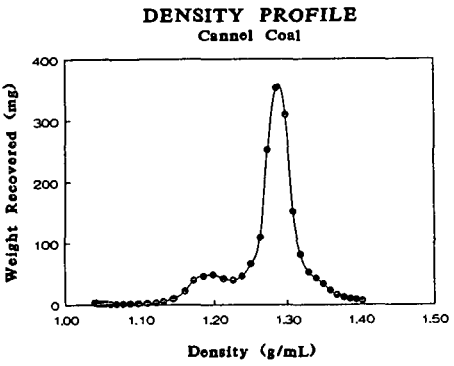

Figure 5. A density profile of a cannel coal. The main peak is vitrinite and the low density peak is sporinite.

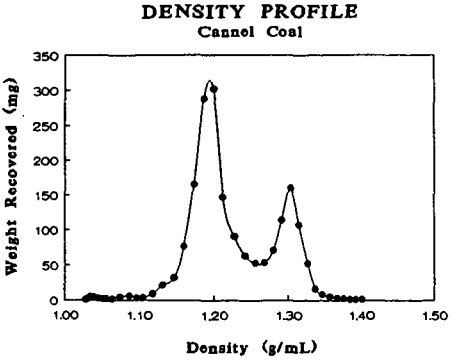

Figure 6. A density profile of another cannel coal which is extremely sporinite rich. In this case the dominant peak is sporinite and the smaller peak is vitrinite.

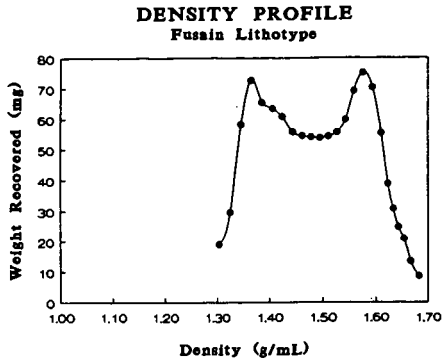

Figure 7. A density profile of a fusain lithotype. Note that it contains only inertinite macerals. The two peaks represent semifusinite (lower density) and fusinite (higher density).

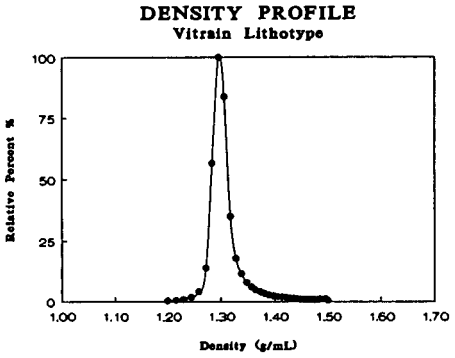

Figure 8. A density profile of a vitrain lithotype consisting of vitrinite and very little else.

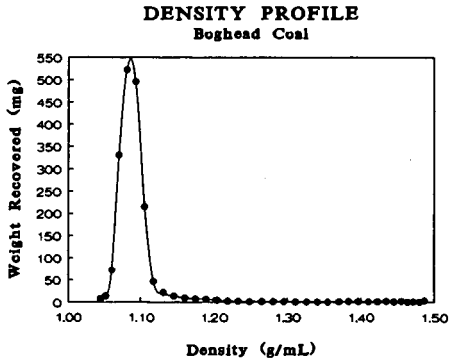

Figure 9. A density profile of a boghead coal that is essentially momomaceralic consisting of alginite.

Adventures in Maceral Separation

Gary R. Dyrkacz
Chemistry Division,
Argonne National Laboratory
9700 S. Cass Ave
Argonne, Illinois 60439

Introduction

Understanding coal structure tasks the best researchers with the latest equipment. The problems start with the raw materials to produce coal - the profusion of plant tissues and minerals of the peat swamps. The problems are further compounded by environmental processing of this raw material through a host of biochemical, chemical and thermal transformations.[1] The resulting coal is then physically and chemically heterogeneous, both in terms of the organic material and the mineral components. Just how heterogeneous is not even clear. Indeed, from the organic chemistry perspective, it is not even known whether any regular structure can even be assigned to coal.

Physically we divide coal into macroscopic or microscopic components called macerals as one measure of the physical heterogeneity. Some macerals are relatively easily associated with certain living tissues such as spores or algae. More often the identity of the original material is uncertain. Partly this is due to the accepted methods of preparing samples for microscopic observation, but often the original peat is so extensively degraded that any remnants of the original physical structure are gone.[2]

Because macerals are the first level of heterogeneity that can be readily observed, separating them to obtain more pure species would appear to be worthwhile. This is true even for a single maceral type, such as vitrinite, which can still be heterogeneous. However, it is notable that maceral separations are not routinely done, even when fundamental structure studies are anticipated. This is contrary to many other fields (e.g. plant science or bioscience areas) where physical and chemical separations of complex organic materials is a mandatory first stage in unraveling structures. One reason may have been a lack of maceral separation science. One of our goals has been to put maceral and, lately, submaceral separations on a more scientific basis.

The methodology of maceral separations can be broken down into several processes which are listed in Table 1. Each of these processes, when viewed in depth, is intertwined with complex and often little understood issues of coal's physical and chemical structure. As a result viable separation procedures are achieved mostly by guessing, faith and a lot of work. For efficient maceral separations to be realized, all these subprocesses must interlock in concert. We have been able to either thread our way through or skirt a number of the problems. However, there is still a largely unexplored vein of information within each area that is specifically important to maceral separations, and probably generally to coal science. A complete idea of where work is needed to improve separations cannot be fully addressed here. Only a brief overview and flavor of where work stands can be given.

Discussion

Liberation

Coal constituents must be liberated from each other for optimal separation even to be possible. Without sufficient liberation some macerals may not be liberated at all. At best, they can only be enriched. Incomplete liberation also affects other constituents by limiting the pure materials that can be separated. This can potentially bias the type of material that is recovered as monomaceral particles. For example, liptinites are usually difficult to liberate cleanly from vitrinites. In density separations, these bimaceral particles will usually be found mixed in with low density monomaceral vitrinite particles. This vitrinite is different from any of the other vitrinite material.[3] Eliminating this portion of material to obtain pure vitrinite can lead to differences in vitrinite properties that do not reflect the original coal.

Mechanical grinding has been the primary method for liberation. The small size of many maceral species means that the coal must be ground very fine - on the order of 10 microns. Fluid energy

mills appear to be particularly effective at producing coal particles in this range. They also appear to cause the least amount of reaccretion or rehomogenization of the coal.[4]

What is the appropriate stage to stop grinding? This question is not only important from the aspect of maceral separation, but can extend to how we perceive the chemical heterogeneity of coal. Ideally, grinding needs to be continued until all particles are completely monomaceral. This goal is opposed by the problem of identification of the ground material. Simple optical identification based on reflectance differences between the macerals is not possible below about 2 microns. In addition, another limiting factor is reached in the submicron range (<0.5 microns). Particles in this range can strongly interact with separation media giving quite different densities than larger particles with the same density.[5]

The preceding demands of maceral liberation critically depend on the maceral concept and maceral identification. But what is the nature of chemical heterogeneity within even a single monomaceral particle? If coal is ground to submicron sizes will new distinct particulate species appear? This would suggest that macerals themselves consist of chemical domains of regular structure? Often vitrinite will exhibit detailed substructures, when coal samples are polished and etched.[1,2] Alternatively, what if no further resolution occurs? This would be true if coal is so heterogeneous that it's structure varies on a nanometer scale, or if monomaceral particles are chemically homogeneous. These questions are not easy to answer, but point to a level of physical separation that has received only a small amount of attention.[4]

Demineralization

The common minerals found in coal have densities from ~1.5 to 4 times that of the organic coal material. Thus, a small amount of included mineral can have a large influence on maceral particle density. Optimum separation of macerals demands that the coal be as mineral free as possible. Mechanical demineralization by density methods is not sufficient to remove the inorganic materials.[5] Chemical demineralization using strong acids is the alternative, but the effect of this procedure on the chemical structure of coal is still uncertain. Fortuitously, pyrite, which has a density of ~4.5 g cm^{-1} and is particularly difficult to remove chemically, is nearly completely liberated from the coal particles during fluid energy mill grinding.

Wetting and Dispersion

Most maceral separations are based on differences in maceral densities in liquid suspensions. If coal particles extensively aggregate in a medium, then separation will be inefficient. There are two related components to the problem: 1.The coal particles must be completely wetted by the media. 2. The particles must remain isolated from one another or undergo nearly elastic collisions over the separation time. Wetting is a necessary condition for dispersion. Just what governs the effectiveness of a particular media for maceral particle dispersion is not clear. The result is that the dispersion remains in the realm of "shake-the-shelf " chemistry. An example of the importance of dispersion can be seen in Figure 1. This data is taken from a study of centrifugal sink/float separations for coal in a variety of commonly used suspension media.[6] SI is a separation index, which is a measure of the efficiency of separation. An SI value of 0 represents no separation relative to the original coal while 1 represents a complete disengagement of the float and sink material. A negative value is due to aggregation effects. RI is the recovery index and represents the fraction of float or sink phase found after separation, relative to the maximum fraction of material expected from a perfect separation. Thus, a value of 0 represents no desired phase found, while 1 represents all the phase isolated. Of the five media systems investigated, only two stood out: aqueous CsCl/Brij-35 and $Ca(NO_3)_2$/Brij-35. (Brij-35 is the nonionic surfactant polyoxyethylene-23-lauryl ether.) Other commonly used media, such as $ZnCl_2$ or organic systems based on CCl_4, were not as effective. Contrary to expectations, recycling material in aggregating media showed no further separation. Although Brij-35 seems to be a magic material that fixes all dispersion problems, it is not. Separations in aqueous $ZnCl_2$ /Brij-35 solutions were only moderately better than $ZnCl_2$ solutions. Thus, the effect of the media can be subtle. Much more work is needed to understand what drives the interactions.

Separation

The heart of maceral enrichment is the separation step. Sedimentation methods are the most commonly used, particularly centrifugal sink/float. A relative newcomer on the maceral separation scene is density gradient centrifugation(DGC). This technique is superior to any type of sink/float separation. It has the highest density resolving ability of any maceral separation method, and

functions both as a separation and characterization method. DGC methods are definitely the method of choice for optimum enrichment of macerals. However, DGC methods do have limitations on the amount of material than can be obtained in any single separation cycle. This can be overcome by first using sink/float methods to isolate desired density regions.

In some studies high density resolution of macerals may not be necessary. Thus, sink/float techniques will remain an alternate separation method or at least an adjunct to DGC separations. With this in mind, we have recently examined the process of centrifugal sink/float (S/F) separations to understand its limitations and provide guidance in its use.[5,7]. In addition, we have explored in detail a continuous flow centrifugation (CFC) technique that allows much larger amounts of material to be separated in a shorter time than by simple centrifugal sink/float.[8-10] Both studies could not have been done without the resolving power and speed of analytical density gradient centrifugation (ADGC) methods. Each study required over two hundred separate ADGC analyses of float or sink phases.

Several general observations emerged from the sink/float studies. The effect of media has already been discussed. Figure 2 displays the ADGC results of a complete separation sequence on a single high volatile bituminous coal using CsCl/Brij-35. The vertical bars represent the nominal solution densities used for each fractionation. This particular separation sequence was from low density to high density. Note that several fractions are not very pure. This is a consequence of two effects. First, even though a density separation may have a constant separation efficiency (i.e., the fraction of mass that will report to the proper phase), the amount of contamination depends on the efficiency factor and the density distribution. Hence, separations made near large bands will be more contaminated than separations further from the main band. We were able to predict the purity of fractions based on the former effect with only moderate success. The second general observation is that float phases invariably contaminates the sink phase due to solution instabilities during the centrifugation process. Much more work is needed to optimize and predict the dynamics of such separations. In the course of this work, we also realized that the density interval of a fraction can also dramatically effect the purity. The narrower the density interval between successive separations, the more contaminated will be the resulting fractions. This is due to the fact that the separation inefficiency is constant, but the mass of a fraction will be smaller as the density interval between separations decreases. DGC is not as affected by this phenomena; this is one reason for its high resolving power. Generally, the S/F separations produced fractions with purities >60 %. Many fractions were routinely better than 80% pure.

Continuous flow centrifugation separations, another version of sink/float separations, had very similar constraints to the simple centrifugal sink/float. Even the overall fraction purities were about the same. CFC separations are carried out in a special centrifuge that allows the continuous removal of liquid from the rotor. Float material is entrained with the expelled liquid, while sink material is retained in the rotor (or in more sophisticated centrifuges, separately ejected). Very dilute solutions can be used so that particle aggregation can be minimized. Single density separations with up to 300g of coal can be accomplished within a day. This is far more than can be conveniently handled by simple centrifugal sink/float methods for finely ground coal. We believe that the efficiency of CFC separations can be substantially improved. For one the rotor dynamics appeared to be more complicated than generally believed. We suspect that there are regions within the separation section of the rotor where the particles are not subjected to the expected flow and centrifugal dynamics. Detailed studies of this device are needed to corroborate this. Modifications to the rotor may be necessary to increase the efficiency.

Isolation

Isolation is included in Table 1 mainly because of its impact on time for a complete separation cycle. The largest fraction of time in the separation of ultrafine coal is spent filtering and washing the separated samples. It is often wise to use membrane filters to avoid selective loss of fine coal, which further slows the filtration process.

Summary

Progress has been made in recent years in the science of maceral separation. However, there are many areas that can improved, and new areas to be investigated. The power of DGC to physically resolve macerals and submaceral species coupled with other instrumental techniques is particularly attractive for defining the limits of coal heterogeneity as well as investigating the ability of other separation methods.

Acknowledgement

This work was performed under the auspices of the Office of Basic Energy Sciences, Division of Chemical Sciences, U. S. Department of Energy, under contract number W-31-109-ENG-38.

References

1. Stach, E., Mackowsky, M.-Th., Teichmuller, M., Taylor, G. H., Chandra, D., Teichmuller, R., Murchinson, D.G., and Zienke, F., 'Stach's Textbook of Coal Petrology', 2nd Edn., Gebruder Borntraeger, Berlin, 1975.
2. Kroger, C., *Erdol und Kohle Erdgas Petrochem.*, 1964, 17, 802-812.
3. Dyrkacz, G. R., Bloomquist, C. A. A., and Ruscic, L. R., *Fuel*, 1984, 63, 1166-1173.
4. Dyrkacz, G. R., Bloomquist, C. A. A., in preparation.
5. Dyrkacz, G. R., and Horwitz, E. P., *Fuel*, 1982, 61, 3 -12.
6. Dyrkacz, G. R., Ruscic. L.R., and Fredericks, J., *Energy and Fuels*, 1992, 6, 720-742.
7. Dyrkacz, G. R., Ruscic. L.R., *ibid.*, 1992, 6, 743-752..
8. Dyrkacz, G. R., Bloomquist, C. A. A.,*ibid*, 1992, 6, 357-374.
9. Dyrkacz, G. R., Bloomquist, C. A. A.,*ibid.*, 1992, 6, 375-386.
10.Dyrkacz, G. R., Bloomquist, C. A. A., Ruscic. L.R.,*ibid.*, 1992, 7, 655-660.

Table 1. Coal Maceral Separation Subprocesses.

Liberation of constituents
Demineralization
Wetting and dispersion of maceral particles
Separation
Isolation

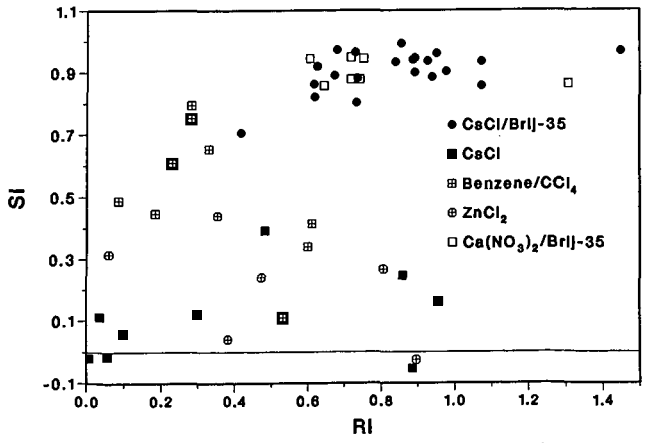

Figure 1. S/F Separation and recovery indices for float fractions from three high volatile bituminous coal.

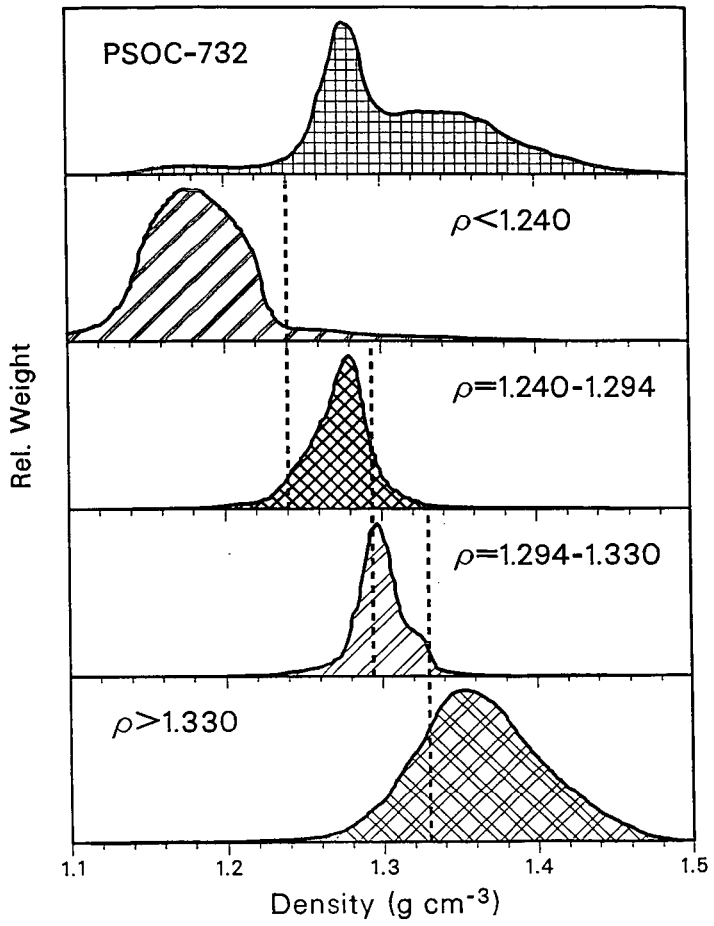

Figure 2. Sequential S/F Separation of a high volatile bituminous cool distributions are normalized to peak values.

Oxidation of NO into NO_2 over Activated Carbon Fibers

Isao Mochida*, Seiki Kisamori, Motohiro Hironaka and Shizuo Kawano
Institute of Advanced Material Study, Kyushu University;
6-1 Kasugakoen, Kasuga-shi, Fukuoka 816, Japan.

Catalytic oxidation of NO into NO_2 was studied over activated carbon fibers at room temperature to trap the unreacted NO as well as the oxidized product as the acid or salts.The heattreatment of pitch based activated carbon fiber was found to enhanced markedly the activity to allow the conversion of 82% in dry and 25% in wet air at 25℃ by W/F of 1.0×10^{-2}g · min · ml^{-1}. The strong retardation by humidity on the activity of as-received fiber was moderated by the heattreatedment. The rate of oxidation was examined by varying concentration of NO ,H_2O and NO_2. The catalytic activities of other fibers were also examined in dry and wet air.

Introduction

NO in flue gas or even in the atmosphere has been continuously expected to be removed or converted into unharmful species more extensively and more efficiently. Selective catalytic reducion of NO in flue gases from various sources has been performed in a commercial scale, using vanadium on TiO_2 catalyst in a honey comb from at a temperature range of 300 to 400℃, where the complete decomposition of $(NH_4)_2SO_4$ is achieved.[1] Although such a SCR process appears proven and established, there remain several problems such as a high reaction temperature which requires reheating, large volume of reactor and necessity of reductant ammonia. The process is not applicable to NO from mobile sources or in very low concentration at ambient temperature as observed in urban areas.

Low temperature SCR processes have been explored around 100-150℃ using zeolite and active carbon as the catalysts and ammonia as the reductant.[2] Complete removal of SO_2 before SCR is strictly necessary because $(NH_4)_2SO_4$ tends to plug the reactor as well as the catalyst bed. The present authers have proposed such a process catalyzed by activated carbon fiber (ACF) to reduce NO of 10ppm at room temperature in the atmosphere.[3,4] However, severe retardation by humidity, necessity of ammonia and further activation of ACF with H_2SO_4 may increase the cost to be unceptable .

In the present paper, we describe the catalytic activity of activated carbon fibers and their heattreated ones for the oxidation of NO in flue or air to be captured as the nitric acids or salts. Such an oxidation catalyzed by active carbon has been reported for a long time.[5,6,7] The unsatisfactory activity and strong retardation by humidity so far restricts further development in the practical application.

The present authors have revealed that the surface preperties of activated carbon fiber can be controlled by the selection of precursor, activation conditions and post-modification such as heattreatment as well as chemical treatment. Hence we examined in the present study the catalytic activity of pitch and PAN based activatied fibers and their heattreated ones to explore the high humidity-resistive activity. Very preliminary trials to capture the oxidized nitric species in water and aq bases are also included.

Experimental

Pitch based (OG-5A,-10A,-20A) and PAN-based (PAN-FE300) active carbon fibers (ACFs) were supplied by Osaka Gas and Toho Rayon, respectively in yarn forms.Their propeties are summarized in Table 1.

The fibers were heattreated in N_2 at 200 to 1000℃ for 4h. Properties of the fibers heattreated at 800℃ (H800) are listed also in Table 1. Oxidation of NO was preformed in a fixed bed U-shaped flow type reactor. The weight and length of fiber bed, flow rate, the concentrations of NO in N_2 containing 4-15% O_2, and reaction temperatures were 0.5g, 70mm, 50ml · min^{-1}, 380ppm, and 25-125℃, respectively. Air was humidified at 25℃. Reactant and product gases were analyzed by NOX meter (ECL-77A, YANAGIMOTO Co.,Ltd.).

The Oxidized gas was washed in a washing bottle after the reaction before the analyzer to examine the capture of NO_2 and remaining NO.Water and aq.KOH (1mol/l) were placed in the bottle by the depth of 70mm (100ml).

Results

1. Catalytic activity of a pitch based ACF, OG-5A

Figure 1 illustrates the compositional change of a model gas at the outlet of the reactor at 25℃ over as-received OG-5A. NO in dry air decreased its concentration from 380ppm to 75ppm by passing through the OG-5A for the first 2h and then increased it gradually to 170ppm by 20h. Up to this time, no nitric species except for NO was found in the outlet gas, adsorption of the species being suggested although so far their form is not identified.

At 20h after the gas flow started, NO_2 started to be found in the outlet gas. The concentration of NO_2 steadily increased, while NO both found and missed, being calculated from N balance, decreased. At 40h, the concentrations of NO and NO_2 became stationous to be 100 and 300ppm, respectively, N balance being now obtained. Such staitionary conversions continued at least for 40h.

Increasing humidity in the air decreased the adsorption amount of N species and conversion of NO into NO_2 at the stationary states, shortening the time to reach the stationary state. Although the retardation of humidity was slight when the humidity was below 60%, humidity above 80% retarded very markedly and humidity of 100% decreased severely the NO conversion into NO_2 to

only null.

2. Influence of heattreatment

Figure 2 illustrates the activity of OG-5A heattreated at 800℃ (OG-5A-H800) for the oxidation of NO at 25℃. Although the profile for NO adsorption and oxidation over OG-5A-H800 was similar to that over as-received OG-5A, the activity was certainly much higher by the heattreatment. The stationary conversion of NO into NO_2 in dry air increased to 80 % by the same W/F. The humidity in air reduced the conversion to 87% at 60% r.h., 55% at 80%r.h., 15% at 100%r.h.. Such reduction was certainly much less with the heattreated OG-5A than that with the as-received one. The activity at 80%r.h. should be noted.

Figure 3 summarizes the stationary conversions of NO into NO_2 over OG-5A heatreated at 400 to 1000℃. The heattreatment increased slightly the activity in dry air, providing the largest activity at 800℃. Either lower or higher temperature decreased the conversion. The increase of activity by the heattreatment at 800℃ was most marked when the relative humidity was 80%. Activity increase by four times in comparison with that of as-received OG-5As was very significant. Further higher humidity reduced the conversions over all OG-5A regardless of the heattreatment. Nevertheless OG-5A-H800 exhibited the highest conversion of only 15%. Although the activity increase may be remarkable even under 100%r.h. because the as-received OG-5A exhibited no activity at all under the same conditions.

3. Influences of reaction conditions

Figure 4 summarizes the influences of relative humidity on the conversion of NO over as-received and a heattreated OG-5A-H800 ones. Although the humidity reduced the conversion slightly below 60% but severaly above 60%r.h. especially over 80%r.h., the marked influence of the heattreatment was observed at 80%r.h.. (The activity under 100%r.h. was composed in more detail, varying the W/F.)

The oxygen concentration above 7% provided the same conversion of NO over OG-5A-H800 regardless of relative humidities at 25℃.

Figure 5 illustrates the conversion of NO in a temperature range of 30 to 125℃ over OG-5A-H800 at 4% O_2 in dry and humid airs. Air was humidified at 30℃ to carry 30.4g/m^3 H_2O. Hence, the relative humidity decreased at the higher reaction temperature. The conversion in dry air decreased monotonously with rising the reaction temperature.[5,6] The decrease was marked above 50℃. In contrast, the conversion increased with rising temperature upto 75℃ in the humid air. The conversion decreased above 75℃ as observed in dry air. Higher oxygen concentration of 15% increased more markedly the conversion in humid air at 75℃.

Table 1 summarized the the conversions of NO into NO_2 over PAN, pitch ACFs and their heattreated ones. OG-5A exhibited the largest activity in dry air among the as-received ones. The larger surface areas of pitch ACFs tended to show lower activity. Pitch ACF was more active than PAN-ACF. The heattreatment at 800℃ enhanced the activity of all ACFs, OG-5A-H800 exhibiting the largest activity in dry air. Superiority of pitch ACF was more marked in wet air of 80%, where OG-5A-H800 and PAN-FE-300-H800 exhibited the conversions of 65 and 38%, respectively.

4. Capture of Oxidized NO

Figure 1 illustrates the extent of captured NO_2 and NO at the outlet of the reactor after the catalytic oxidation of NO over OG-5A as-received. Under the conditions described, NO of 380ppm was oxidized into NO_2 by the conversion of 73% as described above. Water in the washing bottle (100ml, depth the of water 70mm.) captured 70% of produced NO_2, passing remaining NO_2 and unreacted NO. Aq.KOH (1mol/l) of 100ml captured all NO_2 produced and 58% of unreacted NO, a removing 91% of NO of the inlet gas. More efficient contact of gas with water or aq.KOH can remove more NO as well as NO_2.

Discussion

The present paper describes the significant catalytic activity of pitch based activated carbon fiber, especially after the heattreatment at 800℃, for the oxidation of NO into NO_2 at 25℃, which is captured rather easily with water or aq. basic solution. Two points may be worthwhile for discussion.

The first point is related to the retardation by humidity as reported in the past[5,6] : The important feature is that the heattreatment improved the resistivity against the humidity, allowing the significant activity at room temperature in air of humidity up to 80%, where the ACF as-received lost the activity very severely.

The hydrophobic surface may be induced on the particular ACF surface of potentially high graphitizability. The removal of oxygen functional groups in forms of CO or CO_2 is well established for the ACF surface.[8] Certain graphitization may be achieved by such a treatment, although the ACF experienced such a temperature in the activation stages. The preference of the pitch based fiber to PAN based fiber is ascribed to the graphitization potential of the former fiber.

Second point is related to the active site for the oxidation on the ACF surface. The heattreatment appears to induce more number or more active sites for the oxidation of NO as well as SO_2 as described in a preceding paper.[9,10] The site is induced by the liberation of CO and CO_2 in contrast to the expectation that the oxidation active site is connected to the oxygen functional group. Unidentified site for oxidation appears to be introduced by the heattreatment. Surface carbon of unsaturation in its valence may be induced.

The interesting point is that PAN and pitch based ACFs exhibited the reverse order of catalytic activity for the oxidation of SO_2 and NO.[11,12]

Different ways of H_2O intervention in the two oxidation reactions may cause the different activity in humid air. The activity in dry air may reflect the different interactions of such substrate with the ACF-surface. Detail characterization of surface is necessary.

In conclusion, the combination of PAN-ACF and pitch ACF after the heattreatment at 800℃ may allow the oxidative removal of both SO_2 and NO at room temperature in their acid forms, providing a base for novel technology for treatment of both flue and atmosphere. The successive application of both ACFs can recover H_2SO_4 and HNO_3, separately.

References

1) M.Grove, W.sturu, Ceram.Eng.Sei.Pore., 1989, *10*, 325.
2) W.Held, A.Konig, T.Richte, L.Puppe, SEApaper, 1990, *13*.
3) I.Mochida, S.Kawano, H.Fujitsu, T.Maeda, Nippon Kagaku Kaishi, 1992, *3*, 275.
4) S.Kawano, S.Kisamori, I.Mochida, H.Fujitsu, T.Maeda, Nippon Kagaku Kaishi, 1993, *6*, 694.
5) O.Kircher, O.A.Hougen, A.I.Ch.E.Jaurnal, 1957, *3*, 331.
6) Chieh CHU, O.A.Hougen, Chem.Eng.Prog., 1961, *57*, 51.
7) M.Iwamoto, N.Mizuno, Catal., 1990, *32*, 462.
8) I.Mochida, S.Kisamori, S.Kawano, H.Fujitsu, Nippon Kagaku Kaishi, 1992, 1429.
9) I.Mochida, T.Hirayama, S.Kisamori, S.Kawano, H.Fujitsu, Langmdir, 1992, *8*, 2290.
10) S.Kisamori, S.Kawano, I.Mochida, Chem.Lett., 1993, 1899.
11) I.Mochida, S.Kawano, S.Kisamori, Prepr.Am.Chem.Soc.Div.Fuel.Chem., 1993, *38*(2), 421.
12) I.Mochida, S.Kawano, S.Kisamori, Prepr.Am.Chem.Soc.Div.Fuel.Chem., 1994.

Table 1 Some Properties of ACFs

ACFs	Ultmate analysis (wt%)						Surface area (m^2/g)	Pore vol. (ml/g)
	C	H	N	O	S	Ash		
OG-5A(As-received)	89.6	1.1	0.7	8.3	tr	0.3	480	0.25
OG-10A(As-received)	91.6	0.9	0.5	6.7	tr	0.3	710	0.37
OG-20A(As-received)	93.9	0.9	0.3	4.6	tr	0.5	1550	0.81
PAN-EF300(As-received)	83.4	0.9	4.7	9.2	0	1.8	875	0.46
OG-5A-H800[a)]	92.1	1.0	0.5	5.8	0	0.6	450	0.23
OG-10A-H800	94.0	0.8	0.4	4.4	0	0.4	620	0.32
OG-20A-H800	95.8	0.6	0.3	2.8	0	0.5	1320	0.68
PAN-FE300-H800	86.9	0.7	3.6	5.8	0	3.0	810	0.42

a) Calcined at 800℃ in N_2

Table 2 Catalytic Activities of ACFs for NO Oxidation in Dry and Humidified Carrier

ACFs	NO conversion (%)		
	r.h.=0%	r.h.=60%	r.h.=80%
OG-5A(As-received)	73	58	18
OG-10A(As-received)	71	56	14
OG-20A(As-received)	64	49	16
PAN-EF300(As-received)	60	43	4
OG-5A-H800	82	74	65
OG-10A-H800	80	71	56
OG-20A-H800	75	66	51
PAN-FE300-H800	71	57	38

NO : 380ppm (N_2 Balance), O_2 : 4.0%
W/F=1×10^{-2} g · min/ml, W=1.0g
Reaction temp. : 25℃
Conversion was observed 40h after the reaction started.

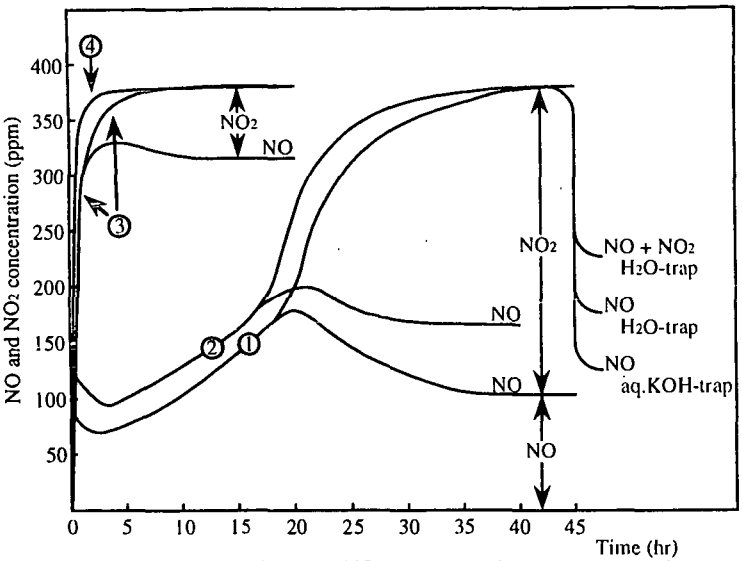

Fig.1 Oxidation of NO into NO_2 over As-received Pitch Based ACF OG-5A

ACF : OG-5A(As-receiced), W=1.0g
NO : 380ppm (N_2 Balance), O_2 : 4.0%
W/F=1×10^{-2}g · min/ml, Reaction temp. : 25℃
Relative humidity : ①0% ②60% ③80% ④100%
Outlet gas passed through washing a botlle.
H_2O : 100ml, depth 70mm, T=25℃
aq.KOH(1mol) : 100ml, depth 70mm, T=25℃

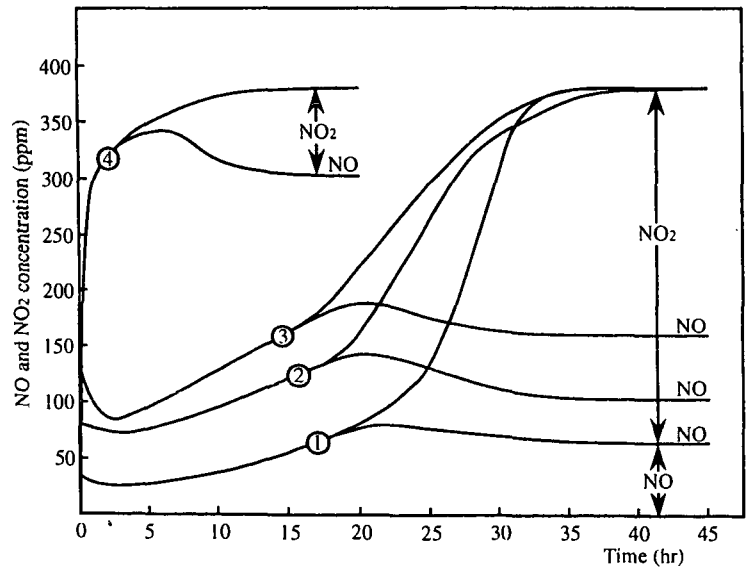

Fig.2 Oxidation of NO into NO_2 over OG-5A Heattreated at 800℃ (OG-5A-H800)

ACF : OG-5A-H800, W=1.0g
NO : 380ppm (N_2 Balance), O_2 : 4.0%
W/F=1×10^{-2}g · min/ml, Reaction temp. : 25℃
Relative humidity : ①0% ②60% ③80% ④100%

A METAL CHELATE PROCESS FOR REMOVAL OF NITRIC OXIDE FROM FLUE GAS

David Littlejohn
Eric K. Pham
S. G. Chang
Energy & Environment Division
Lawrence Berkeley Laboratory
University of California
Berkeley, California 94720

Key words: nitric oxide, flue gas clean-up, metal chelates

INTRODUCTION

Control of sulfur dioxide (SO_2) in flue gases has been achieved by utilization of its high solubility in aqueous solutions. Unlike sulfur dioxide, nitric oxide (NO) has low solubility in aqueous solutions. Consequently, achieving simultaneous control of sulfur dioxide and nitric oxide in flue gas has been difficult to achieve. Nitric oxide can be oxidized to nitrogen dioxide (NO_2), which is more soluble. However, many oxidants are expensive and some of the oxidant material may consumed by the oxidation of dissolved sulfur dioxide. Much of the effort of research for the control of nitric oxide has focused on the development of additives that enhance the solubility of nitric oxide in aqueous solutions. Of the additives investigated, the most promising compounds appear to be metal chelates which are capable of reacting with nitric oxide to form nitrosyl complexes. In particular, many ferrous ion complexes have a high affinity for nitric oxide [1]. Some of the ferrous ion complexes that have been studied have some shortcomings. In particular, ferrous ion-polyaminocarboxylic acid complexes, such as Fe^{2+}(EDTA), are susceptible to oxidation by residual oxygen in the flue gas. The nitrosyl complexes they form react with dissolved sulfur dioxide to form nitrous oxide (N_2O) and nitrogen-sulfur compounds [2]. In recent years, we have investigated thiol-based ligands complexed with ferrous ions that have superior oxidation resistance and NO absorbing capacity [3]. We report here the results of our study of a new thiol-based iron complex using 2,3-dimercapto-1-propane sulfonate (DMPS). It is superior to Fe^{+2}(EDTA) chelate in three aspects: (a) the ability to reduce Fe^{+3} to Fe^{+2}, (b) the absence of nitrogen-sulfur byproducts, and (c) the ease of regeneration using electrochemical reduction. We present here results of the NO removal chemistry of $Fe^{+2}(DMPS)_2$ and the electrochemical regeneration of $Fe^{+2}(DMPS)_2$. Also presented are results of NO thermal desorption studies, which is an alternative regeneration method.

EXPERIMENTAL

NO Absorption Experiments The absorption of NO by $Fe^{+2}(DMPS)_2$ was studied by flowing the gas mixture through a frit at the bottom of a Pyrex column (5cm dia. x 42cm). The $Fe^{+2}(DMPS)_2$ solution was adjusted to pH 5-7 and the temperature of the solution was maintained at 55°C. Simulated flue gas (N_2 with 300-600 ppm NO and 5% O_2) was bubbled through the solution at a flow rate of about 1 L/min, providing a contact time of about 6 seconds. The NO concentration was monitored with a Thermoelectron 14A chemiluminescent NO_x analyzer. The gases were flowed until the NO concentration in the outlet gas matched that of the inlet gas.

Cyclic Voltammetry The electrolytic cell consisted of two flasks separated by an anion-exchange membrane. The cell contained a 0.7 cm dia. glassy carbon working electrode and a platinum foil counter electrode. A saturated calomel electrode was used as reference and 1M Na_2SO_4 was used for the supporting electrolyte. The experiments were performed with a Princeton Applied Research Model 173 potentiostat and a EG&G Model 175 universal programmer. The output was recorded on an XY recorder. All potentials reported are versus SCE.

Electroregeneration of $Fe^{+2}(DMPS)_2$ A somewhat larger electrochemical cell was used for regeneration of the solutions. The cell contained a 11 cm dia. glassy carbon working electrode and a platinum counter electrode separated by an anion exchange membrane. To increase current flow, a barium titanate ultrasonic

transducer was attached to the glassy carbon electrode. During the electroreduction, the solutions in both compartments were agitated with a flow of nitrogen. Under these conditions, the observed current was consistently in the range of 1.5 - 2.0 A for a 0.025 M $Fe^{+2}(DMPS)_2$ solution. Ammonia produced by the reduction was collected in a trap containing 100mL sulfuric acid connected to the electroreduction cell gas outlet. A Dionex 2010i ion chromatograph with a conductivity detector and a CS12 cation column was used to determine the concentration of NH_4^+ in the trap following electroreduction.

Thermal Regeneration of $Fe^{+2}(DMPS)_2$ In these experiments, solutions of 50 mM $Fe^{+2}(DMPS)_2$ were saturated with nitric oxide at 55°C. For thermal desorption, the flow of NO (only) was stopped and the temperature of the $Fe^{2+}(DMPS)_2NO$-containing solution was raised to 95°C. After a fixed amount of time (5 min - 2 h) at 95°C, the solution was cooled down to 55°C. The nitric oxide flow was then restarted to assess the NO removal efficiency of the regenerated solution.

RESULTS AND DISCUSSION

To determine the absorption capacity of $Fe^{+2}(DMPS)_2$ solutions, NO was bubbled through a 10 mM $Fe^{+2}(DMPS)_2$ solution, and the NO absorption capacity was measured with the NO_x analyzer. The NO absorption profile for $Fe^{+2}(DMPS)_2$ exposed to 580 ppm NO at 55°C and pH 6.6 is shown in Figure 1a. By graphically integrating the absorption trace, the amount of NO absorbed was determined, and the concentration of $Fe^{+2}(DMPS)_2NO$ was found to be 7.5 mM in the absence of oxygen. NO absorption under the same conditions except for the addition of 5% oxygen to the gas stream is shown in Figure 1b. It was found that the introduction of 5% O_2 reduces the NO absorption capacity of the solution by 44%. For comparison, a nitric oxide absorption by a 10 mM Fe^{+2}(EDTA) solution under similar conditions is shown in Figure 1c. The solution formed only 2.6 mM of the NO adduct. Introducing 5% O_2 into the gas stream results in a 83% reduction in NO absorption by the Fe^{+2}(EDTA) solution, as shown in Figure 1d. From these measurements, we find that $Fe^{+2}(DMPS)_2$ has 2.5 times larger NO absorption capacity than Fe^{2+}(EDTA) at typical scrubber conditions in the absence of oxygen. Its performance in the presence of oxygen is even better, absorbing 7.5 time more NO than Fe^{+2}(EDTA) in the presence of 5% O_2.

The efficient removal of the NO group from the $Fe^{+2}(DMPS)_2NO$ complex to regenerate $Fe^{+2}(DMPS)_2$ for sustained NO absorption is important in the development of a practical flue gas scrubbing system. Chemical reduction of the coordinated nitric oxide is one such approach that has been used with a number of ferrous nitrosyl complexes. The nitrosyl group of many ferrous ion complexes will react with sulfite ion. However, unlike Fe^{+2}(EDTA)NO and other complexes, the coordinated NO in the $Fe^{+2}(DMPS)_2NO$ complex does not react with SO_3^{2-}/HSO_3^-, even at temperatures up to 95°C. This is advantageous in that no undesirable products such as N_2O and nitrogen-sulfur compounds are formed [2]. At present, no suitable chemical agent has been found to regenerate the $Fe^{+2}(DMPS)_2$ complex due to the relative inertness of the NO group.

In an earlier study, the addition of SH-containing compounds, such as penicillamine, or ß,ß'-dimethylcysteine, had been found to enhance the NO removal ability of ferrous cysteine solutions, resulting in an increase in its NO absorption capacity [4]. However, addition of excess thiolated reagents such as cysteamine, cysteine, or DMPS, showed no notable increase in the NO absorption of $Fe^{+2}(DMPS)_2$. This is illustrated in Figure 2 which shows the effect of excess DMPS on the NO absorption capacity of a 10 mM $Fe^{+2}(DMPS)_2$ solution. There is no appreciable increase in NO absorption beyond a 2:1 complex, $Fe^{+2}(DMPS)_2$.

Since flue gas typically contains 2-8% O_2, it can oxidize Fe^{2+} to Fe^{3+}. DMPS rapidly reduces Fe^{3+} back to Fe^{2+} by electron transfer. However, the resulting oxidation of the SH moiety in DMPS leads to a disulfide (S-S) linkage. To maintain its activity, oxidized DMPS must be reduced to its original form. Electrochemical reduction of the disulfide bond to a thiol has been used to convert cystine to cysteine [5]. We have found that oxidized DMPS can be reduced electrolytically to its original state. Electroreduction can also be used to eliminate the nitrosyl group of the

$Fe^{+2}(DMPS)_2NO$ complex. Cyclic voltammograms of $Fe^{+2}(DMPS)_2NO$ were taken at pH 6 with a scan rate of 50 mV/s using glassy carbon and platinum electrodes. They showed a wave due to the reduction of NO at -0.75 V vs. SCE, in addition to waves associated with the reversible Fe(II)/Fe(III) redox couple. Reduction of S-S linkages has been reported to occur at about -1 V [5], where there is interference from hydrogen evolution with the electrodes. Measurements in our laboratory suggest that the potential that is needed may be somewhat lower.

The fate of the coordinated NO following electroreduction is of interest. Results from our analysis of the reduction products by ion chromatography indicate that the NO is reduced to NH_3 with quantitative yield. There is no evidence, based on gas chromatography analysis, of either N_2 (2-electron reduction) or N_2O (1-electron reduction) being formed. Controlled-potential bulk electrolysis of $Fe^{+2}(DMPS)_2NO$ solutions indicates that current densities of 15-20 mA/cm^2 can be routinely achieved using ultrasound vibration and nitrogen bubbling. Under these conditions, the NO desorption rates, as measured from NO absorption experiments on the electroregenerated $Fe^{+2}(DMPS)_2$ solutions, are 6×10^{-5} mol/min and 1.2×10^{-5} mol/min, in the absence and presence of 5% O_2, respectively. More importantly, there is no attenuation in the NO removal capacity of the electroregenerated $Fe^{+2}(DMPS)_2$ after repeated electroreduction cycles. This indicates that electrolytic decomposition of the chelate is unlikely. Therefore, electrolysis of $Fe^{+2}(DMPS)_2NO$ solutions accomplishes dual tasks in the regeneration of $Fe^{+2}(DMPS)_2$: (1) it electrochemically removes bound NO, and (2) it electroreduces the S-S linkage to reform the S-H groups. This is illustrated in the following scheme:

$$Fe^{+2}(DMPS)_2 + NO = Fe^{+2}(DMPS)_2NO \quad (1)$$

$$Fe^{+2}(DMPS)_2NO + 5H_2O + 5e^- \rightarrow Fe^{+2}(DMPS)_2 + NH_4^+ + 6OH^- \quad (2)$$

$$Fe^{+2}(DMPS)_2 \xrightarrow{O_2} Fe^{+3}(DMPS)_2 \quad (3)$$

$$Fe^{+3}(DMPS)_2 \rightarrow Fe^{+2} + DMPS + \text{oxid. DMPS} + H^+ \quad (4)$$

$$\text{oxid. DMPS} + 2H_2O + 2e^- \rightarrow DMPS + 2OH^- \quad (5)$$

Thermal desorption of NO from $Fe^{+2}(DMPS)_2NO$ represents a simple and attractive method for the regeneration of $Fe^{+2}(DMPS)_2$. We have determined the extent of NO desorption by heating a 50 mM $Fe^{+2}(DMPS)_2$ solution, under anaerobic conditions: the NO-saturated solution containing the resulting 37 mM $Fe^{+2}(DMPS)_2(NO)$ was subjected to several cycles of heating to 100°C for fixed amounts of time followed by NO absorption experiments at 55°C to quantify the amount of NO desorbed. The results are shown in Figure 3 which plots the percentage of $Fe^{+2}(DMPS)_2$ recovered as a function of heating time (from 55°C to 100°C to 55°C). Up to 7.5% of the 37 mM of absorbed NO can be removed by heating the spent solution to 100°C for 2h. Heating times of more than 2h become impractical due to significant water evaporation. There is also no evidence of a linear increase in the amount of NO removed following more than 2h of 100°C heat. These results are reproducible over additional thermal cycles, thus precluding the possibility of thermal decomposition of $Fe^{+2}(DMPS)_2$ and its NO adduct.

In the presence of 5% O_2 and under similar experimental conditions, a 50 mM $Fe^{+2}(DMPS)_2$ solution absorbs 17 mM of NO. Of this amount, only 5% could be desorbed in the presence of 5% O_2 after 2h of heat treatment at 100°C. However, there is a rapid drop off to negligible NO desorption in the second thermal cycle due to the oxidation of DMPS. Thus, to make the process recyclable, electrochemical regeneration of DMPS which is needed to reduce Fe^{+3} to Fe^{+2} for sustained NO absorption must still be used. Even so, a comparison of the NO removal efficiencies in the absence of oxygen clearly indicates that thermal desorption is not as efficient as electroreduction in regenerating $Fe^{+2}(DMPS)_2$.

ACKNOWLEDGEMENTS
This work was supported by the Assistant Secretary for Fossil Energy, U.S. Department of Energy, under contract DE-AC03-76SF00098 through the Pittsburgh Energy Technology Center, Pittsburgh, PA.

REFERENCES

1. Littlejohn, D. and S.G. Chang, Kinetic Study of Ferrous Nitrosyl Complexes. *J. Phys. Chem.*, **1982**. *86*, 537-540.

2. Littlejohn, D. and S.G. Chang, Reaction of Ferrous Nitrosyl Chelates with Sulfite and Bisulfite Ions. *I&EC Res.*, **1990**. *29*, 10-14.

3. Chang, S.G., D. Littlejohn, and D.K. Liu, Use of Ferrous Chelates of SH-Containing Amino Acids and Peptides for Removal fo NO_x and SO_2 from Flue Gases. *I&EC Res.*, **1988**. *27*, 2156-2161.

4. Liu, D.K., L.P. Frick, and S.G. Chang, A Ferrous Cysteine Based Recyclable Process for the Combined Removal of NO_x and SO_2 from Flue Gas. *Environ. Sci. Technol.*, **1988**. *22*, 219-223.

5. Zagal, J.H. and P. Herrera, Electrochemistry of Cysteine and Cystine on Metal-Phthalocyanines Adsorbed on a Graphite Electrode. *Electrochim. Acta*, **1985**. *30*, 449-454.

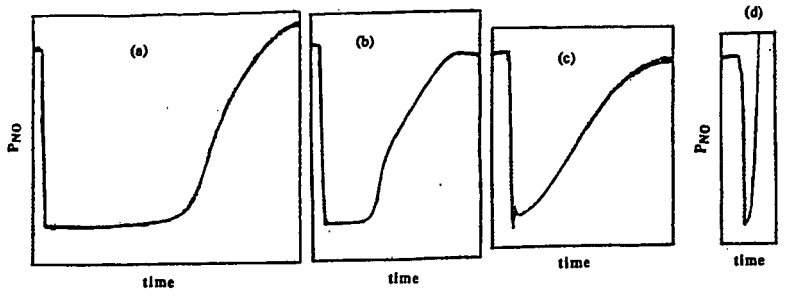

Figure 1. Comparison of NO absorption by $Fe^{+2}(DMPS)_2$ and Fe^{2+}(EDTA) solutions, with and without the presence of 5% oxygen.

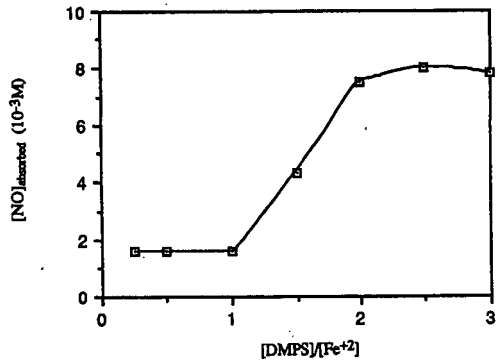

Figure 2. Effect of Fe^{2+}:DMPS ratio on the absorption of nitric oxide.

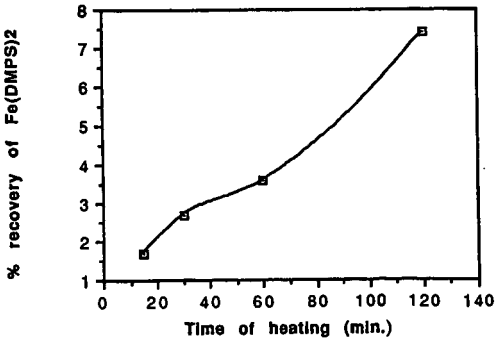

Figure 3. Percent recovery of $Fe^{+2}(DMPS)_2$ as a function of time of heat treatment (55°C –> 100°C –> 55°C) of a 37mM $Fe^{+2}(DMPS)_2(NO)$ solution generated from 50mM $Fe^{+2}(DMPS)_2$ + 550ppm NO (pH 6, 55°C).

SULFUR CAPTURE CAPACITY OF LIMESTONES IN COMBUSTION GASES: EFFECT OF THERMALLY INDUCED CRACKING

Ye Liu, Joel L. Morrison and Alan W. Scaroni
The Pennsylvania State University
402 Academic Activities Building
University Park, PA 16802

Keywords: limestone; thermally induced cracking; sulfation capacity.

INTRODUCTION

Limestones and dolostones can be used in coal-fired, fluidized bed power plants as sorbents to capture SO_2 from the combustion gases. The physical properties of calcined sorbents, especially pore size distributions, and the relationship between these properties and subsequent sulfur capture behavior have been subjects of extensive study[1-4]. In general, calcines of limestones and calcines of dolostones differ not only in chemical composition, but more importantly in physical structure, and this is manifested as a difference in sulfation behavior. Prediction of the development of pore volume and characteristics upon calcination, is usually based on the chemical composition of the starting sorbents[1-3]. These models predict that limestones and dolostones will have different pore structures during and after calcination. They also predict that two limestones or two dolostones with the same chemical compositions will have the same pore structures after calcination.

However, there are numerous examples to show that the pore structures of calcined sorbents differ significantly from those predicted from chemical properties[1,5]. The reasons for this, and the effect this has on sulfation behavior are not well understood.

The work presented here is a study of the sulfur capture capacities of two limestones with high $CaCO_3$ contents (99.4 and 98.5, respectively). The limestones are therefore chemically similar, however, they are petrographically different. Significant differences existed between the physical properties of the calcines and in their sulfation behavior. An explanation for the differences is presented.

EXPERIMENTAL

Two limestones with high $CaCO_3$ contents were collected from different quarries in Pennsylvania (from the Linden Hall and Annville formations). Their physical and chemical properties are given in Table 1.

Calcination and sulfation experiments were conducted in a Perkin-Elmer Series 7 thermogravimatric analyzer (TGA). The reactive gas flow consisted of 15 volume % CO_2, 4% O_2, 2,000 ppm SO_2 and the balance N_2. The flow of 125 standard cubic centimeters per minute (SCCM) was controlled by Brooks Electronic mass flow controllers and was passed downwards over the sample, which was held in a platinum pan of 5 mm diameter. From 4 to 10 mg of sample were used for each run, depending on the particle size. Before starting the rapid heating, the system was thoroughly purged with the reactant gas. To simulate the practical situation in a fluidized bed combustor where sorbent particles are introduced into a high temperature gaseous environment, the samples were heated at the maximum setting of 200 °C/min. to the final temperature of 875°C.

Surface area measurements were performed on an Autosorb-1 gas adsorption system (Quantachrome Corporation) using nitrogen as the adsorbate. The pore size distributions were obtained using an Autoscan mercury porosimeter (Quantachrome Corporation).

Morphological analyses were performed on an EM-30 Environmental Scanning Electron Microscope (ESEM) (ElectroScan). Unlike the traditional SEM, the ESEM is capable of examining specimens without coating. In addition, the examination can be conducted on a hot stage where the specimen can be heated up to 1000° C.

RESULTS AND DISCUSSION

It is generally accepted that at atmospheric pressure and high temperature, it is the CaO formed by the thermal decomposition of $CaCO_3$ that reacts with SO_2 and O_2 according to:

$$CaCO_3 \rightarrow CaO + CO_2 \qquad (1)$$

$$CaO + SO_2 + 1/2\ O_2 \rightarrow CaSO_4 \qquad (2)$$

instead of the direct sulfation of limestone by:

$$CaCO_3 + SO_2 + 1/2\ O_2 \rightarrow CaSO_4 + CO_2 \qquad (3)$$

Figure 1 illustrates typical TGA profiles of the Linden Hall and Annville samples in a simultaneous calcination and sulfation test. The profiles consist of two characteristic portions. At first, the weight loss due to calcination by reaction (1) dominates. Sulfation starts, however, as soon as CaO is formed. This has been confirmed previously by comparing data obtained with and without SO_2 in the calcining gas [6]. During active calcination, the sulfur uptakes were about 5 % (on a S/Ca molar ratio basis) and 10 % for the Linden Hall and Annville samples, respectively, for the particle size of 60x100 mesh. In the second portion of the TGA trace, the sample weight increases with time due to the occurrence of sulfation. The sulfur uptake by reaction (2) is initially rapid, then gradually decreases as pore plugging occurs [7].

Despite similar chemical compositions, for the size fraction of 60x100 mesh, the performance of the Annville sample was much better than that of the Linden Hall sample. This can be related to the larger pore volume in pores greater than 1 μm for the Annville calcine, as shown in Figure 2. Ulerich et al [4] found higher sulfation capacities for calcines with larger pores even though the pore volume and surface area may have been lower than those of calcines with smaller pores. The larger pores facilitate rapid sulfur capture and produce high sulfur capture capacity due to the more rapid transport of SO_2 to the interior of sorbent particles and because the pore plugging effect is minimized [7].

The particle size dependency of the sulfur capture capacity for the Linden Hall and Annville samples is given in Figure 3. The S/Ca molar ratio was calculated from the following equation:

$$\text{S/Ca (molar ratio)} = \frac{[W_i - W_0(1\text{-LOI})] / 80}{W_0\, CaCO_3\% / 100}$$

where:

W_i: Sample weight during sulfation reaction at time t_i,
W_0: Initial sample weight,
LOI: Loss on ignition,
80: Molecular weight of SO_3 (see reaction 2)
100: Molecular weight of $CaCO_3$.

The sulfur capture capacity of the Linden Hall sample increases significantly as the particle size decreases. In a 200 minute run, the S/Ca molar ratio increased from 0.07 for 20x25 mesh particles to 0.47 for 200x270 mesh particles; in comparison, the sulfation performance of the Annville sample had a relatively weak dependence on particle size. As the particle size was changed over the same range, the S/Ca molar ratio only increased from 0.24 to 0.36.

Consequently, for the larger particle size, the Annville sample was superior to the Linden Hall sample, while for the smaller particle size, the opposite was the case. This dependency of performance on particle size is important from a practical viewpoint in that a conclusion that one sample is superior to another based on a test of one particular particle size fraction may not be valid for other particle sizes. In terms of the pore size distributions of the 60x100 mesh particles, it is understandable that for larger particles, the Annville sorbent displayed better performance because of the larger pore volume in larger sized pores. For the Linden Hall sample, the pore plugging effect prevents the interior surface from being accessible to SO_2 and O_2. However, in the case of smaller particles, the above reasoning is not applicable.

The Linden Hall and Annville limestones are chemically similar but geologically different. The Linden Hall is a fine-grained (micritic) limestone and the Annville has undergone recrystallization producing a coarse-grained texture. Their detailed petrographic characterizations are described elsewhere [5]. The petrographic properties of carbonate rocks and their relationship to SO_2 sorption were studied by Harvey and Steinmetz [8,9]. The grain size was found to be an important indicator of sulfation capacity. Among the carbonate rocks tested (including limestone, dolostone, marble and chalk), in general, the finer the grain size of the rock, the higher the sulfation capacity. However, the limestone samples tested exhibited increasing sulfation capacity with increasing grain size [9]. More recently, Zarkanitis and Sotirchos found that fine-grained Greer limestone had a stronger sulfation dependency on particle size than Georgia marble which consisted of coarse calcitic grains [7]. Morrison et al [5] showed using ESEM the occurrence of cracking within the Linden Hall and Annville samples during particle heat up. Extensive cracks developed among the grain boundaries for the Annville sample. For the Linden Hall sample, some particles contained only one or two randomly oriented fractures within the fine-grained structure. The conditions used for these experiments were low pressure (3 torr water vapor) and low heating rate (10 °C/min.).

Figure 4 presents ESEM photographs of Linden Hall and Annville samples, calcined in the TGA in the absence of SO_2. For the Annville sample with larger grains, extensive cracks occurred along the grain boundaries of the 45x60 mesh particles (Figure 4a). As the particle size was decreased to 200x270 mesh, which is of the order of the grain size, there was essentially no fracturing within the grains, as shown in Figure 4b. Few fractures developed in the Linden Hall particles, as typified by the particles shown in Figures 4c and 4d. It should be noted that the surface structure of the calcined Linden Hall particles is much more porous than that of the Annville particles.

The occurrence of cracking in the larger particles of the Annville limestone benefits the sulfur capture process. It also facilitates rapid calcination. Figure 5 shows the ratio of the time to 50% calcination (t_{50}) between the Linden Hall and Annville samples as a function of particle size. For the 200x270 mesh particles (mean size = 63 μm), the calcination rate of the Annville sample is lower than that of the Linden Hall sample. However, for the 60x100 mesh particles (mean size = 193 μm) , the calcination rate of the Annville sample is greater than that of the Linden Hall sample. It is hypothesized that the fractures facilitate the rapid evolution of CO_2 produced by the decomposition of $CaCO_3$, thereby decreasing the CO_2 pressure inside the particle, and this increases the calcination rate.

The importance of the occurrence of fractures within the particles during heat up to the subsequent sulfation behavior is supported by the sulfur distributions within the Linden Hall and Annville particles. The sulfur distribution maps, obtained from a Camera SX50 microprobe, are shown in Figure 6. For the Linden Hall sample, sulfur is concentrated in an outer layer around the particles, while for the Annville sample, sulfur penetrated into the particles and is distributed

along the grain boundaries. Reaction took place at the external surface of the Linden Hall particles, gradually closing the pores and blocking the pathway to the particle interior. This leads to significant intraparticle diffusion effects in the vicinity of the external surface. For the Annville sample, however, SO_2 penetrated into the particle interior through fractures along the grain boundaries and reaction occurred at the external surfaces of grains, which leads to intragrain diffusion effects.

CONCLUSIONS

This investigation examined the dependency of the sulfur capture capacity of two high $CaCO_3$ content limestones on particle size. The extent of sorbent utilization is dependent on the extent of sulfur penetration into the particles or sulfur penetration into the individual grains which comprise a single particle. The occurrence of cracking within particles had a strong impact on the sulfur capture behavior, since it produced significant accessible surface area.

The petrographic properties of sorbents play an important role in determining calcination and sulfation behavior. It has been shown that the cracking pattern is related to grain size, grain-grain interlocking and particle size. The present experiments indicated that cracking occurred between grains rather than within grains, i.e. no cracking occurred in a particle consisting of a single grain. The Annville sample with the larger grains showed a greater cracking tendency. The Linden Hall sample with smaller grains withstood the imposed stress better.

ACKNOWLEDGMENTS:

Financial support for this work was provided by the Pennsylvania Energy Development Authority and the Pennsylvania Aggregates and Concrete Association. Ronald Wincek is thanked for his help in modifying the TGA.

REFERENCES

1 Vogel, G. J., Johnson, I., Lee, S. H., Lenc, J. F., Lescarret, S. A., Montagna, J., Nunes, F. F., Shearer, J. A., Snyder, R. B., Smith, G. W., Swift, W. M., Teats, F. G., Tumer, C. B., Wilson, W. I., Jonke, A. A. *"Supportive Studies in Fluidized Bed Combustion"*, Argonne National Laboratory, ANL/CEN/FE-77-3, Annual Report, July 1976-June 1977.

2 Haji-Sulaiman, M. Z. and Scaroni, A. W. *Fuel*, 1991, **79**, 169

3 Rubiera, F., Fuertes, A. B., Pis, J. J., Artos, V. and Marban, G. *Thermochimica Acta*, 1991, **179**, 125

4 Ulerich, N. H., O'Neill, E. P. and Keairns, D. L. *Thermochimica Acta*, 1978, **26**, 269

5 Morrision, J. L., Liu, Y., Romans, D. E., Pisupati, S. V., Scaroni, A. W. and Miller, S. F. *Proceedings of SO_2 Capture Seminar "Sorbent Option and Considerations"*, National Stone Association, Cincinnati, Ohio, September 19-21,1993

6 Romans, D. E., Liu, Y., Pisupati, S. V. and Scaroni, A. W. *Proceedings of 7th International Conference on Coal Science*, International Energy Agency, Banff, Canada, September 11-17, 1993

7 Zarkanitis, S and Sotirchos, S. V. *AIChE Journal*, 1989, **35**, 821

8 Harvey, R. D. *Environ. Geology Notes, Illinois State Geological Survey*, **38**, 1970

9 Harvey, R. D. and Steinmetz, J. C. *Environ. Geology Notes, Illinois State Geological Survey*, **50**, 1971

TABLE 1 Properties of the Linden Hall and Annville limestones

Limestone	Linden Hall	Annville
BET Surface area (N_2, m^2/g)	0.215	0.155
Porosity (vol. %)	1.0	1.8
Loss on Ignition (wt%)	43.4	43.2
CaO (wt%)	55.7	55.2
MgO (wt%)	0.41	0.54
SiO_2 (wt%)	0.69	0.74
Al_2O_3 (wt%)	0.31	0.35
Fe_2O_3 (wt%)	0.07	0.05
Other minor oxides (wt%)	0.22	0.12
Total (wt%)	100.8	100.2

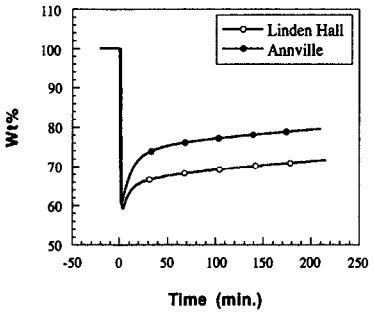

Figure 1 TGA profiles during simultaneous calcination and sulfation of 60x100 mesh sorbent particles

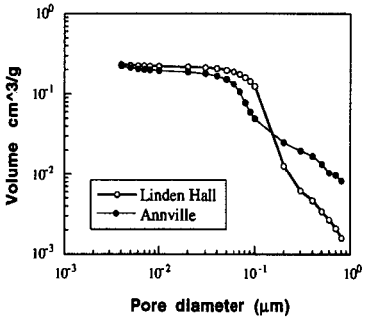

Figure 2 Pore size distributions of calcined 60x100 mesh sorbent particles

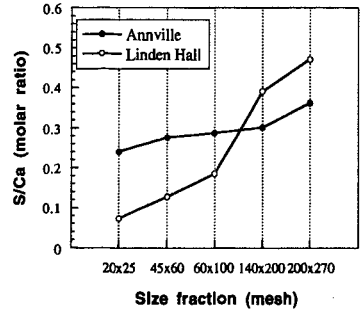

Figure 3 Dependency of sulfur uptake capacity on particle size for a 200 min test

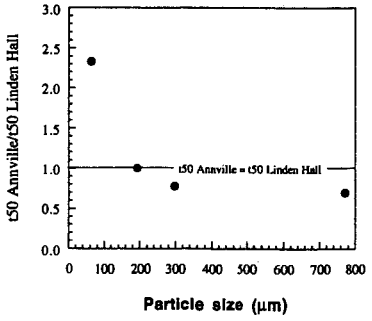

Figure 6 Dependency of the relative calcination time on particle size

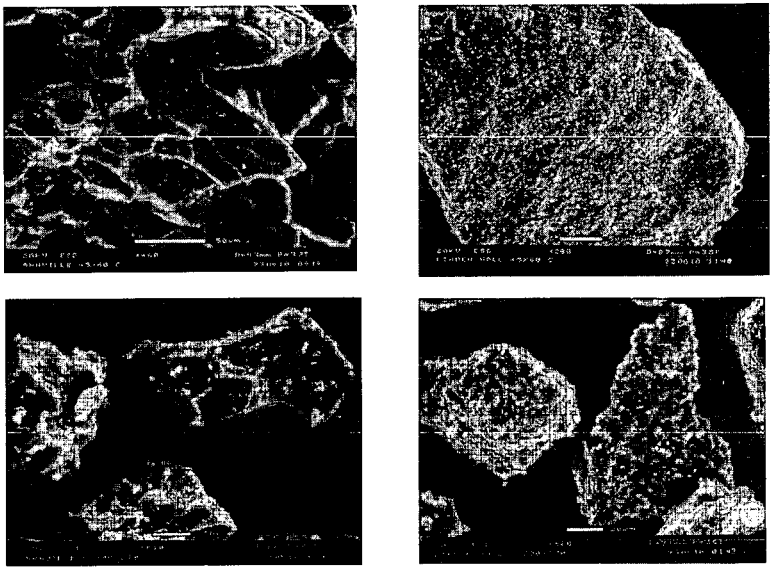

a (above) Annville 45x60 mesh
b (bottom) Annville 200x270 mesh
c (above) Linden Hall 45x60 mesh
d (above) Linden Hall 200x270 mesh

Figure 4 ESEM photographs of calcined Annville and Linden Hall samples

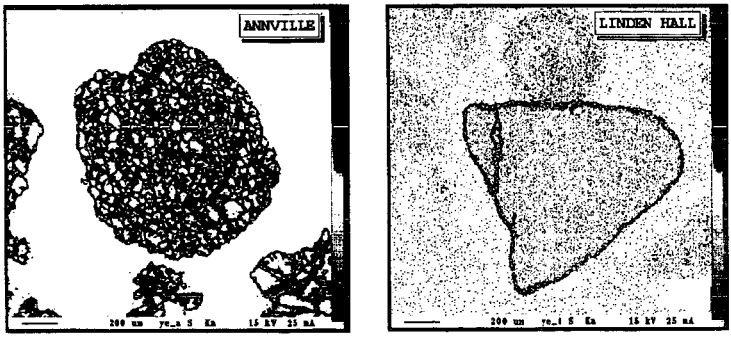

Figure 5 Sulfur distribution maps of sectioned Annville and Linden Hall sulfated particles

EXPERIMENTAL INVESTIGATION OF HIGH-TEMPERATURE, SHORT RESIDENCE-TIME CALCINATION AND SULFATION OF LIMESTONE AND DOLOSTONE SORBENTS

Naiyi Hu, Ye Liu, Sharon Falcone Miller and Alan W. Scaroni
The Pennsylvania State University
402 Academic Activities Building
University Park, PA 16802

Key words: sorbent furnace injection, calcination, sulfation.

INTRODUCTION

Sulfur dioxide emissions from coal-fired utility boilers and furnaces continue to be of significant regulatory concern. One approach to reducing these emissions that has received considerable attention[1-4] is the injection of dry, pulverized sorbent (limestone or dolostone) into the combustion chamber. This technology has been applied to conventional coal-fired utility boilers[1,2] and is considered to be a good candidate for use in coal-fired heat engine applications.[3,4] During the process, the injected limestone or dolostone particles are rapidly heated by the hot combustion gases and calcined by the reactions $CaCO_3 \rightarrow CaO + CO_2$ and $CaMg(CO_3)_2 \rightarrow CaO + MgO + 2CO_2$, respectively. The CaO produced then reacts with SO_2 and excess O_2 in the combustion gases to form $CaSO_4$.

Experimental data on the rates of calcination, sintering and sulfation have been reported by Borgwardt and others.[5-8] The physical structure of the calcined sorbents has also been investigated,[5,9,10] and a number of models have been developed describing the calcination and sulfation processes.[10,11,12] The primary application of dry sorbent injection is to conventional coal-fired utility boilers. The sorbent particle size used is either small (in the range of 1 to 30 μm) in pulverized coal applications or large (in the range of 0.25 to 1 mm) for fluidized-bed applications. Few investigations have been carried out using 30 to 100 μm particles, which is the size range of interest for coal-fired heat engine applications.[3,4]

This study investigated the calcination and sulfation behavior of three different sorbents (two limestones and one dolostone) in the size range from 37 to 105 μm. The time required for heating and calcination, the effect of the calcination process on sulfation behavior, and the effect of sorbent type on sulfation behavior were of primary interest.

EXPERIMENTAL

The calcination and sulfation experiments were conducted in the entrained-flow reactor illustrated in Figure 1. It consists of a preheater, a side-heated sorbent injector, and a vertical reactor. The preheater, injector and reactor were electrically heated to provide the desired gas preheating temperature and reactor temperature. The inside diameter of the ceramic reactor tube is 50.8 mm and it has an isothermal zone length of 600 mm. Dry air was used as the entrainment gas and was preheated to the same temperature as that in the reactor isothermal zone (±13 °C). The total gas flow rate was 60.7 l/min. As the preheated air passes through the injector section, the heat loss caused by contacting the injector wall is compensated for by the heat transferred from the heating wire wound around the outside of the injector. The sorbent was fed by a calibrated fluidized bed feeder. Room temperature air was used for sorbent injection and it comprised 5 % by mass of the total air flow to the reactor. A flow stabilizer was used to eliminate pulsations of the feed material caused by the fluidized feeder. SO_2 was doped into the gas flow by a mass flow controller to provide an SO_2 concentration of 2000 ppmv in the reactor. The sorbent feed rate was adjusted to achieve a Ca/S molar feed ratio of 2.0. Solid samples were collected through a nitrogen-purged, water-cooled sampling probe. During sampling, the nitrogen was used to increase the cooling rate of the sample. The nitrogen comprised 50 % of the total gas flow through the probe. Calculations indicated that 89 μm particles were cooled from 1,100 to 700 °C within 0.03 second after entering the sampling probe.

The stratigraphic formations, chemical compositions and the specific BET surface areas of the two limestone and one dolostone sorbents tested are shown in Table 1. The materials were crushed and wet sieved to size fractions of 74-105 μm (140x200 US mesh), 53-74 μm (200x270 US mesh) and 37-53 μm (270x400 US mesh). The sieved materials were dried in an oven at 105 °C for 48 hours.

The solid samples extracted from the reactor were analyzed for loss-on-ignition (using a Leco MAC-400 proximate analyzer), BET surface area (using a Quantachrome Autosorb-1 analyzer system with nitrogen), and sulfur content (using a Leco SC-132 sulfur analyzer with V_2O_5 catalyst). Some hydration occurred during sample collection and transfer. The extent of hydration was determined (using the Leco MAC-400 proximate analyzer) and the calcination and sulfation data corrected accordingly.

RESULTS AND DISCUSSION

CALCINATION BEHAVIOR

The extents of calcination of the Linden Hall limestone at gas temperatures of 1,000 and 1,100 °C are shown in Figures 2 a and b, respectively. The initial calcination rate is slow, followed by a rapid increase, and then a decline as the calcination process approaches completion.

An initial slow rate of calcination was observed for all three sorbents studied and this was attributed to the use of ambient air as the injecting medium, and the time needed for the sorbent particles to reach their decomposition temperatures.

Effects of Ambient Air Sorbent Injection and Time Required for Particle Heating: Sorbent injection systems typically use ambient air as the injecting medium. To simulate this condition, the sorbents were entrained in air at room temperature. As previously indicated, the sorbent-entraining air comprised 5 %, by mass, of the total air flow to the reactor tube. This ambient air, when mixed with preheated air in the top of the reactor, reduced the reactor inlet temperature. Figure 3 shows the measured gas temperature profiles along the reactor. It was found that the gas temperature, at a location corresponding to 0.1 second after injection, was 40 °C lower than the gas temperature at the same location when no ambient air injection occurred. The lower inlet gas temperature caused by the ambient air injection resulted in a delay in the initial calcination of the sorbents.

Another reason for the significant delay in calcination was the heating time required for the relatively coarse sorbent particles to reach their decomposition temperature. Figure 4 shows the calculated temperature profiles of 10 and 63 μm particles as a consequence of convective heat transfer. It takes much longer for the relatively coarser sorbent particles (in the range of 37 to 105 μm) to heat up than for a 10 μm particle. The characteristic heating time for a 105 μm sorbent particle is 92 ms and that for a 10 μm sorbent particle is only 0.8 ms. This latter time is negligible for conventional utility boilers firing pulverized-coal where the effective sorbent reaction time is about 2 seconds. However, the characteristic heating time for 63 μm sorbent particles is 33 ms, which is significant in heat engine applications.

Effect of Sorbent Particle Size on the Calcination Process: Over the sorbent size range from 45 to 89 μm, the effect of particle size on the calcination process at 1,000 °C is shown in Figures 2 and 5. For the three sorbents studied, the extent of calcination was not significantly dependent on the sorbent particle size.

From the classical shrinking-core model, the extent of calcination can be expressed as:

$$x = 1 - (1 - k \cdot t / dp)^3 \qquad (1)$$

where dp is the particle diameter, k is the calcination rate constant and t is the calcination time. In Equation (1), the extent of calcination has a strong dependency on particle size. Borgwardt[5] demonstrated that, when the resistances of intraparticle and interparticle mass transfer were eliminated, the calcination rate of small limestone particles could be described by a model that assumed a direct relationship with the specific BET surface area of $CaCO_3$. This calcination model has the form:

$$d(CaCO_3) / dt = k \cdot S_g \cdot (CaCO_3) \qquad (2)$$

where $(CaCO_3)$ is the weight of the undecomposed carbonate and S_g is the specific BET surface area of $CaCO_3$. By integration, the extent of calcination is related to the specific BET surface area by:

$$x = 1 - \exp (- k \cdot t / S_g) \qquad (3)$$

Milne et al.[10] employed a modified shrinking-core model to interpret the experimental data of Borgwardt[5]. A good fit was obtained when the particle diameter dependency was reduced to the 0.6 power, and the empirically modified equation was:

$$x = 1 - (1 - k \cdot t / dp^{0.6})^3 \qquad (4)$$

Comparison of the calcination models with the experimental data for the Linden Hall limestone at 1,000 °C is shown in Figure 6. This data indicate that the calcination model based on the specific BET surface area of $CaCO_3$ is a better predictor of the experimental data than the modified shrinking core model. A comparison of the calcination models with the data for the Bossardsville and Nittany sorbents results in the same conclusion.

To be able to apply the modified shrinking-core model to the experimental data of this study requires that the particle size dependency be reduced to a power of between 0.2 to 0.3, depending on the particular sorbent. The very weak particle size dependency implies that these sorbents had very rough surfaces and the different size dependencies of the different sorbents may be related to the physical structures of the sorbents as well as to the chemical reactions that occur on the surface. This issue will be clarified in future studies.

SULFATION BEHAVIOR

The sulfation data for the three sorbents at a gas temperature of 1,000 °C are shown in Figure 7. The extent of sulfation is expressed as the molar ratio of sulfur to calcium in the solid sample. The data reveal that the sulfation process for the limestone and dolostone particles in this size range was different than that associated with small particles (~5 μm) and precalcined sorbents.[13] There were no initial rapid sulfur capture periods as was the case for most small particles and precalcines.[13] The sulfation rates increased steadily and monotonically. In addition, the low calcium dolostone exhibited a greater sulfur capture capability than the high calcium limestone for the same experimental conditions. The 1,100 °C sulfation data for the three sorbents showed the same trends.

Effect of Calcination Rate on Sulfation Rate: Figure 8 shows the calcination and sulfation curves for 45 μm Bossardsville limestone particles at a gas temperature of 1,000 °C. The experimental

data of Cole et al.[13] using precalcined limestone at similar sulfation conditions are also shown in Figure 8 (indicated by the square data points). Comparing the sulfation curves of the 45 μm limestone particles used in this study and that of Cole's study, the initial rapid sulfur capture period, typical of precalcines and small particles, was not apparent. Based on the calcination curves generated in this study, it is concluded that the delay in calcination is responsible for the initial lower extent of sulfur capture. For the 63 μm Bossardsville limestone particles, the extent of calcination was only 8 % for a 0.2 seconds particle residence time. Though the sulfation rate of the CaO produced was very high, there was not sufficient CaO available at that time for extensive sulfation to occur. As a consequence, the sulfur capture (based on the molar ratio of sulfur to calcium) was low. Despite the initial sulfation delay, the slope of the sulfation curve at longer residence times did not level off. The ongoing calcination process produced fresh CaO surface to be sulfated. The production of a $CaSO_4$ layer from the CaO initially produced resulted in a slower rate of sulfation due to product layer diffusion limitations. However, the sulfation rate of newly created CaO was rapid, thereby compensating for the slower rate of sulfation of the CaO beneath the $CaSO_4$ layer. For particle residence times up to one second, which corresponded to an 80 to 90 % extent of calcination, no significant decrease of the apparent sulfation rate was observed.

Effect of Sorbent Type on Sulfation: As shown in Figure 7, the different sorbents exhibited different sulfation performances at the same experimental conditions. For the sulfation tests with 45 μm particles at 1,000 °C and 1.1 second residence time, the calcium utilization of the Linden Hall limestone was 9 %, that of the Bossardsville limestone was 12 %, while that of the Nittany dolostone was 28 %. On the basis of sorbent utilization (rather than calcium utilization), the performance of the lower purity Bossardsville limestone was not significantly different than that of the high purity Linden Hall limestone. The Nittany dolostone, which contained only 50 % calcium carbonate, displayed better performance than the high purity Linden Hall limestone. At a Ca/S molar feed ratio of 2.0, the 45 μm Nittany dolostone particles reduced the SO_2 in combustion gas by 56 % in 1.1 seconds at 1,000 °C.

CONCLUSIONS

1. Simulating the dry sorbent furnace injection process by using ambient temperature air as the injection medium increased the heating time of 37 to 105 μm diameter particles and delayed the calcination process.
2. The extent of calcination was insensitive to particle size in the range studied. The calcination model based on the specific BET surface area of the raw sorbent produced the best fit of the experimental data.
3. The calcination delay significantly affected the apparent sulfation rate for up to 0.2 seconds after sorbent injection. Between 0.2 and 1.0 seconds, the apparent sulfation rate was almost constant.
4. High purity limestones may not be the best choice for use in dry sorbent furnace injection processes. Low calcium dolostone may display better sulfation performance.

ACKNOWLEDGMENTS

Financial support for this work was provided by Manufacturing and Technology Conversion International, Inc. under DOE Contract #DE.AC21-89MC26288. The cooperation of the staff of The Combustion Laboratory is also acknowledged.

REFERENCES

1. Proceedings: *1990 SO_2 Control Symposium,* Session 3A, EPRI GS-6963, Electric Power Research Institute, Sept. 1990
2. Proceedings: *First Combined Flue Gas Desulfurization and Dry SO_2 Control Symposium,* Session 4A, EPRI GS-6307, Electric Power Research Institute, April 1989
3. Abichandani, J. S., *Gas Stream Cleanup Papers from DOE/METC Sponsored Contractors Review Meetings,* DOE/METC-89/6099, Morgantown, WV, 1988, p.167
4. Lawson, W. F., Maloney, D. J., Shaw, D. W. Richards, G. A., Anderson, R. J., Cook, J. M., Siriwardane, R. V., Poston, J. A. and Colaluca, M. A., *Proceedings of Seventh Annual Coal-fueled Heat Engines and Gas Stream Cleanup Systems Contractors Review Meeting,* DOE/METC-90/6110, Morgantown, WV, 1990, p.283
5. Borgwardt, R. H., *AIChE J.*, 1985, **31**, 103
6. Borgwardt, R. H. and Bruce, K. R, *AIChE J.*, 1986, **32**, 239
7. Borgwardt, R. H., Roache, N. F. and Bruce, K. R., *Ind. Eng. Chem. Fundam.*, 1986, **25**, 165
8. Powell, E. K. and Searcy, A. W., *Metallurgical Trans.*, 1980, **11B**, 427
9. Newton, G. H., Chen, S. L. and Kramlich, J. C., *AIChE J.*, 1989, **35**, 988
10. Milne, C. R., Silcox, G. D. and Pershing, D. W., *Ind. Eng. Chem. Res.*, 1990, **29**, 139
11. Milne, C. R., Silcox, G. D. and Pershing, D. W., *Ind. Eng. Chem. Res.*, 1990, **29**, 2201
12. Dam-Johansen, K., Hansen, P. F. B. and Østergaard, K.,*Chem. Eng. Sci.* 1991, **46**, 847
13. Cole, J. A., Kramlich, J. C., Seeker, W. R., Silcox, G. D., Newton, D. W., Harrison, D. J. and Pershing, D. W., Proceedings: *1986 Joint Symposium on Dry SO_2 and Simultaneous SO_2/NO_x Control Technologies,* Vol. 1, 16-1, EPRI CS-4966, Electric Power Research Institute, Dec. 1986

Table 1. Stratigraphic formations, chemical compositions and BET surface areas of the sorbents

Formation	$CaCO_3$	$MgCO_3$	SiO_2	Al_2O_3	Fe_2O_3	BET surface area (m^2/g)		
						45μm	63μm	89μm
Linden Hall	99.42	0.86	0.69	0.31	0.07	0.422	0.396	0.351
Bossardsville	86.93	1.91	8.07	1.46	0.95	0.648	0.613	0.579
Nittany	49.62	39.30	8.01	1.41	0.53	0.534	0.477	0.376

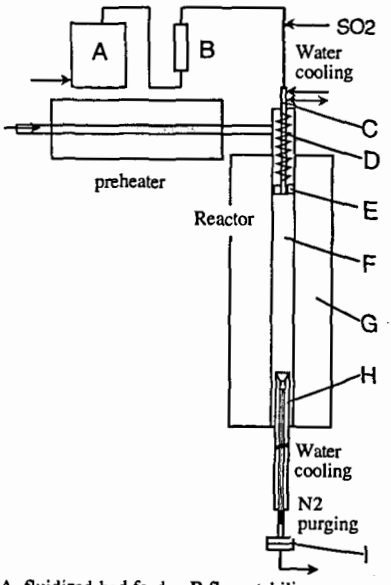

A fluidized-bed feeder, B flow stabilizer
C sorbent and SO2 injector
D injector outside heating
E flow straightener, F reactor tube
G electric furnace, H solid sampling probe
I sample filter

Fig. 1 Schematic diagram of entrained-flow reactor

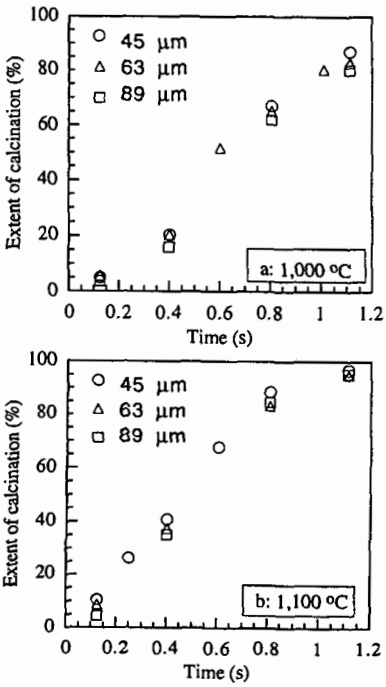

Fig. 2 Time dependency of the extent of calcination of the Linden Hall limestone at a) 1,000°C and b) 1,100°C for various particle sizes

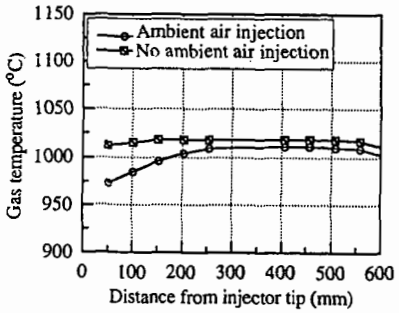

Fig. 3 Effect of injecting sorbent with ambient air on the gas temperature profile along the reactor

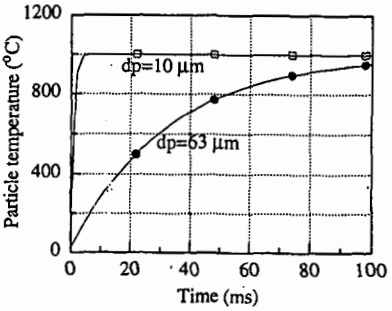

Fig. 4 Calculated sorbent particle temperature profiles during convective heating for 10 and 63 μm particles

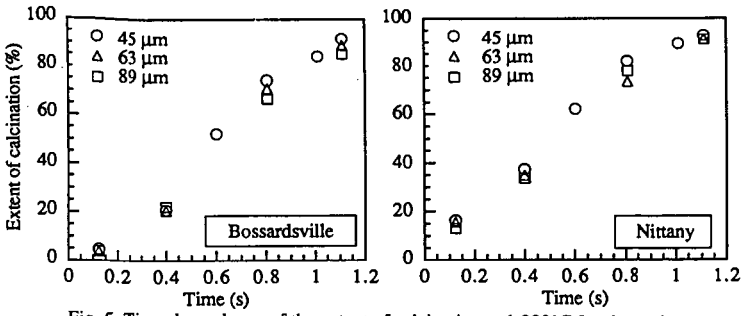

Fig. 5 Time dependency of the extent of calcination at 1,000°C for the various particle sizes of the Bossardsville and Nittany sorbents

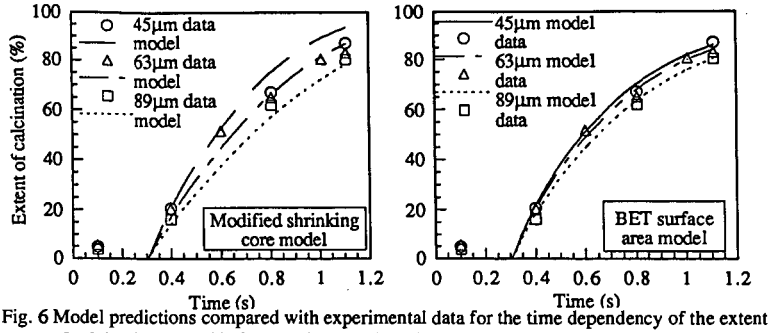

Fig. 6 Model predictions compared with experimental data for the time dependency of the extent of calcination at 1,000°C for various particle sizes of the Linden Hall limestone

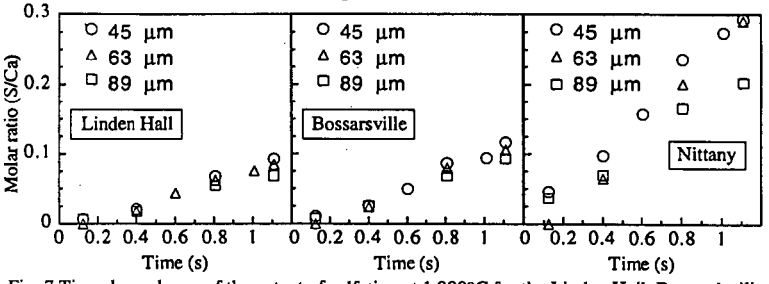

Fig. 7 Time dependency of the extent of sulfation at 1,000°C for the Linden Hall, Bossardsville and Nittany sorbents

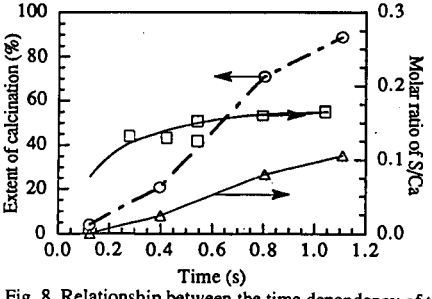

Fig. 8 Relationship between the time dependency of the extents of calcination and sulfation at 1,000°C of 63 μm Bossardsville limestone particles

MODIFIED PEROVSKITES, $La_{1-x}Mg_xMO_3$, - EXCELLENT De-SOx AGENTS.

Jin S. Yoo, C. A. Radlowski, and J. A. Karch*, Amoco Research Center, P.O. Box 3011, Naperville, IL 60566, *UOP, 25 E. Algonquin Road, Des Plaines, IL 60017-5017

Keywords: $DeSO_x$, modified perovskites, FCC regenerator

INTRODUCTION

The De-SO_x catalyst, cerium containing mixed spinel materials, $Ce/MgO \cdot MgAl_{2-x}M_xO_4$ M=Fe, V, Cr, Mn etc) has been effective for the SO_x and NO_x removal from the emission of the fluid catalytic cracking (FCC) regenerator [1,2]. Another type of mixed metal oxides structurally analogous to the naturally occurring mineral perovskite ($CaTiO_3$) have for decades formed the testing and breeding ground for ideas in solid state chemistry. The properties of perovskites that are important in catalysis are primarily the stability of mixed valence states of Co, Mn, Ti, etc., the stabilization of unusual oxidation states, and in particular, the mobility of oxygen ions.

For the automotive application, encouraging results were obtained with manganite and cobaltate perovskites in the oxidation of CO and the reduction of NO. The sensitivity of these particular perovskites to deactivation by SO_2 dampened the initial enthusiasm for their application in automotive exhaust catalysis. Since then, the deactivation mechanism has been understood, the SO_2 resistant catalysts such as $La_{0.6}Sr_{0.4}Co_{1-x}M_xO_3$ has been found [3]. IR spectroscopy indicates that SO_2 absorbed on B sites ions in perovskite, AB_3, deactivate the catalyst by blocking the surface sites that are necessary for CO absorption and lattice oxygen replenishment. The poisoning is due to the stable sulfate formation on B sites with SO_3 formed by oxidation of SO_2 in O_2 [4]. This prompted us to look into application of these types of mixed oxides materials for SO_x removal from the emission of FCC regenerator.

EXPERIMENTAL

Catalyst preparation - over recent years specialized catalyst preparation techniques such as freeze-drying and various types of sol-gel process have been used to produce oxides in a fine partiuclate form. In particular the amorphous citrate process [5] and chemical vapor deposition technique [6] have been shown to be effective because of the high yields of uniformly dispersed mixed oxides with high surface area. However, the modified perovskites studied in this work were prepared by the coprecipitation method for simplicity. The preparation of modified perovskites is described using $La_{0.5}Mg_{0.2}CoO_3$ as an example. The catalyst was precipitated from the aqueous nitrate solutions of La, Mg, and Co with n-butylamine according to the procedure discussed in a previous paper [7]. These nitrates of La, Mg, and Co were dissolved in the minimum amount of water. The pH of aqueous solution of La, Mg, and Co were 0.50, 4.75, and 0.76, respectively. These three metal nitrate solutions were mixed with agitation, and the n-butylamine was added dropwise to produce a coprecipitate over an hour. A spectacular color change and an exothermicity were observed. After amine addition was complete, the slurry pH was 9.46, and the pH of the mother liquor was 9.64. The final slurry was extremely viscous and required vigorous stirring. The slurry was filtered, a water wash followed by an ethanol wash to remove final trace of n-butylamine. The resulting cake was allowed to dry in air and further dried in a vacuum oven at 100°C for 12 hours. The dried cake was a crumbly multi-colored solid. The solid was a uniform color after grinding to 40 minus mesh. The 40 minus mesh grind size was fluidized while cartying out calcination at 732°C for 3 hours. The empirical formular of the final dark-brown product was $La_{0.5}Mg_{0.2}CoO_3$.

The SO_x pickup half cycle - Absorption of SO_3 on the catalyst was measured on an Omni Thermal Analysis System which employs a model 35000 Data Reduction system and a rebuilt Du pont 951 Thermogravimetric Analyzer (TGA). The TGA analyzer was equipped with a special reaction cell to allow the use of corrosive gases (i.e. SO_2) without affecting the delicate balance mechanism. The following test procedure was followed: 1) Approximately 8 mg of catalyst was placed on a quartz pan on the TGA balance. 2) The reaction cell was connected to gas lines and exhaust line. Purged with nitrogen at a flow rate of 200 cc/min throughout an entire run to sweep reacting gases away from balance and out exhaust line. 3) Nitrogen was passed at 100 cc/min while sample was heated at 25°/min to 732°C. 4) After the reactor temperature stabilized at 732°C, the N_2 gas was shut off and the gas blend containing 1.5% SO_2 and 5.9% O_2 in N_2 was introduced over the sample at 100 cc/min. 5) Maintained a weight gain for 15 min while the data point was taken every 10 seconds. 6) At the end of 15 min, the reactor was allowed to cool down, shut off the SO_2 blend gas and switched to air (100 cc/min) for 5 min. When the reactor was cooled to 500°C, air was switched to N_2. It was assumed that a net weight gain was attributed to the SO_3 uptake, and % sulfur was calculated from the net weight gain.

The H_2 reduction half cycle - The sulfated sample resulting from the SO_x pick-up half cycle was reduced with H_2. 1) The sulfated sample was heated to 677°C (in some cases 677 – 732°C) under the N_2 flow of 100 cc/min at a rate of 25°C/min. 2) After the

temperature was stabilized, N_2 is shut off and H_2 was admitted at a rate of 100 cc/min. A weight loss was monitored for 10 min (data points were taken every 2 seconds). 3) At the end of 10 min., the oven was shut off, H_2 was shut off and then N_2 was admitted at 100 cc/min. A catalyst cycle was complete by conducting the SO_x pick-up half cycle and then the H_2 reduction half cycle in sequence. The catalyst stability was determined by the prolonged catalyst cycle tests.

RESULTS AND DISCUSSTIONS

The oxidative SO_x pick-up half cycle - A series of modified perovskite type mixed oxides, $La_{1-x}Mg_xMO_3$, where M=Mn, Co, Cu, Fe were prepared by the coprecipitation procedure. The evaluation of the calcined materials was conducted according to the procedure described in the experimental section. A feed consisting of 1.5% SO_2, 5.9% O_2 and the balance N_2 passed over the catalyst on a pan in the cell of du pont 951 Thermogravimetric Analyzer for 15 min at 732°C. The typical results for manganite, cobaltate, ferrate and cuprate are compared in Figure 1.

H_2 reduction half cycle - The sulfated manganite such as $MgMnO_3$ and $La_{0.2}Mg_{0.8}MnO_3$ and modified cobaltate such as $La_{0.8}Mg_{0.2}CoO_3$ and $La_{0.5}Mg_{0.5}CoO_3$ in the SO_x pick-up half cycle was subjected to the H_2 reduction half cycle. After the catalyst blend in a FCC equilibrium catalyst was sulfated in the SO_x pick-up half cycle, the sulfated system was flushed with nitrogen, brought back to 677°C, reduced in flowing H_2 for 5 minutes, flushed with N_2, and then retested for the SO_x pick-up reaction. The catalytic cycle, SO_x pick-up half cycle followed by H_2 reduction half cycle, was repeated with these catalysts. The weight change (mg) occurred in each half cycle was presented along with calculated S% on the catalyst in Table 1, and plotted in Figure 2. Among these catalyst, $La_{0.8}Mg_{0.2}CoO_3$ appears to be the most stable and promising one.

It has been well known that perovskites are able to exchange oxygen quite easily as the oxidation state of the metals changes due to oxidation or reduction. Reller and colleagues [8] have shown the following conversion: $CaMn^{+4}O_3 \rightleftharpoons CaMn^{+2}O_2 + H_2O$ under H_2 at 500-600°C. It is thus difficult to measure the reduction capability of a sulfated perovskites by TGA. The reaction we want to observe is: $M\text{-}O\text{-}SO_3 + H_2 \rightarrow M\text{-}O + H_2 + SO_2$, where the weight loss is solely due to the loss of SO_3. But the abstraction of labile oxygens from the perovskite lattice complicates the interpretation of the weight loss observed. This phenomenon has been observed in reductions of the sulfated peroskites. The final weight after reduction is lower than the initial weight of the sample (before sulfation) in our own work as well. Any pickups occurred subsequent to the reduction will not only indicate the weight gain of SO_3 but also the replacement of any oxygen missing from the lattice. Because the TGA indicates only weight losses and gains, one must report to final testing of the perovskite catalysts in a cyclic unit where actual pick-up of SO_2 after the sulfate reduction step can be monitored. This will indicate whether or not sulfur is being removed by the reduction or picked up on the catalyst.

Non-oxidative SO_x pick-up chemistry

The same modified cobaltate, manganite, and ferrate were also subjected to non-oxidative SO_x uptake in a feed containing 1600 ppm SO_2 in N_2 by varying the reaction temperatures. The results shown in Table 2 indicate that some of the samples were excellent for SO_x uptake. Catalyst D, $La_{0.8}Mg_{0.2}CoO_3$, exhibited the highest activity in the non-oxidative system among the catalysts studied. Figure 3 is a plot of non-oxidative SO_x pick-up as a function of temperature. Main reactions occurring in the non-oxidative system are believed to be disproportionation of metal sulfite, MSO_3, into sulfate and sulfide [9], and direct reduction of SO_2 to elemental sulfur by the reducing agent such as CO [10]. These results suggest that modified perovskites can be used either in oxygen rich or in oxygen starved FCC regeneration mode.

CONCLUSIONS

A series of modified perovskites, $La_{1-x}Mg_xMO_3$, where M=Co, Mn, Cu, Fe, x=0-1, was found to be effective for removing SO_x from the emission of the fluid catalytic cracking regenerator. Typical modified perovskite samples such as $La_{0.2}Mg_{0.8}MnO_3$, $La_{0.8}Mg_{0.2}CoO_3$, $La_{0.5}Mg_{0.5}CoO_3$, and $La_{0.8}Mg_{0.2}FeO_3$ were prepared by the coprecipitation method. These materials were evaluated for the SO_x removal activity in the two types of feed streams containing 1.5% SO_2 in N_2 with or without 5.9% oxygen. These samples exhibited a remarkable SOx absorption activity in both streams. The catalyst stability of $La_{0.8}Mg_{0.2}CoO_3$ was demonstrated with the catalyst cycle test in an automated laboratory reactor. It is encouraging to find that these materials are also very active under the non-oxidative stream. This suggests that these materials can be used either in the oxygen rich or in oxygen starved FCC regeneration modes.

REFERENCES

1. J. S. Yoo, A. A. Bhattacharyya, C. A. Radlowski, and J. A. Karch, Appl. Catal. B: Environmental, 1 (1992) 169.
2. J. S. Yoo, A. A. Bhattacharyya, and C. A. Radlowski, I&EC Res., 30 (1991) 1444.
3. W. Li, Q. Hwang, W. Zhang, B. Lin, and G. Lee, Stud. Surf. Sci. Catal., 30 (1987) 405.
4. M. Yu. Sultanov, I. S. Al'tsshel, and Z. Z. Makhmudova, Kinet. Katal., 28(1) (1987) 236.
5. H. Zhang, Y. Teraoka, and N. Yamazoe, Chem. Lett., (1987) 665: M. S. G. Baythoun and F. R. Sale, J. Mater. Sci., 17 (1982) 2757.
6. J. S. Yoo, J. A. Donohue, M. S. Kleefisch, P. S. Lin and S. D. Elfline, Appl. Catal. A: General 105 (1993) 83.
7. T. Nakamura, M. Misono, T. Uchijima, Y. Yoneda, Nippon Kagaku Kaishe, No.11 (1980) 1680.
8. A. Reller, G. Davoodabady, H. Oswald, Thermochimica Acta, 83 (1985) 121.
9. C. Castelliani, Gass Chim. Ital., 93(10) (1963) 1252; 93(11) (1963) 1444; 92 (1962) 447; 91 (1961) 173.
10. D. B. Hibbert and R. H. Campbell, Appl. Catal., 41 (1988) 273.

Table 1

The catalytic cycle test, SO_x pick-up half cycle and sulfate reduction half cycle
Catalyst: A:$MgMnO_3$, B:$La_{0.2}Mg_{0.8}MnO_3$, C:$La_{0.5}Mg_{0.5}CoO_3$. D:$La_{0.8}Mg_{0.2}CoO3$,
Surface area. m^2/g: C:22, D:1

	S pick-up, mg				S removed, mg				S% on catalyst			
Catalyst	A	B	C	D	A	B	C	D	A	B	C	D
# of cycle												
1	49	46	46	35	34	18	29	13	13.0	12.4	12.4	10.2
2	33	14	32	17	26	13	31	17	13.4	12.2	13.5	11.5
3	23	9	30	14	23	9.6	30	12	12.8	11.4	13.5	10.9
4	18	7	26	15	19	8.6	27	13	11.8	10.8	12.8	11.4
5	16	8	24	14	20	8.3	-	-	11.2	10.7	12.2	11.2
6	18				18				10.7			

Table 2

The SO_x pick-up test in a non-oxidative system
2% blend of catalysts in an FCC equilibrium catalyst
Catalyst D: $La_{0.8}Mg_{0.2}$ CoO_3, E:$La_{0.2}Mg_{0.2}MnO_3$, F:$La_{0.8}Mg_{0.2}FeO_3$

Catalyst	% SO_x picked up					Activity	
Temp. °F	500	800	1000	1200	1350	1200	1350
D	12	16	31	63		28	
E					52		22
F					36		14

Fig. 1. Comparison of oxidative SOx pick-up results - S% vs time
La.5Mg.5MO3, M = Mn, Co, Fe, Cu

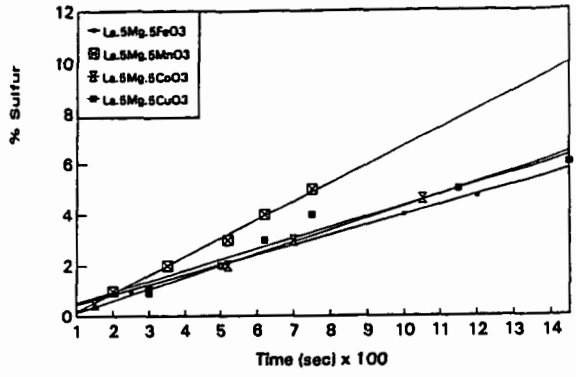

Fig. 2. The stability study of modified perovskites - SOx activity vs catalyst cyle
Repeating a catalyst cycle, SOx pickup half cycle followed by H2 reduction half cycle

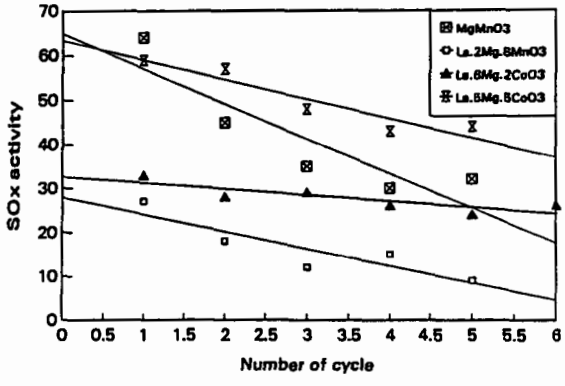

Fig. 3. Non-oxidative SOx pick-up of modified perovskite
SOx pick-up vs temperature, 1600 ppm SO2 in N2

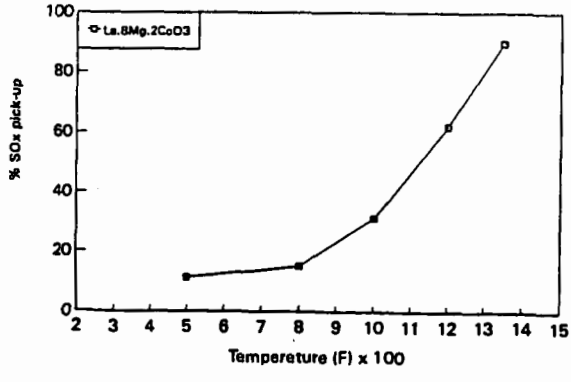

Oxidative Removal of SO_2 and Recovery of H_2SO_4 over Polyacrylonitrile-Based Active Carbon Fiber

S. Kisamori, K. Kuroda, S. Kawano, and I. Mochida
Institute of Advanced Material Study, Kyushu University,
6-1 Kasuga-koen, Kasuga, Fukuoka 816

Keywords : SO_2 removal, SO_2 Oxidation, Activated Carbon Fiber

Abstract

SO_2 was adsorbed, oxidized, hydrated, and recovered continuously as aq. H_2SO_4 at 30-100℃ on a polyacrylonitrile based active carbon fiber (PAN-ACF-FE-300). SO_2 of 1000 ppm in a model flue gas was removed completely for longer than 60 h at 30 and 50℃ by W/F=5.0×10^{-3} g min ml^{-1} by supplying sufficient humidity of 10 and 20 vol%, respectively. The heat-treatment of the ACF at 800℃ was found very effective to enhance the catalytic activity, the temperature appearing very best between 30 to 1000℃. A pitch based activated carbon fiber exhibited less activity than PAN-ACF.

Introduction

More energy-saving, deeper removal of SO_2 in the flue gas has been expected to be developed for the better environment with smaller increase of the cost. Although the wet desulfurization of flue gas using calcium hydroxide in water has been widely commercialized[1], desulfurization of higher efficiency is expected. The conventional desulfurization consumes calcium hydride, to produce gypsum of low value as by-product, or solid waste, requiring a large amount of water and leaking ca. 50 ppm of SO_2. Oxidative adsorption of SO_2 in the form of H_2SO_4 on active carbon or coke around 130℃ is a basis for a dry process[2-4]. The present authors have reported a remarkably large capacity of PAN-ACF among various ACFs for such an oxidative adsorption[5,6]. Such a dry process using carbon adsorbents should heat up the adsorbents after the SO_2 adsorption to recover SO_2 adsorbed in the form of H_2SO_4 on the carbon surface and to regenerate the adsorption ability. At the same time, oxygen functional groups which are introduced by adsorption and desorption of SO_2 should be removed because such oxygen functional groups reduce SO_2 adsorption ability of ACF[7,8]. The reduction of SO_3 into SO_2 at the recovery consumes the carbon as carbon dioxide or monoxide. The carbon adsorbent loses its weight and adsorption ability very rapidly, when flue gas of large SO_2 concentration is charged. Such energy and carbon consumption is one of the critical disadvantages[2,7]. Hitachi has proposed extraction of adsorbed SO_2 on active carbon with water, however, it took so much water to obtain a diluted H_2SO_4[9].

The present paper proposes a solution of the problems, by recovering aq. H_2SO_4 continuously from the surface of PAN-ACF at the SO_2 removal temperature without any carbon loss. PAN-ACF is certainly active to oxidize catalytically SO_2 into SO_3 even at room temperature. Hence continuous hydration of SO_3 may allow the flow of aq. H_2SO_4 from the ACF surface to the reservoir, liberating the active sites to continue the oxidation and hydration of the successive SO_2 molecule. The present process can be applicable to remove SO_2 in the atmosphere as well as flue gas without any difficulty.

Experimental

FE series of PAN-ACFs were supplied by Toho Rayon Co. OG series of pitch ACFs were supplied by Osaka gas. They were heat-treated in nitrogen at 30 to 1000℃. Some of them properties are summarized in Table 1.

SO_2 removal was carried out at 30-100℃ using a fixed bed flow reactor which is illustrated in Fig.1. A model flue gas containing SO_2 of 1000 ppm, O_2 of 5 vol% and H_2O of 10-30 vol% in nitrogen was used. H_2SO_4 was trapped at the outlet of the reactor as illustrated in Fig.1. A part of H_2O was condensed to dew drops in the reactor when water vapor of 10 and 20 vol% was introduced at 30 and 50℃, respectively. Therefore, concentrations of SO_2 and O_2 in the model gas were increased slightly and the total flow rate was decreased slightly in these cases compared

with other cases. SO_2 concentrations in inlet and outlet gases were observed continuously by a frame photometric detector (FPD). Weights of ACF examined and the total flow rate were 0.25, 0.5, and 1.0 g, and 100 ml min^{-1}, respectively.

Results

Figure 2 illustrates the break-through profiles of SO_2 at 30℃ through the beds of two PAN-ACFs and three pitch ACFs of all as-received forms. The gas carried 10 vol% water in all cases. Over PAN-ACF FE-300 which exhibited the largest adsorption capacity, SO_2 was adsorbed completely until 1.6 h (the break-through time T_0), no SO_2 being detected at all at the outlet of the reactor and then SO_2 started to leak concentration increasing rather gradually to 15% of the inlet SO_2 after 5 h. The concentration was kept at this level for at least 13 h, major SO_2 of 80% was removed continuously from the flowing gas.

Other ACFs exhibited similar profile of SO_2 adsorption and removal, although the T_0 and the level of SO_2 stationary concentration were dependent on ACFs. The levels of the stationary concentration were 18% over PAN-ACF-FE 300, 22% over FE-100, 38% over OG-5A and OG-20A, and 45% over OG-10A. The higher activity of PAN-ACF for SO_2 removal was definite. The value of T_0 ranged 0.5 to 18 h, PAN-ACF exhibiting slightly longer break-through time.

Figure 3 illustrates effects of heat-treatment on break-through profiles over PAN-ACF-FE-200 and FE-300 at 30℃, 10 vol% of H_2O. The heat-treatment was very effective to decrease the level of SO_2 stationary concentration as well as to prolong the break-through time as reported before[11]. A particular temperature of 800℃ was found most favorable for both FE-200 and FE-300. The complete removal of SO_2 by both ACFs continued for in least 60 h at 25℃ by W/F of 5.0×10^{-3}g min ml^{-1}. Further higher temperature reduceed the activity.

Figure 4 illustrates the break-through profiles of SO_2 at several temperatures through the bed of FE-300-800. SO_2 was adsorbed completely at 100℃ until 5.1 h, no SO_2 being detected at all at the outlet of the reactor, and then SO_2 started to leak, its concentration increasing rather rapidly to 100% of the inlet SO_2 after 10.5 h. SO_2 of 4.0 mmol g^{-1} was captured on the ACF at 100℃. Lower temperature of 80℃ extended the break-through time to 8.5 h until SO_2 was detected at the outlet of the reactor. After the break-through, SO_2 concentration at the outlet increased rather gradually by 24 h until it reached to 65% of the inlet concentration, and that of the outlet stayed at the same level later on until at least 45 h. Further lower temperature of 50℃ extended the break-through time to 10.5 h. At this temperature, the outlet concentration increased very slowly to 25% after 25 h. While the removal of SO_2 continued, some elusion of aq. H_2SO_4 was observed at outlet of the reactor. At room temperature of 30℃, SO_2 was completely removed at least 60 h while no SO_2 was observed at the outlet. Elusion of aq. H_2SO_4 was clearly observed at the outlet.

Figure 5 summarizes the influences of H_2O concentration on the break-through profiles of SO_2 through FE-300-800 at 100, 80 and 50℃. Higher concentration of H_2O (20 and 30 vol%) extended slightly the break-through time at 100℃ and allowed the stationary removal of SO_2 at the outlet after the concentration became steady. The stationary concentrations under 10 and 20 vol% H_2O were 100 and 80%, respectively. Higher concentrations of H_2O were more pronounced at 80 ℃. The stationary concentrations of SO_2 under 10, 20 and 30 vol% H_2O were 60, 55 and 10%, respectively while the break-through time was extended to 7 to 10 h. The influence of H_2O concentration was more drastic at 50℃. H_2O concentration of 20 vol% allowed a steady SO_2 removal of 100%, no SO_2 being detected for 60 h, whereas 10 vol% H_2O provided 30% steady concentration at the outlet. When the steady removal of SO_2 was achieved, elusion of aq. H_2SO_4 was observed. Hence, SO_2 is adsorbed, oxidized, and hydrated into aq. H_2SO_4 on the ACF surface which flows out from the bed to be stored in the reservoir at the reactor outlet (Fig.1). Thus, the removal of SO_2 is expected to continue. Enough water is necessary to hydrate SO_3 and to dilute H_2SO_4 to flow smoothly through the ACF bed.

Figure 6 summarized the influences of W/F (Flow rate was fixed at 100 ml min^{-1}) on the break-through profiles of SO_2 through FE-300-800 at 100 and 30℃ when humidity was fixed at 10 vol%. In the case of 100℃, break-through time (T_0) was extended drastically with increasing of W/F. When the weight of the ACF increased from 0.25 g to 1.0 g, T_0 was extended markedly from

1.8 h to 18 h. The concentration of SO_2 at the outlet was saturated to be 100% by 10-15 h when ACF of 0.25 and 0.5 g was used, respectively. When the ACF was increased to 1.0 g, SO_2 concentration at the outlet increased very slowly but continuously even 45 h after SO_2 adsorption started. Larger amount of ACF may allow the better contact of the gas with the fiber and some storage of adsorbed H_2SO_4 to fill the void in its bed.

The ACF removed SO_2 completely for 60 h at least by W/F = 5.0×10^{-3} g min ml^{-1} at 30℃. However, 0.25 g of ACF removed SO_2 completely for 2.0 h, and then SO_2 started to leak. SO_2 concentration in the outlet increased continuously to 10% by 7.5 h, and stayed at the level until 15 h at least, leaving aq. H_2SO_4 in the reservoir. The highest concentration of H_2SO_4 trapped in the reservoir at the outlet of the reactor, was 7.3 normal when the PAN-ACF-FE-300-800 was used at 30℃ with 10 vol% H_2O. The concentration should depend on the SO_2 concentration and conversion, and vol% of H_2O. Hence the ACF of the highest activity and the largest amount for the complete conversion and lower temperature which allows lower concentration of H_2O are favorable to increase the concentration of recovered H_2SO_4.

Discussion

The oxidation and hydration of adsorbed SO_2 were found to proceed on the ACF surface at a temperature range of 30-100℃. The surface of the activated carbon was found to oxidize SO_2 efficiently and rapidly. The key point of the present study is to achieve the continuous recovery of aq. H_2SO_4 by supplying H_2O vapor onto ACF. The results indicate that the necessary concentration of water vapor is very much dependent on the reaction temperature, being 20 vol% at 50℃ and 10 vol% at 30℃ when the W/F was large enough. Higher reaction temperature requires more supply of water. H_2SO_4 can flow only when it is diluted to a certain concentration by the sufficient water on the ACF surface. Water is condensed on the ACF from the gas phase basically according to the relative humidity, although H_2SO_4 itself may adsorb water.

Fiber form of ACF may be favorable for smooth flow of aq. H_2SO_4 through the adsorbent bed. Flue gas sometimes requires further reduction of NOx after the desulfurization. Hence the temperature of desulfurization should be balanced since higher temperature is favorable for the reduction while lower desulfurization temperature requires less water. The flow of aq. H_2SO_4 may depend also on the surface structure of ACF.

It is worthwhile to note that the heat-treatment at 800 ℃ increased significantly the ability of SO_2 recovery. The oxidation appears to be enhanced. Such treatment may introduce the active site for adsorption[6,7] and oxidation[10] of SO_2 through the evolution of CO and CO_2 by decomposition of surface oxygen functional groups on ACF. Another interesting point is that PAN-ACF showed much higher activity than pitch ACF. Their surface structure is interestingly compared. NO probably co-existing in the flue gas may pass through ACF bed with least oxidation under the present condition as discussed in the following paper. Hence we expect separate recoveries of H_2SO_4 and HNO_3.

References

1) Y. Miura, *Nenryo Kyokaishi*, 1978, **57**, 817.

2) K. Knoblauch, E. Richter, and H. Juntgen. *Fuel*, 1981, **60**, 832.

3) Y. Komatsubara, I. Shiraishi, M. Yano, and S. Ida, *Nenryo Kyokaishi*, 1985, **64**, 255.

4) I. Keiichiro, Y. Niwa, and Y. Morita, *Nenryo Kyokaishi*, 1985, **64**, 338.

5) I. Mochida, Y. Masumura, T. Hirayama, H. Fujitsu, S. Kawano, and K. Gotoh, *Nippon Kagaku Kaishi*, 1991, **1991**, 296.

6) I. Mochida, T. Hirayama, S. Kisamori, S. Kawano, and H. Fujitsu, *Langmuir*, 1992, **8**, 2290.

7) I. Mochida, S. Kisamori, S. Kawano, and H. Fujitsu, *Nippon Kagaku Kaishi*, 1992, **1992**, 1429.

8) S. Kisamori, S. Kawano, and I. Mochida, Extended Abstr., 21th Biennial Conf. on Carbon, 478, Buffalo, June 1993.

9) K. Yamamoto, K. Kaneko, and M. Seki, *Kogyo Kagaku Kaishi*, 1971, **74**, 84.

10)S. Kisamori, S. Kawano, and I. Mochida, *Langmuir*, in press.

11)S. Kisamori, S. Kawano, and I. Mochida, *Chemistry Letters*, 1993, **11**,1899.

Table 1. Some properties of ACFs

ACFs	Elemental Analysis(wt%)					Surface area
	C	H	N	O diff.	Ash	($m^2 g^{-1}$)
FE-100	77.5	1.8	9.7	11.0	0.3	446
FE-200	75.8	1.7	5.8	16.7	0.3	887
FE-300	78.1	1.4	4.5	16.0	0.3	1141
OG-5A	89.6	1.1	0.7	8.3	0.3	480
OG-10A	91.6	0.9	0.5	6.7	0.3	710
OG-20A	93.9	0.9	0.3	4.6	0.5	1150

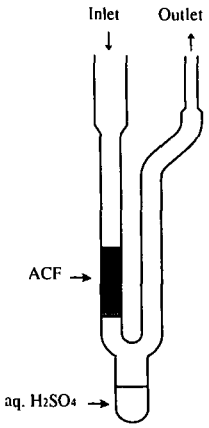

Fig.1 Reactor

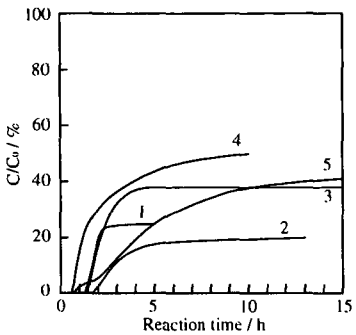

Fig.2 Breakthrough profiles of SO_2 over as-received ACFs
SO_2 1000ppm, O_2 5 vol%, H_2O 10 vol%
W/F = 5.0×10^{-3}g min ml^{-1}
Reaction temp. = 30℃
1 : FE-100 (PAN, 450$m^2 g^{-1}$)
2 : FE-300 (PAN, 1140$m^2 g^{-1}$)
3 : OG-5A (Pitch, 480$m^2 g^{-1}$)
4 : OG-10A (Pitch, 710$m^2 g^{-1}$)
5 : OG-20A (Pitch, 980$m^2 g^{-1}$)

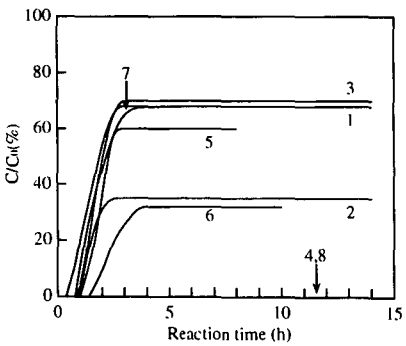

Fig.3 Breakthrough profiles of SO_2 over heat-treated FE-200 and FE-300 at 30℃
SO_2 1000ppm, O_2 5 vol%, H_2O 10 vol%
W/F = 2.5×10^{-3}g min ml^{-1}(1-3, 5-7)
5.0×10^{-3}g min ml^{-1}(4, 8)
1 : FE-200-600; 2,4 : FE-200-800; 3 : FE-200-1000
5 : FE-300-600; 6,8 : FE-300-800; 7 : FE-300-1000

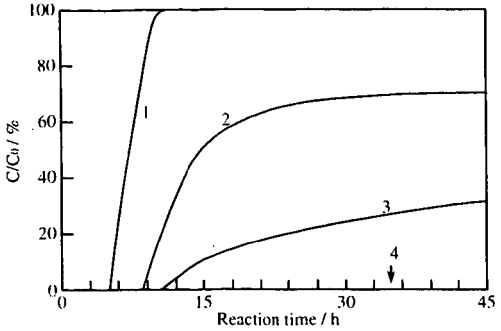

Fig.4 Breakthrough profiles of SO_2 at several temperatures over FE-300-800
SO_2 1000ppm, O_2 5 vol%, H_2O 10 vol%
W/F = 5.0×10^{-3}g min ml^{-1}
1 : 100℃, 2 : 80℃, 3 : 50℃, 4 : 30℃
No.4 adsorbed SO_2 completely for least 60 hours

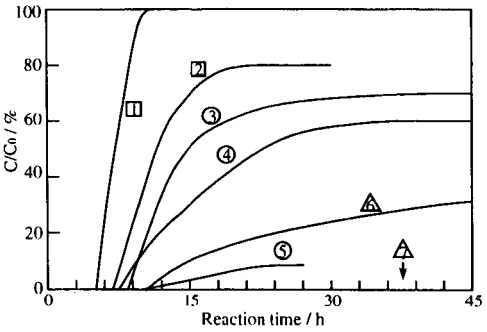

Fig.5 Effect of H_2O concentration for SO_2 removal over FE-300-800
SO_2 1000ppm, O_2 5 vol%, W/F = 5.0×10^{-3}g min ml^{-1}
1 : 100℃, H_2O 10 vol%, 2 : 100℃, H_2O 20 vol%,
3 : 80℃, H_2O 10 vol%, 4 : 80℃, H_2O 20 vol%,
5 : 80℃, H_2O 30 vol%, 6 : 50℃, H_2O 10 vol%,
7 : 50℃, H_2O 20 vol%
No.7 adsorbed SO_2 completely for least 60 hours

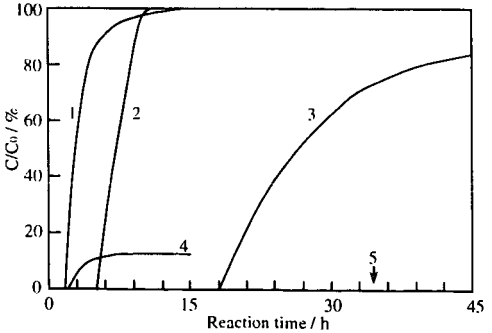

Fig.6 Influence of W/F for SO_2 removal of FE-300-800
SO_2 1000ppm, O_2 5 vol%, H_2O 10 vol%
1 : 100℃, W/F=2.5×10^{-3}g min ml^{-1}
2 : 100℃, W/F=5.0×10^{-3}g min ml^{-1}
3 : 100℃, W/F=1.0×10^{-2}g min ml^{-1}
4 : 30℃, W/F=2.5×10^{-3}g min ml^{-1}
5 : 30℃, W/F=5.0×10^{-3}g min ml^{-1}

CATALYTIC REDUCTION OF SULFUR DIOXIDE TO ELEMENTAL SULFUR

Yun Jin, Qiquan Yu, and S. G. Chang, Energy and Environment Division, Lawrence Berkeley Laboratory, University of California Berkeley, CA 94720

Keywords: sulfur dioxide, catalytic conversion, elemental sulfur

INTRODUCTION

There are several regenerable flue gas desulfurization processes; some of them have been commercilized, while others are still emerging. In the regenerable processes, sulfur dioxide from flue gas is first absorbed into an alkaline solution (Wellman-Lord, Tung, Cansolv, and Dow processes) or adsorbed on a solid substrate (NOXSO and CuO processes), and is subsequently desorbed to produce a stream of high concentration sulfur dioxide. It is desirable to convert sulfur dioxide to elemental sulfur for storage, transportation, and/or conversion to valuable chemicals.

Sulfur dioxide can be reduced with synthesis gas, derived from coal ($H_2/CO = 0.3\text{-}1.0$) or methane ($H_2/CO = 3$), to produce elemental sulfur at elevated temperatures according to the reaction

$$0.875\ SO_2 + 0.75\ H_2 + CO \text{ ----------> } 0.438\ S_2 + CO_2 + 0.75\ H_2O \quad (1)$$

$$2\ SO_2 + 3\ H_2 + CO \text{ ----------> } S_2 + CO_2 + 3\ H_2O \quad (2)$$

These reactions are facilitated with catalysts. In addition to elemental sulfur, these reactions may produce several undesirable byproducts. These include hydrogen sulfide, carbonyl sulfide, carbon disulfide, and elemental carbon. Numerous research efforts have been carried out to develop catalysts for these reactions so that they can proceed with high conversion of sulfur dioxide and high selectivity to elemental sulfur at low temperatures. However, the results obtained so far show only limited successes and do not warrant a commercial application. Using synthesis gas to reduce SO_2, Akhmedov et. al. [1] developed several catalysts and obtained the following results: a 64-65 % sulfur yield with a bauxite-bentonite catalyst at 350 C with a feed gas at a molar ratio ($CO + H_2$)/SO_2 of 2 and a space velocity of 1000 h^{-1}; a 82.0 % sulfur yield with a NiO/Al_2O_3 catalyst at 300 C with a space velocity of 500 h^{-1} [2]; a 82.0 % and 87.4 % sulfur yield with a Co_2O_3/Al_2O_3 catalyst [3] at 300 C with a space velocity of 1000 h^{-1} and 500 h^{-1} respectively; a 82.3 % and 78.6 % sulfur yield with a $NiO+Co_3O_4$ catalyst [4] at 400 C with a space velocity of 500 h^{-1} and 1000 h^{-1} respectively. The development of a catalyst capable of obtaining better than 90 % yield of sulfur with a high space velocity at low temperatures would be required to warrant a commercial application. This paper reports the evaluation results of a promising catalyst formulated in our lab.

EXPERIMENTAL

Catalyst Preparation

Catalysts were composed of a combination of several metal oxides supported on $-Al_2O_3$. Two sizes of $-Al_2O_3$ were used: 1. 30-40 mesh particles, and 2. 3mm dia. by 5 mm height granules. By mixing appropriate amounts of metal nitrate solutions with $-Al_2O_3$, the mixture underwent stepwise heating to form the activated catalyst. The ratio of the active catalyst to carrier was about 0.3 by weight.

Apparatus and Procedure

A schematic flow diagram of the apparatus is shown in Figure 1. The experimental setup consists of three separate sections: the gas supply section, the main reactor, and the detection and analysis section. Gases are supplied from compressed gas cylinders (Matheson Gas Products) to gas flow meters before entering a gas mixer. The tubular reactor is fabricated from a 1.4-cm-o.d. with a 1-mm wall thickness quartz tube. The entire reactor is mounted inside a tubular furnace. The reactor, which is 5 cm long, consists of three zones. The inlet or the preheating zone (2.5 cm long) is packed with 20 mesh quartz chips, the reaction zone (1.5 cm long) is packed with either particles (30-40 mesh) or granules (d. 3mm x h. 5mm) activated catalysts on alumina, and the outlet zone (1 cm long) is packed with quartz chips (20 mesh), mainly for the purpose of supporting the catalyst, which sat on a perforated quartz plate having seven holes for gas exit. A thermocouple, reaching the center of the catalytic packing, provide measurement of the temperature of catalytic reactions. After the last section of the reactor, the gases pass through a sulfur collector at room temperatures, and then enter into an on-line trap cooled in an ice bath to condense water before entering a six-port sampling valve which is used to inject the products of the catalytic reactions into the gas chromatograph. Finally, the exit gases pass into a scrubber containing concentrated NaOH.

The inlet and exit gases are analyzed by using a gas chromatograph equipped with a column switching valve and a thermal conductivity detector. A 2-meter Porapak QS (80-100 mesh) column was employed. The operating conditions were at 60 mA and at column temperature of 100 C. The carrier gas is helium.

RESULTS AND DISCUSSION

The inventive catalyst (Cat-S) consists of active metal oxide components and carriers (-Al_2O_3). In order to study the kinetics of the reactions and the diffusivity of the reactants, two carrier sizes were used. The smaller size carrier is 30-40 mesh -Al_2O_3 particles, which were used typically in laboratory scale experiments to obtain kinetic information. The larger size carrier has a dimension of 3 mm diameter by 5 mm height cylindrical granules, which were used in scale up tests. The parametric studies were conducted on particles and granules for comparison. The lifetime experiments were performed on particles.

Particles (30-40 mesh)

Parametric Studies

The effect of temperatures, space velocity, molar ratios of reductants to SO_2 ($R = F_{(H2+CO)}/F_{SO2}$), and molar ratios of H_2 to CO ($r = F_{H2}/F_{CO}$) on the activity of the catalyst (Cat-S) were investigated in order to determine the optimum operating conditions.

Tables 1 and 2 summarize the results of temperature dependence studies at a space velocity of 10,000 h^{-1} and 15,000 h^{-1}, respectively. The experiments were carried out at r = 3, and R = 2. The results show that the conversion of SO_2 is > 95 % when the temperature is > 380 C at both space velocities. Over the temperature range (340 C - 480 C) studied, the yield of H_2S does not show any appreciable and systematic changes: between 0.716 % and 3.31 % at a S.V.=10,000 h^{-1}, and between 0.919 % and 4.96 % at a S.V.=15,000 h^{-1}. However, the yield of COS shows a decrease with an increase of temperatures: Y_{COS} =2.75 % and 0.749 % at 340 C and 480 C, respectively (at a S.V.=10,000 h^{-1}); Y_{COS} =10.5 % and 0.178 % at 340 C and 480 C, respectively (at a S.V.=15,000 h^{-1}). AT a S.V.=10,000 h^{-1}, the yield of elemental sulfur, Y_{S2} is 93.7 % at 380 C and reaches a maximum value of 95.1 % at 420 C; it decreases slightly to 94.4 % with further increase of the temperature to 480 C. At a S.V.=15,000 h^{-1}, Y_{S2} is 92.8 % at 380 C, and reaches 94.9 % at 420 C.

The effect of space velocity on the catalyst was shown in Table 3. The conversion of SO_2 remains fairly stable (95.8 % - 98.7 %) in a S.V. range of 5,000 to 15,000 h^{-1}. At a S.V. =15,000 h^{-1}, it was observed that the temperature of the catalyst increased 60 degree C, which could be attributed to the liberation of heat from the reactions (exothermic reactions). Y_{H2S} remains at very low level (0.269 % - 0.716 %) when the S.V. is less than 10,000 h^{-1}, it shows a slight increase to 2.21 % as the S.V is increased to 13,750 h^{-1}, but it reaches 4.96 % as the S.V. is further increased to 15,000 h^{-1}. Y_{COS} remains very small (0.095 % - 1.32 %), and does not appeared to be affected systematically by the change of the space velocity. Y_{S2} remains very high value (95.1 % -97.5 %) for S.V. up to 13,750 h^{-1}, it decreases to 92.3 % when the S.V. is increased to 15,000 h^{-1}.

Lifetime tests

The lifetime test was carried out continuously for 1080 h (45 days). The flow rate of H_2, CO, and SO_2 were 2286, 3047, and 2667 ml/h respectively. These correspond to R=2 and r=0.75. The amount of catalyst used was 1 g. These correspond to a space velocity of 10,000 h^{-1}. The catalytic activity was evaluated at three temperatures: 440, 460, and 480 C. The arithematic mean of the experimental results of all 45 days is shown in Table 4. Also given in Table 10 is the arithematic mean of results of an additional experimental condition which was implemented after 15 days lifetime test , and used r =3 to cover the composition of synthesis gas produced from methane.

The results indicate that the activity of the Cat-S, including the conversion and the selectivity, is very stable and does not show any changes during the entire 1080 h of the lifetime test. Table 10 shows that the yield of elemental sulfur ranges between 93.1 and 96.5 %, which is far superior to results so far reported in the literatures [2,3,4]. These high yields were achieved at a space velocity of 10,000 h^{-1} , compared with a reported result of obtaining 69.3 - 72.8 % yield of elemental sulfur at a space velocity of 2,000 h^{-1}, and a 82.8 % sulfur yield at a space velocity of only 500 h^{-1}. Table 10 shows that the yield of H_2S ranges between 1.28 and 2.82 %, which is far better than those of other catalysts: 13.4 % for NiO/Al_2O_3 [2] at a space velocity of 2000 h^{-1} and at 400 C; 3.80 % for Co_2O_3/Al_2O_3 [3] at a space velocity of 2000 h^{-1} and at 300 C; 13.9 % for NiO + Co_3O_4 [4] at a space velocity of 2000 h^{-1} and at 450 C. The yield of H_2S increases along with the increase of the reaction temperatures. Therefore, it is remarkable to observe the low yield of H_2S for the Cat-S at a temperature of 440 to 480 C.

Granules (d. 3 mm x h. 5 mm)
Parametric Studies
The effect of temperature, space velocity, and molar ratio of reactants on the activity and selectivity of the Cat-S catalyst on granules was studied. Table 5 and 6 show the effect of temperature on the catalyst at r = 0.4 and 3 respectively. The results indicate that at a given temperature, C, Y_{S2}, and S_{S2} increase, while Y_{H2S} and Y_{COS} decrease along with the increase of r. Meanwhile, C, Y_{H2S}, and S_{S2} show an increase, while Y_{COS} decreases, as the reaction temperature is increased at a given r value. At a space velocity of 2100 h^{-1} and R = 2 (i.e. a stoichiometric ratio), the yield of sulfur increases to more than 90% when the temperature is above 560 C, 520 C, and 460 C with r = 0.4, 0.75, and 3 respectively. It is worthy noting that the yield of sulfur reaches 97.8% at 560 C and a space velocity of 2100 h^{-1} with synthesis gas derived from methane (i.e. r = 3).

The effect of the space velocity on the catalyst for r = 3 was shown in Table 7 (480 C). The temperature of this series of experiments were chosen such that Y_{S2} could achieve more than 90%. The results indicate that C, Y_{H2S}, and Y_{S2} decrease, while Y_{COS} increases along with the increase of the space velocity. S_{S2} remains fairly constant under the experimental conditions employed.

The effect of R on the Cat-S at r = 3 was summarized in Table 8 (480 C). The results show that at a given r value, C, Y_{H2S}, and Y_{COS} show a slight increase along with the increase of R until R reaches 2. Beyond that however, Y_{H2S} exhibits a drastic growth with the increase of R; Y_{COS} also shows some growth with R, but to a much lesser extent than Y_{H2S}. It is obvious that Y_{S2} is the greatest when R is 2 regardless of the ratio of r.

High Efficiency Recovery
Because of the incomplete conversion of SO_2, and the production of unwanted byproducts, H_2S and COS, either a tail gas treatment step or recycling the byproducts for combustion is necessary. Many technologies have been developed for the treatment of tail gas from a Claus process. However, the tail gas treatment cost is substantial. The combustion treatment would increase the concentration of SO_2 in flue gas. Therefore, it is desirable to maximize the yield of elemental sulfur and to minimize the production of byproducts.

The operating conditions of the Cat-S to obtain a Y_{S2} of 97 % have been determined. Table 9 and 10 show the effect of space velocity and temperature on the catalytic reduction of SO_2 by synthesis gas derived from methane to achieve a more than 93% Y_{S2}. Y_{S2} reaches between 96.9% and 97.1% at 520 C and a space velocity from 1,800 h^{-1} to 2,000 h^{-1}; further increase of space velocity to 3,000 h^{-1}, Y_{S2} decreases to 93%. To achieve a Y_{S2} of 96% at a space velocity of 3,000 h^{-1}, the temperature of the catalytic reactions would have to be increased to 580 C (Table 28).

An alternative technology for the conversion of SO_2 to elemental sulfur involves two steps: 1. the combustion of SO_2 in a hydrocarbon flame under reduced conditions to form H_2S, 2. the employment of a Claus process to react SO_2 with H_2S to produce elemental sulfur. The first step requires the consumption of an excess amount of hydrocarbon, compared with the need of only a stoichiometric amount of synthesis gas for SO_2 reduction in the present invention. The Claus process requires three stages to achieve a 96-97% Y_{S2} at a space velocity of 1,500 -3,000 h^{-1}, while the new technology needs only a single stage reactor to obtain the same Y_{S2} at a comparable space velocity, 2,000 - 3,000 h^{-1}.

CONCLUSION
We have developed a catalyst for reduction of SO_2 by synthesis gas. This catalyst is composed of a mixture of common transition metal oxides supported on -alumina and is inexpensive.

The inventive catalyst can achieve a high conversion efficiency of SO_2 by synthesis gas with a high selectivity to elemental sulfur. Unlike the Claus process, the reaction of SO_2 with synthesis gas to form elemental sulfur is not a reversible process. As a result, a high efficiency recovery of sulfur can be achieved in a single stage reactor.

A lifetime (1080 h) test has been successfully performed on the Cat-S in 30-40 mesh particle sizes. The test was conducted at 480 C, S.V. = 10,000 h^{-1}, R = 2, and at r = 3 and 0.75. The activity of the catalyst remains very stable during the entire period of the lifetime test. The yield of sulfur was 96.5% and 94.1% at r = 3 and 0.75 respectively.

The mass balance of sulfur and carbon has been checked satisfactory by measuring the aforementioned products.

It has been demonstrated that the byproducts, H_2S and COS, produced during the conversion of SO_2 to sulfur can be circulated back to the feed gas for subsequent conversion on inventive catalysts without resulting in further accumulation of the said byproducts.

This catalyst can achieve 97% yield of elemental sulfur at 540 C with a space velocity of 2,000 h^{-1} or at 640 C with a space velocity of 3,000 h^{-1}. This catalyst requires only a stoichiometric amount of synthesis gas for SO_2 reduction. While the waste of fuel is negligible, the operating cost is small

The inventive catalyst possesses very promising properties. As such, it could be utilized as a basis to develop a new process for high efficiency conversion of SO_2 to elemental sulfur by synthesis gas at a more cost effective manner than technologies available currently.

REFERENCES

(1). Akhmedov, M.M., Shakhtakhtinskii, G. B., Agaev., A.I., Azerb. Khim. Zh. (2) 95 (1983).
(2). Akhmedov, M.M., Gezalov, S.S., Agaev, A.I., Mamedov, R.F., Zh. Prikl. Khim., 61, (1) 16 (1988).
(3). Akhmedov, M.M., Guliev, A.I., Agaev, A.I., Gezalov, S.S., Zh. Prikl. Khim., 61, (8) 1891 (1988).
(4). Akhmedov, M.M., Guliev, A.I., Ibragimov, A.A., Khim. Prom. (1), 37 (1989).

ACKNOWLEDGEMENT

The authors appreciate the support of Perry Bergman, Charles Schmidt, and Charles Drummond. This work was supported by the Assistant Secretary for Fossil Energy, U.S. Department of Energy, under Contract DE-AC03-76SF00098 through the Pittsburgh Energy Technology Center, Pittsburgh, PA.

Table 1 The effect of temperatures on the Cat-S(particles) at (H2/CO)=3.0, and S.V.=10,000 h^{-1}

t (°C)	C (%)	Y_{H2S} (%)	Y_{cos} (%)	Y_{S2} (%)	S_{S2} (%)
340	83.7	1.59	2.75	79.4	94.8
380	95.9	1.66	0.548	93.7	97.7
400	97.9	3.31	0.325	94.2	96.3
420	98.0	2.51	0.314	95.1	97.0
440	97.2	2.19	0.341	94.7	97.4
460	96.3	1.57	0.326	94.4	98.0
480	95.8	0.716	0.749	94.4	98.5

Table 2 The effect of the temperatures on the Cat-S (particles) at (H2/CO)=3.0, and S.V.=15,000 h^{-1}

t (°C)	C (%)	Y_{H2S} (%)	Y_{cos} (%)	Y_{S2} (%)	S_{S2} (%)
340	62.7	0.919	10.5	51.4	81.8
360	74.2	0.218	5.23	68.8	92.7
380	94.8	1.53	0.526	92.8	97.8
400	96.5	1.62	0.489	94.4	97.8
420	97.7	2.45	0.324	94.9	97.2
440	96.9	2.07	0.351	94.5	97.5
460	96.3	1.83	0.363	94.1	97.7
480	97.4	4.96	0.178	92.3	94.7

Table 3 The effect of the space velocity on the Cat-S (particles) at (H2/CO)=3.0, and 480 C

S.V. (h^{-1})	C (%)	Y_{H2S} (%)	Y_{cos} (%)	Y_{S2} (%)	S_{S2} (%)
5000	97.7	0.289	0.095	97.4	99.0
6250	98.2	0.482	0.123	97.5	99.4
7500	97.9	0.349	0.839	96.7	98.8
8750	98.4	0.574	0.102	97.7	99.3
10000	95.8	0.716	0.746	94.4	98.5
11250	96.6	0.269	0.077	96.2	99.6
12500	98.7	2.29	1.32	95.1	96.3
13750	98.5	2.21	0.248	96.0	97.5
15000	97.4	4.96	0.178	92.3	94.7

Table 4 The arithmatic mean values of the lifetime test results at 440 C, 460 C, and 480 C; and at the feed gas molar ratio (H2/CO)=0.75 [* feed gas molar ratio (H2/CO)=3]

t (°C)	C (%)	Y_{H2S} (%)	Y_{cos} (%)	Y_{S2} (%)	S_{S2} (%)
440	95.7	2.30	0.356	93.1	97.0
460	96.2	2.36	0.376	93.5	97.2
480	97.3	2.82	0.366	94.1	96.7
480*	98.2*	1.28*	0.382*	96.5*	98.3*

Table 5 The effect of the temperatures on the Cat-S (granules) at (H2/CO)=0.4, [(H2+CO)/SO2]=2.0, and S.V.=2,105 h^{-1}

t (°C)	C (%)	Y_{H2S} (%)	Y_{cos} (%)	Y_{S2} (%)	S_{S2} (%)
440	81.4	0.949	9.0	71.9	87.1
460	85.7	0.992	6.09	78.6	91.7
480	88.2	1.08	4.95	82.1	93.1
500	91.7	1.37	3.56	86.8	94.6
520	93.0	1.40	2.93	88.7	95.3
540	93.5	1.42	2.42	89.7	95.9
560	94.3	1.53	2.22	90.5	96.1
580	96.7	2.47	2.17	92.0	95.3

Table 6 The effect of the temperatures on the Cat-S (granules) at (H2/CO)=3.0, [(H2+CO)/SO2]=2.0, and S.V.=2,105 h^{-1}

t (°C)	C (%)	Y_{H2S} (%)	Y_{cos} (%)	Y_{S2} (%)	S_{S2} (%)
440	91.4	0.414	2.80	88.2	96.5
460	93.0	0.423	2.29	90.3	97.1
480	94.4	0.442	1.88	92.1	97.5
500	97.0	0.438	1.37	95.5	98.1
520	97.7	0.516	1.13	96.1	98.3
540	98.5	0.524	1.00	96.9	98.3
560	99.3	0.740	0.782	97.8	98.4
580	99.4	0.811	0.748	97.8	98.4

Table 7 The effect of the space velocity on the Cat-S (granules) at (H2/CO)=3.0, [(H2+CO)]/SO2]=2.0, and 480 C

S.V. (h^{-1})	C (%)	Y_{H2S} (%)	Y_{cos} (%)	Y_{S2} (%)	S_{S2} (%)
1000	98.6	2.35	0.789	95.5	96.8
1500	97.3	0.791	1.05	95.5	98.1
1800	96.0	0.696	1.52	93.8	97.7
2000	94.4	0.442	1.88	92.1	97.5
2500	90.6	0.619	1.96	88.0	97.2
3000	86.5	0.623	2.26	83.7	96.7

Table 8 The effect of the molar ratio of reactants on the Cat-S (granules) at (H2/CO)=3.0, [(H2+CO)]/SO2]=2.0, S.V.=2,000 h^{-1}, and 480 C

$\frac{CO + H_2}{SO_2}$	C (%)	Y_{H2S} (%)	Y_{cos} (%)	Y_{S2} (%)	S_{S2} (%)
3.0	99.8	35.1	1.59	63.2	63.3
2.5	99.7	21.0	1.64	77.0	77.3
2.2	99.8	6.61	1.72	91.4	91.7
2.0	94.4	0.442	1.88	92.1	97.5
1.8	92.9	0.339	1.64	91.0	97.9
1.6	88.9	0.293	1.66	87.6	97.8
1.4	84.1	0.302	1.63	82.8	97.7

Table 9 The effect of the space velocity on the Cat-S (granules) at (H2/CO)=3.0, [(H2+CO)]/SO2]=2.0, and 520 C

S.V. (h^{-1})	C (%)	Y_{H2S} (%)	Y_{cos} (%)	Y_{S2} (%)	S_{S2} (%)
1000	98.5	0.990	0.467	97.0	98.5
1500	98.2	0.445	0.772	96.9	98.8
1800	98.9	1.05	0.791	97.1	98.1
2000	98.5	0.624	1.00	96.9	98.3
2500	97.3	0.342	1.24	95.7	98.4
3000	94.8	0.337	1.47	93.0	98.1

Table 10 The effect of the temperatures on the Cat-S (granules) at (H2/CO)=3.0, [(H2+CO)/SO2]=2.0, and S.V.=3,158 h^{-1}

t (°C)	C (%)	Y_{H2S} (%)	Y_{cos} (%)	Y_{S2} (%)	S_{S2} (%)
540	95.3	0.479	1.30	93.5	98.1
560	96.1	0.536	1.06	94.5	98.3
580	97.6	0.614	1.00	96.0	98.3
600	98.3	0.979	0.882	96.5	98.1
620	98.4	0.920	0.755	96.8	98.3
640	98.6	0.931	0.621	97.0	98.4
660	98.8	1.36	0.441	97.0	98.2

THE EFFECT OF NONUNIFORM LIQUID DROPLETS CONCENTRATION DISTRIBUTION ON ABSORPTION OF SO2 IN AN ATOMIZING SCRUBBER

M.Taheri, J.Fathikalajahi,and M.R. Talaie

Shiraz University, Shiraz,Iran

Keywords: Drop Distribution, Scrubber, Absorption

ABSTRACT

Many investigators have predicted SO2 absorption in a scrubber based on uniform concentration of liquid droplets concentration. In this study an investigation was carried out to determine the effect of actual liquid droplets concentration on SO2 absorption in an atomizing scrubber. In this model liquid droplets are dispersed in the polluted gas stream from an area or line source depending on the method of liquid injection. Then the overall performance of the scrubber is obtained by solving the diffusion equation both for liquid droplets and gas absorption. The effect of various operating parameters such as liquid to gas ratio and scrubber size were obtained on cleaning performance of the scrubber. The results of mathematical predictions is compared with the data reported in the literature. The results of prediction with this model indicate a significant improvement compare to the prediction based on uniform liquid droplets concentration.

INTRODUCTION

Atomizing scrubbers are frequently used for absorption of SO2 and some other gaseous pollutants. Gage and Rochelle (1992) have studied the use of this device in flue gas desulphurization processes.Also the capital cost and operating cost of a scrubber is given by Baasel (1988). In an atomizing scrubber the performance of gas absorption is a function of several parameters including ,gas velocity, liquid to gas flow rate ratio, geometry, and the method of liquid injection. In designing a venturi scrubber the above parameters must be adjusted so that the liquid droplets are distributed as uniformly as possible. The purpose of this study was to study the effect of various operating parameters on liquid droplets concentration distribution in a scrubber. This in turn will improve the capability of various mathematical models in predicting gas absorption and particulate removal in a wet scrubber.

Several experimental and theoretical investigations for studying droplets concentration distribution in atomizing scrubbers have been reported in the literature. Taheri and Haines carried out an experimental work to study the effect of water injection on droplets distribution and SO2 absorption in an atomizing scrubber. By photographing the throat of scrubber they showed that the water droplets are distributed nonuniformly across the cross section of scrubber. They also showed that the rate of SO2 absorption and particle collection varied depending on method of water injection. Viswanathan et.al (1984) performed experimental work for determining water droplets distribution in the throat of a venturi scrubber. They showed that the droplets concentration distribution in the throat and down stream of point of water injection is a function of liquid to gas ratio. Calvert(1970) developed a mathematical model to predict particulate removal efficiency in a scrubber. He fitted the results of the experimental work by applying a correction factor in his model which included the non-uniformity effect of droplets distribution. Taheri and Shieh (1975) used a plume dispersion equation to predict water droplets concentration in an atomizing scrubber. They have shown that by considering nonuniform distribution of droplets the particulate removal efficiency are in close agreement with experimental data.

MATHEMATICAL MODEL

The detail of the mathematical model developed in this work is

given by Talaei (1993). This model is based on a three dimensional dispersion of droplets and pollutants such as SO2 by convection and eddy diffusion. The gaseous pollutants are absorbed by liquid droplets while they are moving co-currently in the scrubber. The rate of gas absorption in the scrubber is influenced by distribution of droplets population. The steady state equation expressing material balance for droplets is as follows:

$$\frac{\partial(V_{d_x})}{\partial x} = E_d\left(\frac{\partial^2 C_d}{\partial y^2} + \frac{\partial^2 C_d}{\partial z^2}\right) + S \qquad (1)$$

In the above equation the droplets are convected in the x direction, while they are dispersed in y and z direction by eddy diffusion. In addition it is assumed that droplets are generated by a line or area source depending on method of water injection. This area source is located by an empirical correlation for calculating liquid jet penetration length which has been obtained by Viswanathan et.al (1984):

$$\frac{h^*}{d_j} = 0.1145\frac{V_j\rho_j}{V_g\rho_g} \times \left(\frac{P_j}{P_g}\right)^{1/2} \qquad (2)$$

The water droplets velocity V is adjusted to the ambient gas stream velocity according to the following equation:

$$\frac{dV_d}{dX} = \frac{3}{4}\frac{C_{D_\ell}}{D_d}\frac{\rho_g}{\rho_l}\frac{(V_g - V_d)^2}{V_d} \qquad (3)$$

The Transport equation for gaseous pollutant such as SO2 is as follows:

$$\frac{\partial(V_{g_x}C_g)}{\partial x} = E_g\left(\frac{\partial^2 C_g}{\partial y^2} + \frac{\partial^2 C_g}{\partial z^2}\right) - N_A\pi D_d^2 C_d \qquad (4)$$

The eddy diffusivity E depends on the flow situation and is a function of the degree of mixing and turbulence. The gas stream eddy diffusion was obtained by using a Peclet number :

$$\frac{V_g D}{E_g} = N_{Pe} \qquad (5)$$

The value of Pecklet number was found to be 130 for a venturi scrubber. Droplets because of their inertia can not follow the random motion of gas stream. As a result their eddy diffusion is reduced. The effect of droplets inertia on eddy diffusivity was obtained by Talaie (1993):

$$\frac{E_d}{E_g} = \frac{l_d^2}{l_g^2} \qquad (6)$$

NUMERICAL SOLUTION

Equations (1),(2) and (3) are the main equations for the present model.Equation (3) is integrated analytically and the droplets velocity U is computed. With all the other parameters Known , the problem is then reduced to solving C,and C by a numerical technique.

RESULTS

The comparison between the result of simulation and Viswanathan

data for water droplets distribution is given in Figure (1). This Figure indicates a very good agreement between predicted value s and experimental data.
Figure (2) indicates the comparison between Calculated and experimental data performed by The Office of Air Program. These data are reported by Wen and Fan (1975). This figure indicates a very good agreement compare to applying a uniform water droplets concentration. The results indicate that water droplets concentration distribution plays an important role in scrubber performance and must be considered in any realistic model.

SUMMERY AND CONCLUSION

From the results of simulation the following conclusions can be drawn:
The factors which increases the uniformity of droplets distribution also increases removal efficiency.The highest uniformity of droplets distribution is attained in a scrubber for a jet penetration of 20 to 30% of scrubber width. Some of the factors which affects the uniformity of droplets distribution are as follows:
a) Increasing liquid to gas flow ratio, to some limit at constant gas velocity increases uniformity
b) When L/G and Vg are constant,increasing cross sectional area of the scrubber increases uniformity by increasing droplets eddy diffusivity.

ACKNOWLEDGEMENT

This research was supported by Shiraz University Research Council.

NOTATION

C	=	Droplets concentration	No./m^3
C	=	Gas concentration	gmole/m^3
D	=	Throat diameter of scrubber	m
D	=	Drop diameter	m
d	=	Nozzle diameter	m
E	=	Eddy Diffusivity	m^2/s
h	=	Penetration length	m
l	=	Mixing length	m
L/G	=	Liquid to gas flow rate ratio	m^3/1000 m^3
N	=	Overall mass transfer rate of component A	gmole/m^2.s
P	=	Pressure of liquid jet at injection point	(atm)
S	=	Source strength	No./m^2.s
V	=	Velocity	m/s
x	=	Rectangular coordinate in the direction of flow	m
y,z		Rectangular coordinate perpendicular to the direction of flow	m

Subscripts

d	=	Droplets
g	=	Gas
J	=	Jet

References

Baasel,W.D. (1988) Journal of Air Pollution Control Association, Volume 38,327
Calvert,S.(1970) AIChE Journal,16,392
Gage,C.L., and G.T. Rochelle,(1992) Journal of Air and Waste Management Association, Volume 42,926
Taheri,M. and G.F. Haines,(1969) Journal of Air Pollution Control Association,19,427
Taheri,M., and C.M.S. Sheih,(1975),AIChE Journal,21,153

Talaei,M.R.(1993) M.S. Thesis, Chemical Engineering Department, Shiraz University, Shiraz,Iran
Viswanathan,S,A.W.Gnyp, and C.C.St. Pierre.(1984) Ind.Eng.Chem. Fundamental,23,303
Wen, C.Y.,and L.T. Fan, (1975)"Models for flow systems and chemical reactors",Marcel Dekker Inc.New York

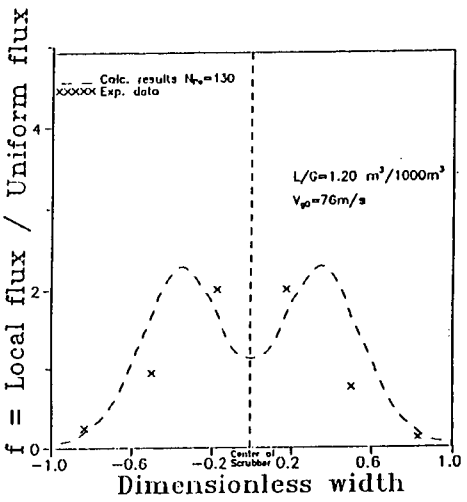

Figure 1 Variation of Normalized Flux With Dimensionless Width

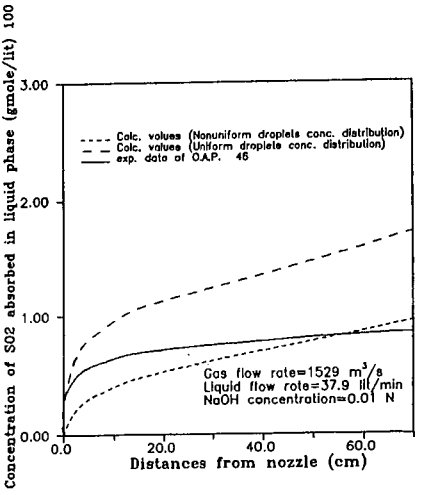

Figure 2. Variation of Liquid Phase Concentration Along the Scrubber for O.A.P. Data

PhOSNOX PROCESS FOR COMBINED REMOVAL OF SULFUR DIOXIDE AND NITROGEN OXIDES FROM FLUE GAS

S.G. Chang and S. M. Wang , Energy and Environment Division, Lawrence Berkeley Laboratory, University of California, CA 94720, U. S. A.

Keywords: nitric oxide, flue gas cleanup, phosphorus

INTRODUCTION

Wet FGD (flue gas desulfurization) systems are the most widely used technology for control of sulfur dioxide emissions from power plants. However, these systems are incapable of removing nitrogen oxides because most of the nitrogen oxides in flue gas is nitric oxide which is barely soluble in aqueous solutions.

This paper addresses a new and cost-effective method for the generation of ozone to allow a wet scrubber system to remove SO_2 and NO_x simultaneously. In addition, a new method to suppress the formation of nitrogen-sulfur compounds in scrubbing liquors is discussed. The major oxidation product of yellow phosphorus is phosphoric acid mists which can be recovered for byproducts credit. The size of mists and the concentration of phosphoric acid in the mists were measured in order to determine an appropriate device for acid collection and concentration. An economic projection of the PhoSNOX process has been performed.

EXPERIMENTAL

The experiments were conducted on a 600 liter/min bench-scale spray tower absorber. A simulated flue gas mixture with about 5% oxygen was prepared by passing liquid nitrogen through a vaporizer column and by mixing the gas with compressed air to obtain the desired oxygen concentration. NO and SO_2 were blended in to give concentration of 60-600 ppm and 1500-2500 ppm, respectively. CO_2 concentration could be adjusted up to approximately 10% of the total gas flow. The gas stream flowed at a rate of 600 liter/min through an electric air heater where it was heated to a temperature of 450 K (350 F). The heated gas then entered a spray tower absorber. The absorber was a 10 cm diameter by 120 cm long glass column installed with spray nozzles (Figure 1). A scrubbing liquor, which was composed of an aqueous mixture of yellow phosphorus was sprayed in the absorber. The liquid flow rate ranged between 1 and 4 gallons/min. A 2-liter Erlenmeyer flask was used as a holding tank for the liquid mixture from the spray column. The liquid mixture was recirculated with a centrifugal pump to the top of the spray column. The pH of the scrubbing liquor was controlled by feeding an aqueous mixture of sodium sulfite or calcium carbonate from a thermostated reservoir (55 C) to the hold tank by a Masterflex pump. The pH range studied was 4.5 to 7.5. The holding tank temperature was controlled at 55 C. A countercurrent flow of flue gas entered at the base of the absorber and passed upward through the falling spray of liquors. The superficial velocity of flue gas in the absorber is about 4 ft/sec. The contact time of flue gas with spraying solution was approximately 2 seconds. The contact time can be varied by changing the flow rate of flue gas; correspondingly, this would vary the L/G ratio, given a constant liquid flow rate. The SO_2 fluorescent analyzer and the NO_x chemiluminescent analyzer have intake connections to the gas stream at various points along the system. The SO_2, NO, and NO_2 concentrations can thus be measured and the effectiveness of the absorber operation can be evaluated.

The major oxidation product of P_4 is phosphoric acid mists which can be recovered as a valuable commercial product. Experiments were performed to determine the size distribution of mists in order to determine an appropriate collector for use in scale-up tests. The size of mists was measured by means of a cascade impactor and a laser optical particle counter. The mists produced from the bench-scale spray tower flowed through thermostated tubings. Then, the mists were sucked into a Mark V Pilat Cascade Impactor, which was installed inside an oven at a controlled temperature. The application of the laser optical particle counter has limitations in that it can not measure particles with size less than 0.5 um, nor can it measure particles with density more than 10^6 particles/ml. Consequently, the dilution of phosphoric acid mists with air is sometimes necessary. A stream of conditioned mists was allowed to pass through a measuring port of an Insitec PCSV-P laser optical particle counter. The size distribution of the mists was determined from the scattering light of a laser beam. In addition, a mist collector using the impactor and capillary action principles was constructed. The phosphoric acid mists were collected. The concentration of phosphoric acid in the mists was determined by an ion chromatography.

RESULTS AND DISCUSSIONS

The removal of NO from flue gas in the PhoSNOX process is based on the P_4-induced oxidation of NO to produce more soluble NO_2. The chemistry involved can be described by the following reactions:

$$P_4 + O_2 \xrightarrow{} P_4O + O \qquad (1)$$

$$P_4O \xrightarrow[n\,O_2]{} P_4O_{10} + m\,O \qquad (2)$$

$$O + O_2 \xrightarrow[M]{} O_3 \qquad (3)$$

$$NO + O_3 \longrightarrow NO_2 + O_2 \quad (4)$$

$$P_4O_{10} + 6\,H_2O \longrightarrow 4\,H_3PO_4 \quad (5)$$

P_4 reacts with O_2 to produce O and O_3 according to reaction (1) thru (3). Subsequently, O and O_3 oxidize NO to NO_2. NO_2 can be removed by scrubbing liquors through direct dissolution (6), by dissolution after forming N_2O_3 with NO (7), or by reaction with SO_3^{2-} or HSO_3^- ion (8).

$$2\,NO_2 + H_2O \longrightarrow NO_2^- + NO_3^- + 2\,H^+ \quad (6)$$

$$NO_2 + NO \quad N_2O_3 \longrightarrow 2\,NO_2^- + 2\,H^+ \quad (7)$$

$$NO_2 + SO_3^{2-}/HSO_3^- \longrightarrow NO_2^- + SO_3^-/HSO_3 \quad (8)$$

The presence of SO_3^{2-}/HSO_3^- at a concentration of greater than 1 mM in scrubbing liquor can cause[2] most of the NO_2 to react via (8) rather than (6). Consequently, most of the dissolved NO_2 is intially converted to HNO_2.

1. Removal Efficiency

The results of typical runs on the removal efficiency of NO are shown in Figure 2. Greater than 95 % NO removal efficiency were achieved at initial NO concentrations ranging from 58 to 610 ppm with an L/G of 16 liter/m^3 and a gas-droplet contact time of about 2 sec. The flue gas was under continuous flow conditions, whereas the P_4 reagent was under batch conditions with a limited amount of P_4 in the circulating liquors. The concentration of P_4 decreased with time, which resulted in the drop of NO removal efficiency. The removal efficiencies of SO_2 were greater than 95 % in these experiments, but were deleted from the figures to avoid confusion.

The NO removal efficiencies as a function of L/G and P_4 concentration in spray liquors are shown in Figure 3. The results were obtained from a set of experiments which were conducted by varying the flow rate of flue gas at a constant flow rate of recycling liquors. As a result, the contact time of the flue gas with the spray varied. The removal efficiency did not reach 90% until an L/G of 10 liter/m^3 with spray liquors of 0.5% P_4 concentration. The increase of P_4 concentration from 0.5% to 0.8% reduced the required L/G from 10 liter/m^3 to 8 liter/m^3 in order to achieve a 90% NO removal efficiency.

Because the diameter of the spray column is 4 inches, the droplets hit the wall a short distance after being sprayed. The liquor then flows down the wall of the column and exhibits poor contact with flue gas. Consequently, the mixing in the bench-scale system is not as effective as that in a commercial scale system at a given L/G. The consideration of the contact time of the droplets with flue gas may be more meaningful. Figure 4 shows a plot of the NO removal efficiencies as a function of contact time. The gas-droplet contact distance was estimated to be 2 ft. The contact time can be varied by changing the flow rate of the flue gas. The NO_x removal reached 90% efficiency with a contact time of 1.4 secs, which is less than that (2-5 secs) in a commercial system. However, it must be realized that the size of the droplets is smaller than those in a commercial system. Consequently, the mass transfer from gas to liquid is more effective in our bench absorber than in a commercial absorber. The utilization efficiency of P_4 can be expressed in terms of P/NO ratio. A P/NO ratio of as low as 0.6 has been achieved.

2. Byproducts Formation

The analysis[3,4] of scrubbing liquors from a bench-scale experiment revealed that less than 10% of the NO removed was converted to NO_3^-. The majority of NO removed was found to be in the form of nitrogen-sulfur compounds, which were produced as a result of the reaction of NO_2^- with HSO_3^-

$$NO_2^- + 2\,HSO_3^- \longrightarrow HON(SO_3)_2^{2-} + OH^- \quad (9)$$

$$HON(SO_3)_2^{2-} + H_2O \longrightarrow HOHNSO_3^- + HSO_4^- \quad (10)$$

$$HON(SO_3)_2^{2-} + HSO_3^- \longrightarrow N(SO_3)_3^{3-} + H_2O \quad (11)$$

$$N(SO_3)_3^{3-} + H_2O \longrightarrow HN(SO_3)_2^{2-} + HSO_4^- \quad (12)$$

$$HN(SO_3)_2^{2-} + H_2O \longrightarrow H_2NSO_3^- + HSO_4^- \quad (13)$$

These nitrogen-sulfur compounds can be converted to ammonium sulfate under extremely acidic conditions

$$H_2NSO_3^- + H^+ + H_2O \longrightarrow NH_4^+ + HSO_4^- \quad (14)$$

Alternative ways to remove the nitrogen-sulfur compounds from scrubbing liquors include the precipitation as potassium salts and the use of an electrodialysis technique. We have recently developed a new approach to suppress the formation of the aforementioned nitrogen-sulfur compounds. This approach involves the use of a sulfamic acid additive which can be produced from the reaction of urea and sulfuric acid. As a result of the addition of sulfamic acid in scrubbing liquors, the absorbed NO is converted to N_2.

$$HNO_2 + H_2NSO_3H \longrightarrow N_2 + HSO_4^- + H_2O + H^+ \qquad (15)$$

The majority of yellow phosphorus was oxidized by oxygen in flue gas to form P_4O_{10}, which subsequently absorbed moisture to form phosphoric acid mists. The analysis of spraying liquors by ion chromatography showed that only about 10% of these mists were absorbed into scrubbing liquors. The remaining 90% of mists stayed with the flue gas, as evidenced by its heavy white appearance. These mists must be removed from flue gas so that a valuable by-product, phosphoric acid, could be recovered and that the flue gas discharged from a stack could comply with opacity regulations.

3. Characterization of Phosphoric Acid Mists

The size distribution of the mists was determined in order to choose an appropriate collection device for the mists. Two different techniques, a cascade impactor and a laser optical particle counter, were employed to measure the size of mists for comparison. The results obtained from these two techniques are in good agreement. Table 1 shows that the geometric mean diameter of mists increases from 0.65 um to 1.1 um as the residence time extends from 0.7 sec to 11 sec. The size of the mists increases along with the residence time of the mists, which was attributed to the coagulation. However, a small decrease of temperature during the transit of the mists may result in the grow of the size from the condensation of moisture in spite of the temperature control along the pathway of the mists. The size distribution of the mists, in terms of mass frequency vs size, was measured by the optical particle counter. The size distribution of the mists peaked at 0.5 um, 0.9 um, and 1.2 um with a residence time of 0.7, 5.6, and 11.2 sec, respectively.

The concentration of phosphoric acid in the mists was about 10% by weight. This was determined by the collection of the mists with a sinter glass impactor. The solutions soaked in the sinter glass was sucked into a container through a capillary tube. The solutions collected was analyzed by an ion chromatography.

From the results of size and concentration measurements, the use of a submicron mist collector such as an Aerosep multi stage aerosol separation system may be necessary to recover the phosphoric acid mists. The residence time of phosphoric acid mists in a prescrubber or a scrubber is expected to be less than 5 sec. As a result, a substantial fraction of the mists is less than 1 um. In addition, the acid recovered has to be concentrated to about 75 wt % in order to produce a marketable byproducts.

4. Process Configuration

A conceptual process configuration of a wet PhoSNOX system with throw-away wastes may be derived as shown in Figure 5. An aqueous mixture of P_4 and an alkaline reagent such as limestone or soda ash may be sprayed in a scrubber. A mist collector is required to recover the phosphoric acid mists to comply with the opacity regulation and for by-product credit. An air-purged oxidation tank is installed to ensure the complete conversion of residual P_4 to phosphate ions before discharge. Besides the addition of a mist collector and an air-purged oxidation tank, this is a typical process configuration of a throw-away wet flue gas desulfurization system.

An alternative process configuration (Figure 6) may be derived where an aqueous mixture of P_4 and sulfamic acid is injected into a prescrubber or a section of the duct upstream from the scrubber where an alkaline solution/slurry is used to absorb acid gases. An Aerosep mist collector is installed between the prescrubber and the scrubber. A slip stream of liquor from a scrubber loop was fed into a prescrubber loop to ensure the conversion of absorbed NO_x to N_2.

5. Process Economic Projection

Pre-pilot plant economic projections for the PhoSNOX process have been made based on a preliminary conceptual process configuration with the following features:

- Injecting a phosphorus emulsion into an existing wet limestone scrubber, or injecting an aqueous mixture of yellow phosphorus and sulfamic acid into a new prescrubber
- Adding an "Aerosep" system downstream of the scrubber (or prescrubber) to capture and convert the P_2O_5 to phosphoric acid byproduct
- Installing necessary equipment to recover other phosphate byproducts
- Adding new fan capacity to compensate for the additional pressure drop
- Adding new equipment for phosphorus and byproducts storage
- Installing fire & safety protection equipment on phosphorus unloading, storage, and handling system.

The PhoSNOX process economics are compared with those reported in the literature for the Selective Catalytic Reduction (SCR) process, as shown in Table 2.

CONCLUSION

The PhoSNOX process is based on the addition of yellow phosphorus in wet flue gas desulfurization systems to allow simultaneous removal of SO_2 and NO_x from flue gas. The NO_x removal efficiency of PhoSNOX at 90+% could potentially be achieved at the actual conditions employed in wet FGD systems. Pre-pilot plant economic projections for the PhoSNOX process indicates that the capital installation costs for PhoSNOX are lower and operating costs are comparable when the process is compared with SCR.

REFERENCES

1. S.G. Chang, and D. K. Liu, "Removal of Nitrogen and Sulphur Oxides from Waste Gas Using a Phosphorus/Alkali Emulsion," Nature, 343, 151(1990).
2. D. Littlejohn, and S. G. Chang,"Modeling of the Chemistry of Wet Limestone Flue Gas Desulfurization Systems," Energy & Fuels, 5, 249 (1991).
3. D. Littlejohn, and S.G. Chang,"Determination of Nitrogen-Sulfur Compounds by Ion Chromatography," Anal. Chem.,58,158 (1986).
4. D. Littlejohn, and S.G. Chang,"Identification of Species in a Wet Flue Gas Desulfurization and Denitrification system by laser Raman Spectroscopy,"Environ. Sci. & Technol.,18, 305 (1984).

Table 1 Comparison of the Mean Diameters of Mists from Laser Scattering and Cascade Impactor Measurements

	Residence Time(sec)			
Methods	0.7	2.8	6.5	11.2
Laser	0.66 um	0.72 um	0.97 um	1.10 um
Impactor	0.67 um	0.67 um	0.83 um	

Table 2. Economics Comparisons: NO_x Removal Processes (500 MW, 300 ppm NO_x)

	Capital, $/kW	Levelized, mills/kWh
PhoSNOX (90% NO_x Removal; P/NO_x=0.5)		
W/O prescrubber	28	4.2
With prescrubber	43	4.7
SCR (80% NO_x Removal)		
EPRI (1991 NO_x Symposium Summary)	100	5 - 7
EPRI (1989 NO_x Symposium Summary)	78 - 101	4 - 9

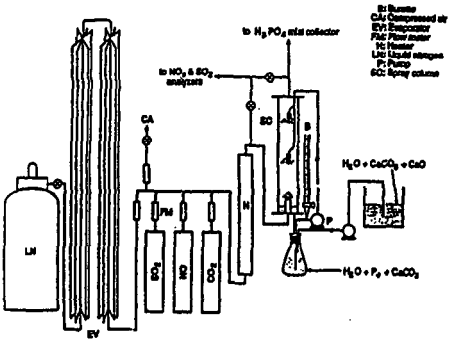

FIGURE 1. A schematic diagram of a 20 cfm [9.44 x 10^{-3} m^3/sec] bench-scale wet scrubber using yellow phosphorus and an alkaline for combined removal of SO_2 and NO, from a simulated flue gas.

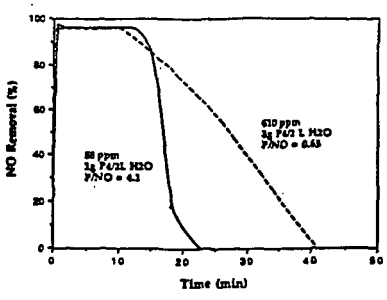

FIGURE 2. The removal efficiency of NO for NO concentrations of 58 and 610 ppm in a simulated flue gas.

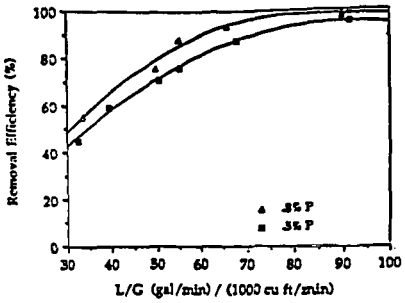

FIGURE 3. The removal efficiency of NO as a function of L/G [1 liter/m³ = 7.48 gal/1000 cu ft] with initial yellow phosphorus concentration of 0.5% and 0.8%.

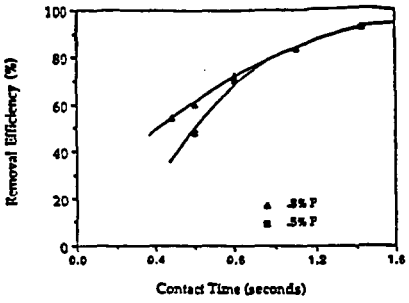

FIGURE 4. The removal efficiency of NO as a function of the contact time of spray droplets with a simulated flue gas.

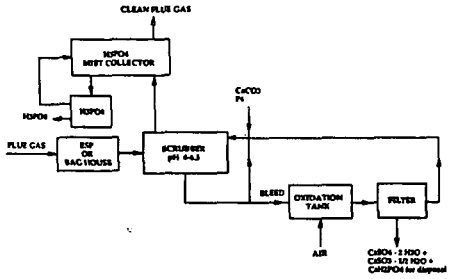

Figure 5 A conceptual process configuration of a wet PhoSNOX system with throw-away wastes

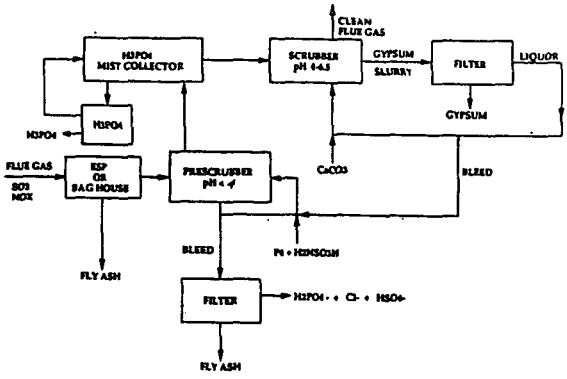

Figure 6 A conceptual process configuration of a wet PhoSNOX system with salable byproducts

ADVANCED IN-DUCT SORBENT INJECTION PROCESS FOR SO_2 CONTROL

J. A. Withum, W. A. Rosenhoover, M. R. Stouffer,
N. J. Delullis, D. C. McCoy
CONSOL Inc.
Research & Development
4000 Brownsville Road
Library, PA 15129

KEYWORDS: SO_2 Control; Hydrated Lime; Flue Gas Desulfurization; Sorbent Injection; Flue Gas Humidification

SUMMARY

This paper describes the status of development of an advanced duct-sorbent-injection process for the control of SO_2 emissions from coal-fired power plants. The technical objective of the project is to develop a low-capital-cost process capable of over 90% SO_2 removal as a retrofit option for compliance with the 1990 Clean Air Act Amendments. A complementary objective is to achieve sufficiently high sorbent utilization (60% with hydrated lime) so that levelized costs are lower than wet limestone scrubbing costs over a wide range of coal types and plant sizes.

The SO_2 removal and sorbent utilization objectives were achieved. The original performance targets of 90% SO_2 removal and 60% sorbent utilization were exceeded in 0.3 MWe pilot plant operations through a combination of equipment design improvements and sorbent recycle optimization. The 90% SO_2 removal target was achieved at sorbent utilizations of 70-75%. Up to 99% SO_2 removal was attained at 60% sorbent utilization. A simplified equipment design was tested and its operability was confirmed in pilot plant operation.

An interim economic evaluation was completed based on these results. Projected capital costs are approximately 40% lower than wet limestone scrubbing costs over the range of coal sulfur contents (1.5-3.5%) and plant sizes (160-500 MWe) evaluated. Levelized SO_2 control costs are competitive with wet limestone scrubbing over the range of cases studied. Potential design and operating improvements were identified which can reduce capital and levelized costs. These improvements will be evaluated in ongoing pilot plant development work. Current work also includes the development and testing of improved sorbents.

The advanced duct-sorbent-injection process (Advanced Coolside) involves flue gas humidification to the adiabatic saturation point using a contacting device which simultaneously removes fly ash from the flue gas. A sorbent (hydrated lime), injected into the highly humid flue gas downstream of the contactor, captures SO_2 before being removed in the existing particulate collector. The high humidity allows high SO_2 removal. High sorbent utilization is achieved by sorbent recycle. Greater recycle is possible than for previous duct-sorbent-injection processes because the fly ash is removed by the contactor prior to sorbent injection.

BACKGROUND

In-duct dry sorbent injection technology has been actively developed in the U.S. since the early 1980s. The performance of these processes has been well-established through the development of the Coolside process (CONSOL)[1-3] and the HALT process (Dravo)[4] and through the DOE duct injection technology development program.[5] These development efforts have included pilot-scale tests, proof-of-concept tests, and a full-scale utility demonstration. Established performance is in the range of 40-50% SO_2 removal at 2/1 Ca/S molar ratio and 20-25°F approach to adiabatic saturation temperature using hydrated lime as the sorbent. Additionally, the 105 MWe demonstration of the Coolside process at the Ohio Edison Edgewater Station[3] showed that an SO_2 removal of 70% can be attained by improving calcium hydroxide sorbent activity with sodium-based additive injection at a 0.2 Na/Ca molar ratio (~32% sorbent utilization).

Process performance data and economic analyses support the attractiveness of duct sorbent injection for site-specific applications.[6] However, the applicability as a compliance option for the Clean Air Act or other regulations can be expanded by improving SO_2 removals and sorbent utilizations. The performance targets for developing an advanced process (90% SO_2 removal and 60% sorbent utilization) represent a substantial improvement over previous technology.

The Advanced Coolside process is being developed using a 1000 acfm pilot plant.[7] The pilot plant was used in previous development of the Coolside process;[1,2] it was modified to include all elements of the Advanced Coolside process. Process development has focused on improving the design of the contactor and on improving sorbent utilization by optimizing sorbent recycle. A test program to investigate sorbent improvement was recently initiated. This report will discuss progress in these areas, results of the interim economic study and approaches for future process improvement.

DESCRIPTION OF ADVANCED COOLSIDE PROCESS

Figure 1 shows a schematic of the Advanced Coolside process. The process achieves higher SO_2 removal and sorbent utilization than previous duct sorbent injection processes by operating at a higher flue gas humidity and by more fully exploiting the potential of sorbent recycle. The key to the process is a gas/liquid contacting device downstream of the air preheater. The contactor serves two purposes: to nearly saturate the flue gas with water, and to remove most of the coal fly ash from the flue gas. The sorbent is injected downstream of the contactor into the highly humid flue gas. Hydrated lime is very

active for SO_2 capture near the saturation point. Because the flue gas is already humidified prior to sorbent injection, there is no strict residence time requirement for droplet evaporation. SO_2 is removed in the duct and by the sorbent collected in the existing ESP or baghouse. The heat of reaction between SO_2 and hydrated lime raises the temperature of the flue gas by roughly 9°F for each 1000 ppm of SO_2 removed. Therefore, it is possible to operate the particulate collector at a practical approach to saturation without flue gas reheat. However, because hydrated lime activity is highly sensitive to the approach to saturation, this reaction heat effect can also act as a limiting mechanism for SO_2 capture.

The spent sorbent is captured by the existing particulate collector as a dry powder. It can be disposed of with the fly ash or separately. Sorbent recycle is an integral component of the Advanced Coolside process. Recycle sorbent is quite active for SO_2 capture at high humidity. The potential for recycle is increased because fly ash is removed separately before sorbent injection. Furthermore, recycle sorbent performance can be improved by a simple physical pre-treatment step prior to re-injection; the nature of this pre-treatment step is currently a proprietary feature of the process.

Design optimization has focused on the flue gas/water contactor. For the initial pilot plant testing the contacting device was a Waterloo scrubber.[8] This is a commercially available device, marketed by Turbotak, Inc., and used primarily for removal of submicron particles. The Waterloo scrubber consists of a conditioning zone, a centrifugal fan and a mist eliminator, and uses two-fluid nozzles to finely atomize water sprays at a liquid/gas ratio of about 1 gal/1000 acf.

DISCUSSION

Recycle Optimization. The improvement in desulfurization performance which allowed project performance targets to be exceeded resulted primarily from recycle optimization. By more fully exploiting recycle, sorbent utilization efficiencies of 70-75% were attained, while maintaining SO_2 removal around 90%. Also, high SO_2 removals ranging from 90% to over 99% were attained, while maintaining sorbent utilization of 60%.

Recycle optimization tests were conducted in the 1000 acfm pilot plant in a semi-continuous manner. Spent sorbent was removed frequently from the pilot baghouse. A portion of the material was discarded and the remainder, after pretreatment, was returned in a batch to the recycle feeder. Test duration was sufficiently long to assure that steady-state continuous recycle was simulated closely (typically 20-70 hr).

Tables 1 and 2 list process conditions and results for pilot recycle optimization tests. Tests 1 through 4 (Table 1) were conducted with reheat before the baghouse (to a 25°F approach) to minimize baghouse SO_2 removal. The purpose was to simulate conditions in a retrofit application with an existing ESP. In this case, SO_2 removal in the ESP would be limited by gas phase mass transfer. Based on literature information and on theoretical calculations, an ESP removal of 30% of the SO_2 remaining in the ESP inlet gas is a reasonable assumption. As shown in Table 1, SO_2 removal in the baghouse with reheat averaged 5% (absolute). Tests 5-9 (Table 2) were conducted with no baghouse reheat. The 9 to 12°F baghouse approach temperature was a result of the flue gas temperature rise from the heat of reaction. In these tests SO_2 removal in the baghouse was greater than with reheat, although the large majority of SO_2 was still removed in the duct.

The recycle test results indicate that for systems with an existing ESP, 90% SO_2 removal can be achieved at sorbent utilizations of 70-75%, substantially higher than the original target of 60% utilization. For example, with a fresh Ca/S mol ratio of 1.2, duct and system SO_2 removals were 87% and 90%, respectively (Test 2, Table 1).

The results also indicate that high efficiency SO_2 removal can be attained in systems with a baghouse operated at close approach. For example, 99% SO_2 removal was attained at 61% sorbent utilization (Test 9, Table 2). In this test most of the SO_2 removal (88%) occurred in the duct. The capability to achieve very high SO_2 removal may be attractive to new units using a baghouse for fly ash collection.

In the recycle tests in Tables 1 and 2, recycle ratios ranged from 3.3 to 6.9 lb/lb fresh lime. Relatively high recycle ratios are possible because fly ash is removed upstream of sorbent injection. Total dust loading ranged from 9.5 to 14.5 gr/scf. Pilot testing indicated that recycle sorbent particles tended to agglomerate during handling, pretreatment and reaction; this could improve the ability of an existing ESP to handle higher dust loadings.

As shown in Tables 1 and 2, the recycle tests were relatively long-term. With one exception, operating durations ranged from 21 to 115 hr. This allowed process operability to be evaluated. It also provides added confidence in data reliability.

Data reliability also was confirmed by comparing utilizations based on gas analysis with those based on solids analysis. As shown in Tables 1 and 2, utilizations by the two independent methods agreed very well. This confirms the accuracy of process performance data; it also confirms that steady-state continuous recycle conditions were established. In addition, in-duct SO_2 removal data for selected run periods were confirmed by manual flue gas sampling using EPA Method 6.

Design Optimization. A major portion of the process development is devoted to contactor simplification. The contactor is a key capital cost component, and the contacting device initially tested was designed for more stringent applications (i.e., submicron particulate control) than required for Advanced Coolside. Because the process is applied upstream of an existing particulate collector, some fly ash slippage through the contactor is acceptable. It is only necessary to remove a large portion of the particulate mass (ca. 90%) to avoid recycling much of the inert fly ash. Approaches to reduce the capital and operating

cost of the contactor included eliminating the fan, an integral component of the original Waterloo scrubber system, and redesigning the contactor to reduce water and atomization air requirements.

Preliminary pilot plant studies indicated that these approaches are feasible. Tests were conducted using the original Waterloo scrubber system with and without its centrifugal fan under a wide range of atomizing air pressures and water flow rates. The test results (Figure 2) indicated that high flue gas relative humidities can be achieved with or without the fan, as long as sufficient water droplet surface area is generated in the contactor. The test results also showed that the atomization energy can be reduced to below typical operating conditions (40-45 psig) with a relatively minor effect on flue gas humidity. Particulate removal tests indicated that removal efficiency was not sensitive to the nozzle operating conditions over the ranges tested and that the scrubber fan was not needed to achieve fly ash removal greater than 90 wt %. These results indicate that there was flexibility for design and operating modifications.

Based on the tests using the original contactor, a mechanically simpler contactor was designed by Turbotak Inc. (Figure 3). The new contactor consists of a spray chamber and a downstream mist eliminator. Most of the particles and water droplets are removed in the spray chamber. The mist eliminator removes remaining droplets from the flue gas. The Waterloo scrubber fan was eliminated, significantly reducing the cost of the contactor.

Tests were performed which verified the humidification performance, particulate collection efficiency, and operability of the simplified contactor. Optimization tests were conducted to reduce atomization air pressure and flow and water flow relative to the design conditions of Turbotak. Table 3 shows the result of using the alternative operating conditions identified in these tests. Water and air flow requirements were reduced by about half. The air pressure requirement was reduced from 45-50 to ~30 psig, while maintaining humidification (>95% relative humidity) and fly ash removal efficiency (> ca. 90%). These alternative operating conditions will result in lower operating and capital costs.

Operability Observations. Pilot plant operating experience in tests up to 115 hr in duration is a positive indication of the operability and retrofit potential of the Advanced Coolside process. Although the pilot plant is not of sufficient scale to make a complete assessment of process operability, observations of pilot plant operation provide initial information on key operability issues.

The contactor operability was simplified by the elimination of the fan. The mist eliminator was washed periodically to maintain contactor pressure drop at about 1.5 inches of H_2O.

Accumulation of solids on the duct walls was not an operating problem, even at very close approach to saturation and with different duct configurations having short straight-run residence times (<0.5 sec) and numerous changes in flow direction. There was generally a light surface coating of dry solids. At bends, there was somewhat more accumulation. The amount of solids on the duct surface tended to reach a steady value after 10 to 30 hr of operation, after which the rate of accumulation approached zero. The solids were loose and easily removed.

No major problems were encountered in preparing, handling and feeding the recycle sorbent. Operability of the pneumatic transport system was similar to that with hydrated lime. Operability of the recycle handling system was observed to deteriorate at very high sorbent utilization (>70%). This was alleviated by adding the fresh lime to the recycle material during pre-treatment and co-injecting the sorbents.

Baghouse operability was good at the close approaches to adiabatic saturation (down to 10°F) investigated in this program. The material did have a tendency to compact under compression at the lowest baghouse approach temperature, an important consideration for a larger scale design.

Sorbent Optimization. Sorbent improvement can increase the attractiveness of the Advanced Coolside process in several ways. Increasing sorbent utilization reduces sorbent usage and waste disposal requirements. Increasing sorbent activity can reduce the required level of sorbent recycle and could increase the applicability of the process for high SO_2 removal levels. Finally, the results of sorbent studies could allow use of lower cost sorbents by reducing process sensitivity to sorbent source.

Pilot plant tests reported previously in this paper were all conducted with a single commercial hydrated lime. A sorbent optimization test program was recently begun. The program includes work in three areas: a lime hydration study, evaluation of alternate sorbents, and evaluation of additive enhancement.

The objectives of the lime hydration study are to determine the effect of hydration variables on the properties of hydrated lime and to determine the effect of lime properties on desulfurization performance. The hydration study is being conducted in cooperation with Dravo Lime Co. using their continuous pilot hydrator. Hydration variables being investigated in a statistical experimental design include the following: quicklime source, quicklime grind size, hydration water temperature, residual H_2O in the product, and hydrator residence time. Hydrated limes will be characterized for chemical composition and physical properties such as particle size, surface area, and pore size. Desulfurization performance will be measured in laboratory reactors and in the pilot plant.

Evaluation of alternate sorbents will include testing of different commercial hydrated limes and testing of other sorbents, for example, specially prepared high surface area hydrated limes. Recycle tests were conducted for two commercial hydrated limes. In these tests at 1.2 Ca/S mol ratio, system SO_2 removals (with baghouse reheat to simulate ESP removal) were 90% and 86% for the hydrated limes with surface areas of 22 and 14 m^2/g, respectively. Also, once-through screening tests of different commercial hydrated limes from different geographic regions and with varying surface areas showed only small differences in SO_2 removals. These results suggest that process performance is relatively insensitive to

surface area and to commercial lime source. This may be an economic advantage, allowing use of the lowest cost sorbent available.

Previous laboratory studies[7] simulating Advanced Coolside process conditions indicated that sodium-based additives can substantially increase the utilization of hydrated lime (by over 20% absolute). In the current test program, different approaches for additive promotion will be investigated, including addition to lime during hydration. Based on previous lab studies and literature information, additives to be evaluated include Na_2CO_3, NaCl, and $CaCl_2$. Chloride additives are of interest because they could be generated by neutralization of contactor recycle water. One pilot plant test was conducted with NaCl promotion. Results are encouraging, indicating that sorbent utilization can be increased to 80-85% using very small amounts of additive — 0.025 Na/S mol/mol, about 1/15 of that employed in the conventional Coolside process.[1-3] Further testing is under way using different additives and additive dosages, and varying process conditions.

Process Economics. An interim process economic study was completed based on current process performance data with a commercial hydrated lime and a conceptual process design. The objectives for this study were to confirm the potential economic advantages of the Advanced Coolside process and to identify priorities for further process development. A final economic study will be conducted at the conclusion of the pilot-scale development program.

The economic study compared costs of Advanced Coolside with limestone wet scrubbing. Economic assumptions (Table 4) were selected to assure comparison on an equivalent basis. The limestone wet FGD costs are based on a design which includes forced oxidation and a single absorber module. Both processes were evaluated for 90% SO_2 removal efficiency, an assumed capital life of 30 years and using the same retrofit factors. The analysis was based on an "nth" plant design philosophy, using an 18% contingency for each process.

The economic study confirmed a substantial capital cost advantage for the Advanced Coolside process. Figure 4 shows that for a 2.5% sulfur coal the capital cost was about 40% less than forced oxidation limestone scrubbing, over the 150-500 MWe range of plant sizes studied. The relative difference in capital cost was about the same for 1.5 and 3.5% sulfur coals. The lower capital cost can be important to utilities in making compliance decisions because it reduces financial and regulatory risk.

The economic study quantified the potential SO_2 control cost advantages of the Advanced Coolside process. Figure 5 shows that the process has a lower levelized cost ($/ton SO_2 removed) than limestone wet FGD over a wide range of coal sulfur contents and plant sizes. The cost differential ranged from 21% for 1.5% sulfur coal and a 150 MWe plant, to 11% for 2.5% sulfur and 250 MWe, to breakeven for 3.5% sulfur and 500 MWe.

The interim study also indicated that there is potential for further improvement of the Advanced Coolside process and identified areas for improvement with the greatest potential impact on economics, including reduction in sorbent cost and reduction in equipment capital cost for certain process systems. Areas for equipment cost reduction include further contactor optimization and improvement in other systems on which optimization studies have not yet focused (e.g., recycle handling, waste handling, and flue gas handling). The goal of further development is to establish at least a 20% levelized cost advantage over wet FGD over a wide range of compliance situations. This would make it more attractive for utilities to employ a newer, less established technology.

FUTURE WORK

Based on the process economic study, the focus of future process development will be to increase the cost advantage of Advanced Coolside over commercial technology through equipment design optimization and sorbent improvement. For the economic study, Turbotak, Inc. developed preliminary full-scale designs for the simplified contactor based on the test results with the original contactor. The results of pilot tests using the new contactor will be used by Turbotak to develop a commercial design to further reduce costs. Equipment design optimization efforts will be expanded to look at other systems with potential impact on process capital cost, as identified in the economic study. The sorbent improvement work under way will continue as described above. The goals are to reduce sorbent usage and to allow use of lower cost sorbent sources. Another area for future investigation is air toxics control, particularly that of mercury. A literature analysis under way suggests that the Advanced Coolside process has potential for Hg reduction. The capability for air toxics control would provide an additional incentive to use this technology for SO_2 compliance.

ACKNOWLEDGMENT

This work was conducted under partial sponsorship of the U.S. Department of Energy Contract DE-AC22-91PC90360. The authors are grateful to C. J. Drummond, T. D. Brown and others at DOE/PETC for their support and encouragement of this project.

REFERENCES

1. Yoon, H.; Stouffer, M. R.; Rosenhoover, W. A.; Withum, J. A.; Burke, F. P. "Pilot Process Variable Study of Coolside Desulfurization", *Environ. Progress* **1988**, 7(2), 104-11.
2. Stouffer, M. R.; Yoon, H.; Burke, F. P. "An Investigation of the Mechanisms of Flue Gas Desulfurization by In-Duct Dry Sorbent Injection", *I&EC Research* **1989**, 28(1), 20.
3. Withum, J. A.; Yoon, H.; Burke, F. P.; Statnick, R. M. "Coolside Desulfurization Demonstration at Ohio Edison Edgewater Power Station", *ACS Div. Fuel Chem. Preprints* **1990**, 35(4), 1463-72.

4. Babu, M.; College, J.; Forsythe, R. C,; Herbert, R.; Kanary, D. A.; Kerivan, D.; Lee, K. "5 MW Toronto HALT Pilot Plant", Proceedings, 4th DOE-PETC Contractors' Meeting, Pittsburgh, PA, August 1988.
5. Felix, L. G.; Gooch, J. P.; Merritt, R. L.; Klett, M. G.; Hunt, J. E.; Demian, A. G. "Scale-Up Tests and Supporting Research for the Development of Duct Injection Technology", Presented at the 1991 SO_2 Control Symposium, Washington, DC, December 1991.
6. Nolan, P. S.; McCoy, D. C.; Statnick, R. M.; Stouffer, M. R.; Yoon, H. "Economic Comparison of Coolside Sorbent Injection and Wet Limestone FGD Processes", Presented at the 1991 SO_2 Control Symposium, Washington, DC, December 1991.
7. Stouffer, M. R.; Rosenhoover, W. A.; Withum, J. A. "Advanced Coolside Desulfurization Process", Presented at the 1992 Summer National Meeting of the American Institute of Chemical Engineers, Minneapolis, MN, August 9-12, 1992.
8. Spink, D. R. "Handling Mists and Dusts", *CHEMTECH* 1988, 364-8.

TABLE 1. Advanced Coolside Pilot Plant Recycle Tests with Flue Gas Reheat Prior to the Baghouse.

Test	1	2	3	4
Test Duration, hr	36	115	13	73
Process Conditions				
Fresh Ca/S, mol	1.4	1.2	1.5	1.2
Recycle Ratio, lb/lb fresh lime	4.5	6.9	4.4	6.7
Recycle Pretreatment	Yes	Yes	Yes	Yes
Baghouse Approach Temp., °F	23	23	24	22
Hydrated Lime	A	A	A	B
Process Performance				
SO_2 Removal, %, In-Duct	83	67	84	80
System	90	90	90	86
Baghouse	7	3	6	6
Sorbent Utilization, %, By Gas Analysis	63	75	60	70
By Solid Analysis	63	70	59	71

Common Condition: SO_2 Content: 1500 ppm

TABLE 2. Advanced Coolside Pilot Plant Recycle Tests with No Flue Gas Reheat Prior to the Baghouse.

Test	5	6	7	8	9
Test Duration, hr	40	28	21	25	23
Process Conditions					
Fresh Ca/S, mol	1.2	1.5	1.2	1.6	1.6
Recycle Ratio, lb/lb fresh lime	3.3	3.5	4.9	3.9	3.6
Recycle Pretreatment	Yes	Yee	Yes	Yee	Yes
Baghouse Approach Temp., °F	9	12	9	11	12
Hydrated Lime	A	A	A	A	A
Process Performance					
SO_2 Removal, %, In-Duct	60	70	61	91	88
System	84	90	88	97	99
Baghouse	24	20	7	6	11
Sorbent Utilization, %, By Gas Analysis	67	61	71	80	61
By Solid Analysis	68	63	68	56	61

Common Condition: SO_2 Content: 1500 ppm

TABLE 3. Optimization of Contactor Operating Conditions.

	Base Design	Alternative
Conditions		
Nozzle Water Flow	1.13 gpm/1000 acfm	0.6 gpm/1000 acfm
Nozzle Air Pressure	45-50 psig	30 psig
Nozzle Air Flow	17 scfm/1000 acfm	9 scfm/1000 acfm
Performance		
Exit Humidity	>98%	>98%
Fly Ash Collection	>95%	~95%

TABLE 4. Key Assumptions of Interim Process Economic Study.

	Advanced Coolside	Forced Oxidation Wet FGD
Delivered Sorbent Cost	$60/ton, 7% inerts (hydrated lime)	$15/ton (limestone)
Waste Disposal Cost	$6.50/ton	$6.50/ton
SO_2 Removal	90%	90%
Capacity Factor	65%	65%
Capital Life	30 years	30 years
Retrofit Factor	Medium (1.22-1.34)	Medium
Location Factor	1.06	1.06
Design Philosophy	"nth" plant, 18% capital contingency	"nth" plant, 18% capital contingency
Sparing	Auxillary equip. only, no major equip.	Auxillary equip. only, no major equip.
Indirect Costs	37.2% of direct	37.2% of direct

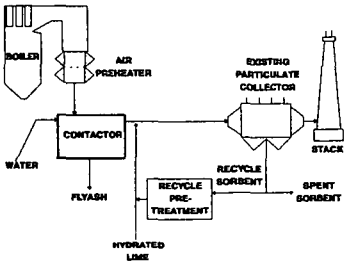

Figure 1. Advanced Coolside Process Schematic.

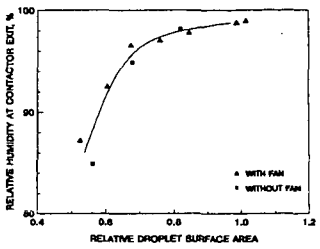

Figure 2. Initial Pilot Test Data for Contactor Simplification.

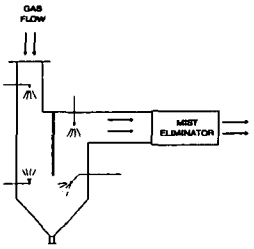

Figure 3. Simplified Contactor Design.

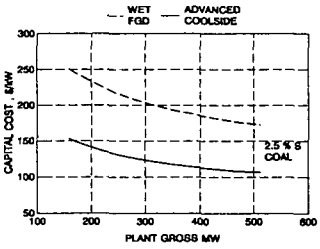

Figure 4. Comparison of Capital Costs for Advanced Coolside and Wet Limestone Forced Oxidation FGD at 2.5% Coal Sulfur Content and Varying Plant Sizes.

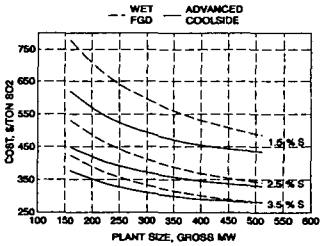

Figure 5. Comparison of Levelized SO_2 Control Costs for Advanced Coolside and Wet Limestone Forced Oxidation FGD as a Function of Coal Sulfur Content and Plant Size.